Capacitive reverse electrodialysis cells for osmotic energy harvesting : Toward real brines and power enhancement

Nan Wu

To cite this version:

Nan Wu. Capacitive reverse electrodialysis cells for osmotic energy harvesting : Toward real brines and power enhancement. Inorganic chemistry. Université Paris sciences et lettres, 2024. English. NNT : 2024UPSLS019 . tel-04809571

HAL Id: tel-04809571
https://pastel.hal.science/tel-04809571v1

Submitted on 28 Nov 2024

THÈSE DE DOCTORAT
DE L'UNIVERSITÉ PSL

Préparée à l'ESPCI Paris PSL, Laboratoire CBI-MIE UMR 8231

Capacitive reverse electrodialysis cells for osmotic energy harvesting: Toward real brines and power enhancement

Cellule capacitive d'électrodialyse inverse pour la récupération d'énergie osmotique : Vers des saumures réelles et augmentation de puissance

Soutenue par
Nan Wu
Le 18 septembre 2024

École doctorale n°397
Physique et Chimie des matériaux

Spécialité
Physico-chimie, Electrochimie

Composition du jury :

Véronique BALLAND Professeur, Université Paris Cité	*Présidente*
Marie-Caroline JULLIEN Directrice de recherche, Institut de Physique de Rennes	*Rapporteuse*
Cyril PICARD Maître de conférence, Université Grenoble Alpes	*Rapporteur*
Virginie LAIR Professeur, Chimie ParisTech - PSL	*Examinatrice*
Mikhael BECHELANY Directeur de recherche, Institut Européen des Membranes	*Examinateur*
Annie COLIN Professeur, ESPCI Paris - PSL	*Directrice de thèse*

ESPCI PARIS | PSL

To my parents.

Acknowledgements

J'aimerais remercier tout d'abord ma directrice de thèse, Annie Colin, qui m'a accueilli chaleureusement à Paris et m'a donné l'opportunité de faire ce travail de thèse. Je suis toujours impressionnée par sa passion vers la science et son efficacité de travail. Elle reste toujours disponible pour une discussion scientifique ou sociale. Elle m'a encouragé à explorer de nombreux projets intéressants et m'a laissé également beaucoup d'autonomie pour réaliser ces travaux. Elle m'a permis de présenter mon travail à de nombreuses conférences internationales. Elle est non seulement ma directrice de thèse mais aussi ma directrice de la vie. J'aimerai également remercier Youcef Brahmi pour sa guidance et son soutien inconditionnel au début de ma thèse. Il m'a transféré beaucoup de conseils précieux pour continuer le projet scientifique.

Je remercie Véronique Balland pour avoir accepté d'être la présidente de mon jury de thèse. Je remercie également Marie-Caroline Jullien et Cyril Picard pour avoir accepté d'être les rapporteurs de ma thèse, ainsi que Virginie Lair et Mikhael Bechelany pour avoir accepté d'être membres de mon jury de thèse. Je vous remercie pour les échanges et les discussion scientifiques ainsi que pour votre retour bienveillant sur l'ensemble de mon travail.

Je remercie également les ingénieurs de l'IPGG et la plateforme technologique, Bertrand Cinquin et Audric Jan qui m'ont aidé à réaliser mes montages expérimentaux, ainsi que Bruno Bresson pour son soutien au MEB.. Merci également à Hélène Dodier et Isabelle Borsenberger pour les commandes et l'aide administrative.

Je tiens à remercier tous mes collègues du MIE et en particulier Marion, Soufiane, Youcef, Edwige, Adrien, Corentin, Mathieu, Timothée, Zhiyi, Houyeme, Aderito, Milad que j'ai eu la chance de rencontrer et avec qui j'ai partagé des moments magnifiques. Je remercie également les doctorants du LCMD pour les discussions et les moments sympathiques.

Merci à tous mes amis et en particulier, Ruiwen, Zhuang, Sizhuo, Donghao, Peixin, Zhibo, Zeyuan, Chaohe, Dongjiu, Burebi, Menghua, pour avoir m'accompagné pendant 3 ans de thèse. Je remercie également tous mes amis en Chine, qui ont gardé le contact et m'ont accueilli chaleureusement en Chine.

Je tiens à remercier le financement CSC (China Scholarship Council).

Pour finir, je remercie mes parents, et mon compagnon qui me soutiennent inconditionnellement en Chine.

Résumé en français

Cette thèse est l'aboutissement des recherches que j'ai effectuées au laboratoire Chimie Biologie Innovation dans le groupe Matériaux Innovants pour l'Énergie sous la direction d'Annie Colin. Ils ont mené à la publication de quatre articles[1–4] et un brevet.

Contexte général

L'énergie a été un facteur essentiel pour les êtres humains tout au long de leur existence sur Terre. Les types d'énergie utilisés ont évolué au fil du temps. Initialement, les humains comptaient sur leur propre énergie musculaire et celle des animaux. Cependant, reconnaissant les limitations de ces sources, ils se sont tournés vers les combustibles fossiles tels que le pétrole, le gaz naturel et le charbon. La consommation de combustibles fossiles est rapidement devenue omniprésente avec le début de la révolution industrielle. Malgré leur utilisation généralisée, les combustibles fossiles sont considérés comme une forme d'énergie finie et non renouvelable qui nécessite des millions d'années pour se reformer. De plus, leur combustion libère du CO_2, contribuant à l'accumulation de gaz à effet de serre et au changement climatique subséquent.

Pour atténuer ces impacts environnementaux et éviter des catastrophes potentielles, les experts conseillent de réduire de moitié les émissions de CO_2 d'ici 2050. Ainsi, la nécessité urgente d'une transition vers des sources d'énergie renouvelables avec un impact environnemental minimal devient évidente. Parmi tous les modèles, l'énergie éolienne et solaire sont appelées à diriger cette transition, offrant une capacité propre à faible coût et rapide à fournir. On rapporte que l'énergie éolienne et solaire a atteint plus de 10% de la part mondiale de la production d'électricité. Malgré leur forte croissance, la diversification des sources d'énergie renouvelable reste un défi. L'énergie osmotique, libérée lors du mélange de solutions de concentrations différentes, demeure une ressource énergétique inexploitée avec un potentiel significatif. De plus, la récolte d'énergie osmotique a des émissions de gaz à effet de serre limitées et une empreinte écologique minimale sur la planète. Par conséquent, le développement de technologies de récolte d'énergie osmotique fiables, efficaces et économiquement viables est d'une grande importance.

Dans ce manuscrit, nous présentons des études approfondies visant à promouvoir le développement des systèmes d'électrodialyse capacitive (CRED). L'innovation principale des systèmes CRED réside dans leur combinaison du processus de création de flux ionique dans les systèmes d'électrodialyse inverse (RED) avec l'utilisation d'électrodes capacitives peu coûteuses dans les systèmes de mélange de capacité (Capmixing). Avec de nombreux avantages tant sur le plan technique qu'économique, le CRED émerge comme un excellent candidat méritant une enquête approfondie pour la récolte d'énergie osmotique. Cependant, en tant que technologie nouvellement développée, elle manque d'études systématiques dans le domaine de la recherche. Dans ce travail de thèse, nous fournirons tout d'abord une description détaillée du mécanisme de fonctionnement du système CRED, sur la base duquel une stratégie efficace d'amélioration des performances énergétiques est proposée. Ensuite, nous évaluons les performances énergétiques du système CRED dans des scénarios réels, dans le but de progresser vers l'industrialisation. Enfin, nous élargissons le champ d'application des systèmes CRED en développant un système de gradient de pH sous un cadre similaire, démontrant son application étendue dans tous les processus de récolte d'énergie basés sur les gradients de concentration.

Résumé du manuscrit

Ce manuscrit est divisé en 5 chapitres différents. Le Chapitre 1 propose une étude bibliographique des technologies de pointe pour la récolte d'énergie osmotique. À la fin de ce chapitre, nous définissons les objectifs de ce travail de thèse. Les Chapitres 2, 3 et 4 sont trois travaux de recherche distincts sur le système CRED. Le chapitre 2 décrit une stratégie de boosting qui permet l'amelioration de la densité de puissance pour le système CRED. Le chapitre 3 décrit l'impact des ions divalents pour le système CRED pour rapprocher à l'application réelle. Le chapitre 4 conçois une cellule à partir d'un gradient de pH qui récolte l'énergie osmotique génère lors de la capture de CO_2. Enfin, le Chapitre 5 offre une conclusion générale du travail de thèse et des aspects intrigants à explorer davantage dans les futurs travaux de recherche.

Chapitre 1: Introduction

Le premier chapitre offre une revue complète des études de pointe sur les systèmes de récolte d'énergie osmotique. Nous commençons par introduire les concepts généraux de l'énergie osmotique, en mettant en évidence son potentiel significatif estimé à l'échelle mondiale. Ceci est suivi par un résumé des trois principales technologies de récolte d'énergie osmotique : l'Osmose à Pression Rétardée (PRO), l'Électrodialyse Inverse (RED) et le Capmixing. En bref, la PRO est une technologie semi-membranaire dans laquelle le flux d'eau induit par l'effet osmotique entraîne une augmentation du volume de la chambre de solution sous pression de haute concentration. Cette énergie mécanique est ensuite utilisée pour actionner les systèmes de turbines afin de produire de l'électricité. De manière similaire, la RED est également une technologie basée sur la membrane, où des membranes d'échange d'ions sont utilisées pour créer un flux ionique sous l'effet osmotique, qui est ensuite converti en courant électrique par des réactions d'oxydoréduction aux électrodes. Les systèmes de Capmixing conçoivent un cycle précis et ingénieux pour exploiter l'expansion de la double couche sur les électrodes capacitives afin de récolter l'énergie osmotique. Pour chaque technologie, nous fournissons des détails sur le principe de fonctionnement, les performances énergétiques et l'analyse économique. Après une comparaison approfondie et une analyse, nous décidons de nous concentrer sur le système d'électrodialyse capacitive inverse (CRED), qui se situe à la croisée des chemins entre la RED et le Capmixing. Nous définissons le cadre de ce travail de thèse et esquissons le plan de recherche.

Chapitre 2: Amélioration des performances de densité de puissance des systèmes CRED par stratégie de boosting

Un système CRED composé d'une membrane échangeuse de cations unique et de deux électrodes capacitives à base de carbone est construit dans ce travail. De l'eau salée et de l'eau douce sont injectées en continu dans le système CRED pour former une ressource énergétique osmotique. Séparé par la membrane échangeuse de cations, un flux cationique directionnel est dirigé de la chambre d'eau salée vers la chambre d'eau douce sous l'effet osmotique. Les électrodes capacitives sont capables de convertir ce flux ionique en un flux électronique par phénomène d'adsorption/désorption des ions. Ainsi, une caractéristique majeure du système CRED est la suppression des réactions redox à l'intérieur du processus. Pour mieux décrire les systèmes CRED, il est possible d'établir un circuit équivalent de type RC. Le modèle correspondant décrit bien les performances énergétiques des systèmes CRED. Les expériences démontrent qu'il existe un écart de densité de puissance substantiel entre le système CRED et la valeur maximale théorique. Suite aux résultats expérimentaux et à l'analyse théorique basée sur le circuit équivalent, cet écart est principalement dû à l'efficacité de conversion flux ionique-électronique faible dans les électrodes capacitives. Pour pallier cette limitation, nous proposons l'application d'un signal électrique supplémentaire synchronisé avec la tension de la cellule pour optimiser le régime de fonctionnement du système CRED. Les expériences et la modélisation confirment que cette stratégie de boosting est efficace pour améliorer la densité de puissance. Elle est capable d'optimiser le régime de fonctionnement du système CRED, ce qui se traduit par des performances énergétiques optimisées pour le CRED comparables à celles du système RED. En considérant un coût réduit pour les électrodes capacitives, le CRED présente un avantage économique supérieur pour un développement ultérieur.

Chapitre 3: Atténuation de l'influence des ions divalents sur les performances du système CRED

Pour progresser vers des applications concrètes, nous évaluons les performances du système CRED sous des solutions composées de mélanges d'ions multivalentes. Nous caractérisons systématiquement la tension de la cellule, comprenant la contribution liée à la membrane et la contribution liée aux électrodes, sous le mélange d'ions divalents de différentes fractions. Il est démontré que le mélange d'ions divalents a un impact énorme sur la tension de la membrane, mais que la tension liée aux électrodes reste stable. Selon les expériences, la chute de tension de la membrane dans le système CRED peut être entièrement expliquée par l’effet ascendant (Uphill effect), où les ions divalents migrent de la partie diluée à la partie concentrée. Ce phénomène est fondamentalement différent de celui observé dans les systèmes RED, où l’empoisonnement de la membrane entraîne une importante baisse de la sélectivité de la membrane et une augmentation considérable de la résistance de la membrane. Contrairement à la chute significative de 75 % de la densité de puissance observée dans les systèmes RED classiques, le système CRED présente seulement une légère baisse de 35 % à la fois de la tension de la cellule et des performances énergétiques lorsqu’il est soumis à des solutions avec mélange d’ions divalents de plus de 60 %. Ce phénomène est attribué au renversement périodique de la chambre d’eau, qui atténue l’effet d’empoisonnement de la membrane. Ce résultat est en outre validé par des tests à long terme avec des solutions réelles. Ce travail propose une méthode simple de commutation de la chambre d’eau pour supprimer le problème de l’empoisonnement de la membrane, qui perturbe le domaine de recherche des systèmes RED depuis plus de dix ans. En considérant la légère baisse de densité de puissance dans des scénarios réels, cela ouvre la voie au passage à l’échelle industrielle du système CRED.

Chapitre 4: Cellule à gradient de pH pour la récolte d’énergie

Pour généraliser le système CRED à un spectre plus large, on peut envisager tous les types de systèmes de récolte d’énergie basés sur les gradients de concentration. Contrairement aux gradients de salinité qui sont limités par la solubilité du sel, le gradient de pH présente une gamme plus large et existe largement dans le domaine industriel. Un scénario passionnant consiste à exploiter la variation de pH survenue dans les processus de capture du carbone et à convertir cette énergie osmotique basée sur le gradient de pH en électricité. Cette méthode de récolte d’énergie pourrait éventuellement réduire le coût global du processus de capture du carbone. Plus précisément, le pH diminuera lors de la capture du CO_2 dans l’électrolyte. Il augmentera lorsque de l’air est pompé dans l’électrolyte ou lorsqu’il est soumis à un traitement thermique venant des usines. La combinaison de ces deux électrolytes entraînera une différence de pH géante allant jusqu’à 3,9. Nous proposons une cellule à gradient de pH composée d’une membrane non sélective et de deux électrodes de pseudo-capacité en MnO_2 pour récolter l’énergie osmotique établie. Il est démontré que la cellule à gradient de pH fonctionne de manière similaire à un processus capacitif comme le système CRED, car elle peut être bien décrite par un circuit équivalent de type RC. De manière inattendue, la cellule à gradient de pH présente une augmentation inhabituelle de la densité de puissance sous la stratégie de boosting, dépassant sa prédiction maximale théorique de densité de puissance. Nous sommes convaincus que ce phénomène inhabituel provient de la contribution supplémentaire de la tension des électrodes due au changement de couverture fractionnelle dans les électrodes composites de MnO_2. Ce point est vérifié par un circuit équivalent RC adapté, qui décrit les performances énergétiques sous boosting. Il convient de mentionner que la cellule à gradient de pH reste dans le cadre du régime capacitif et que les réactions redox restent réversibles à ce stade. Cependant, lorsque la densité de courant dépasse 2 $mA.cm^{-2}$, nous observons une perte de matériau sévère dans les électrodes, suggérant la survenue de réactions redox irréversibles.

Chapitre 5: Conclusion et Perspectives

Ce chapitre conclusif présente un aperçu complet de la récolte d'énergie osmotique à travers les systèmes d'électrodialyse capacitive inverse (CRED). De plus, nous décrivons nos futures investigations prévues. Plus précisément, nous approfondirons l'étude de l'industrialisation du système CRED, en nous concentrant sur deux directions principales. Premièrement, nous explorerons la construction de cellules CRED avec des surfaces effectives plus grandes. Deuxièmement, nous avons l'intention de mettre en œuvre des unités CRED en série. De plus, nous prévoyons d'intégrer des systèmes CRED basés sur les gradients de salinité en tant que systèmes de boosting dans les systèmes à gradient de pH. Enfin, nous explorons l'intégration potentielle de cellules à gradient de pH dans les processus de capture et de stockage du carbone (CCS) en mer.

Les annexes apportent des informations complémentaires aux différents chapitres et reproduisent les quatre articles publiés à *Lab on a chip*, *Nano Energy*, *Environmental Science & Technology* et *Scientific Reports*.

Table of contents

Nomenclature

Common Abbreviations

AEM	Anion Exchange Membrane
CA	Chronoamperometry
CCS	Carbon Capture and Storage
CD	Fixed Charge Density
CDLE	Capacitive energy extraction based on Double Layer Expansion
CDP	Capacitive energy extraction based on Donnan Potential
CEM	Cation Exchange Membrane
CP	Chronopotentiometry
CRED	Capacitive Reverse Electrodialysis
CV	Cyclic Voltametry
ECC	Electrochemiluminescence
ECP	External Concentration Polarization
ED	Electrodialysis
EDL	Electrical Double Layer
FIB	Focused Ion Beam
FO	Forced Osmosis
HIT	Hydration Innovation Technology
ICP	Internal Concentration Polarization
IEC	Ion Exchange Capacity
IEM	Ion Exchange Membrane
LCOE	Levelized Cost Of Energy
NIPS	Non-Solvent Induced Phase Seperation

OCV	Open-circuit Voltage
PAO	Pressure Assisted Osmosis
PCC	Post-combustion Capture
PRO	Pressure Retarded Osmosis
RED	Reverse Electrodialysis
RO	Retarded Osmosis
RSF	Reverse Salt Flux
SD	Swelling Degree
SE	Soft Electrode
ssRED	Solid Salt Reverse Electrodialysis
SWRO	Seawater Reverse Osmosis
TEM	Transmission Electron Microscopy
TFC	Thin Film Composite
TIPS	Thermal Induced Phase Seperation
TRCPC	Thermally regenerative CO_2 induced pH gradient cell

Material Abbreviations

BNNT	Boron Nitride Nanotube
CA	Cellulose Acetate
CDQs	Carbon quantum dots
CNTs	Carbon NanoTubes
CTA	Cellulose Tricetate
DI water	Deionized water
EDA	Ethylenediamine
MEA	Monoethanolamine
PA	Polyamide
PAA	Polyacrylic acid
PAI	Polyamide-imide
pAMPSA	Poly(2-acrylamido-2-methyl-1-propanesulfonic acid)
PAN	Polyacrylonitrile

PBO	Polybenzoxazole-co-imide
PDA	Polydopamine
pDADMAC	Poly(diallyldimethylammonium chloride)
PE	Polyethylene
PEI	Polyethylenimine
PES	Polyethesulfone
PET	Polyester
PMA	Polymethyl acrylate
PSf	Polysufone
PVA	Polyvinvlalcohol
PVDF	Polyvinylidenefluoride
PVP	Polyvinylpyrrolidone
SHPG	Sulfonated Hyperbranched Polyglycerol
sPEEK	Sulfonated Poly (ether ether kefone)
TBP	Tributyl phosphate
Symbols	
α	Membrane permselectivity
$\Delta\pi$	Osmosis pressure difference
τ	Electrical characteristic time for RC circuit defined as $\tau = (R_{load} + R_{cell})C$
τ_{fill}	Time required to fulfill the water chamber. It is defined by the flow rate Q and the chamber volume
c_L, c_H	salt concentration in diluted solution, concentrated solution.
C	Inner cell capacitance of a CRED system
E_0	Boosting voltage
E_{cap}	potential drop across the capacitor, defined as $E_{cap} = \frac{q}{C}$
E_{eff}	Effective electromotive force in CRED system
E_{elec-c}	Electrode related potential difference in CRED system
E_{elec-f}	Electrode related potential difference in RED system
E_{elec}	Electrode related potential difference in RED or CRED system. It depends upon local salt concentration.

E_{load}	Voltage applied onto the load resistor
E_m	Membrane voltage
E_{OCV-c}	Open-circuit voltage in CRED system
E_{OCV-f}	Open-circuit voltage in RED system
E_{OCV}	Open-circuit voltage of a cell, it is composed of membrane contribution E_m and electrode contribution E_{elec}
I	Electrical current in CRED system
P	Instantaneous power density dissipated in a load resistor in CRED system
$P_{b-boost}$	Temporal average power density provided by a booster system under boosting strategy
$P_{b-gross-th}$	Temporal average gross power density dissipated in a load resistor under boosting strategy calculated by theoretical models
$P_{b-gross}$	Temporal average gross power density dissipated in a load resistor under boosting strategy
$P_{b-net-th}$	Temporal average net power density of a CRED system under boosting strategy calculated by theoretical models
P_{b-net}	Temporal average net power density of a CRED system under boosting strategy. It is defined as $P_{net} = P_{gross} - P_{boost}$
P_{max}	Maximum electrical power density of an ideal RED system
P_{nb-th}	Temporal average power density output of a CRED system without boosting strategy calculated by theoretical models
P_{nb}	Temporal average power density output of a CRED system without boosting strategy
Q	Flow rate
q	Charge accumulated in a capacitor
R	Perfect gas constant
R_{cell}	Inner cell resistance
R_{eff}	Effective resistance in CRED system under boosting strategy
R_{load}	Electrical resistance of a load resistor
R^*_{load}	Optimized load resistance to recover the maximum power density
S	Effective surface area in a RED or CRED system
T_s	Switching period for CRED system
V	System volume

X	Extent of fractional coverage of the surface or inner structure of MnO_2 composite electrode
Z	Impedance of CRED system
z_i	Valence of ion of species i
γ_i	Activity coefficient of species i for a system consists of N species
μ_i, μ_i^*	Chemical potential, standard chemical potential, of species i for a system consists of N species
c_i	molar concentration of species i for a system consists of N species
G	Gibbs energy
G_H, G_L	Gibbs energy of seawater of high salinity, Gibbs energy of freshwater of low salinity
$G_{mix}, \Delta G_{mix}$	Gibbs energy of brackish water after mixing, Gibbs free energy released of mixing
J	Molar transport of divalent ions towards concentrated solution in uphill effect
n_i	Mole number of species i for a system consists of N species
P	Pressure
Ra	Salinity ratio
T	Temperature
x_i	mole fraction of species i for a system consists of N species
ΔP	Hydraulic pressure in PRO
A_m	Effective surface area of the membrane in PRO
A_x	Membrane permeability in PRO
J_w	Solvent flux across the semipermeable membrane in PRO
P_{gross}	Gross power density in PRO
$\bar{\phi}_L$, $\bar{\phi}_H$	Electrical potential on the internal side of the membrane in diluted solution, concentrated solution
$\bar{a}_{i,L}$, $\bar{a}_{i,H}$	Ion activity of species i on the internal side of the membrane in diluted solution, concentrated solution
$\Delta\phi_{D,L}$, $\Delta\phi_{D,H}$	Donnan potential in diluted solution, concentrated solution
ΔE	Voltage applied onto a capacitor
ΔE_{OCV}	Instantaneous voltage drop in CP measurement
γ_L, γ_H	Activity coefficient in diluted solution, concentrated solution.

ϕ_L, ϕ_H	Electrical potential on the external side of the membrane in diluted solution, concentrated solution
ϕ_L^{SDL}, ϕ_H^{SDL}	Difference of potential created by Stagnant Double Layers that build up close to the membrane in diluted solution, concentrated solution
τ_{1H}, τ_{2H}	Potential equilibrium time for electrode 1, 2 in concentrated solution
τ_{1L}, τ_{2L}	Potential equilibrium time for electrode 1, 2 in diluted solution
A	Membrane surface in a RED stack
$a_{i,L}$, $a_{i,H}$	Ion activity of species i on the external side of the membrane in diluted solution, concentrated solution
C_{EDL}	Capacitance of Electrical Double Layer
e, w, l	Thickness, width and length of the water chamber in CRED
I_{CP}	Constant electrical current applied in CP measurement
k	Slope of the linear decrease in CP measurement
m_{wet}, m_{dry}	Ion Exchange Membrane weight in its wet phase, dry phase
N	Number of membranes in a RED stack
t_+, t_-	Transport number of cations, anions

General Introduction

Energy has been an essential factor for human beings throughout their existence on Earth. The types of energy utilized have evolved overtime. Initially, humans relied on their own muscular energy and that of animals. However, recognizing the limitations of these sources, they turned to fossil fuels such as oil, natural gas, and coal. The consummation of fossil fuels quickly became ubiquitous with the onset of the industrial revolution. Despite their widespread use, fossil fuels are considered as a finite and non-renewable type of energy that requires millions of year to reform. Additionally, their combustion releases CO_2, contributing to the accumulation of greenhouse gases and subsequent climate change. To mitigate these environmental impacts and avert potential disasters, experts advise halving CO_2 emissions by 2050. Hence, the pressing necessity for a shift towards renewable energy sources with minimal environmental impact becomes apparent. Across all models, wind and solar are set to lead this shift, offering low cost and quick-to-deliver clean capacity. It is reported that wind and solar energy reached over 10% of the global power share. Despite their strong growth, diversifying renewable energy sources remains a challenge.

In this context, osmotic energy released during the mixing of solutions of different salinities is a promising avenue to explore. This lesser-known energy source holds significant potential. Mixing 1 m^3 of seawater with 1 m^3 of freshwater yields 1.4 MJ of energy. We estimate a potential global power output of 2.4 Terawatts, which is comparable to the world's total electrical power. However, osmotic energy also appears on a smaller scale, such as in the biological salinity gradients found in physiological fluids across cell membranes or organs. Additionally, it can be generalized into other forms, like pH gradient-based osmotic energy, which has a much broader range compared to salinity gradients limited by solubility. In fact, natural cells store free energy by maintaining different concentrations of molecules in separate "compartments." As with many processes, humans should draw inspiration from nature. By carefully engineering the energy harvesting process, artificial systems can effectively utilize this clean and sustainable osmotic energy source.

There are overall three major osmotic energy harvesting technologies, including pressure retarded osmosis (PRO), reverse electrodialysis (RED) and Capmixing. Briefly speaking, PRO is a semi-membrane based technology where water flux driven by osmotic effect results in the volume increase of the pressurized solution chamber of high concentration. The mechanical energy is then used to propel the turbine systems for electricity generation. Similarly, RED is also a membrane-based technology. Ion-exchange membranes (IEMs) are used to create an ionic flux under osmotic effect, which is then converted into electric current by redox reactions at electrodes. Capmixing systems designs a precise and engineered cycle to use double layer expansion on capacitive electrodes for osmotic energy harvesting. To combine the advantages of both RED and Capmixing technologies, we design a capacitive reverse electrodialysis (CRED) system to harness the osmotic energy.

In this manuscript, we provide firstly a bibliographical study of the state of art technologies for osmotic energy harvesting. After fixing the goal of this thesis work, we present three major research works realized for CRED system. We will provide an in-depth description of the operational mechanism of the CRED system, upon which we will propose an effective strategy to enhance its energy performance. Following this, we will assess the energy performance of the CRED system in real-world scenarios, aiming to progress towards industrialization. Lastly, we will expand the application potential of CRED systems by developing a pH gradient system within a similar framework, showcasing its versatility in all concentration gradient-based energy harvesting processes. In the concluding chapter, we offer a comprehensive summary, accompanied by three promising research avenues for future exploration.

Chapter 1

Introduction

In this chapter, a complete bibliographical study concerning the present osmotic energy harvesting technologies is presented. We will firstly present the world wide energy crisis and the urgent demand for clean energy transition. Among all the alternative energy resources, osmotic energy, also named as blue energy, remains an untapped resource with large potential of exploitation. We then present different blue energy harvesting technologies, including pressure retarded osmosis (PRO), reverse electrodialysis (RED) and Capmixing. A detailed description and techno-economic analysis is provided for each technology. After the comparison among these major energy harvesting technologies, we focus on an innovative technology called capacitive reverse electrodialysis (CRED) which combines well the advantages of both RED and Capmixing.

The bibliography study presented in this chapter is published in Lab on a Chip[1] and Nano Energy[2]. The articles can be found in Appendix A.

1.1 Energy crisis

According to the Global Electricity Review of 2023, the global electricity demand remained at a growth rate of 2.6% in the decade of 2010-2021[5]. Such energy consumption continues to grow in the future. In terms of the energy structure, the majority of the energy consumed worldwide still comes from the fossil fuels, with oil being the major energy source, followed by coal and gas (Fig 1.1)[6]. However, the use of fossil fuels is not only unsustainable due to the limited reservoir, but also environmentally devastating. The planet is experiencing severe global warming issues due to the CO_2 emission contributed by fossil fuel burning. This has profound and widespread impacts in the atmosphere, ocean, cryosphere and biosphere[7]. Facing such emerging global environmental challenges, the International Energy Agency set out a Paris-Agreement-compatible pathway in its Net Zero Emissions scenario published in the report of Net Zero by 2050. The objective is to put the global power sector on track for 1.5 degrees[7].

Due to the rising energy demand and the severe environmental crisis, people call for the world wide reduction of conventional fossil fuel consummation to limit greenhouse gas emission[8, 9]. The above mentioned pathway requires an important expansion in the development of clean energy generation. Alternative energy sources with limited impacts on environment attract much attention in both scientific and industrial fields[10]. In this sector, solar and wind resources are important candidates with mature and industrial exploitation technologies. In the report of Thinktank published in 2022, wind and solar energy reached over 10% of the global power share[11]. Despite their strong growth, diversifying renewable energy sources remains a challenge.

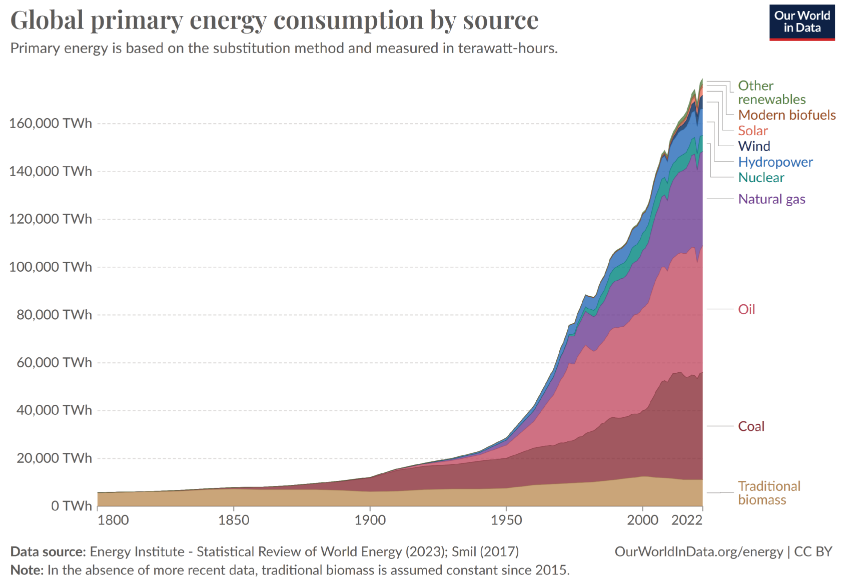

Global primary energy consumption by source

Primary energy is based on the substitution method and measured in terawatt-hours.

Data source: Energy Institute - Statistical Review of World Energy (2023); Smil (2017)

OurWorldInData.org/energy | CC BY

Note: In the absence of more recent data, traditional biomass is assumed constant since 2015.

Fig. 1.1 Global energy consumption by source (Figure and captions adapted from Our World in Data[6])

In this context, the osmotic energy, which is released during the mixing of solutions of different salinity, is a promising avenue to explore. As an untapped large resource of energy, blue energy presents no greenhouse gas emissions and limited ecological footprint on the planet[12]. It is recognized as a renewable energy by European Commission in 2021. In the following sections, we will provide a detailed bibliographical study of osmotic energy. We will firstly start by the general explanation of the osmotic energy. Then we will explain in details about the major osmotic energy harvesting technologies developed in the scientific research and in industrial field.

1.2 Osmotic energy harvesting

The energy produced by mixing solutions of varying salinity, known as osmotic energy, is a clean and renewable resource often referred to as "blue energy."[13, 14]. Naturally, a spontaneous and irreversible mixing of river water and sea water happens at the estuary, resulting in an entropy increase of the system[15]. A precise and engineering control of this entropy change procedure enables the blue energy harvesting. The potential of blue energy can be estimated by thermodynamics studies. The non-expansion work released from the mixing of seawater and freshwater can be described by the Gibbs free energy of mixing ΔG_{mix} at a constant pressure P and at absolute temperature T.

$$\Delta G_{mix} = G_{mix} - (G_H + G_L) \tag{1.1}$$

Here, G_{mix}, G_H and G_L represents the Gibbs free energy of brackish water after mixing, seawater of high salinity and freshwater of low salinity, respectively.

As the Gibbs free energy is defined as $G = \sum_{i=1}^{N} \mu_i n_i$, where μ_i and n_i represent the chemical potential and the mole number of species i for a system consists of a number of N species. The chemical potential μ_i is defined as $\mu_i = \mu_i^* + RT ln(\gamma_i x_i)$ where μ_i^* is the standard chemical potential, R perfect gas constant. γ_i and x_i represent the coefficient of activity and the mole fraction of species i, respectively. For a system of volume V, the molar concentration is defined as $n_i = c_i V$, where c_i is the molar concentration of species i. Thus the Gibbs free energy of mixing can be calculated as[16]:

$$\Delta G_{mix} = \sum_{i=1}^{N}[c_{i,mix}V_{i,mix}RTln(\gamma_{i,mix}x_{i,mix}) - c_{i,H}V_{i,H}RTln(\gamma_{i,H}x_{i,H}) - c_{i,L}V_{i,L}RTln(\gamma_{i,L}x_{i,L})] \tag{1.2}$$

The theoretical available amount of energy from mixing 1 m^3 river water with a large surplus of seawater is around 2.5 MJ, which is equivalent to the hydraulic energy generated by water dams with water falling from 250 m high[17, 18]. Development of efficient and robust energy harvesting technologies is of great importance for the exploitation of this untapped renewable energy. In the following of this section, a review of blue energy harvesting technologies and their applications is explained in details. We first describe pressure retarded osmosis (PRO), and then move to reverse electrodialysis (RED), Capmixing and capacitive reverse electrodialysis (CRED).

1.3 Pressure retarded osmosis

As an emerging energy harvesting system, the technology of pressure retarded osmosis (PRO) is attracting much attention[19, 20]. Semipermeable membranes, which allow the passage of water molecules and block the passage of ions, are used in the configuration of PRO systems[21]. To better illustrate the power generation principle of PRO, an introductory explanation of the osmotic process across the semipermeable membrane is given in the following paragraph.

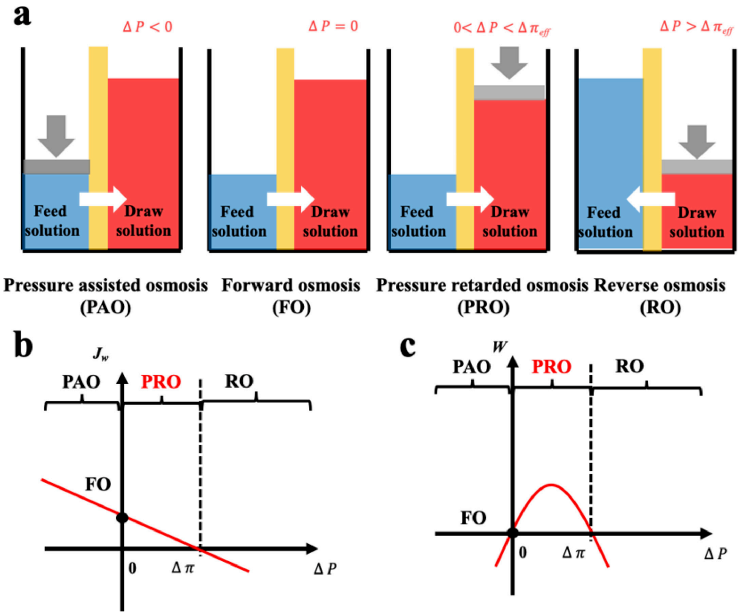

Fig. 1.2 Schematic illustration **a**, and analysis **b, c**, of four classic membrane-based osmotic processes of pressure assisted osmosis (PAO), forward osmosis (FO), pressure retarded osmosis (PRO) and reverse osmosis (RO). (Figures and captions reproduced from [22] with permission from Elsevier, copyright 2021.)

The observation of osmotic phenomenon was firstly documented by Jean-Antoine Nollet. It describes the spontaneous movement of a solvent flux moving across the semipermeable membrane towards a solute of higher concentration, in the way of balancing solute concentrations on both sides of the membrane[23]. The concentration difference across the membrane results in an osmosis pressure difference $\Delta\pi$. Additional hydraulic pressure ΔP could be applied on the system to influence the solvent flux. Description of the water (solvent) flux J_w is an essential parameter in the description of osmotic phenomenon. It can be theoretically described as a function of the applied hydraulic pressure difference ΔP and the effective osmosis pressure difference $\Delta\pi$ for an ideal membrane as $J_w = A_x(\Delta\pi - \Delta P)$. Here A_x refers to the permeability of the membrane[24].

Based on the comparison between ΔP and $\Delta\pi$, osmotic process can be briefly classified into four categories as illustrated in Fig 1.2(a)[22]. The Forward osmosis (FO) corresponds to a trivial case where ΔP is zero, indicating no mechanical work in this process. In this case, water flux is driven by the osmotic driving force, penetrating the semipermeable membrane and proceeding to the draw solution side. While applying a hydraulic pressure difference on the feed solution compartment ($\Delta P < 0$), the above-mentioned process is further assisted and accelerated in the so-called procedure of pressure assisted osmosis (PAO). In the case where $\Delta P > \Delta\pi$, the direction of the water flux is reversed (from draw solution to feed solution) due to the external hydraulic pressure. This procedure is named as Reverse osmosis (RO) and has intriguing applications in water desalination. It is to mention that both PAO and RO are energy consuming processes. On the contrary, PRO is the only power generating process where the water molecules move from feed solution towards the pressurized draw solution under osmotic effect ($0 < \Delta P < \Delta\pi$). The pressurized solution is then utilized to drive turbine systems for electricity power generation. A complete description of the water flux (J_w) and the power density (W) of each osmotic process is illustrated in Fig 1.2(b,c)[22].

Fig 1.3 presents a typical configuration of the PRO plant. Feed solution and draw solution are both filtered and pumped into the PRO module. Under the osmotic effect, a water exchange flow rate (ΔQ) is created near the semipermeable membrane moving from feed water side towards draw water side. The brackish water received in the feed water chamber presents a higher flow rate of ($\Delta Q + Q_H$) and a higher hydrostatic pressure P_H. The brackish water is then divided into two streams, where one stream is depressurized to drive turbine systems and produce electricity and the other one is delivered into a pressure exchanger to maintain the incoming pressure of draw solution[25]. Here the gross power density of a PRO system can be experimentally calculated as[26]

$$P_{gross} = \frac{\Delta Q \Delta P}{A_m} = \Delta P J_w \tag{1.3}$$

where A_m refers to the effective surface area of the membrane, ΔP refers to the trans-membrane hydraulic pressure and J_w refers to the water flux across the membrane[27].

1.3.1 Major challenges in PRO

Although PRO is a promising technology for energy harvesting, PRO modules still suffer from limiting factors in practical use. As illustrated in Fig 1.4, a semipermeable membrane is composed of an active layer and a support layer[22]. An ideal membrane is expected to have high water permeability while maintaining a high salt selectivity. However, it was demonstrated in the work of Straub et al. the existence of tradeoff between these two factors (Figure 1.5(A))[26].

One of the major obstacles of membrane applications is the polarization effect, which refers to the ion accumulation phenomenon near the semipermeable membrane. The internal concentration polarization (ICP) corresponds to an immobile area clogged with ions in the dense support layer[29]. External concentration polarization (ECP) occurs at the interface between active layer and the draw solution (dilutive ECP) or feed solution (concentrative ECP). Concentration polarization effect deteriorates the osmotic driving force across the membrane, thus leads to lower effective membrane performances and power density output[30]. In addition,

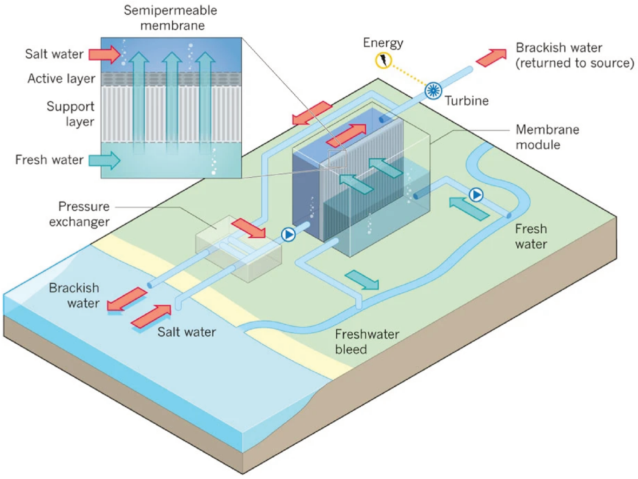

Fig. 1.3 Schematic illustration of the working principle of PRO systems. Feed solution and draw solution are injected continuously into water compartments which are separated by semipermeable membranes. Driven by effective osmotic force, water flux flows across the membrane from freshwater compartment towards saltwater compartment, resulting in a concentration decrease and a flow rate increase in draw solution compartment. The pressurized water flux is then split into two fluid streams: one fluid stream is used for electricity generation by driving an installed turbine, while the other stream returns to a pressure exchanger to maintain the pressure of draw solution. (Figures and captions reproduced from [28] with permission from Springer Nature, copyright 2012.)

the imperfection of membranes could lead to ion leakage from draw solution to feed solution, which is named as Reverse salt flux (RSF)[31]. The trace leakage might cause more severe ICP effect in the system, lower the power density output, and could possibly promote membrane fouling problems[32], which is also one of the major limitations on PRO power density output. A theoretical analysis of the impact of ICP and RSF was conducted by Straub et al., as illustrated in Fig 1.5(B). An apparent drop in power density is observed under the synergistic effect of ICP and RSF[26].

Biofouling is a common problem for the industrial application of membranes. It influences severely the membrane performances in practical use, hinders the lifespan of membranes and raises additional fees for water pre-treatment[33]. The mechanical strength of membranes is also the key point for the development of PRO performances and its commercialization[22].

In general, ideal PRO membranes should reach the following criteria: large water permeability, high salt rejection (high membrane selectivity), low reverse flux, limited biofouling problems and reinforced mechanical strength[34]. Precise engineering of the membrane's properties, including layer thickness, geometry configuration, porosity, selectivity and etc., is summarized in the following paragraph.

1.3.2 PRO membrane development

At the early stage of PRO technology development, commercial membranes developed for RO and FO applications were used. In the pioneer work of PRO, Loeb et al.[35] used ‘Minipermeators’ with asymmetric hollow fibers of Du Pont Permasep B-10 initially developed for RO applications on sea water desalination. Later, Mehta et al.[36] realized a series of tests of the commercial membranes for RO and FO applications. Investigations on spiral-wound minimodules of cellulose acetate brackish water membrane and hollow fiber minipermeators were realized. Then

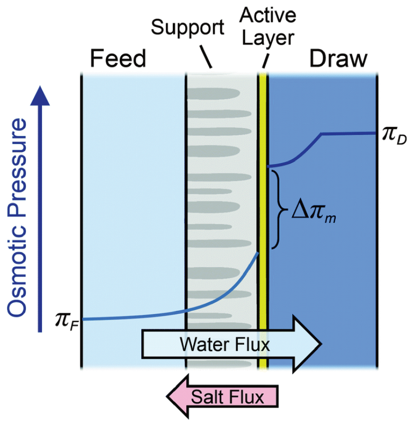

Fig. 1.4 Illustration of the semipermeable membrane cross section composed of an active layer and a support layer. A qualitative presentation of osmotic pressure profile across the membrane is presented.(Figures and captions reproduced from with permission [26] with permission from Royal Society of Chemistry, copyright 2016.)

the initial cellulose-based membranes designed for PRO applications with superior hydrophobicity and mechanical strength was used in studies[37]. These flat-sheet cellulose acetate membranes, including cellulose acetate (CA) and cellulose triacetate (CTA), were developed by HIT (Hydration innovation technology)[38]. The early studies indicate a low energy harvesting performance of PRO mainly due to the use of unsuitable and bulky membrane structures, which causes severe ICP effect and reverse water flux problems[39]. In recent years, development in membrane design and surface modification promotes a vast progress for PRO membranes. The present membranes for PRO applications could be classified into two categories: the thin film composite (TFC) flat sheet membranes and thin film composite hollow fiber[40].

Flat-sheet PRO TFC membranes consist of a highly-porous support layer and an active layer to reinforce its selectivity[41]. Polyamide (PA) is commonly chosen as the active layer, which is polymerized over the interface of the support layer through the phase inversion polymerization[34]. Various works were realized to optimize the permeability and structure integrity, aiming to ameliorate the power density output of PRO systems.

Table 1.1 lists the present work of flat-sheet PRO TFC membranes in literature.

It was demonstrated that membrane post-treatment of PA active layer could significantly increase the power density of PRO systems. Yip et al.[42] compared the performance of membranes with and without NaOCl and $NaHSO_3$ solution immersion and heat treatment. The highest power density output is predicted to be 10 $W.m^{-2}$ with proper post-treatment. A detailed study on membrane post-treatment was conducted by Han et al.[43] An optimal post-treatment condition was reported to generate a power density of 12 $W.m^{-2}$ under a hydraulic pressure of 15 bar. Integrating additives into support layer is another common strategy applied in membrane research for PRO applications. Li et al.[44] realized polydopamine (PDA) modification onto the polyamide-imide (PAI) support layer. Son et al. [45] successfully embedded carbon nano tubes (CNTs) into the polyethersulfone (PES) support layer, obtaining a power density output of 1.6 $W.m^{-2}$ at a hydraulic pressure of 6 bar, using deionized (DI) water and NaCl solution of 0.5 M. Wei et al.[46] realized polysulfone (PSf) support layer reinforced by polyvinylpyrrolidone (PVP), and obtained a maximum power density of 12.9 $W.m^{-2}$ at hydraulic pressure of 22 bar.

Flat sheet membranes could also be prepared by electrospun polymeric supports of high porosity and tortuosity. A highly-porous support layer was realized by Bui et al.[47] by electrospinning polyacrylonitrile (PAN) nanofibers

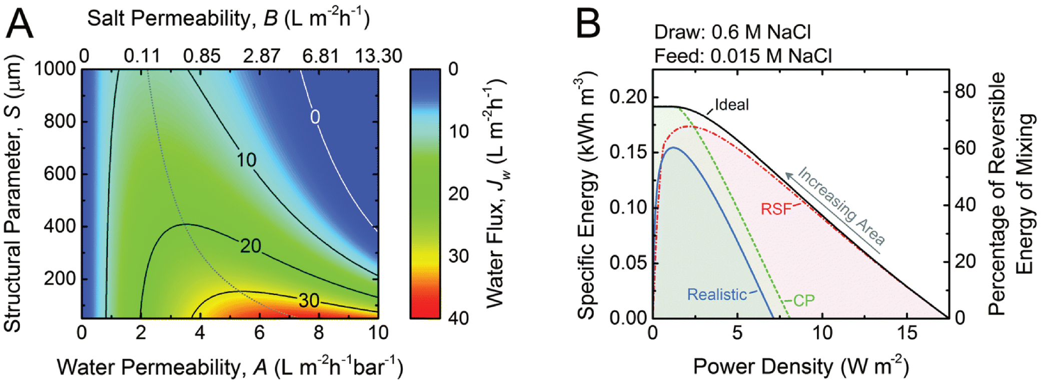

Fig. 1.5 **A**. Coupon-scale water flux J_w as a function of the water permeability coefficient, A; NaCl permeability coefficient, B; and support layer structural parameter, S. The water permeability and salt permeability are linked by the permeability-selectivity trade-off. **B**. Specific energy and power density for counter-current membrane modules with increasing membrane area from right to left. Data for three types of membranes are shown: ideal (solid black line), RSF (dash dotted red line) and CP (dashed green line) and realistic (solid blue line) (Figures and captions reproduced with permission.(Figures and captions reproduced from [26] with permission from Royal Society of Chemistry, copyright 2016.)

onto a polyester (PET) fabric substrate. Tian et al.[48] prepared tiered polyethylenimine (PEI) nanofibrous support incorporated with multi-walled CNTs. Use of such membrane in PRO system generates a power density of 17.3 W.m^{-2}. A dual layer of PSf/GO (graphene oxide) and PSf/HNT (halloysite nanotube) of nanocomposite on PET was prepared by Lim et al.[49] to ameliorate water permeability.

The possibility of incorporating nano-sized materials into conventional membranes has been well developed by researchers. Gonzale et al.[50] incorporated Schiff base network-1 (SNW-1) nanocomposite into the PA active layer preparation. The PRO system reached its maximum performance of 12.1 W.m^{-2} with DI water and brine water of 1M. Kwon et al.[51] realized a toluene-assisted interfacial polymerization to fabricate active layer of PA onto a polyvinyl alcohol (PVA)-coated polyethylene (PE) support. An astonishing power density of 35.7 W.m^{-2} was reported for a hydraulic pressure of 20 bar. Recently, a Korean research group reported a novel thermally rearranged TFC membrane containing polybenzoxazole-co-imide (TR-PBO) combined with a PA layer[52]. A giant power density increase towards 40 W.m^{-2} was reported in its first work. Later, modification with fluorination on TR-PBO membranes ameliorate the output power density towards 87.2 W.m^{-2} in PRO applications[53].

There is no doubt that tremendous advances were achieved in flat-sheet PRO TFC membranes. However, most published works presented here focus on gross power densities, calculated by Equation.1.3. Actually, the module gross power densities presented here differ from the net power density due to the irrecoverable pumping energy input and the energy losses during electricity generation in turbine systems[54]. Taken into consideration the pumping energy inputs and energy losses, the net power density in published works might be much lower than its gross value. A detailed economic analysis of PRO systems will be given later.

In conventional PRO configuration using flat-sheet membrane, a feed spacer is needed to maintain the feeding channel geometry and reinforce the mass transfer near the membrane[55]. Such configuration decreases the hydraulic pressure and results in an energy loss in the PRO system[56]. In addition, feed spacers might cause membrane deformation at high hydraulic pressure, inducing severe reverse solute diffusion of the membrane and leading to performance loss[34].

Different from flat-sheet membranes, hollow fiber PRO TFC membranes have a self-supporting tubular shape of higher effective surface area. Such geometry avoids the use of feed spacers, thus limit the deformation failure in flat-sheet based PRO systems. The PRO module using hollow fiber membranes could also achieve a higher pack density, which could efficiently ameliorate output performances[57]. The major preparation method of the hollow fiber membrane is the phase separation spinning, including non-solvent induced phase separation (NIPS) or thermal induced phase separation (TIPS)[25].

The first work dealing with hollow fiber TFC membranes for PRO application was realized by Chou et al.[58] They successfully prepared a tubular self-supporting membrane made of PES as the supporting substrate and PA as the selective layer. A maximum power density of 10.6 $W.m^{-2}$ could be achieved by using the home-made hollow fiber PRO membrane with a salt concentration of 40 mM and 1 M for fresh and salt water chambers, respectively. The same group prepared a novel hollow fiber TFC membrane using PEI as the supporting substrate[59]. This PEI based hollow fiber membrane presents superior mechanical strength and shows a better power density output of 20.9 $W.m^{-2}$ under a hydraulic pressure of 15 bar.

Similar to flat-sheet PRO TFC membranes, chemical modifications on selective layer and the supporting substrate are both widely investigated in the research field. The work of Ingole et al.[60, 61] proves the effectiveness of PDA coating on PES supporting substrates in PRO applications. A power density increase from 1.62 $W.m^{-2}$ to 3 $W.m^{-2}$ is realized due to the additional coating. Grafting of chemical groups on supporting substrates were also reported in literature[62, 63].

Ingole et al.[64] prepared CA layer treated with Tributyl phosphate (TBP) onto the supporting substrate of PES with PDA coating. An improved power density of 3.9 $W.m^{-2}$ is achieved with the same brine water and fresh water conditions used in their previous work. Zhang et al.[65] reported a novel supporting substrate of PES with PDA coating, grafted with dendritic-architecture sulfonated hyperbranched polyglycerol (SHPG). A superior resistance to protein adhesion and bacterial attachment is achieved due to the high wettability of the polymer brushes. A maximum power density at hydraulic pressure of 15 bar is reported to be 18.8 $W.m^{-2}$.

An emerging trend nowadays is to incorporate nanocomposites into membrane preparation. Zhao et al.[66] grafted carbon quantum dots (CDQs) onto the PDA coating of the PES supporting substrate by covalent bonding during the hollow fiber membrane preparation. They obtained a maximum power density of 11 $W.m^{-2}$ at a hydraulic pressure of 15 bar. Another work of incorporating CDQs in PA selective layer was realized later by Gai et al.[67] They reported a better power density of 34.2 $W.m^{-2}$ at hydraulic pressure of 23 bar. Park et al.[68] incorporated graphene oxide nanosheets with PES supporting substrate.

In addition, numerous research work investigated on modifications of hollow fiber membranes to limit biofouling problems. Synthetic sea brine solutions with complex components were used in fouling experiments and the power density of PRO systems was tracked along the procedure. Zhao et al.[69] reported the use of MPC (2-methacryloyloxyethylphosphorylcholine)-PDA coating on PES support layer to enhance anti-fouling capacities of the system. Le et al.[70] presented the effect of using grated zwitterionic poly(sulfobetaine) on PA selective layers.

Table 1.2 lists the present work of hollow fiber PRO TFC membranes in literature.

Table 1.1 A summary of present PRO systems using flat-sheet PRO TFC membran

Materials	Concentration gradient	Hydraulic pressure (bar)	Power density (W.m^{-2})	Comments
PA/PSf-PET	DI/0.5M	12	10	NaOCl, $NaHSO_3$ and heat treatment
PA/PI	DI/1.0M	15	7-12	NaOCl, $NaHSO_3$ and MeOH treatment
PA/PAN	DI/3.5%(w/w)	10	2.6	NaOCl and $NaHSO_3$ treatment
PA/PAI	DI/3.5%(w/w)	6	2.84	PDA coating and NaOCl, $NaHSO_3$, EtO
PA/PI	DI/1.0M	9	6.0	PA blended with moderate p-xylylenedia
PA/PAN	80mM/1.06M	22	15.2	NaClO treatment
PA/PI	DI/1.0M	22	18.1	PA modified with DMF and SDS
PA/PAN-PE	DI/0.5M	11.5	8.0	PA selective layer of mTFC/ pTFC
CTA membrane	DI/3.0M	48	60	/
PA/PEI	10mM/1.0M	17.2	12.8	/
PA/PEI	DI/1.0M	16.9	17.3	Tiered PEI nanofibrous support with mul
PA/PSf-PET	10mM/1.0M	18.4	7.1	/
PA/PES	DI/0.5M	6	1.6	CNT-embedded-PES with NaOCl and N
PA/PSf	DI/1.0M	22	12.9	PSf support layer reinforced by PVP
PA/PES-PET	DI/1.0M	25	12.5	/
PA/PK	DI/0.6M	28	6.1	PK reinforced by PED non-woven fabric
GO membrane	17mM/1.0M	6.9	12.8	/
PA/PET	DI/1.0M	21	12.1	PSf/GO and PSf/HNT (dual layer) nanoc
PA/TR-PBO	DI/1.0M	15	17.9	TR-PBO (thermally rearranged polybenz
PA/PAI	DI/1.0M	21	12.1	PA incorporated with SNW-1 nanocomp
PA/TR-PBO	DI/3.0M	27	87.2	TR-PBO ESMs exposed to direct flurina
PA/TR-PBO	DI/1.0M	21	26.6	TR-PBO modified with PVA coating
PA/PE	DI/1.0M	20	35.7	PA formed by toluene-assisted IP

Table 1.2 A summary of present PRO systems using hollow fiber PRO TFC membra

Materials	Concentration gradient	Hydraulic pressure (bar)	Power density (W.m^{-2})	Comments
PA/PES	40mM/1M	9	10.6	/
PA/PEI	1mM/1.0M	15	20.9	/
PA/PI	DI/1.0M	16	14	/
PAN-PVP/PBI-POSS	10mM/1.0M	7	2.5	/
PA/PI	DI/1.0M	20	7.6	PDA coating
PA/PES	DI/1.0M	20	24.3	/
PA/P84 co-polyimide	DI/1.0M	21	12	/
PAN-PVP/PBI-POSS	10mM/1.0M	15	5.1	PAN/PVP with APS post-t
PA/PI	DI/1.0M	15	16.5	/
PA/PES	DI/0.6M	6	1.62	/
PA/PES	DI/0.6M	7	3	PDA coating
PA/PES	DI/0.6M	8	3.9	PA treated with TBP with
PA/PES	DI/3.5%(w/w)	16	6.7	PES grafted with HPG
PA/PI	DI/1.0M	16.2	12	/
PA/PES	DI/1.0M	18	11.2	/
PBI/PVP/PAN	10mM/1M	22	6.2	Triple layer
PA/PES	DI/1.0M	20	7.8	/
PA/PES	DI/1.0M	20	22.1	Pre-stabilization
PA/PEI	DI/1.0M	17	9.6	Pre-wetting
PA/PEI	DI/1.0M	13	13	PA modified with APTMS
PA/PES	wastewater/0.81M	15	7.7	PES with MPC- PDA coati
PA/PEI	DI/1.0M	15	19.2	/
PA/PEI	/	17	9.5	/
PA/PES	DI/1.0M	22	10.7	/
PA/PES	DI/1.0M	20	22	/
PA/PES	DI/1.0M	15	10.7	PA dual layer on both side
PA/PEI	DI/1.0M	15	16.2	PA with LbL depostion of
PA/PES	DI/0.81M	15	11	PDA coating grafted with
PA/PES	DI/1.0M	20	20	PES with $CaCl_2$ additive t
PA/PES	wastewater/0.81M	20	18.8	PDA coating grafted with
PA/PEI	DI/1.0M	15	8.9	/
PA/PES	DI/1.0M	23	34.2	PA incorporated with CD
PA/PAI	wastewater/1.0M	13	4.3	PAH post-treatment
PA/PES	DI/1.0M	16.5	14.6	PES incorporated with GO
CTA/CA T-NIPS	DI/1.0M	18	5.5	/
PA/PES	DI/1.0M	17	14.6	PA incorporated with PP-S

1.3.3 Economic analysis

Ever since the appearance of PRO system, the debate on its technological and economical feasibility has never stopped. In 2008, the power density threshold for PRO commercialization was reported to be 5 $W.m^{-2}$[103]. This result was taken as reference for the PRO application of Stakraft in Norway and for numerous studies published later. However, based on the novel economic framework developed by Chung et al.[54], the economical viable threshold of PRO power density was revalued. The net power density enabling the commercial interest of PRO to compete with present solar photovoltaic power plants is estimated to be 56.4 $W.m^{-2}$, with a suggestion of membrane cost at 15 $\$.m^{-2}$. Here, the levelized cost of energy (LCOE) is set to be 0.074 $ per kWh. Net power density and gross power density fundamentally differ because of the inherent overhead associated with the PRO process in the form of irrecoverable pumping energy input. The importance of using net power density in PRO system characterization is emphasized for better guidance of the technology development.

Several evaluations focused on different cases were also reported. Mashrafi et al.[104] provide an environmental and economic case study of PRO system implantation in Tampa Florida. A LCOE between 0.62 - 0.97 $ per kWh is estimated for feed water of different salinities. Based on the analysis model, suggestions including waste water treatment (as feed water) or PRO installation near waste water source (within 1km) could effectively reduce the LCOE down to 0.14 $ per kWh. Khasawneh et al.[105] analyzed the feasibility of installing PRO power plants with Red Sea-Dead sea waters. It was demonstrated that the project is technically and economically feasible, with a LCOE of 0.056 $ and a power of 134.5 MW. The membrane cost is estimated to be 25 $ per meter square. Based on hypersaline water sources, the extractable energy density in this case study surpass the conventional river-sea water sources, providing a positive estimation on installation of PRO systems.

Straub et al.[26] reported a thorough energetic analysis of PRO system harvesting blue energy in river water and sea water. An estimation for energy inputs and outputs in the system was presented separately. Overall, the expected energetic inputs will most likely surpass outputs, resulting in a negative power generation. The major cause is the insufficient energy density extractable in mixing of river and sea sources. However, systems with higher concentration gradients can sufficiently overcome the energy output limit mentioned above, though technical problems including biofouling and selectivity decrease remain to be solved. Touati. et al.[19] confirmed the viability of open-loop PRO and close-loop PRO by using low-concentration feed solutions. However, the analysis of hybrid SWRO-PRO systems results in a negative energy generation.

Though the debate of the viability of PRO system never stops, industrial attempts using PRO prototypes continues in the globe. The first commercialized plant was conducted by Stakraft in Norway from December 2009[106]. The aim of the project is to produce an 8-inch spiral wound module of 2000 m^2 which is able to produce a total of 10 kW of power, corresponding to a power density of 5 $W.m^{-2}$[107]. However, the actual performance of the PRO plant failed to reach the initial objective, delivering a total power of 2 kW, which corresponds only to 20% of the designed power[108]. Due to the lack of membrane optimization and high cost in accessory systems, the sale price of a PRO plant reaches 70-100 euros per MWh and showed low economic interests, compared with the actual electricity price of 30-40 euros in Norway. The whole system was unfortunately shut down in 2013. Researchers and engineers performed another prototype experiment in Quebec, Canada[107]. The main objective of the project is to carry out process optimization studies of performing water pretreatment to prevent biofouling problems. A novel project was started in Japan to install an additional prototype PRO module, using commercial CTA hollow fiber membrane modules, to the Fukuoka WRO desalination plant to form a RO-PRO joint system[107]. A maximum power density of 13.3 $W.m^{-2}$ was achieved by a 10-inch hollow fiber membrane module. Nowadays, a similar hybrid RO-PRO project is developed jointly by Saudi Arabia and

Japan, aiming to develop efficient PRO systems for energy recovery and environmentally friendly high saline water treatment used in RO desalination processes[109].

Overall, stand-alone PRO systems with sources of higher salinity difference seem to be more promising due to a higher extractable energy density. The development of commercialized inexpensive PRO membranes is of key importance, which could sufficiently increase the system performances and reduce the production and maintenance costs. Considering the rising electricity price in Europe due to the lack of gas and the emerging technology development in PRO systems, the economic threshold of PRO system might be reached in the near future.

1.4 Reverse electrodialysis

Proposed by Pattle et al. in 1954 [110] , reverse electrodialysis (RED) is the earliest technology proposed for blue energy extraction. In a classic RED configuration, sea water and river water were injected respectively into two different compartments separated by an ionic exchange membrane (IEM). This approach corresponds to the reversed process of the electrodialysis (ED), where IEMs are used with an electric current to remove salts from sea water for pure water production. Years after, no significant development has done until 70s, when Lacey in 1980 developed his model for the RED[111]. To understand how an RED device works, it is necessary to understand how an ion exchange membrane behaves when it separates two salt solutions of different concentrations. This question will be answered in the following subsection.

1.4.1 An ionic exchange membrane separating two different salted solutions.

An electrical potential difference occurs between two solutions of different salinity when an ion exchange membrane separates them. As illustrated in Fig 1.6, this potential difference is the sum of several terms [112] and writes: $E_m = \Delta\phi_{D,L} - \Delta\phi_{D,H} + \phi_{m,L-H} + \phi_L^{SDL} + \phi_H^{SDL}$.

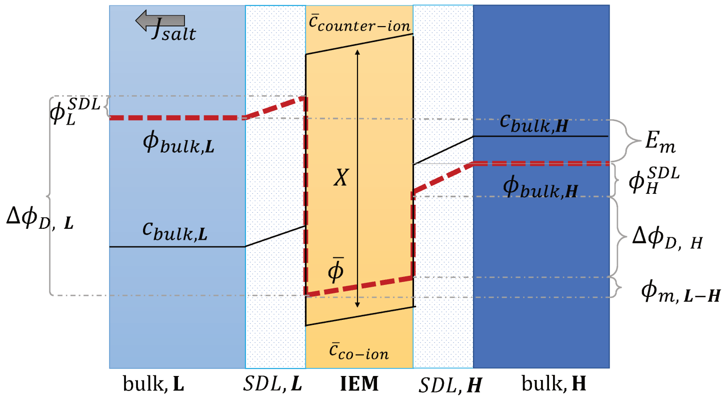

Fig. 1.6 Schematic representation of concentration, c, and potential, ϕ, profile in the bulk solutions, the stagnant diffusion layers (SDLs), and in an ion exchange membrane (IEM).(Figures and captions adapted from [112] with permission from FIMTEC & MPRL, copyright 2016.)

$\Delta\phi_{D,L}$ is called the Donnan potential in the diluted solution. It comes from the difference in ion concentration at the solution-membrane interface. In this context, the equality of chemical potentials leads to :

$$\mu_i^0 + RTln(a_{i,L}) + z_iF\phi_L = \mu_i^0 + RTln(\bar{a}_{i,L}) + z_iF\bar{\phi}_L \tag{1.4}$$

$$\Delta\phi_{D,L} = \frac{RT}{z_iF}ln(\frac{\bar{a}_{i,L}}{a_{i,L}}) \tag{1.5}$$

where F is the Faraday constant, z_i the valence of the ion, R the gas constant, T the temperature, $a_{i,L}$ and $\bar{a}_{i,L}$ are the activity of the ions on the external and the internal side of the membrane in the diluted electrolyte, respectively. ϕ_L and $\bar{\phi}_L$ are the electrical potential on the external and the internal side of the membrane in the diluted electrolyte, respectively. $\Delta\phi_{D,H}$ is the Donnan potential characterizing the concentrated solution. $\phi_{m,L-H}$ is the difference of potential occurring inside the membrane. ϕ_L^{SDL} and ϕ_H^{SDL} are the difference of potential created by Stagnant Double Layers (Boundary layer) that build up close to the membrane. These layers, also named as polarization layers, have fundamental impacts with the presence of electric current. As we will see later, they are usually considered as non-ohmic resistances in the analysis of RED systems. The modeling of all these terms is complex and requires complicated numerical simulations.

A simple limit can be found. In the absence of electric current through the membrane, in the case of a rigorously selective membrane, the diffusion potential vanishes. Neglecting the Stagnant Double Layers, the open circuit voltage writes:

$$E_m = \frac{RT}{z_i F} ln(\frac{\gamma_H c_H}{\gamma_L c_L}) \tag{1.6}$$

where γ_H and γ_L the activity coefficients, and c_H and c_L are the concentrations of concentrated and diluted respectively. with a_i=γ_i c_i.

Under the assumption of an open circuit and neglecting the polarization layers, this equation can be generalized to a non-selective membrane by writing: $E_m = \alpha \frac{RT}{z_i F} ln(\frac{\gamma_H c_H}{(\gamma_L c_L})$. where $\alpha = \frac{t^+ - t^-}{t^+ + t^-}$ with t^+ the transport number of the cation and t^- the transport number if the anion. To go further and calculate α, the modeling of all these terms is required. The most widely used description comes from the Teorell-Meyer-Sievers [113] theory which is a one-dimensional model that does not take into account the ions concentrations variations in the pore section of the membrane, nor the fluid transport by convection. The space charged model developed by Osterle and colleagues [114] takes into account these two points. Recently, interactions with surfaces and electro-osmotic effects have been taken into account in calculations to explain the strong ionic currents generated by charged but a priori non-selective nanotubes of more than 20 nanometers in diameter [115]. We will return to this point later in the text.

In a more pragmatic way, this description of the membrane potentials leads to propose an electrical scheme for a membrane. In the presence of different salt concentrations on both sides of the membrane, the membrane behaves like a voltage generator E_{OCV} which is the open circuit voltage in series with a resistor and with elements that account for the polarization layers. These double layers are resistors in parallel with phase elements or simply resistors[116, 117].

1.4.2 The RED cell

The RED device takes advantage of the potential difference that appears on an ion exchange membrane when it separates two saline solutions of different concentrations. A classic RED stack configuration is illustrated in Fig 1.7. Two types of IEMs are used in this configuration: anionic exchange membranes (AEMs) which allow the passage of anions and cationic exchange membranes (CEMs) which allow the passage of cations. These membranes are separated by spacers and are placed alternatively so as to form alternative water compartments. Diluted and concentrated solutions are injected continuously in water compartments by pumps. At two ends of the stack, two electrodes are placed with circulating electrolytes for energy conversion by redox reactions. In each compartment of the cell, where the solutions can circulate generally through a spacer to ensure an uniform flow, the ions try to move from the concentrated solution to the dilute solution to balance the chemical potentials, but due to the charge of the IEMs, only one type of ion is allowed to pass and the other type will be rejected. Thus, an ionic flux is generated allowing an electrochemical potential to establish in the surface of the membrane called Donnan potential. This potential is converted to electricity by faradaic reactions at the end of the cell by the electrodes and electrolytes.

In the following we will detail all the elements of the cell.

Electrodes

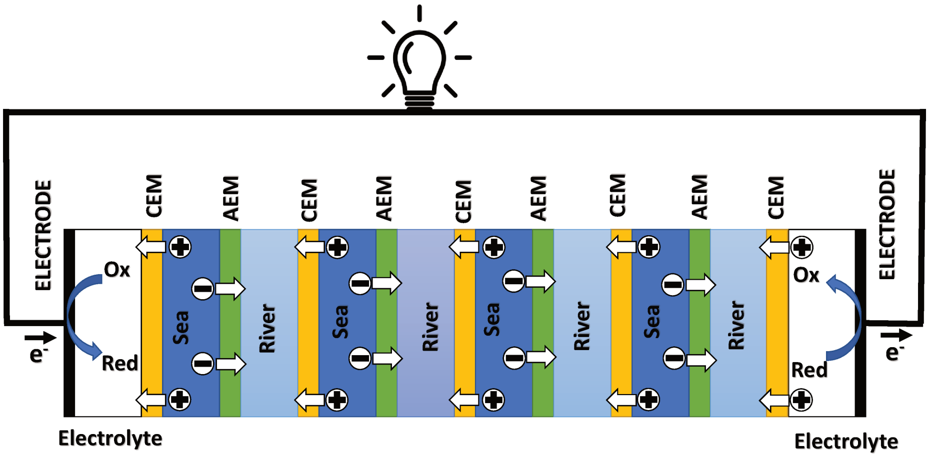

Fig. 1.7 A schematic illustration of the RED process.

Electrodes are used in RED stacks for the conversion of osmotic-driven ionic flux into an electric current by faradaic reactions. The choice of electrodes is of great importance for the optimization of energy conversion efficiency in RED stacks[118].

Several electrodes were proposed for RED systems, from participating electrodes like Ag/AgCl to inert ones like Pt, and with redox reactions ranging from hydrogen/oxygen reactions to more complex like $Fe(CN)_6^{3-}/Fe(CN)_6^{4-}$. These electrodes are classified to three main types summarized in the Table 1.3. The oldest electrodes[110, 119] were made of two metals immersed in a solution containing the metal ions. The metal (or the amalgam such as Ag/AgCl) participates directly in the red-ox reaction. Thereby, the electrodes were consumed during the process and their life span remains limited. For theses reasons, participating electrodes were dropped out in the latest development [120][121]. After that, inert electrodes were proposed to avoid the regeneration problem. They interact directly with the electrolytes and forming gases which is their major drawback[122]. Inert electrodes are used jointly with redox couples dissolved in the circulating electrolytes to enable the redox reactions for energy conversion. Inert electrodes present enormous applications in RED systems due to good chemical/ environmental advantage. The consumed ions in one electrode will be generated in the other one, and thus leading to no net chemical reaction at the end. At the same time, the electrolyte will be conserved and over-potential related to gas formation will be suppressed. The problem with this category is the nature of the couple: for the $FeCl_2/FeCl_3$ system, low pH is needed to prevent formation of solid (hydr)oxides[120]and for the Fe-complex couple, it is not stable during long time especially if exposed to light[123].

Ionic exchange membrane

The RED is a membrane based osmotic process where IEMs are considered as the main engine of the energy recovery. Membranes are usually characterized by several properties based on the amount, structure, type and the charge of the functional groups in the membrane. These proprieties are linked. IEMs are divided to three main classes: CEMs, AEMs and bipolar membranes according to the surface charge. CEMs possess negative charges with a fixed chemical group. Generally, chemical groups of strong acids, like sulphonate ($-SO_3{}^{-}$) and phosphorate ($-PO_3^{-}$), or weak acids like carboxyl groups ($-COO^{-}$) are used in CEMs. Due to the presence of negative charges in CEMs, anions in solutions are repulsed and the cations pass. For AEMs, cations are repulsed due to the positively charged chemical groups including ammonium ($-NR_3^{+}$), primary amine ($-NH_2$), secondary

Table 1.3 A summary of electrodes used in the RED

Type	Electrodes	Electrolyte	Advantage	Disadvantage	Ref
Inert electrodes with	Ti-RU/Ir mesh	$K_4Fe(CN)_6$ / $K_3Fe(CN)_6$	No electrolysis voltage losses	Sensible to light	[124]
reversible reactions	Ti-Ru/It mesh	$Fe(Cl)_2$ / $Fe(Cl)_3$	No net chemical reaction	Sensible to pH	[120]
			Bidirectional system		
Inert electrodes with	Ti-RU/Ir mesh	NaCl	No net chemical reaction	Voltage loss	[122]
irreversible reactions	Ti-Pt mesh	Na_2SO_4		H_2/Cl_2 Generation	[125]
Participating	Ag/AgCl	NaCl	No net chemical reaction	Switching flows	[126]
electrodes	Cu	$CuSO_4$	No electrolysis voltage losses	Electrodes	[110]
	Zn	$ZnSO_4$		regeneration	[119]

amine (-NRH) and tertiary amine (-NR_2). Bipolar membranes have simultaneously negative and positive chemical groups and display fascinating applications in water splitting. The main characteristics of commercial membranes, i.e. the swelling degree, the ion exchange capacity, the fixed charge density, the permselectivity, and the membrane resistance are reported in the Table 1.5 and Table 1.4.

The swelling degree (SD) characterizes the ability of a dry membrane to absorb water. It measures the mass change ratio of a dry membrane before and after water immersion :

$$SD = \frac{m_{wet} - m_{dry}}{m_{dry}} \times 100 \tag{1.7}$$

Where m_{wet} is weight of the wet IEM and m_{dry} is weight of membrane in its dry phase.

Ion exchange capacity (IEC) determines the number of fixed charges inside the IEM per unit of mass of a dry membrane.

The fixed charges in the membrane are usually in equilibrium with the ions in the electrolytes, This equilibrium is given by the Fixed charge density (CD) and it is defined as the milli-equivalents of charged groups per gram of water in the membrane. It is given by :

$$CD = \frac{IEC}{SD} \tag{1.8}$$

The permselectivity (α) is one of the most important parameters for ionic exchange membranes. It describes the ability of a membrane to reject co-ions (ions of same charge) and allow the passage of counter ions. An ideal membrane, which blocks all co-ions and allows passage of 100% of counter ions, is characterized by a selectivity of 1. In practical applications, the effective selectivity can be calculated by the ratio between the electrical potential measured between the electrodes and the theoretical one for an ideal membrane under a given gradient.

The membrane is a part of an electrochemical cell where the ionic current is converted to an electrical one. This current is directly affected by the conductivity of this membrane (ohm loss) and can influence the power density. This resistance is reported to a unit of area. It depends on the the material's property and its structure (see Table 1.4 and Table 1.5).

These properties depend on the conditions of use such as the concentrations of the saline solutions, the value of the difference in salinity, the acidity, the temperature. Using a very high concentration can reduce membrane selectivity even though it gives better conductivity [117, 121]. A high temperature [121] decreases the permselectivity of the membrane.

The characteristics of the membranes depend on the mode of production based on which IEMs are classified into homogeneous IEMs and heterogeneous IEMs. For the first class, the membrane is prepared using just one product, generally, by polymerization of a charged/can be charged monomers or followed by grafting functional monomers on a film/dissolved polymer [127]. On the other hand, heterogeneous IEMs contain two parts, an ionic exchange resin mixed with an uncharged polymer matrix without any chemical bound. Homogeneous IEMs exhibit excellent electrochemical properties, very low resistances and high permselectivity [128]. Their thickness is between 1 and 30 µm. However, their production is more complicated and more expensive. In contrast, heterogeneous IEMs are easier and less expensive to prepare with a good mechanical and chemical stability especially for the AEMs in alkaline electrolyte. However, their high resistance is still a major challenge for the RED technology. [129]. Recently, N.D. Pismenskaya et al.[128] modified an heterogeneous membrane by grafting functional quaternary ammonium groups to increase its electrochemical performance. The results are encouraging and close to that of a homogeneous IEM.

Table 1.4 A summary of the most used CEMs in literature

Membrane	Thickness (μm)	IEC (meq.g^{-1})	SD (%)	CD (meq.g^{-1} H_2O)	α (%)	R (Ω.cm^2)
CEM						
Neosepta CMX	164	1.62	18	9.0	99	2.91
Neosepta CMS	150	–	–	–	97	1.4–1.8
Neosepta CM-1	133	2.3	20	11.5	97.2	1.67
Neosepta CIMS	150	2.3	30	7.7	–	2.49
Fumasep FKD	113	1.14	29	3.9	89.5	2.14
Fumasep FKS-20	20	1.24	–		99	1.7
Fumasep FKE	34	1.36	12	11.3	98.6	2.46
Selemion CSO	–	1.04	16	6.4	92.3	2.26
Selemion CMV	101	2.01	20	10.1	98.8	2.29
Fujifilm V1	125	–	–	–	93	1.6
Fujifilm CEM RP1 80050-04	120	1.45	–	–	96	2.55
Nafion -115	139	0.9	–	8	–	–
Nafion-117	201	0.9	–	7.7	–	–
Ralex CMH	764	2.34	31	7.5	94.7	11.33
Qianqiu CEM	205	1.21	33	3.7	82	1.97
Tailor-made SPEEK 65	72	1.76	35.6	–	89.1	1.22
Tailor-made SPEEK 40	53	1.23	23	–	95.3	2.05

Table 1.5 A summary of the most used AEMs in literature

Membrane	Thickness (μm)	IEC (meq.g^{-1})	SD (%)	CD (meq.g^{-1} H_2O)	α (%)	R (Ω.cm
AEM						
Neosepta AM-1	126	1.77	19	9.3	91.8	1.84
Neosepta AFN	163	3.02	43	7	88.9	0.7
Neosepta AMX	134	1.25	16	7.8	90.7	2.35
Neosepta ACS-8T	150	1.9	–	–	–	2.41
Fumasep fad	74	0.13	34	0.4	86	0.89
Fumasep fas-20	20	1.5	31.25	4.8	95.5	0.5
Selemion DSV	121	1.89	1.03	183.5	89.9	1.03
Selemion APS	138	0.29	147	0.2	88.4	0.68
Selemion AMV	110	2.2	21	10.5	95	2.44
Fujifilm TYPE I	115	–	–	–	91.9	1.3
Fujifilm AEM RP1 80045-01	120	1.28	–	–	96	1.83
Fujifilm V3B	84	1.7	23	7.39	87	1.36
Fuji V3A	66	2.2	23	9.57	82	0.87
Fujifilm V1	139	1.8	23	7.83	90	1.05
Fujifilm V2	53	1.6	23	6.96	86	0.67
Ralex AMH-PES	714	1.97	56	3.5	89.3	7.66
Qianqiu AEM	294	1.33	35	3.8	86.3	2.85
Tailor-made PECH A	77	1.31	32.2	4.1	90.3	2.05
Tailor-made PECH B2	77	1.68	49	3.4	87.2	0.94
Tailor-made PECH B1	33	1.68	49	3.4	86.5	0.82

1.4.3 The power density

The maximal electrical power density in a RED cell is given by [122]

$$P_{max} = \frac{E_{ocv}^2}{4R_{cell}} \tag{1.9}$$

Where E_{ocv} is the potential generated using an ionic exchange membrane between two solutions under a salinity gradient. It can be described by the following equation:

$$E_{ocv} = \alpha N \frac{RT}{zF} ln(\frac{c_H \gamma_H}{c_L \gamma_L}) \tag{1.10}$$

With α the selectivity of one membrane, N the numbers of membranes, T the temperature, z the valence (z=1 for Na$^+$), R the gas constant, F the Faraday constant, γ_H and γ_L the activity coefficients, and c_H and c_L are the concentrations of concentrated and diluted solutions, respectively. And R_{cell} is the cell resistance which consists of two main parts, an ohmic one that represents the conductivity of cell components (including membrane, solutions, spacers, and etc.) and a non-ohmic part which involves the concentration change inside the cell. The non-ohmic part is caused by the polarization effect near membranes and by the salt concentration variation along the water channel.

To develop a production cell, it is necessary to choose the number of membranes to be used. A priori, it is interesting to increase the number of membranes. Using a large number of membranes should make the whole device more compact. When the salinity of the solutions is fixed, E_{ocv}, and P_{max} increases theoretically linearly with the number of cell pairs and is independent of the flow rate. The power density is therefore independent upon the number of membranes. Experimentally, H.Kim et al.[138] observe a different behavior. When the stack is supplied with a constant flow, the gross and net power density decrease when the number of membranes becomes higher than 200. These phenomena are caused by the polarization of the cell. When the pairs of cells are more numerous, the local flow rate decreases in each cell which favors mixing, the appearance of a concentration gradient along the flow and the growth of the thickness of stagnant ionic layers.

In fact, due to the polarization phenomenon, the open circuit potential increases with the number of cell pairs but the growth law between the two is weaker than a linear law. When the number of cells is fixed, the open circuit potential increases slightly with the flow rate. As the number of cells increases, the throughput in each cell is lower and the polarization effects along the cell but also the thickness of the depleted layers increases. Both effects induce a decrease of the open potential.

According to Equation 1.9, an efficient way for power density optimization is to increase the open-circuit voltage E_{ocv}. Several research works managed to ameliorate the membrane selectivity α or increase the number of IEM pairs used in RED systems. Güler et al. [136] tested several IEMs and found that the permselectivity could be independent of the thickness. H. Kim et al.[138] showed that the using a big number of cell pair will affect the residence time of the ions inside and therefore the concentration polarization inside the cell will cause a diminishing of the potential compared to the theoretical value.

For the non-ohmic resistance, the challenge is always present. Vermass et al.[139] attempted to improve mixing inside the cell to reduce the boundary layer using a specific spacer with filled channels and with sub-corrugations (see Fig 1.8.B) without much success.

For the use of more than 45 membranes in the RED system, Pattle et al.[110] reported a mild power density of 0.2 W.m^{-2} because of the low efficiency of their stack. Numerous studies continues today in the hope of promoting output power density of RED systems. In 2007, Długołecki et al.[129] investigated the performance of several membranes used generally in the RED, and estimated that a power density of 6 W.m^{-2} can be achieved by commercial IEMs. A year after, a power density of 0.84 W per square metre of membrane was obtained in the work of Turek et al.[125] with a high salinity gradient (around 200) and even a 0.9 W.m^{-2} is reached by Veerman et al.[140] with a salinity difference of 30 g.L^{-1} vs 1 g.L^{-1} of NaCl for the concentrated and the diluted solution respectively. High cell resistance hinders the electrical performance of RED systems[122]. It was reported that the diminution of spacer thickness (from 485 μm to 100 μm) could effectively reduce the ohmic resistance of the system by 4[124]. With these RED improvements, Vermaas et al.[124] obtained a gross power density of 1.8 W.m^{-2} using just 5 pairs of IEMs. However, for thinner spacers, a higher pressure loss was reported. A net power density of 1.2 W.m^{-2}, which remains the highest experimental net power density documented until present, was achieved in this work. The same team tried to removed the spacers and employed profiled membranes to reduce water volume (higher conductivity). While a significant ohmic resistance drop of 30% was achieved, the profiled membranes suffered from severe polarization problems which reduces the ohmic resistance around 30% but the polarization resistance was significantly higher[141]. Adding sub-corrugations to disturb the uniform flow and enhance the mixing was insufficient to increase the net energy power[139].

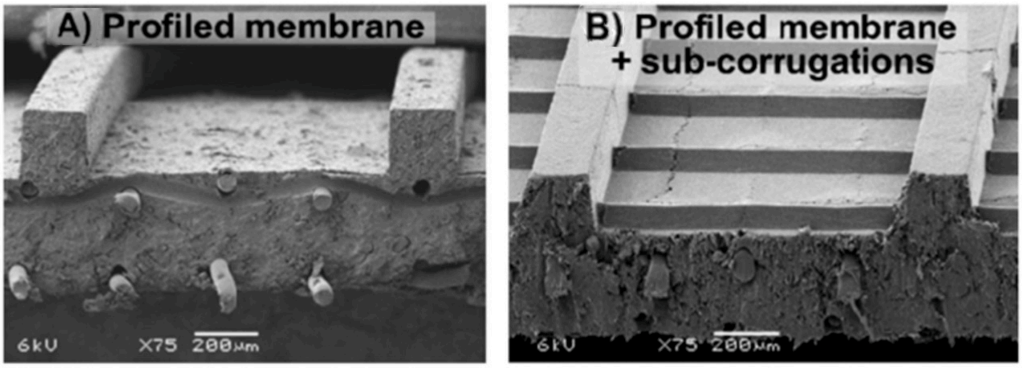

Fig. 1.8 Images obtained from a scanning electron microscope for **(A)** the profiled membranes **(B)** and profiled membranes with sub-corrugations. (Figures and captions reproduced from [139]with permission from Elsevier, copyright 2014.)

As already described, the potential E$_{OCV}$ between the stack's electrodes is directly related to the gradient. Daniilidis et al.[121] investigated the RED stack for hypersaline solution like the Dead sea, with a concentration close to the saturation (around 5 M) with a river water of 0.01 M concentration and they obtained a gross power density 3.8 W. m^{-2} at 25 °C and more than 6.5 W. m^{-2} at 60°C in 5 membrane pairs cell, even if the selectivity was lower with the increasing of the temperature and the gradient. This power density corresponds to a gross power. It's worth to note that even though this energy was experimentally measured, no pumping energy consumption was subtracted. In the same topic, and to show the effect of temperature and gradient, Tedesco et al.[132] used a hypersaline solution at 5 M and a brackish solution with 0.1 M, and reached a gross power of 6 W. m^{-2} at 40°C in a cell with 50 membrane pairs. In this situation, the resistance of membrane pairs is low.

In fact, the recorded experimental gross power density without correction was around 4.75 W. m^{-2} with 2-2.5 W. m^{-2} of dissipated power due to the pressure drop inside the cell. Increasing the unit size to the double and the number of the membrane pairs had only a slight reduction in the power density caused by the non-uniform distribution of fluids concentration. The amount of the theoretical power is very huge, it is estimated to be more than 2 TW in the world rivers and oceans[9]. Just a part of this power is actually exploitable by the blue energy harvesting technologies. The efficiency is defined as the ratio between the recoverable energy and the available Gibbs free energy in the water mixing of unit volume. Higher energy efficiency is achieved when the feed waters are recycled (multiple pass) [124] and a lower current density is applied (due to ionic shortcut currents)[140].

$$\eta = \frac{P_{max} . A}{\Delta G_{mix} . Q} \tag{1.11}$$

Where A is the membrane area and Q the flow rate. For the RED process, it depends on the flow rate and on the capacity of the membrane to exchange ions. As represented in the table 1.6, the efficiency remains under 50 %.

Table 1.6 The summary of processes of RED reviewed literature

Membrane	C_H (M)	C_L (M)	Temperature (°C)	Power density ($W.m^{-2}$)	Efficiency
Fumasep FKD/FAD	0.507	0.017	25	0.93	18 %
Neosepta CMX/AMX	1.899	0.01	-	0.72	-
Fumasep FKS/FAS	0.507	0.017	25	2	32 %
Fumasep FKS/FAS	0.507	0.017	25	1.8	∼ 15 %
Ralex Profiled CMH/AMH	0.507	0.017	25	0.8	< 1 %
Tailor-made SPEEK65/PECH B2	0.513	0.017	25	1.28	-
Qianqiu CEM/AEM	0.513	0.017	25	0.83	-
Custom-made composite/Selemion CEM/ASV	0.5	0.017	25	1.3	-
Ralex Profiled+sub-corrugations CMH/AMH	0.507	0.017	-	0.9	< -
Neosepta CMS/ACS	5	0.01	25	3.8	∼ 7 %
Neosepta CMS/ACS	5	0.01	60	6.7	∼ 20 %
Fumasep FK-20/FAS-20	5	0.1	40	4.75	< 1 %
Fujifilm CEM 80045-04/AEM 80045-01	4-5	0.03	23	1.35	2-3 %
Fujifilm CEM-80050/AEM-80045	0.762	0.005	20	0.3	-
Fujifilm CEM-80050/AEM-80045	0.762	0.005	60	0.705	-
Nafion/Neosepta N117/AMX	4	0.5	25	1.38	-

1.4.4 Nano RED

One way to increase the collected current density is to decrease the cell resistance and thus the membrane resistance. To do this, it has been proposed to work with membranes with nanometric sized holes. This attractive idea is based on the initial work on single nanotube. Remarkably, a giant ionic current was measured when a non-selective boron nitride nanotube (BNNT) is placed in a salt gradient (see Fig 1.9).

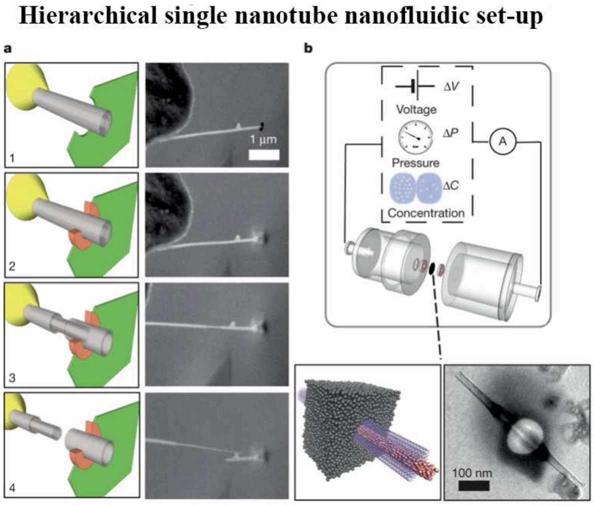

Fig. 1.9 **a**, In situ nanomanipulation of a BNNT (left, sketch; right, scanning electron microscope (SEM) images): 1, insertion of a BNNT (grey) through a nanopore drilled in a SiN membrane (green) using a focused ion beam (FIB); 2, carbon sealing of the FIB-drilled hole using local electron-beam-induced deposition (orange); 3, telescopic retraction of internal walls of the BNNT; 4, finalized transmembrane BNNT device. **b**, Top, schematic of the experimental set-up for measuring fluid transport through the single BNNT. Bottom, sketch of the final transmembrane BNNT for nanofluidic measurements (left) and its experimental realization, imaged by transmission electron microscopy (TEM) (right). (Figures and captions reproduced from [115] with permission from Springer Nature copyright 2013.)

For a BNNT placed between a 1 M and 0.01 M NaCl solution the authors measure [115] an electric current of 1 nA and a power density of 4 kW.m^{-2} for a nanotube (see Fig 1.10). This point is very remarkable. This potential is created by an electrophoretic flux due to the surface charge of the nanotube. Boron Nitride surfaces bear a large surface charge.

The ion concentration profile of the salt solution placed above this surface is given by: $C_{\pm}(x,z) = C_{\infty}(x)exp^{(-\pm\phi(z))}$ where $\phi(z)$ is the electrical potential, z the vertical position normal to the surface, x the position along the direction of the surface, $C_{\infty}(x)$ the concentration in salt far from the surface, $C_{+}(x,z)$ the concentration in positive counterions, $C_{-}(x,z)$ the concentration in negative counterions as a function of x and z. The balance along the z direction between the pressure forces acting on a fluid particle and the electrostatic forces links the pressure and concentration fields. This writes : $P(x,z) = P_{\infty} + 2k_BTC_{\infty}(x)cosh(\phi(z)-1)$ The concentration gradient along the loaded surface induces thus a pressure gradient along the same surface. This pressure gradient is at the origin of a Stokes flow in the nanotube whose maximum speed is given by: $V = \frac{k_BT}{2\pi\eta l_b} ln(1-\gamma^2)\frac{dlogC_{\infty}}{dx}$ with $\gamma = tanh(\frac{e\phi_o}{4k_BT})$ and ϕ_o the surface potential. The diffusio-osmotic flow drags the ions and produce an electric current by convection of the ions in excess. We recall that as the surface is charged, and as the liquid plus the surface is neutral, the

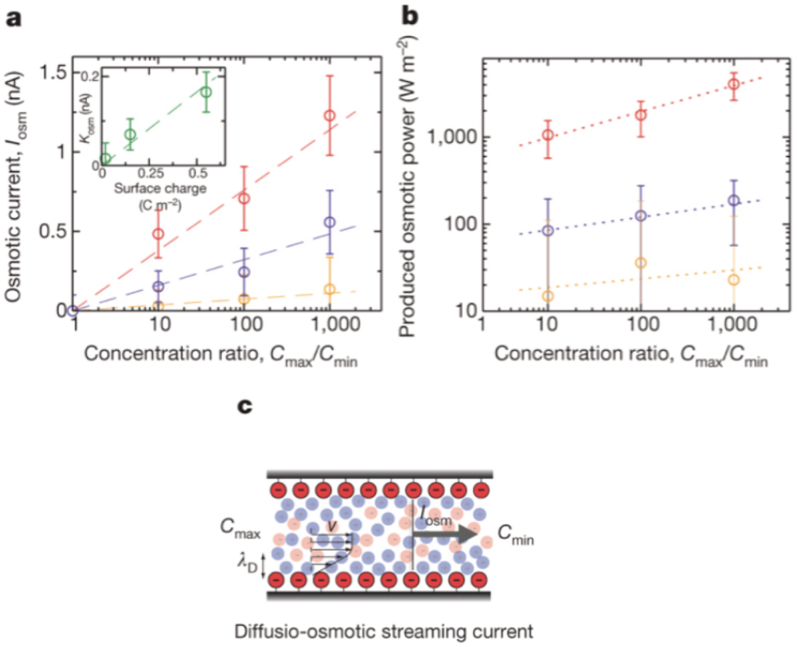

Fig. 1.10 **a**, Osmotic streaming current versus concentration difference for a t-BNNT with R, L 5 40 nm, 1,250 nm and pH 5.5 (yellow), 9.5 (purple) and 11 (red). The experimental points show measurements for various salt concentrations in the two reservoirs, with C_{min} and C_{max} in the range 10^{-3}–1 M. Error bars follow from the corresponding error analysis. Dashed lines are linear fits: $I_{osm} \propto log\frac{C_{max}}{C_{min}}$. **Inset**, osmotic mobility versus surface charge. Surface charge is obtained from independent conductance measurements. The dashed line is a linear fit with proportionality factor of 0.33 for the chosen units. **b**, Corresponding power density (per unit surface of the BNNT) for the three values of pH. Dotted lines are a guide to the eye. In the present graph, the minimum concentration is fixed to $C_{min}= 10^{-3}$ M. **b**, Sketch of the osmotically driven streaming current under a salt concentration difference, C_{max}-C_{min}. (Figures and captions reproduced from [115] with permission from Springer Nature, copyright 2013.)

liquid alone bears a charge which is opposed to the surface one. The obtained electrical current and potential drop are proportional to $\Delta logC_{\infty}$. This modeling is in quantitative agreement with the measurements.

A quantitative analysis of these equations shows that the power gain in the system comes from the very low electrical resistance of the nanopores. The potential difference across the nanotube is not exacerbated and remains about 100 millivolts under classic experimental conditions. The theory recovers an expression close to the one presented for the selective membrane when the radius of the nanopore goes to zero and when the surface charge is high.

This study has prompted many groups to prepare membranes with nanopores to increase the performance of the RED. At this stage, all the attempts end in failure to create large-scale membranes. Fig 1.11 compares the power and extrapolated on 1 m^2 surfaces and the powers measured on membranes. Clearly there is no correspondence between the two and the maximum powers obtained remain below 10 W.m^{-2}. This results comes from the existence of collective effects between nano-channels that prevent the generalization and extrapolation of the results obtained on a single nanotube. When the nanotubes are too close together in the membrane, the formation of ion depletion layer results in an effective concentration difference much smaller than the imposed one. The transport of an electrolyte within a single nanotube is therefore very different from that within a membrane

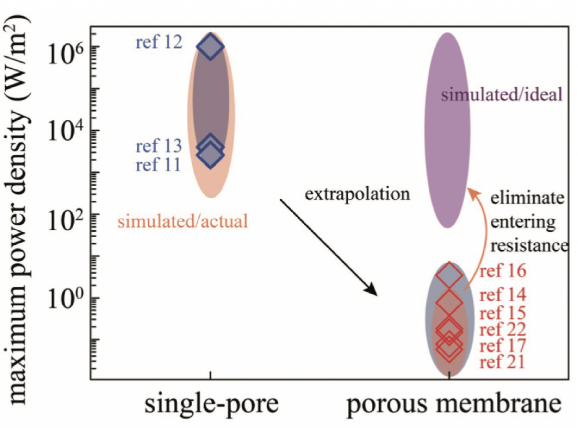

Fig. 1.11 Comparison between literatures reported power density and our simulated results. The range of simulated actual power density (upper left and lower right orange ovals) is approximately in agreement with that reported by literatures (blue diamond represents reported values) for both single-pore and nanoporous membrane systems, suggesting that our intuitive resistance paradigm semi-quantitatively explains the orders- of-magnitude power density gap between single-pore and nanoporous membrane systems. Remarkably, by eliminating the entering resistance, the simulated ideal power density (upper right oval) of membrane mate- rials can be brought back to the single-pore level. (Figures and captions reproduced from [145]with permission from John Wiley and Sons, copyright 2019.)

[145]. The results obtained, although disappointing at the level of extrapolation, are nevertheless better than the powers obtained in the experiments with polymeric membranes. It is necessary to comment on this point. All the experiments conducted on large hole membranes are done on systems with very small surfaces generally smaller than 0.01 mm^2. The system that allows the measurement of powers includes large volume of electrolyte and electrodes of large size. In this case the ionic resistance of the compartments is negligible compared to the resistance of the membrane, which is absolutely not the case in the RED experiments. It is therefore impossible to compare these data to the RED experiments.

Liu et al. [146]have developed a nanoporous carbon membrane via the thermal crossing of polycyclic aromatic hydrocrabons. They obtained a mechanically robust membrane of size 1 cm with 3.6 ± 1.8 nm pores and a thickness of 2.0 ± 0.5 nm. The pore density is close to 10^{10} pore by cm^2.They carry out RED experiments on a membrane 1 micrometer in diameter. They obtain by mixing artificial seawater (0.5 M NaCl) and river water (0.01 M NaCl) a power density of 67 W.m^{-2} for a circuit resistance of 15 MΩ. In the context of the experiment, the dominant resistance corresponds to the resistance of the membrane. The resistance of the electrolyte compartments is negligible. The resistance of the membrane can therefore be calculated and estimated to 0.19 $\Omega.cm^2$. This figure takes into account the resistance of the membrane and the resistance of the double layer near the membrane. It forgets the ohmic resistance of the solutions and the polarization resistance due to the drop of the concentration gradient along the membrane. Note that the values reported on Table 1.4 and Table 1.5 are closed to this one even though they do not take into account the resistance of the double layer near the membrane. To conduct a fair comparison, calculations of magnitude's order are necessary. The power generated by this membrane in the nanofluidic system is 67 W.m^{-2}. To generate such power, a flow rate equal to $Q = \frac{P}{\Delta G_{mix}}$= 4.7 × 10^{-5}m^3.s^{-1} is required assuming an efficiency of 100%. This corresponds to a viscous power by unit area of $P_{vis} = \frac{12\eta Q^2}{e^3 b^2}$ of 26 MW.m^{-2} for a gap e of 1 μm and 26 W.m^{-2} for a gap e of 100 μm. The ohmic resistance of a 0.01 M saline solution is equal to 7.8 Ω.cm^2 for a gap e equals to 100 μm. This value is much higher than the resistance of the membrane and must be added to it to calculate the performance in a device of 1 square meter. Clearly it will therefore be impossible to achieve such high performance in a device of one square meter in area. It is not possible to compare the power from nanofluidic devices and centifluidic devices with conventional membranes. An interesting study would be to measure the resistance of classical ion exchange membranes such as Nafion in nanofluidic systems.

In the previous framework, the creation of an ionic current in nanopores of several nanometers in diameter comes from the surface charge. Another way to do this is to be inspired by nature by creating nanopores covered by a very thin selective membrane. The realization [147]of robust mushroom- shaped (with stem and cap) nanochannel array membrane with an ultrathin selective layer and ultrahigh pore density, has notably allowed to obtain a power of 15 W.m^{-2} with a 10 mM/0.5 M salt gradient. The experiments are performed on a membrane of 8000 μm^2. From the data of the article, it is possible to calculate the resistance of the membrane. This resistance is 1.6 $\Omega.cm^2$. As discussed previously, such feature is very close to the one of classical membranes, which is unlikely to present exceeded performances in our point of view.

1.4.5 Impacts of multivalent ion mixing

In order to demonstrate the feasibility of the RED approach, complex salt components, including various multivalence ions, are added into concentrated and diluted solutions to simulate natural solutions in RED systems.

Post et al. reported in 2009 the impact of multivalent ion mixing on energy performance of RED system[148]. They observed a significant stack voltage drop, due to the presence of multivalent ions. This effect is especially remarkable while multivalent ions present in the dilute solution. This is explained by the uphill effect, which results in a reversed transportation of multivalent ions against the concentration gradient. In addition to his phenomenon, they observed an increase of membrane resistance. To reduce the limit on energy performance, they suggested the use of monovalent-selective membranes. As reported in the work of Vermaas et al.[134], the introduction of $MgSO_4$ in feed solutions in RED systems led to a reduction in stack voltage, leading to a detrimental power density decrease of up to 50 % compared with artificial solutions composed of NaCl (Fig 1.12). Multivalent ions negatively impact the membrane in RED systems in several ways: they increase membrane resistance, reduce permselectivity, and lead to uphill transport, where ions move against their concentration gradient, causing a loss of power output. Long-term issues arise as multivalent ions become trapped in the membrane, neutralizing fixed charges and reducing ion exchange capacity and permselectivity, ultimately diminishing the system's efficiency. The negative effect due to the presence of multivalent ions is confirmed in various research works[149, 150]. Based on all the power loss mechanism originated from the multivalent ion presence, Pintossi et al. developed a model to conclude the three major aspects, including membrane resistance increase, uphill effect and membrane selectivity loss[151]. The model provides accurate description of the RED system performance with multivalent ion mixing. To provide further insight into the influence of multivalent ions, Jin and Jin reported Nernst-Planck based framework to analyze the RED model[152].

More specifically, studies were carried out to understand different mechanisms. In the work of Avci et al., where evidence of the uphill transport of divalent ions Mg^{2+} is confirmed by Ion Chromatography analysis conducted on inlet and outlet streams of the RED system[135, 144]. It is demonstrated theoretically by Moya that the uphill effect is especially remarkable while multivalent ions present in the dilute solution[153]. This result is in accordance with the previous experimental data. To further reveal the impact of multivalent ion mixing on ion exchange membranes, Fontananova et al. conducted systematic studies to evaluate the common ions as

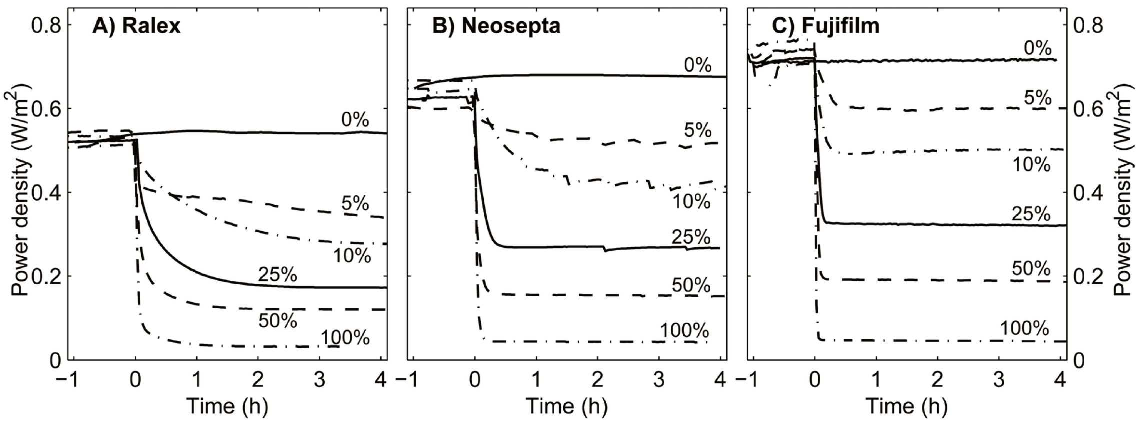

Fig. 1.12 Power density as a function of time, for stacks with (A) Ralex membranes, (B) Neosepta membranes and (C) Fujifilm membranes. At time = 0 h, the feed water source is switched from NaCl solutions to salt solutions with a certain percentage of $MgSO_4$ (as indicated in the graphs) and the remaining percentage of NaCl. Small deviations in power density are observed for all stacks with 5 % $MgSO_4$ and the Neosepta stack with 10 % $MgSO_4$, which are due to temporary entrapment of air in the feed water. (Figures and captions reproduced from [134]with permission from Royal Society of Chemistry, copyright 2014.)

Mg^{2+}, Ca^{2+} and SO_4^{-2}[154]. They identified a strong negative effect of divalent ions on both ionic resistance and permselectivity of ion exchange membranes.

Oh et al. confirmed that as divalent ions of small hydrated radius presents higher electrical resistance in CEMs[155]. Gomez-Coma et al. studied experimentally the effect of multivalent ion species on membrane resistance[156]. They provided firstly a mathematical correlation to further predict the energy performance of RED stacks for saline solutions of different concentrations. To go further, a theoretical description of resistance based on Donnan exclusion theory for the gel phase is proposed by Veerman et al[157].

To go beyond lab-scale experiments, pilot scale experiments were carried out with real-world solutions. Under the framework of EU-founded project REAPOWER, Tufa et al. designed a similar RED system and conducted a performance measurement by using real brackish water and brine from a solar pond in Italy[158]. While the system reaches a maximum gross power density of 3.04 W.m^{-2} per membrane pair operated with a salinity difference of NaCl 5M vs NaCl 0.1M, it presents a dramatic drop both in cell voltage and in energy performance with real solutions. A remarkable increase of stack resistance of 75 % and a significant loss of power density of 64 % is reported. The study identifies Mg^{2+} responsible for the consequent power density depletion. At larger scales, Tedesco et al. performed energy performance on full-scale RED pilot plant by the use of natural streams[143]. They discovered a power density of 1.6 W.m^{-2} per membrane pair using brackish water and saturated brine with a salinity difference of $NaCl_{equivalent}$ 0.03 M vs 5M. They observe an increase of 60 % while using NaCl solutions, with a power density of 2.7 W.m^{-2} per membrane pair. Later in 2017, the same group conducted real solution tests on a scale-up of the pilot plant, with a total membrane surface over 400 m^2[159]. Similarly, they observed a drop of 50 % on power density while real saline solutions were performed. While with artificial NaCl solutions RED stack delivers a net power output of 250 W, this figure is reduced to 100 W due to the presence of complex ions. The study of RED stack project in the Netherlands confirmed as well the power density drop under uphill effect[160].

To overcome this problem, monovalent-selective ion exchange membranes were proposed to replace conventional membranes. Rijnaarts et al. suggested the use of monovalent-selective membranes and multivalent-permeable membranes for mitigate the impact of divalent ions[161]. According to their experimental results, monovalent membranes block divalent transport, thus reduce the uphill effect related voltage drop. Multivalent-permeable membranes reduces the resistance increase in membranes. Both strategies improves the energy performance of RED system in solutions containing complex ions. Similarly, Moreno et al. conducted series of studies to evaluate different types of CEMs[130] . They tried two different strategies to minimise the negative effect of uphill transport (multivalent ions transport against the concentration gradient). The first one is using a highly cross-linked cationic monovalent membrane. This type of IEMs select the ions with the same charge based on their size (hydrated ionic radius). It blocks the multivalent ions and allows the transport of monovalent ions only. The second strategy is based on the charge rejection. A standard CEM with a thin positively charged layer on the membrane surface. A constant OCV was obtained using a mixing between NaCl and $MgCl_2$ compared to pure NaCl solution for the monovalent CEM. Also, for the coated CEM, a slight decrease in the OCV was observed. The membrane resistance was higher due to the lower ion mobility of magnesium ions inside these membranes. Hence, the power density was lower. Great efforts are being made in the design of efficient and cost-effective monovalent-selective membranes[142, 162–164].

At pilot scale, Mehdizadeh et al. reported the energy performance of a pilot-scale RED stack in Okinawa Island in Japan[131]. It is the first pilot scale RED stack using asymmetric monovalent selective membranes. Comparing the energy performance between artificial solutions and natural solutions, they observe a power density decrease of around 35 %. This drop is lower than that reported for REAPOWER. It originates from the fact that the monovalent selective membranes effectively reduce the uphill effect. Using natural salt-lake brines, Zhu et al. reported also a significant power density amelioration of around 120 % due to the use of monovalent selective membranes[165].

As suggested by Veerman, there are still numerous challenges and unresolved methods to address in order to reduce power losses in the presence of multivalent ions[166]. There is a lack of standardized methods for evaluating the impact of multivalent ion mixing on membrane resistance. While various studies have shown improvements in power generation through the use of monovalent-selective membranes, there is still a need for long-term performance reports and associated economic analyses. Significant attention is being directed towards membrane development, but it is also crucial to explore other strategies for reducing the uphill effect or mitigating membrane poisoning issues. Overall, the development of efficient and economically viable technologies for the partial recovery of osmotic energy in challenging conditions could potentially revolutionize the energy balance and carbon footprint of industrial processes.

1.4.6 Fouling

The natural solutions are even more complicated and contain more species than the ions. Several works studied the behavior of RED stacks with natural feed. Kingsbury et al.[167] evaluated the response of a RED unit fed with five different pairs of real waters and wastewaters. They reported that natural organic matters reduced power densities by up to 43%. Cosenza et al.[168] tested different solutions from oil industrial wells, where the high concentrated solution contains an important amount of organic and dissolved solids, and the diluted solution was prepared with 0.7 $g.L^{-1}$ NaCl solution. They measured a greater resistance (around 40% at less concentrated solution) for the natural one compared to a NaCl-artificial salt water causing a 17 % power loss. That effect was even worse when natural solutions from Licetto River and Tyrrhenian Sea in Italy were used in concentrated and diluted compartments, respectively[144].

In addition to this negative effect, fouling remains a tricky problem in long-term experiment, causing severe resistance increase and permselectivity hindrance. In 2012, Vermaas et al.[169] established RED stacks with water feeds of naturel river water (Van Har-inxmakanaal- Netherland) and naturel sea water (Wadden Sea- Netherland) filtered by a 20 μm diameter filter. During the 25-day continuous test, they observed a significant resistance rise, along with a slight decrease in membrane permselectivity, which results in a power loss of 60% of the RED system. This result was confirmed by the work of Vital et al.[170], where after 54 days, the power density decrease by 25%. This fouling comes in two major parts of the RED stack, the IEMS and the spacers. For the IEM we can determine two kinds of fouling depending on the charge of the membrane: The organic and the bio-fouling, generally negatively charged, are more occurred on the AEMs. In contract of the CEM, where the main problem is scaling and the solid particles. In the other hand, the fouling in the spacer can directly detect by a drop pressure jump inside the cell [169] and channel clogging, shown by Cosenza et al.[168], due to bacteria growing in the channels of the RED unit and in the dilute solution circuit, hence, The fouling is most probably in river water.

To control this fouling, various strategies are proposed at different levels: before pumping the steams, inside the RED stack, by slowing the formation of fouling and after by removing all blocking particles.

The first barrier can be a simple pretreatment a 20 µm pore size mesh filter, proposed by Vermaas et al.[169], to filtrate the biggest particles. Vital et al.[170] add to this last a second filter media composed by a 50 cm layer of anthracite (1.2–2.0 mm Ø) on top of a 50 cm layer of sand (0.5–1.0 mm Ø), placed into 11 cm Ø polyvinyl chloride (PVC) pipe. An optimization of the spacers was proposed to reduce the fouling by Vermass et al.[141] where they replaced the traditional spacers and IEMs by profiled membranes, and they found that the pressure drop increased four times slower and the power density remained relatively higher. He et al.[171] confirmed this importance of the spacers and proposed a new type with different inlet and outlet to enhance the hydraulic performance and the power density.

Another solution is to modify the anionic exchange membrane surface to make it less attractive to biofouling. Vaselbehagh et al.[172] coated a polydopamine layer on the surface of an AEM and found that it reduces bacterial attachment.

Various methods, suggest treating the IEMs with some polymer layer to make them selective for monovalent ions and to reduce the uphill effect and the fouling[130]. From these methods, we can find Gao et al.[163] who realized a deposition of two polymers poly(styrenesulfonate) (PSS) and poly(ethyleneimine) (PE) on the surface of an AEM to compare it with commercial one and they showed a good monovalent-anion selectivity comparable, a better anti-organic fouling potential and slightly lower gross power density due to the membrane resistance.

The last strategy is occurred when the fouling is already present. A physical cleaning is used by increasing the pressure or the flow rate for few seconds (a pulse) inside channels to destroy the substances clogging the channels. A chemical washing could be beneficial using some acid and alkaline solutions. To avoid bacteria and algae proliferation, a UV lamp could be installed. With these strategies, they were able to ensure a positive net power density value for more than 18 days using feed from oil well industry[168].

1.4.7 Scale up

After the lab test, researchers tried to exploit the RED technology at an industrial scale (Table 1.7). In 2014, a group from a research institution (Wetsus in Netherlands) succeeded to open the first RED plant called REDSTACK with a final power capacity of 50 kW using the freshwater from Lake IJssel and the saltwater of the North Sea available at Afsluitdijk, in Netherlands.

A year after, a pilot plant is started in south of Italy with a RED unit equipped with 50 m^2 of membranes, and working with natural concentrated brine from saltworks basins and brackish water from a shoreline well over a

Table 1.7 A summary of RED Pilot

Year	σ_H (mS.cm^{-1})	σ_L (mS.cm^{-1})	Membrane Area (m^2)	Membrane pair number	Gross Power density (W.m^{-2})	Reference
2016	150-220	3.4	48.4	125	0.8	[143]
2017	150-220	3.4	435	1125	0.76	[159]
2019	52.9-53.8	1.3-5.7	250	1000	0.38	[173]
2020	83.5-92.3	1.3-2.2	40	200	0.54	[174]
2021	51.9±1	0.34± 0.05	179.4	299	0.62	[131]
2021	81.9± 1	0.34± 0.05	179.4	299	0.96	[131]
2022	31.4± 4.1	0.52±0.02	3.1 + 6.2	32 + 64	0.4	[160]

period of five months during the summer. The gross power density was around 0.75-0.85 W.m^{-2} corresponding to 40 W with an average net power of 25 W [143]. This pilot[159] has scaled up to reach more than 400 m^2 of total membrane area, delivering a 330 W of gross power capacity which is equivalent to around 0.76 W.m^{-2} of power density. After that, a south Korean group built a cell with around 1000 cell pairs with a total area of 250 m^2 and tested it with Ocean lava seawater and wastewater effluent from a sewage treatment plant located beside the sea in Jeju, Korea. The pilot plant was able to produce 95.8 W of power (0.38 W.m^{-2}) [173]. Recently, Yasukawa et al.[174] obtained 0.46 W. m^{-2} net power density with a stack of 200 pairs of IEMs, corresponding to 40 m^2 of total effective membrane area, and streams from a seawater reverse osmosis (SWRO) desalination plant, Mamizu Pia (Fukuoka, Japan), and the Wagiro water treatment center (Fukuoka, Japan). The same team evaluated the performance of the RED pilot plant (RED stack) with 299 cell pairs and a 179.4 m^2 membrane effective area, installed in the sea water desalination unit of Okinawa islands in Chatan town, Japan, using one-side monovalent exchange membranes to reduce the u-phill effect [131]. Surface water was used as the diluted solution, while the sea water and brine from the desalinisation process were used as concentrated solution. The maximum gross power output of 171.6 W (0.96 W.m^{-2}) for the brine/river water and 110.6 W (0.62 W.m^{-2}) for the combination sea-river solutions.

1.4.8 Miniaturized Systems

One of the major advantages of RED technologies is its potential in both scaling up and miniaturization. Emerging researches focus on the development of mini-RED stacks in order to power future wearable devices, implantable sensors, bio-compatible and clinical implant systems, etc. To realize mini-RED devices, researchers can always find an exquisite and highly efficient example from nature: the electric organ of eels[175]. The electric organ is composed of long and thin cells separated by ion gradients[176]. The adjustment of K^+ channels and Na^+ channels could efficiently switch between rest stage (where zero voltage is generated) and firing stage (where a voltage of 150 mV appears across one single cell)[177], as illustrated in Figure 1.13(a) and (b).

Inspired by electrocyte in an electric eel which can generate potentials of 600 V, Xu and Lavan proposed in 2008 the artificial cell conception for biological ion concentration gradient harvesting[178]. Based on the model established for natural electrogenic cell, they proposed methods for constructing artificial cells which have higher power density output and energy conversion efficiency according to their theoretical calculation. Also inspired by electric-eel organs, Schroeder et al. realized an excellent design of scalable stacking of miniature polyacrylamide hydrogel compartments coupled with series of alternative cation- and anion- selective hydrogel membranes[177]. Such design consists of a mini-RED repeating module composed of concentrated salinity hydrogel, cation-selective gel membrane, diluted salinity hydrogel and anion-selective gel membrane (Figure 1.13(c) and (d)). While stacking these modules in series up to 2449 units, an open-circuit potential of 110 V, along

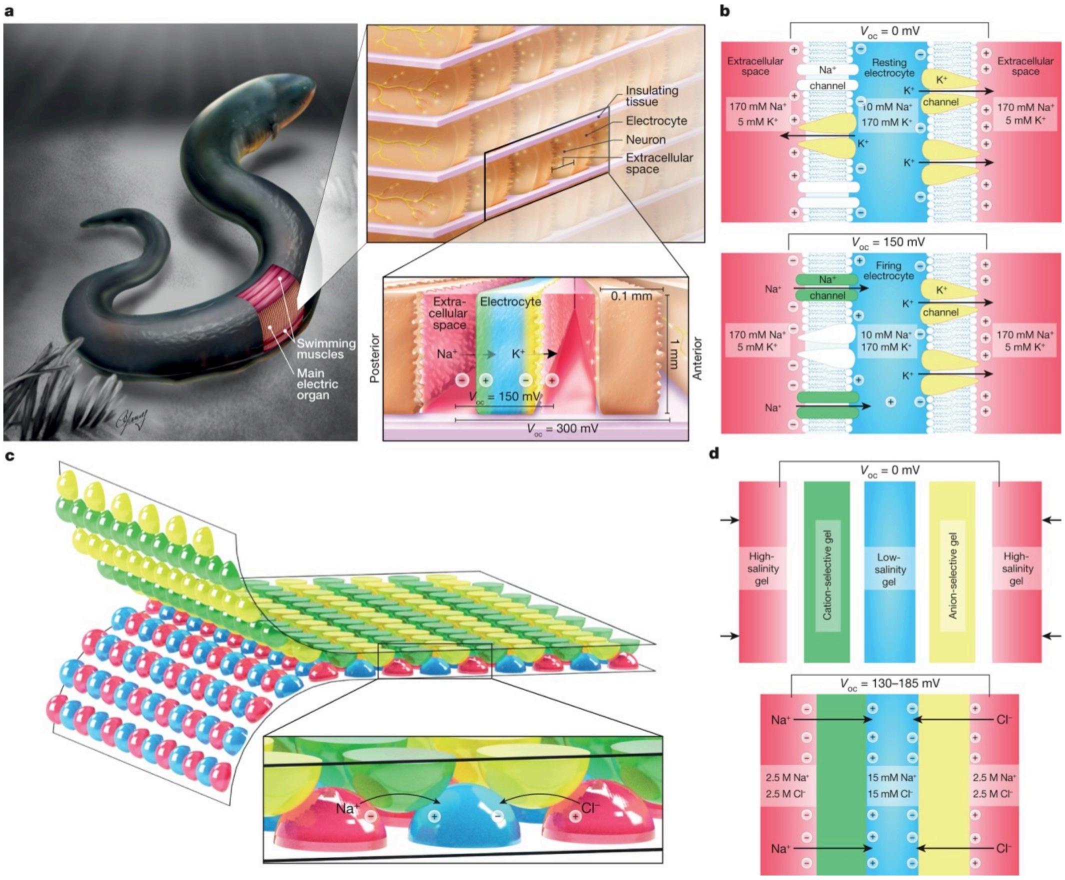

Fig. 1.13 Morphology and mechanism of action of the eel's electric organ and the artificial electric organ. (a), Electrophorus electricus. The top inset shows the arrangement of electrocytes within the electric organs of Electrophorus electricus. The bottom inset shows ion fluxes in the firing state. (b), Mechanism of voltage generation in electrocytes. (c), Artificial electric organ in its printed implementation. (d), Mechanism of voltage generation in the artificial electric organ. Figures and captions reproduced from [177] with permission from Springer Nature, copyright 2017.

with a power density of 27 mW.m^{-2} per tetrameric gel cell is reported. The afore-mentioned work was followed by a similar ionic hydrogel battery in a microfluidic version realized by He et al.[179] They designed typical well arrays and microfluidic channels to enable fast hydrogel assembly within several minutes. This microfluidic design avoids the time-consuming step for hydrogel assembling and provides a further insight for the wide application of power supply for soft and wearable devices.

To fulfill the power supply demand of small scale devices, miniaturized batteries are being extensively studied. In the work of Banan Sadeghian et al., miniaturized RED systems with a diameter of 5 mm are developed for energy generation[180]. Such system is coupled with a microfiltration AEM and copper electrodes. To avoid the use of pumping systems, the solution in the reservoir is not refreshed. This miniaturized system is reported to obtain a maximum energy density of 0.4 mJ.cm^{-3} with an operation time of 3 h when connected with a 2 kΩ resistor. Considering the low energy efficiency estimated at 0.44%, system optimization is required to open up its application field. Tsai et al. reported a circular microchamber system containing a home-made Nafion microchannel with a typical surface of 23×500 μm^2 and a channel length of 1-3 mm[181]. Ag/AgCl electrodes

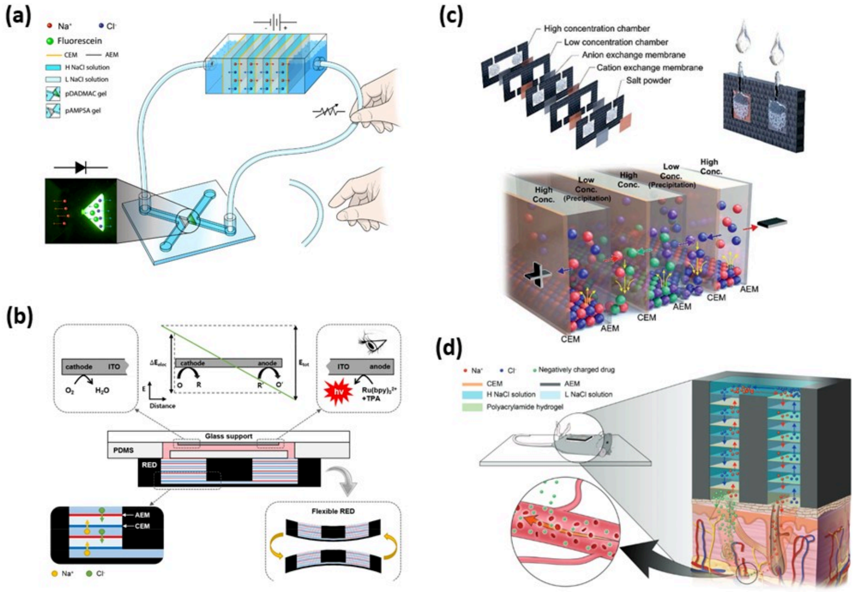

Fig. 1.14 Miniaturized RED-integrated ionic devices, analytical sensors and biomedical applications. (a), Illustrative schematic of ionic circuit powered by RED. Voltage generated from RED is applied to microfluidic polyelectrolyte diode directly via tubes filled with electrolyte. Figure and captions reproduced from [183] with permission from Springer Nature, copyright 2017. (b), Schematic Design of the RED-Powered Biosensing System. Figure and captions reproduced from [184] with permission from American Chemical Society, copyright 2018. (c), Schematic diagram of ssRED composition, its working principle and the activation process. Entry of water through inlets and dissolution of solid salts in high concentration chambers activate the ssRED. Figure and captions reproduced from [185] with permission from Royal Society of Chemistry, copyright 2018. (d), Schematic representation of the electrodeless RED patch attached on the mouse skin. Figure and captions reproduced from [186] with permission from John Wiley and Sons, copyright 2018.

and KCl solutions of a concentration ratio of 2000:1 are used in the experiment, resulting in a maximum power density of 755 mW.m^{-2}. Chang et al. reported a pump-less paper-based RED system for power supply[182]. The unique design avoids the use of traditional pumping systems. In fact, both concentrated solution and diluted solution are driven into the paper-based system under capillary effect. Based on a specific channel design, the injection flow rates are maintained at a constant level. This unique design reduces the system cost and enables an practical integrated power supply device. Despite the low power density (275 nW.cm^{-2}) reported in the work, such system presents a rather high operating time (1h), which presents potentials in powering disposable and cost-less analytical devices.

Lin et al. developed a hydrogel-based RED system, comprising two agarose hydrogel chambers with different potassium chloride concentrations and a cation-selective gellan gum membrane[187]. The RED system is fully designed with bio-compatible materials and presents a open-circuit voltage of 177 mV. In this work, the first TENG-RED combined system is reported. An auxiliary TENG system based on Chitonsan/glycerol and PTFE materials as tribo-layers is developed. The TENG system serves as the charging component while connected with a full-wave rectifier. A maximum charging voltage of RED system is reported at 350 mV.

Informative signals are delivered by electrons in a traditional electronic circuit. However, in biologic systems, information transmission is realized by ions and molecules. The concept of iontronics is positioned between these two systems, where only ions are used for signal transmission in polyelectrolyte gels or electrolytes in aqueous solutions[188]. Currently, various ionic components are extensively studied to complete the iontronic toolbox[189–191]. The development of iontronics aims to realize biocompatible information processors to open up the possibility of biological communications directly with living organs[191]. Hopefully, based on this neuron-like and biocommunicable system, an aqueous computer could be developed in the future.

One of the essential obstacles is to design stable and bio compatible power supply systems. The integration of conventional electronic power generators requires the use of electrodes, where faradaic reactions and interfacial resistances could hinder its practical use. In this case, miniaturized electrodeless RED systems become an excellent candidate to power ionic circuits. Han et al. firstly reported a RED-driven complete iontronic circuit as a polyelectrolyte diode[183]. As illustrated in Figure 1.14(a), a 25-IEM-packed RED system serves as the power supply of an ionic diode composed of a pair of positively charged poly(diallyldimethylammonium chloride) (pDADMAC) and negatively charged poly(2-acrylamido-2-methyl-1-propanesulfonic acid) (pAMPSA) prepared on a microfluidic chip. A flexible and ion-conducting tube is used for the connection between RED and chip. Experimental results demonstrate the forward bias state and reverse bias state of the ionic diode powered by miniaturized RED system. The combination of 2 ionic diodes enables the creation of a logic OR gate, which is also experimentally demonstrated in the work.

Miniaturized RED systems could become an excellent candidate for power supply of disposable bio-sensors and microfluidic analytical devices. They possess the advantages of direct ionic flow creation, along with an instant electrical potential difference establishment and IEM stack based scaling up potential, which could be directly integrated into analytical devices to provide electrical energy.

The electrochemiluminescence (ECL)-based bioanalysis platform is a powerful analytical tool while combining with bipolar electrodes (BPE). While faradaic reactions appear on bipolar electrodes under external voltage, the ECL signals could provide information concerning the quantitative analytes on BPE surface. As demonstrated in Figure 1.14(b), Baek et al. introduced the use of patch-type mini RED systems to power such platform in an electrode-less and environment-friendly way[184]. The direct ionic flow creation by RED system could avoid the voltage drop and faradaic reaction problems in conventional battery power supply. An integrated analytical system for glucose detection, coupled with RED stack powering system, was demonstrated in their work. The work of Yeon et al., has further promoted the development of disposable solid salt RED (ssRED) power source[185]. They designed a one-shot water-activated RED source where two kinds of salts ($Ag_2SO_4/BaCl_2$) are used alternatively in high concentration chambers (Figure 1.14(c)). The activation step requires simply the addition of water into the chambers. As CEMs and AEMs are used alternatively, ions in high concentration chambers penetrated into diluted chambers become insoluble precipitations (AgCl or $BaSO_4$) through metathesis reactions. This ensures a stable concentration ratio, thus a longer operation time of the system. The integration of such system with above-explained BPE system and Ionic diodes are well demonstrated in their work.

Miniaturized RED systems are also widely used in skin-wearable biomedical devices. As presented in the work of Kwon et al., patch-type RED stacks are designed to power active transdermal drug delivery platforms[186]. The electrodeless design of RED patches present excellent advantages in biocompatibility and cost reduction. By adjusting the inserted number of membrane stacks, a controllable voltage is applied on the drug delivery platform to pump ionic drugs to penetrate the skin, as described in Figure 1.14(d). Experimental results proved the feasibility of such systems for in vitro drug delivery of 3 representative drugs. Such design could be generalized and integrated for other portable biomedical devices. Pakkaner et al. reported a miniaturized RED driven biopower cell designed for auto-powered implantable medical devices[192]. The power supply is designed to harness the concentration gradient in physiological fluids in renal artery and vein for example. This fluidic device is designed with alternative CEMs and AEMs with a concentration ratio of 7.2 g/L and 9.0 g/L and is kept at 37 °C in order to imitate in vivo conditions. The same group reported an effective way for performance amelioration of the biopower cell: an additional salt-cartridge for concentration ratio boost[193]. Polysulfone (PSf) hollow fiber membranes saturated with NaCl solutions are prepared as salt cartridge. A diluted stream is divided into diluted sub-stream, which is pumped directly into freshwater chambers, and a feed acceptor stream, which passes through the salt cartridge for salinity increase and serves as saltwater chamber reservoirs. A 3-fold increase of OCV of the cell is reported for the salt-cartridge boosted biopower system. It is to mention that although these two works present excellent potentials for miniaturized systems for biomedical applications, the feasibility of practical RED-driven implantable devices is yet to be verified by in vivo experiments.

1.4.9 Economic analysis

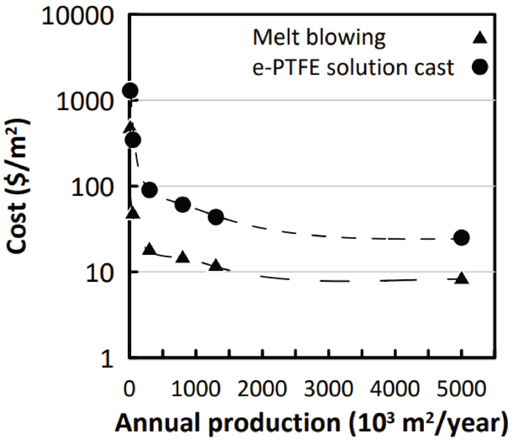

Fig. 1.15 Cost estimation of PFSA electrolyte membrane produced by two different methods as a function of the total yearly production. (Figures and captions reproduced from [135] with permission from MDPI, copyright 2020.)

Several works discussed the economic and financial feasibility of RED for different scenarios. It was shown that the dominating influential factors include the membrane price, which remains very high at present, followed by the inflation, the relatively low experimental power generation and finally the cost of water pre-treatment and pumping[194].

Thin homogeneous membranes with low resistance are generally of high prices (above 80 €.m^{-2}) [195]. In 2007, Turek at al.[196] found a very high cost equal to 6.5 €.kWh^{-1} by using an experimental power density value of 0.92 W.m^{-2} of cell pair and considering a total investment cost of 96 €.m^{-2} of installed membrane. In 2010 Post et al. [197] fixed a viable power density of 2 W.m^{-2} with a membrane price of 2 €.m^{-2} and cost of 0.08 €.kWh^{-1} for the electricity. Daniilidis et al.[194] suggest that if the membrane technology will be developed by using cheap raw materials and manufacturing procedures in the near future, same as in the ED technology with heterogenous membrane, allowing a membrane price below 4.3 €.m^{-2}. A net power density of 2.7 W.m^{-2} will be sufficient to start producing energy. And with a LCOE fixed at 0.16 €.kWh^{-1} will make RED electricity competitive against conventional and established renewable technologies. Another study was done by Toupin et al.[198] on the cost of Nafion and other perfluorinated sulfonic acid (PFSA) polymer electrolyte membranes.

They estimated that with a higher annual production (around 5 million m²), the cost of 1 m² of membrane will be below 10 $ for the melt blowing method [135][198](see Fig 1.15).

In 2019, Giacalone et al.[199] estimate the Levelized Cost of electricity ranging from 0.27 to 0.33 €.kWh^{-1} based on membrane cost of 15 €.m^{-2}, and using brine and freshwater. This cost is lower than the actual electricity prices in certain countries in Europe ,that achieve 0.56 €.kWh^{-1} last August in Germany. It's worth to note that with the latest events in Ukraine, the fast inflation in the world, and the energy price rise (especially for the natural gas) may make the RED competitive with other power sources.

1.5 Capmixing

Firstly proposed in 2009 by Brogioli[200], Capmixing is an emerging blue energy harvesting energy with tremendous potential. Unlike PRO and RED where energy conversion is realized through intermediate steps of mechanical turbine systems and electrochemical redox reactions, Capmixing generates electricity directly from a controlled mixing procedure[18]. In a classic configuration of Capmixing illustrated in Fig 1.16(A), two porous carbon electrodes are dipped into high concentration solutions at initial state. It is an energy consuming state where electrodes are charged by an imposed external electric source. Thus, electrical double layers (EDL) are formed near each electrode to maintain a local electron neutrality in the solution[13]. In state II, the system is in open-circuit state and the high concentration solution in the system is replaced by solution of lower concentration. As the ionic strength lowering of the electrolyte results in a thickness expansion of the EDL, the overall capacitance of EDL C_{EDL} decreases[201]. Considering the total charges accumulated in the electrodes q remain unchanged, the potential difference between these electrodes ΔE increases as predicted by the following equation $q = C_{EDL}\Delta E$. In state III, a load resistor is connected with the Capmixing system. Discharging in electrodes delivers current to produce useful work in the load resistor. At the same time, the thickness of EDL decreases due to the discharging. At final state IV, system switches into open-circuit state and fresh water is replaced by salt water to close the operation loop. As illustrated in fig 1.16(B), the produced work in state III is larger than the energy consumed in state I, a net power is harvested using this so-called capacitive energy extraction based on double layer expansion (CDLE) technology[16]. In the pioneer work of CDLE, Brogioli presented this innovative configuration with a mild power density of 7 mW per square meter of electrodes harvested by two activated carbon porous electrodes[200]. Later, Brogioli et al.[202] analyzed the spontaneous potential and the leakage current of different activated carbon electrodes. Based on this analysis, they proposed several suitable couples of activated carbon materials that could possibly enlarge the energy extraction. Using porous carbon electrodes of A-PC-2 and NS30 (two commercial activated carbon films) in CDLE system, a remarkable power density of 50 mW.m^{-2} was reported.

In CDLE, capacitive electrodes suffer from self-discharging problems due to faradic reactions on the surface of the carbon. Porada et al.[203] summarized these reaction into three types: the first one is the conversion of quinone group on the carbon's surface with two protons to form two hydroquinone. Secondly, the carbon oxidation from carbon to CO_2. And finally, the electrochemical reactions where components in the water react at the carbon surface. Some of them require molecular oxygen in solution. Brogioli et al. found that removing oxygen by bubbling nitrogen partially reduces the self-discharge [204]. An alternative solution of using selective faradaic electrodes in the CDLE configuration was proposed in 2011 by Mantia et al[205]. The so-called 'Mixing entropy battery' was experimentally demonstrated by using $Na_{2-x}Mn_5O_{10}$ electrode for Na^+ and Li^+ capturing and Ag/AgCl electrode for Cl^- capturing. In this conception, extracted energy from salinity difference is stored inside the bulk crystal structure of the electrode material in chemical energy form. A power density of 138 mW.m^{-2} was reported for a salinity gradient of 0.03 M and 1.5 M of LiCl solutions. The main problems of this technique, in

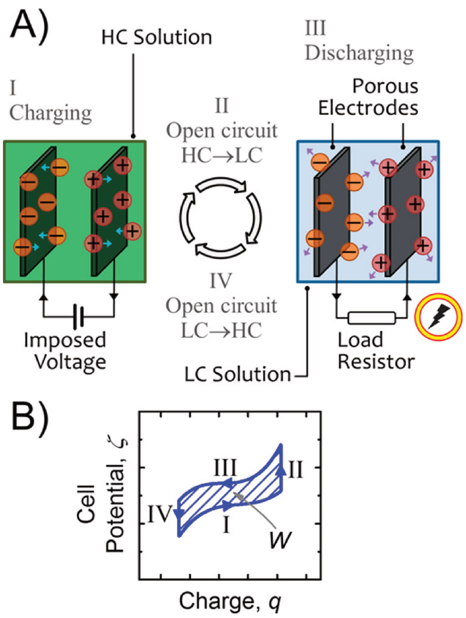

Fig. 1.16 **(A)** Illustration of the working principle of capacitive energy extraction based on double layer expansion (CDLE) and **(B)** the qualitative plot of useful work W produced in an unit Capmixing cycle. (Figures and captions reproduced from [18] with permission from American Chemical Society, copyright 2016.)

addition to the high cost of the electrodes is the relatively short lifespan of the Ag/AgCl electrodes and the low specific capacity of the NMO. Also, the pre-charging step promotes the energy investment[206]. To overcome all that, Ye et al.[206] proposed a charge-free MEB with low-cost electrode materials with Prussian Blue for the cationic electrode to capture the Na^+, and polypyrrole to capture the Cl^- for anions.

The conventional CDLE configuration requires the external electrical charging system to enable the energy harvesting, which requires higher installation costs and reduce the system efficiency. In 2010, Sales et al.[17] proposed to replace auxiliary charging process by using IEMs, so as to use the Donnan potential established across the membrane for system charging. This technology is called capacitive energy extraction based on Donnan potential (CDP). According to their work, Neosepta CEM (or AEM) was placed between the porous carbon electrode and the spacer. While fresh water and salt water were injected alternatively into the spacer, cations and anions were transported through CEM and AEM under the Donnan potential driving force, forming alternative ionic flows (Fig 1.17). The initial work of CDP reported a power density of 11.6 $mW.m^{-2}$ for solution concentration of 10 mM and 510 mM for fresh water and salt water, respectively. Based on the principle of CDP, modifications of electrodes and membranes were conducted for performance amelioration. Hatzell et al.[207] proposed to use flow electrodes containing activated carbons in CDP configuration, which significantly increased the system performance towards 50.9 $mW.m^{-2}$. In 2021, Hwang et al.[208] realized systematic research on flow electrodes on varying particle components and concentration, the optimum flow electrodes containing expanded graphite was reported to provide a power density of 480 $mW.m^{-2}$. Further optimization on current collector (Graphene coated Ti mesh) could even promote the system performance towards 750 $mW.m^{-2}$, according to the recent work of Lee et al.[209]

Another emerging strategy similar to CDP is the soft electrodes (SE), where IEMs are replaced by polyelectrolytes to form direct anionic and cationic layers onto electrodes. A pioneering work was realized in 2014 by Ahualli

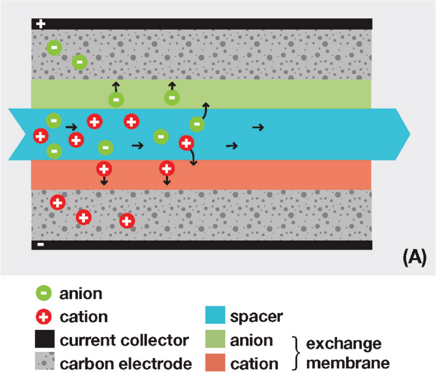

Fig. 1.17 Illustration of the composition and working principle of capacitive energy extraction based on Donnan potential (CDP). IEMs are used to replace external charging sources so that anions and cations move from spacer channel into porous electrodes. (Figures and captions reproduced from [17] with permission from American Chemical Society, copyright 2010.)

et al.[210] by using polyelectrolyte-coated carbon electrodes with a power output of 12.1 mW.m^{-2}. In 2020, Siekierka et al.[211] prepared electrodes coated with EDA and PAA/PMA, reaching a maximum power of 293 mW.m^{-2}. However, it is to notice that considerable viscous loss is expected in flow electrode related systems due to the highly viscous properties of flow electrodes.

Numerous theoretical analyses of Capmixing systems were reported[204, 212–214], providing guidelines for optimization of Capmixing. Further strategies, including thermal assisted Capmixing[215, 216], additional charging[217] and module scaling up[146, 218], were also developed for performance enhancement.

1.6 CRED

An innovative configuration combining RED and Capmixing presents a higher power density output with numerous advantages compared with conventional blue energy harvesting technologies.

It was firstly reported by Vermaas et al.[219] in 2013, suggesting the use of capacitive electrodes in RED configurations (CRED). As illustrated in Fig 1.18, such configuration allows the installation of multiple cationic and anionic membrane stacks for higher potential generation and at the same time avoids the redox reactions in the system. In their work, a layer of activated carbon is deposited on a Ti/Pt mesh to form the capacitive electrodes. Such electrodes convert the ionic flux to electronic flux by ion adsorption and storage without the occurrence of redox reactions. To avoid the problem of saturation in capacitive electrodes, a periodic switch of solution chambers, combined with the switch of electrical current directions, is systematically conducted. As larger range in voltage and accumulated charge is achieved compared with conventional capmixing technologies, a maximum power density of 0.9 W.m^{-2} can be achieved in cell configuration of a stack of 30 membranes with a salinity difference of 0.017 M and 0.508 M for fresh water and salt water, respectively. Their work is the first proof-of concept for CRED system.

This original CRED cell configuration is further studied by Oh et al., with a systematic study of a scaled-up CRED system of 20 – 80 cell pairs[220]. In this case, the CRED system presents a high stack voltage ranging from 0.9 to 5.0 V, surpassing the voltage for water electrolysis occurrence. They discovered that the cutoff output voltage, the voltage where the feed solutions are switched, is the major factor to control the undesired irreversible faradaic reactions in CRED system. By well engineer the cutoff voltage, the increase of stack voltage has an

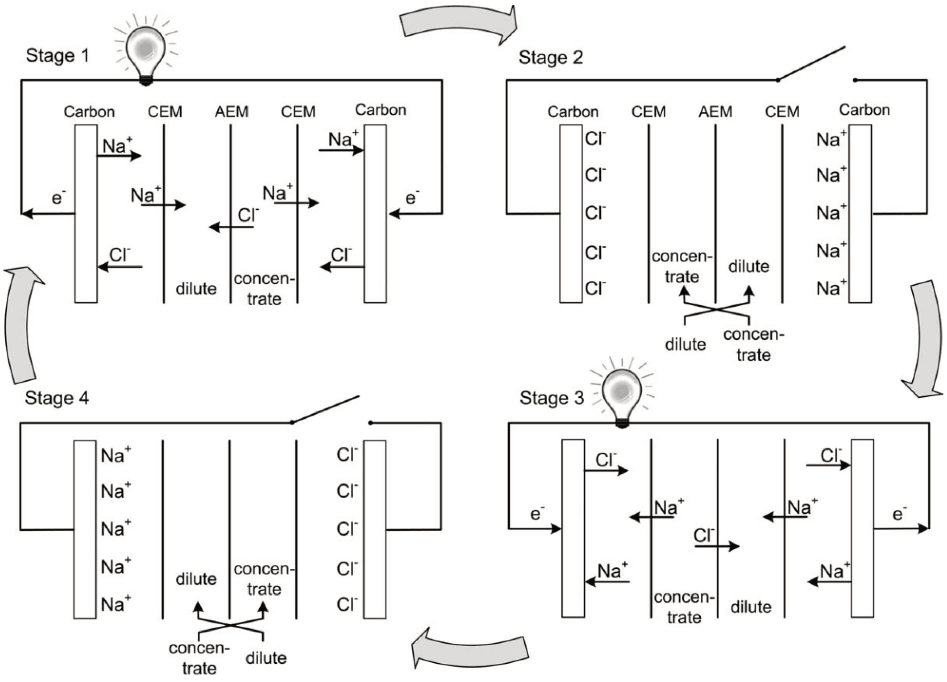

Fig. 1.18 Principle of CRED in four stages, in this case for 1 cell (CEM, AEM, dilute, concentrate). Multiple membrane cells can be stacked between the electrodes. (Figures and captions reproduced from [219] with permission from Royal Society of Chemistry, copyright 2013.)

insignificant impact on faradaic reactions. It provides us thus an effective strategy for stable power generation of CRED system at large scales.

Following the previous CRED study, Zhan et al., designed a CRED system composed of an ion exchange membrane and two graphene hydrogel electrodes[221]. The composite electrodes are mainly composed of graphene oxide negatively charged by residual carboxyl functional groups. They prepared two different cell assemblies, by combining the graphene hydrogel electrodes with CEM and AEM, respectively. The power density measurements indicate a better energy performance of the AEM-assembly, showing an average power density of 482.4 mW.m^{-2} compared with that of 141.4 mW.m^{-2} for CEM-assembly. The experimental results are obtained for a salinity gradient of 0.02M/0.500 M for NaCl solution. Zhu et al. developed a similar CRED system constructed with two identical carbonized peat moss electrodes with a CEM [222]. The composite electrode is mainly composed of peat moss powders, carbon black and polyvinylidenefluoride (PVDF), presenting an excellent capacitance as demonstrated in cyclic voltammetry tests. Similar power density measurement is realized with a fixed switching period of 100 s. They report an average power density of 0.95 W.m^{-2} for a salinity difference of 30 g.L^{-1} vs. 1 g.L^{-1}.

As illustrated in Fig 1.19, a novel cell design composed of a single selective membrane and two inexpensive capacitive electrodes was presented in the work of Brahmi et Colin[117]. A home-made slurry composed of activated carbon particles, carbon nanotubes and PVDF is homogeneously deposited onto a porous carbon electrode to form a capacitive layer. As capacitive electrodes are charged by ion adsorption while immersed in solutions, periodic water compartment switching is necessary to deblock the saturation regime. Fig 1.20 illustrates the two working regimes of CRED before and after water compartment switch. An alternative capacitive current is generated when an electrical resistance is directly connected to the system. The overall CRED structure is

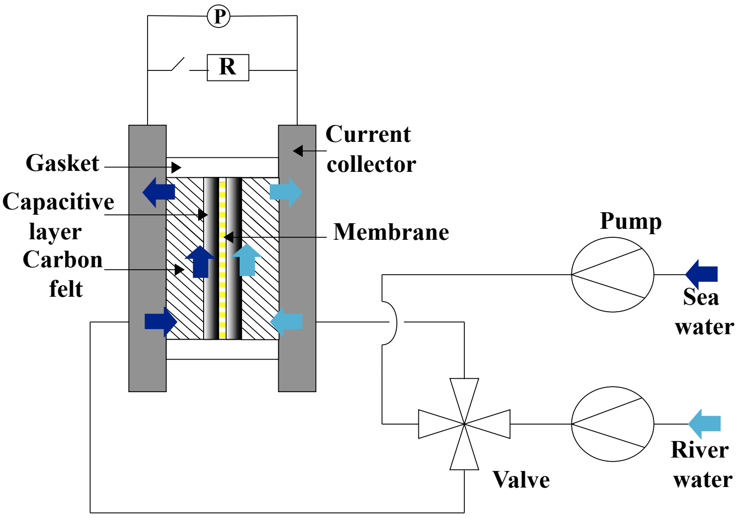

Fig. 1.19 Scheme of the experimental millifluidic set up used for the salinity gradient harvesting with one membrane and a 6 mm water compartment. (Figures and captions reproduced from [117] with permission from Elsevier, copyright 2022.)

optimized to reduce the cell resistance and viscous loss. A net power density output of 2 W.m^{-2} was reported, with a gradient of 300 (0.017 M/5.1 M) for a simple configuration of a single cationic membrane combined with two inexpensive electrodes. The net power density takes into account the viscous loss in the cell and remains the maximum power density output for CRED systems. It is to notice that a RC type equivalent circuit is established for the CRED system based on electrochemical characterizations. The CRED system can be modelled as the combination of a constant voltage supply, a cell resistor and a capacitor. The theoretical modelling based on this equivalent circuit predicts well its experimental power density performance.

Apart from the static capacitive electrode based CRED system, there is another growing trend of integrating flow capacitive electrodes in CRED systems. To the best of our knowledge, the work of Liu et al. was the first reported literature to realize a proof-of-concept dispositif that uses capacitive flow electrodes in CRED system[223]. The capacitive flow electrodes were suspensions composed of 5 – 15 % powdered activated carbon loaded in 0.5 M NaCl solution. It is continuously recirculated at a flow rate of 20 mL.min^{-1} in solution chambers. They report a maximum power density of 260 mW.m^{-2}, an energy performance slightly lower than the static capacitive electrode assembly reported to be 290 mW.m^{-2}. Simoes et al. conducted a systematic study of the capacitive flow electrodes based CRED system by varying the slurry composition[224]. Six different slurry compositions comprising activated carbon, carbon black and graphite powder were carefully characterized and tested in their work. The best energy performance is achieved for a mixture of activated carbon and carbon black at a total concentration of 20 wt %, reported to be 0.7 W.m^{-2} for a salinity difference of 30 g.L^{-1} vs. 1 g.L^{-1}.

Overall, CRED system enables the continuous electricity generation and presents systematically higher power density performances compared with Capmixing process. As the process is enabled by ion adsorption/desorption, CRED system avoids redox reaction related problems, including the material loss in faradaic electrodes, use of additional toxic or hazardous electrolyte, over potential problems and side reactions. From an economical point of view, capacitive electrodes are stable, cost-less and easy for industrial scale-up. If the CRED system exhibits

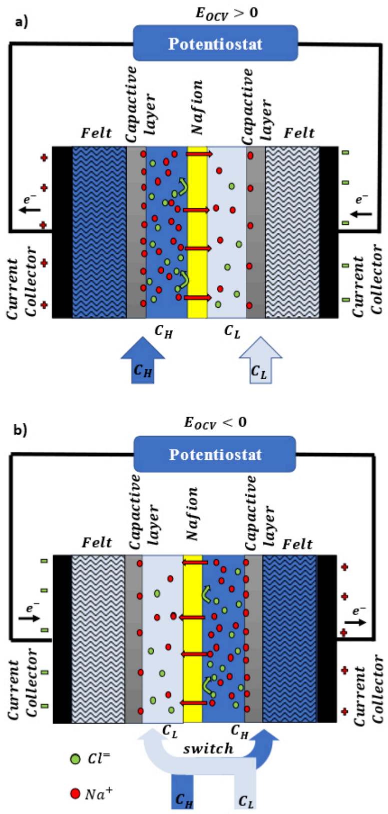

Fig. 1.20 Illustration of two working regimes for a capacitive salinity-gradient cell before **(a)** and after **(b)** water compartment switch. (Figures and captions reproduced from [117] with permission from Elsevier, copyright 2022.)

similar power density performance to that of faradaic RED systems, CRED becomes economically preferable for further development. However, the reported power densities in CRED systems are systematically lower than that reported for faradaic RED system. Taking the example of the work of Brahmi and Colin, the reported power density represents about 50 % of its theoretical value $P_{max} = \frac{E^2_{OCV}}{4SR_{cell}}$, calculated based on open-circuit voltage E_{OCV}, cell resistance R_{cell} and membrane surface S. Considering the fact that the power density corresponds well with the RC type equivalent circuit, such power density drop originates from the capacitive nature of the system. It is necessary to develop strategies to further ameliorate the energy performance of CRED system.

1.7 Generalization towards concentration cells

It is worth mentioning that osmotic energy is not solely generated by salinity gradients, such as those between river water and seawater. Various concentration gradients can also yield substantial energy resources. Osmotic energy exists in diverse forms and at different scales, offering a wide range of applications. One can imagine the application in industrial field of energy and waste treatment sector, but also at smaller scale in biomedicine[186], implant battery design[192], sensors[184] etc. In this section, we aim to broaden the understanding of osmotic energy harvesting to encompass a wider scope. In fact, another significant concentration gradient is established by protons. Unlike the salinity gradient, which is limited by salt dissolution (360 g.L^{-1}, 25°C for NaCl), the pH gradient has a much broader range and is ubiquitous.

If we examine examples in nature, modern cells are known to rely on electrochemical proton gradients for energy transduction and metabolism, providing an excellent illustration of osmotic energy storage and release[225].

From an industrial perspective, various scenarios can be envisioned to establish pH-based osmotic energy reservoirs. In industrial processes, both acidic and alkaline waste streams are commonly generated[226, 227]. Unless neutralized, such streams cannot be discharged into public watercourses[228]. Currently, the pH neutralization process for waste streams is primarily considered a necessary step for waste treatment[229]. However, the pH gradient established between acidic and basic streams can be viewed as an ideal osmotic energy reservoir to be harnessed through a carefully engineered mixing process. This presents a prime example of a waste-to-energy process, which is a significant strategy in the field of waste treatment[230].

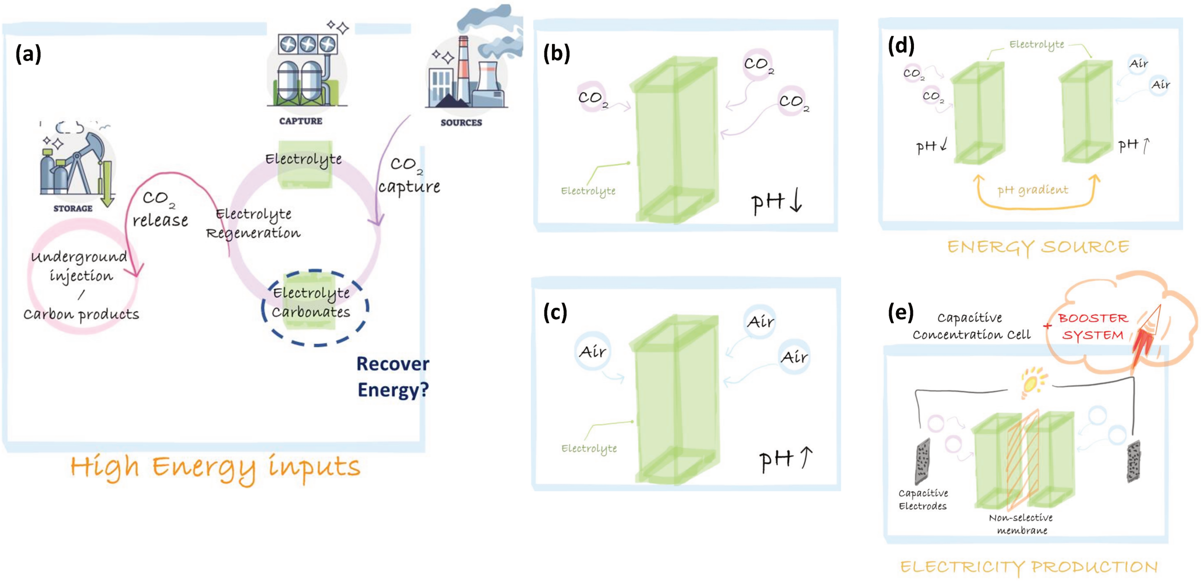

Fig. 1.21 Integration of a pH gradient cell into the Carbon Capture and Storage process. (a). Illustration of a electrolyte based CO_2 capturing process. It is possible to integrate a pH gradient cell for overall energy cost reduction. The dissolution of CO_2 gases results in a pH decrease in the electrolyte (b), while the air pumping results in a pH increase (c). (d). Combining the above mentioned electrolytes results in a pH difference which can be considered as a giant osmotic energy resource. (e). It is thus possible to design a pH gradient energy harvesting system to convert the osmotic energy into electricity.

To go further, we recognize exciting opportunities to integrate pH gradient cells into the Carbon Capture and Storage (CCS) processes[231, 232]. In post-combustion capture (PCC), CO_2 is separated from flue gases using a chemical sorbent rather than being emitted directly into the atmosphere[233]. The most developed and economically viable technology for PCC is the amine-based absorption (amine scrubbing) unit[234, 235]. Osmotic energy harvesting has the potential to reduce the overall energy costs for carbon capture, thereby advancing the maturation of technology. Figure 1.21 illustrates a classic CCS process. The industrial waste gases are pumped into a carbon capturing electrolyte so that CO_2 gases are removed to form carbonates in the electrolyte. The electrolyte is regenerated by heat or electrochemical process to restart the CO_2 capturing process. The released

CO_2 gas is then utilized for fuels and carbon based products or injected underground for further storage. The entire process requires high energy inputs.

Here, to reduce the overall energy cost, it is possible to integrate a pH gradient energy harvesting system to recover certain energy. In fact, the CO_2 dissolution results in a reduced pH in the electrolyte. If we divide the electrolyte into two parts, with one part pumped with CO_2 gas of low pH and another part purged with air or waste heat treatment of high pH, we can easily create a pH difference between them. The pH difference is considered as a giant osmotic energy source. With a well controlled mixing process, it is possible to convert this energy into electricity (Fig 1.21).

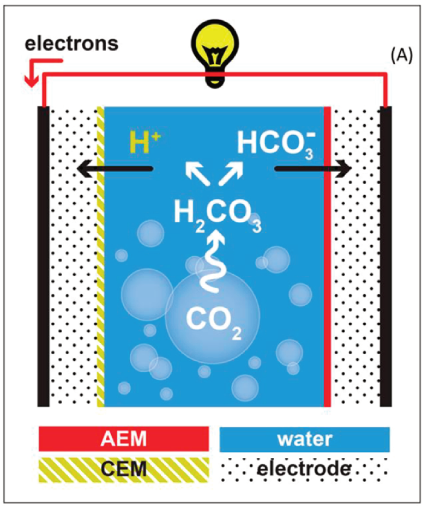

Fig. 1.22 Illustration of energy harvesting from CO_2 emissions in capacitive electrochemical cells. Dissolved CO_2 dissociates in protons and bicarbonate ions, which diffuse into different electrodes due to the ion-selectivity of the membranes placed in front. The resulting membrane potential leads to the spontaneous generation of current. (Figures and captions reproduced from [236] with permission from American Chemistry Society, copyright 2014.)

As illustrated in Fig 1.22, Hamelers et al. developed firstly a pH gradient cell combining with the carbon capture process. The osmotic energy is established by CO_2 or air pumping in electrolytes[236]. The cell configuration used in this work is similar to that of CDP with pairs of porous electrodes and two ion-exchange membranes. They reported an improved power density of 4.5 $mW.m^{-2}$ for MEA solutions compared with that of water (0.28 $mW.m^{-2}$). To better elucidate the underlying mechanism of such system, the same group proposed a physicochemical and mathematical model for the generation of electrical energy from mixing CO_2 saturated solutions using capacitive cells[238, 239]. Later in 2019, the same group examined the impact of different cell designs, namely "conventional", "flow-by (wire)" and "flow-by (flat)", on pH gradient cell performance[240]. They found that an optimized configuration of "flow-by (flat)" results in a doubled energy performance compared with that reported previously.

Porada et al. explored the possibility of combining the capacitive pH gradient cell with capacitive deionization process in order to realize a continuous energy generation process[241]. The main originality of this work relies in the use of flow capacitive electrodes. Kim et al. chose to use 30 wt % N-methyldiethanolamine (MDEA) as the CO_2 capturing electrolyte in their system called carbon capture with reverse-electrodialysis[242]. The cell is composed of five pairs of ion-exchange membranes and two inert electrodes coupled with $[Fe(CN)_6]^{3-}/[Fe(CN)_6]^{4-}$

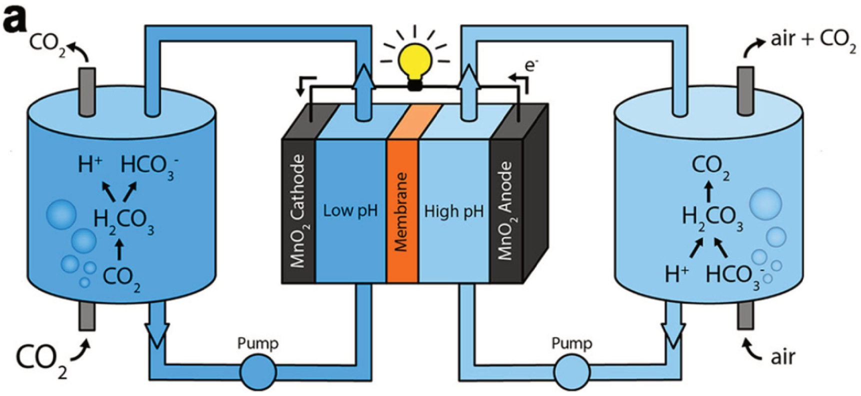

Fig. 1.23 Schematic of the pH-gradient flow cell for converting CO_2 into electricity. The flow cell consisted of two identical MnO_2 electrodes (black) divided by a nonselective membrane (orange) placed between channels. The channels were simultaneously fed 1 M $NaHCO_3$ solutions with a lower pH value (7.7, dark blue) or a higher pH value (9.4, light blue) that was generated by sparging the solutions with CO2 (pH 7.7) or air (pH 9.4), respectively. (Figures and captions reproduced from [237] with permission from American Chemistry Society, copyright 2017.)

reversible redox couples. They reported a peak power density of 1 $W.m^{-2}$, which is 220 times higher than the previous work. They attributed this energy performance amelioration to the enhanced electrical conductivity and the decrease of inner resistance of CCRED cell.

Following the previous attempts, Kim et al. reported a novel pH gradient cell configuration of CRED type [237]. As previously described in Fig 1.23, they established a pH gradient based osmotic energy resource by the pumping of CO_2 gas and air in aqueous bicarbonate buffer solutions, respectively. The pH gradient cell is composed of two identical supercapacitive inexpensive MnO_2 composite electrodes and a nonselective membrane. A systematic chamber reversal is realized due to the blocking characteristic of pseudocapacitive electrodes. They report an average power density of 0.82 $W.m^{-2}$ for a pH difference of 1.7, which is 200 times higher than the first work of Hamelers et al.

Similarly, Cheng et al. designed a low-grade thermally regenerative CO_2 induced pH-gradient cell (TRCPC) to recycle waste CO_2 and thereby produce durable electricity[243]. They demonstrated the reproductivity of the electrolyte and the stability of the cell system. The proposed system displayed a peak power density of 0.578 $W.m^{-2}$. In both experiments, MnO_2 electrodes presenting typical pseudocapacitances are used. Chen et al. designed a pH gradient cell with Ag/AgCl electrodes and a cellulose based membrane[244]. They used monoethanolamine (MEA), an industrialized amine based electrolyte, for CO2 capturing process. The pH difference is created as described in Figure 1.21. They report a power density of 2.6 $W.m^{-2}$ for a tiny system with a effective membrane surface of several square millimeters. It is to notice that this value will drop dramatically while we increase the membrane surface[145].

1.8 Objectives of this thesis

According to the above presented literature review, there are three major osmotic energy harvesting methods : PRO, RED and Capmixing. PRO is considered as the most mature technologies developed today, however it requires numerous facilities including pumps and turbines for mechanical-electrical energy conversion. This requires complex infrastructure installation and raises the overall electricity production cost. The RED system converts directly osmotic energy into electricity by redox reactions. Nevertheless, due to the high cost of ion exchange membranes and expensive electrodes, the electricity generated is of high cost. The occurrence of redox reactions in RED systems results in the depletion of electrode materials, necessitates the use of potentially hazardous or toxic electrolyte rinsing solutions, and may give rise to unintended over-potential problems and side reactions. These factors raise concerns regarding the environmental footprint and carbon impact of RED systems. As for Capmixing, although cost-less capacitive electrodes are used in the system, the system presents systematically low power performance compared with the above-mentioned technologies.

The comparison of these methods leads us to the study of CRED systems, which stands at the crossroad of Capmixing and RED system. The CRED system offers notable advantages. Carbon-based capacitive electrodes are cost-effective compared to the expensive faradaic electrodes, such as Ag/AgCl electrodes, utilized in conventional RED systems. In addition, these electrodes are inert and stable, presenting limited electrode material loss during energy harvesting operation. As there is no presence of redox reaction in the procedure, it prevents us from the use of toxic or hazardous electrolytes and suppresses over-potential problems. The carbon based capacitive materials of large quantities are widely produced at industrial scale. The use of capacitive electrodes simplifies the scale up process for industrial use. On the other hand, compared with Capmixing, CRED system presents a much higher power density output, reaching the order of magnitude of RED systems. Furthermore, a great advantage is that CRED system allows for continuous energy generation, outperforming the sequential production approach utilized in capmixing processes.

Based on this analysis, it is clear that the CRED system merges the high power density output advantage of RED systems with the cost-effectiveness and suppression of redox reactions inherent in Capmixing. It stands as a promising candidate for developing efficient and cost-effective osmotic energy harvesting. Nonetheless, as an emerging technology in the field of osmotic energy harvesting, CRED systems lack comprehensive systematic studies. The primary objective of this thesis is to investigate the fundamental mechanism of the CRED system, aiming to enhance its energy performance and broaden its range of applications.

Following this introductory chapter, in Chapter 2, we will uncover the underlying mechanism of CRED system. We will demonstrate the intrinsic ionic-electronic conversion efficiency problems in capacitive electrodes, verified both by theoretical and experimental methods. Based on this understanding, a boosting strategy is proposed to optimize the working regime of capacitive electrodes, aiming to further enhance the power density performance of CRED system.

In Chapter 3, we take a step forward to the real-world applications where multivalent ions present in the feeding solutions. We verify the energy performance of CRED system under divalent mixing process and uncover the mechanism behind. Based on this study, it is possible to further evaluate the feasibility of such technology in industrial scale-up.

To go further, we extend the research scope into concentration based energy harvesting system. In Chapter 4, we explore the possibility of harnessing pH gradient based osmotic energy in the framework of CRED system. We build up a pH gradient cell with pseudo-capacitive electrodes. The pH gradient based osmotic energy is created within a carbon capturing process, aiming to reduce the overall cost. We study the working mechanism of the novel system and test the boosting strategy for further power density amelioration.

1.9 Conclusion

Conclusion

Human activities, primarily through greenhouse gas emissions, have unequivocally contributed to global warming issues. Given the substantial emissions from the energy sector, finding clean and sustainable energy resources to replace conventional fossil fuels is of paramount importance. Osmotic energy, released during the mixing of solutions of different concentrations, remains an untapped energy resource with significant potential. The development of reliable, efficient and economically viable osmotic energy harvesting technologies is of great importance. The comparison of the present osmotic energy harvesting methods leads us to the study of capacitive reverse electrodialysis (CRED) systems, which combine the advantages of both RED and Capmixing technologies. Although several proof-of-concept CRED system designs are reported, it lacks a systematic study of the underlying working principle of CRED system. Numerous questions remain to be further studied.

What is the underling working mechanism of the CRED system? How does the capacitive behavior impact the energy performance of CRED system? What is the origin of the significant power density performance gap between CRED systems and faradaic RED systems? How to further enhance the power density performance of CRED system? How does the energy performance vary while encountering with real-world solutions in industrial applications? Is it possible to generalize CRED system into a larger scope of concentration gradient based energy harvesting?

To answer these questions, we will firstly focus on uncovering the working mechanism of CRED system. The thorough understanding leads us to an effective strategy for the amelioration of energy performance of CRED systems (Chapter 2. The energy performance amelioration of CRED system by boosting strategy). To further study the energy performance of CRED system in real life electrolytes, we will study the impact of divalent ions on CRED system performance (Chapter 3. The influence of divalent ions on CRED system). Finally, we will try to generalize the CRED system into concentration gradient based systems. We demonstrate the feasibility of combining pH gradient cells with carbon capture and storage CCS technologies to reduce the overall energy cost (Chapter 4. Extension towards pH gradient cell system).

Chapter 2

Power density performance amelioration of CRED systems by boosting strategy

2.1 Preamble

This work is based on the previous work in the lab MIE by Dr. Youcef Brahmi, who invented the capacitive RED system[117]. The system stands at the crossroad of RED and Capmixing, with the use of an ion exchange membrane and two inexpensive carbon based capacitive electrodes. The creation of cationic/anionic flux across the ion exchange membrane under osmotic effect is identical to the procedure in RED systems. The major difference lies in the conversion between ionic flux and electronic flux. Unlike the conversion realized by redox reactions in faradaic RED systems, it is realized under ion adsorption phenomenon for capacitive electrodes. Due to the "blocking" feature of the capacitive electrodes, a periodic water chamber is realized to systematically reverse the direction of of both ionic and electronic flux to enable the continuous functioning of the CRED system.

As already discussed in the Chapter 1, CRED system presents numerous advantages. Nevertheless, we discovered a significant difference of power density performance between the experimental results and the theoretical prediction. For example, in the case of a NaCl salinity gradient of 5.13 mol.L^{-1} and 0.171 mol.L^{-1}, we measured a power density of 2.5 W.m^{-2} for CRED system, which corresponds to a drop of a factor 2 compared with theoretical maximum power density of 5.44 W.m^{-2}[245]. What is the origin of this power density gap? How to ameliorate CRED system to enhance its power density performance?

The objective of this chapter is to understand the mechanism behind this power gap in CRED systems and ameliorate energy conversion of capacitive electrodes to reach the theoretical maximum limits. In the following, we will firstly describe the CRED system established in this study. We will present in details of the cell structure, its working principle, the system characterization and the theoretical modelling. Based on such CRED system, we will then integrate a boosting system to further enhance the energy performance in the second section. A detailed description of the boosting system setup, its working principle and its modelling is provided. In addition, we provide a thorough understanding of the mechanism of boosting strategy. Finally, a techno-economic analysis of CRED technology is carried out.

The results presented in this chapter have been published in ACS Environmental Science & Technology[3]. The published paper is available in Appendix A.

2.2 CRED system

2.2.1 CRED cell set-up

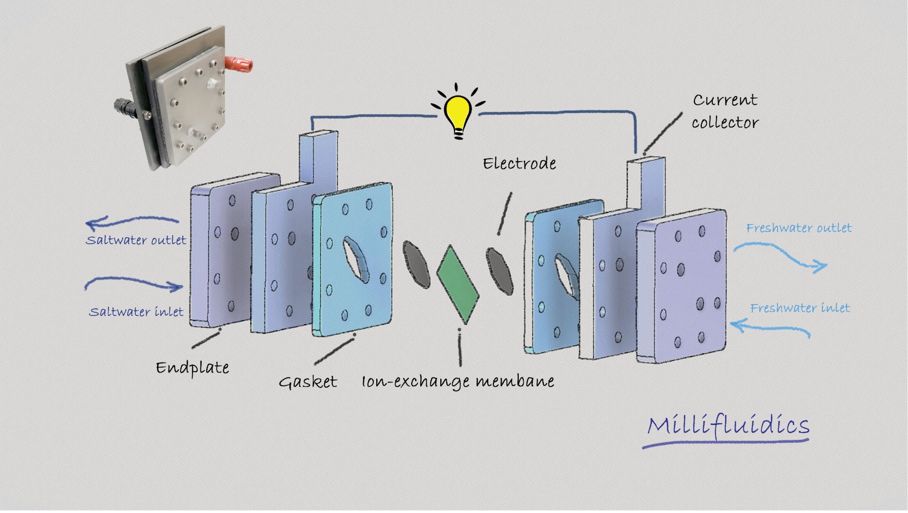

Fig. 2.1 CRED cell set-up.

A similar cell configuration is used as in the previous work of Brahmi et al.[117]. The cell is of symmetric geometry, with an ion-exchange membrane (Nafion^{TM}117, Chemours) placed in the middle of two water compartments of different salt concentration (Fig 2.1). This membrane has a thickness of 183 μm (dry form) to obtain an average conductivity of more than 0.1 S.cm^{-1} and a total acid capacity between 0.95 and 1.01 meq.g^{-1}. The effective surface area of the ion-exchange membrane used in our experiment is 2.24 cm^2. Two capacitive electrodes made of carbon felt (Kynol Activated Carbon Felt) are placed separately in two gaskets on both sides of the membrane. Separated by a distance of 1.4 mm from the membrane, two current collectors of graphite are directly connected to capacitive electrodes, respectively. It is possible to measure the cell electric voltage E_{OCV} by connecting two current collectors with the potentiostat on mode OCV (open-circuit voltage). The direct connection of resistors with the cell is applicable to realise a power density measurement. The whole system is entirely fixed and closed by two stainless steel endplates and 8 bolts with a torque of 2 N.m. Two ports are reserved for gaskets and endplates to ensure the water inlet and outlet propelled by a peristaltic pump (Multichannel Peristaltic pump, Longer) at a fixed flow rate (10 mL.min^{-1}). As the system reaches its saturation after a complete capacitive charging, a switch of water compartments is realized by an automatic 4-port valve with a fixed switching period T_s to unblock the saturation regime, which enables the delivery of a periodic alternative current by the cell. The salt water and fresh water used in this work are NaCl (Sigma Aldrich) solutions of different concentrations.

Capacitive electrodes made of carbon felt are used in this work. To further ameliorate the performance of these capacitive electrodes, an essential step of cyclic voltammetry is realized. This electrochemical step is set between -0.6 V and 0.6 V with a scanning velocity of 2 mV.s^{-1}. The capacitance of the cell is greatly increased after this process, reaching a value of 1.2-1.25 F (see Fig 2.2). In fact, the surface charge of these capacitive electrodes increases during the preparation of the electrode and its cycling by a redox reaction involving the oxygen present in the brine.

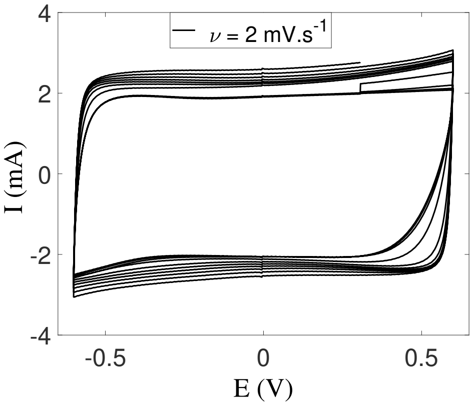

Fig. 2.2 The cyclic voltametry of the cell with a scanning rate of 2 mV.s^{-1} .

2.2.2 Working principle of CRED

The general principle of the capacitive salinity-gradient cell with a single membrane is illustrated in Figure 2.3 **(a)**. A cationic ion-exchange membrane (CEM) is placed in middle of the cell between two compartments of different salinity. This membrane allows the passage of cations and blocks the anions and water molecules[246, 247]. Thanks to this selectivity, an electrical potential difference appears between these two solutions of different salinity. In open-circuit cases, the cell voltage E_{OCV} is the sum of the Donnan potential E_{mem} and of electrode potentials E_{elec}. E_{elec} results from the ion adsorption on the electrodes and depends upon the value of the local salt concentration.

When the circuit is closed as in Figure 2.3 **(a)**, the potential drop between the two electrodes includes the ohmic ionic dissipation both in the membrane and in the electrolyte, as well as the non-ohmic dissipation in the polarization layers built up around the membrane and the electrode. The closing of the circuit also involves the ohmic potential difference in the load resistance and the capacitive potential jump at the electrodes. The presence of capacitance causes the electric current to decay over time. When the capacitor is fully charged, the potential difference across its terminals balances the membrane potential E_{mem} and the potential created by the adsorbed layers E_{elec}. As a result, the produced electric current stops. It is then necessary to switch the fresh water and salt water supplies in order to reverse the membrane and electrode potential to unblock the electricity production. This generates an electric current in the opposite direction. In fact, we fix a switching period T_s to realize the solution reversal by an automated valve. The CRED system will eventually deliver an alternating and periodic electrical signal as output.

2.2.3 CRED system characterization

Based on electrochemical characterizations, it is possible to measure the open-circuit voltage E_{OCV}, cell inner resistance R_{cell}, and its capacitance C. For the case of Nafion 117 membranes, using a NaCl ratio of 30 (5.13 M vs 0.17 M), the open-circuit voltage E_{OCV} measured is around 0.144 V. The cell capacitance and cell resistance are measured to be 1.27 F and 5.39 Ω, respectively. A systematic CRED system characterization result is available in the Table 2.1.

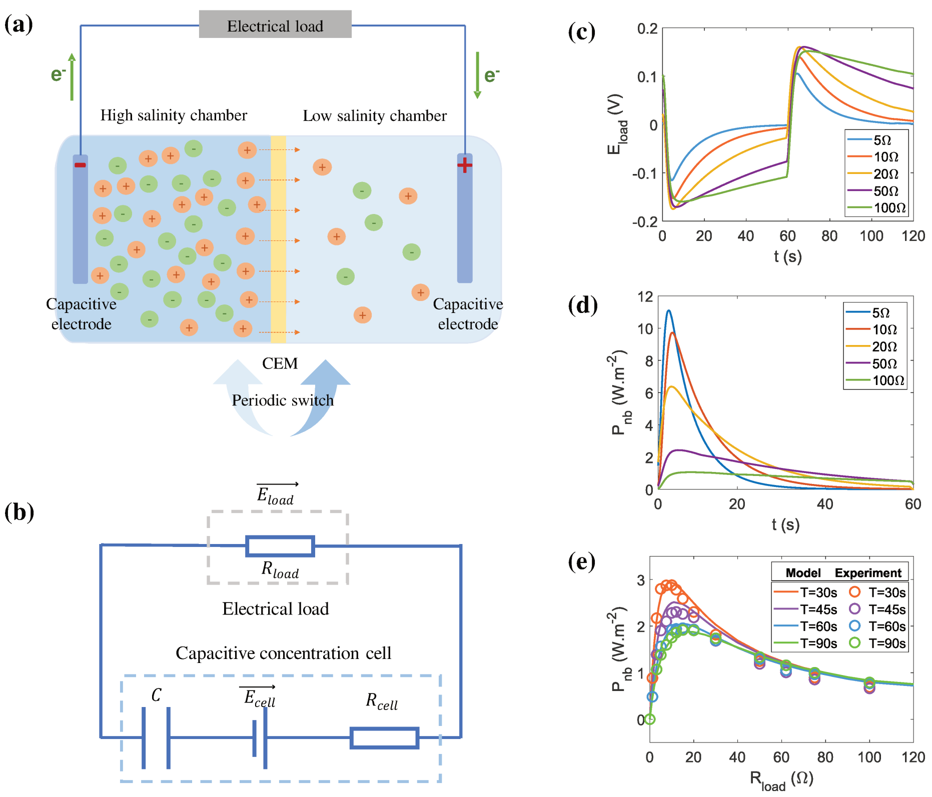

Fig. 2.3 Illustration of a capacitive concentration cell and its power density performance measurement curves. **(a)** Principle of energy conversion of the system with water compartment switch. **(b)** The equivalent electric circuit established based on electrochemical characterization of the capacitive concentration cell. **(c)** Chronovoltammetric measurements of E_{load} for a cell connected with a series of load resistor R_{load} with a fixed switching period T_s = 60 s. **(d)** The power density curve corresponding to the measurement in **(c)** within a fixed switching period T_s. **(e)** Net power density curves P_{nb} as a function of R_{load} for a series of switching periods T_s. The solid lines present the theoretical simulations obtained by the equivalent R-C circuit and the dots present the experimental data. A good agreement between theoretical and experimental data confirms the validity of the equivalent R-C circuit. The experimental conditions of **(c)**, **(d)** and **(e)** are as following: a salinity ratio of 0.17 M and 5.13 M, injecting flow rate of 10 mL.min^{-1} and Nafion 117 used as CEM.

Measurement of Open-circuit voltage E_{OCV}

To measure the open circuit voltage E_{OCV}, we firstly realize a short-circuit state by connecting two cell electrodes with a simple wire. The current tends quickly to zero and the capacitor carries an initial charge of $-CE_{OCV}$. $-E_{OCV}$ is the value of the drop of potential across the membrane and the electrodes, which equals to $E_{mem} + E_{elec}$. We then connect the cell to the potentiostat on mode open circuit voltage (OCV) where the internal resistance of the potentiostat is 10 MΩ. The measured drop of potential across the terminals of the potentiostat E_{cell} is given by $E_{cell} = E_{mem} + E_{elec} - E_{cap}$ where E_{cap} is the drop of potential across the capacitor. After switching the concentrations, the measured potential increases then saturates. As the circuit is open, the potential over the capacitance E_{cap} remains equal to $-E_{OCV}$. $E_{mem} + E_{elec}$ goes from $-E_{OCV}$ to $+E_{OCV}$ due to the switch.

The potential measurement in open circuit after short circuit of the cell corresponds thus to $2E_{OCV}$. A detailed explanation of the open circuit voltage measurement is available in the work of Brahmi et al[117].

Measurement of R_{cell} and C

In order to characterize the electrical resistance R_{cell} and the capacitance C of the cell, it is possible to apply the classical electrochemical technique: chronopotentiometry (CP) which is widely used in battery and flow cell studies. The system setup is the same as in measurement E_{OCV} and the characterisation is realised in a 2-step procedure: mode OCV and mode CP. E_{OCV} is firstly measured by the potentiostat in the first step. Then the mode CP imposes a constant electrical current I_{CP} of 2 mA while measuring the voltage variation of the cell as a function of time. The voltage measured by the potentiostat shows an instantaneous drop ΔE_{OCV} at the switching moment from OCV to CP, followed by a linear decrease with a slope k. The electrical resistance of the cell R_{cell} can be calculated as:

$$R_{cell} = \frac{\Delta E_{OCV}}{I_{CP}} \tag{2.1}$$

And the experimental results are shown in Table 2.1.
For the equivalent capacitance C, it can be estimated as:

$$C = \left|\frac{I_{CP}}{k}\right| \tag{2.2}$$

Table 2.1 The CRED characteristics in function of fresh and salted water concentrations using Nafion 117 membrane.

c_H (M)	c_L (M)	E_{OCV} (mV)	R_{cell} (Ω.cm^2)	C (F)
5.13	0.017	230	35.8	1.13
5.13	0.051	190	20.2	1.12
5.13	0.102	163	15.5	1.11
5.13	0.17	146	12.3	1.1
5.13	0.513	105	9.6	1.15
5.13	1.71	61	8.1	1.16

2.2.4 Power density measurement

To measure the power density output of the cell system, a resistor is directly connected to electrodes in order to close the circuit. As explained earlier, periodic water compartment switching is performed to unblock the saturation state. Throughout the text, we refer to the time between two concentration reversals as the period of time when the cell supports the same salt supply, i.e. salt concentrations that do not vary in the compartments. Strictly speaking, T_s would be the half period of the salt concentration signal. Here, salt and fresh water flows are injected into water compartments with a fixed flow rate of 10 mL.min^{-1}. The potentiostat in OCV mode is placed in parallel with the resistor of resistance R_{load} to realize a voltage measurement of the resistor E_{load} as a function of time.

In Fig 2.3 **(c)**, a typical measurement curve of the E_{load} as a function of time is illustrated. The recorded signals have an oscillating behavior in phase with the concentration inversion. When water flows of new concentrations arrive in the compartments, the membrane potential and the electrode potential change rapidly (compared with cell filling time τ_{fill}, which is defined as the time required to realize a complete concentration change during water chamber switch. $\tau_{fill} \approx 2$ s in our experiments). However, the potential carried by the capacitor does not change immediately. The peak to peak potential drop for a load resistor E_{load} is equal to $\frac{R_{load}}{R_{load}+R_{cell}} \times 2E_{OCV}$ (see Fig 2.3 **(c)** T_s=60 s). After compartment switching, we observe an electric current reversion and capacitor charge changes. This variation in charge tends to create a potential difference E_{cap} which opposes the new sum of the potential difference carried by the membrane and that carried by the capacitive layers. Thus the potential E_{load} tends towards zero and the system evolves towards a blockage. At this moment, a new switch restarts the process.

The power density output P_{nb} of the cell in a complete switching period can be calculated as follows:

$$P_{nb} = \frac{1}{S.2T_s} \int_0^{2T_s} \frac{E_{load}(t)^2}{R_{load}} dt \tag{2.3}$$

where S refers to the effective surface of the ion-selective membrane, which is 2.24 cm^2 in our experiments.

Fig 2.3 **(d)** presents the instantaneous harvested power density P_{nb} as a function of time for a series of load resistance R_{load} within a fixed switching period.

However, it is to notice that the measured maximal value (3 W.m^{-2}) for T_s=30 s is systematically lower than the theoretical value $P_{max} = \frac{E_{OCV}^2}{4SR_{cell}}$ (4.29 W.m^{-2}) described for an ideal cell (i.e. perfect ionic-electronic flux conversion efficiency, with zero over-potential problems at the electrodes and zero electrode resistance). In addition, the maximal power is obtained for a load resistance equal to 12 Ω which differs from the resistance of the cell 5.4 Ω.

2.2.5 CRED modelling

Based on the electrochemical characterization of the system, it is then possible to establish an equivalent R-C circuit for this capacitive concentration cell, as illustrated in Fig 2.3**(b)**. The equivalent circuit describes well the capacitive system and can be used to predict power density performances.

According to an analysis of the electrochemical impedance spectroscopy, a R-C model is proposed as a simplified fitting model for the cell-booster system [117], as illustrated in Fig 2.3 **(b)** in the paper. The system inner resistance R_{cell} and capacitance C can be quantitatively characterized by a chronopotentiometry (CP) measurement using a potentiostat. $E_{mem}(t)$ is the potential drop over the membrane, $E_{elec}(t)$ the electrical potential due to the salt adsorption on the electrodes, $R_{cell}(t)$ the resistance of the cell (including the ohmic and non ohmic resistance of the solvent, the membrane, the carbon felt and the current collector). The temporal variation of $R_{cell}(t)$, $E_{mem}(t)$ and $E_{elec}(t)$ are due to the temporal variation of the ion concentration profile including osmotic potential, diffuse layer establishment, cell filling process after water compartment switching and etc. In the following we will assume that these characteristic times and the filling time of the cell are negligible compared with the switch half period T_s. Thus, these functions will be modeled simply by window functions:for $0 < t < T$, $E_{mem}(t) + E_{elec}(t) = E_{OCV}$ and for $T < t < 2T$, $E_{mem}(t) + E_{elec}(t) = -E_{OCV}$. In this framework, $R_{cell}(t)$ does not depend upon t.

Following these conditions, we establish the theoretical model for a pure cell-resistor circuit in absence of boosting by the equations below:
For $0 < t < T_s$:

$$(R_{load} + R_{cell})I(t) + \frac{q_1(t)}{C_1} + \frac{q_2(t)}{C_2} = E_{OCV} \tag{2.4}$$

For $T_s < t < 2T_S$:

$$(R_{load} + R_{cell})I(t) + \frac{q_1(t)}{C_1} + \frac{q_2(t)}{C_2} = -E_{OCV} \tag{2.5}$$

R_{load} the resistance of the load resistor, C_1 and C_2 are the capacitances of the capacitive layers, q_1 and q_2 the charge on the capacitive layers, $I(t) = \frac{dq_1(t)}{dt} = \frac{dq_2(t)}{dt}$ the current intensity. In the following, we will assume that both capacitive layers are initially uncharged. Since the same current flows through them, $q_1(t) = q_2(t) = \int_0^t i(u)du = q(t)$. The fact of having two different capacitances is therefore of no major consequence in this description. We'll see that this is slightly different when the mixing phase is taken into account. The equations finally writes :
For $0 < t < T_s$:

$$(R_{load} + R_{cell})I(t) + \frac{q(t)}{C} = E_{OCV} \tag{2.6}$$

For $T_s < t < 2T_s$:

$$(R_{load} + R_{cell})I(t) + \frac{q(t)}{C} = -E_{OCV} \tag{2.7}$$

where $\frac{1}{C} = \frac{1}{C_1} + \frac{1}{C_2}$.
In absence of boosting we find:

$$P_{nb-th} = \frac{2}{ST_s} \frac{CE_{OCV}^2 R_{load}}{R_{load} + R_{cell}} tanh(\frac{T_s}{2(R_{load} + R_{cell})C}) \tag{2.8}$$

A comparison of this model with the experimental data is displayed in Fig 2.3 **(e)** for various concentration reversal period (T_s=30 s, T_s=45 s, T_s=60 s and T_s=90 s). Fig 2.3 **(e)** displays the evolution of the harvested power density P_{nb} as a function of the load resistance R_{load}. The solid lines present the theoretical simulations obtained by the equivalent R-C circuit and the dots present the experimental data. A perfect agreement is found for all the periods, while no fitting parameters are used.

The validity of this simple model is based on the assumption that E_{OCV} is a window function and that the cell resistance is constant over time. In our experiments, this is correct because the filling time of the cell, the equilibrium times of the membranes and the potentials of the adsorbed layers are small compared to the period of concentration inversion T_s.

2.3 Booster system

We discovered that there is a significant power density gap between experimental results of CRED system and theoretical prediction of an ideal cell. In order to further narrow the energy performance gap, we proposed a boosting strategy by which it is possible to largely enhance the power density performance of CRED system. In the following part, an alternating voltage power supply (called Booster system) synchronized to the switching period of the cell is placed in series with the cell to promote the power output. The electrical potential signal delivered by the power supply corresponds to a rectangular wave with its maximum voltage equals to E_0 and its minimum voltage $-E_0$. As illustrated in Fig 2.4, the electric potential signal is synchronized in the way that the signs of E_{load} and E_0 remain the same.

2.3.1 Boosting system set-up

The booster system is realized by a 2-step CA (chronoamperometry) mode program controlled by a potentiostat (SP300, Biologic), where a constant positive voltage E_0 is delivered in the first period T_s and an inversed constant

(a) **Phase 1: $0 < t < T$**

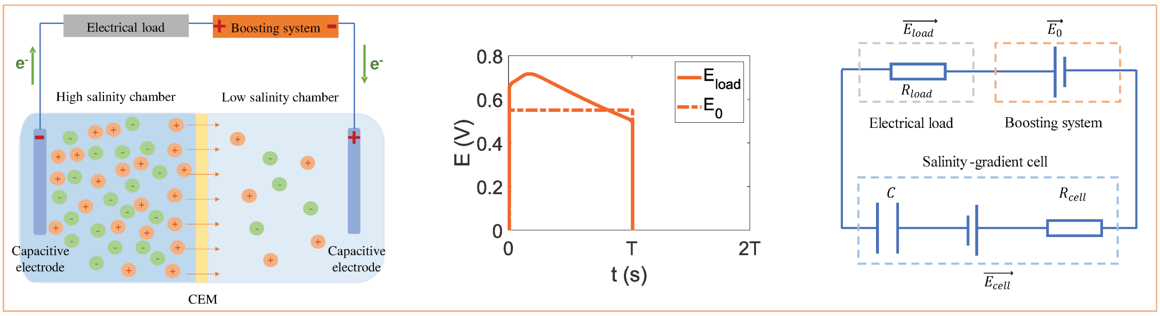

(b) **Phase 2: T< t < 2T**

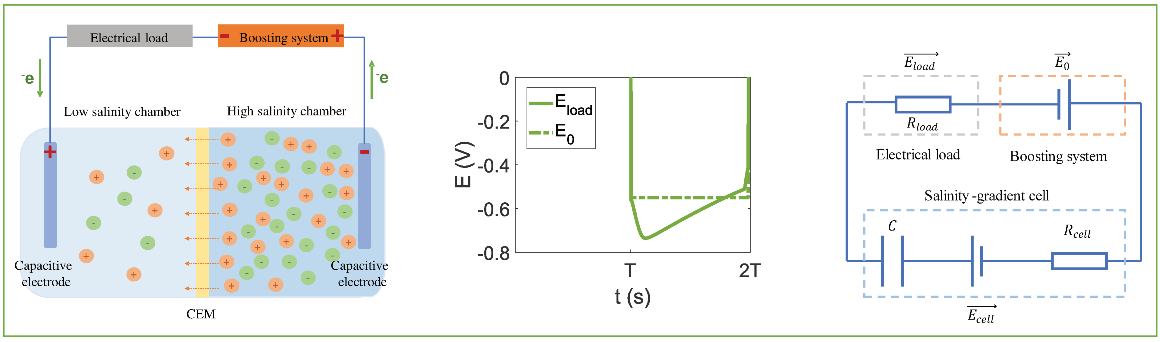

Fig. 2.4 Illustration of the capacitive concentration cell coupled with a booster system in two working phases. **(a)**, phase 1: $0 < t < T$ and **(b)**, phase 2: $T < t < 2T$. For each phase, we illustrate the temporal measurement of E_{load} and E_0 within a fixed period T_s. An equivalent circuit is established for each phase based on electrochemical characterizations, respectively.

voltage $-E_0$ in the second period T_s. It is also possible to realize the booster system with a constant voltage power supply controlled by an electronic chip.

Here, for power density measurement of the cell-booster system, an electrical resistor is directly connected to the cell-booster system to enclose the circuit. A potentiostat is placed in parallel with the resistor for temporal voltage measurement E_{load}. Therefore as presented in Figure 2.4, in a cell-booster system circuit, the voltage applied on the resistor E_{load} remains always the sum of E_0 and E_{cell}.

Thus, the power density directly measured for the resistor is considered as a gross power density $P_{b-gross}$:

$$P_{b-gross} = \frac{1}{S.2T_s} \int_0^{2T_s} \frac{E_{load}(t)^2}{R_{load}} dt \tag{2.9}$$

We recall that S refers to the effective surface of the ion-selective membrane.

To obtain the net power density, it is necessary to remove the additional input energy provided by the booster system, which is calculated as follows:

$$P_{b-boost} = \frac{1}{S.2T_s} \int_0^{2T_s} E_0(t) I(t) dt \tag{2.10}$$

Where E_0 refers to the boosting voltage applied in chronoamperometry (CA) mode by the potentiostat. I refers to the measured boosting current of the electrical circuit.

Thus, the net power density of the boost-cell system is calculated as following:

$$P_{b-net}(E_0) = P_{b-gross} - P_{b-boost} = \frac{1}{S.2T_s}\int_0^{2T_s} \frac{E_{load}(t)^2}{R_{load}}dt - \frac{1}{S.2T_s}\int_0^{2T_s} E_0(t)I(t)dt \tag{2.11}$$

2.3.2 Experimental results and analysis

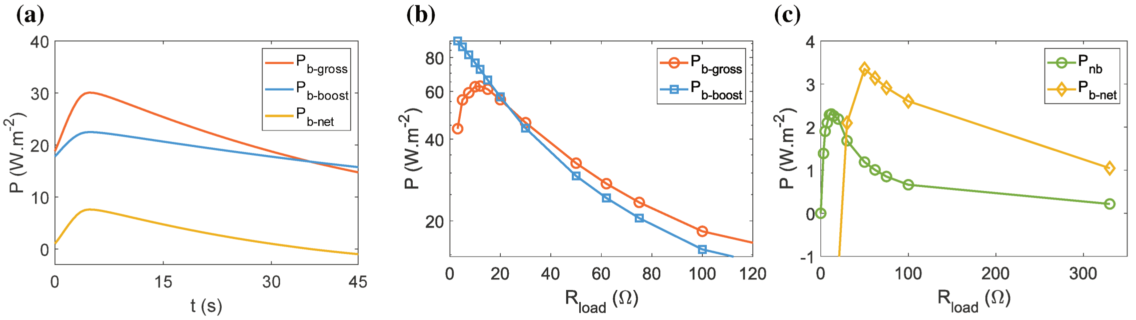

Fig. 2.5 Power density characterisation curves for a capacitive cell coupled with a booster system. **(a)** Power density measurements of $P_{b-gross}$, $P_{b-boost}$ and P_{b-net} as a function of time within a fixed switching period T_s. Here the load resistance R_{load} is fixed at 75 Ω. **(b)** Gross power density curve $P_{b-gross}$ and boosting power density curve $P_{b-boost}$ as a function of load resistance R_{load}. **(c)** Net power density curves as a function of R_{load} for a capacitive cell with P_{b-net} and without P_{nb} a booster system, respectively. The maximum net power density with booster system surpass that without booster system. The experimental conditions in **(a)** - **(c)** are as follows: salinity ratio of 30 (fresh water 0.17 M and salted water 5.13 M), flow rate of 10 mL.min^{-1}, switching period of 45 s, CEM of Nafion 117 and the boosting voltage E_0 is set as 550 mV.

In Fig 2.5 **(a)**, power density measurement curves of $P_{b-gross}$, $P_{b-boost}$ and P_{b-net} as a function of time are illustrated. To obtain the maximal power density of the cell-booster system, it is important to describe the variations of $P_{b-gross}$ and $P_{b-boost}$ as a function of a series of load resistors R_{load}. Fig 2.5 **(b)** presents the power density curves as a function of electrical resistances for $P_{b-gross}$ and $P_{b-boost}$. It is clear that $P_{b-gross}$ firstly presents a sharp increase at lower electrical resistances, then reaches its maximum at an optimal resistance and starts the declination for higher electrical resistances. However, $P_{b-boost}$ remains monotonic decreasing as a function of resistance. According to the definition equation mentioned above, it is possible to calculate the net power density P_{b-net} received in a cell-booster system circuit.

Fig 2.5 **(c)** illustrates the net power density curve as a function of resistance for a cell coupled with a booster system P_{b-net} and without a booster system P_{nb} in the case where the concentration is fixed at $c_H = 5.13$ M for the salt water compartment and $c_L = 0.17$ M for the fresh water compartment. The water flows are injected at a fixed flow rate of 10 mL.min^{-1} into the cell with a fixed switching period of 45 s. A cell-booster circuit is enclosed with a boosting voltage of 550 mV.

For a cell-booster system, P_{b-net} remains negative for low resistances. However, it reaches its maximum at a higher optimal resistance and decreases for higher resistances. It is interesting to notice that the maximal power density recorded in the load resistance surprisingly surpasses that of a pure cell system in the situation of a booster cell system. In this example, the capacitive cell coupled with a booster system could reach a maximum power density of 3.35 W.m^{-2}, which corresponds to a 45.4% increase compared with its maximal power density of 2.30 W.m^{-2} without the booster system.

2.3.3 Booster system modelling

Similarly, it is possible to establish a R-C equivalent circuit for CRED coupled with a booster system as illustrated in Fig 2.4. The major difference is the additional booster system. In the case of boosting, as the cell coupled with a booster system serves as an alternating voltage supply, it is modelled as a constant voltage source of an alternating polarity with a fixed switching period $2T$. Thus for $0 < t < T$, $E_0(t) = E_0$ and for $T < t < 2T$, $E_0(t) = -E_0$. Here, $E_0(t)$ is the secondary boosting voltage.

As the overall voltage drop through the circuit is zero, for a boosted circuit, it is possible to describe the circuit as in Equation 2.12 and 2.13:

For $0 < t < T_s$:

$$(R_{load} + R_{cell})I(t) + \frac{q(t)}{C} = E_{OCV} + E_0 \tag{2.12}$$

For $T_s < t < 2T_s$:

$$(R_{load} + R_{cell})I(t) + \frac{q(t)}{C} = -E_{OCV} - E_0 \tag{2.13}$$

The measured signal is a periodic and continuous signal. Initial conditions are required to solve these equations analytically. We consider that in the established oscillatory regime, q is the same at $T = 0$ and $2T$. We solve analytically these equations and calculate the electrical power recovered by the load resistor.

In presence of boosting we get:

$$P_{b-gross-th}(E_0) = \frac{2}{ST_s}\frac{C(E_{OCV}+E_0)^2R_{load}}{R_{load}+R_{cell}}tanh(\frac{T_s}{2(R_{load}+R_{cell})C}) \tag{2.14}$$

$$P_{b-net-th}(E_0) = \frac{2}{ST_s}\frac{C(E_{OCV}+E_0)}{R_{load}+R_{cell}}tanh(\frac{T_s}{2(R_{load}+R_{cell})C})(E_{OCV}R_{load} - E_0R_{cell}) \tag{2.15}$$

In the case of boosting, a model-experiment data comparison of the net power density of capacitive concentration cell is illustrated in Fig 2.6. No fitting parameters are used. The calculation is based on characterization of the cell features, including open-circuit voltage E_{OCV}, cell resistance R_{cell} and cell capacitance C. The solid lines describe the theoretical prediction of the power density profile realised by the model mentioned above, and solid dots represent the experimental data realised in laboratory experiments.

For T_s higher or equal to 45 s, experimental results fit well with the theoretical model prediction for various boosting voltages, indicating an excellent theoretical description of the cell-booster system. Note that we did not modify the characteristics of the cell to achieve this agreement. This means that the boosting voltage does not influence the polarization phenomena that occur in the cell in a significant way. We did not have to change the value of the ohmic or non-ohmic part of the cell resistance.

The maximal power density correlates positively with the boosting voltage. As explained before, each maximal power density is related to an optimal electrical resistance. The optimal resistance value increases as a function of the boosting voltage. Note that the data displayed for T_s=90 s in Fig 2.6 **(d)** are obtained with a cell displaying different electrical features i.e different cell resistance, and a different capacity from the one used in Fig 2.6 **(a,b,c)**. It is thus not possible to compare the numerical values between them. However, a quantitative model-experiment agreement is also validated in this case.

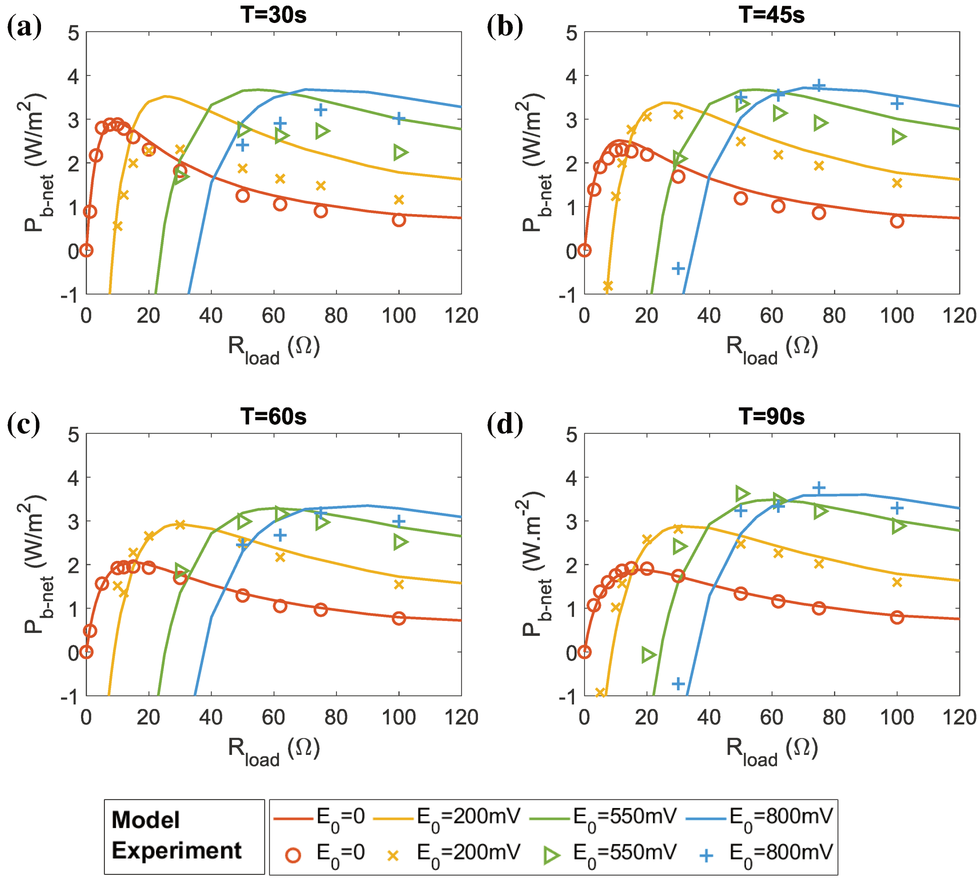

Fig. 2.6 Evolution of the net harvested power density P_{b-net} as a function of the load resistance R_{load} under a series of boosting voltage E_0. The solid lines correspond to modelling results with fitting parameters fixed at E_{OCV}=144 mV, R_{cell} = 6 Ω and C = 1.2 F in the case of **(a)**-**(c)**, and E_{OCV}=148 mV, R_{cell} = 6 Ω and C = 1.4 F in the case of **(d)**. Experimental dots are presented for various boosting voltages E_0 in the following conditions: salinity gradient of 30 (fresh water concentration 0.17 M, salted water concentration 5.13 M) , flow rate of 10 mL.min^{-1}, and CEM of Nafion 117. A quantitative agreement between theoretical and experimental data is found in **(b)**-**(d)** with a switching period T_s of 45 s, 60 s and 90 s, respectively. An experiment-theory gap is found in **(a)** with a switching period T_s of 30 s.

For T_s equals to 30 s, the model does not capture the boosting process whereas it does in absence of boosting. We believe that these disagreements come from the incomplete modelling. A detailed explanation of this point is available in the discussion part.

2.4 Discussions

Influence of switching period T_s

An important influential factor is the switching period T_s of the cell-booster system. In the presence or absence of boosting, the model predicts that the shortest periods lead to the highest powers. In the absence of boosting, the recovered power decreases as a function of the concentration reversal period in the studied period range in perfect agreement with the model (see Fig 2.6). In the case of boosting, the power measured for periods greater than 45 s decreases with the value of the period, as in the case without boosting. The model is in perfect agreement with the data for T_s=45, 60, 90 s. However, the harvested power density is measured to be systematically lower in the case of T_s=30 s than for T_s=45 s, for all different boosting voltages E_0. In the case of T_s=30 s, a power density decrease is even noted for a boosting value of 200 mV compared to a system without booster system (see Fig 2.6).

The fact that we do not measure a higher power density for a period T_s=30 s originates from the neglected processes during model establishment. The filling time of the cell τ_{fill} is not taken into account for the modelling. We recall that the filling time is around 2 s. To understand this point, we further developed a numerical model that takes into account the equilibrium of cell potentials during mixing by introducing a characteristic time scale for mixing.

This numerical analysis shows that the mixing phase affects the process in the presence and absence of boosting, and reduces the power recovered. It also shows that the process without boosting is less affected by the mixing phase. In other words, it shows that a good agreement can be expected with the simple model without taking mixing into account for T_s=35 s in the absence of boosting. Periods longer than 50 seconds are required in the presence of boosting.

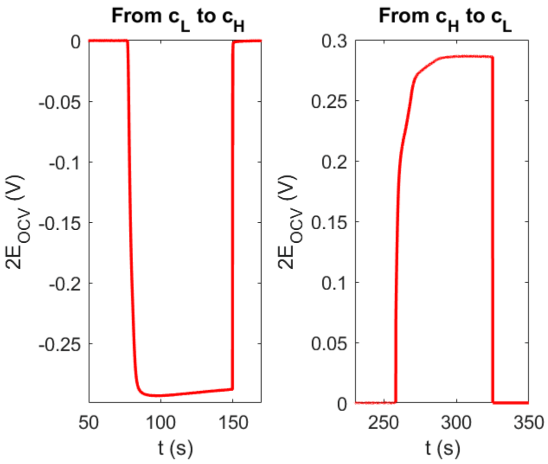

Fig. 2.7 Open-circuit voltage measurement for a capacitive concentration cell. The characteristic time for a potential change equilibrium is different in the case where the solution changes from from c_L to c_H or from c_H to c_L within a water compartment.

The electrical boosting signal $E_0(t)$ and the cell potential $E_{OCV}(t)$ do not have exactly the same time dependency. The electrical boosting signal changes instantaneously from $-E_0$ to E_0 and corresponds to an Heaviside signal. When the concentrations are inverted, for a short period of time the concentration of the solution is not the same throughout the cell. The area near the fluid inlet of one compartment contains salt water, while the outlet contains fresh water, and vice versa for the other compartment. The signal of cell potential variation is therefore not an Heaviside function, but a slower-varying function that can be modeled by an exponential relaxation with a characteristic time of 2 seconds (2 seconds is the filling time of our cell considering the applied flow rate and the dimensions of the cell).

Let us highlight, that if the two electrodes are slightly different and have different capacitances, the equilibrium times of the cell potential may be different depending on which compartment is supplied with the diluted solution. This is easily explained. Potential equilibrium time is the longest time required to equilibrate each electrode potential. This time depends on electrode geometry, filling conditions in each compartment and salt concentration. When electrode 1 (respectively 2) is in contact with the dilute solution of concentration c_L, this time is $\tau_{1L} = f(c_L)$ (respectively $\tau_{2L} = g(c_L)$). When electrode 1 (respectively 2) is in contact with the concentrated solution of concentration c_H , this time is $\tau_{1H} = f(c_H)$ (respectively $\tau_{2H} = g(c_H)$. So when compartment 1 contains dilute solution and compartment 2 concentrated solution, the characteristic time is the maximum of τ_{1L} and τ_{2H}. When compartment 2 contains dilute solution and compartment 1 concentrated solution, the characteristic time is the maximum of τ_{1H} and τ_{2L}. These two characteristic times are slightly different. Experimentally, this is what is measured on the cell during open-circuit experiments. The two times are slightly different when going from c_L to c_H in compartment 1 (Left in Fig 2.7) and from c_H to c_L in compartment 1 (Right in Fig 2.7).

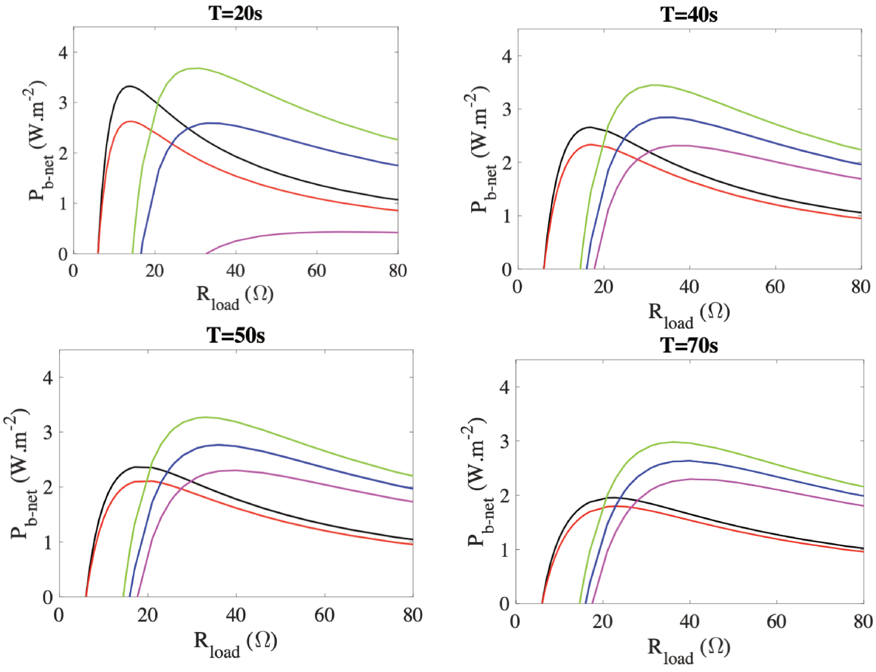

Fig. 2.8 Evolution of the surface density harvested power as a function of the load resistance. Each graph corresponds to different concentration inversion periods T_s=25, 40, 50, 70 s. The black lines correspond to experiments without boosting and a Heaviside cell potential signal. The red lines correspond to experiments without boosting and a cell potential signal exhibiting an exponential relaxation with a characteristic time τ=2 s. This situation models the effect of mixing. The green lines correspond to experiments with boosting and a cell potential signal of Heaviside type. The blue lines correspond to experiments with boosting and a cell potential signal exhibiting exponential relaxation with an identical characteristic time τ=2 s. The magenta lines corresponds to experiments with boosting and a cell potential signal exhibiting two exponential relaxation τ_1=2 s, $\tau_2 = 6$ s. This situation models the effect of mixing. Mixing affects the boosting strategy to a greater extent. The simulation parameters are as follows: E_{OCV}=0.144 V; E_0=0.2 V; S=2.24 cm^2; C=1.2 F and R_{cell}=6 Ω.

To take the mixing effect into account and following the model of CRED system[117], we slightly modify the model and write:

In absence of boosting:

For $0 < t < T_s$:

$$(R_{load} + R_{cell})I(t) + \frac{q(t)}{C} = E_{OCV}(1 - 2exp(-t/\tau_1)); \tag{2.16}$$

For $T_s < t < 2T_s$:

$$(R_{load} + R_{cell})I(t) + \frac{q(t)}{C} = -E_{OCV}(1 - 2exp(-t/\tau_2)); \tag{2.17}$$

τ_1 and τ_2 are the characteristic times. They are related to the filling time of each compartment, their permeability, the geometry of the electrode.

In presence of boosting :

For $0 < t < T_s$:

$$(R_{load} + R_{cell})I(t) + \frac{q(t)}{C} = E_{OCV}(1 - 2exp(-t/\tau_1)) + E_0 \tag{2.18}$$

For $T_s < t < 2T_s$:

$$(R_{load} + R_{cell})I(t) + \frac{q(t)}{C} = -E_{OCV}(1 - 2exp(-t/\tau_2)) - E_0 \tag{2.19}$$

Fig 2.8 displays the obtained results. In all cases, the mixture affects and reduces the recovered power. Let us first consider the situation with an identical characteristic time $\tau_1 = \tau_2$. The Fig 2.8 shows that in the presence of boosting, mixing has a greater effect on power density drop. For a period of 20 s, due to the mixing effect, the maximum power density drops by 0.7 W.m^{-2} without boosting and by 1.1 W.m^{-2} in the presence of boosting. These figures drop as the concentration inversion period increases, and is much longer than the mixing time. The maximum power density drops by 0.27 W.m^{-2} without boosting and by 0.5 W.m^{-2} in the presence of boosting for T_s=50 s. The maximum power drops by 0.2 W.m^{-2} without boosting and by 0.4 W.m^{-2} in the presence of boosting for T_s=65 s. Let us then comment the situation where τ_1=2 s differs from τ_2=6 s. As you might have guessed, the power density drop is comparable with that of an identical characteristic time. And it is worse than that which would have been obtained with an identical characteristic time based on the shortest time.

Influence of boosting voltage E_0

The boosting voltage E_0 is the additional voltage injected by the booster system. To study its impact on the power density, we measure the power density as a function of electrical resistances for various boosting voltage E_0 at a fixed switching period T_s. We limit our study to low boosting voltage (below 1 V) to avoid water hydrolysis.

The gain increases at low boosting voltage and then saturates. This phenomenon is fully described by the model (see Fig 2.9 **(a)**) and comes directly from the electrical equations of the system.

Influence of salinity gradient

It is interesting to note that the salinity ratio can have two paradoxical effects on the power density output (see Fig 2.9 **(b)**). An increase in salinity ratio raises the ionic flux across the membrane induced by osmotic effect, thus results in a higher open-circuit voltage of the cell. As the power density is positively associated with open-circuit voltage in square, higher salinity ratio can effectively lead to a higher power output of the system. Meanwhile, the decrease in salt concentration of the fresh water compartment indicates an electrical resistance increase of the entire cell system, which limits the power output. In the case of a cell-booster system, the simulation prediction indicates that boosting principle is much more efficient for cells with lower electrical resistances (Fig 2.9 **(b)**). The

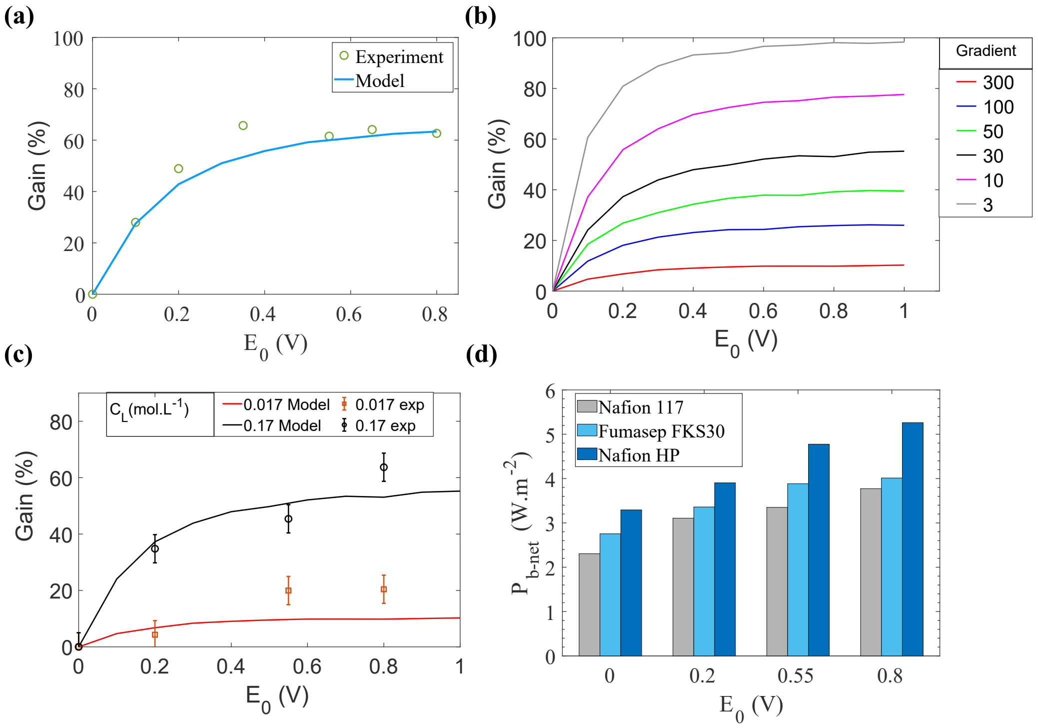

Fig. 2.9 **(a)** The gain of the harvested power density as a function of the boosting voltage E_0. The experimental conditions are as following: salinity ratio of 30 (fresh water concentration of 0.17 M and salted water concentration of 5.13 M) , flow rate of 10 mL.min^{-1}, switching period of 60 s, and CEM of Nafion 117. **(b)** Simulation results of gain as a function of the boosting voltage E_0 and the salinity gradient for a fixed concentration of salt solution (5.13 M) and T_s= 45 s. **(c)** Impact of the salinity gradient on power density gain for capacitive salinity-gradient cell coupled with a booster system. The concentration of salt solution and the period are fixed at 5.13 M and 45 s, respectively. **(d)** Net power density measured for other types of CEMs, including Nafion HP, Nafion 117 and Fumasep FKS-30. The experimental conditions are as following: salinity ratio of 30 (fresh water concentration of 0.17 M and salted water concentration of 5.13 M), flow rate of 10 mL.min^{-1}, and a switching period T_s of 45 s.

gain is higher when the salt concentration are set to 5.13 M vs 1.7 M. This simulation is based on the theoretical model explained above and the cell parameters measured by OCV and CP experiments (Table 2.1).

Such phenomenon is verified by experimental results (see Fig 2.9 **(c)**). When the salt concentrations are set to 5.13 M vs 0.17 M, the period at T_s=45 s and the boosting voltage at 800 mV, the gain can reach 64 %, corresponding to a maximum power density of 3.77 W.m^{-2}. By changing the concentration of the diluted solution to 0.017 M and for the the same conditions, this system generated a maximum power density of 4.29 W.m^{-2}, which corresponds to only 20 % increase compared with its maximal power density of 3.53 W.m^{-2} without the booster system. This can be explained by the fact that, in the second case the resistance of the cell and the salt ratio are higher than in the first one.

Other cation-exchange membranes

The boosting strategy is proved to be applicable to other commercial cationic membranes according to our research results. Here three examples of commercial ion-exchange membranes are presented, including Nafion

117 (Chemours), Nafion HP (Chemours) and Fumasep FKS-30 (Fumatech). The experimental results displayed on Fig 2.9 **(d)** are all achieved in the following conditions: salinity ratio of 30 (fresh water concentration of 0.17 M and salted water concentration of 5.13 M), flow rate 10 mL.min^{-1} and switching period fixed at 45 s, boosting voltage $E_0 = 0.8V$.

Table 2.2 Net power density performances of capacitive concentration cell with different commercial CEMs under boosting strategy of $E_0 = 0.8V$

Materials	E_{OCV} (V)	R_{cell} (Ω)	P_{nb} (W.m^{-2})	P_{b-net} (W.m^{-2})
Fumasep FKS-30	0.157	6.08	2.75	4.01
Nafion HP	0.158	4.92	3.29	5.26
Nafion 117	0.145	5.4	2.3	3.8

2.5 Mechanism

We have demonstrated in the preceding section that the boosting strategy could effectively enhance the net power density output of the CRED system. This point is verified both by experimental results and by theoretical modelling. However, it still lacks the underlying the mechanism of the boosting strategy. In this section, we conduct complete studies based on the equivalent circuit of an ideal system, a CRED system and a CRED system under boosting strategy, respectively. We pointed out that the energy performance gap is due to the "inefficient regime" of CRED system, where a significant capacitive current decay hinders the overall energy conversion efficiency. Boosting strategy actually helps to enlarge the "efficient regime" working window. By optimizing the working regime under boosting, CRED system could approach the theoretical power density output limit.

As illustrated in Fig 2.10, an ideal battery is featured by an electromotive force equal to E_{OCV}, an internal resistance R_{cell}, and ideal electrodes with no over-potential and no resistance. While enclosed by a load resistance R_{load}, such system delivers a maximum power of $\frac{E_{OCV}^2}{4R_{cell}}$ in the situation of $R_{cell} = R_{load}$. Indeed, we're looking to supply power to the load resistance and not to the internal resistance, which means that we must have $R_{cell} < R_{load}$. In the situation where the electrodes are ideal (faradaic without overvoltage and no resistance), the current intensity is constant, as described by the following equation: $I = \frac{E_{OCV}}{R_{load}+R_{cell}}$. It is therefore maximum for the smallest R_{load}. Combining both conditions leads to $R_{load}^* = R_{cell}$, where R_{load}^* is the resistance that allows to recover the maximum power $P_{max} = \frac{E_{OCV}^2}{4R_{cell}}$.

While equipped with capacitive electrodes, concentration cells behave differently. As demonstrated in Fig 2.10, an additional capacitor is added into the equivalent circuit, forming a typical R-C circuit. In this case, the current intensity $I(t)$ varies upon time. The effective electromotive force E_{eff} equals to the difference between the electromotive force of the battery and the potential difference across the capacitor of the capacitive electrode $E_{eff} = E_{OCV} - \frac{q(t)}{C}$. For R-C circuits, the electrical characteristic time $\tau = (R_{cell} + R_{load})C$ represents the time required for capacitor charging or discharging. It plays an important role in electrical performances of the capacitive concentration cells. For operation time T_s much less than the characteristic time τ, the capacitor does not have sufficient time for charging. Thus, the effective electromotive force E_{eff} remains close to E_{OCV}. We name this case an "efficient regime". While the electric capacitor charge remains low in this regime, the current intensity maintains a rather high value close to $I = \frac{E_{OCV}}{R_{load}+R_{cell}}$. The efficient regime reaches the situation of an ideal cell. Thus the maximum power is obtained when $R_{load}^* = R_{cell}$. The recorded density power at R_{load}^* remains constant with time and equals to $P_{max} = \frac{E_{OCV}^2}{4R_{cell}}$. For T_s comparable or even higher than τ, we can no longer neglect the capacitor charging process. The system behaves in a so-called "inefficient regime". As described by the definition

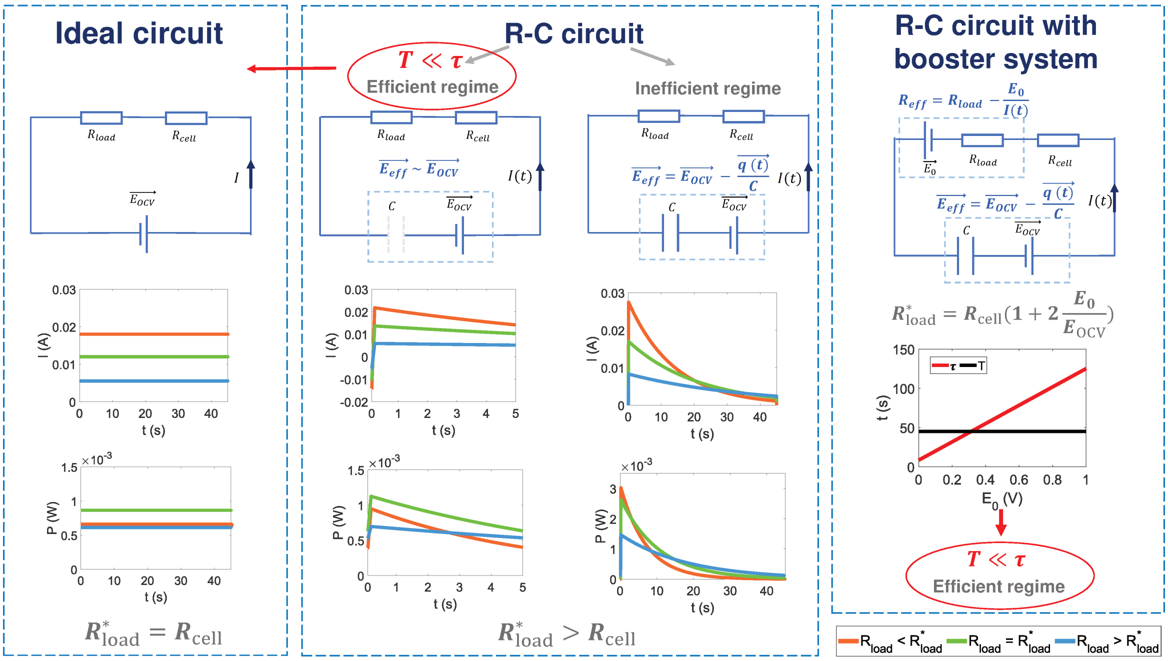

Fig. 2.10 Theoretical analysis of power density performance for the ideal circuit, R-C circuit, and R-C circuit with a booster system, respectively. We illustrate the electrical current curve and power curve within the fixed period T_s for each case. The power performance loss is due to the current decay in R-C circuits which fails to satisfy the condition $T \ll \tau$ in "inefficient regime". The use of an additional booster system enlarges the time window and shifts the working regime towards "efficient regime".

of effective electromotive force E_{eff}, the presence of a capacitor reduces the electromotive force and therefore reduces the power dissipated in the load resistor. In addition, the optimal resistance R^*_{load} is higher than in the previous case. This is due to the decay of current intensity over time. The previous balance between voltage divider and electrical current results in an optimal condition of $R^*_{load} = R_{cell}$ for ideal cell performance optimization. For capacitive concentration cells, the load resistor R_{load} has an impact on the electrical characteristic time τ. A higher load resistance could prevent current decay in RC circuits and thus is beneficial for power density amelioration. This additional factor tilts the balance towards a higher optimal load resistance. In summary, R^*_{load} is therefore greater than R_{cell} in the situation of capacitive electrodes. The recorded density power varies with time and is less than $P_{max} = \frac{E^2_{OCV}}{4R_{cell}}$.

Based on the analysis, it is clear that capacitive systems present systematic lower power density performances compared with ideal cells. The performance gap is due to the capacitive current decay response of a typical R-C circuit. However, it is possible for capacitive systems to behave as ideal cells and reach the maximum theoretical value of P_{max}. The key issue is to ensure the condition $T \ll \tau$, so that the capacitive system operates at an “efficient regime”.

For capacitive concentration cells, a trivial way to satisfy the condition is to shorten the switching period T_s. However, such method is constrained in practical use. While making water compartment switch, the saltwater reservoir (freshwater reservoir) will be replaced by freshwater flows (saltwater flows). The uncontrolled mixing procedure will lead to a decreasing energy harvesting efficiency and remains an inevitable dynamic transition. The filling time is given by $\tau_{fill} = \frac{ewL}{Q}$ where Q is the flow rate, w is the cell width, and L is the cell length. To ensure the energy harvesting efficiency, it is essential to ensure $\tau_{fill} \ll T$. A fast filling time does not lead to a long constant for discharge but ensure the efficiency of the process by suppressing the period where the electrical potential is not well defined. This can be done by decreasing e and increasing Q. This approach has its limits, as it leads to an increase in viscous losses [117]. For an industrial cell, this constraint can be suppressed by keeping e to 1.4 mm, w to 1 m and L to 12.5 cm. This results in a filling time of 9 s, which is shorter than the concentration inversion time of 90-100 s. We anticipate that boosting will make it possible to use very long inversion times while maintaining efficient power production.

Another way of increasing the efficiency of capacitive electrodes is to use supercapacitors, i.e. capacitors with very high capacitances[248–250]. In this case, the electrical characteristic time τ is prolonged to satisfy the condition $T \ll \tau$. From a practical point of view, to recover maximum power, $T < 2\tau$ is required. Assuming $T = 90$ s and taking $T = 0.1 \times 2\tau$ as a criterion, this leads to a characteristic time of 450 s. For a capacitive cell of 1 m^2, the resistance is estimated at 9.6×10^{-4} Ω. The cell capacitance must be 468 750 $F.m^{-2}$, i.e. 46.8 $F.cm^{-2}$. It is difficult to achieve such high capacitance density in conventional systems.

In this work we present a novel strategy to ensure an ‘efficient regime’ for capacitive concentration cells. Our boosting strategy consists in connecting the capacitive cell to a secondary source of voltage E_0. In this case, the net power output is defined as the difference between gross power dissipated in the load resistor and the additional power supplied by the secondary source $P_{b-net} = R_{load}I(t)^2 - E_0 I(t)$, which is equal to the power supplied by the battery minus the power stored in the capacitor and the power dissipated in the internal resistance $E_{OCV}I(t) - \frac{I(t)q(t)}{C} - R_{cell}I(t)^2$. We underline that P_{b-net} is the net power delivered by the battery which is effectively produced by the circuit and can be stored. The power consumed by the secondary source $E_0 I(t)$ has been taken into account and subtracted.

A closer look at the expression of net power P_{b-net} shows that the secondary electromotive force acts as if it were lowering the effective value of the load resistor (Fig 2.10). It is thus possible to define an effective load resistance as $R_{eff} = R_{load} - \frac{E_0}{I(t)}$. If the effective load resistance is negative i.e $R_{load} < \frac{E_0}{I(t)}$, the power harvested in the load resistance is less than the power given by the secondary source of voltage. The balance of the circuit is negative. If the effective load resistance is positive i.e $R_{load} > \frac{E_0}{I(t)}$, the power harvested in the load resistance is higher than the power given by the secondary source of voltage. The balance of the circuit is positive and a net energy is produced. We produce in the load resistance an energy that is higher than the energy given by the secondary voltage. This situation can be analyzed in more detail by continuing the analogy with classical capacitive electrodes without secondary voltage. The net power recovered is that which would be recovered by an effective resistance equal to $R_{eff} = R_{load} - \frac{E_0}{I(t)}$ in a circuit made up of a battery with an electromotive force E_{OCV}, an internal resistance R_{cell} and an electrical characteristic time equal to $\tau = (R_{load} + R_{cell})C$. We're looking to supply power to the effective resistance and not to the internal resistance, which means that we must have $R_{cell} < R_{eff}$ i.e. $R_{cell} + \frac{E_0}{I(t)} < R_{load}$. This criterion differs from the one in absence of boosting. It will lead to an increase in the value of the optimal load resistance R^*_{load}, and therefore to an increase in the characteristic time τ for resistances close to this optimal resistance. The time window governing the "efficient regime" (i.e $t < \tau$) is enlarged. In this regime, the intensity is almost constant $I(t) \approx I(0) = \frac{E_0 + E_{OCV}}{R_{cell} + R_{eff}}$. The maximum recovered net power is reached for $R^*_{eff} = R_{cell}$ i.e for $R^*_{load} = R_{cell}(1 + 2\frac{E_0}{E_{OCV}})$ and is given by $R_{eff}I(0)^2 = R_{load}I(0)^2 - E_0 I(0) = \frac{E^2_{OCV}}{4R_{cell}}$. For resistances which values are close to the optimal resistance R^*_{load}, the characteristic electrical time τ is close to $2R_{cell}C(1 + \frac{E_0}{E_{OCV}})$. Note that the gross power recovered in the load resistor is $R_{load}I^2$ and not $R_{eff}I^2$. $\frac{E^2_{OCV}}{4R_{cell}}$ corresponds to the extra power recorded. Although additional energy consumption is required in boosting, due to the efficiency increase, our system not only recovers the additional energy provided by the booster system, but also presents higher net power density output. A rigorous calculation is presented in supporting information.

In short, to increase the efficiency of capacitive electrodes, the key issue is to ensure the condition $T \ll \tau$. The trivial solution of decreasing the switching period T_s is restricted by the dynamic filling regime during water switch. The use of supercapacitors seems quite difficult due to the high capacitance required. To enhance the power density performance, we suggest the use of a secondary source to enlarge the time window and force the capacitive electrodes into the so-called efficient operating regime.

2.6 Techno-economic analysis

In order to realize an economical analysis of our system, two commercially available membranes of low cost are tested under same experimental conditions: salinity ratio of 30 (300 g.L^{-1} vs. 10 g.L^{-1}), switching period T_s of 45 s, flow rate of 10 mL.min^{-1} and boosting voltage E_0 of 0.8V (for Selemion membranes) and 0.3 V (for Celgard membranes). The boosting strategy is proved to be applicable to these commercial membranes according to our research results. Fig 2.11 displays the results obtained for a capacitive concentration cell with and without boosting.

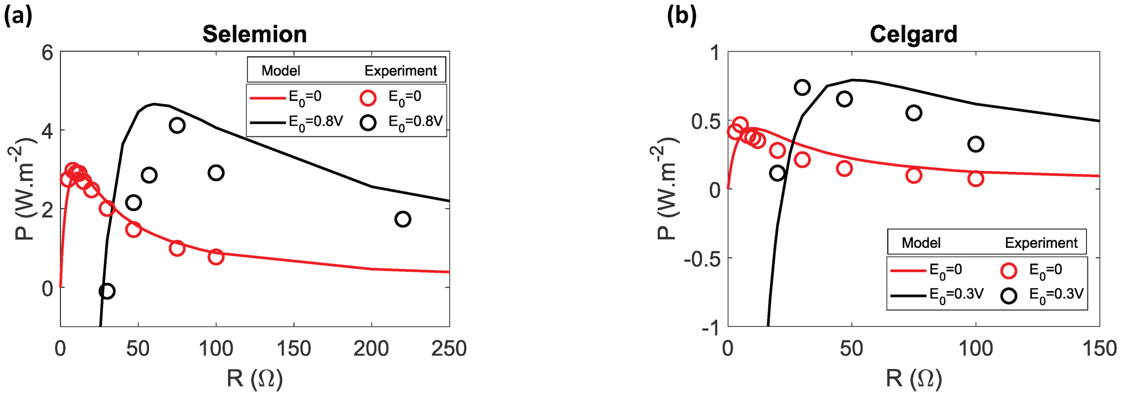

Fig. 2.11 Power density measurement for Selemion and Celgard membranes with and without boosting strategy. For Selemion membranes, the solid lines correspond to modelling results with fitting parameters fixed at E_{OCV}=148 mV, R_{cell} = 5 Ω and C = 1.2 F. For Celgard membranes, the solid lines correspond to modelling results with fitting parameters fixed at E_{OCV}=55 mV, R_{cell} = 3.3 Ω and C = 1.2 F. Experimental dots are obtained in the following conditions: experimental conditions: salinity ratio of 30 (300 g.L^{-1} vs. 10 g.L^{-1}), switching period T_s of 45s, flow rate of 10 mL.min^{-1} and boosting voltage E_0 of 0.8V (for Selemion membranes) and 0.3V (for Celgard membranes)

We tested Selemion CMVN (AGC), which is at a cost of 100 euros per m ^{2}. It presents a power density of 3 W.m^{-2} without boosting and a power density of 4.11 W.m^{-2} with a boosting voltage of 0.8 V. The performance is comparable to that of Nafion, but the price represents only 10%. We also tested Celgard 3401 membrane (Celgard) at a cost of 20 euros per m^2. This is a non-selective membrane, thus we will lose the potential contribution of the membrane E_m. We measure a power density of 0.46 W.m $^{-2}$ without boosting and a power density of 0.74 W.m $^{-2}$ with a boosting voltage of 0.3 V. Although the power density presents 20% of Nafion membrane, the cost remains 3% of Nafion membrane. In addition, both membranes could be fabricated in large volumes. From an economical point of view, these membranes are well worth exploring for large-scale uses in industrial field.

The cost of a RED system was estimated by Post[197, 251] in 2010 at 890,000 euros for a system producing 200 kW. The calculation includes the costs of construction, filtration, liquid pumping and maintenance. The fluids pass through the system only once, at a speed comparable to our experiments. The calculation takes into account a membrane price of 2 euros per m^2 and a power of 2 W per m^2. It's important to note that no membrane currently achieves this cost price. The lowest PRO membrane prices are 10 euros per m^2, and the US Dept of Energy's target price is 40 euros per m^2. 10 euros per m^2 is also the price of sPEEK's supposed membranes, which has been mentioned in recent articles but not yet in the following cited articles[252, 253]. Following these considerations, we propose an analysis at 10 euros per m^2 and one at 40 euros per m^2 as an extension and modification of the work of Post[197, 254]. The viscous loss is estimated at 0.2 W per m^2 of membranes. We have previously measured similar viscous losses in our devices (0.1 W per m^2). To this figure we need to add the power required to reverse the flows. Power ball valves type BW3-100-AW1-230AC valves from JP Fluid Control are suitable for reversing flows of 1-100 $L.min^{-1}$ (This range of flow rates correspond to the experimental conditions of our study extrapolated to a 1 m^2 device i.e 1 $L.min^{-1}$ for a surface of 1 m^2). The valves require a power supply of 6 W and cost around 150 €. In our set-up, they are only used for one second out of the period. The power lost is therefore 0.13 W. The losses in our device are thus comparable to the one of Post (0.23 $W.m^{-2}$ compared to 0.2 $W.m^{-2}$).

The characteristic fluid velocity is 3 $cm.s^{-1}$, that of our experiments 1 $cm.s^{-1}$. Membrane lifetime is 7 years, with production running 8,000 hours an year. The cost of the system is 890,000 euros. Taking inflation into account, this corresponds to a current cost of 1,130,000 euros (First column of Table S2.3). This results in a production cost equal to 0.104 € per kWh, i.e. 104 euros per MWh. This figure is in line with current electricity production costs (solar energy 40 € par MWh, wind off shore 120 €per MWh[255]). However, this analysis is over-optimistic, as there are as yet no high-performance membranes at 2 € by m^2. This is probably one of the reasons why there are no industrial blue energy devices. An analysis based on the U.S. Department of Energy's target for membrane cost leads to 451 € par MWh. That is too expensive and not profitable.

Table 2.3 Cost break-down for a membrane reverse electrodialysis unit (membrane surface 100 000 m^2). Post's data [254] have been updated to take account of inflation since 2009 at 27%[256]. This situation corresponds to the production of energy starting from sea water and river water. A scenario : Post analysis taking into account inflation with a membrane price of 10 euros by m^2. This situation corresponds to the production of energy starting from sea water and river water. B scenario: Post analysis taking into account inflation with a membrane price of 40 euros by m^2 as targeted by the US Dept of Energy. This situation corresponds to the production of energy starting from sea water and river water. C scenario: Selemion membrane for desalination plants. D scenario: Celgard membrane for desalination plants.

Part	Post scenario Construction Costs	A scenario Construction Costs	B scenario Construction Costs	C scenario Construction Costs	D scenario Construction Costs
Membrane cost	254 000	1000000	4000000	11 000 000	2 000 000
Piping, fittings and pumps	406 400	406 400	406 400	406 400	406 400
Valves	0	0	0	150 000	150 000
Electronics for boosting	0	0	0	100 000	100 000
Filtration	469 900	469 900	469 900	0	0
Total	1 130 300	1 876 300	4 876 300	11 656 400	2 656 400
Net Power	200 kW	200 kW	200 kW	388 kW	50 kW
MWh cost (€)	104	173	451	536	948

In this context, our study allows us to take a small step forward. We were able to produce 5 W.m $^{-2}$ with salinity fluids of 300 g.L $^{-1}$ and 10 g.L^{-1}. These are not the conditions found at river mouths, but rather in desalination plants. In this framework, the solutions are already filtered. The cost of this operation has no longer to be included in the cost of electricity production.

The cost of the membranes remains an issue. An exhaustive study of all types of membranes is not the subject of this paper. However, the above mentioned two membranes could provide us with a cost range of our capacitive concentration system. The Selemion CMVN membrane at a cost of 100 € per m ^{2} presents a power density of 3.88 W.m^{-2} if we take into account the hydrodynamic losses. The non-selective Celgard membrane at a cost of 20 euros per m^{2} presents a maximal net power density of 0.5 W.m^{-2} if we take into account the hydrodynamic losses. These two membranes are the limits in terms of efficiency. Nafion is a highly efficient selective membrane, while Celgard is a non-selective membrane. Table 2.3 displays the cost break-down for a membrane reverse electrodialysis unit (membrane surface 100 000 m^{2}) following the hypothesis of Post[254]. The cost of the capacitive carbon layers and electrodes is set to 10 € by m^{-2}. The cost of electronics for boosting to 100 000 € assuming that AC/DC converters are less to 1 € a piece. These figures are 5 to 9 times higher than the limits of profitability. They are set to fall as a result of scale and market expansion. The development of blue energy techniques requires the discovery of efficient membranes, i.e. membranes that are selective and avoid mixing. At this stage, the discoveries of recent years give grounds for optimism [252, 253]. Sulfonated poly (ether ether ketone) (SPEEK) membranes are of interest[257–260]. These articles claim that they will cost less than 10 € per m^{2} and they are selective. Note that they are not yet commercialized. Following our analysis, their use will reduce the cost to 81 € per MWh, if their supposed price is maintained.

2.7 Conclusion

Conclusion

To conclude this chapter, we studied the power density gap between experimental results and theoretical value of CRED systems and proposed an effective strategy for energy performance amelioration.

1. We discovered the intrinsic problem of energy conversion efficiency due to the use of capacitive electrodes. The power density gap is strongly related to the capacitive current decay phenomenon, which impacts the ionic-electronic conversion efficiency in the CRED system.

2. The ionic-electronic conversion efficiency of capacitive electrodes depends on the relationship between the RC circuit characteristic time τ and switching period T_s. While $T \gg \tau$, CRED systems presents significant current decay within each period, leading to an important conversion efficiency limitation in "inefficient regime". However, with $T \ll \tau$, CRED system maintains well its capacitive current within each period, reaching its theoretical power density performance in "efficient regime".

3. Based on the understanding of the underlying mechanism, we proposed a novel boosting strategy by using a secondary voltage source in order to enhance power density output of capacitive RED processes. The net power density is defined as the gross power received in the resistor minus the power supplied by the secondary source. A maximum net power density of 5.26 W.m^{-2} is achieved under experimental conditions. Theoretical analysis indicates that the use of a booster system increases the optimal resistance of the electrical circuit, which results in a higher characteristic time τ. This leads to an enlarged time window of the “efficient regime” for capacitive concentration cells. In such “efficient regimes”, capacitive concentration cells approach the maximal power density performance of ideal cells.

4. According to our techno-economic analysis for different scenarios, CRED system coupled with boosting strategy presents a cost of 5 to 9 times higher than the profitability of 100 €/MWh. However, this cost is set to fall with the development of cost-effective membranes, such as sPEEK membranes.

Chapter 3

Influence of divalent ions on CRED system performance

3.1 Preamble

It is to notice that there is a giant gap between lab research and industrial application of blue energy harvesting systems. The majority of the studies have been conducted using artificial seawater and freshwater with a predominant presence of NaCl. However in real industrial processes involve mixing of salinity gradients, such as production water, desalination plants, salt mining etc, feed waters are of complex composition with significant presence of divalent ions[261]. The complex composition of the real-world feed waters can lead to important energy performance loss. Such phenomenon is partially originated from the impurities such as organic particles, clay particles, micro-organisms that may plug the membrane[169].

Beyond those problems, the presence of divalent ions seems to affect the behavior of energy recovery devices. The inclusion of multivalent ions, particularly Mg^{2+} and Ca^{2+}, has an adverse impact on osmotic energy production efficiency. For example, Post et al. [148] observed that the introduction of $MgSO_4$ into the diluted stream led to a reduction in stack voltage compared to using NaCl alone in the feed. Vermaas et al. [134] identified a detrimental effect of multivalent ions on RED performance in real-world feed waters. When using a mixture with a molar fraction of 10% $MgSO_4$ and 90 % of NaCl in both feed waters, the experimentally obtained power density in steady state decreases up to 50 % compared to the case where the feed solutions contain only NaCl as a salt. Veerman et al.[157] studied a RED module for salinity gradient energy extraction made of 20 membranes pairs of FKS-75 and FAS-75. When only sodium chloride was included in the feed stream of typical composition of 0.5 M for the artificial sea water and 0.02 M for the artificial river water , the harvested power density was equal to 0.743 $W.m^{-2}$ of membranes. It decreases to 0.5 $W.m^{-2}$ when 0.06 M is added to the more concentrated brine and 0.0024 M to the more dilute one. This corresponds to a power decrease of 33 % when a 10% molar fraction of $MgCl_2$ is added.

Four major process are at the origin of this decrease [151]: decrease of the open circuit potential, uphill transportation, increase of the resistance of the membrane, and loss of the selectivity of the membrane. From a thermodynamic point of view, the membrane potential decreases when divalent ions are introduced. Firstly, the membrane potential scales as the valence of the ion at the power minus one. Secondly, the ratio of the activity coefficients of divalent ions is lower than that of divalent ions. Because of the valence of the ion, the electromotive force of the monovalent ions is larger than that of the divalent ions. This causes a reversed transportation of multivalent ions against the concentration gradient called uphill transport. The salinity difference is decreased and the harvested power is lower. Uphill transport of divalent ions Mg^{2+} was evidenced experimentally by Avci et al. using Ion Chromatography analysis conducted on inlet and outlet streams of the RED system [135, 144].

Additionally, multivalent ions have larger radii, charges and dehydration energies. Their transport across membranes is slowed down, leading to the trapping of multivalent ions in the membrane due to electrostatic bridging of ionic charges with fixed membrane charges. As a result, the electrical resistance of the membrane increases and selectivity decreases. The decrease in selectivity is aided by another phenomenon. Multivalent ions drag along co ions with the same charge as the membrane, reducing the membrane's selectivity[262]. Fontananova et al. conducted systematic studies to evaluate the common ions as Mg^{2+}, Ca^{2+} and SO_4^{2-}[154]. They identified a strong negative effect of divalent ions on both ionic resistance and permselectivity of ion exchange membranes. Oh et al. confirmed that as divalent ions of small hydrated radius presents higher electrical resistance in CEMs[155]. Gomez-Coma et al. studied experimentally the effect of multivalent ion species on membrane resistance[156]. Other possibilities for reducing membrane fouling and avoiding loss of selectivity are to frequently change the direction of the electric current, for example by applying short electric pulses as reported by Cifuentes-Araya et al.[263] or by changing the feed water as reported by Allison [264].

Up to present, the electrochemcial characterizations and energy performance evaluation of CRED system are conducted only in NaCl based artificial solutions. More evaluations should be carried out with real-world solutions to verify the feasibility of CRED system in industrialization. What is the impact of divalent ions on energy performance of CRED systems? Is there a significant power density drop in CRED systems as described for faradaic RED systems? What is the power density drop mechanism of divalent ion mixing? To reply to these questions, we perform a systematic study on CRED system with complex solutions of different divalent ion fractions.

In this chapter, we start by presenting the experimental set-up of the CRED system and the complex solution preparation. We measure cell potentials, membrane potentials, open-circuit electrode potentials and cell impedance as a function of monovolent ions concentrations and mixture of monovalent and divalent ions. Maximum recoverable powers are then measured and compared with faradaic RED results. We focus on two types of evaluations: first, we study the power recovered at short times (i.e. when the membrane is soaking in the electrolyte for less than 1 hour), then we carry out long-time cycling (i.e. over 8 hours). In addition, application cases with real-life solutions are presented. Finally, we complete the study with a techno-economic analysis of CRED system under real-life complex solutions.

3.2 Experiment set-up

In this section, we present the experimental set-up used in the research study. Overall, the cell voltage measurement, electrochmeical studies and power density measurement are all performed on a CRED system. In order to gain insight into the membrane potential and electrode potential, a faradaic cell with Ag/AgCl electrodes is used to complete the cell voltage study. Solutions of different divalent ion fractions are prepared and injected in CRED system to study the impact of divalent ions.

3.2.1 CRED system

The CRED cell configuration is similar to that used in Chapter 2. As illustrated in Fig 3.1 (a), the cell exhibits symmetrical geometry, featuring an ion-exchange membrane (Nafion^{TM}HP, Chemours) sandwiched between two water compartments containing varying salt concentrations. The effective surface area of the ion-exchange membrane used in our experimentation measures 10.15 cm^2. Carbon felt capacitive porous electrodes (Kynol Activated Carbon Felt) are separately positioned within gaskets on either side of the membrane. The graphite current collectors are situated at a distance of 1.4 mm from the membrane and are directly linked to the carbon felt capacitive porous electrodes. The entire assembly is securely sealed by stainless steel endplates and held together using eight bolts torqued to 2 N.m. Note that after the cell has been clamped, there is no space between the electrodes and the capacitive tissue. Saline solutions flow into the pores of the capacitive tissue. Two ports facilitate water inlet and outlet, driven by a peristaltic pump (Longer Multichannel Peristaltic pump) operating at a consistent flow rate of 15 mL.min^{-1}.

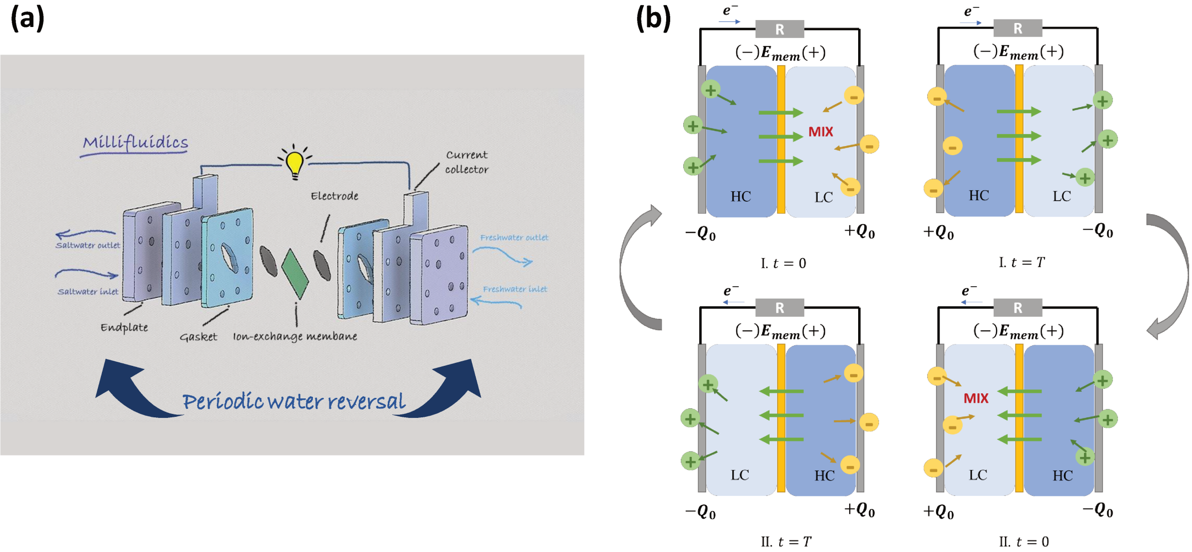

Fig. 3.1 Schematic illustration of the capacitive cell. (a) The capacitive system assembly illustration. (b) The working principle of the CRED system. The periodic water solution reversal is necessary to ensure the continuous electricity production. The eventual electrical signal delivered by the CRED system will be periodic and alternating.

While concentrated solution and diluted solution are injected continuously into the capacitive system, a cationic flow is generated from the concentrated part towards the diluted part under the osmotic effect. The cation exchange membrane blocks the anions and water molecules from free passing. In order to generated electricity, it is necessary to convert this cationic flux into a flux of electrons. In a capacitive system, ions are adsorbed onto the capacitive electrode, inducing the movement of electrons in the outer circuit. Due to charge accumulation inside the capacitive electrodes, the system reaches eventually a saturation regime where the fully charged capacitor blocks the creation of cationic flux (Fig 3.1 (b)). To deblock the saturated regime of capacitive charging, an automated 4-port valve switches water compartments at fixed intervals of T_s. By doing the solution reversal in the chamber, one can reverse the direction of both ionic and electronic flux, thus discharging the accumulated charges in capacitive electrodes and restart the charging process in a reversed direction. This repeated transition within a fixed period T_s unblocks the saturation state, enabling the cell to deliver periodic alternating current.A detailed model can be found in [3].

In open-circuit cases, the cell voltage E_{OCV} is the sum of the Donnan potential E_{mem} and of electrode potentials E_{elec}. The Donnan potential is given by the Nernst equation, corrected for the activity of the feed waters and the apparent permselectivity of the non-perfect membrane. It is given by :

$$E_m = \frac{\alpha RT}{z_i F} log \frac{a_{i,1}}{a_{i,2}} \tag{3.1}$$

where E_m represents the electromotive force across the membrane (in volts, V), R stands for the universal gas constant (8.314 J mol^{-1} K^{-1}), T is the temperature, z_i represents the valence of the ionic species i (dimensionless), F is the Faraday constant (96,485 C mol^{-1}), and a_i signifies the activity of ionic species i in the feed water (in molarity, M).α is the selectivity of the membrane, $\alpha = 1$ corresponds to a perfect selective membrane. In the situation of a cation exchange membrane, $\alpha = 1$ corresponds to a membrane that allows the free passage of cations but blocks all the anions. The subscripts 1 and 2 indicate the side of the membrane. Equation 3.1 illustrates that a salinity ratio of monovalent ions (such as Na^+, Cl^-) results in twice the voltage generated by an equivalent salinity ratio of divalent ions (such as Mg^{2+}, ${SO_4}^{2-}$), assuming constant activities and apparent membrane permselectivity.

We suggest readers to refer to the CRED section in Chapter 2 for more details of the CRED system and its characterization methods. We perform systematic characterization of the system open-circuit voltage, inner resistance and capacitance under different solutions.

3.2.2 Open-circuit Voltage measurement of CRED system

To evaluate the inherent potential of the circuit, we initially link the two cell electrodes. One compartment is filled with a high salt concentration while the other contains a low salt concentration. We then wait for equilibrium to be established.

Modeling the temporal progression of the potential necessitates understanding the behavior of both the electrodes and the membrane. Across the entirety of the circuit, there is no voltage drop. This can be expressed as follows:

$$R_{load}I + R_{cell}I + \frac{q}{C} = E_m(t) + E_{elec-c}(t) \tag{3.2}$$

Here, $E_m(t)$ represents the voltage drop across the membrane, $E_{elec-c}(t)$ signifies the voltage drop across the capacitive layer, I denotes the current intensity, and R_{cell} is the ohmic resistance of the cell, which encompasses the resistance of the solvent, carbon felt, and current collector.

Changes in the concentrations of ions over time cause the temporal evolution of $E_{elec-c}(t)$ and $E_m(t)$. These variations stem from cell filling and the creation of a diffuse ion layer near the electrodes when altering the salt concentration.

At $t = 0$, the system is in a stable state with $I(0) = 0$ and $q(0) = q_0 = C(E_m(\infty) + E_{elec-c}(\infty)$. For t less than 0, the sum of membrane and capacitive layer potentials is given by $E_m(\infty) + E_{elec-c}(\infty)$; at $t = 0$, the flow in both compartments reverses and the signs of membrane and capacitive layer potentials change. Upon reaching steady state after reversal, membrane and capacitive layer potentials are determined by $-E_m(\infty) - E_{elec-c}(\infty)$.

The solution to Equation 3.2 is straightforward. We arrive at:

$$q = \exp^{-\int_0^t \frac{du}{RC}} \int_0^t -\frac{E_m(s) + E_{elec-c}(s)}{R} \exp^{-\int_0^s \frac{du}{RC}} ds + q_0 \exp^{-\int_0^t \frac{du}{RC}} \tag{3.3}$$

$$A(t) = \frac{1}{RC} \exp^{-\int_0^t \frac{du}{RC}} \int_0^t -\frac{E_m(s) + E_{elec-c}(s)}{R} \exp^{-\int_0^s \frac{du}{RC}} ds \tag{3.4}$$

$$I(t) = A(t) - \frac{q_0}{RC(t)} \exp^{-\int_0^t \frac{du}{RC}} - \frac{E_m(t) + E_{elec-c}(t)}{R} \tag{3.5}$$

$q_0 = C(E_m(\infty) + E_{elec-c}(\infty))$.

This leads to $RI(\infty) = E_{OCV-c} = -2(E_m(\infty) + E_{elec-c}(\infty))$. To conclude, as noted in the main text, the open-circuit measurement for a capacitive cell corresponds to twice the steady-state membrane potential and capacitive layer values.

Experimentally, to measure E_{OCV-c}, we continuously feed the compartments with solutions of different salinities for 300 s, then reverse the flows for 300 s. This process is repeated 5 times. We record the evolution of the open-circuit voltage signal. The cell delivers no electrical current, and only ionic flows are responsible for the measured signal. The signal stabilizes in less than 100 seconds after the flow reversals. The signal is averaged over the 50 seconds preceding the change in concentration. E_{OCV-c} is measured by taking the quarter of the difference in signals when saltier water flows into the right-hand compartment and when saltier water flows into the left-hand compartment. The absolute values of the two measurements may differ slightly (by plus or minus 5%) if the two electrodes are not the same. In this situation, we measure the electrode potential plus the electrode membrane. It should be noted that these values are flow-dependent, due to the non-perfect selectivity of membranes.

3.2.3 Impedance characterization

Each compartment of the cell is supplied with a different saline solution under a constant flow rate. The circuit is open, and we wait for steady-state. We then apply 10 mV oscillatory perturbations over the open-circuit voltage. We use a logarithmically spaced frequency range from 200 kHz to 10 mHz for a fixed salinity ratio of 30 $g.L^{-1}$ vs. 1 $g.L^{-1}$ situation with different divalent ion mixing fraction. A Nyquist plot can be plotted corresponding all to a sweep over a frequency range from 200 kHz to 10 mHz. Note that the exact value of the impedance depends on the tightening. Here, we used the impedance data measured at 10 mHz to characterize the cell inner resistance and capacitance. Variations of 0.5 (Ω cm^2) in real part are measured on consecutive experiments despite the care taken to make the clamping procedure repeatable.

3.2.4 Faradaic RED system

In order to fully determine the membrane voltage E_m and capacitive electrode related voltage E_{elec-c}, we used faradaic cell with Ag/AgCl electrodes as well in the experiment. To gain insight into the individual impact of the membrane and the electrodes on the potential, we conducted separate measurements of the open-circuit potential of the membrane, denoted as E_m. These measurements were performed while subjecting the membrane to salt gradients, utilizing custom-made Faradaic Ag/AgCl electrodes.

In this scenario, the measured potential can be expressed as

$$E_{ocv-f} = E_{mem} + E_{elec-Ag/Agcl} \tag{3.6}$$

With

$$E_{elec-Ag/Agcl} = \frac{RT}{zF} ln(\frac{c_H \gamma_H}{c_L \gamma_L}) \tag{3.7}$$

It corresponds to the Nernst contribution from the Ag/AgCl electrodes. Activity coefficients γ_H and γ_L are calculated using Debye Huckel theory and taken directly from a Dortmund Data Bank database for concentrated solutions.

Here, the symbols R, T, z, F, γ, and c stand for the gas constant, temperature, ion valence, Faraday constant, mean activity coefficient, and salt concentration, respectively. The subscript H pertains to the concentrated solution, while L pertains to the dilute one. Knowing the salt concentrations it is possible to measure using Ag/Agcl electrodes the potential drop of potential across the membrane. We measured directly E_{elec-f} eventually.

To gain insight into the individual impact of divalent ion mixing on membrane voltage and electrode voltage, we conducted separate electrochemical measurements with both capacitive cells and faradaic cells. The capacitive cell assembly is described above and we measure the open-circuit voltage E_{OCV-c} for solutions of different salinity ratio with different mixing molar fraction. As explained above, the OCV voltage of a capacitive cell corresponds to twice the sum of the membrane voltage and capacitive electrode voltage.

$$E_{OCV-c} = 2(E_m + E_{elec-c}) \tag{3.8}$$

On the other hand, a faradaic cell composed of the same membrane but with custom-made Faradaic Ag/AgCl electrodes is used. We measure the open-circuit voltage E_{OCV-f} under the same experimental conditions, i.e. solutions of different salinity ratio with different mixing molar fraction. For a faradaic cell, the OCV voltage corresponds to the sum of the membrane voltage and the faradaic electrode voltage.

$$E_{OCV-f} = E_m + E_{elec-f} \tag{3.9}$$

Thus in order to obtain the membrane voltage E_m, it is necessary to measure the faradaic electrode related voltage E_{elec-f}. In our experiment, we immersed the two home-made Ag/AgCl electrodes into concentrated solution and diluted solution in two beakers separately. The solutions used in experiments follows the same experimental conditions as mentioned above for E_{OCV-c} and E_{OCV-f} measurements (solutions of different saliniy ratios with different divalent molar mixing fractions). The whole circuit is closed by the use of a home-made salt bridge (KCl saturated). Then the electrode potential difference E_{elec-f} is measured by using a potentiostat. Following the above two equations (Equation 3.8 and Equation 3.9), we can easily calculate the membrane voltage E_m and capacitive electrode voltage E_{elec-c}.

3.2.5 Preparation and composition of the salted solutions

NaCl, $MgCl_2$, $CaCl_2$ and KCl were purchased from Sigma Aldrich. In this study, we prepared solution mixtures of different concentrations. The compositions of these solutions are described in Table 3.1.

3.3 Impact of divalent ions on CRED

3.3.1 Cell voltage

In order to perform insight studies of the impact of divalent ion mixing on electrical voltages, we conducted measurements to study separately the membrane voltage E_m and capacitive electrode related voltage E_{OCV-c}. This is realized by open-circuit voltage (OCV) measurements both in capacitive and faradaic cells. In the capacitive situation, E_{OCV-c} is twice the sum of the membrane potential E_m and of the electrode potentials E_{elec-c}. In the faradaic situation, E_{OCV-f} is the sum of the membrane potential E_m and of the Ag/AgCl electrode potentials

Table 3.1 Brine composition

NaCl - $CaCl_2$ solution composition

	Concentrated solution				Diluted solution				Ratio ;
NaCl molar fraction	NaCl g.L $^{-1}$	NaCl mol.L^{-1}	$CaCl_2$ g.L^{-1}	$CaCl_2$ mol.L^{-1}	NaCl g.L^{-1}	NaCl mol.L^{-1}	$CaCl_2$ g.L^{-1}	$CaCl_2$ mol.L^{-1}	Experiment number
1	100	1.711	0	0	1	0.017	0	0	100;1
0.8	80	1.369	50.311	0.342	0.8	0.014	0.503	0.003	100;2
0.6	60	1.027	100.623	0.684	0.6	0.010	1.006	0.007	100;3
0.4	40	0.684	150.934	1.027	0.4	0.007	1.509	0.010	100;4
1	30	0.513	0	0	1	0.017	0	0	30;5
0.8	24	0.411	15.093	0.103	0.8	0.014	0.503	0.003	30;6
0.6	18	0.308	30.187	0.205	0.6	0.010	1.006	0.007	30;7
0.4	12	0.205	45.280	0.308	0.4	0.007	1.509	0.010	30;8
1	10	0.171	0	0	1	0.017	0	0	10;9
0.8	8	0.137	5.031	0.034	0.8	0.014	0.503	0.003	10;10
0.6	6	0.103	10.062	0.068	0.6	0.010	1.006	0.007	10;11
0.4	4	0.068	15.093	0.103	0.4	0.007	1.509	0.010	10;12

NaCl - $MgCl_2$ solution composition

	Concentrated solution				Diluted solution				Ratio ;
NaCl molar fraction	NaCl g.L $^{-1}$	NaCl mol.L^{-1}	$MgCl_2$ g.L^{-1}	$MgCl_2$ mol.L^{-1}	NaCl g.L^{-1}	NaCl mol.L^{-1}	$MgCl_2$ g.L^{-1}	$MgCl_2$ mol.L^{-1}	Experiment number
1	30	0.513	0	0	1	0.171	0	0	30;13
0.8	24	0.411	20.872	0.102	0.8	0.014	0.695	0.003	30;14
0.6	18	0.308	41.745	0.205	0.6	0.010	1.389	0.007	30;15
0.4	12	0.205	62.618	0.308	0.4	0.007	2.084	0.010	30;16

E_{elec-f}. E_{elec-f} is measured separately in a simple set-up containing two electrodes immersed in two beakers containing solutions of different concentration and linked by a salt bridge. As E_m does not depend upon the nature of the electrode, it is then possible to deduce $E_{elec-c} = E_{OCV-c} - E_m$ from the measurement of the open circuit potential performed on a cell equipped with the membrane and capacitive electrodes.

In this section, we will firstly study a highly selective membrane, Nafion (Nafion^{TM} HP, Chemours). We will then display some data on two others less expensive and less selective commercial membranes, Fumasep (FUMASEP^{TM} FS720, Fumatech) and sPEEK (FUMASEP^{TM} E-620 (K), Fumatech).

We carried out a series of 16 experiments with NaCl solutions mixed with $MgCl_2$ and $CaCl_2$ solutions. The compositions of the different solutions used are given in the Table 3.1. Compared to solutions with only NaCl, part of the NaCl was replaced by $MgCl_2$ or $CaCl_2$, in order to maintain the molarity of the inflowing feed (and hence the conductivity, to a certain degree) constant. The results obtained concerning different electrical voltages under the influence of divalent ion mixing are displayed in the Table 3.2, 3.3 and Figure 3.2.

Data obtained in the absence of divalent ions are comparable to measurements obtained previously in the literature [117]. In these situations, E_m corrected by measured Ag/AgCl electrode potential are 0.107, 0.074 and 0.05 V for Ra value of 100, 30 and 10 respectively. The membrane potential is given by $E_{mem} = \alpha \frac{RT}{F} ln(\frac{\gamma_H c_H \gamma_H}{\gamma_L c_L \gamma_L}).\alpha$ is the selectivity of the membrane, $\alpha = 1$ corresponds to a perfect selective membrane, that allows the free passage

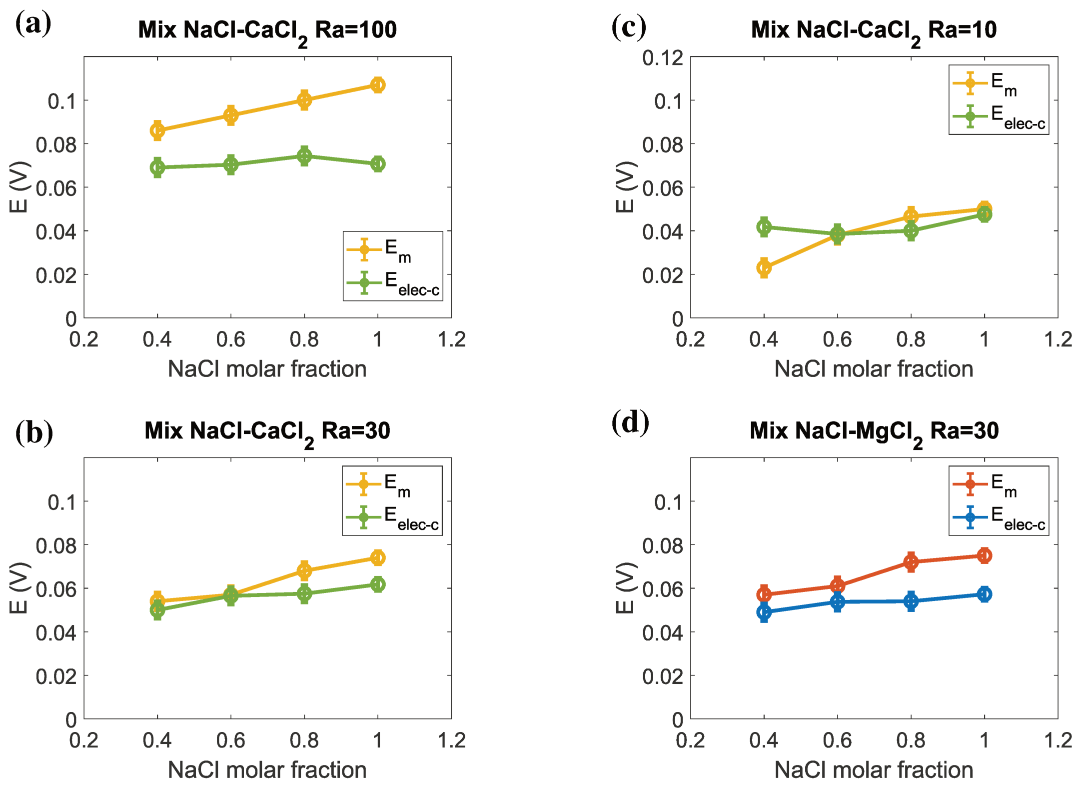

Fig. 3.2 Electrical voltage over membrane E_m and over capacitive electrodes E_{elec-c} as a function of NaCl molar fraction. (a), (b) and (c) represents the variation of voltage of mixing between NaCl and $CaCl_2$ for salinity ratio of 100, 30 and 10, respectively. (d) represents the mixing case of NaCl and $MgCl_2$ for a salinity ratio of 30. As molar fraction of divalent ions gets higher, E_m drops significantly while E_{elec-c} remains constant.

of cations but blocks anions. Activity coefficients γ_H, γ_L are obtained with the extended Debye–Hückel equation .

$$log(\gamma) = \frac{-0.51z^2\sqrt{(I)}}{1+\frac{A}{305}\sqrt{(I)}} \tag{3.10}$$

where I is the ionic strength $I = 0.5\Sigma z_i^2 C_i$ and A stands for the diameter of the hydrated ion (in pm). Some values for A are: Na^+: 450 pm, Mg^{2+}: 800 pm, Ca^{2+}: 600 pm. Based on previous values, the selectivities α are calculated to be 0.99, 0.99 and 0.99 for Ra value of 100, 30 and 10 respectively.

In presence of divalent ions, the membrane voltage decreases compared with solutions composed of pure mono-valent ions, as illustrated in Figure 3.2. As the molar fraction of divalent ions increases, the membrane voltage shows significant further decrease. For a fixed salinity ratio of 100 (30 or 10, respectively) , the membrane potential decreases from 107 mV to 86 mV (75 mV to 63 mV in the case of ratio 30, and 50 mV to 23 mV in the case of 10, respectively) for a molar fraction of 0.4 $CaCl_2$ and a total salt concentration of 1.71 mol/L (0.51 mol/L, 0.17 mol/L, respectively). The nature of divalent ions does not change E_m and E_{elec}. There are no major difference between the case of $MgCl_2$ and $CaCl_2$. In presence of $MgCl_2$, the drop of potential is comparable to that in presence of $CaCl_2$. For a NaCl salt fraction of 0.4, *Ra*=30, the membrane potential is equal to 54 mV in presence of $MgCl_2$ and to 57 mV in presence of $CaCl_2$. We have supplemented this series of measurements

Table 3.2 Electrical voltage measurement split-up table for mixing between NaCl and $CaCl_2$. The electrical voltages measured by experiments consist of open-circuit voltage of a capacitive cell E_{OCV-c} (which corresponds to $2(E_m + E_{elec})$), open-circuit voltage of a faradaic cell E_{OCV-f}, and electrical voltage on faradaic electrodes E_{elec-f}. Based on these measurements, it is possible to deduce the electrical voltage across the membrane E_m and the electrical voltage on capacitive electrodes E_{elec-c}. The measurements are conducted by using solution mixing between NaCl and $CaCl_2$ of different molar fractions (1, 0.8, 0.6 and 0.4 for NaCl molar fraction) for salinity ratios of 10, 30 and 100, respectively. The measurement uncertainties mainly come from the electrode potential contribution in faradaic system E_{elec-f} with a error bar estimated as 1 - 3 mV for different experiment series.

NaCl fraction	$CaCl_2$ fraction	Salinity ratio Ra	E_{OCV-c} (V) $2(E_m + E_{elec-c})$ (V)	E_{OCV-f} (V)	E_{elec-f} (V)	E_m (V)	E_{elec-c} (V)
1	0	100	0.355	0.203	0.096	0.107	0.071
0.8	0.2	100	0.349	0.194	0.094	0.100	0.074
0.6	0.4	100	0.327	0.184	0.091	0.093	0.070
0.4	0.6	100	0.310	0.176	0.090	0.086	0.069
1	0	30	0.272	0.149	0.075	0.074	0.062
0.8	0.2	30	0.251	0.141	0.073	0.068	0.058
0.6	0.4	30	0.227	0.128	0.071	0.057	0.057
0.4	0.6	30	0.208	0.117	0.063	0.054	0.050
1	0	10	0.195	0.101	0.051	0.050	0.048
0.8	0.2	10	0.173	0.095	0.049	0.047	0.040
0.6	0.4	10	0.153	0.086	0.048	0.038	0.039
0.4	0.6	10	0.130	0.070	0.047	0.023	0.042

Table 3.3 Electrical voltage measurement split-up table for mixing between NaCl and $MgCl_2$ for a fixed salinity ratio Ra of 30. Two scenarios are investigated here: The mixing in both concentrated and diluted solutions, and mixing only in the diluted solution. The measurement uncertainties mainly come from the electrode potential contribution in faradaic system E_{elec-f} with a error bar estimated as 1 - 3 mV for different experiment series.

NaCl fraction	$MgCl_2$ fraction	Salinity ratio Ra	E_{OCV-c} (V) $2(E_m + E_{elec-c})$ (V)	E_{OCV-f} (V)	E_{elec-f} (V)	E_m (V)	E_{elec-c} (V)
Mixing of NaCl-$MgCl_2$ in both solutions							
1	0	30	0.265	0.145	0.070	0.075	0.057
0.8	0.2	30	0.252	0.139	0.067	0.072	0.054
0.6	0.4	30	0.230	0.131	0.070	0.061	0.054
0.4	0.6	30	0.212	0.120	0.065	0.055	0.051
Mixing of NaCl-$MgCl_2$ only in the diluted solution							
1	0	30	/	0.144	0.070	0.074	/
0.8	0.2	30	/	0.142	0.069	0.073	/
0.6	0.4	30	/	0.139	0.069	0.070	/
0.4	0.6	30	/	0.131	0.069	0.062	/
0.2	0.8	30	/	0.120	0.069	0.021	/

with membrane potential measurements when divalents are only present in the dilute solution (see Table 3.3). The results show that the potential is less affected by the presence of divalents in this situation than in the case where divalent ions are present on both sides of the membrane. We will come back to this point in the section of modelling.

The potential of the electrodes behaves differently. It seems less affected than membrane potential by the presence of divalent ions. It depends little on the amount of divalent added and on the nature of the ions. These results have important implications for cell potential. The cell potential consists the sum of the electrode and membrane contribution. While the molar fraction of NaCl drops from 1 to 0.4, the voltage contribution of membranes E_m shows a significant drop of 19.6%, 27.0% and 54.0% for salinity ratio Ra of 100, 30 and 10, respectively. In the same situations, the voltage contribution of electrodes E_{elec-c} shows a drop of 3%, 19% and 12.4% for salinity ratio Ra of 100, 30 and 10, respectively. While the molar fraction of NaCl drops from 1 to 0.4, this induces for a capacitive cell a decrease of the total cell voltage E_{OCV-c} of 12.8%, 23.4%, and 33.6% for salinity ratio Ra of 100, 30 and 10, respectively. This decrease is thus much less important than the one occurring for the membrane potential.

We remind the reader that in a RED-type arrangement with an assembly of a large number of membranes, only the membrane potential comes into play. However, in a capacitive type cell scaling-up, both capacitive electrodes and membrane is considered as a repeating unit, thus the contribution of membrane voltage is less important.

We complete this study with some measurements established on less selective membranes. The measured features are displayed on Table 3.4. The FUMASEP^{TM} FS720 and FUMASEP^{TM} E-620 (K) membrane have a lower initial selectivity than the Nafion membrane respectively 0.87 and 0.74. When divalents are added, the OCV potential measured in a CRED falls by a similar amount to that of the Nafion membrane respectively 26.5 % and 26.4 % compared to 30 %.

To conclude this paragraph, it should be noted that these figures are achieved in a CRED cell where fluxes are permanently exchanged, which is not the case in faradaic cells. We'll come back to this point later.

Table 3.4 Characterization of FUMASEP^{TM} FS720 and FUMASEP^{TM} E-620(K) membrane in presence of divalent ions.

Membrane	Salinity ratio	NaCl fraction	$MgCl_2$ fraction	R(Ω cm^2)	C(F cm^{-2})	E$_m$ (mV)	α
FS720	30	1	0	38	0.4	68	0.87
FS720	30	0.4	0.6	34	0.42	50	
E-620(K)	30	1	0	44	0.375	57.9	0.74
E-620(K)	30	0.4	0.6	45	0.38	42.6	

3.3.2 Electrochemical properties

In order to characterize changes in cell resistance R_{cell} and cell capacity C as a function of the nature of the salt solutions, we carried out impedance spectroscopy measurements. As an equivalent *R-C* circuit can be established for the capacitive cell, for each solution mixture, it is possible to measure the corresponding inner cell resistance and its capacitance by using the Nyquist plot plotted by the PEIS method. Here, by using the impedance result measured at 10 mHz, we characterized R and C for different divalent mixing scenarios. The electrochemical measurement results are illustrated in the Table 3.5 for two different mixing scenarios: NaCl-$CaCl_2$ and NaCl-$MgCl_2$ with a fixed salinity ratio of 30. It is clear that while the quantity of divalent salts in the mixing is increased, the cell resistance decreases slightly. We believe that this is related to the increase of molar concentration of chloride ions inside the solution.

Table 3.5 R-C characterization result table for the capacitive cell system with a fixed salinity ratio of 30 of different divalent ion fraction.

NaCl-$CaCl_2$				NaCl-$MgCl_2$			
NaCl fraction	$CaCl_2$ fraction	R (Ω)	C (F)	NaCl fraction	$MgCl_2$ fraction	R (Ω)	C (F)
1	0	3.750	4.259	1	0	3.750	4.259
0.8	0.2	3.426	4.737	0.8	0.2	3.155	4.889
0.6	0.4	3.098	5.010	0.6	0.4	2.874	5.084
0.4	0.6	2.832	5.204	0.4	0.6	2.800	5.257

3.3.3 Energy performance

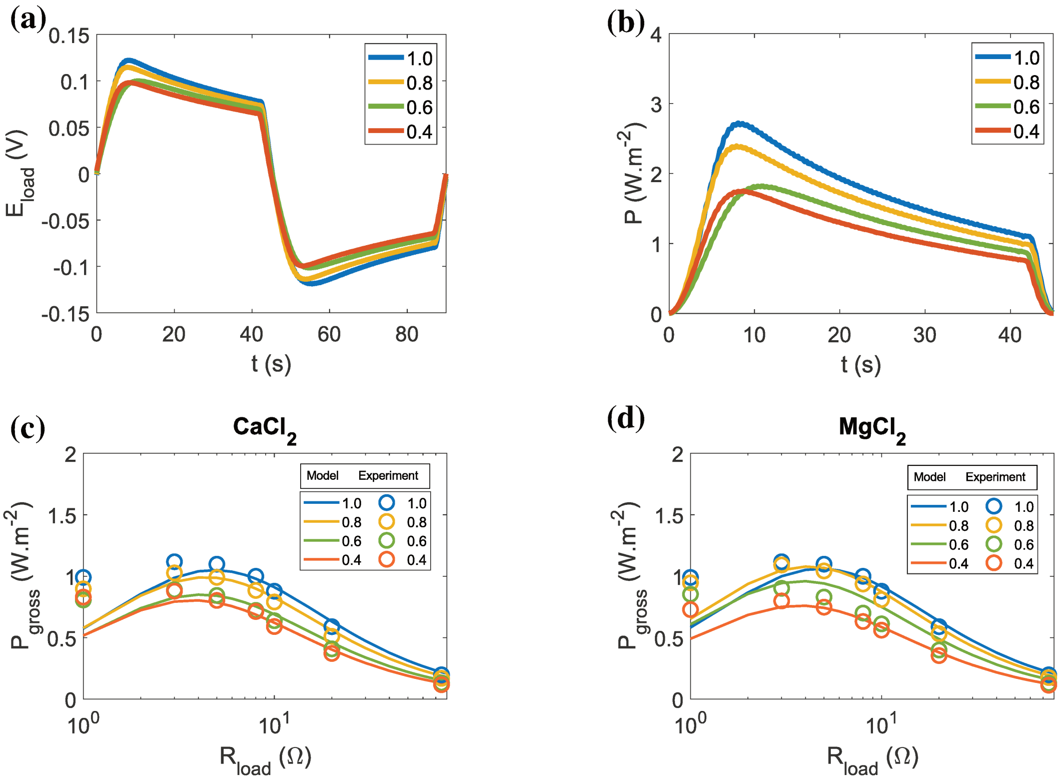

Fig. 3.3 Power density measurement curves. (a) Instantaneous voltage measurement as a function of time for a mixing solution of NaCl and $CaCl_2$ of different fractions. A load resistor of 10 Ω is connected to the capacitive cell. The voltage drop on the load resistor E_{load} is measured by a potentiostat. As the solution reversal is realized for a fixed period T_s = 45 s, an alternating electrical signal is measured. (b) The instantaneous power density P dissipated on the load resistor corresponding to the measurement in (a) for a series of mixing fractions. (c) The temporal averaged power density P_{gross} as a function of load resistance for divalent ion mixing of NaCl and $CaCl_2$ for a salinity ratio of 30. The solid lines represent the theoretical prediction based on the R-C equivalent circuit. The dots represent the experimental data obtained for a capacitive salinity gradient cell. (d) The temporal averaged power density P_{gross} as a function of load resistance for divalent ion mixing of NaCl and $MgCl_2$ for a salinity ratio of 30. The number presented in the legend corresponds to the molar fraction of NaCl.

It is important to characterize the energy performance of the capacitive cell. We will firstly explain the power density characterization method for a simple capacitive cell using pure mono-valent ion based solutions. In general, we connect a load resistor directly to the CRED system. We measure the voltage drop on the load resistor $E_{load}(t)$ as a function of time by using the OCV mode in a pontetiostat, as illustrated in Figure 3.3 **(a)**. Based on these measurements, it is possible to determine the instantaneous power density output on the load resistor $P(t) = \frac{E_{load}(t)^2}{R_{load}}$, as illustrated in Figure 3.3 **(b)**.

The mean gross power density $P_{gross}(t)$, which is the power density without compensating for pumping losses, is a function of time. It is assessed by averaging the signal recorded across the resistance over a time interval of T_s. S denotes the area of the membrane. The expression is as follows:

$$P_{gross}(t) = \frac{1}{T_s \cdot S} \int_t^{T_s+t} \frac{E_{load}^2(u)}{R_{load}} du \tag{3.11}$$

A priori, $P_{gross}(t)$ depends on time t. In fact, in all our experiments, this power does not depend on time, as shown in the Figure 3.4 (b) for a few experiments. Figures 3.3 (c), 3.3 (d) show the value of stationary power, which is measured from the stationary cycles.

It's noteworthy that these measurements constitute direct assessments that mirror real-world scenarios. To assess the influence of divalent ion mixing in the capacitive cell, we measure the harvesting power in various salinity gradients with different divalent ion mixing fraction. For each mixing case, the experimental results are presented by dots in Figure 3.3. The measured power densities show classic variations according to the load resistance. For each mixing case, the experimental results are presented by dots in Figure 3.3. Maximum power recovery decreases from 1.15 W.m^{-2} to 0.8 W.m^{-2} (respectively 0.75 W.m^{-2}) when the $CaCl_2$ (respectively $MgCl_2$) proportion in the brine increases from 0 to 60%. The experimental data corresponds well with the theoretical curves calculated by RC models. A detailed explanation of the model is available in the modelling part.

3.3.4 Membrane poisoning in Faradaic RED cell

In order to be able to compare the CRED and RED devices, it is necessary to carry out new experiments on the membranes we use. The effects of divalents are highly membrane-dependent, and it is not possible to be satisfied with the information available in the literature. To do this, it would be possible to compare the power generated. We have not chosen this approach, however, as it would be complex to construct capacitive cells and Faradaic cells with the same efficiency coefficients, i.e. to recover the same share of the maximum accessible potential. To understand the mechanisms involved, we preferred to focus on how divalent ions modify the intrinsic properties of the membrane.

To probe this more precisely, we close the circuit with the Ag/AgCl electrodes on a resistor which value is closed to R_{cell}. An ionic current passes through the membrane during the experiment. This phase lasts 20 minutes. The current remains constant in the case of the Nafion HP membrane, but drops in the case of the FUMASEP^{TM} FS720 and FUMASEP^{TM} E-620 (K) membranes. Such phenomenon indicates the power density loss in RED system within 20 minutes. We then measure the membrane potential in the Ag/AgCl cell using the OCV measurement method. This measurement slightly disturbs the state of the membrane because it requires a reversal of flow. Two flow reversals are used to limit the impact of the measurement on the results. This allows us to calculate membrane selectivity before and after measurement. E_m in presence of divalent varies from 57.9 mV to 56.4 mV in the case of Nafion HP over 20 minutes, from 50 mV to 42 mV in the situation of FUMASEP^{TM} FS720 and from 42.6 mV to 35 mV in the situation of FUMASEP^{TM} E-620 (K) . We find that the selectivity of

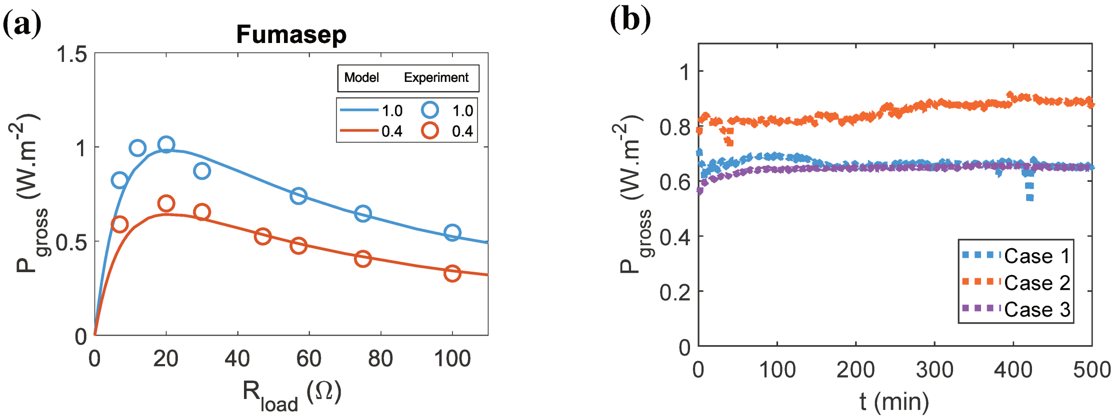

Fig. 3.4 Power density performance characterization. (a) The temporal averaged power density P_{gross} as a function of load resistance for artificial NaCl (blue dots) or NaCl (40%) - $CaCl_2$ (60%) mixed solution (red dots) of 30 g.L $^{-1}$ vs 1 g.L $^{-1}$. The solid lines represent the theoretical model, the dots represent the experimental results. The result is measured for a CRED system with a FUMASEP^{TM} FS720 membrane with a effective surface of 2.24 cm^2. The figure in the legend refers to the NaCl molar fraction in the mixing. The power density presents a drop of around 30 % in artificial NaCl (40%) - $CaCl_2$ (60%) mixed solution of 30 g.L $^{-1}$ vs 1 g.L $^{-1}$. (b) Mean gross Power density measurement $P_{gross}(t)$ (see definition Equation 3.11) of a capacitive salinity gradient cell during an operation duration of 500 min for three different cases. Note that while instantaneous power is a periodic signal due to the capacitive process, power averaged over a period is not. Case 1: the use of artificial NaCl (80%) - $CaCl_2$ (20%) mixed solution with a salinity ratio of 30 g.L $^{-1}$ vs 1 g.L $^{-1}$). The membrane used here is Nafion 117 with a load resistor of 10 Ω. Case 2: the use of production water (equivalent NaCl concentration 107 g.L $^{-1}$) with a salinity ratio of 30. The membrane used here is Nafion 117 with a load resistor of 10 Ω. Case 3: the use of artificial NaCl (40%) - $CaCl_2$ (60%) mixed solution with a salinity ratio of 30 g.L $^{-1}$ vs 1 g.L $^{-1}$). The membrane used here is FUMASEP^{TM} FS720 with a load resistor of 30 Ω. In all cases, we fix the switching period as T_s = 45s. The power density variation after 10h of operation is within 6%.

the Nafion membrane is unaffected. The selectivity of the FUMASEP^{TM} FS720 membrane decreases by 16% and the one of FUMASEP^{TM} E-620 (K) by 17.8%.

3.4 Underlying Mechanism

3.4.1 Cell open-circuit voltage modelling

The preceding measurements show us that divalent ions affect the value of the cell performance of our device and more precisely the open circuit voltage. At this stage, it's important to understand which phenomena induce the drop in potential: is it simply due to the migration of divalents into the concentrated compartment as a result of their charge? Or is it a phenomenon linked to the variation in membrane selectivity and membrane poisoning? Vermass et al. [134] has developed a model to quantify the first point. Comparing our data with this model will enable us to answer the question.

In their analysis, they propose that the open-circuit equilibrium membrane potential is equal to a potential that cancels out the displacement of divalent ions[134]. This is only possible if a local transfer of matter takes

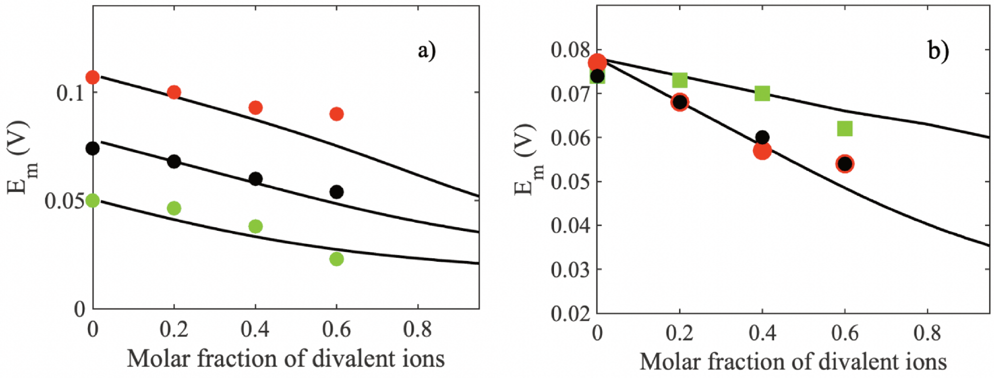

Fig. 3.5 Theoretical interpretation of the membrane voltage E_m decreases as a function of divalent ion molar fraction. (a) Theoretical prediction (solid lines) and experimental data (dots) of E_m of different salinity ratio Ra of 100, 30 and 10, respectively, for a mixing between NaCl and $CaCl_2$. (b) Membrane voltage E_m decrease in two different cases: mixture in both concentrated and diluted solutions, and mixture only in the diluted solution. The feed solution used here is a mixture of NaCl and $MgCl_2$ or NaCl and $CaCl_2$ with a fixed salinity ratio Ra of 30. Green squares refer to the case where the $MgCl_2$ is present only in the river water. Black dots refer to the case where NaCl and $MgCl_2$ are present in both feeding solutions. Red dots refer to the case where NaCl and $CaCl_2$ are present in both feeding solutions.

place, inducing a different concentration in the layer of matter near the membrane. More precisely, ion transport across a membrane is a complex phenomenon when monovalent and multivalent ions exist on both sides of an ion exchange membrane. In such situations, ions are exchanged across the membrane to achieve chemical potential equilibrium on both sides. When solutions of NaCl and MgCl are present on either side of a cation exchange membrane (CEM) at varying concentrations but with the same ratio, the electromotive force E_{OCV} resulting from the difference in concentration of Na^+ is greater than that of Mg^{2+} due to the valence of the ions. We recall that $E_{OCV} = \frac{\alpha RT}{zF} log \frac{a_{i,1}}{a_{i,2}}$. As a result, Mg^{2+} ions are transported from the dilute to the concentrated solution, while twice as many Na^+ ions move in the opposite direction. This exchange ensures electroneutrality on both sides of the membrane and is described in the literature as uphill transport, corresponding to the movement of Mg^{2+} against the concentration gradient. Using Donnan Equation 3.1 and assuming that the apparent permselectivity is equal for both ionic species, this stationary situation is reached when the ion activities at either side of the membrane obey:

$$\frac{\alpha RT}{z_{Na^+}F} log \frac{a_{Na^+,1}}{a_{Na^+,2}} = \frac{\alpha RT}{z_{Mg^{2+}}F} log \frac{a_{Mg^{2+},1}}{a_{Mg^{2+},2}} \tag{3.12}$$

This leads us to :

$$E_m = \frac{\alpha RT}{z_{Na^+}F} log\frac{a_{Na^+,1}}{a_{Na^+,2}} \quad (3.13)$$

$$a_{Na^+,2} = \gamma_{Na^+,2}(c_{Na^+,2} + 2J/V_2) \quad (3.14)$$

$$a_{Na^+,1} = \gamma_{Na^+,1}(c_{Na^+,1} - 2J/V_1) \quad (3.15)$$

$$\frac{\gamma_{Na^+,1}(c_{Na^+,1} - 2J/V_1)}{\gamma_{Na^+,2}(c_{Na^+,2} + 2J/V_2)} = (\frac{\gamma_{Mg^{2+},1}(c_{Mg^{2+},1} + J/V_1)}{\gamma_{Mg^{2+},2}(c_{Mg^{2+},2} - J/V_2)})^{(1/2)} \quad (3.16)$$

J is the molar transport (mol) of Mg^{2+} towards the seawater compartment, and V_1 and V_2 are the volume of the compartments.Activity coefficients in the lower concentration range are obtained with the extended Debye–Hückel equation.

Figure 3.5 shows a comparison between the model and membrane potential measurements. An excellent agreement is found between measurements and simulation. This agreement shows that the selectivity of the Nafion membrane is not affected when it is used in a capacitive device where the ionic current changes of direction on each half period. In the case of Nafion, no loss of selectivity was neither measured when the ionic current flowed in the same direction for 20 minutes i.e . In all likelihood, Nafion's loss of power is limited to the uphill effect.

In the case of membrane with a poisoning effect as FUMASEP^{TM} FS720, the selectivity is equal to 0.87 in presence of NaCl. The membrane potential drops from 68 to 50 mV in presence of 0.6 Mol $MgCl_2$. This corresponds to a ratio equal to 0.73. The potential of the Nafion membrane drops from 75 mV to 55 mV. This corresponds also to a ratio equal to 0.73. The fact that the two figures are the same shows that the selectivity of the FUMASEP^{TM} FS720 membrane is not affected by the divalent ions in the CRED. We recall that no variation of the open potential is measured for more than 8 hours in the CRED. It's not the same thing when a direct ionic current flows through the membrane for 20 minutes as in the Faradaic cell. The membrane potential falls to 42 mV, which corresponds to a loss of selectivity of 16%. Same results are obtained with the FUMASEP^{TM} E-620 (K). In the CRED the membrane potential is equal to 43 mV in presence of divalent ions and to 58 mV in absence of divalent. This corresponds to a ratio 0.74, same figure than previously , suggesting that the permselectivity is not affected by the divalent ions in the CRED. In the Faradaic situation the membrane potential falls to 35 mV, which corresponds to a loss of selectivity of 17.8 %.

To conclude this section, the voltage drop in CRED is fully explained by the uphill effect model. However, in faradaic RED system, we observe additional contribution of voltage drop related to the selectivity loss in membrane.

3.4.2 Harvested power modelling

In this part, we will verify if the open circuit potential drop is sufficient to explain the recovered power losses. To check this, we will compare the results with a R-C model that we have validated in previous studies when the cell filling time is small compared to the period. Details can be find in the work of Brahmi et al.[117] and in the CRED modelling section in Chapter 2. This modeling predicts that the power is given by:

$$P_{th} = \frac{2}{ST_s}\frac{CE_{OCV}^2 R_{load}}{R_{load} + R_{cell}} tanh(\frac{T_S}{2(R_{load} + R_{cell})C}) \quad (3.17)$$

The theoretical prediction is presented by solid lines in Figure 3.3, it does not involved any fitting parameters. It is demonstrated that experimental power density performances are perfectly described by the classical modeling. For each brine solutions, we have used the measured resistance and capacitance values.

From the model of uphill effect and the model of RC circuit, we can deduce that the drop in power measured simply results from the uphill effect, where a reversed flow of divalent ions migrates towards the concentrated part. There is no other hidden mechanism that could be the cause of this decrease.

3.4.3 Analysis

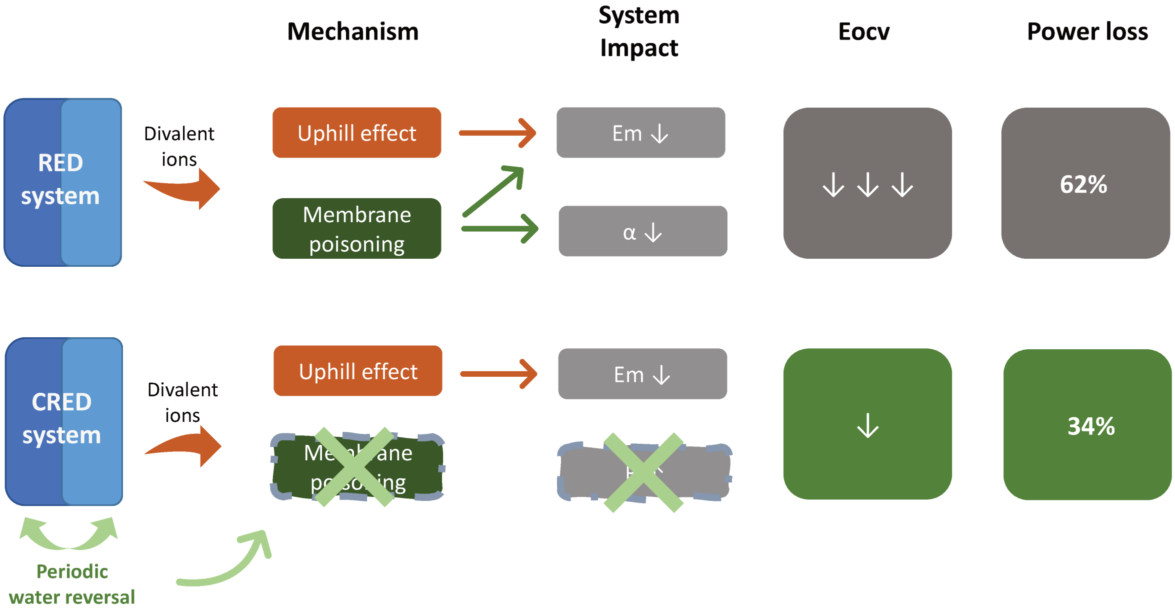

Fig. 3.6 Schematic illustration of the divalent impact mitigation mechanism of CRED system. The diagram summarizes the mechanisms that induce power loss in the presence of divalent ions. In the CRED context, only the uphill mechanism affects membrane potential. Electrode potential remains unaffected. This reduces the impact of divalents on the cell potential, which is the sum of the membrane potential and the electrode potential. Flow reversal prevents membrane poisoning. For a molar fraction of 0.6 of $MgCl_2$, this results in a 34% reduction in power. Under the same conditions and for a poorly selective Fumasep-type membrane, membrane poisoning and the cell potential, which is affected twice by the uphill phenomenon, lead to a 62% power density reduction.

The reduction of the harvested power density due to divalent ions is being mitigated when a CRED cell is used. Divalent ions affect the properties of RED devices for two main reasons. The first is the uphill phenomenon, which modifies the membrane potential. This phenomenon is of course common to RED cells with capacitive electrodes and CRED cells. This phenomenon only applies to the membrane potential, not to the electrodes. The CRED cells consist only a single membrane and two electrodes. They can be placed in series by repeating this electrode-membrane-electrode unit. In this way, the basic capacitive cell potential is the membrane potential plus the electrode potential. As the latter is not affected by the presence of divalent ions, the potential of a series of single-membrane capacitive cells is less affected than that of a RED cell. The reduction in open-circuit potential is half that of a RED cell. The fact that the impact of divalents is limited in capacitive devices therefore stems primarily not from the capacitances themselves, but from the fact that it is possible to sum the electrode potentials by creating single-membrane cells. It should be remembered that, because of the overpotential on faradic electrodes, it is not possible to use a single-membrane faradic cell efficiently. Furthermore, putting faradic cells in series would raise the problem of high electrode costs and the use of large quantities of toxic electrolytes.

Under these conditions it is possible to calculate the power loss in the presence of divalent ions in the CRED and compare it to the RED if there is no loss of membrane selectivity. It should be remembered that the loss of selectivity only occurs on membranes with low selectivity and during a direct ionic current. Assuming that the anionic membrane follows the same trends as the cationic membrane, the open-circuit voltage in a RED device of n membranes equals to $n.E_m$. To simply the calculation, we take the case of a single membrane. The open circuit voltage in a RED device will drop from 107 mV to 86 mV for a salinity ratio of 100, from 77 mV to 54 mV for salinity ratios of 30 and from 50 mV to 23 mV for salinity ratios of 10 when the molar fraction of Na decreases to 0.4. In a CRED for salinity ratio Ra of 100, the open circuit voltage will drop from 178 mV to 155 mV for a salinity ratio of 100, from 132 mV to 105 mV for salinity ratios of 30, from 98 mV to 66 mV or salinity ratios of 10 when the molar fraction of Na decreases to 0.4. These figures lead to a decrease of power of 35.4 % for a salinity ratio of 100, of 50.8 % for a salinity ratio of 30, of 78.8 % for salinity ratio of 10 when the molar fraction of Na decreases to 0.4 in a RED device. In comparison, the drop in power in a CRED is equal to 24.2 % for a salinity ratio of 100, of 36.7 % for a salinity ratio of 30, of 54.6 % for salinity ratio of 10 when the molar fraction of Na decreases to 0.4. These figures are obtained with the measurement realized by Nafion HP membrane. The results are summarized in Table 3.6.

Table 3.6 Comparison of power density drop prediction under divalent ion mixing cases of NaCl and $CaCl_2$ for a fraction of 0.4 of NaCl. The voltage values for CRED system corresponds to the open-circuit voltage E_{OCV-c}. The voltage figures for RED system corresponds to a single membrane voltage E_m, as a simplified case for RED stacks. The calculations are realized for Nafion HP membrane.

		Ratio 10	Ratio 30	Ratio 100
CRED	NaCl solution	98 mV	132 mV	178 mV
	NaCl-$CaCl_2$ mixing, fraction 0.4	66 mV	105 mV	155 mV
	Power density drop	54.6%	36.7%	24.2%
RED	NaCl solution	50 mV	77 mV	107 mV
	NaCl-$CaCl_2$ mixing, fraction 0.4	23 mV	54 mV	86 mV
	Power density drop	78.8%	50.8%	35.4%

The second reason relates to membrane poisoning. Membrane poisoning is influenced by the chemical composition of the membranes. It is relatively rare in Nafion-type membranes but quite common in FUMASEP membranes. This is probably due to the very high surface charge of Nafion membranes, which enables them to avoid poisoning by divalent ions [265]. It leads to a reduction in membrane selectivity, a reduction in electrical potential membrane . The fact that the capacitive process is an alternative process prevents divalent ions from adsorbing permanently to the membrane, which is not the case with continuous processes. The improved properties of CRED compared with RED are once again an indirect effect of the alternating flow of the two solutions. It should be noted that this strategy could be applied to RED, as proposed by Vermaas. From a numerical point of view, assuming that the anionic membrane follows the same trends as the cationic membrane, the open circuit voltage in a RED device will drop from 68 mV to 42 mV for a salinity ratio of 30 when the molar fraction of Na decreases to 0.4 along with the selectivity decrease. In a CRED for salinity ratio of 30, the open circuit voltage will drop from 125 mV to 101 mV for salinity ratios of 30 when the molar fraction of Na decreases to 0.4. Under these conditions, the power generated by a RED device will fall by 34 % and the power generated by a CRED device by 62 %.

The overall underlying mechanism is illustrated in Figure 3.6.

3.5 Towards real-world solutions

To complete our study, we designed a series of experiments to test the feasibility of CRED in applications, where complex solution mixtures are used. The composition of these complex real solutions are listed in the Table 3.7 below.

Table 3.7 Experiments reproducing possible applications: compositions of solutions

Scenario 1: Production water / seawater

	Salinity ratio	NaCl equivalent $g.L^{-1}$	NaCl $g.L^{-1}$	KCl $g.L^{-1}$	$CaCl_2$,$2H_2O$ $g.L^{-1}$	$MgCl_2$,$6H_2O$ $g.L^{-1}$
Production water	4.28	107	93.9	0.628	11.25	9.32
Sea water	4.28	25	23.63	0.77	0.11	0.20

Scenario 2: Dead Sea water / ×30 diluted

	Salinity ratio	NaCl equivalent $g.L^{-1}$	Na $g.L^{-1}$	K $g.L^{-1}$	Ca $g.L^{-1}$	Mg $g.L^{-1}$
Dead Sea water	30	324.87	32.177	9.27	27.503	62.23
Diluted Dead Sea water	30	10.83	1.073	0.309	0.917	2.074

Scenario 3: Salt caverns

	Salinity ratio	NaCl equivalent $g.L^{-1}$	NaCl $g.L^{-1}$	KCl $g.L^{-1}$	$CaCl_2$,$2H_2O$ $g.L^{-1}$	$MgCl_2$,$6H_2O$ $g.L^{-1}$
Salt cavern extraction water	300	300	300	0	0	0
River water	300	1	0.4	0	1.509	0

These imaginary scenarios serve as proxies for some real-life applications, as detailed below, or allow to test some bottlenecks expected in these applications.

In the first scenario (Figure 3.7 **(a)**) we consider produced water from an oil well mixing with seawater. Here we used synthetic production water and synthetic seawater prepared in a laboratory from data provided from a field (see composition in [261]). The obtained power density 0.35 $W.m^{-2}$ was similar to what what was obtained with NaCl solutions at similarly low salinity ratio of around 4. The amount of osmotic energy is low due to the small difference in salinity. We could conclude that although our results show the feasibility of energy harvesting from production water, unaffected by the presence of divalent ions, advantage of further development of this application is site dependent.

In the second scenario we used real water from the evaporation ponds at the Dead Sea, mixed with the same solution diluted by 30 times (Figure 3.7 **(b)**). The extreme salinity conditions of this test could be relevant to projects like the Red sea-Dead sea conveyance, or similar. Remarkably, the high power density of over 2 $W.m^{-2}$ indicate the unprecedented feasibility of such application.

According to our experimental analysis, the total dissolved salts content in the dead sea solution is on the average 324.9 $g.L^{-1}$. The dominant cation is Mg (62.3 $g.L^{-1}$), followed by Na (32.2 $g.L^{-1}$), Ca (27.5 $g.L^{-1}$) and K (9.3 $g.L^{-1}$). We demonstrated that even in the case where divalent ions (Mg and Ca presenting around 55%) dominate, the measured power density obtained in a capacitive cell is comparable to the value 2.2 $W.m^{-2}$

obtained in a pure solution composed of NaCl salts with similar concentration gradients (300 g.L^{-1} vs. 10 g.L^{-1}) as reported by Wu et al.[3].

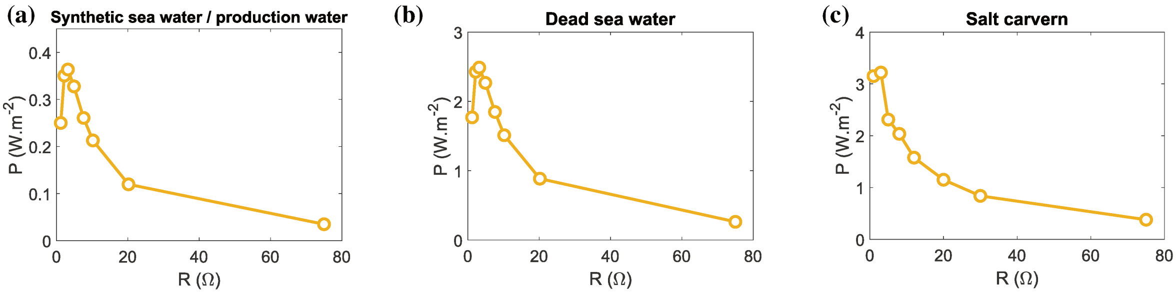

Fig. 3.7 Power density curves for real solutions. (a) Power density measurement for the case of synthetic seawater and production water with a salinity ratio of 4. (b) Power density measurement for the case of Dead sea water with a salinity ratio of 30. (c) The case of salt cavern with highly concentrated sea water corresponding to a pure NaCl salt solution of 300 g.L^{-1} coupled with an artificial river water. The salinity ratio is 300. All the detailed solution composition is available in the method section. In all cases, the switching period is fixed as $T_s = 45$ s.

In the third scenario we imagine creation of salt caverns, either for salt mining or for subsequent hydrogen storage. The caverns are created by dissolution in water, of salinity available on site, injected into the salt deposit. The concentrated solution is therefore saturated brine, mostly composed of NaCl 300 g.L^{-1}, and the diluted solution is fresh (used) water or river water, replaced here for simplicity by a 1 g.L^{-1} artificial mixture solution of composed of NaCl (40%) and $CaCl_2$ (60%). In this case, a maximum power density of 3.2 W.m^{-2} is obtained. The power density shows limited decrease compared with NaCl pure solutions of 300 g.L^{-1} and 1 g.L^{-1}, which shows a maximum power density of 4 W.m^{-2} in the capacitive cell. This scenario also resembles that of a facility constructed between the Great Salt Lake, utilizing water from the lake along with treated wastewater, or a facility situated within the Ettore e Infersa saltworks in Marsala (Trapani, Italy). The Italian location provides freshwater from a coastal well and nearly saturated brine[143, 159, 199].

In our study, the experiments performed with water production and sea water are close to the result obtained with equivalent monovalent ion based solutions as the divalent ions are of low molar fraction (6.7 % in the case of production water and 0.4 % in the case of sea water [261]). For most real sea water solutions, divalent ions are of low molar fraction, as in the example of Mediterranean sea water which contains 3.7% of Mg^{2+} and 1.2% of Ca^{2+} and 33% of Na^{+} [199]). When it comes to Dead Sea water, it is actually dominated by the presence of divalent ions. However, according to our experimental studies, capacitive system presents minor performance decay in this case. We believe that the same results will be obtained when river water containing high levels of divalent ions is taken into account (see Figure 3.2 d). For example, the Amazon river water contains 2.4% of Mg^{2+} and 15% of Ca^{2+} and 3.1% of Na^{+}[199].

We conclude that, within a capacitive cell system, the composition of the brine has a limited impact on performance. We highlight that these performances might be enhanced using an external voltage source [3].

3.6 Life cycle and techno-economic analysis

Our study shows that capacitive cells can achieve significant power levels compared with the literature when real solutions are used. At this point, it becomes important to ask where blue energy technology stands from an economic and ecological point of view. The current literature can be confusing. Some articles mention the enormous power measured on a single nanotube and extrapolate the enormous power that can be recovered[115], while others write that these techniques will never be marketable and is even not suited for the ecological transition[145, 266]. We believe that the situation is halfway between these statements.

3.6.1 Life cycle analysis

Let us first comment on the ecological footprint of the blue energy. A study of the life cycle analysis of our process is outside the scope of this article. However, before making an economic analysis of our process, we would like to remind a few points.

Mueller et al.[12] display in 2021 the the first comprehensive life cycle assessment (LCA) of reverse electrodialysis (RED). They conduct a LCA of 1MWh RED plant using natural waters or concentrated brines and compare the results to existing renewable energy technologies, including wind and solar photovoltaics. They studied 9 impact categories: acidification, ecotoxicity eutrophication, global warming, ozone depletion, photochemical oxidation, carcinogenics, non carcinogenics, and respiratory effects. In all the cases, the environmental impacts from RED are found to be comparable to, and sometimes lower than, established renewable energy technologies. The single drawback deals with eutrophication, ecotoxicity, and carcinogenic impacts which are slightly larger for RED than other technologies under the natural water scenario and not the brine one. Processes associated with membrane manufacture are primary contributors to these impact categories. We anticipate that these impacts may be thus decreased by using biosourced membranes such as cellulose membranes in the natural water situation. The authors conclude by saying that RED performs as well as or better than other renewable energy technologies in terms of ecological impact.

The footprint is not analyzed in this article, but it is comparable to or better than that of photovoltaic plants. Indeed, despite a power density 30-50 times lower than that of photovoltaic energy, it is possible to produce the same power as a photovoltaic plant on smaller surfaces, because RED cells can be stacked on top of each other. Taking into account a thickness of 0.4 mm for two membranes and two liquid compartments (i.e. for the cell repeat pattern) and a density power of 1 $\mathrm{W.m^{-2}}$, it is possible to estimate the power of a 1 m × 1 $\mathrm{m^2}$ cell at 5 kW. The basic RED modules will therefore take up 20 times less space than the basic photovoltaic modules, whose density power is estimated at 100 $\mathrm{W.m^{-2}}$. Discharges of saltwater solutions are not analyzed in this article, and at this stage there are no studies to show how the fragile ecosystem that makes up an estuary can be affected by withdrawals and discharges of saltwater mixtures. Without getting too far ahead of ourselves in this not-so-simple debate, it is nevertheless important to note that osmotic energy devices mix seawater and river water. It may therefore be possible for the estuary, which does the same, to discharge this water at a point where the salinity is close to that of the mixture.

Finally, this impact is less significant when the brine systems studied are industrial brines. In this case, the problem of discharge is already part of the process. All these points are very positive and lead us to ask why RED technology is failing to emerge. One crucial point is the cost. High-performance membranes are expensive membranes. It is important to analyze this point in greater detail and to compare our work with existing results. To do this, we will draw on a techno-economic analyses carried out on RED systems[197, 199, 251].

3.6.2 Techno-economic analysis

Post estimated the cost of a RED device in 2010 for a system producing 200 kW. The calculation includes the costs of construction and membrane (200 000 €), filtration (320 000 €), liquid pumping and maintenance (370 000 €). The fluids pass through the system only once, at a speed 1 $cm.s^{-1}$ comparable to our experiments. The calculation takes into account a membrane price of 2 euros per m^2 and a power of 2 W per m^2. Membrane lifetime is 7 years, with production running 8000 hours a year. 9% of the construction and functioning cost are considered to be the exploitation cost over 7 years. Taking inflation into account, this corresponds to a current cost of 1 232 027 euros . This results in a production cost equal to 0.111 € per kWh, i.e. 111 euros per MWh. This figure is in line with current electricity production costs (solar energy 40 € per MWh, wind off shore 120 € per MWh[255]). In this calculation, the price of the membrane is certainly underestimated while the production power is overestimated.

More realistically, on the basis of our experimental results, we can envisage several different cases and display two other scenarios in the table. We have measured a power of 3.2 $W.m^{-2}$ for a ratio of 300 between a high salinity solution and a fresh water solution in presence of magnesium and calcium. This case mimics that of a plant built between the Great Salt Lake and using water from the lake plus treated wastewater or a plant located in the Ettore e Infersa saltworks in Marsala (Trapani, Italy). The Italian site supplies fresh water from a well on the coast) and almost saturated brine [143, 159] [199]. These cases are very interesting because all these brines do not require filtration. Algae and microorganisms do not grow in such high salinities and the desalination effluents, treated water effluents or water from a shoreline well are rather clean [143].

We propose an analysis based upon a power density of 3.2 $W.m^{-2}$ (equal to our previous measurement) and two cost of membranes.The cost of membrane is difficult to estimate. Post's calculation takes into account a membrane price of 2 euros per m^2 . It's important to note that no membrane currently achieves this cost price. It 's also important to note that the price we pay for a lab scale membrane differs from the commercial price in case of industrialization of the RED process. Because we are interested in real-world greenhouse applications, we will use the commercial price in our cost analysis. Taking into account a lab-scale to commercial cost ratio of Fujifilm membrane equal to 2.8 (based on the lab-scale to commercial cost ratio of the Neosepta membranes), Ahdab et al. [267] propose to use a cost equal to 58 €/m^2 for a Fujifilm membrane. We assume the commercial cost will be same for FUMASEP® FS720 membrane. Note that the lab scale price for a FUMASEP® E-620 (K) membranes is 57 €/m^2. We therefore propose a scenario A based on a construction cost of 60 €/m^2 for the membranes in the cell. This cost takes into account the cost of the membrane and the carbon felt.

Table 3.8 Cost break-down for a membrane reverse electrodialysis unit (membrane surface 100 000 m^2).

	Post scenario	A scenario	B scenario
Membrane cost (€)	254 000	6 000 000	1 500 000
Piping, fittings and pumps (€)	406 400	406 400	406 400
Valves (€)	0	150000	150000
Filtration (€)	469 900	0	0
Total (€)	1 130 300	6 556 400	2 056 400
Annual Costs (9%) (€)	101 727	590 076	185 076
Total (€)	1 232 027	7 146 476	2 241 476
Net Power (kW)	200	320	320
MWh cost (€)	111	399	125

In another realistic techno-economic analysis, Giacalone et al. [199] consider that the price of highly selected membrane is 15 €per m^2. This price is in line with the recent development of sulfonated poly-ether-ether-ketone, sPEEK membrane. Owing to the low cost of raw material (61.5 €/kg for PEEK polymer), Zhu [268] and Yuan [259] estimate the cost of sPEEK membrane to be as low as 12€/m^2, which is at least 20 or 30 times lower than that of commercially available Nafion membranes. We will thus propose a B Scenario based over a cost of 15 €/m^{2}for the membrane and the carbon felt.

The viscous loss is estimated at 0.2 W per m^2 of membranes. We have previously measured similar viscous losses in our devices (0.1 W.m^{-2}). We thus take into account the same cost of viscous loss and filtration when required. To this figure we need to add the power required to reverse the flows. To estimate the cost of valves additionally used in the capacitive system, we estimate the cost at around 35% of the cost related to piping, fittings and pumps.

This analysis shows that the very salty solutions is economically viable and comparable to other renewable energies 111 € per MWh, if we consider a membrane plus felt price of 15 €/m^2. It remains however high, 399 € per MWh, in the situation where the price of the membrane plus felt equals 60 €/ m^2. Note that the obtained values are better than the one predicted following the results of Tedesco [143] and the analysis of Giacalone [199] because the power density is higher (3.2 W.m^{-2}), we have considered no filtration and the plant is different as it encompasses 100 000 m^2 of membranes. The main contribution of our work is the fact that we are able to limit the role of the divalent ions. Considering the Dead sea water scenario (a plant built between the Dead sea and a desalination plant[199]) and following the same analysis, the cost will be reaching 200 €/ MWh. This was the scenario 2 of our study. Lastly, considering sea water mixed with river water, the harvested power remains slightly higher than 1 W per m^2 and leads to a cost of 400 €/ MWh which is too high even in the situation of sPEEK membranes. It will correspond to a cost of 1276 €/ MWh for a membrane cost of 60 €/ m^2.

3.7 Conclusion

Conclusion

In this chapter, we studied the impact of divalent ions mixing on CRED systems to evaluate the feasibility of osmotic energy harvesting in real-life solutions. We studied experimentally the impacts of divalent ions on cell voltage, electrochemical characteristics and power density performances, respectively.

1. The mixture of divalent ions in solutions results in a potential drop in CRED system. More precisely, the membrane potential is severely influenced by the presence of divalent ions, while the electrode potential remains stable.

2. The theoretical modelling of uphill effect predicts well the decrease of membrane potential in CRED system. Such analysis indicates that the potential drop is mainly due to the uphill effect. The membrane poisoning phenomenon has minor impact in CRED system.

3. CRED system with divalent ion mixing shows minor power density decrease compared with the performance in pure NaCl solution. Such performance is maintained in 500 cycles of around 8h. In comparison, the membrane selectivity decreases within 20 minutes. The theoretical modelling based on equivalent R-C circuit describes well the experimental results. It indicates that power density drop results solely from the membrane potential drop under uphill effect. No other hidden mechanism exists in CRED system.

4. Different from the significant power density drop reported towards 75 % in faradaic RED systems while the feeding solution contains over 50 % of divalent ions, CRED systems present limited power density drop of 35 % in the presence of 60 % divalent ions. This is mainly due to the periodic water chamber reversal which prevents the membrane from poisoning problems.

5. Techno-economic analysis suggests that CRED system is worth of further development. The key point relies in the development of cost-less and efficient ion-exchange membranes.

Chapter 4

pH gradient cell for energy harvesting

4.1 Preamble

In previous chapters, our research focused on CRED systems to enhance energy performance and assess the feasibility of industrial scale-up, with the aim of expediting technology maturation. However, it's important to note that the osmotic energy derived from salinity gradients is limited by salt solubility, typically estimated at 260 g.L^{-1} for NaCl, for example. To explore a broader concentration difference range, one avenue is to develop pH gradient-based energy harvesting systems. In this chapter, we will generalize the understanding of salinity gradient based CRED system into a pH gradient cell.

From an industrial perspective, the pH neutralization process is already a matured industrial practice for waste treatment. In fact, with well-controlled mixing in a pH gradient cell, it's possible to simultaneously perform waste treatment and electricity production.

Another interesting possibility of using pH gradient cell is to couple with Carbon capturing process. Today, the global scientific community is deeply engaged in tackling CO_2 capture, exploring numerous technological avenues to separate it from flue gas. Various methods such as chemical and physical absorption, cryogenic separation [269], gas-separation membranes [270] are under scrutiny. Among these, the predominant approach in thermal power plants involves post-combustion capture (PCC) scrubbing the gas with an amine solution. This method is particularly effective for diluting CO_2 streams from sources like coal combustion flue gases, typically containing 12 to 15% of CO_2 by volume [234, 235]. However, the drawback of this process lies in the substantial energy demand during the regeneration phase of the amine absorbent. Research by Dallos et al. revealed that the thermal energy required for regeneration exceeds half of the total capture energy [271]. Consequently, numerous research groups are directing efforts towards minimizing regeneration energy to foster the development of economically viable CO_2 capture processes [272].

To reduce the overall energy cost, it is possible to integrate a pH gradient energy harvesting system to recover certain energy. Kim et al. already reported a feasible pH gradient cell for energy harvesting process[237]. They used MnO_2 electrodes with a non-selective membrane to form the cell. In fact, the CO_2 dissolution results in a reduced pH in the electrolyte. If we divide the electrolyte into two parts, with one part pumped with CO_2 gas of low pH and another part purged with air or waste heat treatment of high pH, we can easily create a pH difference between them. The pH difference is considered as a giant osmotic energy source. With a well controlled mixing process, it is possible to convert this energy into electricity. A typical power density output of 0.82 W.m^{-2} is reported for a pH difference of 1.7. Similar works have been reported for the pH gradient cell[145, 243, 244].

Comparing the pH gradient cell with the salinity gradient based CRED system reported in previous chapters, we find a major common point in its capacitive behavior. This is verified in several facts. Both systems require the periodic water chamber reversal to remove the saturation state caused by the capacitive behavior of electrodes. Both systems outperform the Capmixing process in terms of power density but fall short of matching the power density of the RED system. However, due to the use of MnO_2 composite electrodes in the pH gradient cell, it is hard to determine if the system performs in capacitive or faradaic regime. How does the MnO_2 composite electrodes behave in the pH gradient cell for different electrical current densities? Will there be similar capacitive current decay problems as observed in CRED systems? Is it possible to enhance its power density performance by applying the boosting strategy? Will there be any differed phenomenon due to its possibility of faradaic working modes?

In this chapter, we begin by outlining the experimental setup of the pH gradient cell and elucidating its operational principles. Subsequently, we conduct electrochemical characterizations and develop a capacitive RC-type equivalent circuit for the pH gradient cell. The power density performance is assessed through experimental measurements and theoretical modeling, with an examination of the validity of the RC circuit description. To further enhance the power density output, we implement the boosting strategy discussed in Chapter 2. We measure the net power density achieved in the pH gradient cell and compare this result with the boosting equivalent circuit. Finally, we engage in a discussion on the observed unusual increase in power density, proposing possible mechanisms.

4.2 pH gradient cell

4.2.1 Experimental set-up

MnO_2 particles preparation

Over all, the MnO_2 particles are prepared by a so-called co-precipitation method, as reported in the literature[237, 273]. We prepare a solution of 0.2 M $KMnO_4$ and a solution of 0.3 M $MnSO_4$. The solution of $MnSO_4$ is then mixed with $KMnO_4$ in a large flask with vigorous stirring for 3 hours. The MnO_2 particles are washed and collected after a centrifugation treatment. The particles are dried at 80 °C with a hot plate. The particles are then collected and grilled to minimize the particle aggregation. The chemical products used here are purchased from Sigma Aldrich.

All the Scanning Electron Microscopy images are obtained by Quattro ESEM (Thermo Fisher Scientific). The MnO_2 powders are placed onto a double-sided carbon tape that was adhered to an aluminum SEM stub. Then Nitrogen is used to verify the particle adhesion before placing the sample into the SEM holder. The overall MnO2 particles present an average diameter of 200 - 300 nm.

The X-ray diffraction (XRD) pattern of the prepared MnO_2 powders indicates that the material is amorph.

MnO_2 based electrode preparation

A similar method as reported by Brahmi and Colin for the preparation of the MnO_2 composite electrodes is used in this work[117]. Here, we firstly mix the poweders consist of 0.8 g MnO_2, 0.22 g Carbon Nanotubes (Carbon nanotube, multi-walled, Sigma Aldrich), 0.19 g Carbon Black (Alfa Aesar) and 0.17 g Polyvinylidene Difluoride (PVDF, Sigma Aldrich). Here, carbon nanotubes and carbon black powders are used to further increase the conductivity and the capacitance of the composite electrodes. The PVDF serves as a binder for the mixture. We add 10-11 mL of 1-Methyl-2-pyrrolidinone (NMP, Sigma Aldrich) as a solvent. The overall slurry is well stirred

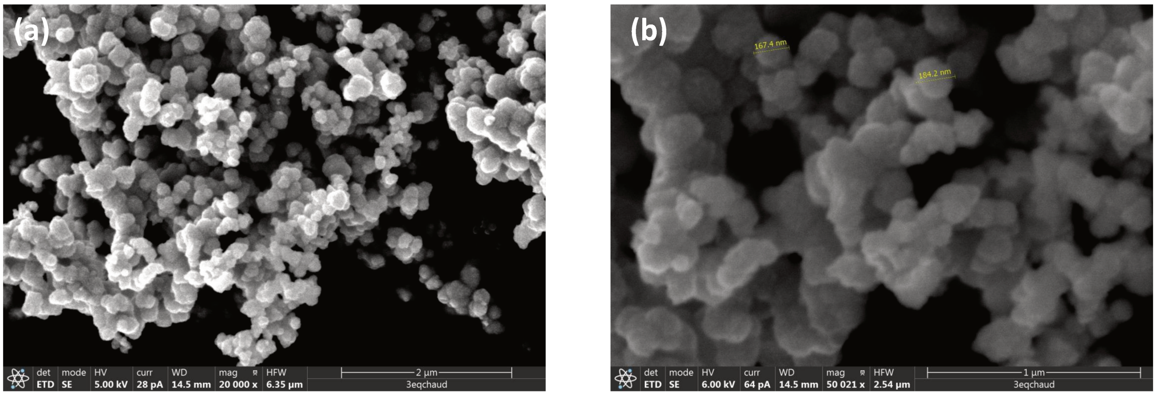

Fig. 4.1 SEM images of MnO_2 particles synthesised by the co-precipitation method.

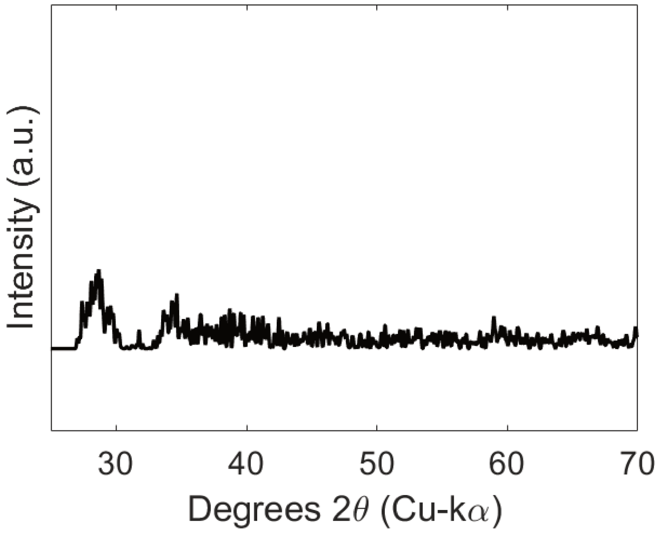

Fig. 4.2 X-ray diffraction (XRD) pattern of MnO_2 powders prepared by the co-precipitation method.

overnight to ensure the homogeneity. Then the slurry is spread onto a carbon cloth (Panex PW06 Carbon Fiber Fabric, Zoltek) by the method of doctor blade. The carbon cloth with the deposited slurry is firstly heated at 50 °C on a hot plate overnight to evaporate the solvent and avoid cracks. The composite is then heated up to 300 °C for over 4 hours. The composite electrode is washed and then dried for use in cell assembly.

For MnO_2 composite electrode, we cut a small piece of the electrode and stick it onto an aluminum SEM stub. All samples are prepared without further coating process.

pH gradient cell set-up

The pH gradient cell employed in this study features a symmetric design (Fig 4.4). It comprises two water chambers separated by a non-selective membrane (Celgard), specifically Celgard 3401, a 25 μm Monolayer Microporous Membrane (PP). The membrane's effective surface area, totaling 5.5 cm^2 (3 cm wide, 1.8 cm long), is determined by the membrane gasket's surface. Within the cell, two MnO_2 composite electrodes, each covering

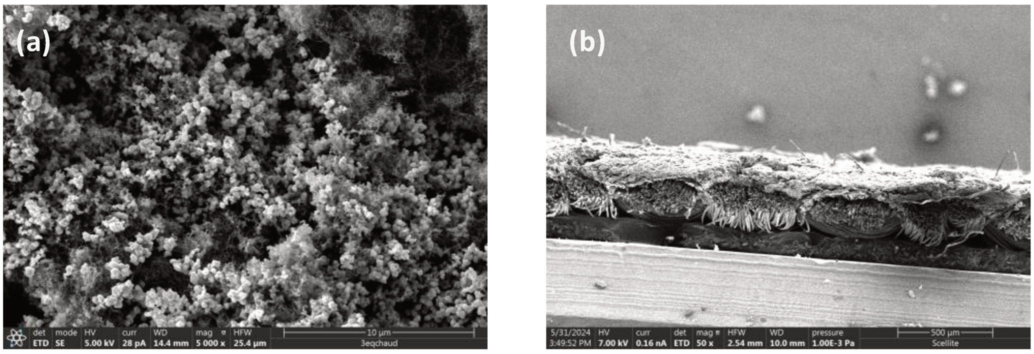

Fig. 4.3 SEM images of a MnO_2 composite electrode.

10 cm^2 , are positioned in individual electrode gaskets. These electrodes are in direct contact with graphite current collectors (Fuel Cell Store). The spacing w between the two electrodes is 400 μm. The whole system is well fixed by the use of two endplates made of stainless steel and then closed by 12 bolts with a torque of 2 N.m. At each side of the cell, two ports are reserved for all cell parts to ensure a water inlet and outlet. Solutions of low pH and of high pH are propelled by a peristaltic pump (BT100-1L Multi-channels Peristaltic Pump, Longer) with a fixed flow rate q of 15 mL.min^{-1}. The mean velocity of the electrolyte V is given by $V = \frac{q}{wL}$ where $L = 3.5$ cm is the width of the cell, V=1.7 cm/s. The pH gradient cell system will be blocked by its saturation regime due to its capacitive feature. We perform a periodic water chamber reversal by the use of an automatic 4-port valve controlled by electronic chip in order to unblock the saturation situation. Eventually, the system delivers a periodic alternative current.

4.2.2 Working principle

The general working principle of a pH gradient cell is illustrated in the Fig 4.4 **(a)**. Here, two different solutions are pumped into the water chambers separately in the pH gradient cell. On the one hand, CO_2 gas is pumped continuously which results in an electrolyte of low pH. On the other hand, air pumping or heat treatment is used in order to keep an electrolyte of high pH. This result in a significant pH difference which varies from 0 to 3.9. In the case of the maximum pH difference, the solutions used in the each chamber is composed of 1 M $NaHCO_3$ (pH 7.8) in the low pH chamber and of 0.5 M Na_2CO_3 (pH 11.7) in the high pH chamber. The CO_2 gas and air pumping is kept all along the experiments.

Different from classic RED systems, only a non-selective membrane is used in the system to prevent the two solutions from direct mixing. Thus the open-circuit voltage E_{OCV} in a pH gradient cell consists only of the potential difference related to electrodes $E_{OCV} = E_{elec}$. Here the contribution of membrane potential is zero, which is quite different from classic RED systems where both membrane and electrodes contribute to the overall open-circuit voltage ($E_{OCV-RED} = E_{mem} + E_{elec}$)[1].

It is to mention that MnO_2 composite only remains stable under basic conditions. During the establishment of pH difference, it is important to avoid acidic environment where we observe a significant composite electrode dysfunction due to the MnO_2 dissolution. Here, due to the use of bicarbonate buffers, the minimum pH in the system remains higher than 7.8.

To convert osmotic energy established by the pH difference into electricity, redox reactions occur on the MnO_2 composite electrodes.

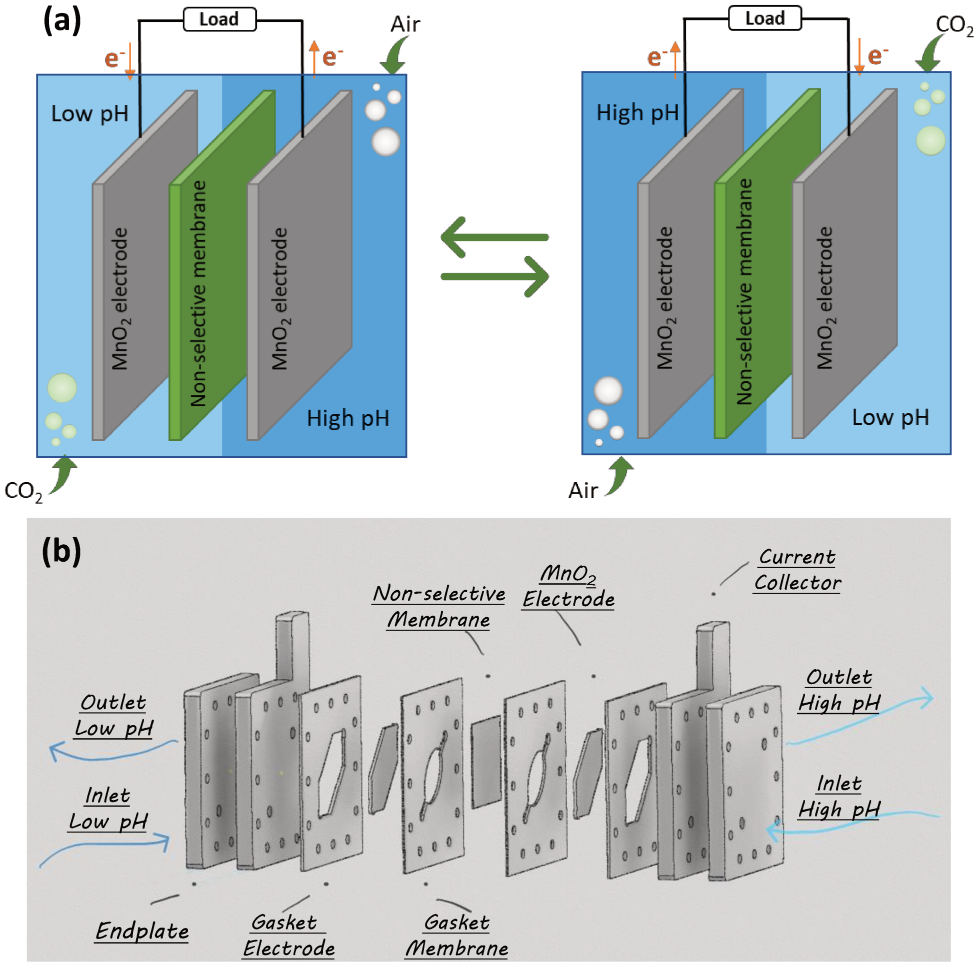

Fig. 4.4 (a) Illustration of the experimental set-up. The pH gradient cell is divided into two identical water chambers with two MnO_2 based electrodes and a non-selective membrane. Electrolyte purged with CO_2 presents lower pH, while electrolyte purged with air or with heat treatment is of higher pH. Two solutions are injected into the pH gradient cell and a water chamber switch is realized at a fixed period T. (b) Detailed illustration of the composition of the pH gradient cell. It is of symmetric structure with end plates, current collectors, gaskets for electrodes, MnO_2 electrodes, gaskets for membranes, and a non-selective membrane.

4.2.3 System characterization of pH gradient cell

In the following, we perform electrochemical characterization measurements of the pH gradient cell. More specifically, we are interested in the open-circuit voltage E_{OCV}, inner cell resistance R_{cell} and capacitance C of the cell.

Measurement of open-circuit potential

Experimentally, we measure the open-circuit of the pH gradient cell by using the OCV function of a potentiostat. While solutions of different pH are injected at a flow rate of 15 mL.min $^{-1}$ into the cell system, we connect the

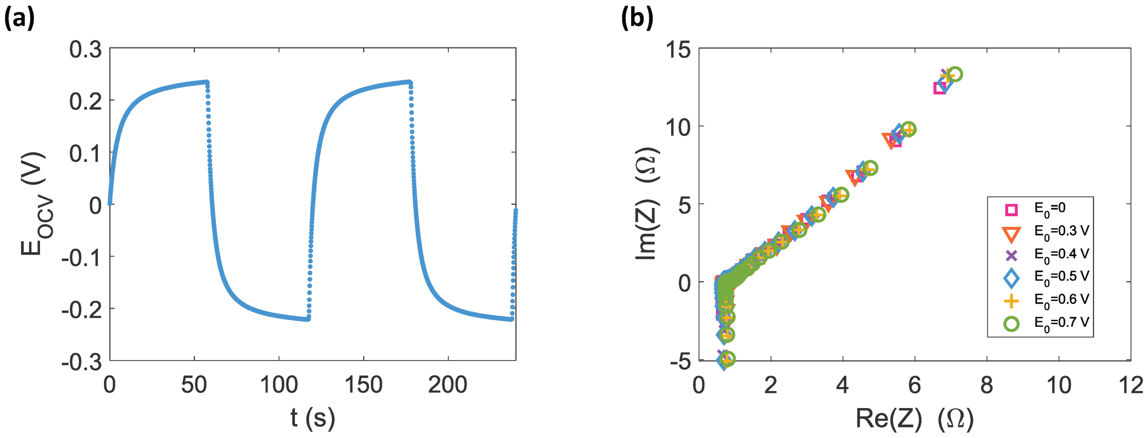

Fig. 4.5 Electrochemical characterizations of the pH gradient cell. (a) Open-circuit voltage E_{OCV} measured in the experiment. The experimental conditions are as follows: we use 1 M of $NaHCO_3$ in the low pH chamber and 0.5 M of Na_2CO_3 in the high pH chamber with a flow rate of 15 mL.min^{-1} and a switching period of 60 s. (b) The PEIS measurement of pH gradient cell after different experiments. Here, we performed systematic PEIS measurement after power density measurement under different boosting voltages. The Nyquist plot presented here provides information concerning the capacitance C and the inner cell resistance R_{cell}.We conclude from the Nyquist plot that the electrochemical characteristics of pH gradient cell remains stable in our experiments.

two current collectors with the potentiostat channel. Here the potentiostat is used as a voltmeter. A periodic water chamber switch is realized each 60 s. In the case of the max pH difference of 3.9, the measured potential curve is illustrated in Fig 4.5 **(a)** as a function of time. The experimental value for E_{OCV} is 0.227 V.

Here in both water chambers, the activity of sodium ions Na^+ remains identical, a potential difference is established due the the pH difference on the electrodes. According to the work of Kim et al.[237], the electrode potential variation varies linearly with the pH difference and follows the Nenst equation as follows:

$$E = E^0 + \frac{RT}{F} ln(a_{H^+}) \tag{4.1}$$

where E is the electrode potential, E^0 is the standard electrode potential, R is the gas constant, T_s is the absolute temperature, F is the Faraday constant and a is the activity.

According to Equation 4.1, at room temperature of 25 °C, it is possible to describe the cell voltage as a function of pH difference Δ pH as[237]:

$$E_{OCV-th} = \Delta E_{elec} = 0.059 \times \Delta pH \tag{4.2}$$

The theoretical prediction by Nernst equation E_{OCV-th} is estimated as 0.231 V for a max pH difference of 3.9. The open-circuit voltage E_{OCV} measured in the experiment corresponds well with the theoretical prediction by Nernst equation.

It is also reported in the work of Kim et al. that the overall response of the pH gradient system is capacitive[237]. We observe capacitive current decay phenomenon and thus perform periodic water reversal to maintain the continuous electricity generation. These facts may seem contradictory with the fact that the system follows a Nernst law. It may come from the fact that the chemical matter available for redox reactions is present in small quantity. We will admit these two points in the following sections before returning to a detailed discussion.

Impedance measurement

Here we perform systematic impedance characterization to measure the inner resistance R_{cell} and capacitance C of the pH gradient cell. A Potentiostatic Electrochemical Impedance Spectroscopy (PEIS) measurement is realized for the cell under different experimental conditions. The result is shown as a Nyquist plot in Figure 4.5 **(b)**. The inner cell resistance R_{cell} and capacitance C is determined using the impedance measurement at 7 mHz as the following Equation 4.3 and 4.4.

$$R_{cell} = Re(Z) \tag{4.3}$$

$$C = \frac{1}{2\pi f \mid Im(Z) \mid} \tag{4.4}$$

where Z refers to the impedance of the cell system measured at 7 mHz, $Re(Z)$ is the real part of the impedance, $Im(Z)$ is the imaginary part of the impedance and f is the measurement frequency.

In the case of max pH difference, we measure a inner cell resistance R_{cell} of 5.5 Ω and a capacitance C of 1.9 F. The PEIS curve has a similar geometry compared with CRED systems, thus we propose a similar R-C type of equivalent circuit for the pH gradient cell system (Fig 4.6 **(c)**). Based on such equivalent circuit, a theoretical model could be established to further predict the energy performance of the pH gradient cell. More details will be provided in the section of power density measurement.

It is also to mention that the Nyquist plot curves under different experimental conditions superpose well among them. Here, we perform power density measurement of the pH gradient cell under boosting voltages E_0. Details of the boosting experiments are available in the section of boosting strategy. It indicates an excellent system abundance of the pH gradient cell, with all electrochemical characteristics remaining stable in all experiments performed in this work.

4.3 Results and discussions

4.3.1 Power density measurement

In order to further characterize the power density performance of the pH gradient cell, we close the circuit by connecting the pH gradient cell with a load resistor R_{load}. Here, we inject solutions of low pH (1 M $NaHCO_3$, pH = 7.8) and of high pH (0.5 M Na_2CO_3, pH = 11.7) into the cell system at a flow rate of 15 mL.min^{-1}. A potentiostat is connected in parallel with the load resistor in order to measure the voltage applied onto the resistor E_{load}. A systematic water chamber switch is realized at a fixed period T_s of 60 s. Such measurement is repeated for a series of load resistors. Fig 4.6 **(a)** illustrates the voltage measurement curve during 2 complete water chamber switch periods. A symmetric voltage curve is observed before and after water chamber switch. It is clear that a higher voltage output is observed while increasing the load resistance, which is explained by the voltage divider rule.

Following the E_{load} measurements, it is then possible to determine the instantaneous power density output P of the pH gradient cell system. It is defined as the following Equation 4.5. The instantaneous power density curve is illustrated in Fig 4.6 **(b)**.

$$P(t) = \frac{E_{load}(t)^2}{R_{load}S} \tag{4.5}$$

where S refers to the effective membrane surface in the cell. It is also possible to define the average power density within a fixed period T_s as in Equation 4.6.

$$P_{nb} = \frac{1}{S.T_s}\int_0^{T_s} P(t)dt = \frac{1}{S.T_s}\int_0^{T_s} \frac{E_{load}(t)^2}{R_{load}}dt \tag{4.6}$$

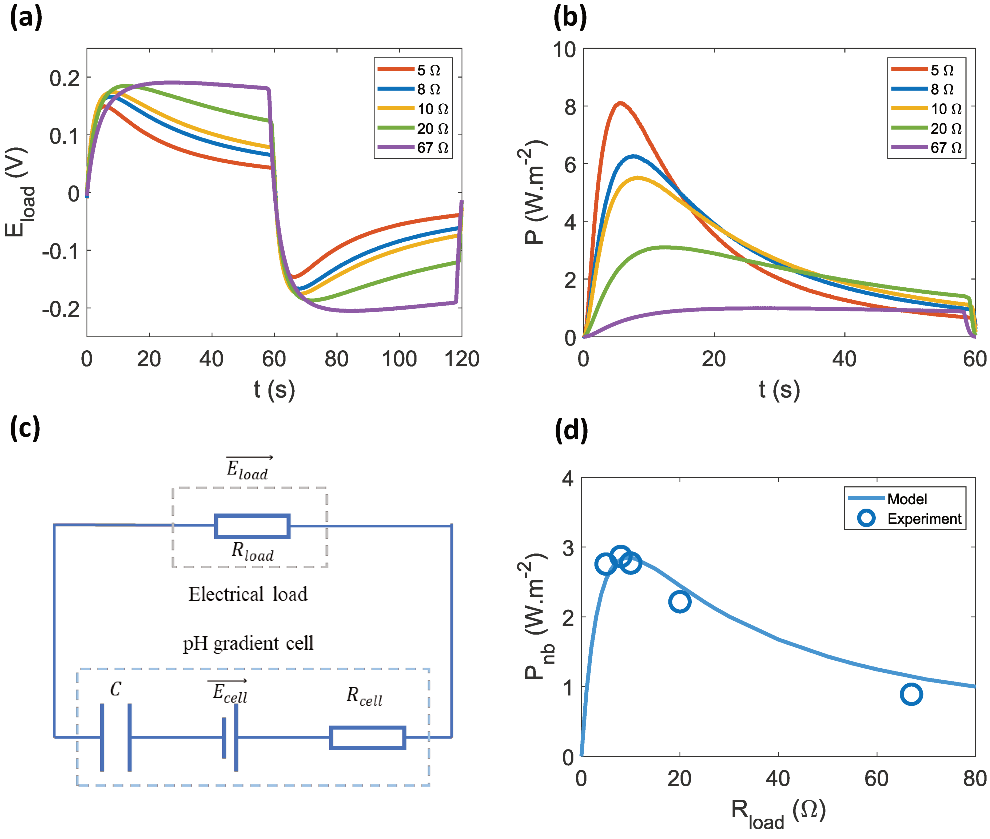

Fig. 4.6 Power density measurement of the pH gradient cell with a series of load resistors R_{load}. (a). The applied voltage E_{load} on different load resistors R_{load} as a function of time t. (b). The instantaneous power density P of pH gradient cell as a function of time t for various load resistances. The result is calculated from the measurement of E_{load} by $P = \frac{E_{load}^2}{R_{load}}$. (c) An equivalent RC type circuit established for the pH gradient cell. The system parameters are characterized by PEIS measurements. (d). The averaged power density P_{nb} with the switching period T_s as a function of load resistance R_{load}. The solid line in the figure refers to the simulation result by modeling. The dots in the figure represents the experimental data. A good agreement is achieved. In all figures, the experimental conditions are as follows. We use 1 M of $NaHCO_3$ in the low pH chamber and 0.5 M of Na_2CO_3 in the high pH chamber with a flow rate of 15 mL.min^{-1} and a switching period of 60 s.

As already discussed in the cell characterization part, we establish a RC type equivalent circuit for the pH gradient cell (Fig 4.6 **(c)**). It is then possible to describe the equivalent circuit by writing the Equation 4.7 and 4.8 below.
For $0 < t < T_s$:

$$(R_{load} + R_{cell})I(t) + \frac{q(t)}{C} = E_{OCV} \tag{4.7}$$

For $T_s < t < 2T_s$:

$$(R_{load} + R_{cell})I(t) + \frac{q(t)}{C} = -E_{OCV} \tag{4.8}$$

where $I(t)$ refers to the electrical current in the closed circuit and $q(t)$ is the accumulated charges in the capacitor.

In the case of a pH gradient cell, as the characteristic times related to the ion concentration profile and the filling time of the cell are negligible compared with the switching period T_s, R_{cell} and E_{OCV} are simplified as window functions. Only electrical current $I(t)$ and accumulated charges $q(t)$ are assumed to be time dependent. Solving the theoretical models enables the prediction of power density as in Equation 4.9.

$$P_{nb-th} = \frac{2}{S.T_s}\frac{CE_{OCV}^2 R_{load}}{R_{load} + R_{cell}} tanh(\frac{T_s}{2(R_{load} + R_{cell})C}) \tag{4.9}$$

In Fig 4.6 **(d)**, we compare the results obtained by model prediction and by experiments. The solid line represents the power density predicted by Equation 4.9. The parameters used in equation are obtained by electrochemical characterization. The dots correspond to the experimental data measured in a pH gradient cell. An excellent agreement is achieved in this case. It confirms once again the validity of the equivalent established for the pH gradient cell system.

However if we compare the measured power density with the theoretical maximum value, we notice a similar power density drop as previously reported for CRED systems. The maximum power density measured in experiments is 2.86 W.m^{-2}, while the maximum power density predicted by $\frac{E_{OCV}^2}{4R_{cell}S}$ is 3.51 W.m^{-2}. In fact, E_{load} curve presents a similar capacitive current decay phenomenon as reported in CRED systems. This is different from a faradaic RED system where the electric current remains constant. The current decay phenomenon results in a power density drop. According to previous studies, it originates from the low ionic-electronic conversion efficiency of capacitive electrodes. It is not surprising that such power density gap exists also for MnO_2 composite electrodes due to the significant capacitive behavior. In the following section, we will apply the boosting strategy onto the pH gradient cell system to further enhance the power density output.

4.3.2 Boosting strategy

As reported in the Chapter 2 and in the work of Wu et al.[3], boosting strategy leads to efficient power density performance amelioration for CRED systems. The power density of CRED system under boosting strategy approaches eventually the theoretical maximum value $\frac{E_{OCV}^2}{4R_{cell}S}$. As the pH gradient cell presents similar capacitive current decay problems, the boosting strategy is applied on pH gradient cell in the hope of further increasing the power density output.

To apply the boosting strategy, an additional booster system is placed in series with the load resistor in the circuit (Fig 4.7**(a)**). The booster system composition is explained in the section of Materials and Methods. It delivers an electrical voltage E_0 well synchronized to the signal E_{OCV} delivered by the pH gradient cell in the way that E_0 and E_{OCV} are always of identical sign. As the booster system presents as a secondary source in the circuit,

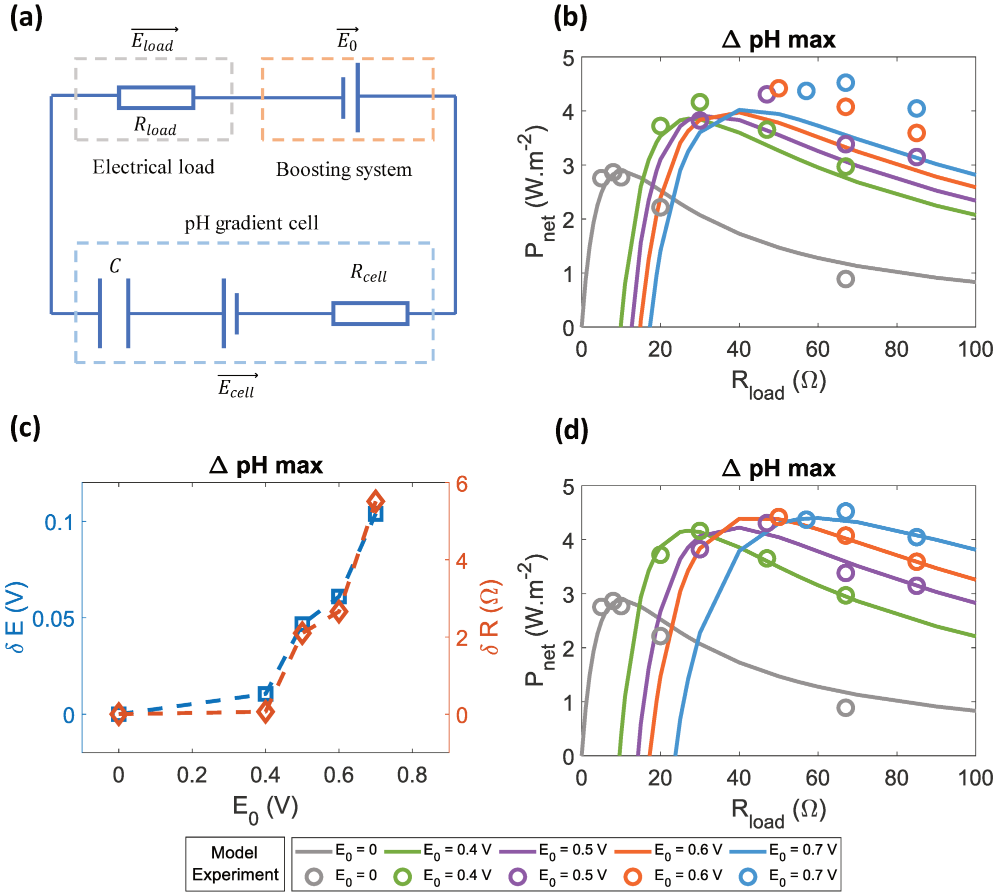

Fig. 4.7 Power density measurement of the pH gradient cell under boosting strategy. (a). The equivalent circuit of the pH gradient cell coupled with an additional booster system. The electrical voltage E_0 delivered by the booster system is synchronized with the signal E_{OCV} delivered by the pH gradient cell. (b). Comparison between theoretical modeling of boosting and experimental data for a pH difference of 3.9. The theoretical modelling is performed with the cell parameters as follows: $E_{OCV} = 0.227$ V, $R_{cell} = 5.5\ \Omega$ and $C = 1.9$ F. These parameters are obtained through electrochemical characterization. Experimental data are obtained by net power density measurement P_{net} as a function of load resistance R_{load} for different boosting voltages E_0 for a pH difference of 3.9. All the net power densities are calculate by the following equation $P_{net} = P_{gross} - P_{boost}$. The model predicts well the power performance of pH gradient cell without boosting strategy. However, a significant difference is noticed between modeling and experiment under boosting strategy. (c). Two fitting parameters δE and δR to adapt equivalent circuit for the description of energy performance under boosting strategy. Both parameters show a significant increase with a rising boosting voltage E_0. The model adjustment considers an increased effective open-circuit voltage E_{eff} and effective cell inner resistance R_{eff} due to the solid state change of MnO_2 electrodes under boosting strategy. (d). Comparison between modified theoretical modeling of boosting and experimental data for a pH difference of 3.9. By adding two fitting parameters in the model, we achieve an good agreement between modeling and experiment under boosting strategy.

while calculating the net power density dissipated in the load resistor, we need to subtract the additional energy provided by the booster system.

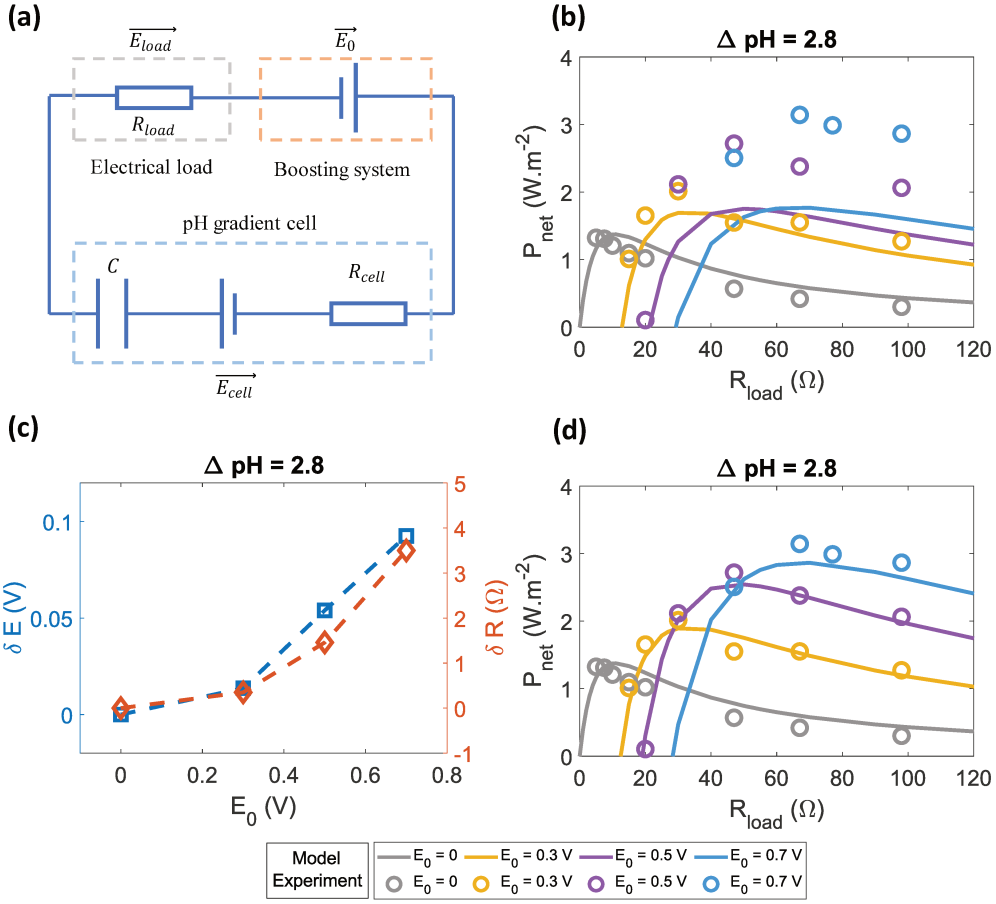

Fig. 4.8 Power density measurement of the pH gradient cell under boosting strategy. (a). The equivalent circuit of the pH gradient cell coupled with an additional booster system. The electrical voltage E_0 delivered by the booster system is synchronized with the signal E_{OCV} delivered by the pH gradient cell. (b). Comparison between theoretical modeling of boosting and experimental data for a pH difference of 2.8. The theoretical modelling is performed with the cell parameters as follows: $E_{OCV} = 0.165$ V, $R_{cell} = 6.8\ \Omega$ and $C = 2.0$ F. These parameters are obtained through electrochemical characterization. Experimental data are obtained by net power density measurement P_{net} as a function of load resistance R_{load} for different boosting voltages E_0 for a pH difference of 2.8. All the net power densities are calculate by the following equation $P_{net} = P_{gross} - P_{boost}$. The model predicts well the power performance of pH gradient cell without boosting strategy. However, a significant difference is noticed between modeling and experiment under boosting strategy. (c). Two fitting parameters δE and δR to adapt equivalent circuit for the description of energy performance under boosting strategy. Both parameters show a significant increase with a rising boosting voltage E_0. The model adjustment considers an increased effective open-circuit voltage E_{eff} and effective cell inner resistance R_{eff} due to the solid state change of MnO_2 electrodes under boosting strategy. (d). Comparison between modified theoretical modeling of boosting and experimental data for a pH difference of 2.8. By adding two fitting parameters in the model, we achieve an good agreement between modeling and experiment under boosting strategy.

In power density measurement experiments, we measure at the same time the gross power density dissipated in the load resistor P_{gross} and the additional power density provided by the booster system P_{boost}. Then we calculate the net power density output of the pH gradient cell using the following Equation 4.10.

$$P_{net} = P_{gross} - P_{boost} \tag{4.10}$$

We perform the power density measurements for a series of load resistances and for a series of boosting voltages. The experimental results are presented in Fig 4.7**(b)**. Here the experimental results are obtained for a pH difference of 3.9, with a pH of 7.8 in low pH chamber and 11.7 in high pH chamber. It is clear that the net power density output of the pH gradient cell shows a significant increase under boosting strategy. In the best cases with a boosting voltage E_0 at 0.7 V, the power density increases from 2.86 W.m^{-2} towards 4.52 W.m^{-2}, which corresponds to a giant increase of 158%. It is astonishing to notice that the power density obtained under boosting strategy even surpasses the theoretical maximum value ($\frac{E_{OCV}^2}{4R_{cell}S}$) predicted to be 4.26 W.m^{-2}. In the case of pH difference 2.8, we obtain a power density increase from 1.32 W.m^{-2} towards 3.14 W.m^{-2}. Similarly, the measured max power density surpasses its theoretical maximum value of 1.82 W.m^{-2} (Fig 4.8).

Based on the equivalent circuit established for pH gradient cell coupled with a boosting system, it is possible to modify the theoretical models. Here the boosting system is modeled as an alternative voltage generator E_0 synchronized with E_{OCV}. It is simplified as a window function.

For $0 < t < T_s$:

$$(R_{load} + R_{cell})I(t) + \frac{q(t)}{C} = E_{OCV} + E_0 \tag{4.11}$$

For $T_s < t < 2T_s$:

$$(R_{load} + R_{cell})I(t) + \frac{q(t)}{C} = -E_{OCV} - E_0 \tag{4.12}$$

Similarly, we get a net power density prediction by solving the modeling under boosting strategy.

$$P_{net-th}(E_0) = \frac{2}{ST}\frac{C(E_{OCV}+E_0)}{R_{load}+R_{cell}} tanh(\frac{T}{2(R_{load}+R_{cell})C})(E_{OCV}R_{load} - E_0 R_{cell}) \tag{4.13}$$

Fig 4.7**(b)** compares the theoretical model prediction with the experimental data obtained under boosting strategy. The solid lines represent the theoretical prediction based on modelling, while the dots represent the net power density obtained experimentally. The theoretical model predicts well the power density performance in absence of boosting. However, we notice an astonishing power density increase in experiments which is not predicted by the modelling by RC equivalent circuit in the case of boosting. In the following, we try to uncover the underlying mechanism of this unusual power density increase.

4.3.3 Mechanism discussion

Pseudocapacitance of MnO$_2$

It is reported in the work of Augustyn et al. that there are typically two major charge storage mechanisms for MnO$_2$ electrodes[274]. Firstly, charge storage is realized by surface charge adsorption/desorption. This process is very similar to the surface electrical double layer (EDL) charging process and can be described by the Equation below.

$$MnO_2 + H^+ + e^- = (MnO_2^- H^+) \tag{4.14}$$

One might wonder if the surface charge adsorption/desorption process is sufficient to describe the capacitive behavior in the pH gradient cell system. In fact, it is demonstrated in the work of Brahmi and Colin that in a single membrane based CRED system, the capacitive electrode related potential difference can be described as a

"Nernst" type equation, and that the diluted part is of higher potential[117]. However, this result is in contrast with the experimental result in a pH gradient cell, where the concentrated part (low pH) presents a higher potential.

This point clearly shows that the capacitive behavior observed in the pH gradient cell does not originate from the ion adsorption/desorption mechanism described for the electrical double layer. Another underlying mechanism should be considered.

In addition to the above mentioned capacitive charge storage process similar to EDL ion adsorption, MnO_2 electrode could also experience redox reactions both at the surface and in the bulk structure[273, 275]. This is reported mainly for crystalline MnO_2 materials but evidences show that ions insert into subsurface sites in amorph MnO_2 materials as well. This process can be described as the following equation.

$$MnO_2 + H^+ + e^- = MnOOH_{(s)} \tag{4.15}$$

Considering the presence of carbonate species in the electrolyte, we cannot eliminate the another redox reaction possibility. Further research work should be conducted to identify the redox reactions occurred in the pH gradient cell.

$$MnO_2 + HCO_3^- + 2e^- + 3H^+ = MnCO_{3(s)} + 2H_2O \tag{4.16}$$

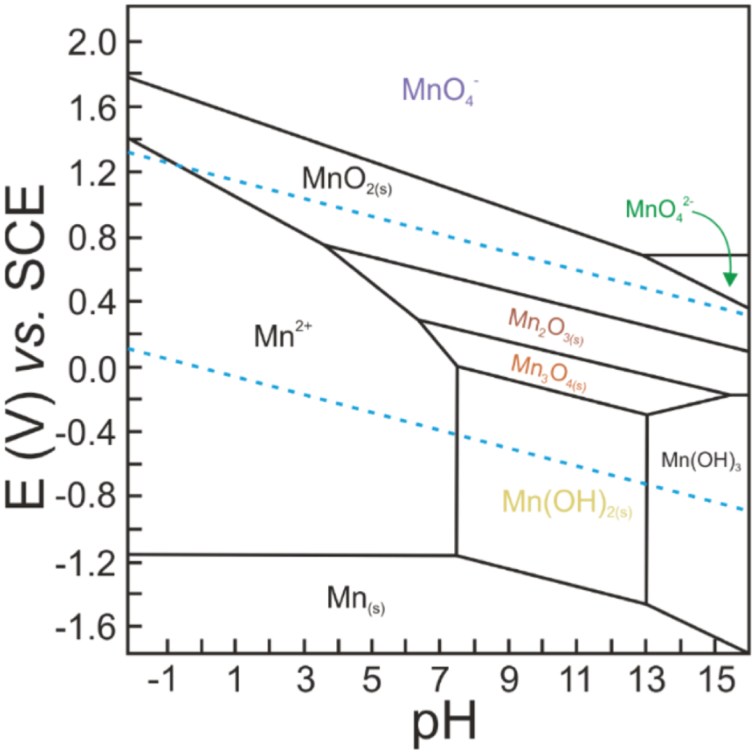

Fig. 4.9 Pourbaix diagram showing the possible thermodynamically stable phases of manganese. The boundaries representing the 50/50% presence of states is represented by solid lines and the stability of water in the system is represented by dashed lines. (Figures and captions adapted from [276] with permission from Elsevier, copyright 2022.)

In fact, the experimentally measured open-circuit potential can be well described by the Nernst Equation 4.1. This suggests the occurrence of faradaic redox reactions. At the same time, the redox reactions remain stable and the pH gradient cell system shows excellent capacitive behavior as verified both by impedance measurement and by equivalent circuit modeling.

Then question arises as to what sets the electrode potential. In practice, the MnO_2 electrode in salt solutions is at abandonment potential. MnOOH sites must appear to define this potential. These sites appear as a result of oxide-reduction reactions with oxygen and water, as shown in the Pourbaix diagram in Fig 4.9. The rate of MnOOH coverage is determined by this equilibrium and by the potential to be applied to the electrode. With the electrode comprising these two surface groups, it is then easy to understand the capacitive behavior, which is an exchange between the MnOOH and MnO_2 sites between the two electrodes of the two different compartment.

Unexpected boosting result

For a purely capacitive system, as reported for CRED, the equivalent RC circuit accurately describes the experimental energy performance, both in the absence and presence of boosting[3]. It is reported that the power density gap of CRED system originates from the low conversion efficiency between ionic flux and electronic flux. It is an inherent characteristic of capacitive electrodes. It slows down and even blocks the electrical current in the circuit, resulting in a significant capacitive current decay phenomenon. In this case, the capacitive system works in an "inefficient regime" and leads to a significant power density drop. To avoid the power density decrease, the boosting strategy is able to enlarge the "efficient regime" window so that the capacitive system presents limited current decay and approaches the theoretical limit.

In a pH gradient cell, due to the pseudo-capacitance of the MnO_2 electrodes, a similar RC type equivalent circuit is established. It describes well the power density output of the pH gradient cell in absence of boosting. It predicts as well the power density gap due to the electrode's capacitive behavior. While applying the boosting strategy, the net power density obtained in experiments surprisingly surpasses that predict by the RC model. Here, the electrochemical characteristics of the pH gradient cell remains stable after the boosting experiments, as the Nyquist plots in PEIS measurement superpose well among them (Fig 4.5(**b**)). This suggests an invariant cell system before and after each experiment. It indicates a temporal electrochemical characteristic modification during the boosting experiments. Here, we propose a possible mechanism with evidences already reported in literature.

In the review work of Augustyn et al., an additional electrode related potential is suggested for materials of pseudo-capacitance[274]. It is reported that the coverage rate of the electrode surface or the inner structure has an impact on the electrode potential. More specifically, the coverage rate related potential variation was already well studied for the composite electrodes made of MnO_2 and MnOOH in 1950s[277, 278]. It was reported by Vosburgh and coworkers that a progressive and continuous electrode potential variation is observed due to the proton/electron accommodation. This point was verified by experiments and was concluded to originate from the formation of a solid solution with a continuous range of Mn (III) and Mn (IV) states[279]. Such phenomenon is eventually well described by the Equation 4.17.

$$E \sim E^0 - \frac{RT}{nF} ln(\frac{X}{1-X}) \tag{4.17}$$

Here n is the ion valence and X is the extent of fractional coverage of the surface or inner structure. To summarize, the solid composition change in MnO_2 composite electrode might result in an additional electrode potential difference. And it is highly related to the fractional coverage X of MnO_2. Thus it is reasonable to include both a proton concentration difference (Δ pH) related term and a fractional coverage difference (ΔX) related term in the description of cell voltage.

Based on this understanding, one possible mechanism is as follows. In absence of boosting, the pH gradient cell works in its capacitive regime. The difference of fractional coverage status of the MnO_2 remains negligible due to the limited redox reactions. Thus the open-circuit voltage is dominated by the potential difference created by the pH difference. The pH gradient cell remains in a capacitive mode with its energy performance well described by the equivalent RC circuit. While applying boosting voltage E_0, there is a significant fractional coverage change due to the forced redox reactions. This results in a further potential contribution related to the fractional coverage difference ΔX. As the fractional coverage change is related to the redox reaction, it strongly depends on the boosting voltage E_0.

To verify this point, we adapt our equivalent circuit with an adapted voltage $E_{OCV-eff}$ defined as $E_{OCV-eff} = E_{OCV} + \delta E$ and an adapted resistance $R_{cell-eff}$ defined as $R_{cell-eff} = R_{cell} + \delta R$. Under boosting strategy, by using these two additional parameters, we obtain a modified model as follows:

$$P_{adapt}(E_0) = \frac{2}{ST}\frac{C(E_{eff}+E_0)}{R_{load}+R_{eff}}tanh(\frac{T}{2(R_{load}+R_{eff})C})(E_{eff}R_{load}-E_0R_{eff}) \tag{4.18}$$

$$= \frac{2}{ST}\frac{C(E_{OCV}+\delta E+E_0)}{R_{load}+R_{cell}+\delta R}tanh(\frac{T}{2(R_{cell}+\delta R+R_{load})C})((E_{OCV}+\delta E)R_{load}-E_0(R_{cell}+\delta R))$$

Through fitting the experimental data with the modified model, we derive insights into δR and δR. Illustrated in Fig 4.7**(c)**, these additional fitting parameters vary with the boosting voltage E_0. Notably, as the boosting voltage E_0 increases, both the system voltage and cell resistance show an increase. By incorporating these adjustments in cell voltage and inner resistance, the RC circuit effectively predicts the power performance of the pH gradient cell under the boosting strategy (Fig 4.7**(d)**). This indicates that the system still works in a capacitive regime. Under boosting conditions, significant surface coverage fraction changes occurred under redox reactions, but these changes remain reversible. For the boosting case of pH difference at 2.8, a good agreement is achieved as well by doing both potential and resistance fitting in RC equivalent circuit (Fig 4.8).

In the maximum boosting cases of 0.7 V, we estimate a temporal voltage increase of 100 mV. If we attribute this increase to the fractional coverage difference, we estimate ΔX to be 34 %. This point is further verified by a simple estimation based on MnO_2 electro-deposition process. Through experimental results, a total charge of 8 C is estimated to form a MnO_2 electrode of the same capacitance. The total charge variation during the boosting case of 0.7 V is in measured to be 0.6 C. We estimate thus a fractional coverage difference of 30% during each boosting period, which is in line with the above mentioned calculation.

To go further, the boosting strategy is applicable under a limit current density of 2 $mA.cm^{-2}$. Beyond this limit, we observe an irreversible electrode deterioration which quickly leads to electrode dysfunction. We believe that in this case, the system enters the faradaic regime and the redox reactions occurred in MnO_2 composite electrodes lead to severe material structural expansion and material loss.

4.3.4 Techno-economic analysis

Following these measurements, a question emerges. How much energy can be recovered from a PCC pilot, and where else should this type of device be integrated? The main issue is the available solvent quantity. The solvent flow and the amount of solvent in the process is constrained by the amount of energy required to regenerate the amine solution. In order to make an estimate, it is thus necessary to approach a real case study. In the following, we will take advantage of the analysis of a pilot plant for CO_2 recovery of 2 ton-CO_2/day from flue gas emitted from a 500 MW coal fired power plant performed by Kwak et al. [272]. In this study, the CO_2 poor solution has a CO_2 concentration of 0.2 mol/mol MEA, while the CO_2 rich solution has a CO_2 concentration of 0.5 mol/mol

MEA. In both cases the concentration in MEA in water is set to 30% in weight. This corresponds to a difference of pH of 2.5 [280]. The electrical and ionic conductivity of these solvents is comparable to our study, so we can expect to produce 3 $W.m^{-2}$ of membrane. The flow rate of the amine solutions is 1300 $L.h^{-1}$. In the case of our cell, this flow enables 177 cells with a width of 0.3 m to be fed, and therefore 46 MJ to be produced per day. Our data are obtained at 25°C, so we can expect higher capacities at 40°C. In addition, unlike the RED-type device, the membranes used are low-cost, so there are no filtration costs in the process. As a result, the cost of electricity produced is low. Assuming a membrane - electrode unit price of 10 € per m^2 (laboratory price), a collected power of 3 $W.m^{-2}$ and a membrane life of 10 years, the cost of the energy produced is 69 € per MWh taking into account the auxiliary equipments[3]. This figure is in line with current electricity production costs (solar energy 40 € per MWh, wind off shore 120 € per MWh[255]). This energy is not intermittent and does not require storage.

4.4 Conclusion

Conclusion

In this chapter, we generalized the salinity gradient based energy harvesting system into concentration gradient based systems. More specifically, we designed a pH gradient based energy harvesting cell to be integrated in the carbon capture process for overall cost reduction.

1. The CO_2 capturing in carbonate solutions results in a pH decrease. Combining electrolytes with CO_2 trapping and electrolytes with air pumping or heat treatment, we create a significant proton concentration difference with Δ pH ranging from 0 to 3.9 , which is used as an osmotic energy source in this work.

2. The pH gradient cell consists of two home-made inexpensive MnO_2 composite electrodes and a non-selective membrane. The overall cell voltage is delivered by the electrode potential difference which is well predicted by Nernst Equation.

3. Due to the pseudo-capacitance of the MnO_2 composite electrodes, the pH gradient cell has similar capacitive behaviors as in CRED systems both in electrochemical characterizations and in power density measurement. It delivers a maximum power density of 2.86 $W.m^{-2}$ for a maximum pH difference of 3.9. The pH gradient cell can be accurately modeled by an RC equivalent circuit, with its power density performance well-described by this model, suggesting that MnO_2 operates within a capacitive regime.

4. We propose the application of a boosting strategy to further enhance power density. However, we observe an astonishing increase in power density towards 4.52 $W.m^{-2}$, surpassing theoretical predictions based on $\frac{E_{OCV}^2}{4SRcell}$. The equivalent circuit-based modeling fails to account for this unusual increase in power density. Considering a potential additional contribution related to fractional coverage changes in MnO_2 electrodes, we further adjust the model under the boosting strategy, incorporating two fitting parameters to account for the observed increase. The corrected model aligns excellently with experimental data, suggesting a reversible redox reaction occurring within the MnO_2 electrodes.

5. While the electrical current exceeds a limit of 2 $mA.cm^{-2}$, we observe severe electrode dysfunction and material loss, indicating the occurrence of irreversible redox reactions.

Chapter 5

Conclusion and Perspectives

This concluding chapter provides a comprehensive overview of osmotic energy harvesting through capacitive reverse electrodialysis (CRED) systems. We also offer insights into our planned future investigations. Specifically, we will investigate deeper into studying the industrialization of the CRED system, focusing on two primary directions. Firstly, we will explore the construction of CRED cells with larger effective surface areas. Secondly, we intend to implement CRED units in series. Moreover, we plan to integrate salinity gradient-based CRED systems as booster systems in pH gradient systems. Lastly, we explore the possibility of integrating pH gradient cells into ocean-based Carbon Capture and Storage (CCS) processes.

5.1 General conclusion

In this thesis, we study the capacitive reverse electrodialysis (CRED) systems for osmotic energy harvesting. Based on the previous work in this group, we designed a CRED cell composed of two inexpensive capacitive electrodes and a single ion exchange membrane. While the CRED system offers significant advantages such as cost reduction, ease of industrial scale-up, elimination of over-potential issues, avoidance of redox reactions, and high stability, it also exhibits significant challenges in its power density output. The "blocking nature" of the capacitive electrodes requires a periodic solution chamber reversal to ensure the continuous osmotic-electric energy conversion. The experimental results reveal a notable decrease in power density, with over a 50% drop observed in the CRED system compared to its theoretical maximum. To further enhance the power density output of the CRED system, we conduct systematic study to reveal the underlying mechanism of this power density gap and provide an effective strategy for energy performance amelioration.

The giant power density gap is essentially due to the capacitive current decay phenomenon within each period. It is the result of an inefficient ionic-electronic flux conversion in capacitive electrodes. If the capacitive current shows important decrease within the fixed working period, the system presents low conversion efficiency between ionic flux and electronic flux. Thus it presents a significant energy performance drop under a so-called "Inefficient regime". However, if the capacitive current remains stable and shows limited decrease, it enters the "efficient regime" where the power density output approaches the maximum theoretical value. Based on this mechanism understanding, we propose the use of a secondary voltage source placed in series with the CRED system for power density output enhancement. This so-called "Boosting strategy" delivers an additional electrical signal well synchronized with the CRED cell electrical voltage. It enlarges the effective "efficient regime" window and thus alleviates the current decay problem for CRED system. By shifting the CRED system towards "efficient regime", it optimizes the ionic-electronic flux conversion in capacitive electrodes and enhances effectively the energy performance of the CRED system. This point is verified both by experimental results and by numerical simulations realized on an equivalent circuit of the CRED system. In the most optimized cases, for a salinity difference of 300 g.L^{-1} vs 10 g.L^{-1}, the net power density increases from 3.29 W.m^{-2} towards 5.26 W.m^{-2} under boosting strategy.

Thanks to the boosting strategy, the CRED system now demonstrates outstanding energy performance which is comparable to theoretical maximum predictions. Given its numerous advantages, particularly its cost-effectiveness compared to classic RED systems, further investigation into its feasibility at an industrial scale is intriguing. The aforementioned studies were conducted using artificial solutions composed solely of NaCl salts, which diverges from real-life applications. One crucial aspect is to explore the impact of divalent ion mixing, as encountered in real-world solutions.

We conducted a systematic study to investigate the impact of divalent ion mixing on cell open-circuit voltage, electrochemical characteristics and power density performance, respectively. According to experimental results, the mixing of divalent ions results in a significant cell voltage drop in CRED system. To further analyze this voltage decrease, we study the details in its membrane related contribution and its electrode related contribution, respectively. The experimental data demonstrates a major decrease in membrane potential while the electrode related potential remains stable. Different from classic RED scale up of series connection, the CRED repetition unit comprises capacitive electrodes. Thus in a CRED scale up configuration, 50 % of the overall cell voltage of CRED is electrode related contribution and it remains stable. This presents a major advantage for CRED system.

Further investigations are conducted to reveal the underlying mechanism of the membrane voltage drop. Two possible mechanisms could be the reasons behind this drop. In divalent mixing solutions, we observe a so-called uphill phenomenon which results in a decrease of membrane voltage. Due to Donnan equation, the electromotive force of monovalent ions are two times higher than that of divalent ions. In order to obtain equilibrium in chemical potential at both sides of the membrane, divalent ions are transported from the diluted part towards the concentrated part to compensate the monovalent ion transportation, to obey the electron-neutrality at both sides of the membrane. The theoretical modelling of uphill effects describes well the voltage drop in CRED system. This experiment-model accordance effectively eliminates the possibility of membrane poisoning issues. This phenomenon arises from the permeation of co-ions through non-ideal membranes, leading to a decrease in apparent membrane selectivity and an increase in cell resistance. Unlike previous studies on classic RED systems, the CRED system exhibits a limited decrease in cell voltage and power density performance. In the case of a mixed solution comprising 60 % $CaCl_2$ and 40 % NaCl, we observe a power density drop of only 35 % in the CRED system compared to scenarios where the feed solutions contain only NaCl as a salt. In contrast to the significant power density drops over 75 % observed in classic RED systems, the CRED system is much less affected by the presence of divalent ions, thanks to the elimination of membrane poisoning issues. Experimental results show that the membrane poisoning is alleviated by the periodic chamber solution reversal in the CRED system. To complete this study, we conduct power density studies on the CRED system using various real-world solutions. Similarly, the CRED system exhibits limited power density drop solely due to the uphill effect, a performance that is sustained even during 500 cycles of around 8 hours.

The limited impact of multivalent ions on the energy performance of the CRED system is indeed exciting and paves the way for further advancements toward its industrialization. To evaluate its potential, we've conducted a systematic techno-economic analysis based on results obtained with real-world solutions. In scenarios involving seawater and riverwater solutions, the estimated electricity production cost remains prohibitively high. However, in applications with very salty solutions, such as a Dead Sea desalination scenario, the estimated electricity production cost of 125 € becomes comparable to that of other renewable energies. This estimation is based on the novel sPEEK membrane with a cost estimated at 12 € in literature.

Osmotic energy manifests in various forms. Unlike salinity gradients, which are severely restricted by salt solubility, pH gradients present a broad spectrum, offering an important ion concentration difference in various scenarios. We extend our salinity gradient-based CRED system into a concentration-based framework. Specifically, we introduce a pH gradient-based system comprising two inexpensive MnO_2 electrodes and a non-selective membrane. This system is well-suited for integration into the Carbon Capture and Storage process, facilitating overall energy cost reduction. The dissolution of CO_2 induces a significant pH shift in the electrolyte. By combining electrolytes with CO_2 dissolution and air purging, we establish an osmotic energy source with a pH difference of up to 3.9. The pH gradient cell enables the conversion of osmotic energy into electricity. Due to the pseudo-capacitance of the MnO_2 electrodes, the pH gradient cell exhibits typical capacitive behavior under current limitations. Consequently, a similar capacitive current decay issue leads to relatively low power density performance.

To enhance power density performance further, we implement the same boosting strategy for the pH gradient cell. With a maximum pH difference of 3.9, the net power density increases from 2.86 $W.m^{-2}$ to 4.52 $W.m^{-2}$. It's remarkable to observe that the experimental power density exceeds the theoretical maximum prediction. The equivalent circuit-based modeling fails to explain this unexpected rise in power density. This surprising increase is attributed to the additional potential and resistance contributions linked to fractional coverage changes in MnO_2 electrodes. The adjusted model, incorporating two fitting parameters, closely matches experimental data, indicating a reversible redox reaction taking place within the MnO_2 electrodes.

5.2 Perspectives

In this section, we outline several intriguing plans for future studies. Specifically, we will delve deeper into studying the industrialization of the CRED system, focusing on two primary directions: effective surface area increase and implementation of CRED unit in series. Furthermore, we plan to integrate salinity gradient-based CRED systems as booster systems in pH gradient systems. Lastly, we aim to integrate pH gradient cells into ocean-based Carbon Capture and Storage (CCS) processes.

5.2.1 CRED system scale up

In this thesis work, we showcased an effective boosting strategy for CRED systems, resulting in outstanding power density performance that approaches its theoretical limit. Further investigations revealed that the CRED system is minimally affected by the mixing of multivalent ions in real-world solutions, thanks to the periodic water chamber reversal. This advancement represents a significant step toward its industrial applications. As indicated by the techno-economic analysis, there is immense potential to scale up CRED systems.

In future studies, it would be fascinating to pursue the scale-up of CRED systems in two distinct directions: first, by increasing the effective surface areas, and second, by implementing CRED units in series.

Surface area increase

One interesting direction is to enlarge the effective surface of the system. At present, we conduct lab-scale studies with CRED systems of 2-10 cm^2 as effective membrane surface. For further development towards industrialized CRED system, it is essential to design CRED systems of 0.1-1 m^2 for example.

In a larger CRED system, complex problems that are negligible at lab-scale are to be well studied. We will focus on the effect of the extension of the length - along the flow - and the width – perpendicular to the flow. The extension of the length highlights the problem of the filling time. Ideally, we expect a filling time as small as possible in order to realize an instantaneous potential establishment towards a square type signal. Otherwise, we need to spend much energy against viscous dissipation, which leads to power density loss problems. As the cell size increases significantly, the ion concentration profile across the surface becomes no longer homogeneous. This could impact directly the overall cell voltage and inner resistance. Extending the length also exhibits the non-ideal selectivity of the membrane requiring an adjustment of the relative volume flows of the saline solutions. Preliminary results showed that during a switch, the potential of the cell is mostly given by the Donnan potential and its spatial mean considering a plug flow.

Regarding the width, the matter differs. As the system displays an invariance regarding the flow, the main goal is to improve the transmission line along the current collectors that sets a limit width due to the lineic resistance of the collectors[281]. In addition, the structural design of CRED system, for example co-flow or counter-flow design, should be adapted and tested at larger scale.

Stacking capacitive units in series

Another interesting direction is to stack CRED units in series as already developed for faradaic RED systems. To increase the power recovered in the RED devices, a series of cationic and anionic membranes are stacked alternatively in a device with only two faradaic electrodes placed in the end, as illustrated in Fig 5.1. In such configuration, the overall cell voltage is calculated as:

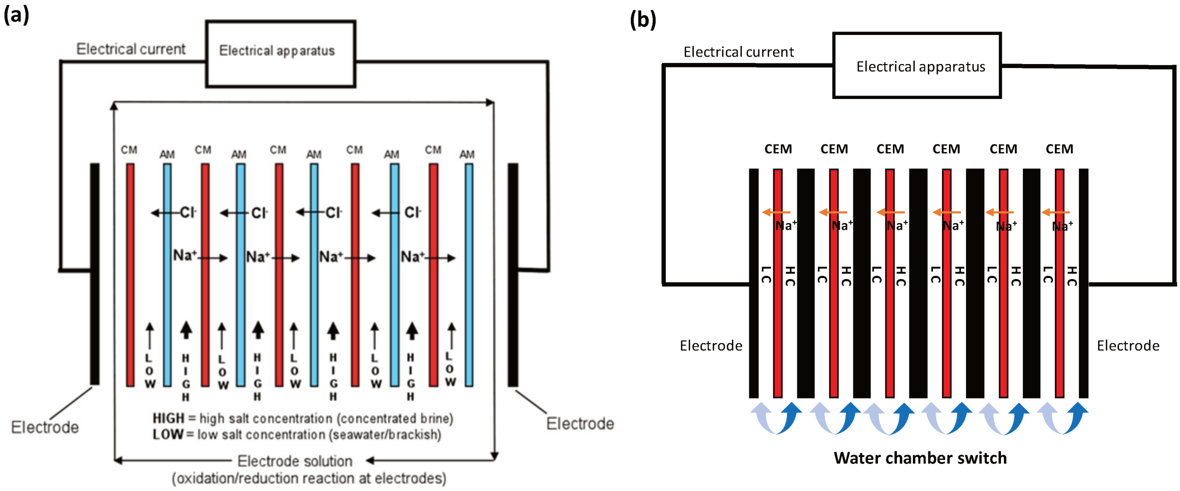

Fig. 5.1 Stacking configurations for faradiac RED systems (a) and CRED systems (b).

$$E_{OCV} = N.E_m + E_{elec} \tag{5.1}$$

where N refers to the number of ion-exchange membranes.

It is to notice that the implementation of CRED systems is slightly different. Capacitive concentration cells, on the other hand, require the use of two electrodes per membrane i.e. by cell (Fig 5.1). As the cost of the electrode and the clamping device is negligible compared to the cost of the membrane, this is not a major disadvantage of capacitive cells. In addition, due to the additional contribution of electrode potential, we replace one ion-exchange membrane used in RED system by a pair of capacitive electrodes. From an economic point of view, such design is cost-less as electrodes are much cheaper than membranes. In such configuration, the overall cell voltage is calculated as:

$$E_{OCV} = N.E_m + N.E_{elec} \tag{5.2}$$

where N refers to the number of ion-exchange membranes, which is equal to the number of pairs of capacitive electrodes.

As discussed in Chapter 3, in the repetition configurations of CRED units, electrode-related potential contributes to 50% of the overall cell voltage. While the mixing of multivalent ions significantly affects membrane potentials, it has minimal impact on electrode-related potentials. Consequently, CRED systems exhibit higher cell voltage in real-world solutions.

Considering the hydraulic aspect, It is recommended to connect in series and feed them all with solutions of the same high and low salinity to limit polarization problems. To reduce the overall system cost, carbon based capacitive felt and sPEEK membranes are recommended.

5.2.2 pH gradient cell optimization

The pH gradient cell expands the potential application scope for CRED systems. Therefore, it is intriguing to explore additional strategies to enhance energy performance or combining CRED system with other technologies. Furthermore, there are other possibilities for integrating such systems into CCS procedures that warrant further exploration.

Combining pH gradient cell with other technologies

It is interesting to combine other concentration gradients into the system to increase the overall power density output. A good example would be the work of Chen et al., where they combine the pH gradient with thermal gradient into a single system[244]. Further test of thermal or solar-assisted pH gradient cell could eventually present higher energy performance.

Currently, we achieve boosting through an external power supply. The use of an accessory power supply could present as a major disadvantage while we imagine the future industrial scale up. To replace the accessory power supply, we can imagine the use of a salinity gradient based cell connected in series with the pH gradient cell. Such coupling has already been reported for water electrolysis[282, 283]. To go further, integrating an inner salt-gradient-based RED system within the pH gradient system could present a more intelligent and feasible solution for the boosting strategy applications[284].

Ocean electrolyte based Carbon capture

In addition, another ocean related CCS process provides an interesting opportunity of pH gradient energy harvesting. While in most of the CCS technologies, a well engineered electrolyte is used to capture CO_2 gas from industrial wastes or directly from ambient air, the ocean already presents as a perfect CO_2 capturing reservoir. Dissolved carbon dioxide in the ocean occurs mainly in three inorganic forms: free aqueous carbon dioxide (CO_2(aq)), bicarbonate (HCO_3^-), and carbonate ion (CO_3^{2-}).

In typical seawater, approximately 2-3% of the CO_2 is dissolved gas in the form of carbonic acid (H_2CO_3), 1% is carbonate (CO_3^{2-}), and the remaining 96-97% is dissolved bicarbonate (HCO_3^-)[285].

$$CO_2 + H_2O \leftrightarrows H^+ + HCO_3^- \leftrightarrows 2H^+ + CO_3^{2-} \tag{5.3}$$

To regenerate the CO_2 accumulated in the ocean, it is important to well push the equilibrium to the left. A possible solution is to reduce the pH. Recently, researchers develop an acidification electrochemical cell to well control the ocean pH level below 6, so that the dissolved carbonates and bicarbonates re-equilibrate to dissolved gas form. On the one hand, the regenerated CO_2 could be further utilized in biofueling or carbon based product production, or injected underground for storage. On the other hand, the CO_2 extraction breaks the CO_2 equilibrium in the ocean. Additional CO_2 in ambient air will then be further trapped into the ocean reservoir. Through ocean based electrolyte, we capture indirectly the CO_2 from ambient air.

Indeed, while the acidified part is utilized for CO_2 extraction, there exists a basic part at the cell outlet. Prior to re-injecting the electrolytes into the ocean, it is essential to mix the acidic and basic parts to equilibrate the pH. At this juncture, we identify an ideal opportunity to integrate the pH gradient cell for energy harvesting. A meticulously engineered mixing process can convert osmotic energy into electricity, thereby undoubtedly reducing the overall energy cost of CCS technology.

In the preliminary tests realized for this process, we converted a electrodialysis cell into an ocean acidification cell with the use of two cation exchange membranes. It requires a typical power density of 100 W.m^{-2} to

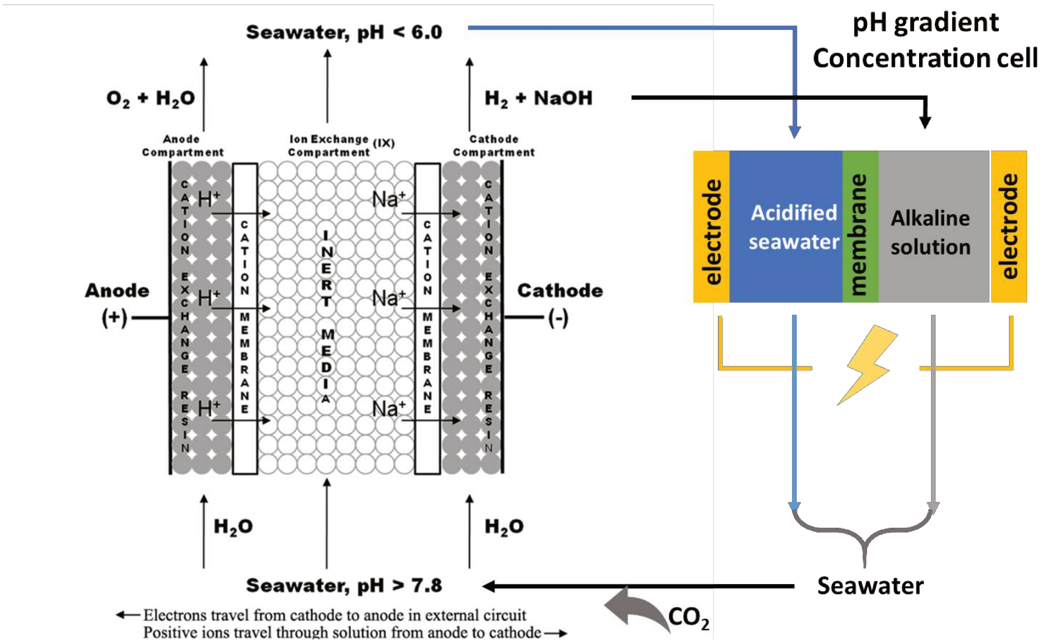

Fig. 5.2 Integration of pH gradient cell into an ocean based CCS technology. (Figures and captions reproduced from [285] with permission from American Chemical Society, copyright 2011.)

convert the seawater (pH 8.31) into the acidified part (pH 5.69) and basic part (pH 10.70) for CO_2 regeneration. Considering the maximum power density achieved in our experiments, it requires approximately 20 pH gradient cells to regenerate the consumed electrical power. In this situation, as carbonate/bicarbonates are of lower presence in the solution, we noticed a severe problem of proton transportation kinetics, which results in a significant power density drop[286].

In the future, we will try to integrate proton exchange medias, such as ion-exchange resins both into the ocean acidification cell and in pH gradient cell. It might reduce the overall cell resistance and promote the system efficiency. For further overall system efficiency amelioration, it is interesting to redesign the ocean acidification cell by using bipolar membranes. This eliminates the production of H_2 and O_2 gases in the system, which eventually leads to a power demand reduction[287].

References

[1] Nan Wu, Youcef Brahmi, and Annie Colin. Fluidics for energy harvesting: From nano to milli scales. *Lab on a Chip*, 23(5):1034–1065, 2023.

[2] Nan Wu, Timothée Derkenne, Corentin Tregouet, and Annie Colin. Comparison of miniaturized mechanical and osmotic energy harvesting systems. *Nano Energy*, 118:109004, 2023.

[3] Nan Wu, Youcef Brahmi, and Annie Colin. A Strategy for Power Density Amelioration of Capacitive Reverse Electrodialysis Systems with a Single Membrane. *Environmental Science & Technology*, 57(40):14973–14982, 2023.

[4] Nan Wu, Michael Levant, Youcef Brahmi, Corentin Tregouet, and Annie Colin. Mitigating the influence of multivalent ions on power density performance in a single-membrane capacitive reverse electrodialysis cell. *Scientific Reports*, 14(1):16984, 2024.

[5] Małgorzata, Wiatros-Motyka, Dave Jones, Hannah Broadbent, Nicolas Fulghum, Chelsea Bruce-Lockhart, Reynaldo Dizon, Phil MacDonald, Charles Moore, Alison Candlin, Uni Lee, Sam Hawkins, Matt Ewen, Bryony Worthington, Harry Benham, Muyi Yang, Aditya Lolla, Achmed Shahram Edianto, Paweł Czyżak, Chris Rosslowe, Richard Black, Marion Bachelet, Krzysztof Bolesta, and Lauri Myllyvirta. Global Electrcity Review 2023. Technical report, Ember, 2023.

[6] Hannah Ritchie, Pablo Rosado, and Max Roser. Energy production and consumption. *Our World in Data*, 2020. https://ourworldindata.org/energy-production-consumption.

[7] Katherine Calvin, Dipak Dasgupta, Gerhard Krinner, Aditi Mukherji, Peter W. Thorne, Christopher Trisos, José Romero, Paulina Aldunce, Ko Barrett, Gabriel Blanco, William W.L. Cheung, Sarah Connors, Fatima Denton, Aïda Diongue-Niang, David Dodman, Matthias Garschagen, Oliver Geden, Bronwyn Hayward, Christopher Jones, Frank Jotzo, Thelma Krug, Rodel Lasco, Yune-Yi Lee, Valérie Masson-Delmotte, Malte Meinshausen, Katja Mintenbeck, Abdalah Mokssit, Friederike E.L. Otto, Minal Pathak, Anna Pirani, Elvira Poloczanska, Hans-Otto Pörtner, Aromar Revi, Debra C. Roberts, Joyashree Roy, Alex C. Ruane, Jim Skea, Priyadarshi R. Shukla, Raphael Slade, Aimée Slangen, Youba Sokona, Anna A. Sörensson, Melinda Tignor, Detlef Van Vuuren, Yi-Ming Wei, Harald Winkler, Panmao Zhai, Zinta Zommers, Jean-Charles Hourcade, Francis X. Johnson, Shonali Pachauri, Nicholas P. Simpson, Chandni Singh, Adelle Thomas, Edmond Totin, Paola Arias, Mercedes Bustamante, Ismail Elgizouli, Gregory Flato, Mark Howden, Carlos Méndez-Vallejo, Joy Jacqueline Pereira, Ramón Pichs-Madruga, Steven K. Rose, Yamina Saheb, Roberto Sánchez Rodríguez, Diana Ürge-Vorsatz, Cunde Xiao, Noureddine Yassaa, Andrés Alegría, Kyle Armour, Birgit Bednar-Friedl, Kornelis Blok, Guéladio Cissé, Frank Dentener, Siri Eriksen, Erich Fischer, Gregory Garner, Céline Guivarch, Marjolijn Haasnoot, Gerrit Hansen, Mathias Hauser, Ed Hawkins, Tim Hermans, Robert Kopp, Noëmie Leprince-Ringuet, Jared Lewis, Debora Ley, Chloé Ludden, Leila Niamir, Zebedee Nicholls, Shreya Some, Sophie Szopa, Blair Trewin, Kaj-Ivar Van Der Wijst, Gundula Winter, Maximilian Witting, Arlene Birt, Meeyoung Ha, José Romero, Jinmi Kim, Erik F. Haites, Yonghun Jung, Robert Stavins, Arlene Birt, Meeyoung Ha, Dan Jezreel A. Orendain, Lance Ignon, Semin Park, Youngin Park, Andy Reisinger, Diego Cammaramo, Andreas Fischlin, Jan S. Fuglestvedt, Gerrit Hansen, Chloé Ludden, Valérie Masson-Delmotte, J.B. Robin Matthews, Katja Mintenbeck, Anna Pirani, Elvira Poloczanska, Noëmie Leprince-Ringuet, and Clotilde Péan. IPCC, 2023: Climate Change 2023: Synthesis Report. Contribution of Working Groups I, II and III to the Sixth Assessment Report of the Intergovernmental Panel on Climate Change [Core Writing Team, H. Lee and J. Romero (eds.)]. IPCC, Geneva, Switzerland. Technical report, Intergovernmental Panel on Climate Change (IPCC), July 2023.

[8] Steven Chu and Arun Majumdar. Opportunities and challenges for a sustainable energy future. *Nature*, 488(7411):294–303, August 2012.

[9] Menachem Elimelech and William A. Phillip. The Future of Seawater Desalination: Energy, Technology, and the Environment. *Science*, 333(6043):712–717, August 2011.

[10] Martin I. Hoffert, Ken Caldeira, Gregory Benford, David R. Criswell, Christopher Green, Howard Herzog, Atul K. Jain, Haroon S. Kheshgi, Klaus S. Lackner, John S. Lewis, H. Douglas Lightfoot, Wallace Manheimer, John C. Mankins, Michael E. Mauel, L. John Perkins, Michael E. Schlesinger, Tyler Volk, and Tom M. L. Wigley. Advanced Technology Paths to Global Climate Stability: Energy for a Greenhouse Planet. *Science*, 298(5595):981–987, November 2002.

[11] Ember global electricity review 2022. Technical report, Ember, 2022.

[12] Katelyn E. Mueller, Jeffrey T. Thomas, Jeremiah X. Johnson, Joseph F. DeCarolis, and Douglas F. Call. Life cycle assessment of salinity gradient energy recovery using reverse electrodialysis. *Journal of Industrial Ecology*, 25(5):1194–1206, 2021.

[13] Ngai Yin Yip, David A. Vermaas, Kitty Nijmeijer, and Menachem Elimelech. Thermodynamic, Energy Efficiency, and Power Density Analysis of Reverse Electrodialysis Power Generation with Natural Salinity Gradients. *Environmental Science & Technology*, 48(9):4925–4936, May 2014.

[14] Richard S. Norman. Water Salination: A Source of Energy. *Science*, 186(4161):350–352, October 1974.

[15] Jan W. Post, Hubertus V. M. Hamelers, and Cees J. N. Buisman. Energy Recovery from Controlled Mixing Salt and Fresh Water with a Reverse Electrodialysis System. *Environmental Science & Technology*, 42(15):5785–5790, August 2008.

[16] Zhijun Jia, Baoguo Wang, Shiqiang Song, and Yongsheng Fan. Blue energy: Current technologies for sustainable power generation from water salinity gradient. *Renewable and Sustainable Energy Reviews*, 31:91–100, March 2014.

[17] B. B. Sales, M. Saakes, J. W. Post, C. J. N. Buisman, P. M. Biesheuvel, and H. V. M. Hamelers. Direct Power Production from a Water Salinity Difference in a Membrane-Modified Supercapacitor Flow Cell. *Environmental Science & Technology*, 44(14):5661–5665, July 2010.

[18] Ngai Yin Yip, Doriano Brogioli, Hubertus V. M. Hamelers, and Kitty Nijmeijer. Salinity Gradients for Sustainable Energy: Primer, Progress, and Prospects. *Environmental Science & Technology*, 50(22):12072–12094, November 2016.

[19] Khaled Touati and Fernando Tadeo. Green energy generation by pressure retarded osmosis: State of the art and technical advancement—review. *International Journal of Green Energy*, 14(4):337–360, March 2017.

[20] S. Sarp, Z. Li, and J. Saththasivam. Pressure Retarded Osmosis (PRO): Past experiences, current developments, and future prospects. *Desalination*, 389:2–14, July 2016.

[21] Fernanda Helfer, Charles Lemckert, and Yuri G. Anissimov. Osmotic power with Pressure Retarded Osmosis: Theory, performance and trends – A review. *Journal of Membrane Science*, 453:337–358, March 2014.

[22] Yongxuan Shi, Mingming Zhang, Hanmin Zhang, Fenglin Yang, Chuyang Y. Tang, and Yingchao Dong. Recent development of pressure retarded osmosis membranes for water and energy sustainability: A critical review. *Water Research*, 189:116666, February 2021.

[23] Wen Yi Chia, Shir Reen Chia, Kuan Shiong Khoo, Kit Wayne Chew, and Pau Loke Show. Sustainable membrane technology for resource recovery from wastewater: Forward osmosis and pressure retarded osmosis. *Journal of Water Process Engineering*, 39:101758, February 2021.

[24] Qianhong She, Rong Wang, Anthony G. Fane, and Chuyang Y. Tang. Membrane fouling in osmotically driven membrane processes: A review. *Journal of Membrane Science*, 499:201–233, February 2016.

[25] Ralph Rolly Gonzales, Ahmed Abdel-Wahab, Samer Adham, Dong Suk Han, Sherub Phuntsho, Wafa Suwaileh, Nidal Hilal, and Ho Kyong Shon. Salinity gradient energy generation by pressure retarded osmosis: A review. *Desalination*, 500:114841, March 2021.

[26] Anthony P. Straub, Akshay Deshmukh, and Menachem Elimelech. Pressure-retarded osmosis for power generation from salinity gradients: Is it viable? *Energy & Environmental Science*, 9(1):31–48, January 2016.

[27] Shihong Lin, Anthony P. Straub, and Menachem Elimelech. Thermodynamic limits of extractable energy by pressure retarded osmosis. *Energy & Environmental Science*, 7(8):2706–2714, July 2014.

[28] Bruce E. Logan and Menachem Elimelech. Membrane-based processes for sustainable power generation using water. *Nature*, 488(7411):313–319, August 2012.

[29] Shichang Xu, Yanqiu Liu, Yue Wang, Mengke Zhang, Qinqin Xiao, and Yawei Duan. Influential analysis of concentration polarization on water flux and power density in PRO process: Modeling and experiments. *Desalination*, 412:39–48, June 2017.

[30] Shuaifei Zhao and Linda Zou. Relating solution physicochemical properties to internal concentration polarization in forward osmosis. *Journal of Membrane Science*, 379(1):459–467, September 2011.

[31] Qianhong She, Xue Jin, and Chuyang Y. Tang. Osmotic power production from salinity gradient resource by pressure retarded osmosis: Effects of operating conditions and reverse solute diffusion. *Journal of Membrane Science*, 401–402:262–273, May 2012.

[32] Jihye Kim, Myoung Jun Park, Minkyu Park, Ho Kyong Shon, Seung-Hyun Kim, and Joon Ha Kim. Influence of colloidal fouling on pressure retarded osmosis. *Desalination*, 389:207–214, July 2016.

[33] Ngai Yin Yip and Menachem Elimelech. Influence of Natural Organic Matter Fouling and Osmotic Backwash on Pressure Retarded Osmosis Energy Production from Natural Salinity Gradients. *Environmental Science & Technology*, 47(21):12607–12616, November 2013.

[34] Muhammad Tawalbeh, Amani Al-Othman, Noun Abdelwahab, Abdul Hai Alami, and Abdul Ghani Olabi. Recent developments in pressure retarded osmosis for desalination and power generation. *Renewable and Sustainable Energy Reviews*, 138:110492, March 2021.

[35] Sidney Loeb, Fred Van Hessen, and Dinah Shahaf. Production of energy from concentrated brines by pressure-retarded osmosis: II. Experimental results and projected energy costs. *Journal of Membrane Science*, 1:249–269, January 1976.

[36] Gurmukh D. Mehta. Further results on the performance of present-day osmotic membranes in various osmotic regions. *Journal of Membrane Science*, 10(1):3–19, March 1982.

[37] Andrea Achilli, Tzahi Y. Cath, and Amy E. Childress. Power generation with pressure retarded osmosis: An experimental and theoretical investigation. *Journal of Membrane Science*, 343(1):42–52, November 2009.

[38] N. Akther, A. Sodiq, A. Giwa, S. Daer, H. A. Arafat, and S. W. Hasan. Recent advancements in forward osmosis desalination: A review. *Chemical Engineering Journal*, 281:502–522, December 2015.

[39] Yu Chang Kim and Menachem Elimelech. Potential of osmotic power generation by pressure retarded osmosis using seawater as feed solution: Analysis and experiments. *Journal of Membrane Science*, 429:330–337, February 2013.

[40] Sophia L. Plata and Amy E. Childress. Limiting power density in pressure-retarded osmosis: Observation and implications. *Desalination*, 467:51–56, October 2019.

[41] Nahawand AlZainati, Haleema Saleem, Ali Altaee, Syed Javaid Zaidi, Marwa Mohsen, Alaa Hawari, and Graeme J. Millar. Pressure retarded osmosis: Advancement, challenges and potential. *Journal of Water Process Engineering*, 40:101950, April 2021.

[42] Ngai Yin Yip, Alberto Tiraferri, William A. Phillip, Jessica D. Schiffman, Laura A. Hoover, Yu Chang Kim, and Menachem Elimelech. Thin-Film Composite Pressure Retarded Osmosis Membranes for Sustainable Power Generation from Salinity Gradients. *Environmental Science & Technology*, 45(10):4360–4369, May 2011.

[43] Gang Han, Sui Zhang, Xue Li, and Tai-Shung Chung. High performance thin film composite pressure retarded osmosis (PRO) membranes for renewable salinity-gradient energy generation. *Journal of Membrane Science*, 440:108–121, August 2013.

[44] Xue Li, Sui Zhang, Fengjiang Fu, and Tai-Shung Chung. Deformation and reinforcement of thin-film composite (TFC) polyamide-imide (PAI) membranes for osmotic power generation. *Journal of Membrane Science*, 434:204–217, May 2013.

[45] Moon Son, Hosik Park, Lei Liu, Hyeongyu Choi, Joon Ha Kim, and Heechul Choi. Thin-film nanocomposite membrane with CNT positioning in support layer for energy harvesting from saline water. *Chemical Engineering Journal*, 284:68–77, January 2016.

[46] Jing Wei, Ye Li, Laurentia Setiawan, and Rong Wang. Influence of macromolecular additive on reinforced flat-sheet thin film composite pressure-retarded osmosis membranes. *Journal of Membrane Science*, 511:54–64, August 2016.

[47] Nhu-Ngoc Bui and Jeffrey R. McCutcheon. Nanofiber Supported Thin-Film Composite Membrane for Pressure-Retarded Osmosis. *Environmental Science & Technology*, 48(7):4129–4136, April 2014.

[48] Miao Tian, Rong Wang, Kunli Goh, Yuan Liao, and Anthony G. Fane. Synthesis and characterization of high-performance novel thin film nanocomposite PRO membranes with tiered nanofiber support reinforced by functionalized carbon nanotubes. *Journal of Membrane Science*, 486:151–160, July 2015.

[49] Sungil Lim, Myoung Jun Park, Sherub Phuntsho, Anne Mai-Prochnow, Anthony B. Murphy, Donghan Seo, and Hokyong Shon. Dual-layered nanocomposite membrane incorporating graphene oxide and halloysite nanotube for high osmotic power density and fouling resistance. *Journal of Membrane Science*, 564:382–393, October 2018.

[50] Ralph Rolly Gonzales, Myoung Jun Park, Tae-Hyun Bae, Yanqin Yang, Ahmed Abdel-Wahab, Sherub Phuntsho, and Ho Kyong Shon. Melamine-based covalent organic framework-incorporated thin film nanocomposite membrane for enhanced osmotic power generation. *Desalination*, 459:10–19, June 2019.

[51] Soon Jin Kwon, Kiho Park, Dal Yong Kim, Min Zhan, Seungkwan Hong, and Jung-Hyun Lee. High-performance and durable pressure retarded osmosis membranes fabricated using hydrophilized polyethylene separators. *Journal of Membrane Science*, 619:118796, February 2021.

[52] Ji Hoon Kim, Sun Ju Moon, Sang Hyun Park, Marcus Cook, Andrew G. Livingston, and Young Moo Lee. A robust thin film composite membrane incorporating thermally rearranged polymer support for organic solvent nanofiltration and pressure retarded osmosis. *Journal of Membrane Science*, 550:322–331, March 2018.

[53] Sun Ju Moon, Ji Hoon Kim, Jong Geun Seong, Won Hee Lee, Sang Hyun Park, Seong Hee Noh, Jae Hoon Kim, and Young Moo Lee. Thin film composite on fluorinated thermally rearranged polymer nanofibrous membrane achieves power density of 87 W m-2 in pressure retarded osmosis, improving economics of osmotic heat engine. *Journal of Membrane Science*, 607:118120, July 2020.

[54] Hyung Won Chung, Jaichander Swaminathan, Leonardo D. Banchik, and John H. Lienhard. Economic framework for net power density and levelized cost of electricity in pressure-retarded osmosis. *Desalination*, 448:13–20, December 2018.

[55] Yu Chang Kim and Menachem Elimelech. Adverse Impact of Feed Channel Spacers on the Performance of Pressure Retarded Osmosis. *Environmental Science & Technology*, 46(8):4673–4681, April 2012.

[56] Qianhong She, Dianxun Hou, Junxian Liu, Kang Hai Tan, and Chuyang Y. Tang. Effect of feed spacer induced membrane deformation on the performance of pressure retarded osmosis (PRO): Implications for PRO process operation. *Journal of Membrane Science*, 445:170–182, October 2013.

[57] Edvard Sivertsen, Torleif Holt, Willy Thelin, and Geir Brekke. Pressure retarded osmosis efficiency for different hollow fibre membrane module flow configurations. *Desalination*, 312:107–123, March 2013.

[58] Shuren Chou, Rong Wang, Lei Shi, Qianhong She, Chuyang Tang, and Anthony Gordon Fane. Thin-film composite hollow fiber membranes for pressure retarded osmosis (PRO) process with high power density. *Journal of Membrane Science*, 389:25–33, February 2012.

[59] Shuren Chou, Rong Wang, and Anthony G. Fane. Robust and High performance hollow fiber membranes for energy harvesting from salinity gradients by pressure retarded osmosis. *Journal of Membrane Science*, 448:44–54, December 2013.

[60] Pravin G. Ingole, Wook Choi, Kee-Hong Kim, Hang-Dae Jo, Won-Kil Choi, Jong-Soo Park, and Hyung-Keun Lee. Preparation, characterization and performance evaluations of thin film composite hollow fiber membrane for energy generation. *Desalination*, 345:136–145, July 2014.

[61] Pravin G. Ingole, Wook Choi, Kee Hong Kim, Chul Ho Park, Won Kil Choi, and Hyung Keun Lee. Synthesis, characterization and surface modification of PES hollow fiber membrane support with polydopamine and thin film composite for energy generation. *Chemical Engineering Journal*, 243:137–146, May 2014.

[62] Feng-Jiang Fu, Shi-Peng Sun, Sui Zhang, and Tai-Shung Chung. Pressure retarded osmosis dual-layer hollow fiber membranes developed by co-casting method and ammonium persulfate (APS) treatment. *Journal of Membrane Science*, 469:488–498, November 2014.

[63] Xue Li, Tao Cai, and Tai-Shung Chung. Anti-Fouling Behavior of Hyperbranched Polyglycerol-Grafted Poly(ether sulfone) Hollow Fiber Membranes for Osmotic Power Generation. *Environmental Science & Technology*, 48(16):9898–9907, August 2014.

[64] Pravin G. Ingole, Kee Hong Kim, Chul Ho Park, Won Kil Choi, and Hyung Keun Lee. Preparation, modification and characterization of polymeric hollow fiber membranes for pressure-retarded osmosis. *RSC Advances*, 4(93):51430–51439, October 2014.

[65] Yu Zhang, Jia Le Li, Tao Cai, Zhen Lei Cheng, Xue Li, and Tai-Shung Chung. Sulfonated hyperbranched polyglycerol grafted membranes with antifouling properties for sustainable osmotic power generation using municipal wastewater. *Journal of Membrane Science*, 563:521–530, October 2018.

[66] Die Ling Zhao, Subhabrata Das, and Tai-Shung Chung. Carbon Quantum Dots Grafted Antifouling Membranes for Osmotic Power Generation via Pressure-Retarded Osmosis Process. *Environmental Science & Technology*, 51(23):14016–14023, December 2017.

[67] Wenxiao Gai, Die Ling Zhao, and Tai-Shung Chung. Novel thin film composite hollow fiber membranes incorporated with carbon quantum dots for osmotic power generation. *Journal of Membrane Science*, 551:94–102, April 2018.

[68] Myoung Jun Park, Sungil Lim, Ralph Rolly Gonzales, Sherub Phuntsho, Dong Suk Han, Ahmed Abdel-Wahab, Samer Adham, and Ho Kyong Shon. Thin-film composite hollow fiber membranes incorporated with graphene oxide in polyethersulfone support layers for enhanced osmotic power density. *Desalination*, 464:63–75, August 2019.

[69] Dieling Zhao, Guanglei Qiu, Xue Li, Chunfeng Wan, Kangjia Lu, and Tai-Shung Chung. Zwitterions coated hollow fiber membranes with enhanced antifouling properties for osmotic power generation from municipal wastewater. *Water Research*, 104:389–396, November 2016.

[70] Ngoc Lieu Le, N. M. S. Bettahalli, S. P. Nunes, and Tai-Shung Chung. Outer-selective thin film composite (TFC) hollow fiber membranes for osmotic power generation. *Journal of Membrane Science*, 505:157–166, May 2016.

[71] Gang Han, Peng Wang, and Tai-Shung Chung. Highly Robust Thin-Film Composite Pressure Retarded Osmosis (PRO) Hollow Fiber Membranes with High Power Densities for Renewable Salinity-Gradient Energy Generation. *Environmental Science & Technology*, 47(14):8070–8077, July 2013.

[72] Sui Zhang, Fengjiang Fu, and Tai-Shung Chung. Substrate modifications and alcohol treatment on thin film composite membranes for osmotic power. *Chemical Engineering Science*, 87:40–50, January 2013.

[73] Xue Li, Tai-Shung Chung, and Tai-Shung Chung. Effects of free volume in thin-film composite membranes on osmotic power generation. *AIChE Journal*, 59(12):4749–4761, 2013.

[74] Xiaoxiao Song, Zhaoyang Liu, and Darren Delai Sun. Energy recovery from concentrated seawater brine by thin-film nanofiber composite pressure retarded osmosis membranes with high power density. *Energy & Environmental Science*, 6(4):1199, 2013.

[75] Yue Cui, Xiang-Yang Liu, and Tai-Shung Chung. Enhanced osmotic energy generation from salinity gradients by modifying thin film composite membranes. *Chemical Engineering Journal*, 242:195–203, April 2014.

[76] Anthony P. Straub, Ngai Yin Yip, and Menachem Elimelech. Raising the Bar: Increased Hydraulic Pressure Allows Unprecedented High Power Densities in Pressure-Retarded Osmosis. *Environmental Science & Technology Letters*, 1(1):55–59, January 2014.

[77] Ye Li, Rong Wang, Saren Qi, and Chuyang Tang. Structural stability and mass transfer properties of pressure retarded osmosis (PRO) membrane under high operating pressures. *Journal of Membrane Science*, 488:143–153, August 2015.

[78] Qianhong She, Jing Wei, Ning Ma, Victor Sim, Anthony G. Fane, Rong Wang, and Chuyang Y. Tang. Fabrication and characterization of fabric-reinforced pressure retarded osmosis membranes for osmotic power harvesting. *Journal of Membrane Science*, 504:75–88, April 2016.

[79] Jaime A. Idarraga-Mora, David A. Ladner, and Scott M. Husson. Thin-film composite membranes on polyester woven mesh with variable opening size for pressure-retarded osmosis. *Journal of Membrane Science*, 549:251–259, March 2018.

[80] Yuchen Sun, Liang Cheng, Takuji Shintani, Yasuhiro Tanaka, Tomoki Takahashi, Takuya Itai, Shengyao Wang, Lifeng Fang, and Hideto Matsuyama. Development of High-Flux and Robust Reinforced Aliphatic Polyketone Thin-Film Composite Membranes for Osmotic Power Generation: Role of Reinforcing Materials. *Industrial & Engineering Chemistry Research*, 57(40):13528–13538, October 2018.

[81] Xin Tong, Xin Wang, Su Liu, Haiping Gao, Chunyan Xu, John Crittenden, and Yongsheng Chen. A freestanding graphene oxide membrane for efficiently harvesting salinity gradient power. *Carbon*, 138:410–418, November 2018.

[82] Sun Ju Moon, Sang Min Lee, Ji Hoon Kim, Sang Hyun Park, Ho Hyun Wang, Jae Hoon Kim, and Young Moo Lee. A highly robust and water permeable thin film composite membranes for pressure retarded osmosis generating 26 W·m-2 at 21 bar. *Desalination*, 483:114409, June 2020.

[83] Feng-Jiang Fu, Sui Zhang, Shi-Peng Sun, Kai-Yu Wang, and Tai-Shung Chung. POSS-containing delamination-free dual-layer hollow fiber membranes for forward osmosis and osmotic power generation. *Journal of Membrane Science*, 443:144–155, September 2013.

[84] Shi-Peng Sun and Tai-Shung Chung. Outer-Selective Pressure-Retarded Osmosis Hollow Fiber Membranes from Vacuum-Assisted Interfacial Polymerization for Osmotic Power Generation. *Environmental Science & Technology*, 47(22):13167–13174, November 2013.

[85] Sui Zhang, Panu Sukitpaneenit, and Tai-Shung Chung. Design of robust hollow fiber membranes with high power density for osmotic energy production. *Chemical Engineering Journal*, 241:457–465, April 2014.

[86] Gang Han and Tai-Shung Chung. Robust and high performance pressure retarded osmosis hollow fiber membranes for osmotic power generation. *AIChE Journal*, 60(3):1107–1119, 2014.

[87] Gang Han, Qingchun Ge, and Tai-Shung Chung. Conceptual demonstration of novel closed-loop pressure retarded osmosis process for sustainable osmotic energy generation. *Applied Energy*, 132:383–393, November 2014.

[88] Si Cong Chen, Chun Feng Wan, and Tai-Shung Chung. Enhanced fouling by inorganic and organic foulants on pressure retarded osmosis (PRO) hollow fiber membranes under high pressures. *Journal of Membrane Science*, 479:190–203, April 2015.

[89] Feng-Jiang Fu, Sui Zhang, and Tai-Shung Chung. Sandwich-structured hollow fiber membranes for osmotic power generation. *Desalination*, 376:73–81, November 2015.

[90] Zhen Lei Cheng, Xue Li, Ying Da Liu, and Tai-Shung Chung. Robust outer-selective thin-film composite polyethersulfone hollow fiber membranes with low reverse salt flux for renewable salinity-gradient energy generation. *Journal of Membrane Science*, 506:119–129, May 2016.

[91] Wenxiao Gai, Xue Li, Jun Ying Xiong, Chun Feng Wan, and Tai-Shung Chung. Evolution of micro-deformation in inner-selective thin film composite hollow fiber membranes and its implications for osmotic power generation. *Journal of Membrane Science*, 516:104–112, October 2016.

[92] Lizhi Zhang, Qianhong She, Rong Wang, Sunee Wongchitphimon, Yunfeng Chen, and Anthony G. Fane. Unique roles of aminosilane in developing anti-fouling thin film composite (TFC) membranes for pressure retarded osmosis (PRO). *Desalination*, 389:119–128, July 2016.

[93] Yunfeng Chen, Laurentia Setiawan, Shuren Chou, Xiao Hu, and Rong Wang. Identification of safe and stable operation conditions for pressure retarded osmosis with high performance hollow fiber membrane. *Journal of Membrane Science*, 503:90–100, April 2016.

[94] Ngoc Lieu Le, Mathias Quilitzsch, Hong Cheng, Pei-Ying Hong, Mathias Ulbricht, Suzana P. Nunes, and Tai-Shung Chung. Hollow fiber membrane lumen modified by polyzwitterionic grafting. *Journal of Membrane Science*, 522:1–11, January 2017.

[95] Zhen Lei Cheng, Xue Li, Yingnan Feng, Chun Feng Wan, and Tai-Shung Chung. Tuning water content in polymer dopes to boost the performance of outer-selective thin-film composite (TFC) hollow fiber membranes for osmotic power generation. *Journal of Membrane Science*, 524:97–107, February 2017.

[96] Chun Feng Wan, Bofan Li, Tianshi Yang, and Tai-Shung Chung. Design and fabrication of inner-selective thin-film composite (TFC) hollow fiber modules for pressure retarded osmosis (PRO). *Separation and Purification Technology*, 172:32–42, January 2017.

[97] Gang Han, Zhen Lei Cheng, and Tai-Shung Chung. Thin-film composite (TFC) hollow fiber membrane with double-polyamide active layers for internal concentration polarization and fouling mitigation in osmotic processes. *Journal of Membrane Science*, 523:497–504, February 2017.

[98] Chun Feng Wan, Tianshi Yang, Wenxiao Gai, Yu De Lee, and Tai-Shung Chung. Thin-film composite hollow fiber membrane with inorganic salt additives for high mechanical strength and high power density for pressure-retarded osmosis. *Journal of Membrane Science*, 555:388–397, June 2018.

[99] Yunfeng Chen, Chun Heng Loh, Lizhi Zhang, Laurentia Setiawan, Qianhong She, Wangxi Fang, Xiao Hu, and Rong Wang. Module scale-up and performance evaluation of thin film composite hollow fiber membranes for pressure retarded osmosis. *Journal of Membrane Science*, 548:398–407, February 2018.

[100] Ye Li, Shanshan Zhao, Laurentia Setiawan, Lizhi Zhang, and Rong Wang. Integral hollow fiber membrane with chemical cross-linking for pressure retarded osmosis operated in the orientation of active layer facing feed solution. *Journal of Membrane Science*, 550:163–172, March 2018.

[101] Young Hoon Cho, Sang Deuk Kim, Jeong F. Kim, Hyeon-gyu Choi, Youngmi Kim, Seung-Eun Nam, You-In Park, and Hosik Park. Tailoring the porous structure of hollow fiber membranes for osmotic power generation applications via thermally assisted nonsolvent induced phase separation. *Journal of Membrane Science*, 579:329–341, June 2019.

[102] Ralph Rolly Gonzales, Yanqin Yang, Myoung Jun Park, Tae-Hyun Bae, Ahmed Abdel-Wahab, Sherub Phuntsho, and Ho Kyong Shon. Enhanced water permeability and osmotic power generation with sulfonate-functionalized porous polymer-incorporated thin film nanocomposite membranes. *Desalination*, 496:114756, December 2020.

[103] Karen Gerstandt, K. V. Peinemann, Stein Erik Skilhagen, Thor Thorsen, and Torleif Holt. Membrane processes in energy supply for an osmotic power plant. *Desalination*, 224(1):64–70, April 2008.

[104] Samar AL Mashrafi, Nancy Diaz-Elsayed, Joshua Benjamin, Mauricio E. Arias, and Qiong Zhang. An environmental and economic sustainability assessment of a pressure retarded osmosis system. *Desalination*, 537:115869, September 2022.

[105] Qais A. Khasawneh, Bourhan Tashtoush, Anas Nawafleh, and Bayan Kan'an. Techno-Economic Feasibility Study of a Hypersaline Pressure-Retarded Osmosis Power Plants: Dead Sea–Red Sea Conveyor. *Energies*, 11(11):3118, November 2018.

[106] The Norwegian American. Crown Princess of Norway to open the world's first osmotic power plant. https://www.norwegianamerican.com/crown-princess-of-norway-to-open-the-worlds-first-osmotic-power-plant/, October 2009.

[107] Chulmin Lee, Sung Ho Chae, Eunmok Yang, Suhun Kim, Joon Ha Kim, and In S. Kim. A comprehensive review of the feasibility of pressure retarded osmosis: Recent technological advances and industrial efforts towards commercialization. *Desalination*, 491:114501, October 2020.

[108] REUK. Osmotic Power Plant Opened | REUK.co.uk, 2009.

[109] Masaru Kurihara and Hiromu Takeuchi. SWRO-PRO System in "Mega-ton Water System" for Energy Reduction and Low Environmental Impact. *Water*, 10(1):48, January 2018.

[110] R. E. Pattle. Production of Electric Power by mixing Fresh and Salt Water in the Hydroelectric Pile. *Nature*, 174(4431):660–660, October 1954.

[111] R. E. Lacey. Energy by reverse electrodialysis. *Ocean Engineering*, 7(1):1–47, January 1980.

[112] AH Galama, JW Post, HVM Hamelers, VV Nikonenko, and PM Biesheuvel. On the origin of the membrane potential arising across densely charged ion exchange membranes: How well does the teorell-meyer-sievers theory work? *Journal of Membrane Science and Research*, 2(3):128–140, 2016.

[113] Torsten Teorell. An attempt to formulate a quantitative theory of membrane permeability. *Proceedings of the Society for Experimental Biology and Medicine*, 33(2):282–285, 1935.

[114] FA Morrison Jr and JF Osterle. Electrokinetic energy conversion in ultrafine capillaries. *The Journal of Chemical Physics*, 43(6):2111–2115, 1965.

[115] Alessandro Siria, Philippe Poncharal, Anne-Laure Biance, Rémy Fulcrand, Xavier Blase, Stephen T. Purcell, and Lydéric Bocquet. Giant osmotic energy conversion measured in a single transmembrane boron nitride nanotube. *Nature*, 494(7438):455–458, February 2013.

[116] Zhepeng Tang, Qiu-An Huang, Yan-Jie Wang, Fangzhou Zhang, Weiheng Li, Aijun Li, Lei Zhang, and Jiujun Zhang. Recent progress in the use of electrochemical impedance spectroscopy for the measurement, monitoring, diagnosis and optimization of proton exchange membrane fuel cell performance. *Journal of Power Sources*, 468:228361, 2020.

[117] Youcef Brahmi and Annie Colin. New membrane and electrode assembly concept to improve salinity energy harvesting. *Energy Conversion and Management*, 254:115297, February 2022.

[118] J. Veerman, M. Saakes, S. J. Metz, and G. J. Harmsen. Reverse electrodialysis: evaluation of suitable electrode systems. *Journal of Applied Electrochemistry*, 40(8):1461–1474, August 2010.

[119] Joseph Jagur-Grodzinski and Riry Kramer. Novel process for direct conversion of free energy of mixing into electric power. *Industrial & Engineering Chemistry Process Design and Development*, 25(2):443–449, 1986.

[120] Joost Veerman, Michel Saakes, Sybrand J. Metz, and G. Jan Harmsen. Electrical Power from Sea and River Water by Reverse Electrodialysis: A First Step from the Laboratory to a Real Power Plant. *Environmental Science & Technology*, 44:9207–9212, 2010.

[121] Alexandros Daniilidis, David A. Vermaas, Rien Herber, and Kitty Nijmeijer. Experimentally obtainable energy from mixing river water, seawater or brines with reverse electrodialysis. *Renewable Energy*, 64:123–131, April 2014.

[122] J. Veerman, R. M. de Jong, M. Saakes, S. J. Metz, and G. J. Harmsen. Reverse electrodialysis: Comparison of six commercial membrane pairs on the thermodynamic efficiency and power density. *Journal of Membrane Science*, 343(1):7–15, November 2009.

[123] J. Veerman and D.A. Vermaas. Reverse electrodialysis. In *Sustainable Energy from Salinity Gradients*, pages 77–133. Elsevier, 2016.

[124] David A. Vermaas, Michel Saakes, and Kitty Nijmeijer. Doubled Power Density from Salinity Gradients at Reduced Intermembrane Distance. *Environmental Science & Technology*, 45(16):7089–7095, August 2011.

[125] M. Turek, B. Bandura, and P. Dydo. Power production from coal-mine brine utilizing reversed electrodialysis. *Desalination*, 221(1):462–466, March 2008.

[126] R. Audinos. Electrodialyse inverse. Etude de l'energie electrique obtenue a partir de deux solutions de salinites differentes. *Journal of Power Sources*, 10(3):203–217, 1983.

[127] M. Y. Kariduraganavar, R. K. Nagarale, A. A. Kittur, and S. S. Kulkarni. Ion-exchange membranes: preparative methods for electrodialysis and fuel cell applications. *Desalination*, 197(1):225–246, October 2006.

[128] N. D. Pismenskaya, E. V. Pokhidnia, G. Pourcelly, and V. V. Nikonenko. Can the electrochemical performance of heterogeneous ion-exchange membranes be better than that of homogeneous membranes? *Journal of Membrane Science*, 566:54–68, 2018.

[129] P Dlugolecki, K Nymeijer, S Metz, and M Wessling. Current status of ion exchange membranes for power generation from salinity gradients. *Journal of Membrane Science*, 319(1-2):214–222, July 2008.

[130] J. Moreno, V. Díez, M. Saakes, and K. Nijmeijer. Mitigation of the effects of multivalent ion transport in reverse electrodialysis. *Journal of Membrane Science*, 550:155–162, 2018.

[131] Soroush Mehdizadeh, Yuriko Kakihana, Takakazu Abo, Qingchun Yuan, and Mitsuru Higa. Power Generation Performance of a Pilot-Scale Reverse Electrodialysis Using Monovalent Selective Ion-Exchange Membranes. *Membranes*, 11(1):27, January 2021.

[132] M. Tedesco, E. Brauns, A. Cipollina, G. Micale, P. Modica, G. Russo, and J. Helsen. Reverse electrodialysis with saline waters and concentrated brines: A laboratory investigation towards technology scale-up. *Journal of Membrane Science*, 492:9–20, October 2015.

[133] Jin Gi Hong and Yongsheng Chen. Nanocomposite reverse electrodialysis (RED) ion-exchange membranes for salinity gradient power generation. *Journal of Membrane Science*, 460:139–147, 2014.

[134] David A. Vermaas, Joost Veerman, Michel Saakes, and Kitty Nijmeijer. Influence of multivalent ions on renewable energy generation in reverse electrodialysis. *Energy & Environmental Science*, 7(4):1434–1445, March 2014.

[135] Ahmet H. Avci, Diego A. Messana, Sergio Santoro, Ramato Ashu Tufa, Efrem Curcio, Gianluca Di Profio, and Enrica Fontananova. Energy Harvesting from Brines by Reverse Electrodialysis Using Nafion Membranes. *Membranes*, 10(8):168, August 2020.

[136] Enver Güler, Rianne Elizen, David A. Vermaas, Michel Saakes, and Kitty Nijmeijer. Performance-determining membrane properties in reverse electrodialysis. *Journal of Membrane Science*, 446:266–276, November 2013.

[137] T. Rijnaarts, J. Moreno, M. Saakes, W. M. de Vos, and K. Nijmeijer. Role of anion exchange membrane fouling in reverse electrodialysis using natural feed waters. *Colloids and Surfaces A: Physicochemical and Engineering Aspects*, 560:198–204, January 2019.

[138] Hanki Kim, SeungCheol Yang, Jiyeon Choi, Jong-Oh Kim, and Namjo Jeong. Optimization of the number of cell pairs to design efficient reverse electrodialysis stack. *Desalination*, 497:114676, January 2021.

[139] David A. Vermaas, Michel Saakes, and Kitty Nijmeijer. Enhanced mixing in the diffusive boundary layer for energy generation in reverse electrodialysis. *Journal of Membrane Science*, 453:312–319, March 2014.

[140] J. Veerman, M. Saakes, S.J. Metz, and G.J. Harmsen. Reverse electrodialysis: Performance of a stack with 50 cells on the mixing of sea and river water. *Journal of Membrane Science*, 327(1-2):136–144, February 2009.

[141] David A. Vermaas, Michel Saakes, and Kitty Nijmeijer. Power generation using profiled membranes in reverse electrodialysis. *Journal of Membrane Science*, 385–386:234–242, December 2011.

[142] Enver Guler, Yali Zhang, Michel Saakes, and Kitty Nijmeijer. Tailor-Made Anion-Exchange Membranes for Salinity Gradient Power Generation Using Reverse Electrodialysis. *ChemSusChem*, 5(11):2262–2270, 2012.

[143] Michele Tedesco, Claudio Scalici, Davide Vaccari, Andrea Cipollina, Alessandro Tamburini, and Giorgio Micale. Performance of the first reverse electrodialysis pilot plant for power production from saline waters and concentrated brines. *Journal of Membrane Science*, 500:33–45, February 2016.

[144] Ahmet H. Avci, Ramato A. Tufa, Enrica Fontananova, Gianluca Di Profio, and Efrem Curcio. Reverse Electrodialysis for energy production from natural river water and seawater. *Energy*, 165:512–521, December 2018.

[145] Jun Gao, Xueli Liu, Yanan Jiang, Liping Ding, Lei Jiang, and Wei Guo. Understanding the Giant Gap between Single-Pore- and Membrane-Based Nanofluidic Osmotic Power Generators. *Small*, 15(11):1804279, 2019.

[146] Xue Liu, Meng He, Dario Calvani, Haoyuan Qi, Karthick B. Sai Sankar Gupta, Huub J. M. de Groot, G. J. Agur Sevink, Francesco Buda, Ute Kaiser, and Grégory F. Schneider. Power generation by reverse electrodialysis in a single-layer nanoporous membrane made from core–rim polycyclic aromatic hydrocarbons. *Nature Nanotechnology*, 15(4):307–312, April 2020.

[147] Chao Li, Liping Wen, Xin Sui, Yiren Cheng, Longcheng Gao, and Lei Jiang. Large-scale, robust mushroom-shaped nanochannel array membrane for ultrahigh osmotic energy conversion. *Science Advances*, 7(21):eabg2183, 2021.

[148] Jan W. Post, Hubertus V. M. Hamelers, and Cees J. N. Buisman. Influence of multivalent ions on power production from mixing salt and fresh water with a reverse electrodialysis system. *Journal of Membrane Science*, 330(1):65–72, March 2009.

[149] Tuğçe Zeynep Kaya, Esra Altıok, Enver Güler, and Nalan Kabay. Effect of Co-Existing Ions on Salinity Gradient Power Generation by Reverse Electrodialysis Using Different Ion Exchange Membrane Pairs. *Membranes*, 12(12):1240, December 2022.

[150] Zhihao Wang, Jianbo Li, Hao Wang, Mengqi Li, Lingjie Wang, and Xiangqiang Kong. The Effect of Trace Ions on the Performance of Reverse Electrodialysis Using Brine/Seawater as Working Pairs. *Frontiers in Energy Research*, 10, August 2022.

[151] Diego Pintossi, Catarina Simões, Michel Saakes, Zandrie Borneman, and Kitty Nijmeijer. Predicting reverse electrodialysis performance in the presence of divalent ions for renewable energy generation. *Energy Conversion and Management*, 243:114369, 2021.

[152] Dongxu Jin and Yunshu Jin. Sustainable power generation from salinity gradients by reverse electrodialysis: Influence of divalent ions. *Chemical Engineering Research and Design*, 198:69–80, October 2023.

[153] A. A. Moya. Uphill transport in improved reverse electrodialysis by removal of divalent cations in the dilute solution: A Nernst-Planck based study. *Journal of Membrane Science*, 598:117784, March 2020.

[154] E. Fontananova, D. Messana, R. A. Tufa, I. Nicotera, V. Kosma, E. Curcio, W. van Baak, E. Drioli, and G. Di Profio. Effect of solution concentration and composition on the electrochemical properties of ion exchange membranes for energy conversion. *Journal of Power Sources*, 340:282–293, February 2017.

[155] Yoontaek Oh, Yejin Jeong, Soo-Jin Han, Chan-Soo Kim, Hanki Kim, Ji-Hyung Han, Kyo-Sik Hwang, Namjo Jeong, Jin-Soo Park, and Soryong Chae. Effects of Divalent Cations on Electrical Membrane Resistance in Reverse Electrodialysis for Salinity Power Generation. *Industrial & Engineering Chemistry Research*, 57(46):15803–15810, November 2018.

[156] Lucía Gómez-Coma, Víctor M. Ortiz-Martínez, Javier Carmona, Laura Palacio, Pedro Prádanos, Marcos Fallanza, Alfredo Ortiz, Raquel Ibañez, and Inmaculada Ortiz. Modeling the influence of divalent ions on membrane resistance and electric power in reverse electrodialysis. *Journal of Membrane Science*, 592:117385, December 2019.

[157] Joost Veerman, Lucía Gómez-Coma, Alfredo Ortiz, and Inmaculada Ortiz. Resistance of Ion Exchange Membranes in Aqueous Mixtures of Monovalent and Divalent Ions and the Effect on Reverse Electrodialysis. *Membranes*, 13(3):322, March 2023.

[158] Ramato Ashu Tufa, Efrem Curcio, Willem van Baak, Joost Veerman, Simon Grasman, Enrica Fontananova, and Gianluca Di Profio. Potential of brackish water and brine for energy generation by salinity gradient power-reverse electrodialysis (SGP-RE). *RSC Advances*, 4(80):42617–42623, September 2014.

[159] Michele Tedesco, Andrea Cipollina, Alessandro Tamburini, and Giorgio Micale. Towards 1kW power production in a reverse electrodialysis pilot plant with saline waters and concentrated brines. *Journal of Membrane Science*, 522:226–236, January 2017.

[160] Catarina Simões, Bárbara Vital, Tom Sleutels, Michel Saakes, and Wim Brilman. Scaled-up multistage reverse electrodialysis pilot study with natural waters. *Chemical Engineering Journal*, 450:138412, 2022.

[161] Timon Rijnaarts, Elisa Huerta, Willem van Baak, and Kitty Nijmeijer. Effect of Divalent Cations on RED Performance and Cation Exchange Membrane Selection to Enhance Power Densities. *Environmental Science & Technology*, 51(21):13028–13035, November 2017.

[162] Abreham Tesfaye Besha, Misgina Tilahun Tsehaye, David Aili, Wenjuan Zhang, and Ramato Ashu Tufa. Design of Monovalent Ion Selective Membranes for Reducing the Impacts of Multivalent Ions in Reverse Electrodialysis. *Membranes*, 10(1):7, January 2020.

[163] Haiping Gao, Bopeng Zhang, Xin Tong, and Yongsheng Chen. Monovalent-anion selective and antifouling polyelectrolytes multilayer anion exchange membrane for reverse electrodialysis. *Journal of Membrane Science*, 567:68–75, December 2018.

[164] Enver Güler, Willem van Baak, Michel Saakes, and Kitty Nijmeijer. Monovalent-ion-selective membranes for reverse electrodialysis. *Journal of Membrane Science*, 455:254–270, April 2014.

[165] Wending Zhu, Xu Zhang, Zhiqi Bao, Xianglu Zhang, Yang Zhang, Yuting Yuan, Chenxiao Jiang, Qiuhua Li, Guanping Jin, and Xiaozhao Han. Sustainable energy recovery from salt-lake brines through a novel selective reverse electrodialysis process. *Chemical Engineering Science*, 292:120006, June 2024.

[166] Joost Veerman. Concepts and Misconceptions Concerning the Influence of Divalent Ions on the Performance of Reverse Electrodialysis Using Natural Waters. *Membranes*, 13(1):69, January 2023.

[167] R. S. Kingsbury, F. Liu, S. Zhu, C. Boggs, M. D. Armstrong, D. F. Call, and O. Coronell. Impact of natural organic matter and inorganic solutes on energy recovery from five real salinity gradients using reverse electrodialysis. *Journal of Membrane Science*, 541:621–632, November 2017.

[168] Alessandro Cosenza, Giovanni Campisi, Francesco Giacalone, Serena Randazzo, Andrea Cipollina, Alessandro Tamburini, and Giorgio Micale. Power Production from Produced Waters via Reverse Electrodialysis: A Preliminary Assessment. *Energies*, 15(11):4177, January 2022.

[169] David A. Vermaas, Damnearn Kunteng, Michel Saakes, and Kitty Nijmeijer. Fouling in reverse electrodialysis under natural conditions. *Water Research*, 47(3):1289–1298, March 2013.

[170] Bárbara Vital, Eduardo V. Torres, Tom Sleutels, M. Cristina Gagliano, Michel Saakes, and Hubertus V. M. Hamelers. Fouling fractionation in reverse electrodialysis with natural feed waters demonstrates dual media rapid filtration as an effective pre-treatment for fresh water. *Desalination*, 518:115277, December 2021.

[171] Zhaolong He, Xueli Gao, Yushan Zhang, Yuhong Wang, and Jian Wang. Revised spacer design to improve hydrodynamics and anti-fouling behavior in reverse electrodialysis processes. *Desalination and Water Treatment*, 57(58):28176–28186, 2016.

[172] Mahboobeh Vaselbehagh, Hamed Karkhanechi, Ryosuke Takagi, and Hideto Matsuyama. Biofouling phenomena on anion exchange membranes under the reverse electrodialysis process. *Journal of Membrane Science*, 530:232–239, May 2017.

[173] Joo-Youn Nam, Kyo-Sik Hwang, Hyun-Chul Kim, Haejun Jeong, Hanki Kim, Eunjin Jwa, SeungCheol Yang, Jiyeon Choi, Chan-Soo Kim, Ji-Hyung Han, and Namjo Jeong. Assessing the behavior of the feed-water constituents of a pilot-scale 1000-cell-pair reverse electrodialysis with seawater and municipal wastewater effluent. *Water Research*, 148:261–271, 2019.

[174] Masahiro Yasukawa, Soroush Mehdizadeh, Tomoyuki Sakurada, Takakazu Abo, Masaya Kuno, and Mitsuru Higa. Power generation performance of a bench-scale reverse electrodialysis stack using wastewater discharged from sewage treatment and seawater reverse osmosis. *Desalination*, 491:114449, October 2020.

[175] Anthony L Gotter, Marcia A Kaetzel, and John R Dedman. Electrophorus electricus as a Model System for the Study of Membrane Excitability. *Comparative Biochemistry and Physiology Part A: Molecular & Integrative Physiology*, 119(1):225–241, January 1998.

[176] M. V. Brown. The electric discharge of the electric EEL. *Electrical Engineering*, 69(2):145–147, February 1950.

[177] Thomas B. H. Schroeder, Anirvan Guha, Aaron Lamoureux, Gloria VanRenterghem, David Sept, Max Shtein, Jerry Yang, and Michael Mayer. An electric-eel-inspired soft power source from stacked hydrogels. *Nature*, 552(7684):214–218, December 2017.

[178] Jian Xu and David A. Lavan. Designing artificial cells to harness the biological ion concentration gradient. *Nature Nanotechnology*, 3(11):666–670, November 2008.

[179] Pei He, Jiankang He, Ziyao Huo, and Dichen Li. Microfluidics-based fabrication of flexible ionic hydrogel batteries inspired by electric eels. *Energy Storage Materials*, 49:348–359, August 2022.

[180] Ramin Banan Sadeghian, Oxana Pantchenko, Daniel Tate, and Ali Shakouri. Miniaturized concentration cells for small-scale energy harvesting based on reverse electrodialysis. *Applied Physics Letters*, 99(17):173702, October 2011.

[181] Tsung-Chen Tsai, Chia-Wei Liu, and Ruey-Jen Yang. Power Generation by Reverse Electrodialysis in a Microfluidic Device with a Nafion Ion-Selective Membrane. *Micromachines*, 7(11):205, November 2016.

[182] Hyung-Kwan Chang, Eunpyo Choi, and Jungyul Park. Paper-based energy harvesting from salinity gradients. *Lab on a Chip*, 16(4):700–708, February 2016.

[183] Seok Hee Han, Seung-Ryong Kwon, Seol Baek, and Taek-Dong Chung. Ionic Circuits Powered by Reverse Electrodialysis for an Ultimate Iontronic System. *Scientific Reports*, 7(1):14068, October 2017.

[184] Seol Baek, Seung-Ryong Kwon, Song Yi Yeon, Sun-Heui Yoon, Chung Mu Kang, Seok Hee Han, Dahye Lee, and Taek Dong Chung. Miniaturized Reverse Electrodialysis-Powered Biosensor Using Electrochemiluminescence on Bipolar Electrode. *Analytical Chemistry*, 90(7):4749–4755, April 2018.

[185] Song Yi Yeon, Jeongse Yun, Sun-heui Yoon, Dahye Lee, Woohyuk Jang, Seok Hee Han, Chung Mu Kang, and Taek Dong Chung. A miniaturized solid salt reverse electrodialysis battery: A durable and fully ionic power source. *Chemical Science*, 9(42):8071–8076, October 2018.

[186] Seung-Ryong Kwon, So Hee Nam, Clara Yongjoo Park, Seol Baek, Joomyung Jang, Xiangguo Che, Su Hong Kwak, Yu-Ra Choi, Na-Rae Park, Je-Yong Choi, Yan Lee, and Taek Dong Chung. Electrodeless Reverse Electrodialysis Patches as an Ionic Power Source for Active Transdermal Drug Delivery. *Advanced Functional Materials*, 28(15):1705952, 2018.

[187] Zong-Hong Lin, Wei-Shan Hsu, Anant Preet, Li-Hsien Yeh, Yung-Hsin Chen, Yu-Ping Pao, Shien-Fong Lin, Sangmin Lee, Jia-Ching Fan, Ligang Wang, Yi-Pin Chiu, Bak-Sau Yip, and Tzu-En Lin. Ingestible polysaccharide battery coupled with a self-charging nanogenerator for controllable disinfection system. *Nano Energy*, 79:105440, January 2021.

[188] Max Tepermeister, Nikola Bosnjak, Jinyue Dai, Xinyue Zhang, Samuel M Kielar, Zhongtong Wang, Zhiting Tian, Jin Suntivich, and Meredith N Silberstein. Soft ionics: Governing physics and state of technologies. *Frontiers in Physics*, page 453, 2022.

[189] Klas Tybrandt, Karin C. Larsson, Agneta Richter-Dahlfors, and Magnus Berggren. Ion bipolar junction transistors. *Proceedings of the National Academy of Sciences*, 107(22):9929–9932, June 2010.

[190] Ji-Hyung Han, Kwang Bok Kim, Hee Chan Kim, and Taek Dong Chung. Ionic Circuits Based on Polyelectrolyte Diodes on a Microchip. *Angewandte Chemie International Edition*, 48(21):3830–3833, 2009.

[191] Per Janson, Erik O. Gabrielsson, Keon Jae Lee, Magnus Berggren, and Daniel T. Simon. An Ionic Capacitor for Integrated Iontronic Circuits. *Advanced Materials Technologies*, 4(4):1800494, 2019.

[192] Efecan Pakkaner, Chase Smith, Christina Trexler, Jamie Hestekin, and Christa Hestekin. Blood driven biopower cells: Acquiring energy from reverse electrodialysis using sodium concentrations from the flow of human blood. *Journal of Power Sources*, 488:229440, March 2021.

[193] Efecan Pakkaner, Jessica L. Orton, Caroline G. Campbell, Jamie A. Hestekin, and Christa N. Hestekin. Development of an Integrated Salt Cartridge-Reverse Electrodialysis (Red) Device to Increase Electrolyte Concentrations to Biomedical Devices. *Membranes*, 12(10):990, October 2022.

[194] Alexandros Daniilidis, Rien Herber, and David A. Vermaas. Upscale potential and financial feasibility of a reverse electrodialysis power plant. *Applied Energy*, 119:257–265, April 2014.

[195] Ramato Ashu Tufa, Sylwin Pawlowski, Joost Veerman, Karel Bouzek, Enrica Fontananova, Gianluca di Profio, Svetlozar Velizarov, João Goulão Crespo, Kitty Nijmeijer, and Efrem Curcio. Progress and prospects in reverse electrodialysis for salinity gradient energy conversion and storage. *Applied Energy*, 225:290–331, September 2018.

[196] M. Turek and B. Bandura. Renewable energy by reverse electrodialysis. *Desalination*, 205(1):67–74, 2007.

[197] J. W. Post, C. H. Goeting, J. Valk, S. Goinga, J. Veerman, H. V. M. Hamelers, and P. J. F. M. Hack. Towards implementation of reverse electrodialysis for power generation from salinity gradients. *Desalination and Water Treatment*, 16(1-3):182–193, 2010.

[198] Mathieu Toupin, Kourosh Malek, and Asmae Mokrini. Techno-Economics of a New High Throughput Process for Proton Exchange Membranes Manufacturing. *World Electric Vehicle Journal*, 8(2):431–442, June 2016. Number: 2 Publisher: Multidisciplinary Digital Publishing Institute.

[199] F. Giacalone, M. Papapetrou, G. Kosmadakis, A. Tamburini, G. Micale, and A. Cipollina. Application of reverse electrodialysis to site-specific types of saline solutions: A techno-economic assessment. *Energy*, 181:532–547, August 2019.

[200] Doriano Brogioli. Extracting Renewable Energy from a Salinity Difference Using a Capacitor. *Physical Review Letters*, 103(5):058501, July 2009.

[201] Pawan Sharma and T. S. Bhatti. A review on electrochemical double-layer capacitors. *Energy Conversion and Management*, 51(12):2901–2912, December 2010.

[202] D. Brogioli, R. Ziano, R. A. Rica, D. Salerno, O. Kozynchenko, H. V. M. Hamelers, and F. Mantegazza. Exploiting the spontaneous potential of the electrodes used in the capacitive mixing technique for the extraction of energy from salinity difference. *Energy & Environmental Science*, 5(12):9870–9880, November 2012.

[203] S. Porada, R. Zhao, A. van der Wal, V. Presser, and P.M. Biesheuvel. Review on the science and technology of water desalination by capacitive deionization. *Progress in Materials Science*, 58(8):1388–1442, October 2013.

[204] D. Brogioli, R. Ziano, R.A. Rica, D. Salerno, and F. Mantegazza. Capacitive mixing for the extraction of energy from salinity differences: Survey of experimental results and electrochemical models. *Journal of Colloid and Interface Science*, 407:457–466, October 2013.

[205] Fabio La Mantia, Mauro Pasta, Heather D. Deshazer, Bruce E. Logan, and Yi Cui. Batteries for Efficient Energy Extraction from a Water Salinity Difference. *Nano Letters*, 11(4):1810–1813, April 2011.

[206] Meng Ye, Mauro Pasta, Xing Xie, Kristian L. Dubrawski, Jianqaio Xu, Chong Liu, Yi Cui, and Craig S. Criddle. Charge-Free Mixing Entropy Battery Enabled by Low-Cost Electrode Materials. *ACS Omega*, 4(7):11785–11790, July 2019. Publisher: American Chemical Society.

[207] Marta C. Hatzell, Kelsey B. Hatzell, and Bruce E. Logan. Using Flow Electrodes in Multiple Reactors in Series for Continuous Energy Generation from Capacitive Mixing. *Environmental Science & Technology Letters*, 1(12):474–478, December 2014.

[208] Insung Hwang, Dongsoo Lee, Yongmin Jung, Keemin Park, Yeon-Gil Jung, Donghyun Kim, Geun-Ho Cho, Sung-il Jeon, Yun-ki Byeun, Ungyu Paik, SeungCheol Yang, and Taeseup Song. Cross Effect of Surface Area and Electrical Conductivity for Carbonaceous Materials in Flow-electrode Capacitive Mixing (F-CapMix) and Flow-electrode Capacitive Deionization (FCDI): Solid-like Behavior of Flow-electrode. *ACS Sustainable Chemistry & Engineering*, 9(40):13514–13525, October 2021.

[209] Dongsoo Lee, Ji Soo Roh, Insung Hwang, Yongmin Jung, Hyungjun Lee, Il Woo Ock, Sungmin Kim, Seho Sun, SeungCheol Yang, Ho Bum Park, Ungyu Paik, and Taeseup Song. Multilayered Graphene-Coated Metal Current Collectors with High Electrical Conductivity and Corrosion Resistivity for Flow-Electrode Capacitive Mixing. *ACS Sustainable Chemistry & Engineering*, 10(23):7625–7634, June 2022.

[210] S. Ahualli, M. L. Jiménez, M. M. Fernández, G. Iglesias, D. Brogioli, and Á V. Delgado. Polyelectrolyte-coated carbons used in the generation of blue energy from salinity differences. *Physical Chemistry Chemical Physics*, 16(46):25241–25246, November 2014.

[211] Anna Siekierka, Katarzyna Smolińska-Kempisty, and Marek Bryjak. Charge-doped electrodes for power production using the salinity gradient in CapMix. *Desalination*, 495:114670, December 2020.

[212] R. A. Rica, R. Ziano, D. Salerno, F. Mantegazza, and D. Brogioli. Thermodynamic Relation between Voltage-Concentration Dependence and Salt Adsorption in Electrochemical Cells. *Physical Review Letters*, 109(15):156103, October 2012.

[213] Xian Kong, Alejandro Gallegos, Diannan Lu, Zheng Liu, and Jianzhong Wu. A molecular theory for optimal blue energy extraction by electrical double layer expansion. *Physical Chemistry Chemical Physics*, 17(37):23970–23976, 2015.

[214] Muhammad Nasir, Yuji Nakanishi, Anindityo Patmonoaji, and Tetsuya Suekane. Effects of porous electrode pore size and operating flow rate on the energy production of capacitive energy extraction. *Renewable Energy*, 155:278–285, August 2020.

[215] Daniel Moreno and Marta C. Hatzell. Efficiency of Thermally Assisted Capacitive Mixing and Deionization Systems. *ACS Sustainable Chemistry & Engineering*, 7(13):11334–11340, July 2019.

[216] S. Ahualli, M. L. Jiménez, Z. Amador, M. M. Fernández, G. R. Iglesias, and A. V. Delgado. Energy production by salinity exchange in polyelectrolyte-coated electrodes. Temperature effects. *Sustainable Energy & Fuels*, 5(13):3321–3329, June 2021.

[217] Zhi Zou, Longcheng Liu, Shuo Meng, and Xiaolei Bian. Comparative study on the performance of capacitive mixing under different operational modes. *Energy Reports*, 8:7325–7335, November 2022.

[218] Guillermo R. Iglesias, Silvia Ahualli, María M. Fernández, María L. Jiménez, and Ángel V. Delgado. Stacking of capacitive cells for electrical energy production by salinity exchange. *Journal of Power Sources*, 318:283–290, June 2016.

[219] David A. Vermaas, Suman Bajracharya, Bruno Bastos Sales, Michel Saakes, Bert Hamelers, and Kitty Nijmeijer. Clean energy generation using capacitive electrodes in reverse electrodialysis. *Energy & Environmental Science*, 6(2):643–651, July 2013.

[220] Yoontaek Oh, Ji-Hyung Han, Hanki Kim, Namjo Jeong, David A. Vermaas, Jin-Soo Park, and Soryong Chae. Active Control of Irreversible Faradic Reactions to Enhance the Performance of Reverse Electrodialysis for Energy Production from Salinity Gradients. *Environmental Science & Technology*, 55(16):11388–11396, August 2021.

[221] Fei Zhan, Zijian Wang, Tingting Wu, Qiang Dong, Changtai Zhao, Gang Wang, and Jieshan Qiu. High performance concentration capacitors with graphene hydrogel electrodes for harvesting salinity gradient energy. *Journal of Materials Chemistry A*, 6(12):4981–4987, March 2018.

[222] Haihui Zhu, Wangwang Xu, Guangcai Tan, Elizabeth Whiddon, Ying Wang, Christopher G. Arges, and Xiuping Zhu. Carbonized peat moss electrodes for efficient salinity gradient energy recovery in a capacitive concentration flow cell. *Electrochimica Acta*, 294:240–248, January 2019.

[223] Fei Liu, Orlando Coronell, and Douglas F. Call. Electricity generation using continuously recirculated flow electrodes in reverse electrodialysis. *Journal of Power Sources*, 355:206–210, July 2017.

[224] Catarina Simões, Michel Saakes, and Derk Brilman. Toward Redox-Free Reverse Electrodialysis with Carbon-Based Slurry Electrodes. *Industrial & Engineering Chemistry Research*, January 2023.

[225] Irene A. Chen and Jack W. Szostak. Membrane growth can generate a transmembrane pH gradient in fatty acid vesicles. *Proceedings of the National Academy of Sciences*, 101(21):7965–7970, May 2004.

[226] Peter Doudoroff and Max Katz. Critical Review of Literature on the Toxicity of Industrial Wastes and Their Components to Fish: I. Alkalies, Acids, and Inorganic Gases. *Sewage and Industrial Wastes*, 22(11):1432–1458, 1950.

[227] Annah Moyo, Anita Parbhakar-Fox, Sebastien Meffre, and David R. Cooke. Alkaline industrial wastes – Characteristics, environmental risks, and potential for mine waste management. *Environmental Pollution*, 323:121292, April 2023.

[228] Johannes Philippus Maree. *Treatment of Industrial Effluents for Neutralization and Sulphate Removal*. Thesis, North-West University, 2006.

[229] H. L. Jacobs. Neutralization of Acid Wastes. *Sewage and Industrial Wastes*, 23(7):900–905, 1951.

[230] Andrea Tabasová, Jiří Kropáč, Vít Kermes, Andreja Nemet, and Petr Stehlík. Waste-to-energy technologies: Impact on environment. *Energy*, 44(1):146–155, August 2012.

[231] Peter Adeniyi Alaba, Shaukat Ali Mazari, Hamisu Umar Farouk, Samuel Eshorame Sanni, Oluranti Agboola, Ching Shya Lee, Faisal Abnisa, Mohamed Kheireddine Aroua, and Wan Mohd Ashri Wan Daud. Harvesting Electricity from CO2 Emission: Opportunities, Challenges and Future Prospects. *International Journal of Precision Engineering and Manufacturing-Green Technology*, 8(3):1061–1081, May 2021.

[232] E. G. Novitsky, E. A. Grushevenko, V. P. Vasilevsky, and A. V. Volkov. Studying the Possibilities of Generating Electric-Power by Reverse Electrodialysis of Monoethanolamine Aqueous Solutions. *Membranes and Membrane Technologies*, 2(2):109–114, March 2020.

[233] Jose Antonio Garcia, Maria Villen-Guzman, Jose Miguel Rodriguez-Maroto, and Juan Manuel Paz-Garcia. Technical analysis of CO2 capture pathways and technologies. *Journal of Environmental Chemical Engineering*, 10(5):108470, October 2022.

[234] Changru Ma, Fabio Pietrucci, and Wanda Andreoni. Capture and Release of CO2 in Monoethanolamine Aqueous Solutions: New Insights from First-Principles Reaction Dynamics. *Journal of Chemical Theory and Computation*, 11(7):3189–3198, July 2015.

[235] Patricia Luis. Use of monoethanolamine (MEA) for CO2 capture in a global scenario: Consequences and alternatives. *Desalination*, 380:93–99, February 2016.

[236] H. V. M. Hamelers, O. Schaetzle, J. M. Paz-García, P. M. Biesheuvel, and C. J. N. Buisman. Harvesting Energy from CO2 Emissions. *Environmental Science & Technology Letters*, 1(1):31–35, January 2014.

[237] Taeyoung Kim, Bruce E. Logan, and Christopher A. Gorski. A pH-Gradient Flow Cell for Converting Waste CO $_2$ into Electricity. *Environmental Science & Technology Letters*, 4(2):49–53, February 2017.

[238] J. M. Paz-Garcia, O. Schaetzle, P. M. Biesheuvel, and H. V. M. Hamelers. Energy from CO2 using capacitive electrodes – Theoretical outline and calculation of open circuit voltage. *Journal of Colloid and Interface Science*, 418:200–207, March 2014.

[239] J. M. Paz-Garcia, J. E. Dykstra, P. M. Biesheuvel, and H. V. M. Hamelers. Energy from CO2 using capacitive electrodes – A model for energy extraction cycles. *Journal of Colloid and Interface Science*, 442:103–109, March 2015.

[240] L. Legrand, O. Schaetzle, M. Tedesco, and H. V. M. Hamelers. Electrical energy from CO2 emissions by direct gas feeding in capacitive cells. *Electrochimica Acta*, 319:264–276, October 2019.

[241] S. Porada, D. Weingarth, H. V. M. Hamelers, M. Bryjak, V. Presser, and P. M. Biesheuvel. Carbon flow electrodes for continuous operation of capacitive deionization and capacitive mixing energy generation. *Journal of Materials Chemistry A*, 2(24):9313–9321, May 2014.

[242] Hanki Kim, Young-Eun Kim, Nam-Jo Jeong, Kyo-Sik Hwang, Ji-Hyung Han, Joo-Youn Nam, Eunjin Jwa, Sung-Chan Nam, Sung-Youl Park, Yeo-Il Yoon, and Chan-Soo Kim. Innovative reverse-electrodialysis power generation system for carbon capture and utilization. *Journal of CO2 Utilization*, 20:312–317, July 2017.

[243] Chun Cheng, Sijia Wang, Yifan Wu, Idris Temitope Bello, Yawen Dai, Rui Cheng, Shuo Zhai, Yifei Wang, Shien-Ping Feng, and Meng Ni. Thermally Regenerative CO2-Induced pH-Gradient Cell for Waste-to-Energy Conversion. *ACS Energy Letters*, 6(9):3221–3227, September 2021.

[244] Chang Chen, Xueli Liu, Renxing Huang, Kuankuan Liu, Shangfa Pan, Junchao Lao, Qi Li, Jun Gao, and Lei Jiang. Nanofluidic osmotic power generation from CO2 with cellulose membranes. *Green Carbon*, 1(1):58–64, September 2023.

[245] Youcef Brahmi. *Nouveau concept pour améliorer l'extraction d'énergie bleue par des couches capacitives*. Theses, Université Paris sciences et lettres, December 2021.

[246] Hanqing Fan, Yuxuan Huang, and Ngai Yin Yip. Advancing ion-exchange membranes to ion-selective membranes: Principles, status, and opportunities. *Frontiers of Environmental Science & Engineering*, 17(2):25, October 2022.

[247] Kuichang Zuo, Kunpeng Wang, Ryan M. DuChanois, Qiyi Fang, Eva M. Deemer, Xiaochuan Huang, Ruikun Xin, Ibrahim A. Said, Ze He, Yuren Feng, W. Shane Walker, Jun Lou, Menachem Elimelech, Xia Huang, and Qilin Li. Selective membranes in water and wastewater treatment: Role of advanced materials. *Materials Today*, 50:516–532, November 2021.

[248] Patrice Simon and Yury Gogotsi. Materials for electrochemical capacitors. *Nature Materials*, 7(11):845–854, November 2008.

[249] Paula Ratajczak, Matthew E. Suss, Friedrich Kaasik, and François Béguin. Carbon electrodes for capacitive technologies. *Energy Storage Materials*, 16:126–145, January 2019.

[250] Waseem Raza, Faizan Ali, Nadeem Raza, Yiwei Luo, Ki-Hyun Kim, Jianhua Yang, Sandeep Kumar, Andleeb Mehmood, and Eilhann E. Kwon. Recent advancements in supercapacitor technology. *Nano Energy*, 52:441–473, October 2018.

[251] Joanna Kuleszo, Carolien Kroeze, Jan Post, and Balázs M Fekete. The potential of blue energy for reducing emissions of co2 and non-co2 greenhouse gases. *Journal of Integrative Environmental Sciences*, 7(S1):89–96, 2010.

[252] Qing-Yun Wu, Chengwei Wang, Ruiliu Wang, Chaoji Chen, Jinlong Gao, Jiaqi Dai, Dapeng Liu, Zhiwei Lin, and Liangbing Hu. Salinity-gradient power generation with ionized wood membranes. *Advanced energy materials*, 10(1):1902590, 2020.

[253] Weipeng Chen, Yun Xiang, Xiang-Yu Kong, and Liping Wen. Polymer-based membranes for promoting osmotic energy conversion. *Giant*, 10:100094, 2022.

[254] Jan Willem Post. *Blue Energy: electricity production from salinity gradients by reverse electrodialysis*. Wageningen University and Research, 2009.

[255] *Types of Energy Ranked by Cost Per Megawatt Hour - Solar Power Guide - Infographic*. https://solarpower.guide/solar-energy-insights/energy-ranked-by-cost. Accessed: 2023-09-17.

[256] Calculateur d'inflation. https://france-inflation.com.

[257] Enver Güler, Rianne Elizen, David A Vermaas, Michel Saakes, and Kitty Nijmeijer. Performance-determining membrane properties in reverse electrodialysis. *Journal of membrane science*, 446:266–276, 2013.

[258] Chuan-Yu Sun, Huan Zhang, Xu-Dong Luo, and Na Chen. A comparative study of nafion and sulfonated poly (ether ether ketone) membrane performance for iron-chromium redox flow battery. *Ionics*, 25:4219–4229, 2019.

[259] Zhizhang Yuan, Lixin Liang, Qing Dai, Tianyu Li, Qilei Song, Huamin Zhang, Guangjin Hou, and Xianfeng Li. Low-cost hydrocarbon membrane enables commercial-scale flow batteries for long-duration energy storage. *Joule*, 6(4):884–905, 2022.

[260] Soryong Chae, Hanki Kim, Jin Gi Hong, Jaewon Jang, Mitsuru Higa, Mohammad Pishnamazi, Ji-Yeon Choi, Ramali Chandula Walgama, Chulsung Bae, and In S Kim. Clean power generation from salinity gradient using reverse electrodialysis technologies: Recent advances, bottlenecks, and future direction. *Chemical Engineering Journal*, 452:139482, 2023.

[261] Aurélie Le Beulze, Nathalie Santos De Pera, Bertrand Levaché, Mathias Questel, Pascal Panizza, François Lequeux, Michael Levant, and Nicolas Passade-Boupat. Jams and Cakes: A Closer Look on Well Clogging Mechanisms in Microscale Produced Water ReInjection Experiments. *Transport in Porous Media*, 147(1):143–156, March 2023.

[262] Timon Rijnaarts, Elisa Huerta, Willem van Baak, and Kitty Nijmeijer. Effect of divalent cations on red performance and cation exchange membrane selection to enhance power densities. *Environmental science & technology*, 51(21):13028–13035, 2017.

[263] Nicolás Cifuentes-Araya, Gérald Pourcelly, and Laurent Bazinet. Impact of pulsed electric field on electrodialysis process performance and membrane fouling during consecutive demineralization of a model salt solution containing a high magnesium/calcium ratio. *Journal of colloid and interface science*, 361(1):79–89, 2011.

[264] Robert P Allison. Electrodialysis reversal in water reuse applications. *Desalination*, 103(1-2):11–18, 1995.

[265] Yris I Werges. Modelling of reverse electrodialysis in the presence of multivalent ions, 2021.

[266] Zhangxin Wang, Li Wang, and Menachem Elimelech. Viability of Harvesting Salinity Gradient (Blue) Energy by Nanopore-Based Osmotic Power Generation. *Engineering*, 9:51–60, February 2022.

[267] Yvana D. Ahdab, Georg Schucking, Danyal Rehman, and John H. Lienhard. Cost effectiveness of conventionally and solar powered monovalent selective electrodialysis for seawater desalination in greenhouses. *Applied Energy*, 301:117425, November 2021.

[268] Hongli Zhu. SPEEK scaling UP. *Joule*, 6(4):718–720, April 2022.

[269] Gang Xu, Feifei Liang, Yongping Yang, Yue Hu, Kai Zhang, and Wenyi Liu. An improved co2 separation and purification system based on cryogenic separation and distillation theory. *Energies*, 7(5):3484–3502, 2014.

[270] Yang Han and WS Winston Ho. Polymeric membranes for co2 separation and capture. *Journal of Membrane Science*, 628:119244, 2021.

[271] A Dallos, T Altsach, and L Kotsis. Enthalpies of absorption and solubility of carbon dioxide in aqueous polyamine solutions. *Journal of thermal analysis and calorimetry*, 65(2):419–423, 2001.

[272] No-Sang Kwak, Ji Hyun Lee, In Young Lee, Kyung Ryoung Jang, and Jae-Goo Shim. A study of the co2 capture pilot plant by amine absorption. *Energy*, 47(1):41–46, 2012.

[273] Mathieu Toupin, Thierry Brousse, and Daniel Bélanger. Charge Storage Mechanism of MnO2 Electrode Used in Aqueous Electrochemical Capacitor. *Chemistry of Materials*, 16(16):3184–3190, August 2004.

[274] Veronica Augustyn, Patrice Simon, and Bruce Dunn. Pseudocapacitive oxide materials for high-rate electrochemical energy storage. *Energy & Environmental Science*, 7(5):1597–1614, April 2014.

[275] Hee Y. Lee and J. B. Goodenough. Supercapacitor Behavior with KCl Electrolyte. *Journal of Solid State Chemistry*, 144(1):220–223, April 1999.

[276] Robert D. Crapnell and Craig E. Banks. Electroanalytical overview: The determination of manganese. *Sensors and Actuators Reports*, 4:100110, November 2022.

[277] D. Thomas Ferrell and W. C. Vosburgh. A Proposed Mechanism for the Discharge of the Manganese Dioxide Electrode. *Journal of The Electrochemical Society*, 98(8):334, August 1951.

[278] Richard S. Johnson and W. C. Vosburgh. Electrodes of Mixed Manganese Dioxide and Oxyhydroxide. *Journal of The Electrochemical Society*, 100(10):471, October 1953.

[279] B. E. Conway. Two-dimensional and quasi-two-dimensional isotherms for Li intercalation and *upd* processes at surfaces. *Electrochimica Acta*, 38(9):1249–1258, June 1993.

[280] Takao Nakagaki, Ippei Tanaka, Yukio Furukawa, Hiroshi Sato, and Yasuro Yamanaka. Experimental evaluation of effect of oxidative degradation of aqueous monoethanolamine on heat of co2 absorption, vapor liquid equilibrium and co2 absorption rate. *Energy Procedia*, 63:2384–2393, 2014.

[281] H. H. Berger. Models for contacts to planar devices. *Solid-State Electronics*, 15(2):145–158, February 1972.

[282] Ramato Ashu Tufa, Jaromír Hnát, Michal Něměček, Roman Kodým, Efrem Curcio, and Karel Bouzek. Hydrogen production from industrial wastewaters: An integrated reverse electrodialysis - Water electrolysis energy system. *Journal of Cleaner Production*, 203:418–426, December 2018.

[283] Mohammadreza Nazemi, James Padgett, and Marta C. Hatzell. Acid/Base Multi-Ion Exchange Membrane-Based Electrolysis System for Water Splitting. *Energy Technology*, 5(8):1191–1194, August 2017.

[284] Jihye Lee, Jeongse Yun, Seung-Ryong Kwon, Woo Je Chang, Ki Tae Nam, and Taek Dong Chung. Reverse Electrodialysis-Assisted Solar Water Splitting. *Scientific Reports*, 7(1):12281, September 2017.

[285] Heather D. Willauer, Felice DiMascio, Dennis R. Hardy, M. Kathleen Lewis, and Frederick W. Williams. Development of an Electrochemical Acidification Cell for the Recovery of CO $_2$ and H $_2$ from Seawater. *Industrial & Engineering Chemistry Research*, 50(17):9876–9882, September 2011.

[286] Paul Akinyemi, Weikun Chen, and Taeyoung Kim. Enhanced Desalination Performance Using Phosphate Buffer-Mediated Redox Reactions of Manganese Oxide Electrodes in a Multichannel System. *ACS Applied Materials & Interfaces*, 16(1):614–622, January 2024.

[287] R. Sharifian, R. M. Wagterveld, I. A. Digdaya, C. Xiang, and D. A. Vermaas. Electrochemical carbon dioxide capture to close the carbon cycle. *Energy & Environmental Science*, 14(2):781–814, February 2021.

Appendix A

Appendix

A.1 Fluidics for energy harvesting: From nano to milli scales

Wu, N., Brahmi, Y., and Colin, A. Fluidics for energy harvesting: From nano to milli scales. 23(5):1034–1065.

In this appendix, we present the review article published on the fluidic energy harvesting systems. It refers to the Chapter 1 of this thesis manuscript.

Lab on a Chip

ROYAL SOCIETY OF CHEMISTRY

CRITICAL REVIEW

View Article Online
View Journal | View Issue

Check for updates

Cite this: *Lab Chip*, 2023, **23**, 1034

Fluidics for energy harvesting: from nano to milli scales

Nan Wu, Youcef Brahmi and Annie Colin*

Received 8th October 2022,
Accepted 16th December 2022

DOI: 10.1039/d2lc00946c

rsc.li/loc

A large amount of untapped energy sources surrounds us. In this review, we summarize recent works of water-based energy harvesting systems with operation scales ranging from miniature systems to large scale attempts. We focus particularly on the triboelectric energy, which is produced when a liquid and a solid come into contact, and on the osmotic energy, which is released when salt water and fresh water are mixed. For both techniques we display the state of the art understanding (including electrical charge separation, electro-osmotic currents and induced currents) and the developed devices. A critical discussion of present works confirms the significant progress of these water-based energy harvesting systems in all scales. However, further efforts in efficiency and performance amelioration are expected for these technologies to accelerate the industrialization and commercialization procedure.

1 Introduction

A large amount of untapped energy sources surrounds us. They derive from human activities or come from ambient energies such as chemical, thermal, radiant and mechanical energies. Energy harvesting from environment is not recent: people have been harvesting energy for centuries at large scale with windmills and nowadays with wind turbines or photovoltaic batteries. After the radiant sources (sun, RF, *etc.*), mechanical energy (vibrations, wind, rain, *etc.*) and salted gradient are the second main environmental source of energy[1–4] The mixing of 1 cm^3 of sea water with 1 cm^3 of river water produces an energy of 1.4 J.[5] The energy of a rainwater drop falling on a surface is of the order of magnitude of 10 μJ (speed of the drops estimated to 1 m s^{-1}). These energies are not negligible and are comparable to the energy demand for powering current electronic devices. It takes 1 mJ to send a text message and 1 μJ to measure a temperature.[6,7] It seems therefore interesting to develop new techniques to recover energy from water by focusing on the mechanical energy contained in the drops of rain, in waves and in a more original way, in the osmotic energy contained in salt solutions. In such an approach, the first goal will be to be

ESPCI Paris, PSL Research University, MIE-CBI, CNRS UMR 8231, 10, Rue Vauquelin, F-75231 Paris Cedex 05, France. E-mail: annie.colin@espci.psl.eu

Nan Wu

Nan Wu received her bachelor's degree and master's degree from Beihang University. She received her general engineering degree from Ecole Centrale de Lyon. She currently holds a position as a Ph. D candidate at the laboratory of Matériaux Innovants pour l'Energie (MIE) in ESPCI-Paris at Paris Sciences & Lettres University (PSL). Her research focuses on developing innovative and efficient blue energy harvesting systems, especially enhancing energy harvesting efficiency of capacitive reverse electrodialysis systems. Her research interests include energy harvesting systems, capacitive reverse electrodialysis and capacitive electrodes.

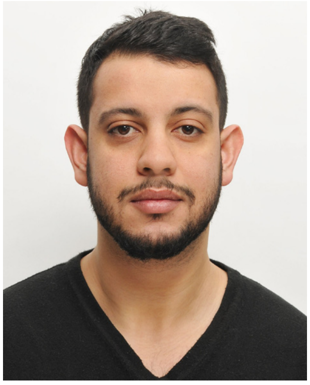

Youcef Brahmi

Youcef Brahmi received his Master degree in Chemical engineering from Ecole Nationale Polytechnique of Algiers and his PhD in physics and chemistry of material from PSL University in 2021. He is currently a post-doc researcher at ESPCI Paris PSL. His research work deals with electrochemistry, materials characterization, chemical engineering and device development.

able to power sensors and embedded electronic devices, which is part of the energy harvesting field. The second goal in the longer term, if the results are there, will be to extend these devices to large scales in order to generate new renewable energy sources to fight against climate change and replace fossil fuels. Researchers estimate that the worldwide salinity gradient energy could reach 2.4–2.6 Terawatts considering all the rivers and effluents running to the sea, among which 1 Terawatt is extractable.[8,9]

In this context, nanofluidics, microfluidics and millifluidics can have an impact in the field of research and development of new strategies to recover blue energy or energy from rain water. Nanofluidics, microfluidics and millifluidics encompasse all techniques for manipulating fluids at nanometer scale (between 1 and 1000 nanometers), micron scale (between 1 and 1000 micrometers) and millimeter scale (between 1 and 1000 millimeters), respectively.

In this review, we focus on emerging techniques for energy harvesting from fluids. In all cases, these techniques involve charge separation mechanisms and the creation of an ionic flow which is then converted into electronic flows either through a capacitive system or a faradic system. The charge separation mechanism is a basic key point in this framework. It remains to this day an open question although much progress has been made recently.[10] It involves the interactions between liquids and solids and the electrification of the contact. In this context it finds its explanations in the mechanics that govern triboelectric phenomena.[11,12]

The remaining part of this review proceeds as follows. In the second part, we will mainly focus on triboelectric energy harvesting systems. We will start with the state of art charge separation mechanisms taking place in liquids, or at the contact between a liquid and a solid surface due to the supply of mechanical energy. Based on these principles, innovative devices for the recovery of the mechanical energy of raindrops or waves are presented. A brief discussion on economic viability is provided at the end of this part. The third part will deal with the recovery of osmotic energy from salted gradient. Here we will present the main techniques including pressure retarded osmosis, reverse electrodialysis, capacitive mixing and capacitive reverse electrolysis. Present technological challenges and economic evaluations of these techniques are discussed in this part. A comprehensive conclusion, which summarizes the present research advancement as well as encouraging perspectives in this field, is provided at the end.

Annie Colin

Annie Colin is a professor at ESPCI Paris PSL and director of the Institut Pierre Gilles de Gennes. She is internationally recognized for her original contributions in the field of soft matter, rheology, materials for energy and microfluidics through her 160 papers and 15 patents.

2 Triboelectric energy harvesting

When two materials or a material and a fluid come into contact by friction, the materials and the fluid become electrically charged. This effect, known since ancient Greece, is called the triboelectric effect. Despite the fact that it is observed on a daily basis, it has only recently been partially explained. In the following section we will clarify this point and in particular illustrate the recent work that explains charge separation. It is possible to take advantage of this phenomenon to create an electric current. The presence of triboelectric charges on the dielectric surfaces can be a force that pushes the electrons in the electrode to flow in order to balance the electric potential drop created. Based on this observation, Wang invented TriboElectric NanoGenerators (TENGs).[13,14] In the second subsection of this part we will see how these devices work by focusing on devices that consist of a liquid and a material. The last subsections are devoted to economic analysis and perspectives of TENGs.

2.1 Contact electrification and charge electrification

2.1.1 Charge separation in liquid due to the amplification of an instability: Lord Kelvin's experiments. The pioneering work of charge separation process in liquids is the well-known Lord Kelvin's experiment. A Kelvin dropper[15] is a device that converts the gravitational potential energy of the drops into a high electrostatic voltage. Two positive feedback loops are constructed in the system to enable continuous ion separation. It consists of a tank equipped with two metallic tubes, two metal rings and two metallic canisters. The canisters are connected to the rings (see Fig. 1) in a well defined way: each canister is connected to the ring that does not feed it. The water drops fall from the two outlets above the conductive rings. When a drop is emitted from the outlet of the capillary nozzles, it has a small charge. The value and the sign of this charge depend on the material of the tube and on the value of the local electric field at the level of the nozzle. Suppose a drop is of positive charge. The metal reservoir will become positively charged as well as the ring facing the second capillary. Drops emitted from the second capillary will be negatively charged and be accumulated in the reservoir connected to the first ring. The phenomenon will be amplified. In a few seconds a voltage difference of several kiloVolts appears between the two tanks. This voltage difference can be so large that it can reach the field breakdown threshold of the air between two plates of a capacitor connected to the two reservoirs. Sparks may appear.

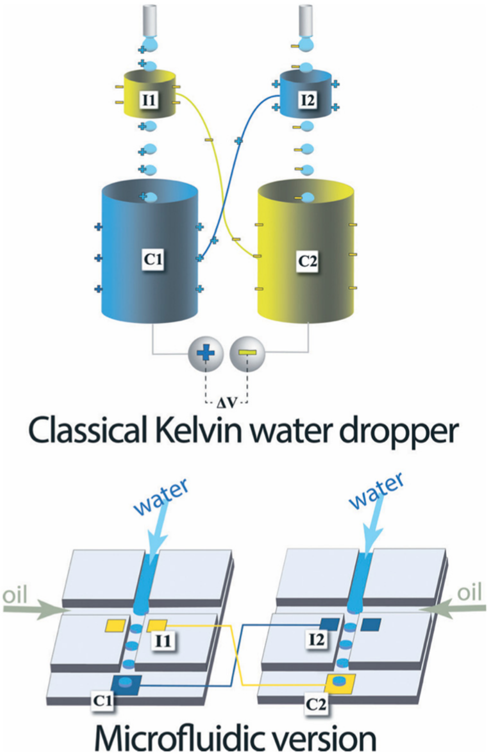

Fig. 1 Top, classical Kelvin water dropper, bottom, representation of the microfluidic version (figures and captions reproduced from ref. 16 with permission from Royal Society of Chemistry, copyright 2013).

This experiment was designed by Lord Kelvin to reproduce the appearance of electrostatic phenomena during thunderstorms. It is to mention that there is no electrical power generated in this system. No electrical currents are involved in the whole procedure, neither of capacitive nature, nor of faradic nature.

At the end of the 20th century, this experience was redesigned to increase the recoverable energy density. Marin *et al.*[16] proposed a microfluidic version of the device in 2013. The device consists of two microfluidic drop generators on different chips. Each chip comprises two types of electrodes: an electrode analogous to the ring of the Kelvin system close to the emission zone of the drops and an electrode further on the channel which recovers the charges. They demonstrated a successful formation of charged liquid drops by this microfluidic system.

2.1.2 Charge separation on graphene. Charge separation phenomena have also been demonstrated by studies on moving drops on graphene.[17,18] The physical mechanism in charge of the production of this electric current has been discussed in many works. It seems to date that a clear picture appears[19] thanks to Density Functional Theory simulations (see Fig. 2). While an ionic liquid drop is deposited onto a graphene surface, cations including H_3O^+ and hydrated Na^+ are preferentially adsorbed on the graphene surface, attracting electrons to accumulate on the upper side of the graphene. This excess of charge under the drop creates a positive charge (an electron deficiency) in the graphene which is distributed on the edges of the drop. When the drop does not advance, there is no potential difference created.

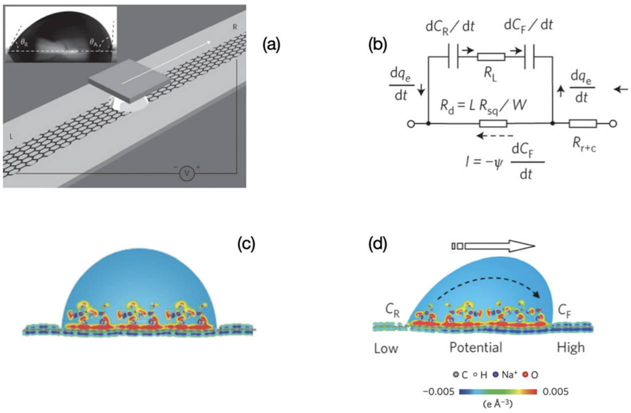

Fig. 2 Mechanism of charge separation on graphene. (a) Illustration of the experimental set-up. A liquid droplet is sandwiched between graphene and a SiO_2/Si wafer, and drawn by the wafer at specific velocities. Inset: A droplet of 0.6 M NaCl solution on a graphene surface with advancing and receding contact angles of 91.98° and 60.28°, respectively. (b) Equivalent circuit for (d). (c) Schematic illustration of the pseudo-capacitance formed by a static droplet on graphene. (d) Schematic illustration of the potential difference induced by a moving droplet (figures and captions reproduced from ref. 19 with permission from Springer Nature, copyright 2014).

When the drop moves, there is a constant supply of positive charge towards the front of the drop. Thus there is a constant supply of electrons at the front interface. Similarly, there is a constant departure of electrons from the back of the drop. These two phenomena induce an electric current in the graphene and a potential difference between the front and the back, with the electric potential at the front being higher than the electric potential at the back. The density power[19] is 19.2 nW cm^{-2} which corresponds to an efficiency of 1%.

Charge separations have also been demonstrated when a graphene-covered surface is dipped in an electrolyte[20] (see

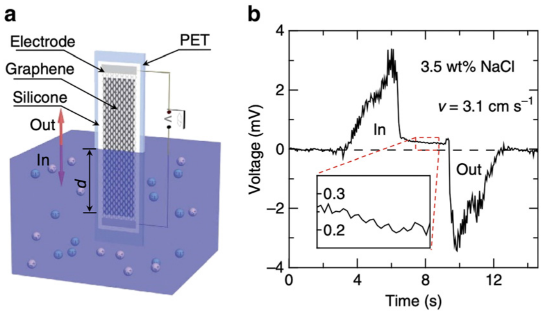

Fig. 3 a, Schematic illustration of the experimental set-up: moving the graphene sample on a polyester terephthalate substrate vertically across the water surface within a container. All the edges of the graphene sheet and silver emulsion electrodes are protected with silicone. b, Typical voltage signals produced as a sample is inserted and pulled out of 0.6 M NaCl solution (3.5 wt%) at a velocity v = 3.1 cm s^{-1} (figures and captions reproduced from ref. 20, with permission from Springer Nature copyright 2014).

Fig. 3). The sodium ions in the electrolyte adsorb rapidly on the surface. Chlorine ions move less rapidly towards the surface from which they are repelled. It therefore takes time to cancel this charge separation. During this time, the electrons in the graphene move closer to the sodium ions, creating holes in the graphene. A difference in the concentration of holes appears along the material and thus leads to the creation of a potential difference and an electric current. When the plate is removed from the liquid, the opposite phenomenon occurs, resulting in an electronic current in the opposite direction. Maximum voltages of 100 mV and maximum currents of 11 μA are measured for surfaces of 20 cm^2. The powers are therefore very low. The authors consider that their work can have an impact in the field of sensors.

At this stage we are not aware of any development of these graphene-liquid systems leading to real efficient devices. However, these new reflections have the merit to improve the understanding of the electrification phenomena. To conclude this section, in the above-mentioned graphene-based charge separation processes, graphene itself presents no permanent static surface charges. The electric current is generated by potential differences and dynamic concentration imbalances. In the following, we will present several charge separation mechanisms involving the creation and use of charged surfaces.

2.1.3 Charge separation and electrification of the liquid/solid contact. The electrification of a contact corresponds to the appearance of charge when two solids or a solid and a liquid are placed in contact. Although known since ancient Greece, the nature of the charge carrier electrons or ions during electrification remains a debate. Using ferrimagnetic solids, Lin *et al.*[21] show that electrification by liquid–solid contact is sensitive to magnetic fields. This result allows to answer the nature of the charge carrier during the contact electrification for ferrimagnetic solids. Indeed, potential charge carriers such as OH^- and H_3O^+ are all in a singlet ground state. They have an extremely weak response to magnetic fields and should not induce a sensitivity of the contact electrification (CE) to magnetic fields. Conversely, the electron spin is sensitive to magnetic field. The transfer of electrons between two species is spin conservative and follows the Pauli exclusion principle. Therefore, the liquid–solid CE should depend on the spin and therefore on the magnetic field if electrons are the charge carriers. These results provide strong evidence that the charge carrier is the electron during electrification of the liquid–solid contact for ferrimagnetic solids. However, these experiments do not allow us to totally reject the participation of ions in the electrification of the contact, especially in the case of other solids such as oxide surfaces or polymers. In recent studies, Lin and his colleagues[10,22] have shown, by performing thermionic emission experiments, that both electrons and ions transfer during the contact electrification between the SiO_2 and deionized water. The electronic transfer corresponds to 75% of the charge transferred in this context. The other 25% corresponds to the reaction between OH^- and SiO_2 which leads to the creation of SiO^-. When the pH is increased to 11 or decreased to 3 the electron transfer remains present but decreases while the ion transfer increases. The electrons transferred to the surface come from the water molecules. This requires during the contact to make appear in a very temporary way ions of type H_2O^+. The existence of the latter is explained by the hybrid layer model of Wang[23] and has been indirectly demonstrated recently by the production of OH radicals and hydrogen peroxide during contact electrification.[24] The surface charges carried by other oxyde[25] or PTFE after contact with water can be explained in the same way. Some of them come from the adsorption of ions during the contact (OH^- adsorption), others from an electron transfer from water to the material.[10]

The electrification of the contact allows to create currents. Let's consider the contact between PDMS (polydimethylsiloxane) and copper lubricated by water. The set-up developed by Lin *et al.*[26] to study this process, encompasses a PDMS layer on which a pyramid-shaped structure has been lithographically etched, a layer of water and a poly(methyl methacrylate) (PMMA) plate covered with a copper film (see Fig. 4). At initial state, a drop of DI water is placed onto the copper thin film, which is noted as electrode 1. For electrode 2, the structured side of the PDMS film is facing the electrode 1, while the other side is covered with a copper thin film. A drop of DI water is deposited onto electrode 1 on the copper surface. When the PDMS comes into contact with the liquid, the ionization of these surface

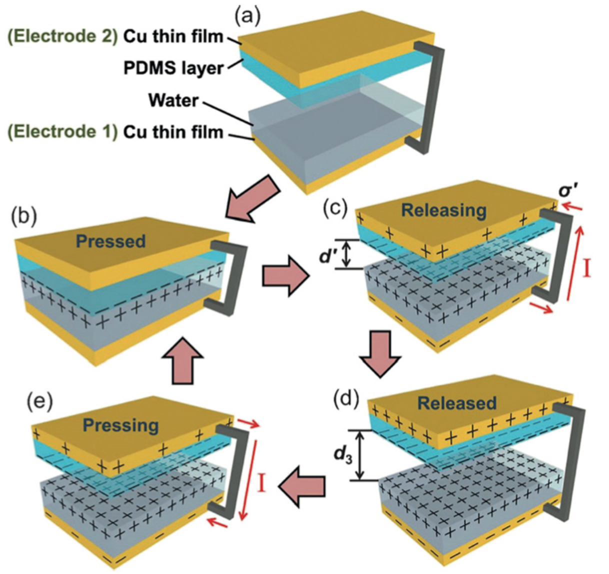

Fig. 4 Working mechanism of the water-TENG. (a) Initial status without any external force applied. (b) External force brings the PDMS layer into contact with water. (c) Removing the PDMS layer from the water surface. (d) PDMS layer returning back to the original position. (e) External force applied makes the PDMS layer contact with water again. For simplification, both PMMA substrates are not shown (figures and captions reproduced from ref. 26) with permission from John Wiley and Sons, copyright 2013.

groups induces the appearance of a positive surface charge in the liquid volume and a negative one on the polymer surface.

When the PDMS is removed from the liquid, its hydrophobic character induces the charge separation. The PDMS carries a net negative surface charge and the liquid a positive charge. This charge is greater the more easily water is drained from the PDMS surface. As said before, the hydrophobic character of PDMS is fundamental to ensure charge separation. A maximum surface charge is generated when the water is completely drained from the PDMS surface in an ideal case. If the two copper films are electrically connected, a flow of electrons occurs between the copper film covered by the PDMS which is negatively charged and the copper film covered by the water drop which is positively charged so as to counterbalance the charges. When the PDMS re-enters the liquid, its charge is locally neutralized by the charge of the liquid. Thus the electrons make the opposite path, results in a capacitive current in the opposite direction. This new prototype of triboelectric contact by charge exchange between a solid surface and a liquid surface produces a current of 2.45 mA m^{-2}, a peak voltage of 52 V and a peak power (not average) of 0.13 W m^{-2} which allows to power 60 LEDs simultaneously. It is worth to be noted that the measured effect strongly decreases when deionized water is replaced by salt water. The power decreases by a factor of 4 when the authors use a 0.6 M NaCl solution instead of deionized water. This explanation is suitable for a surface carrying ionizable groups but is not satisfactory on PTFE surfaces or oxide surface. In this last situation, the interaction of the ions of the solution with the surface is put forward.

Surface charge, wherever it comes from (electrons from water or ions adsorption), seems also to be at the origin of the production of charged drops. We have just seen that the contact of a drop of water on a surface can create surface electrostatic charges and induced currents. A similar mechanism can occur when a liquid flows over a surface. The electrification of the drop after its emission from a nozzle or a capillary has generated a lot of activities over the past 20 years. The surface of the nozzle or capillary[27] has a surface charge.[28] When liquid flows, it will first take away the released counterions which balance the surface charge and reveal a charged surface. Then through the capillary or the nozzle, a layer of counterions will build up at the liquid–wall interface. The whole wall of the tube, electrolyte in the tube is neutral. However, the tube wall and the electrolyte each carry a surface charge which is opposite. The value of the charge depends on the pH, the concentration of electrolytes, the capillary coating and little on the humidity value. This explains why the drops coming out of a capillary are charged. This natural electrification of the droplets does not come from pre-existing free charges on the capillaries but from a charge separation mechanism between a droplet and the surface of the pipette tip which carries a static electric charge. The chemical balance of the surface is not affected by the flow. This causes the upper liquid upstream of the capillary to become inversely charged. The existence of charged drops will be used in the following to generate energy producing devices.

2.2 Applications to energy harvesting devices

2.2.1 Ballistic electrostatic generator. Xie *et al.*[29] developed a device that converts the inertial energy of jet drops into electric current. The device is depicted in Fig. 5. A jet of water is formed at the outlet of a pore of about thirty micrometers in diameter under the action of a strong over-pressure of the order of 100 kPa. Under the effect of Rayleigh Plateau instability, the jet breaks into small drops. These drops possess an electrical charge which is induced by the surface charge of the hole (see above subsection for more details). The charged drops arrive on the target plate which is connected to the ground. In this device, the acceleration of the drops compensates the electric field created between the bottom plate and the electrode. A current of electrons from the ground to the target plate is established. This current is counterbalanced by a current of electrons from the membrane to the ground (see Fig. 5). This device resembles Lord Kelvin's device. However, there are significant differences that make it more efficient. In Kelvin's drop generator, gravity opposes the electric force that slows down the drops, in this device it is the acceleration of the drops. This fundamental difference coupled with the fact that the charges of the drops are 10^4 larger than those of the Kelvin experiment results in higher currents.

The authors claimed that the system displays a conversion efficiency up to 48% and may generate a power density of 160 kW m^{-2} if scale up holds. These figures are excellent. However, although promising, the device is far from being developed as an application. The main disadvantage of this system is that it does not provide for a surface discharge phase. Indeed, in order to produce energy in a system that induces ion flows and then capacitive electron flows, it is necessary either to imagine a process that induces reverse flows, or to set up reactions that consume the charges produced by faradaic reactions. In other words, it is necessary to manage to discharge the surfaces, to depolarize them in order to be able to cycle as in the case of triboelectric systems. Moreover, even if this problem is solved, the system will face the same energy storage problem as triboelectric systems. This system has a very small output impedance and the energy transfer efficiency will be very low. This work has not led to any application developments in the literature but as we said before it is one of the most promising.

2.2.2 Harvesting the rain droplets energy. In this spirit, Xu *et al.*[30] have developed a device that is closer to the application domain. The device consists of several layers of electrodes. An aluminum electrode is placed onto a polytetrafluoroethylene (PTFE) electret, below which an indium tin oxide (ITO) electrode is placed on a glass surface and does not receive liquid drops. It is important to mention the direct connection between aluminum electrode and ITO

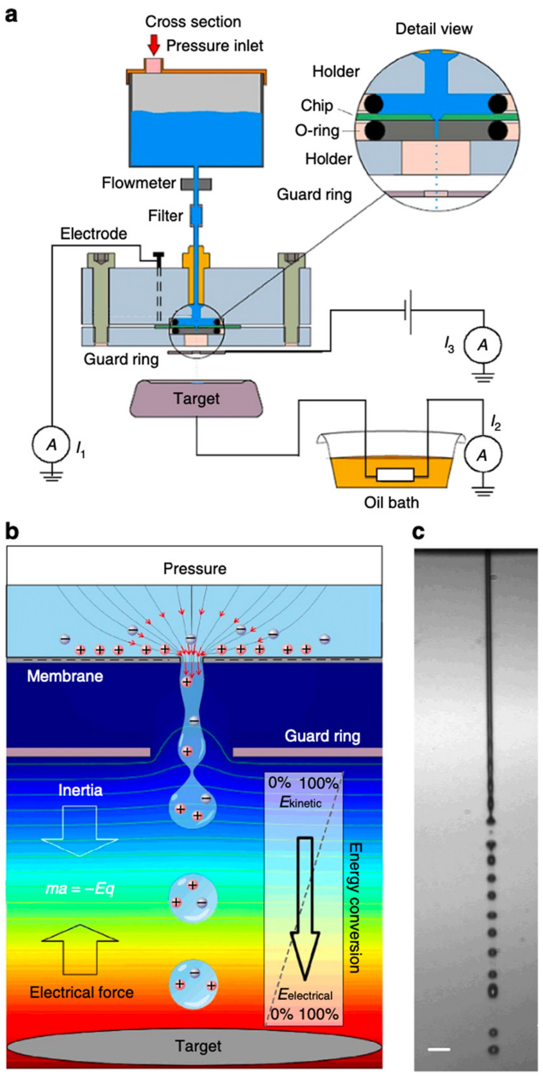

Fig. 5 Concept of energy conversion and set-up. a, Experimental set-up. Aqueous solution is forced by applied air pressure through a 10 or 30 mm diameter circular pore in a 500 nm-thick silicon nitride membrane. A platinum electrode sputtered on the backside of the chip (30 mm pore experiments) or an inserted platinum wire (10 mm pore experiments) was connected to a picoammeter (Keithley 6485). A microjet is formed that breaks up in a droplet stream. The droplets travel through the air and arrive on a metal target placed at 7.5–25 mm distance from the pore opening. The target is connected to electrical ground *via* a high-load resistance. A metal guard ring with an opening of 2 mm diameter is placed at 1.5 mm (10 mm pore) or 5.0 mm (30 mm pore) from the pore exit and maintained at ground potential, or at a negative potential for inductive droplet charging. The current can be measured between ground and the platinum reservoir electrode (denoted I_1), between target and ground (I_2) and between metal guard ring and ground (I_3). b, Conceptual illustration of the conversion principle. Water is accelerated to form a microjet that breaks up into charged droplets. On their air trajectory towards the target, the droplets are decelerated by the electrical force, converting kinetic energy into electrical energy. The background colour from red to blue indicates the voltage distribution from high to low, the lines denote equipotentials. c, Photomicrograph of the microjet from the 10 mm pore taken by double iLIF illumination. Scale bar, 40 mm (figures and captions reproduced from ref. 29 with permission from Springer Nature, copyright 2014).

electrode. This work is directly related to the previous part dealing with electrification by contact between the drops of water and the PTFE. After the impact of 1.6.10^4 drops (ion concentration 3.1 mM salt), the PTFE reaches a steady charge of 49.8 nC.[31] At steady state, when new drops fall, a resistive water bridge closes an electrical circuit which includes the capacitor created by the electret, the capacitor created by the PTFE/water contact and the capacitor created by the aluminum/water contact (see Fig. 6). These last two being very important compared to the capacity of the electret, the transfer of charge in a closed circuit allows the passage of all the electret charges towards the aluminium water contact. When the drop retracts, the water-aluminium capacity goes to zero and the charges return to the electret. This mechanism includes cyclic procedures where positive and negative capacitive currents are generated. The reversibility is confirmed by the measurement of cyclic charge. An instantaneous peak power density of 50.1 W m^{-2} is reported in this work. The theoretical basis of energy production is presented in detail in ref. 32. The average energy-conversion efficiency of device, defined as the harvested electrical energy relative to the input energy of an impinging droplet, is calculated to be roughly 2.2%. This is several orders of magnitude higher than that of the control device without an aluminium electrode.

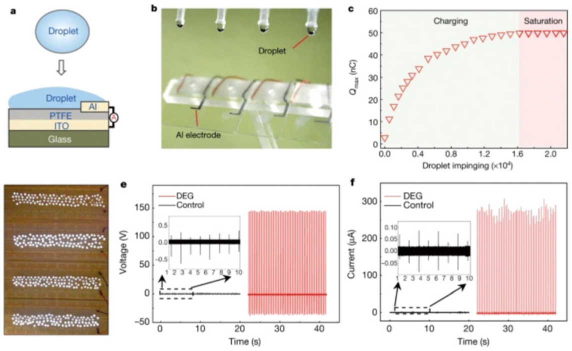

Fig. 6 Schematic illustration of droplet-based electricity generator (DEG). (a) Schematic diagram. (b) Optical image showing four parallel DEG devices fabricated on a glass substrate. The volume of each droplet is 100.0 μl. (c) As individual droplets continue to impinge on the as-fabricated device, the amount of charge on the PTFE surface increases gradually and eventually reaches a stable value. (d) One hundred commercial LEDs can be powered when one droplet, released from a height of 15.0 cm, is in contact with the device. (e) Under the same experimental conditions (for example, the same droplet size and height of release), the output voltage measured from the DEG (in red, with the frequency of impinging droplets being set at 4.2 Hz, and the total number of droplets being about 84) is more than two orders of magnitude higher than that from the control device (in black, with a droplet frequency of 1.0 Hz, and a total of 20 impinging droplets). The negligible electricity generation from the control device is limited by the interfacial effect, although its PTFE surface is loaded with the same amount of charge as the DEG. (f) Comparison of output current from the DEG (in red) and the control device (in black) in response to continuous impinging of individual droplets (figures and captions reproduced from ref. 30 with permission from Springer Nature, copyright 2020).

At this stage we are not aware of the industrial development of this device. The electrification of liquid–solid contacts, that is to say the triboelectric process, is the technique closest to applications and commercialization. We will describe these points in the next subsection.

2.2.3 Harvesting energy of waves. Liquid–solid triboelectric technology is used to collect the energy of waves. A device involving the electrification of a liquid–solid contact was developed by Wang and collaborators[33] to recover wave energy. The material used is a film consisting of PTFE nanoparticles (see Fig. 7). Due to the hydrophobicity of PTFE, the contact angle with water is 110°.

When the water comes into contact with the PTFE, the latter acquires a permanent electrostatic surface charge as explained above in the text.[31,49] During the following phases when the water advances on the surface, the positive ions it contains are adsorbed on the PTFE due to the existence of negative surface charge. As seawater propagates over the surface, this creates a charge gradient on the material, with the emerged part having zero charge and the dry part carrying an unbalanced negative charge. (see Fig. 8). Electrons move away from electrode A whose surface charge is neutralized by the propagating water and head towards electrodes B and C which are both negatively charged (see Fig. 8).

When the water recedes, an electrical reverse current is measured using the same principle. The use of bridge rectifiers makes it possible to recover a current that always flows in the same direction. Thanks to the use of rectifier bridges, it is possible to rectify the current and to sum currents of the same sign, which opens up the possibility of device scaling up. Due to the wetting properties, static charges remain on the PTFE. (We recall that the most probable mechanism responsible for the appearance of this charge is the permanent adsorption of OH^- ions). The authors measure a peak output power of 1.1 mW. This device can power a total number of 10 light emitting diodes.

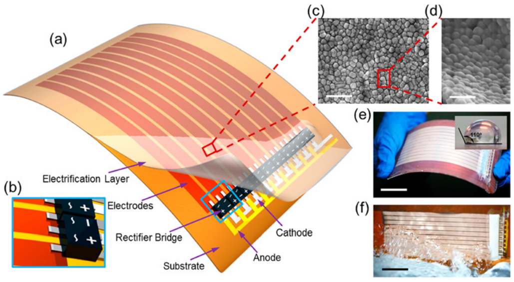

Fig. 7 Structure of a thin-film triboelectric generator (TF-TEG). a, Schematic diagram of an integrated TF-TEG. b, Enlarged sketch of the arrayed bridge rectifiers. c, SEM image of the PTFE nanoparticles on the electrification layer (scale bar = 1 μm). d, Enlarged view of the nanoparticles at a tilted angle of 60° (scale bar = 500 nm). e, Picture of a bendable as-fabricated TF-TEG. Inset: Water contact angle on the nanostructured surface (scale bar = 25 mm). f, Picture of the TF-TEG that is interacting with the water wave (scale bar = 25 mm) (figures and captions reproduced from ref. 33 with permission from American Chemical Society, copyright 2015).

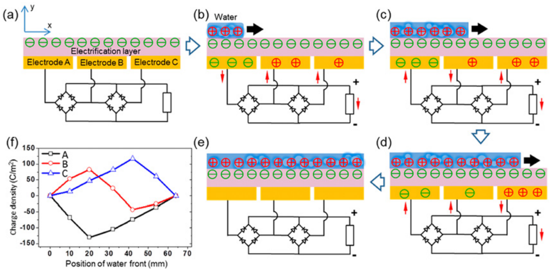

Fig. 8 Electricity-generating process of the TF-TEG. (a) Cross-sectional view of charge distribution when the device is fully exposed from water. Charge distribution when water is propagating across (b) electrode A, (c) electrode B and (d) electrode C. (e) Charge distribution when water fully covers the electrification layer underneath. (f) Charge density on the three electrodes as the water front propagates (figures and captions reproduced from ref. 33 with permission from American Chemical Society, copyright 2015).

In the same spirit, Wang *et al.*[50] have developed a device which recovers the energy dissipated during the navigation on the hull of a boat. The originality of this work, which is complementary to the previous one, consists in the development of a coating that avoids the proliferation of algae and microorganisms on the triboelectric layer. The device has excellent stability and high performance. It allows several LEDs to be illuminated during navigation. Currently, many groups[51,52] are studying PTFE for energy harvesting applications based on liquid–solid contact electrification. This material is one of the most promising. It is possible[38] to recover 3 W m^{-2} in the best conditions.

2.2.4 Harvesting water from unsteady flows. It is possible to generate triboelectric currents in a pipe covered by different materials. Ahn *et al.*[46] inserted a PVDF zone in a silicone tube. They placed a grounded copper electrode on the top of the PVDF zone. A salt water solution circulates in the tube. Silicone and PVDF have different surface charges. Thus the ion concentration in the Stern layer in the vicinity of the Silicone and PVDF is different. During a flow the Stern layers move. The charge in the Stern layer close to the PVDF varies and becomes unbalanced. This causes a current of electrons coming from the ground and trying to cancel the charge separation. When the flow is decreased, the charge concentration in the Stern layer returns to its initial value and a current of electrons in the opposite direction is created. The harvested power reaches 11.5 μW. Using the same approach Cheedarala *et al.*[44] measured a power density of 25 mW m^{-2} with a pulsating flow.

2.2.5 Hybridized triboelectric nanogenerator: coupling charge separation TENG and contact TENG. In the previous examples, the current produced is created by a charge separation mechanism. When a raindrop falls, it brings with it charges but it also brings with it mechanical energy that can produce a current if it causes contact between two solids with different triboelectric properties. A very first approach concerned the coupled recovery of the kinetic energy and the electrostatic energy of water. When a raindrop or water falls, it not only brings charges, but also possesses a large amount of mechanical energy which can be harvested if a liquid/solid contact with different triboelectric properties is designed. Such idea leads to the creation of hybridized TENGs, where a coupled recovery of kinetic energy and electrostatic energy is realized in a single system. Cheng *et al.*[41] have designed an impeller whose blades are composed of superhydrophobic polytetrafluoroethylene (PTFE) thin films with nanostructures. These PTFE blades are used to harvest the electrostatic energy of the flowing water. The water flowing over the blades turns the wheel and sets in rotation a triboelectric disc that collects the mechanical kinetic energy. At a water flow rate of 54 mL s^{-1}, the device involving electrostatic energy has an open circuit voltage of 72 V, a short circuit current of 12.9 μA, and a maximum power of 0.59 W m^{-2}. To this power must be added the power produced by the conventional disk TENG whose open circuit voltage is 102 V, short circuit current is 3.8 μA and maximum power density is 0.03 W m^{-2}. These results show the potential of liquid–solid contact electrification onshore and offshore and even in rainy areas. Following these considerations, hybrid nanogenerators have been developed[36,48] (see Table 1 for the performances). Recently, a fluorinated ethylene propylene (FEP)-based tribonanogenerator has been coupled to a piezoelectric material (PVDF) mounted on a cantilever. The deflection of the cantilever during the passage of the drop allows to capture the kinetic energy of the drop while the FEP coupled to a metallic electrode allows to recover the electrostatic energy.[45]

2.3 Economic analysis

The levelized cost of electricity LCOE is the cost necessary to produce electricity from a process, taking into account the materials, resources needed for the production, the life time and the maintenance during the process. In 2022, The BloombergNEF report estimates LCOE for onshore wind to be 0.044 $ per kW h and 0.042 $ per kW h for solar PV without storage.[53] The LCOE of storage is estimated in the same report to be 0.146 $ per kW h. The US average LCOE of wind projects built in 2021 was 0.031 $ per kW h.[54] It becomes very complex to give that of gas and fossiles combustible in the context of the war in Ukraine. Before the Ukraine war in 2021, the LCEO of gas was 0.081 $ per kW h.[53] The LCOE of triboelectrical generators has been estimated by Ahmed *et al.*[55] and is comprised between 0.02 and 0.09 $ per kW h. Unsurprisingly, this figure is lower than that for renewable and fossil fuels. The triboelectric devices are made of polymers and conductive layers already very present in the industrial world. The costs of these materials are low. Efficiency and module lifetime are the most sensitive factors for the LCOE of TENG. The lowest value of the LCOE assumes a life time of 15 years. In the same work,[55] the authors evaluated the Energy PayBack Time (EPBT) of a TENG, *i.e.* the time needed to produce the same amount of electricity (converted into equivalent primary energy) with the energy consumed during its life cycle. The two generators used have EPBT comprised between 0.1 and 0.25 year. These

Table 1 A summary of present solid–liquid nanogenerator

Materials	Output current (μA)	Power (μW)	Power density (W m^{-2})	Comments	Ref.
CYTOP	30	10^3	—	Water drops plus electret	34
FEP	2.6	1.2×10^5	—	Water drops, an efficiency of 7.7%	35
FEP-PTFE	5.1 + 4.3	41.2 + 3.03	—	Hybrid TENG (interfacial electrification TENG (IE-TENG) + impact-TENG)	36
HCOENPs-coated fabric-PET	3.2	—	0.14	Wearable all-fabric-based triboelectric generator	37
Graphene	1.7	1.92×10^2	—	Efficiency of 1%	19
PDMS-Cu	2.45×10^3 m^{-2}	—	0.13	Water-TENG	26
PDMS-PTFE	5.5	1.2×10^3	3	Water-TENG	38
PTFE	0.553	1.2	—	Water drops	39
PTFE	17	145	—	Superhydrophobic micro–nanostructured polytetrafluoroethylene (PTFE), water drop contact electrification	40
PTFE	12.9 + 3.8	—	0.59 + 0.03	Hybrid TENG (water-TENG + disk-TENG), water flow rate 54 mL s^{-1}	41
PTFE	13	1.1×10^3	—	Thin-film TENG	33
PTFE-FTO	1.8	—	0.01266	Multi-unit transparent TENG, flow rate 45 mL s^{-1}	42
PTFE-ITO	270	—	50.1	Water drop contact electrification	30
PTFE-nylon	0.54	—	1.838	Bi-electrode freestanding mode TENG (BF-TENG)	43
PVDF-Al	1.67	—	0.02653	Unsteady peristaltic flow induced pulsatile flow-TENG (PF-TENG)	44
PVDF-Al-FEP	6.2	1.34×10^4	—	Coupled TENG and piezo ENG	45
PVDF-BOPP	2.4	11.5	—	Fluid-based TENG	46
PVP	5.3	—	0.5	Power peak to peak, water drops	47
Superhydrophobic TiO_2 + SiO_2	43 + 18	—	1.31 + 0.18	Hybrid TENG (water-TENG + contact TENG), flow rate 40 mL s^{-1}	48

values are lower than those of the solar devices which are included between 0.3 and 2.5 years depending upon the different technologies. TENGs are more efficient and have a smaller energy footprint than photovoltaic cells. Indeed their manufacture does not require to purify and to treat silicon or rare elements necessary to the constructions of photovoltaic cells. These processes consume a lot of energy. A comprehensive analysis points out, that to improve these performances, more efforts should be made to increase the lifetime and the efficiency of TENGs rather than to identify cheaper materials and fabrication processes.

2.4 Perspective dealing with TENG

The results presented in this section are very encouraging and show the potential for commercial applications. The performances of some of these devices are reported in Table 1. The power densities that can be obtained are variable and range according to the experimental conditions from mW m^2 to 50 W m^2. Couplings between different devices (*e.g.* PiezoENG coupling with a Water TENG[45] or a Water TENG coupling with a Solid Contact TENG[36,48]) seem very promising. However, there is still a lot of work to be done to bring these techniques to the commercial level. There is a need to increase the energy conversion at the triboelectric layer level. This requires a better understanding of the physical mechanisms related to triboelectricity. Although triboelectric series have been established for a long time, the study of liquid–solid contacts calls for their modification. This requires research into new materials, new composites involving carbon nanotubes,[56] graphene[57] and systematic studies. These materials must be mechanically resistant, hydrophobic and possess a high surface charge. The energy storage at the device output has to be improved. Indeed, most of these devices have very low output impedances which strongly limit their use in the context of charging a battery or a super capacitor. The capacity of a TENG is very small of the order of 100 pF. These characteristics result in a low energy transfer efficiency, whether for charging a battery or powering electronic devices. These later generally have a much higher impedance (100 of μF). In order to transfer a maximum amount of energy, it is important to insert an electronic stage between the battery or the super capacitor that allows to adapt the impedances. This can be achieved by using N capacitors in series on charge and in parallel on discharge (basic switched capacitor convertor) or a fractal design based switched-capacitor-convertor (FSCC).[58] In the last situation, a energy transfer of 94% with an impedance reduction of 750 has been demonstrated. Last but not the least, the durability of the materials has to be improved. Moreover, it should be noted, that polymer devices are easily corroded by seawater.[59] Thus, some of the wave energy harvesting devices involve fully enclosed TENG devices whose review is beyond the scope of this work.[60–64] The power density of some of these devices[64] may reach 10.6 W m^{-3}.

In the following part, we will focus on osmotic energy harvesting. The technologies for saline gradients recovering emerged earlier and thus are more mature than the above-mentioned ones. There were already several pilot-scale attempts in industrial field, as well as other novel trials planned in the future. Considering the present energy crisis, these osmotic based energy harvesting systems might reach the threshold of economical viability soon.

3 Osmotic energy harvesting

The osmotic energy released during the process of mixing solutions of different salinity is clean and renewable energy. It is nicknamed blue energy.[65,66] Naturally, a spontaneous and irreversible mixing of river water and sea water happens at the estuary, resulting in an entropy increase of the system.[67] A precise and engineering control of this entropy change procedure enables the blue energy harvesting. The potential of blue energy can be estimated by thermodynamics studies. The non-expansion work released from the mixing of seawater and freshwater can be described by the Gibbs free energy of mixing ΔG_{mix} at a constant pressure P and at absolute temperature T.

$$\Delta G_{\text{mix}} = G_{\text{mix}} - (G_{\text{H}} + G_{\text{L}}) \tag{1}$$

Here, G_{mix}, G_{H} and G_{L} represents the Gibbs free energy of brackish water after mixing, seawater of high salinity and freshwater of low salinity, respectively.

As the Gibbs free energy is defined as $G = \sum_{i=1}^{N} \mu_i n_i$, where μ_i and n_i represent the chemical potential and the mole number of species i for a system consists of a number of N species. The chemical potential μ_i is defined as $\mu_i = \mu_i^* + RT\,\ln(\gamma_i x_i)$ where μ_i^* is the standard chemical potential, R perfect gas constant. γ_i and x_i represent the coefficient of activity and the mole fraction of species i, respectively. For a system of volume V, the molar concentration is defined as $n_i = c_i V$, where c_i is the molar concentration of species i. Thus the Gibbs free energy of mixing can be calculated as:[68]

$$\Delta G_{\text{mix}} = \sum_{i=1}^{N} \left[c_{i,\text{mix}} V_{i,\text{mix}} RT\,\ln\left(\gamma_{i,\text{mix}} x_{i,\text{mix}}\right) - c_{i,\text{H}} V_{i,H} RT\,\ln\left(\gamma_{i,\text{H}} x_{i,\text{H}}\right) - c_{i,\text{L}} V_{i,\text{L}} RT\,\ln\left(\gamma_{i,\text{L}} x_{i,\text{L}}\right)\right] \tag{2}$$

A maximum power of 0.8 W for fresh water of 1 cm^3 is predicted by theoretical calculations,[69] which is equivalent to the hydraulic energy generated by water dams with water falling from 250 m high.[70] Development of efficient and robust energy harvesting technologies is of great importance for the exploitation of this untapped renewable energy. In the following of this section, a review of blue energy harvesting technologies and their applications is explained in details. We first describe pressure retarded osmosis and then move to reverse electrodialysis and to Capmixing and CRED.

3.1 Pressure retarded osmosis

As an emerging energy harvesting system, the technology of pressure retarded osmosis (PRO) is attracting much attention.[71,72] Semipermeable membranes, which allow the passage of water molecules and block the passage of ions, are used in the configuration of PRO systems.[73] To better illustrate the power generation principle of PRO, an introductory explanation of the osmotic process across the semipermeable membrane is given in the following paragraph.

The observation of osmotic phenomenon was firstly documented by Jean-Antoine Nollet. It describes the spontaneous movement of a solvent flux moving across the semipermeable membrane towards a solute of higher concentration, in the way of balancing solute concentrations on both sides of the membrane.[75] The concentration difference across the membrane results in an osmosis pressure difference $\Delta\pi$. Additional hydraulic pressure ΔP could be applied on the system to influence the solvent flux. Description of the water (solvent) flux J_w is an essential parameter in the description of osmotic phenomenon. It can be theoretically described as a function of the applied hydraulic pressure difference ΔP and the effective osmosis pressure difference $\Delta\pi$ for an ideal membrane as $J_w = A_x(\Delta\pi - \Delta P)$. Here A_x refers to the permeability of the membrane.[76]

Based on the comparison between ΔP and $\Delta\pi$, osmotic process can be briefly classified into four categories as illustrated in Fig. 9(a).[74] The Forward osmosis (FO) corresponds to a trivial case where ΔP is zero, indicating no mechanical work in this process. In this case, water flux is driven by the osmotic driving force, penetrating the semipermeable membrane and proceeding to the draw solution side. While applying a hydraulic pressure difference on the feed solution compartment ($\Delta P < 0$), the above-mentioned process is further assisted and accelerated in the so-called procedure of pressure assisted osmosis (PAO). In the case where $\Delta P > \Delta\pi$, the direction of the water flux is reversed (from draw solution to feed solution) due to the external hydraulic pressure. This procedure is named as reverse osmosis (RO) and has intriguing applications in water desalination. It is to mention that both PAO and RO are energy consuming processes. On the contrary, PRO is the only power generating process where the water molecules move from feed solution towards the pressurized draw solution under osmotic effect ($0 < \Delta P < \Delta\pi$). The pressurized solution is then utilized to drive turbine systems for electricity power generation. A complete description of the water flux (J_w) and the power density (W) of each osmotic process is illustrated in Fig. 9(b and c).[74]

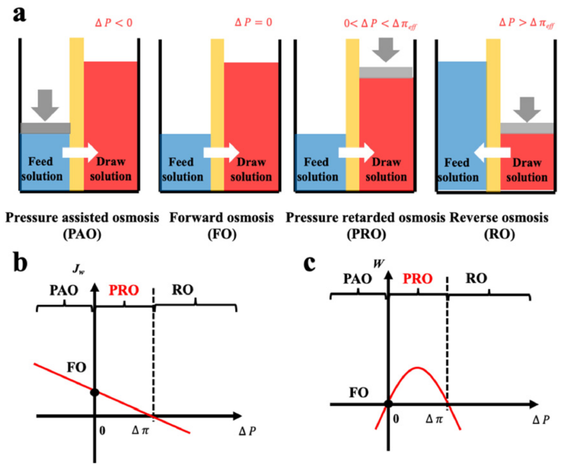

Fig. 9 Schematic illustration a, and analysis b and c, of four classic membrane-based osmotic processes of pressure assisted osmosis (PAO), forward osmosis (FO), pressure retarded osmosis (PRO) and reverse osmosis (RO) (figures and captions reproduced from ref. 74 with permission from Elsevier, copyright 2021).

Fig. 10 presents a typical configuration of the PRO plant. Feed solution and draw solution are both filtered and pumped into the PRO module. Under the osmotic effect, a water exchange flow rate (ΔQ) is created near the semipermeable membrane moving from feed water side towards draw water side. The brackish water received in the feed water chamber presents a higher flow rate of ($\Delta Q + Q_H$) and a higher hydrostatic pression P_H. The brackish water is then divided into two streams, where one stream is depressurized to drive turbine systems and produce electricity and the other one is delivered into a pressure exchanger to maintain the incoming pressure of draw solution.[77] Here the gross power density of a PRO system can be experimentally calculated as[78]

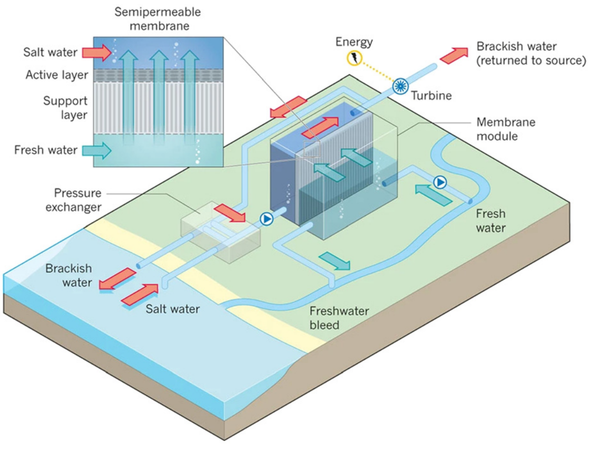

Fig. 10 Schematic illustration of the working principle of PRO systems. Feed solution and draw solution are injected continuously into water compartments which are separated by semipermeable membranes. Driven by effective osmotic force, water flux flows across the membrane from freshwater compartment towards saltwater compartment, resulting in a concentration decrease and a flow rate increase in draw solution compartment. The pressurized water flux is then split into two fluid streams: one fluid stream is used for electricity generation by driving an installed turbine, while the other stream returns to a pressure exchanger to maintain the pressure of draw solution (figures and captions reproduced from ref. 80 with permission from Springer Nature, copyright 2012).

$$P_{\mathrm{gross}} = \frac{\Delta Q \Delta P}{A_{\mathrm{m}}} = \Delta P J_{\mathrm{w}} \tag{3}$$

where A_{m} refers to the effective surface area of the membrane, ΔP refers to the transmembrane hydraulic pressure and J_{w} refers to the water flux across the membrane.[79]

3.1.1 Major challenges in PRO. Although PRO is a promising technology for energy harvesting, PRO modules still suffer from limiting factors in practical use. As illustrated in Fig. 11, a semipermeable membrane is composed of an active layer and a support layer.[74] An ideal membrane is expected to have high water permeability while maintaining a high salt selectivity. However, it was demonstrated in the work of Straub *et al.* the existence of tradeoff between these two factors (Fig. 12(A)).[78]

One of the major obstacles of membrane applications is the polarization effect, which refers to the ion accumulation phenomenon near the semipermeable membrane. The internal concentration polarization (ICP) corresponds to an immobile area clogged with ions in the dense support layer.[81] External concentration polarization (ECP) occurs at the interface between active layer and the draw solution (dilutive ECP) or feed solution (concentrative ECP). Concentration polarization effect deteriorates the osmotic driving force across the membrane, thus leads to lower effective membrane performances and power density output.[82] In addition, the imperfection of membranes could lead to ion leakage from draw solution to feed solution, which is named as reverse salt flux (RSF).[83] The trace leakage might cause more severe ICP effect in the system, lower the power density output, and could possibly promote membrane fouling problems,[84] which is also one of the major limitations on PRO power density output. A theoretical analysis of the impact of ICP and RSF was conducted by Straub *et al.*, as illustrated in Fig. 12(B). An apparent drop in power density is observed under the synergistic effect of ICP and RSF.[78]

Biofouling is a common problem for the industrial application of membranes. It influences severely the membrane performances in practical use, hinders the lifespan of membranes and raises additional fees for water pre-treatment.[85] The mechanical strength of membranes is also the key point for the development of PRO performances and its commercialization.[74]

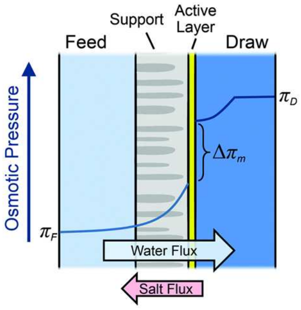

Fig. 11 Illustration of the semipermeable membrane cross section composed of an active layer and a support layer. A qualitative presentation of osmotic pressure profile across the membrane is presented (figures and captions reproduced from with permission ref. 78 with permission from Royal Society of Chemistry, copyright 2016).

In general, ideal PRO membranes should reach the following criteria: large water permeability, high salt rejection (high membrane selectivity), low reverse flux, limited biofouling problems and reinforced mechanical strength.[86] Precise engineering of the membrane's properties, including layer thickness, geometry configuration, porosity, selectivity and *etc.*, is summarized in the following paragraph.

3.1.2 PRO membrane development. At the early stage of PRO technology development, commercial membranes developed for RO and FO applications were used. In the pioneer work of PRO, Loeb *et al.*[87] used 'Minipermeators' with asymmetric hollow fibers of Du Pont Permasep B-10 initially developed for RO applications on sea water desalination. Later, Mehta *et al.*[88] realized a series of tests of the commercial membranes for RO and FO applications. Investigations on spiral-wound minimodules of cellulose acetate brackish water membrane and hollow fiber minipermeators were realized. Then the initial cellulose-based membranes designed for PRO applications with superior hydrophobicity and mechanical strength was used in studies.[89] These flat-sheet cellulose acetate membranes, including cellulose acetate (CA) and cellulose triacetate (CTA), were developed by HIT (Hydration Innovation Technology).[90] The early studies indicate a low energy harvesting performance of PRO mainly due to the use of unsuitable and bulky membrane structures, which causes severe ICP effect and reverse water flux problems.[91] In recent years, development in membrane design and surface modification promotes a vast progress for PRO membranes. The present membranes for PRO applications could be classified into two categories: the thin film composite (TFC) flat sheet membranes and thin film composite hollow fiber.[92]

Flat-sheet PRO TFC membranes consist of a highly-porous support layer and an active layer to reinforce its selectivity.[93] Polyamide (PA) is commonly chosen as the active layer, which is polymerized over the interface of the support layer through the phase inversion polymerization.[86] Various works were realized to optimize the permeability and structure integrity, aiming to ameliorate the power density output of PRO systems.

Table 2 lists the present work of flat-sheet PRO TFC membranes in literature.

It was demonstrated that membrane post-treatment of PA active layer could significantly increase the power density of PRO systems. Yip *et al.*[94] compared the performance of membranes with and without NaOCl and $NaHSO_3$ solution immersion and heat treatment. The highest power density output is predicted to be 10 W m^{-2} with proper post-treatment. A detailed study on membrane post-treatment was conducted by Han *et al.*[95] An optimal post-treatment condition was reported to generate a power density of 12 W m^{-2} under a hydraulic pressure of 15 bar. Integrating

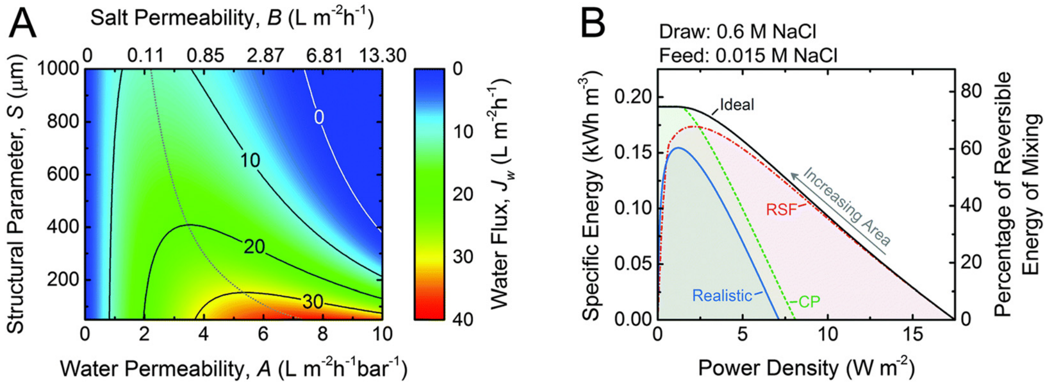

Fig. 12 A. Coupon-scale water flux J_w as a function of the water permeability coefficient, A; NaCl permeability coefficient, B; and support layer structural parameter, S. The water permeability and salt permeability are linked by the permeability-selectivity trade-off. B. Specific energy and power density for counter-current membrane modules with increasing membrane area from right to left. Data for three types of membranes are shown: ideal (solid black line), RSF (dash dotted red line) and CP (dashed green line) and realistic (solid blue line) (figures and captions reproduced with permission from ref. 78 with permission from Royal Society of Chemistry, copyright 2016).

Table 2 A summary of present PRO systems using flat-sheet PRO TFC membranes

Materials	Concentration gradient	Hydraulic pressure (bar)	Power density (W m^{-2})	Comments	Ref.
PA/PSf-PET	DI/0.5 M	12	10	NaOCl, $NaHSO_3$ and heat treatment	94
PA/PI	DI/1.0 M	15	7–12	NaOCl, $NaHSO_3$ and MeOH treatment	123
PA/PAN	DI/3.5% (w/w)	10	2.6	NaOCl and $NaHSO_3$ treatment	124
PA/PAI	DI/3.5% (w/w)	6	2.84	PDA coating and NaOCl, $NaHSO_3$, EtOH treatment	96
PA/PI	DI/1.0 M	9	6.0	PA blended with moderate *p*-xylylenediamine	125
PA/PAN	80 mM/1.06 M	22	15.2	NaClO treatment	126
PA/PI	DI/1.0 M	22	18.1	PA modified with DMF and SDS	127
PA/PAN-PE	DI/0.5 M	11.5	8.0	PA selective layer of mTFC/pTFC	99
CTA membrane	DI/3.0 M	48	60	—	128
PA/PEI	10 mM/1.0 M	17.2	12.8	—	129
PA/PEI	DI/1.0 M	16.9	17.3	Tiered PEI nanofibrous support with multi-walled CNTs	100
PA/PSf-PET	10 mM/1.0 M	18.4	7.1	—	130
PA/PES	DI/0.5 M	6	1.6	CNT-embedded-PES with NaOCl and $NaHSO_3$ treatment	97
PA/PSf	DI/1.0 M	22	12.9	PSf support layer reinforced by PVP	98
PA/PES-PET	DI/1.0 M	25	12.5	—	131
PA/PK	DI/0.6 M	28	6.1	PK reinforced by PED non-woven fabric	132
GO membrane	17 mM/1.0 M	6.9	12.8	—	133
PA/PET	DI/1.0 M	21	12.1	PSf/GO and PSf/HNT (dual layer) nanocomposite on PET	101
PA/TR-PBO	DI/1.0 M	15	17.9	TR-PBO (thermally rearranged polybenzoxazole-co-imide)	104
PA/PAI	DI/1.0 M	21	12.1	PA incorporated with SNW-1 nanocomposite	102
PA/TR-PBO	DI/3.0 M	27	87.2	TR-PBO ESMs exposed to direct fluorination	105
PA/TR-PBO	DI/1.0 M	21	26.6	TR-PBO modified with PVA coating	134
PA/PE	DI/1.0 M	20	35.7	PA formed by toluene-assisted IP	103

additives into support layer is another common strategy applied in membrane research for PRO applications. Li *et al.*[96] realized polydopamine (PDA) modification onto the polyamide-imide (PAI) support layer. Son *et al.*[97] successfully embedded carbon nano tubes (CNTs) into the polyethersulfone (PES) support layer, obtaining a power density output of 1.6 W m^{-2} at a hydraulic pressure of 6 bar, using deionized (DI) water and NaCl solution of 0.5 M. Wei *et al.*[98] realized polysulfone (PSf) support layer reinforced by polyvinylpyrrolidone (PVP), and obtained a maximum power density of 12.9 W m^{-2} at hydraulic pressure of 22 bar.

Flat sheet membranes could also be prepared by electrospun polymeric supports of high porosity and tortuosity. A highly-porous support layer was realized by Bui *et al.*[99] by electrospinning polyacrylonitrile (PAN) nanofibers onto a polyester (PET) fabric substrate. Tian *et al.*[100] prepared tiered polyethylenimine (PEI) nanofibrous support incorporated with multi-walled CNTs. Use of such membrane in PRO system generates a power density of 17.3 W m^{-2}. A dual layer of PSf/GO (graphene oxide) and PSf/HNT (halloysite nanotube) of nanocomposite on PET was prepared by Lim *et al.*[101] to ameliorate water permeability.

The possibility of incorporating nano-sized materials into conventional membranes has been well developed by researchers. Gonzales *et al.*[102] incorporated Schiff base network-1 (SNW-1) nanocomposite into the PA active layer preparation. The PRO system reached its maximum performance of 12.1 W m^{-2} with DI water and brine water of

1M. Kwon *et al.*[103] realized a toluene-assisted interfacial polymerization to fabricate active layer of PA onto a polyvinyl alcohol (PVA)-coated polyethylene (PE) support. An astonishing power density of 35.7 W m^{-2} was reported for a hydraulic pressure of 20 bar. Recently, a Korean research group reported a novel thermally rearranged TFC membrane containing polybenzoxazole-co-imide (TR-PBO) combined with a PA layer.[104] A giant power density increase towards 40 W m^{-2} was reported in its first work. Later, modification with fluorination on TR-PBO membranes ameliorate the output power density towards 87.2 W m^{-2} in PRO applications.[105]

There is no doubt that tremendous advances were achieved in flat-sheet PRO TFC membranes. However, most published works presented here focus on gross power densities, calculated by eqn (3). Actually, the module gross power densities presented here differ from the net power density due to the irrecoverable pumping energy input and the energy losses during electricity generation in turbine systems.[106] Taken into consideration the pumping energy inputs and energy losses, the net power density in published works might be much lower than its gross value. A detailed economic analysis of PRO systems will be given later.

In conventional PRO configuration using flat-sheet membrane, a feed spacer is needed to maintain the feeding channel geometry and reinforce the mass transfer near the membrane.[107] Such configuration decreases the hydraulic pressure and results in an energy loss in the PRO system.[108] In addition, feed spacers might cause membrane deformation at high hydraulic pressure, inducing severe reverse solute diffusion of the membrane and leading to performance loss.[86]

Different from flat-sheet membranes, hollow fiber PRO TFC membranes have a self-supporting tubular shape of higher effective surface area. Such geometry avoids the use of feed spacers, thus limit the deformation failure in flat-sheet based PRO systems. The PRO module using hollow fiber membranes could also achieve a higher pack density, which could efficiently ameliorate output performances.[109] The major preparation method of the hollow fiber membrane is the phase separation spinning, including non-solvent induced phase separation (NIPS) or thermal induced phase separation (TIPS).[77]

The first work dealing with hollow fiber TFC membranes for PRO application was realized by Chou *et al.*[110] They successfully prepared a tubular self-supporting membrane made of PES as the supporting substrate and PA as the selective layer. A maximum power density of 10.6 W m^{-2} could be achieved by using the home-made hollow fiber PRO membrane with a salt concentration of 40 mM and 1 M for fresh and salt water chambers, respectively. The same group prepared a novel hollow fiber TFC membrane using PEI as the supporting substrate.[111] This PEI based hollow fiber membrane presents superior mechanical strength and shows a better power density output of 20.9 W m^{-2} under a hydraulic pressure of 15 bar.

Similar to flat-sheet PRO TFC membranes, chemical modifications on selective layer and the supporting substrate are both widely investigated in the research field. The work of Ingole *et al.*[112,113] proves the effectiveness of PDA coating on PES supporting substrates in PRO applications. A power density increase from 1.62 W m^{-2} to 3 W m^{-2} is realized due to the additional coating. Grafting of chemical groups on supporting substrates were also reported in literature.[114,115]

Ingole *et al.*[116] prepared CA layer treated with tributyl phosphate (TBP) onto the supporting substrate of PES with PDA coating. An improved power density of 3.9 W m^{-2} is achieved with the same brine water and fresh water conditions used in their previous work. Zhang *et al.*[117] reported a novel supporting substrate of PES with PDA coating, grafted with dendritic-architecture sulfonated hyperbranched polyglycerol (SHPG). A superior resistance to protein adhesion and bacterial attachment is achieved due to the high wettability of the polymer brushes. A maximum power density at hydraulic pressure of 15 bar is reported to be 18.8 W m^{-2}.

An emerging trend nowadays is to incorporate nanocomposites into membrane preparation. Zhao *et al.*[118] grafted carbon quantum dots (CDQs) onto the PDA coating of the PES supporting substrate by covalent bonding during the hollow fiber membrane preparation. They obtained a maximum power density of 11 W m^{-2} at a hydraulic pressure of 15 bar. Another work of incorporating CDQs in PA selective layer was realized later by Gai *et al.*[119] They reported a better power density of 34.2 W m^{-2} at hydraulic pressure of 23 bar. Park *et al.*[120] incorporated graphene oxide nanosheets with PES supporting substrate.

In addition, numerous research work investigated on modifications of hollow fiber membranes to limit bio-fouling problems. Synthetic sea brine solutions with complex components were used in fouling experiments and the power density of PRO systems was tracked along the procedure. Zhao *et al.*[121] reported the use of MPC (2-methacryloyloxyethylphosphorylcholine)-PDA coating on PES support layer to enhance anti-fouling capacities of the system. Le *et al.*[122] presented the effect of using grated zwitterionic poly(sulfobetaine) on PA selective layers.

Table 3 lists the present work of hollow fiber PRO TFC membranes in literature.

3.1.3 Economic analysis. Ever since the appearance of PRO system, the debate on its technological and economical feasibility has never stopped. In 2008, the power density threshold for PRO commercialization was reported to be 5 W m^{-2}.[155] This result was taken as reference for the PRO application of Statkraft in Norway and for numerous studies published later. However, based on the novel economic framework developed by Chung *et al.*,[106] the economical viable threshold of PRO power density was revalued. The net power density enabling the commercial interest of PRO to compete with present solar photovoltaic power plants is estimated to be 56.4 W m^{-2}, with a suggestion of membrane cost at 15 \$ per m^2. Here, the levelized cost of energy (LCOE) is set to be 0.074 \$ per kW h. Net power density and gross

Table 3 A summary of present PRO systems using hollow fiber PRO TFC membranes

Materials	Concentration gradient	Hydraulic pressure (bar)	Power density (W m^{-2})	Comments	Ref.
PA/PES	40 mM/1 M	9	10.6	—	110
PA/PEI	1 mM/1.0 M	15	20.9	—	111
PA/PI	DI/1.0 M	16	14	—	123
PAN-PVP/PBI-POSS	10 mM/1.0 M	7	2.5	—	135
PA/PI	DI/1.0 M	20	7.6	PDA coating	136
PA/PES	DI/1.0 M	20	24.3	—	137
PA/P84 co-polyimide	DI/1.0 M	21	12	—	115
PAN-PVP/PBI-POSS	10 mM/1.0 M	15	5.1	PAN/PVP with APS post-treatment	114
PA/PI	DI/1.0 M	15	16.5	—	138
PA/PES	DI/0.6 M	6	1.62	—	112
PA/PES	DI/0.6 M	7	3	PDA coating	113
PA/PES	DI/0.6 M	8	3.9	PA treated with TBP with PDA coating	116
PA/PES	DI/3.5% (w/w)	16	6.7	PES grafted with HPG	115
PA/PI	DI/1.0 M	16.2	12	—	139
PA/PES	DI/1.0 M	18	11.2	—	140
PBI/PVP/PAN triple layer	10 mM/1 M	22	6.2	—	141
PA/PES	DI/1.0 M	20	7.8	—	142
PA/PES	DI/1.0 M	20	22.1	Pre-stabilization	143
PA/PEI	DI/1.0 M	17	9.6	Pre-wetting	122
PA/PEI	DI/1.0 M	13	13	PA modified with APTMS	144
PA/PES	Wastewater/0.81 M	15	7.7	PES with MPC- PDA coating	121
PA/PEI	DI/1.0 M	15	19.2	—	145
PA/PEI	—	17	9.5	—	146
PA/PES	DI/1.0 M	22	10.7	—	147
PA/PES	DI/1.0 M	20	22	—	148
PA/PES	DI/1.0 M	15	10.7	PA dual layer on both sides	149
PA/PEI	DI/1.0 M	15	16.2	PA with LbL deposition of PAH and PAA	146
PA/PES	DI/0.81 M	15	11	PDA coating grafted with CQDs	118
PA/PES	DI/1.0 M	20	20	PES with $CaCl_2$ additive tuning	150
PA/PES	Wastewater/0.81 M	20	18.8	PDA coating grafted with SHPG	117
PA/PEI	DI/1.0 M	15	8.9	—	151
PA/PES	DI/1.0 M	23	34.2	PA incorporated with CDQs	119
PA/PAI	Wastewater/1.0 M	13	4.3	PAH post-treatment	152
PA/PES	DI/1.0 M	16.5	14.6	PES incorporated with GO nanosheets	120
CTA/CA T-NIPS membrane	DI/1.0 M	18	5.5	—	153
PA/PES	DI/1.0 M	17	14.6	PA incorporated with PP-SO_3H	154

power density fundamentally differ because of the inherent overhead associated with the PRO process in the form of irrecoverable pumping energy input. The importance of using net power density in PRO system characterization is emphasized for better guidance of the technology development. Several evaluations focused on different cases were also reported. Mashrafi *et al.*[156] provide an environmental and economic case study of PRO system implantation in Tampa Florida. A LCOE between 0.62–0.97 $ per kW h is estimated for feed water of different salinities. Based on the analysis model, suggestions including waste water treatment (as feed water) or PRO installation near waste water source (within 1 km) could effectively reduce the LCOE down to 0.14 $ per kW h. Khasawneh *et al.*[157] analyzed the feasibility of installing PRO power plants with Red Sea-Dead sea waters. It was demonstrated that the project is technically and economically feasible, with a LCOE of 0.056 $ and a power of 134.5 MW. The membrane cost is estimated to be 25 $ per meter square. Based on hypersaline water sources, the extractable energy density in this case study surpass the conventional river-sea water sources, providing a positive estimation on installation of PRO systems.

Straub *et al.*[78] reported a thorough energetic analysis of PRO system harvesting blue energy in river water and sea water. An estimation for energy inputs and outputs in the system was presented separately. Overall, the expected energetic inputs will most likely surpass outputs, resulting in a negative power generation. The major cause is the insufficient energy density extractable in mixing of river and sea sources. However, systems with higher concentration gradients can sufficiently overcome the energy output limit mentioned above, though technical problems including biofouling and selectivity decrease remain to be solved. Touati *et al.*[71] confirmed the viability of open-loop PRO and close-loop PRO by using low-concentration feed solutions. However, the analysis of hybrid SWRO-PRO systems results in a negative energy generation.

Though the debate of the viability of PRO system never stops, industrial attempts using PRO prototypes continues in the globe. The first commercialized plant was conducted by Statkraft in Norway from December 2009.[158] The aim of the project is to produce an 8 inch spiral wound module of 2000 m^2 which is able to produce a total of 10 kW of power, corresponding to a power density of 5 W m^{-2}.[159] However, the actual performance of the PRO plant failed to reach the initial objective, delivering a total power of 2 kW, which corresponds only to 20% of the designed power.[160] Due to the lack of membrane optimization and high cost in accessory systems, the sale price of a PRO plant reaches 70–100 euros per MW h and showed low economic interests, compared with the actual electricity price of 30–40 euros in Norway. The whole system was unfortunately shut down in 2013. Researchers and engineers performed another prototype experiment in Quebec, Canada.[159] The main objective of the project is to carry out process optimization studies of performing water pretreatment to prevent biofouling problems. A novel project was started in Japan to install an additional prototype PRO module, using commercial CTA hollow fiber membrane modules, to the Fukuoka WRO desalination plant to form a RO-PRO joint system.[159] A maximum power density of 13.3 W m^{-2} was achieved by a 10 inch hollow fiber membrane module. Nowadays, a similar hybrid RO-PRO project is developed jointly by Saudi Arabia and Japan, aiming to develop efficient PRO systems for energy recovery and environmentally friendly high saline water treatment used in RO desalination processes.[161]

Overall, stand-alone PRO systems with sources of higher salinity difference seem to be more promising due to a higher extractable energy density. The development of commercialized inexpensive PRO membranes is of key importance, which could sufficiently increase the system performances and reduce the production and maintenance costs. Considering the rising electricity price in Europe due to the lack of gas and the emerging technology development in PRO systems, the economic threshold of PRO system might be reached in the near future.

3.2 Reverse electrodialysis

Proposed by Pattle *et al.* in 1954,[162] reverse electrodialysis (RED) is the earliest technology proposed for blue energy extraction. In a classic RED configuration, sea water and river water were injected respectively into two different compartments separated by an ionic exchange membrane (IEM). This approach corresponds to the reversed process of the electrolysis (ED), where IEMs are used with an electric current to remove salts from sea water for pure water production. Years after, no significant development has done until 70s, when Lacey in 1980 developed his model for the RED.[163] To understand how an RED device works, it is necessary to understand how an ion exchange membrane behaves when it separates two salt solutions of different concentrations. This question will be answered in the following subsection.

3.2.1 An ionic exchange membrane separating two different salted solutions. An electrical potential difference occurs between two solutions of different salinity when an ion exchange membrane separates them. As illustrated in Fig. 13, this potential difference is the sum of several terms[164] and writes: $E_m = \Delta\phi_{D,L} - \Delta\phi_{D,H} + \phi_{m,L-H} + \phi_L^{SDL} + \phi_H^{SDL}$.

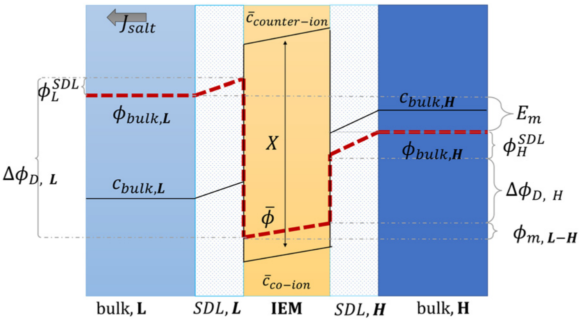

Fig. 13 Schematic representation of concentration, c, and potential, ϕ, profile in the bulk solutions, the stagnant diffusion layers (SDLs), and in an ion exchange membrane (IEM) (figures and captions adapted from ref. 164 with permission from FIMTEC & MPRL, copyright 2016).

$\Delta\phi_{D,L}$ is called the Donnan potential in the diluted solution. It comes from the difference in ion concentration at the solution–membrane interface. In this context, the equality of chemical potentials leads to:

$$\mu_i^0 + RT\ln(a_{i,L}) + z_i F\phi_L = \mu_i^0 + RT\ln(\bar{a}_{i,L}) + z_i F\bar{\phi}_L \tag{4}$$

$$\Delta\phi_{D,L} = \frac{RT}{z_i F}\ln\left(\frac{\bar{a}_{i,L}}{a_{i,L}}\right) \tag{5}$$

where F is the Faraday constant, z_i the valence of the ion, R the gas constant, T the temperature, $a_{i,L}$ and $\bar{a}_{i,L}$ are the activity of the ions on the external and the internal side of the membrane in the diluted electrolyte, respectively. ϕ_L and $\bar{\phi}_L$ are the electrical potential on the external and the internal side of the membrane in the diluted electrolyte, respectively. $\Delta\phi_{D,H}$ is the Donnan potential characterizing the concentrated solution. $\phi_{m,L-H}$ is the difference of potential occurring inside the membrane. ϕ_L^{SDL} and ϕ_H^{SDL} are the difference of potential created by stagnant double layers (boundary layer) that build up close to the membrane. These layers, also named as polarization layers, have fundamental impacts with the presence of electric current. As we will see later, they are usually considered as non-ohmic resistances in the analysis of RED systems. The modeling of all these terms is complex and requires complicated numerical simulations.

A simple limit can be found. In the absence of electric current through the membrane, in the case of a rigorously selective membrane, the diffusion potential vanishes. Neglecting the stagnant double layers, the open circuit voltage writes:

$$E_m = \frac{RT}{z_i F}\ln\left(\frac{\gamma_H c_H}{\gamma_L c_L}\right) \tag{6}$$

where γ_H and γ_L the activity coefficients, and c_H and c_L are the concentrations of concentrated and diluted respectively, with $a_i = \gamma_i c_i$.

Under the assumption of an open circuit and neglecting the polarization layers, this equation can be generalized to a non-selective membrane by writing: $E_{\mathrm{m}} = \alpha \frac{RT}{z_{\mathrm{i}}F}\ln\left(\frac{\gamma_{\mathrm{H}}c_{\mathrm{H}}}{\gamma_{\mathrm{L}}c_{\mathrm{L}}}\right)$, where $\alpha = \frac{t^{+} - t^{-}}{t^{+} + t^{-}}$ with t^{+} the transport number of the cation and t^{-} the transport number if the anion. To go further and calculate α, the modeling of all these terms is required. The most widely used description comes from the Teorell–Meyer–Sievers[165] theory which is a one-dimensional model that does not take into account the ions concentrations variations in the pore section of the membrane, nor the fluid transport by convection. The space charged model developed by Osterle and colleagues[166] takes into account these two points. Recently, interactions with surfaces and electro-osmotic effects have been taken into account in calculations to explain the strong ionic currents generated by charged but *a priori* non-selective nanotubes of more than 20 nanometers in diameter.[167] We will return to this point later in the text.

In a more pragmatic way, this description of the membrane potentials leads to propose an electrical scheme for a membrane. In the presence of different salt concentrations on both sides of the membrane, the membrane behaves like a voltage generator E_{OCV} which is the open circuit voltage in series with a resistor and with elements that account for the polarization layers. These double layers are resistors in parallel with phase elements or simply resistors.[168,169]

3.2.2 The RED cell. The RED device takes advantage of the potential difference that appears on an ion exchange membrane when it separates two saline solutions of different concentrations. A classic RED stack configuration is illustrated in Fig. 14. Two types of IEMs are used in this configuration: anionic exchange membranes (AEMs) which allow the passage of anions and cationic exchange membranes (CEMs) which allow the passage of cations. These membranes are separated by spacers and are placed alternatively so as to form alternative water compartments. Diluted and concentrated solutions are injected continuously in water compartments by pumps. At two ends of the stack, two electrodes are placed with circulating electrolytes for energy conversion by redox reactions. In each compartment of the cell, where the solutions can circulate generally through a spacer to ensure an uniform flow, the ions try to move from the concentrated solution to the dilute solution to balance the chemical potentials, but due to the charge of the IEMs, only one type of ion is allowed to pass and the other type will be rejected. Thus, an ionic flux is generated allowing an electrochemical potential to establish in the surface of the membrane called Donnan potential. This potential is converted to electricity by faradaic reactions at the end of the cell by the electrodes and electrolytes.

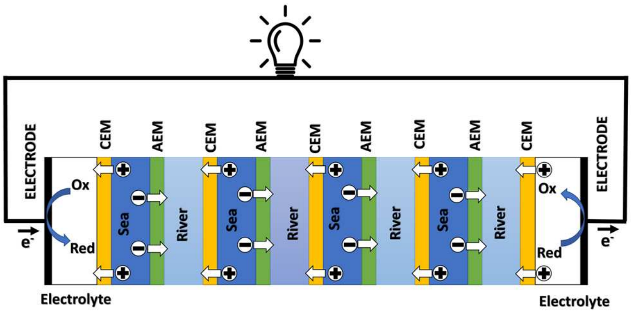

Fig. 14 A schematic illustration of the RED process.

In the following we will detail all the elements of the cell.

Electrodes. Electrodes are used in RED stacks for the conversion of osmotic-driven ionic flux into an electric current by faradaic reactions. The choice of electrodes is of great importance for the optimization of energy conversion efficiency in RED stacks.[170] Several electrodes were proposed for RED systems, from participating electrodes like Ag/AgCl to inert ones like Pt, and with redox reactions ranging from hydrogen/oxygen reactions to more complex like $\mathrm{Fe(CN)_6}^{3-}$/$\mathrm{Fe(CN)_6}^{4-}$. These electrodes are classified to three main types summarized in the Table 4. The oldest electrodes[162,171] were made of two metals immersed in a solution containing the metal ions. The metal (or the amalgam such as Ag/AgCl) participates directly in the red-ox reaction. Thereby, the electrodes were consumed during the process and their life span remains limited. For theses reasons, participating electrodes were dropped out in the latest development.[172,173] After that, inert electrodes were proposed to avoid the regeneration problem. They interact directly with the electrolytes and forming gases which is their major drawback.[174] Inert electrodes are used jointly with redox couples dissolved in the circulating electrolytes to enable the redox reactions for energy conversion. Inert electrodes present enormous applications in RED systems due to good chemical/environmental advantage. The consumed ions in one electrode will be generated in the other one, and thus leading to no net chemical reaction at the end. In the same time, because of this, the electrolyte will be conserved and no over-potential will be appear because of the gas formation. The problem with this category is the nature of the couple: for the $\mathrm{FeCl_2/FeCl_3}$ system, low pH is needed to prevent formation of solid (hydr)oxides[172] and for the Fe-complex couple, it is not stable during long time especially if exposed to light.[175]

Ionic exchange membrane. The RED is a membrane based osmotic process where IEMs are considered as the main engine of the energy recovery. Membranes are usually characterized by several properties based on the amount, structure, type and the charge of the functional groups in the membrane. These proprieties are linked. IEMs are divided to three main classes: CEMs, AEMs and bipolar membranes according to the surface charge. CEMs possess negative charges with a fixed chemical group. Generally, chemical groups of strong acids, like sulphonate ($-\mathrm{SO_3}^{-}$) and phosphorate ($-\mathrm{PO_3}^{-}$), or weak acids like carboxyl groups ($-\mathrm{COO}^{-}$) are used in CEMs. Due to the presence of negative charges in CEMs, anions in solutions are repulsed and the

Table 4 A summary of electrodes used in the RED

Type	Electrodes	Electrolyte	Advantage	Disadvantage	Ref.
Inert electrodes with reversible reactions	Ti–Ru/Ir mesh	$K_4Fe(CN)_6$ $K_3Fe(CN)_6$	No electrolysis voltage losses	Sensible to light	176
	Ti–Ru/Ir mesh	$Fe(Cl)_2/Fe(Cl)_2$	No net chemical reaction Bidirectional system	Sensible to pH	172
Inert electrodes with irreversible reactions	Ti-Ru/Ir mesh	NaCl	No net chemical reaction	Voltage loss H_2 generation	174
	Ti–Pt mesh	Na_2SO_4		Cl_2 generation	177
Participating electrodes	Ag/AgCl	NaCl	No net chemical reaction	Switching flows	178
	Cu	$CuSO_4$	No electrolysis voltage losses	Electrodes regeneration	162
	Zn	$ZnSO_4$			171

Table 5 A summary of the most used IEMs in literature

Membrane	Thickness (μm)	IEC (meq g^{-1})	SD (%)	CD (meq g^{-1} H_2O)	α (%)	R (Ω cm^2)	Ref.
CEM							
Neosepta CMX	164	1.62	18	9.0	99	2.91	179
Neosepta CMS	150	—	—	—	97	1.4–1.8	180
Neosepta CM-1	133	2.3	20	11.5	97.2	1.67	179
Neosepta CIMS	150	2.3	30	7.7	—	2.49	181
Fumasep FKD	113	1.14	29	3.9	89.5	2.14	179
Fumasep FKS-20	20	1.24	—		99	1.7	182
Fumasep FKE	34	1.36	12	11.3	98.6	2.46	179
Selemion CSO	—	1.04	16	6.4	92.3	2.26	183
Selemion CMV	101	2.01	20	10.1	98.8	2.29	179
Fujifilm V1	125	—	—	—	93	1.6	184
Fujifilm CEM RP1 80050-04	120	1.45	—	—	96	2.55	182
Nafion-115	139	0.9	—	8	—	—	185
Nafion-117	201	0.9	—	7.7	—	—	185
Ralex CMH	764	2.34	31	7.5	94.7	11.33	179
Qianqiu CEM	205	1.21	33	3.7	82	1.97	186
Tailor-made SPEEK 65	72	1.76	35.6	—	89.1	1.22	186
Tailor-made SPEEK 40	53	1.23	23	—	95.3	2.05	186
AEM							
Neosepta AM-1	126	1.77	19	9.3	91.8	1.84	179
Neosepta AFN	163	3.02	43	7	88.9	0.7	179
Neosepta AMX	134	1.25	16	7.8	90.7	2.35	179
Neosepta ACS-8T	150	1.9	—	—	—	2.41	181
Fumasep fad	74	0.13	34	0.4	86	0.89	179
Fumasep fas-20	20	1.5	31.25	4.8	95.5	0.5	182
Selemion DSV	121	1.89	1.03	183.5	89.9	1.03	179
Selemion APS	138	0.29	147	0.2	88.4	0.68	179
Selemion AMV	110	2.2	21	10.5	95	2.44	187
Fujifilm TYPE I	115	—	—	—	91.9	1.3	180
Fujifilm AEM RP1 80045-01	120	1.28	—	—	96	1.83	182
Fujifilm V3B	84	1.7	23	7.39	87	1.36	187
Fuji V3A	66	2.2	23	9.57	82	0.87	187
Fujifilm V1	139	1.8	23	7.83	90	1.05	187
Fujifilm V2	53	1.6	23	6.96	86	0.67	187
Ralex AMH-PES	714	1.97	56	3.5	89.3	7.66	179
Qianqiu AEM	294	1.33	35	3.8	86.3	2.85	186
Tailor-made PECH A	77	1.31	32.2	4.1	90.3	2.05	186
Tailor-made PECH B2	77	1.68	49	3.4	87.2	0.94	186
Tailor-made PECH B1	33	1.68	49	3.4	86.5	0.82	186

cations pass. For AEMs, cations are repulsed due to the positively charged chemical groups including ammonium ($-NR_3^+$), primary amine ($-NH_2$), secondary amine ($-NRH$) and tertiary amine ($-NR_2$). Bipolar membranes have simultaneously negative and positive chemical groups and display fascinating applications in water splitting. The main characteristics of commercial membranes, *i.e.* the swelling degree, the ion exchange capacity, the fixed charge density, the permselectivity, and the membrane resistance are reported in the Table 5.

The swelling degree (SD) characterizes the ability of a dry membrane to absorb water. It measures the mass change ratio of a dry membrane before and after water immersion:

$$\mathrm{SD} = \frac{m_{\mathrm{wet}} - m_{\mathrm{dry}}}{m_{\mathrm{dry}}} \times 100 \quad (7)$$

where m_{wet} is weight of the wet IEM and m_{dry} is weight of membrane in its dry phase.

Ion exchange capacity (IEC) determines the number of fixed charges inside the IEM per unit of mass of a dry membrane. The fixed charges in the membrane are usually in equilibrium with the ions in the electrolytes, this equilibrium is given by the Fixed charge density (CD) and it is defined as the milliequivalents of charged groups per gram of water in the membrane. It is given by:

$$\mathrm{CD} = \frac{\mathrm{IEC}}{\mathrm{SD}} \quad (8)$$

The permselectivity (α) is one of the most important parameters for ionic exchange membranes. It describes the ability of a membrane to reject co-ions (ions of same charge) and allow the passage of counter ions. An ideal membrane, which blocks all co-ions and allows passage of 100% of counter ions, is characterized by a selectivity of 1. In practical applications, the effective selectivity can be calculated by the ratio between the electrical potential measured between the electrodes and the theoretical one for an ideal membrane under a given gradient.

The membrane is a part of an electrochemical cell where the ionic current is converted to an electrical one. This current is directly affected by the conductivity of this membrane (ohm loss) and can influence the power density. This resistance is reported to a unit of area. It depends on the material's property and its structure (see Table 5).

These properties depend on the conditions of use such as the concentrations of the saline solutions, the value of the difference in salinity, the acidity, the temperature. Using a very high concentration can reduce membrane selectivity even though it gives better conductivity.[169,173] A high temperature[173] decreases the permselectivity of the membrane.

The characteristics of the membranes depend on the mode of production based on which IEMs are classified into homogeneous IEMs and heterogeneous IEMs.

For the first class, the membrane is prepared using just one product, generally, by polymerization of a charged/can be charged monomers or followed by grafting functional monomers on a film/dissolved polymer.[188] On the other hand, heterogeneous IEMs contain two parts, an ionic exchange resin mixed with an uncharged polymer matrix without any chemical bound. Homogeneous IEMs exhibit excellent electrochemical properties, very low resistances and high permselectivity.[189] Their thickness is between 1 and 30 μm. However, their production is more complicated and more expensive. In contrast, heterogeneous IEMs are easier and less expensive to prepare with a good mechanical and chemical stability especially for the AEMs in alkaline electrolyte. However, their high resistance is still a major challenge for the RED technology.[179] Recently, N. D. Pismenskaya *et al.*[189] modified an heterogeneous membrane by grafting functional quaternary ammonium groups to increase its electrochemical performance. The results are encouraging and close to that of a homogeneous IEM.

3.2.3 The power density. The maximal electrical power density in a RED cell is given by[174]

$$P_{\max} = \frac{{E_{\mathrm{ocv}}}^2}{4R_{\mathrm{cell}}} \quad (9)$$

where E_{ocv} is the potential generated using an ionic exchange membrane between two solutions under a salinity gradient. It can be described by the following equation:

$$E_{\mathrm{ocv}} = \alpha N \frac{RT}{zF} \ln\left(\frac{c_{\mathrm{H}}\gamma_{\mathrm{H}}}{c_{\mathrm{L}}\gamma_{\mathrm{L}}}\right) \quad (10)$$

With α the selectivity of one membrane, N the numbers of membranes, T the temperature, z the valence ($z = 1$ for Na^+), R the gas constant, F the Faraday constant, γ_{H} and γ_{L} the activity coefficients, and c_{H} and c_{L} are the concentrations of concentrated and diluted solutions, respectively. And R_{cell} is the cell resistance which consists of two main parts, an ohmic one that represents the conductivity of cell components (including membrane, solutions, spacers, and *etc.*) and a non-ohmic part which involves the concentration change inside the cell. The non-ohmic part is caused by the polarization effect near membranes and by the salt concentration variation along the water channel.

To develop a production cell, it is necessary to choose the number of membranes to be used. *A priori*, it is interesting to increase the number of membranes. Using a large number of membranes should make the whole device more compact. When the salinity of the solutions is fixed, E_{ocv}, and $P_{\max}$ increases theoretically linearly with the number of cell pairs and is independent of the flow rate. The power density should therefore not be depend upon the number of membranes.

Experimentally, H. Kim *et al.*[196] observe a different behavior. When the stack is supplied with a constant flow, the gross and net power density decrease when the number of membranes becomes higher than.[200] These phenomena are caused by the polarization of the cell. When the pairs of cells are more numerous, the local flow rate decreases in each cell which favors mixing, the appearance of a concentration gradient along the flow and the growth of the thickness of stagnant ionic layers.

In fact it comes from the polarization the open circuit potential increases with the number of cell pairs but the growth law between the two is weaker than a linear law. When the number of cells is fixed, the open circuit potential increases slightly with the flow rate. As the number of cells increases, the throughput in each cell is lower and the polarization effects along the cell but also the thickness of the depleted layers increases. Both effects induce a decrease of the open potential.

According to eqn (9), an efficient way for power density optimization is to increase the open-circuit voltage E_{ocv}.

Several research works managed to ameliorate the membrane selectivity a or increase the number of IEM pairs used in RED systems. Güler *et al.*[186] tested several IEMs and found that the permselectivity could be independent of the thickness. H. Kim *et al.*[196] showed that the using a big number of cell pair will affect the residence time of the ions inside and therefore the concentration polarization inside the cell will cause a diminishing of the potential compared to the theoretical value.

For the non-ohmic resistance, the challenge is always present. Vermaas *et al.*[193] attempted to improve mixing inside the cell to reduce the boundary layer using a specific spacer with filled channels and with sub-corrugations (see Fig. 15B) without much success.

Though the use of more than 45 membranes in the RED system, Pattle *et al.*[162] reported a mild power density of 0.2 W m^{-2} because of the low efficiency of their stack. Numerous studies continues today in the hope of promoting output power density of RED systems. In 2007, Dlugolecki *et al.*[179] investigated the performance of several membranes used generally in the RED, and estimated that a power density of 6 W m^{-2} can be achieved by commercial IEMs. A year after, a power density of 0.84 W per square metre of membrane was obtained in the work of Turek *et al.*[177] with a high salinity gradient (around 200) and even a 0.9 W m^{-2} is reached by Veerman *et al.*[190] with a salinity difference of 30 g L^{-1} *vs.* 1 g L^{-1} of NaCl for the concentrated and the diluted solution respectively. High cell resistance hinders the electrical performance of RED systems.[174] It was reported that the diminution of spacer thickness (from 485 μm to 100 μm) could effectively reduce the ohmic resistance of the system by 4.[176] With these RED improvements, Vermaas *et al.*[176] obtained a gross power density of 1.8 W m^{-2} using just 5 pairs of IEMs. However, for thinner spacers, a higher pressure loss was reported. A net power density of 1.2 W m^{-2}, which remains the highest experimental net power density documented until present, was achieved in this work. The same team tried to removed the spacers and employed profiled membranes to reduce water volume (higher conductivity). While a significant ohmic resistance drop of 30% was achieved, the profiled membranes suffered from severe polarization problems which reduces the ohmic resistance around 30% but the polarization resistance was significantly higher.[191] Adding sub-corrugations to disturb the uniform flow and enhance the mixing was insufficient to increase the net energy power.[193]

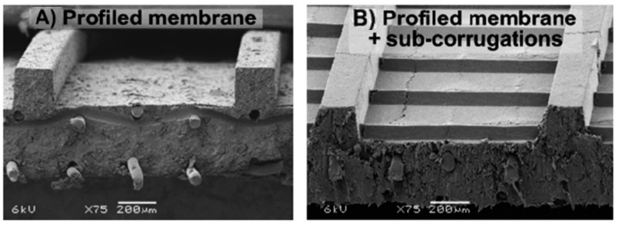

Fig. 15 Images obtained from a scanning electron microscope for (A) the profiled membranes (B) and profiled membranes with sub-corrugations (figures and captions reproduced from ref. 193 with permission from Elsevier, copyright 2014).

As already described, the potential E_{ocv} between the stack's electrodes is directly related to the gradient. Daniilidis *et al.*[173] investigated the RED stack for hypersaline solution like the Dead sea, with a concentration close to the saturation (around 5 M) with a river water of 0.01 M concentration and they obtained a gross power density 3.8 W m^{-2} at 25 °C and more than 6.5 W m^{-2} at 60 °C in 5 membrane pairs cell, even if the selectivity was lower with the increasing of the temperature and the gradient. This power density corresponds to a gross power. It's worth to note that even though this energy was experimentally measured, no pumping energy consumption was subtracted. In the same topic, and to show the effect of temperature and gradient, Tedesco *et al.*[182] used a hypersaline solution at 5 M and a brackish solution with 0.1 M, and reached a gross power of 6 W m^{-2} at 40 °C in a cell with 50 membrane pairs. In this situation, the resistance of membrane pairs is low.

In fact, the recorded experimental gross power density without correction was around 4.75 W m^{-2} with 2–2.5 W m^{-2} of dissipated power due to the pressure drop inside the cell. Increasing the unit size to the double and the number of the membrane pairs had only a slight reduction in the power density caused by the non-uniform distribution of fluids concentration. The amount of the theoretical power is very huge, it is estimated to be more than 2 TW in the world rivers and oceans.[8] Just a part of this power is actually exploitable by the blue energy harvesting technologies. The efficiency is defined as the ratio between the recoverable energy and the available Gibbs free energy in the water mixing of unit volume. Higher energy efficiency is achieved when the feed waters are recycled (multiple pass)[176] and a lower current density is applied (due to ionic shortcut currents).[190]

$$\eta = \frac{P_{\max} \cdot A}{\Delta G_{\mathrm{mix}} \cdot Q} \tag{11}$$

where A is the membrane area and Q the flow rate. For the RED process, it depends on the flow rate and on the capacity of the membrane to exchange ions. As represented in the Table 6, the efficiency remains under 50%.

3.2.4 Nano RED. One way to increase the collected current density is to decrease the cell resistance and thus the membrane resistance. To do this, it has been proposed to work with membranes with nanometric sized holes. This attractive idea is based on the initial work on single nanotube. Remarkably, a giant ionic current was measured when a non-selective boron nitride nanotube (BNNT) is placed in a salt gradient (see Fig. 16).

For a BNNT placed between a 1 M and 0.01 M NaCl solution the authors measure[167] an electric current of 1 nA and a power density of 4 kW m^{-2} for a nanotube (see Fig. 17). This point is very remarkable. This potential is created by an

Table 6 The summary of processes of RED reviewed literature

Membrane	C_H (M)	C_L (M)	Temperature (°C)	Power density (W m^2)	Efficiency	Ref.
Fumasep FKD/FAD	0.507	0.017	25	0.93	18%	190
Neosepta CMX/AMX	1.899	0.01	—	0.72	—	177
Fumasep FKS/FAS	0.507	0.017	25	2	32%	176
Fumasep FKS/FAS	0.507	0.017	25	1.8	15%	176
Ralex Profiled CMH/AMH	0.507	0.017	25	0.8	<1%	191
Tailor-made SPEEK65/PECH B2	0.513	0.017	25	1.28	—	192
Qianqiu CEM/AEM	0.513	0.017	25	0.83	—	192
Custom-made composite/Selemion CEM/ASV	0.5	0.017	25	1.3	—	183
Ralex Profiled + sub-corrugations CMH/AMH	0.507	0.017	—	0.9	—	193
Neosepta CMS/ACS	5	0.01	25	3.8	7%	173
Neosepta CMS/ACS	5	0.01	60	6.7	20%	173
Fumasep FK-20/FAS-20	5	0.1	40	4.75	<1%	182
Fujifilm CEM 80045-04/AEM 80045-01	4–5	0.03	23	1.35	2–3%	194
Fujifilm CEM-80050/AEM-80045	0.762	0.005	20	0.3	—	195
Fujifilm CEM-80050/AEM-80045	0.762	0.005	60	0.705	—	195
Nafion/Neosepta N117/AMX	4	0.5	25	1.38	—	185

electrophoretic flux due to the surface charge of the nanotube. Boron Nitride surfaces bear a large surface charge.

The ion concentration profile of the salt solution placed above this surface is given by: $C_{\pm}(x,z) = C_{\infty}(x)\exp^{(-\pm\phi(z))}$ where $\phi(z)$ is the electrical potential, z the vertical position normal to the surface, x the position along the direction of the surface, $C_{\infty}(x)$ the concentration in salt far from the surface, $C_{+}(x,z)$ the concentration in positive counterions, $C_{-}(x,z)$ the concentration in negative counterions as a function of x and z. The balance along the z direction between the pressure forces acting on a fluid particle and the electrostatic forces links the pressure and concentration fields. This writes: $P(x,z) = P_{\infty} + 2k_BTC_{\infty}(x)\cosh(\phi(z) - 1)$ the concentration gradient along the loaded surface induces thus a pressure gradient

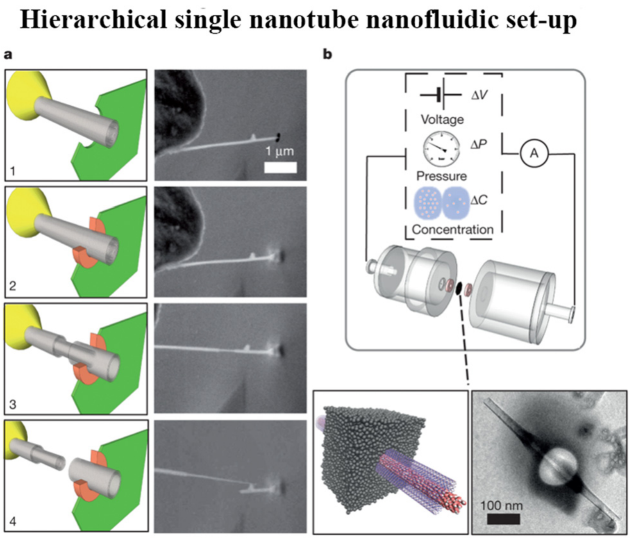

Fig. 16 a, *In situ* nanomanipulation of a BNNT (left, sketch; right, scanning electron microscope (SEM) images): 1, insertion of a BNNT (grey) through a nanopore drilled in a SiN membrane (green) using a focused ion beam (FIB); 2, carbon sealing of the FIB-drilled hole using local electron-beam-induced deposition (orange); 3, telescopic retraction of internal walls of the BNNT; 4, finalized transmembrane BNNT device. b, Top, Schematic of the experimental set-up for measuring fluid transport through the single BNNT. Bottom, sketch of the final transmembrane BNNT for nanofluidic measurements (left) and its experimental realization, imaged by transmission electron microscopy (TEM) (right) (figures and captions reproduced from ref. 167 with permission from Springer Nature copyright 2013).

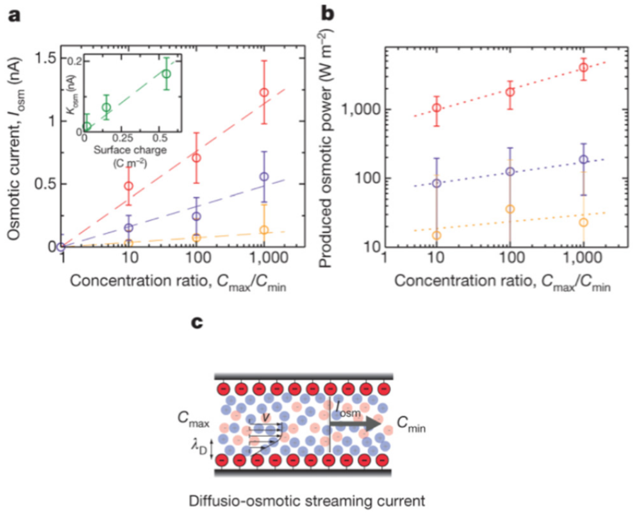

Fig. 17 a, Osmotic streaming current *versus* concentration difference for a t-BNNT with R, L 5 40 nm, 1250 nm and pH 5.5 (yellow), 9.5 (purple) and 11 (red). The experimental points show measurements for various salt concentrations in the two reservoirs, with C_{min} and C_{max} in the range 10^{-3}–1 M. Error bars follow from the corresponding error analysis. Dashed lines are linear fits: $I_{osm} \propto \log\frac{C_{max}}{C_{min}}$. Inset, Osmotic mobility *versus* surface charge. Surface charge is obtained from independent conductance measurements. The dashed line is a linear fit with proportionality factor of 0.33 for the chosen units. b, Corresponding power density (per unit surface of the BNNT) for the three values of pH. Dotted lines are a guide to the eye. In the present graph, the minimum concentration is fixed to $C_{min} = 10^{-3}$ M. b, Sketch of the osmotically driven streaming current under a salt concentration difference, $C_{max} - C_{min}$ (figures and captions reproduced from ref. 167 with permission from Springer Nature, copyright 2013).

along the same surface. This pressure gradient is at the origin of a Stokes flow in the nanotube whose maximum speed is given by: $V = \frac{k_\mathrm{B}T}{2\pi\eta l_\mathrm{b}}\ln\left(1-\gamma^2\right)\frac{\mathrm{d}\log C_\infty}{\mathrm{d}x}$ with $\gamma = \tanh\left(\frac{e\phi_\mathrm{o}}{4k_\mathrm{B}T}\right)$ and ϕ_o the surface potential. The diffusion–osmotic flow drags the ions and produce an electric current by convection of the ions in excess. We recall that as the surface is charged, and as the liquid plus the surface is neutral, the liquid alone bears a charge which is opposed to the surface one. The obtained electrical current and potential drop are proportional to $\Delta\log C_\infty$. This modeling is in quantitative agreement with the measurements.

A quantitative analysis of these equations shows that the power gain in the system comes from the very low electrical resistance of the nanopores. The potential difference across the nanotube is not exacerbated and remains about 100 millivolts under classic experimental conditions. The theory recovers an expression close to the one presented for the selective membrane when the radius of the nanopore goes to zero and when the surface charge is high. This study has prompted many groups to prepare membranes with nanopores to increase the performance of the RED. At this stage, all the attempts end in failure to create large-scale membranes. Fig. 18 compares the power and extrapolated on 1 m^2 surfaces and the powers measured on membranes. Clearly there is no correspondence between the two and the maximum powers obtained remain below 10 W m^{-2}. This results comes from the existence of collective effects between nano-channels that prevent the generalization and extrapolation of the results obtained on a single nanotube. When the nanotubes are too close together in the membrane, the formation of ion depletion layer results in an effective concentration difference much smaller than the imposed one. The transport of an electrolyte within a single nanotube is therefore very different from that within a membrane.[197] The results obtained, although disappointing at the level of extrapolation, are nevertheless better than the powers obtained in the experiments with polymeric membranes. It is necessary to comment on this point. All the experiments conducted on large hole membranes are done on systems with very small surfaces generally smaller than 0.01 mm^2. The system that allows the measurement of powers includes large volume of electrolyte and electrodes of large size. In this case the ionic resistance of the compartments is negligible compared to the resistance of the membrane, which is absolutely not the case in the RED experiments.

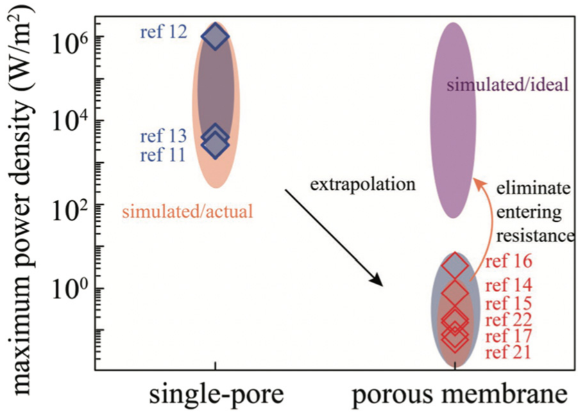

Fig. 18 Comparison between literatures reported power density and our simulated results. The range of simulated actual power density (upper left and lower right orange ovals) is approximately in agreement with that reported by literatures (blue diamond represents reported values) for both single-pore and nanoporous membrane systems, suggesting that our intuitive resistance paradigm semiquantitatively explains the orders- of magnitude power density gap between single-pore and nanoporous membrane systems. Remarkably, by eliminating the entering resistance, the simulated ideal power density (upper right oval) of membrane materials can be brought back to the single-pore level (figures and captions reproduced from ref. 197 with permission from John Wiley and Sons, copyright 2019).

It is therefore impossible to compare these data to the RED experiments. Liu *et al.*[198] have developed a nanoporous carbon membrane *via* the thermal crossing of polycyclic aromatic hydrocarbons. They obtained a mechanically robust membrane of size 1 cm with 3.6 ± 1.8 nm pores and a thickness of 2.0 ± 0.5 nm. The pore density is close to 10^{10} pore by cm^2. They carry out RED experiments on a membrane 1 micrometer in diameter. They obtain by mixing artificial seawater (0.5 M NaCl) and river water (0.01 M NaCl) a power density of 67 W m^{-2} for a circuit resistance of 15 MW. In the context of the experiment, the dominant resistance corresponds to the resistance of the membrane. The resistance of the electrolyte compartments is negligible. The resistance of the membrane can therefore be calculated and estimated to 0.19 Ω cm^2. This figure takes into account the resistance of the membrane and the resistance of the double layer near the membrane. It forgets the ohmic resistance of the solutions and the polarization resistance due to the drop of the concentration gradient along the membrane. Note that the values reported on Table 5 are closed to this one even though they do not take into account the resistance of the double layer near the membrane. To conduct a fair comparison, calculations of magnitude's order are necessary. The power generated by this membrane in the nanofluidic system is 67 W m^{-2}. To generate such power, a flow rate equal to $Q = \frac{P}{\Delta G_\mathrm{mix}} = 4.7\times10^{-5}\ \mathrm{m}^3\ \mathrm{s}^{-1}$ is required assuming an efficiency of 100%. This corresponds to a viscous power by unit area of $P_\mathrm{vis} = \frac{12\eta Q^2}{e^3b^2}$ of 26 MW m^{-2} for a gap e of 1 μm and 26 W m^{-2} for a gap e of 100 μm. The ohmic resistance of a 0.01 M saline solution is equal to 7.8 Ω cm^2 for a gap e equals to 100 μm. This value is much higher than the resistance of the membrane and must be added to it to calculate the performance in a device of 1 square meter. Clearly it will therefore be impossible to achieve such high performance in a device of one square meter in area. It is not possible to compare the power from nanofluidic devices and centifluidic devices with conventional membranes. An interesting study would be to measure the resistance of classical ion exchange membranes such as Nafion in nanofluidic systems.

In the previous framework, the creation of an ionic current in nanopores of several nanometers in diameter comes from the surface charge. Another way to do this is to be inspired by nature by creating nanopores covered by a very thin selective membrane. The realization[199] of robust mushroom-shaped (with stem and cap) nanochannel array membrane with an ultrathin selective layer and ultrahigh pore density, has notably allowed to obtain a power of 15 W m^{-2} with a 10 mM/0.5 M salt gradient. The experiments are performed on a membrane of 8000 μm^2. From the data of the article, it is possible to calculate the resistance of the membrane. This resistance is 1.6 Ω cm^2. As discussed previously, such feature is very close to the one of classical membranes, which is unlikely to present exceeded performances in our point of view.

3.2.5 River and sea water salted solutions. In order to demonstrate the feasibility of the RED approach, complex salt components, including various multi-valence ions, are added into concentrated and diluted solutions to simulate natural solutions in RED systems. Vermaas *et al.*[184] have investigated the influence of multivalent ions on the performance of cell with several membranes and different compositions for the feed solutions. The power density has a drop up to 50% for certain IEMs with the mixing of 10% $MgSO_4$ to the NaCl, and thus because of the uphill transport described in ref. 200. In fact, the valence of divalent ions is the double compared to the monovalent one, create a lower open circuit voltage. But also, the resistance is more important because of the lower diffusion coefficients of multivalent ions compared to Na^+ and Cl^- with a strongest steric hindrance of Mg^{2+}, Ca^{2+} relative to Na^+.[184] The same effect was noticed by Tufa *et al.*[201] when they added Mg^{2+} to the feed: a 64% loss of maximum power was reported. In addition, when they tested imitating real brackish water and exhaust brine with several ions, they got 63% loss in power density.

To overcome this problem, monovalent ion exchange membranes were proposed to replace the usual IEMs. Guler *et al.*[192] compared two commercial monovalent AEMs with a home-modified one, and they found that there is no significant difference on the measured gross power densities between the monovalent and the multivalent IEMs because of their high internal resistance.[180,192] Moreno *et al.*[180] tried two different strategies to minimise the negative effect of uphill transport (multivalent ions transport against the concentration gradient). The first one is using a highly cross-linked cationic monovalent membrane. This type of IEMs select the ions with the same charge based on their size (hydrated ionic radius). It blocks the multivalent ions and allows the transport of monovalent ions only. The second strategy is based on the charge rejection. A standard CEM with a thin positively charged layer on the membrane surface. A constant OCV was obtained using a mixing between NaCl and $MgCl_2$ compared to pure NaCl solution for the monovalent CEM. Also, for the coated CEM, a slight decrease in the OCV was observed. The membrane resistance was higher due to the lower ion mobility of magnesium ions inside these membranes. Hence, the power density was lower.

3.2.6 Fouling. The natural solutions are even more complicated and contain more species than the ions. Several works studied the behavior of RED stacks with natural feed. Kingsbury *et al.*[202] evaluated the response of a RED unit fed with five different pairs of real waters and wastewaters. They reported that natural organic matters reduced power densities by up to 43%. Cosenza *et al.*[203] tested different solutions from oil industrial wells, where the high concentrated solution contains an important amount of organic and dissolved solids, and the diluted solution was prepared with 0.7 g L^{-1} NaCl solution. They measured a greater resistance (around 40% at less concentrated solution) for the natural one compared to a NaCl-artificial salt water causing a 17% power loss. That effect was even worse when natural solutions from Licetto River and Tyrrhenian Sea in Italy were used in concentrated and diluted compartments, respectively.[195]

In addition to this negative effect, fouling remains a tricky problem in long-term experiment, causing severe resistance increase and permselectivity hindrance. In 2012, Vermaas *et al.*[204] established RED stacks with water feeds of naturel river water (Van Harinxmakanaal – Netherland) and natural sea water (Wadden Sea – Netherland) filtered by a 20 μm diameter filter. During the 25 day continuous test, they observed a significant resistance rise, along with a slight decrease in membrane permselectivity, which results in a power loss of 60% of the RED system. This result was confirmed by the work of Vital *et al.*,[205] where after 54 days, the power density decrease by 25%. This fouling comes in two major parts of the RED stack, the IEMS and the spacers. For the IEM we can determine two kinds of fouling depending on the charge of the membrane: the organic and the bio-fouling, generally negatively charged, are more occurred on the AEMs. In contract of the CEM, where the main problem is scaling and the solid particles. In the other hand, the fouling in the spacer can directly detect by a drop pressure jump inside the cell[204] and channel clogging, shown by Cosenza *et al.*,[203] due to bacteria growing in the channels of the RED unit and in the dilute solution circuit, hence, The fouling is most probably in river water.

To control this fouling, various strategies are proposed at different levels: before pumping the steams, inside the RED stack, by slowing the formation of fouling and after by removing all blocking particles.

The first barrier can be a simple pretreatment a 20 μm pore size mesh filter, proposed by Vermaas *et al.*,[204] to filtrate the biggest particles. Vital *et al.*[205] add to this last a second filter media composed by a 50 cm layer of anthracite (1.2–2.0 mm Ø) on top of a 50 cm layer of sand (0.5–1.0 mm Ø), placed into 11 cm Ø polyvinyl chloride (PVC) pipe. An optimization of the spacers was proposed to reduce the fouling by Vermass *et al.*[191] where they replaced the traditional spacers and IEMs by profiled membranes, and they found that the pressure drop increased four times slower and the power density remained relatively higher. He *et al.*[206] confirmed this importance of the spacers and proposed a new type with different inlet and outlet to enhance the hydraulic performance and the power density.

Another solution is to modify the anionic exchange membrane surface to make it less attractive to biofouling. Vaselbehagh *et al.*[207] coated a polydopamine layer on the surface of an AEM and found that it reduces bacterial attachment.

Various methods, suggest treating the IEMs with some polymer layer to make them selective for monovalent ions and to reduce the uphill effect and the fouling.[180] From these methods, we can find Gao *et al.*[208] who realized a deposition of two polymers poly(styrenesulfonate) (PSS) and poly(ethyleneimine) (PE) on the surface of an AEM to compare it with commercial one and they showed a good monovalent-anion selectivity comparable, a better anti-organic fouling potential and slightly lower gross power density due to the membrane resistance.

The last strategy is occurred when the fouling is already present. A physical cleaning is used by increasing the pressure or the flow rate for few seconds (a pulse) inside channels to destroy the substances clogging the channels. A chemical washing could be beneficial using some acid and alkaline solutions. To avoid bacteria and algae proliferation, a UV lamp could be installed. With these strategies, they were able to ensure a positive net power density value for more than 18 days using feed from oil well industry.[203]

3.2.7 Scale up. After the lab test, researchers tried to exploit the RED technology at an industrial scale (Table 7). In 2014, a group from a research institution (Wetsus in Netherlands) succeeded to open the first RED plant called REDSTACK with a final power capacity of 50 kW using the freshwater from Lake IJssel and the saltwater of the North Sea available at Afsluitdijk, in Netherlands.

A year after, a pilot plant is started in south of Italy with a RED unit equipped with 50 m^2 of membranes, and working with natural concentrated brine from saltworks basins and brackish water from a shoreline well over a period of five months during the summer. The gross power density was around 0.75–0.85 W m^{-2} corresponding to 40 W with an average net power of 25 W.[194] This pilot[209] has scaled up to reach more than 400 m^2 of total membrane area, delivering a 330 W of gross power capacity which is equivalent to around 0.76 W m^{-2} of power density. After that, a South Korean group built a cell with around 1000 cell pairs with a total area of 250 m^2 and tested it with Ocean lava seawater and wastewater effluent from a sewage treatment plant located beside the sea in Jeju, Korea. The pilot plant was able to produce 95.8 W of power (0.38 W m^{-2}).[213] Recently, Yasukawa *et al.*[211] obtained 0.46 W m^{-2} net power density with a stack of 200 pairs of IEMs, corresponding to 40 m^2 of total effective membrane area, and streams from a seawater reverse osmosis (SWRO) desalination plant, Mamizu Pia (Fukuoka, Japan), and the Wagiro water treatment center (Fukuoka, Japan). The same team evaluated the performance of the RED pilot plant (RED stack) with 299 cell pairs and a 179.4 m^2 membrane effective area, installed in the sea water desalination unit of Okinawa islands in Chatan town, Japan, using one-side monovalent exchange membranes to reduce the uphill effect.[181] Surface water was used as the diluted solution, while the sea water and brine from the desalination process were used as concentrated solution. The maximum gross power output of 171.6 W (0.96 W m^{-2}) for the brine/river water and 110.6 W (0.62 W m^{-2}) for the combination sea-river solutions.

3.2.8 Economic analysis. Several works discussed the economic and financial feasibility of RED for different scenarios. It was shown that the dominating influential factors include the membrane price, which remains very high at present, followed by the inflation, the relatively low experimental power generation and finally the cost of water pretreatment and pumping.[214]

Thin homogeneous membranes with low resistance are generally of high prices (above 80 \$ per m^2).[215] In 2007, Turek *et al.*[216] found a very high cost equal to 6.5 \$ per kW h by using an experimental power density value of 0.92 W m^{-2} of cell pair and considering a total investment cost of 96 \$ per m^2 of installed membrane. In 2010 Post *et al.*[217] fixed a viable power density of 2 W m^{-2} with a membrane price of 2 \$ per m^2 and cost of 0.08 \$ per kW h for the electricity.

Daniilidis *et al.*[214] suggest that if the membrane technology will be developed by using cheap raw materials and manufacturing procedures in the near future, same as in the ED technology with heterogeneous membrane, allowing a membrane price below 4.3 \$ per m^2. A net power density of 2.7 W m^{-2} will be sufficient to start producing energy. And with a LCOE fixed at 0.16 \$ per kW h will make RED electricity competitive against conventional and established

Table 7 A summary of RED pilot

Year	σ_H (mS cm^{-1})	σ_L (mS cm^{-1})	Membrane area (m^2)	Membrane pairs number	Gross power density (W m^{-2})	Ref.
2016	150–220	3.4	48.4	125	0.8	194
2017	150–220	3.4	435	1125	0.76	209
2019	52.9–53.8	1.3–5.7	250	1000	0.38	210
2020	83.5–92.3	1.3–2.2	40	200	0.54	211
2021	51.9 ± 1	0.34 ± 0.05	179.4	299	0.62	181
2021	81.9 ± 1	0.34 ± 0.05	179.4	299	0.96	181
2022	31.4 ± 4.1	0.52 ± 0.02	3.1 + 6.2	32 + 64	0.4	212

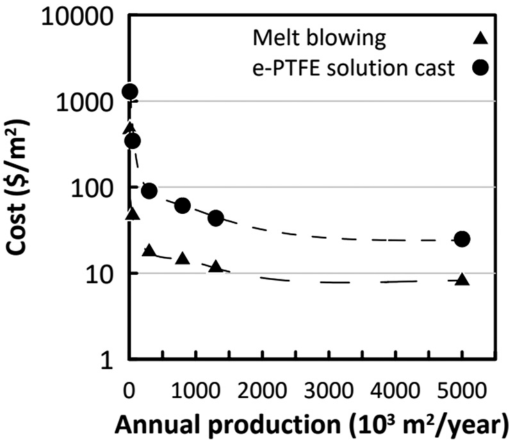

Fig. 19 Cost estimation of PFSA electrolyte membrane produced by two different methods as a function of the total yearly production (figures and captions reproduced from ref. 185 with permission from MDPI, copyright 2020).

renewable technologies. Another study was done by Toupin *et al.*[218] on the cost of Nafion and other perfluorinated sulfonic acid (PFSA) polymer electrolyte membranes. They estimated that with a higher annual production (around 5 million m^2), the cost of 1 m^2 of membrane will be below 10 $ for the melt blowing method[185,218] (see Fig. 19).

In 2019, Giacalone *et al.*[219] estimate the levelized cost of electricity ranging from 0.27 to 0.33 $ per kW h based on membrane cost of 15 $ per m^2, and using brine and freshwater. This cost is lower than the actual electricity prices in certain countries in Europe, that achieve 0.56 $ per kW h last August in Germany. It's worth to note that with the latest events in Ukraine, the fast inflation in the world, and the energy price rise (especially for the natural gas) may make the RED competitive with other power sources.

3.2.9 Miniaturized systems. We have focused in the above approach on the scale up of devices for global energy production. It should be noted that these systems can be miniaturized to power on-board sensors.[220] Sadeglian *et al.*[221] have developed 5 cm diameter cells which miniaturizes a RED system. An IEM is placed between two reservoirs which contain saline solutions of cupric sulphate of different concentrations. The system has a limited production time because it does not include flow or a phase for reconstituting the initial concentration of saline solutions. When the solutions are mixed, it is not possible to return to the initial state. This system makes it possible to obtain a peak power density of 0.7 μW m^{-2} and to deliver an energy of 0.4 mJ cm^{-3}. The previous device has the disadvantage of having a limited power generation time. To overcome this problem, Lin *et al.*[222] have associated an osmotic system composed of two gels containing saline solutions of different concentrations, a selective membrane, faradaic electrodes with a triboelectric system that allows to separate the saline solutions after their mixing. The maximum outpower is 146 μW for an external load resistance of 50 MΩ. This system is efficient and opens the way to use hybrid osmotic–triboelectric systems to power sensors. In the framework seen previously, the triboelectricity is used to reconcentrate the solutions. The advantage compared to a simple triboelectric system is that there is no need for complex impedance matching to perform this charge separation. The results, although preliminary, are comparable to those obtained with piezoelectric[223] or capacitive systems.[2,224] If such systems are proved to work over several cycles, this approach is surely a path for the commercial development of the blue energy. The infrastructure costs are much lower in these miniature devices than those involved in producing energy. Here are a few studies in the literature on the life cycle assessment of blue energy processes, including reverse electrodialysis processes[225–227] Muller *et al.* analyses[225] a functional unit of 1 MW h of net electricity production. They compare their results to wind and solar photovoltaic. Using favorable conditions and assumptions they show that the environmental footprint of the RED is comparable or lower than those of established renewable energy technologies. The main points of focus on RED are the processes associated with membrane manufacturing. The impacts are also greater when lower salt gradients are used due to lower process efficiency. The use of membranes makes eutrophication, ecotoxicity and carcinogenic impacts more significant for RED than for other technologies under certain assumptions.

3.3 Capmixing

Firstly proposed in 2009 by Brogioli,[228] Capmixing is an emerging blue energy harvesting energy with tremendous

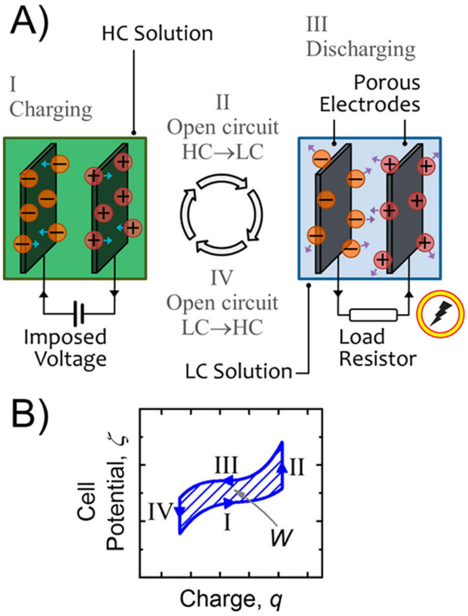

Fig. 20 (A) Illustration of the working principle of capacitive energy extraction based on double layer expansion (CDLE) and (B) the qualitative plot of useful work W produced in an unit Capmixing cycle (figures and captions reproduced from ref. 69 with permission from American Chemical Society, copyright 2016).

potential. Unlike PRO and RED where energy conversion is realized through intermediate steps of mechanical turbine systems and electrochemical redox reactions, Capmixing generates electricity directly from a controlled mixing procedure.[69] In a classic configuration of Capmixing illustrated in Fig. 20(A), two porous carbon electrodes are dipped into high concentration solutions at initial state.

It is an energy consuming state where electrodes are charged by an imposed external electric source. Thus, electrical double layers (EDL) are formed near each electrode to maintain a local electron neutrality in the solution.[65] In state II, the system is in open circuit state and the high concentration solution in the system is replaced by solution of lower concentration. As the ionic strength lowering of the electrolyte results in a thickness expansion of the EDL, the overall capacitance of EDL C_{EDL} decreases.[229] Considering the total charges accumulated in the electrodes q remain unchanged, the potential difference between these electrodes DE increases as predicted by the following equation $q = \Delta C_{EDL}\Delta E$. In state III, a load resistor is connected with the Capmixing system. Discharging in electrodes delivers current to produce useful work in the load resistor. At the same time, the thickness of EDL decreases due to the discharging. At final state IV, system switches into open-circuit state and fresh water is replaced by salt water to close the operation loop. As illustrated in Fig. 20(B), the produced work in state III is larger than the energy consumed in state I, a net power is harvested using this so-called capacitive energy extraction based on double layer expansion (CDLE) technology.[68] In the pioneer work of CDLE, Brogioli presented this innovative configuration with a mild power density of 7 mW per square meter of electrodes harvested by two activated carbon porous electrodes.[228] Later, Brogioli *et al.*[230] analyzed the spontaneous potential and the leakage current of different activated carbon electrodes. Based on this analysis, they proposed several suitable couples of activated carbon materials that could possibly enlarge the energy extraction. Using porous carbon electrodes of A-PC-2 and NS30 (two commercial activated carbon films) in CDLE system, a remarkable power density of 50 mW m^{-2} was reported.

In CDLE, capacitive electrodes suffer from self-discharging problems due to faradic reactions on the surface of the carbon. Porada *et al.*[231] summarized these reaction into three types: the first one is the conversion of quinone group on the carbon's surface with two protons to form two hydroquinone. Secondly, the carbon oxidation from carbon to CO_2. And finally, the electrochemical reactions where components in the water react at the carbon surface. Some of them require molecular oxygen in solution. Brogioli *et al.* found that removing oxygen by bubbling nitrogen partially reduces the self-discharge.[232] An alternative solution of using selective faradaic electrodes in the CDLE configuration was proposed in 2011 by Mantia *et al.*[233] The so-called 'Mixing entropy battery' was experimentally demonstrated by using $Na_{2-x}Mn_5O_{10}$ electrode for Na^+ capturing and Ag/AgCl electrode for Cl^- capturing. In this conception, extracted energy from salinity difference is stored inside the bulk crystal structure of the electrode material in chemical energy form. A power density of 138 mW m^{-2} was reported for a salinity gradient of 0.03 M and 1.5 M of NaCl solutions. The main problems of this technique, in addition to the high cost of the electrodes is the relatively short lifespan of the Ag/AgCl electrodes and the low specific capacity of the NMO. Also, the pre-charging step promotes the energy investment.[234] To overcome all that, Ye *et al.*[234] proposed a charge-free MEB with low-cost electrode materials with Prussian blue for the cationic electrode to capture the Na^+, and polypyrrole to capture the Cl^- for anions.

The conventional CDLE configuration requires the external electrical charging system to enable the energy harvesting, which requires higher installation costs and reduce the system efficiency. In 2010, Sales *et al.*[70] proposed to replace auxiliary charging process by using IEMs, so as to use the Donnan potential established across the membrane for system charging. This technology is called capacitive energy extraction based on Donnan potential (CDP). According to their work, Neosepta CEM (or AEM) was placed between the porous carbon electrode and the spacer. While fresh water and salt water were injected alternatively into the spacer, cations and anions were transported through CEM and AEM under the Donnan potential driving force, forming alternative ionic flows (Fig. 21). The initial work of CDP reported a power density of 11.6 mW m^{-2} for solution concentration of 10 mM and 510 mM for fresh water and salt water, respectively. Based on the principle of CDP, modifications of electrodes and membranes were conducted for performance amelioration. Hatzell *et al.*[235] proposed to use flow electrodes containing activated carbons in CDP configuration, which significantly increased the system performance towards 50.9 mW m^{-2}. In 2021, Hwang *et al.*[236] realized systematic research on flow electrodes on varying particle components and concentration, the optimum flow electrodes containing expanded graphite was reported to

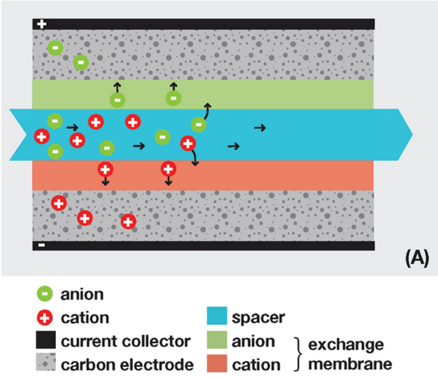

Fig. 21 Illustration of the composition and working principle of capacitive energy extraction based on Donnan potential (CDP). IEMs are used to replace external charging sources so that anions and cations move from spacer channel into porous electrodes (figures and captions reproduced from ref. 70 with permission from American Chemical Society, copyright 2010).

provide a power density of 480 mW m^{-2}. Further optimization on current collector (graphene coated Ti mesh) could even promote the system performance towards 750 mW m^{-2}, according to the recent work of Lee *et al.*[237]

Another emerging strategy similar to CDP is the soft electrodes (SE), where IEMs are replaced by polyelectrolytes to form direct anionic and cationic layers onto electrodes. A pioneering work was realized in 2014 by Ahualli *et al.*[238] by using polyelectrolyte coated carbon electrodes with a power output of 12.1 mW m^{-2}. In 2020, Siekierka *et al.*[239] prepared electrodes coated with EDA and PAA/PMA, reaching a maximum power of 293 mW m^{-2}. However, it is to notice that considerable viscous loss is expected in flow electrode related systems due to the highly viscous properties of flow electrodes.

Numerous theoretical analyses of Capmixing systems were reported,[232,240–242] providing guidelines for optimization of Capmixing. Further strategies, including thermal assisted Capmixing,[243,244] additional charging[245] and module scaling up,[246,247] were also developed for performance enhancement.

3.4 CRED

An innovative configuration combining RED and Capmixing presents a higher power density output with numerous advantages compared with conventional blue energy harvesting technologies. It was firstly reported by Vermaas *et al.*[248] in 2013, suggesting the use of capacitive electrodes in RED configurations (CRED). Such configuration allows the installation of multiple cationic and anionic membrane stacks for higher potential generation and at the same time avoids the redox reactions in the system. In their work, a layer of activated carbon is deposited on a Ti/Pt mesh to form the capacitive electrodes for adsorption and storage of ions. As larger range in voltage and accumulated charge is achieved compared with conventional Capmixing technologies, a maximum power density of 0.9 W m^{-2} can be achieved in cell configuration of a stack of 30 membranes with a salinity difference of 0.017 M and 0.508 M for fresh water and salt water, respectively. Zhan *et al.*[249] proposed similar configurations using graphene hydrogel electrodes combined with a single AEM, obtaining an average power density of 0.417 W m^{-2} for a salinity gradient of 0.02 M/0.500 M for NaCl solution.

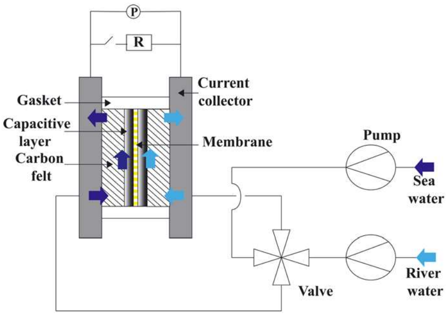

Fig. 22 Scheme of the experimental millifluidic set up used for the salinity gradient harvesting with one membrane and a 6 mm water compartment (figures and captions reproduced from ref. 169 with permission from Elsevier, copyright 2022).

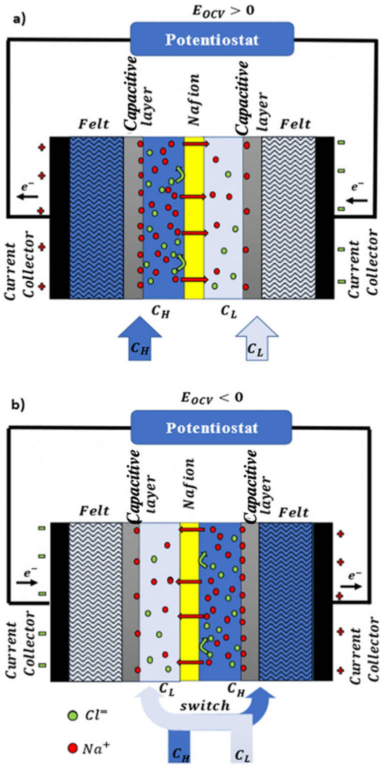

Fig. 23 Illustration of two working regimes for a capacitive salinity-gradient cell before (a) and after (b) water compartment switch (figures and captions reproduced from ref. 169 with permission from Elsevier, copyright 2022).

In 2019, Zhu *et al.*[250] proposed a novel configuration of carbonized peat moss (CPM) electrodes along with a single CEM. They obtained an average power density of 0.95 W m^{-2} for a salinity gradient of 0.017 M and 0.513 M for fresh water and salt water, respectively.

A novel cell design composed of a single selective membrane and two inexpensive capacitive electrodes was presented in the work of Brahmi et Colin (Fig. 22 and 23).[169] A home-made slurry composed of activated carbon particles, carbon nanotubes and PVDF is homogeneously deposited onto a porous carbon electrode to form a capacitive layer. As capacitive electrodes are charged by ion adsorption while immersed in solutions, periodic water compartment switching is necessary to deblock the saturation regime. An alternative capacitive current is generated when an electrical resistance is directly connected to the system. A net power density output of 2 W m^{-2} was reported, with a gradient of 300 (0.017 M/5.1 M) for a simple configuration of a single cationic membrane combined with two inexpensive electrodes. It is to mention that this net power density takes into account the viscous loss in the cell and remains the maximum power density output for CRED systems.

4 Conclusion

In this review, we mainly focus on two different types of water-based energy harvesting systems built on fluidic systems at different scales. Based on the charge separation mechanism, triboelectric energy harvesting systems converts mechanical energy into electrical energy. Osmotic energy harvesting systems realize controlled mixing procedure of solutions of different salinity to recover energies. These two systems have the advantages of being able to be miniaturized[220] as well as being used on a large scale. Though they are not currently in use for electricity production due to many remaining problems, researches of system amelioration are in full development.

We have shown that triboelectric systems can achieve an average power density of a few watt per meter square. The increase of efficiency of triboelectric systems requires a better understanding of charge separation mechanisms but also the implementation of efficient storage processes for the energy generated. Another promising strategy is to investigate in innovative materials. For instance, the composite polymer materials, integrated with conductive particles in order to increase their dielectric constant and their polarizability, could have an important place in future technological developments. It is of great importance to ensure the durability and recycling of these systems. Working with self-healing systems such as vitrimers[251] is a prospect.

The majority of the osmotic energy harvesting systems (PRO, RED and CRED systems) obtain a power density of a few watt per meter square and an energy conversion efficiency below 35%. Though numerous attempts were realized in laboratories and in industrial applications, we now encounter with the bottleneck of performance amelioration, especially for power density and energy conversion efficiency, which remain below the commercialization threshold. The bar of 5 W m^{-2} of net production under industrial production conditions has still not been crossed. The key factor in technology acceleration consists of the amelioration of membrane performance and a significant membrane price reduction. Recent studies have shown that the development of these techniques will not go through the use of membranes resulting from the concepts of nanofluidics or bioinspiration which aroused great interest. To relaunch this track, it is necessary to reduce the polarization effects developed at the entry and exit of membranes with limited energy input. In order to apply these conceptions in membrane engineering, several crucial questions are raised as follows. How to stack nanochannels or slits with large surface charges in space while preventing these nanochannels from interacting with each other? How to optimize electrode arrangement in cell designs so as to avoid the ionic passage through solution compartments (of low ionic conductivity)? How to limit significant pressure drop in energy harvesting systems?

Another promising path, which remains little exploited, is the novel configuration composed of capacitive electrodes and a single membrane. It opens up a novel path of performance enhancement by working on electrode materials. In this context, the use of electrodes exhibiting faradaic surface reactions seems to be a promising track. In terms of device scaling up, it is certain that significant engineering work is required to reduce the filling time during water compartment batching. In general, there is a contribution to be made towards battery technologies to improve these processes.

All these results are very encouraging for powering electronic devices. The applications of the use of saline gradients to supply embedded sensors seem to be a relevant way and can be an important industrial outlet for this technique. The passage to large scales is more futuristic. The economic profitability of triboelectricity is proven. However, it is necessary to improve the lifetimes. The profitability of osmotic energy is less clear. It is true that currently, PRO, RED and Capmixing techniques are not profitable due to the high cost of membranes and water pre-treatments. And the debate of economic viability of osmotic energy harvesting systems has never stopped. However, these economic analyzes should not hinder research. Electricity prices increased by a factor of 20 in 1 year. In such an economic context and because of the scarcity of fossil resources, these techniques will eventually prevail even if they currently remain expensive. The IPCC report reminds us of the importance of taking actions to find solutions for limiting global environmental problems of climate change and greenhouse gas emissions. Our planet is nicknamed the blue planet. 71% of the 509 million m^2 of our planet surface are covered with water,[252] which corresponds to a volume of 140 million km^3. It is therefore a natural idea to develop renewable energies based on salted water resources. Overall, we believe that it is important to continue scientific researches and industrial attempts on these two techniques which could eventually solve the major problem of the 21st century: the ecological transition.

Author contributions

NW, YB, AC wrote, reviewed and edited the manuscript. AC supervised the redaction of the manuscript.

Conflicts of interest

There are no conflicts to declare.

Acknowledgements

NW acknowledges funding from China Scholarship Council (CSC). YB acknowledges funding from the Institut Pierre-Gilles de Gennes (laboratoire d'excellence PSL).

Notes and references

1 S. Priya and D. J. Inman, *Energy harvesting technologies*, Springer, 2009, vol. 21.

2 M. Pruvost, W. J. Smit, C. Monteux, P. Del Corro, I. Dufour, C. Ayela, P. Poulin and A. Colin, *Sci. Rep.*, 2020, **10**, 1–14.

3 D. Guyomar and M. Lallart, *Micromachines*, 2011, **2**, 274–294.

4 A. Harb, *Renewable Energy*, 2011, **36**, 2641–2654.

5 S. E. Skilhagen, J. E. Dugstad and R. J. Aaberg, *Desalination*, 2008, **220**, 476–482.

6 S. Hanson, M. Seok, Y.-S. Lin, Z. Foo, D. Kim, Y. Lee, N. Liu, D. Sylvester and D. Blaauw, *IEEE J. Solid-State Circuits*, 2009, **44**, 1145–1155.

7 S. Jeong, Z. Foo, Y. Lee, J.-Y. Sim, D. Blaauw and D. Sylvester, *IEEE J. Solid-State Circuits*, 2014, **49**, 1682–1693.

8 M. Elimelech and W. A. Phillip, *Science*, 2011, **333**, 712–717.

9 A. Siria, M.-L. Bocquet and L. Bocquet, *Nat. Rev. Chem.*, 2017, **1**, 1–10.

10 S. Lin, X. Chen and Z. L. Wang, *Chem. Rev.*, 2021, **122**, 5209–5232.

11 F.-R. Fan, Z.-Q. Tian and Z. L. Wang, *Nano Energy*, 2012, **1**, 328–334.

12 J. Tian, X. Chen and Z. L. Wang, *Nanotechnology*, 2020, **31**, 242001.

13 Z. L. Wang, *Nano Energy*, 2020, **68**, 104272.

14 Z. L. Wang, *Mater. Today*, 2017, **20**, 74–82.

15 W. Thomson, *Proc. R. Soc. London*, 1868, 67–72.

16 A. G. Marin, W. van Hoeve, P. Garcia-Sanchez, L. Shui, Y. Xie, M. A. Fontelos, J. C. Eijkel, A. van den Berg and D. Lohse, *Lab Chip*, 2013, **13**, 4503–4506.

17 J. P. Tarelho, M. P. S. dos Santos, J. A. Ferreira, A. Ramos, S. Kopyl, S. O. Kim, S. Hong and A. Kholkin, *Mater. Today*, 2018, **21**, 1019–1041.

18 P. Dhiman, F. Yavari, X. Mi, H. Gullapalli, Y. Shi, P. M. Ajayan and N. Koratkar, *Nano Lett.*, 2011, **11**, 3123–3127.

19 J. Yin, X. Li, J. Yu, Z. Zhang, J. Zhou and W. Guo, *Nat. Nanotechnol.*, 2014, **9**, 378–383.

20 J. Yin, Z. Zhang, X. Li, J. Yu, J. Zhou, Y. Chen and W. Guo, *Nat. Commun.*, 2014, **5**, 1–6.

21 S. Lin, L. Zhu, Z. Tang and Z. L. Wang, *Nat. Commun.*, 2022, **13**, 1–9.

22 S. Lin, L. Xu, A. Chi Wang and Z. L. Wang, *Nat. Commun.*, 2020, **11**, 1–8.

23 Z. L. Wang and A. C. Wang, *Mater. Today*, 2019, **30**, 34–51.

24 B. Chen, Y. Xia, R. He, H. Sang, W. Zhang, J. Li, L. Chen, P. Wang, S. Guo and Y. Yin, *et al.*, *Proc. Natl. Acad. Sci. U. S. A.*, 2022, **119**, e2209056119.

25 N. Miljkovic, D. J. Preston, R. Enright and E. N. Wang, *Nat. Commun.*, 2013, **4**, 1–9.

26 Z.-H. Lin, G. Cheng, L. Lin, S. Lee and Z. L. Wang, *Angew. Chem., Int. Ed.*, 2013, **52**, 12545–12549.

27 D. Choi, H. Lee, D. J. Im, I. S. Kang, G. Lim, D. S. Kim and K. H. Kang, *Sci. Rep.*, 2013, **3**, 1–7.

28 J. H. Masliyah and S. Bhattacharjee, *Electrokinetic and colloid transport phenomena*, John Wiley & Sons, 2006.

29 Y. Xie, D. Bos, L. J. De Vreede, H. L. De Boer, M.-J. van der Meulen, M. Versluis, A. J. Sprenkels, A. van den Berg and J. C. Eijkel, *Nat. Commun.*, 2014, **5**, 1–5.

30 W. Xu, H. Zheng, Y. Liu, X. Zhou, C. Zhang, Y. Song, X. Deng, M. Leung, Z. Yang and R. X. Xu, *et al.*, *Nature*, 2020, **578**, 392–396.

31 Q. Sun, D. Wang, Y. Li, J. Zhang, S. Ye, J. Cui, L. Chen, Z. Wang, H.-J. Butt and D. Vollmer, *et al.*, *Nat. Mater.*, 2019, **18**, 936–941.

32 H. Wu, N. Mendel, D. van den Ende, G. Zhou and F. Mugele, *Phys. Rev. Lett.*, 2020, **125**, 078301.

33 X. J. Zhao, G. Zhu, Y. J. Fan, H. Y. Li and Z. L. Wang, *ACS Nano*, 2015, **9**, 7671–7677.

34 S. Jang, M. La, S. Cho, Y. Yun, J. H. Choi, Y. Ra, S. J. Park and D. Choi, *Nano Energy*, 2020, **70**, 104541.

35 G. Zhu, Y. Su, P. Bai, J. Chen, Q. Jing, W. Yang and Z. L. Wang, *ACS Nano*, 2014, **8**, 6031–6037.

36 Y. Su, X. Wen, G. Zhu, J. Yang, J. Chen, P. Bai, Z. Wu, Y. Jiang and Z. L. Wang, *Nano Energy*, 2014, **9**, 186–195.

37 J. Xiong, M.-F. Lin, J. Wang, S. L. Gaw, K. Parida and P. S. Lee, *Adv. Energy Mater.*, 2017, **7**, 1701243.

38 G.-Z. Li, G.-G. Wang, D.-M. Ye, X.-W. Zhang, Z.-Q. Lin, H.-L. Zhou, F. Li, B.-L. Wang and J.-C. Han, *Adv. Electron. Mater.*, 2019, **5**, 1800846.

39 B. K. Yun, H. S. Kim, Y. J. Ko, G. Murillo and J. H. Jung, *Nano Energy*, 2017, **36**, 233–240.

40 Z.-H. Lin, G. Cheng, S. Lee, K. C. Pradel and Z. L. Wang, *Adv. Mater.*, 2014, **26**, 4690–4696.

41 G. Cheng, Z.-H. Lin, Z.-L. Du and Z. L. Wang, *ACS Nano*, 2014, **8**, 1932–1939.

42 Q. Liang, X. Yan, X. Liao and Y. Zhang, *Nano Energy*, 2016, **25**, 18–25.

43 L. Zhao, L. Liu, X. Yang, H. Hong, Q. Yang, J. Wang and Q. Tang, *J. Mater. Chem. A*, 2020, **8**, 7880–7888.

44 R. K. Cheedarala, M. Shahriar, J. H. Ahn, J. Y. Hwang and K. K. Ahn, *Nano Energy*, 2019, **65**, 104017.

45 M. Zhang, C. Bao, C. Hu, Y. Huang, Y. Yang and Y. Su, *Nano Energy*, 2022, 107992.

46 J. H. Ahn, J. Y. Hwang, C. G. Kim, G. H. Nam and K. K. Ahn, *Nano Energy*, 2020, **67**, 104269.

47 S.-H. Kwon, J. Park, W. K. Kim, Y. Yang, E. Lee, C. J. Han, S. Y. Park, J. Lee and Y. S. Kim, *Energy Environ. Sci.*, 2014, **7**, 3279–3283.

48 Z.-H. Lin, G. Cheng, W. Wu, K. C. Pradel and Z. L. Wang, *ACS Nano*, 2014, **8**, 6440–6448.

49 K. Yatsuzuka, Y. Mizuno and K. Asano, *J. Electrost.*, 1994, **32**, 157–171.

50 B. Wang, Y. Wu, Y. Liu, Y. Zheng, Y. Liu, C. Xu, X. Kong, Y. Feng, X. Zhang and D. Wang, *ACS Appl. Mater. Interfaces*, 2020, **12**, 31351–31359.

51 P. Zhao, N. Soin, K. Prashanthi, J. Chen, S. Dong, E. Zhou, Z. Zhu, A. A. Narasimulu, C. D. Montemagno and L. Yu, *et al.*, *ACS Appl. Mater. Interfaces*, 2018, **10**, 5880–5891.

52 C. Cai, B. Luo, Y. Liu, Q. Fu, T. Liu, S. Wang and S. Nie, *Mater. Today*, 2022, **52**, 299–326.

53 BNEF, **https://about.bnef.com/blog/cost-of-new-renewables-temporarily-rises-asinflation-starts-to-bite/**, 2022.

54 Energy.gov, **https://www.energy.gov**, 2022.

55 A. Ahmed, I. Hassan, T. Ibn-Mohammed, H. Mostafa, I. M. Reaney, L. S. Koh, J. Zu and Z. L. Wang, *Energy Environ. Sci.*, 2017, **10**, 653–671.
56 R. Zhang and H. Olin, *ACS Nanosci. Au*, 2021, **2**, 12–31.
57 M. G. Stanford, J. T. Li, Y. Chyan, Z. Wang, W. Wang and J. M. Tour, *ACS Nano*, 2019, **13**, 7166–7174.
58 W. Liu, Z. Wang, G. Wang, Q. Zeng, W. He, L. Liu, X. Wang, Y. Xi, H. Guo and C. Hu, *et al.*, *Nat. Commun.*, 2020, **11**, 1–10.
59 Z. L. Wang, T. Jiang and L. Xu, *Nano Energy*, 2017, **39**, 9–23.
60 X. Wen, W. Yang, Q. Jing and Z. L. Wang, *ACS Nano*, 2014, **8**, 7405–7412.
61 Z. L. Wang, *et al.*, *Nature*, 2017, **542**, 159–160.
62 L. M. Zhang, C. B. Han, T. Jiang, T. Zhou, X. H. Li, C. Zhang and Z. L. Wang, *Nano Energy*, 2016, **22**, 87–94.
63 S. L. Zhang, M. Xu, C. Zhang, Y.-C. Wang, H. Zou, X. He, Z. Wang and Z. L. Wang, *Nano Energy*, 2018, **48**, 421–429.
64 M. Xu, T. Zhao, C. Wang, S. L. Zhang, Z. Li, X. Pan and Z. L. Wang, *ACS Nano*, 2019, **13**, 1932–1939.
65 N. Y. Yip, D. A. Vermaas, K. Nijmeijer and M. Elimelech, *Environ. Sci. Technol.*, 2014, **48**, 4925–4936.
66 R. S. Norman, *Science*, 1974, **186**, 350–352.
67 J. W. Post, H. V. M. Hamelers and C. J. N. Buisman, *Environ. Sci. Technol.*, 2008, **42**, 5785–5790.
68 Z. Jia, B. Wang, S. Song and Y. Fan, *Renewable Sustainable Energy Rev.*, 2014, **31**, 91–100.
69 N. Y. Yip, D. Brogioli, H. V. M. Hamelers and K. Nijmeijer, *Environ. Sci. Technol.*, 2016, **50**, 12072–12094.
70 B. B. Sales, M. Saakes, J. W. Post, C. J. N. Buisman, P. M. Biesheuvel and H. V. M. Hamelers, *Environ. Sci. Technol.*, 2010, **44**, 5661–5665.
71 K. Touati and F. Tadeo, *Int. J. Green Energy*, 2017, **14**, 337–360.
72 S. Sarp, Z. Li and J. Saththasivam, *Desalination*, 2016, **389**, 2–14.
73 F. Helfer, C. Lemckert and Y. G. Anissimov, *J. Membr. Sci.*, 2014, **453**, 337–358.
74 Y. Shi, M. Zhang, H. Zhang, F. Yang, C. Y. Tang and Y. Dong, *Water Res.*, 2021, **189**, 116666.
75 W. Y. Chia, S. R. Chia, K. S. Khoo, K. W. Chew and P. L. Show, *J. Water Process. Eng.*, 2021, **39**, 101758.
76 Q. She, R. Wang, A. G. Fane and C. Y. Tang, *J. Membr. Sci.*, 2016, **499**, 201–233.
77 R. R. Gonzales, A. Abdel-Wahab, S. Adham, D. S. Han, S. Phuntsho, W. Suwaileh, N. Hilal and H. K. Shon, *Desalination*, 2021, **500**, 114841.
78 A. P. Straub, A. Deshmukh and M. Elimelech, *Energy Environ. Sci.*, 2016, **9**, 31–48.
79 S. Lin, A. P. Straub and M. Elimelech, *Energy Environ. Sci.*, 2014, **7**, 2706–2714.
80 B. E. Logan and M. Elimelech, *Nature*, 2012, **488**, 313–319.
81 S. Xu, Y. Liu, Y. Wang, M. Zhang, Q. Xiao and Y. Duan, *Desalination*, 2017, **412**, 39–48.
82 S. Zhao and L. Zou, *J. Membr. Sci.*, 2011, **379**, 459–467.
83 Q. She, X. Jin and C. Y. Tang, *J. Membr. Sci.*, 2012, **401–402**, 262–273.
84 J. Kim, M. J. Park, M. Park, H. K. Shon, S.-H. Kim and J. H. Kim, *Desalination*, 2016, **389**, 207–214.
85 N. Y. Yip and M. Elimelech, *Environ. Sci. Technol.*, 2013, **47**, 12607–12616.
86 M. Tawalbeh, A. Al-Othman, N. Abdelwahab, A. H. Alami and A. G. Olabi, *Renewable Sustainable Energy Rev.*, 2021, **138**, 110492.
87 S. Loeb, F. Van Hessen and D. Shahaf, *J. Membr. Sci.*, 1976, **1**, 249–269.
88 G. D. Mehta, *J. Membr. Sci.*, 1982, **10**, 3–19.
89 A. Achilli, T. Y. Cath and A. E. Childress, *J. Membr. Sci.*, 2009, **343**, 42–52.
90 N. Akther, A. Sodiq, A. Giwa, S. Daer, H. A. Arafat and S. W. Hasan, *Chem. Eng. J.*, 2015, **281**, 502–522.
91 Y. C. Kim and M. Elimelech, *J. Membr. Sci.*, 2013, **429**, 330–337.
92 S. L. Plata and A. E. Childress, *Desalination*, 2019, **467**, 51–56.
93 N. AlZainati, H. Saleem, A. Altaee, S. J. Zaidi, M. Mohsen, A. Hawari and G. J. Millar, *J. Water Process. Eng.*, 2021, **40**, 101950.
94 N. Y. Yip, A. Tiraferri, W. A. Phillip, J. D. Schiffman, L. A. Hoover, Y. C. Kim and M. Elimelech, *Environ. Sci. Technol.*, 2011, **45**, 4360–4369.
95 G. Han, S. Zhang, X. Li and T.-S. Chung, *J. Membr. Sci.*, 2013, **440**, 108–121.
96 X. Li, S. Zhang, F. Fu and T.-S. Chung, *J. Membr. Sci.*, 2013, **434**, 204–217.
97 M. Son, H. Park, L. Liu, H. Choi, J. H. Kim and H. Choi, *Chem. Eng. J.*, 2016, **284**, 68–77.
98 J. Wei, Y. Li, L. Setiawan and R. Wang, *J. Membr. Sci.*, 2016, **511**, 54–64.
99 N.-N. Bui and J. R. McCutcheon, *Environ. Sci. Technol.*, 2014, **48**, 4129–4136.
100 M. Tian, R. Wang, K. Goh, Y. Liao and A. G. Fane, *J. Membr. Sci.*, 2015, **486**, 151–160.
101 S. Lim, M. J. Park, S. Phuntsho, A. Mai-Prochnow, A. B. Murphy, D. Seo and H. Shon, *J. Membr. Sci.*, 2018, **564**, 382–393.
102 R. R. Gonzales, M. J. Park, T.-H. Bae, Y. Yang, A. Abdel-Wahab, S. Phuntsho and H. K. Shon, *Desalination*, 2019, **459**, 10–19.
103 S. J. Kwon, K. Park, D. Y. Kim, M. Zhan, S. Hong and J.-H. Lee, *J. Membr. Sci.*, 2021, **619**, 118796.
104 J. H. Kim, S. J. Moon, S. H. Park, M. Cook, A. G. Livingston and Y. M. Lee, *J. Membr. Sci.*, 2018, **550**, 322–331.
105 S. J. Moon, J. H. Kim, J. G. Seong, W. H. Lee, S. H. Park, S. H. Noh, J. H. Kim and Y. M. Lee, *J. Membr. Sci.*, 2020, **607**, 118120.
106 H. W. Chung, J. Swaminathan, L. D. Banchik and J. H. Lienhard, *Desalination*, 2018, **448**, 13–20.
107 Y. C. Kim and M. Elimelech, *Environ. Sci. Technol.*, 2012, **46**, 4673–4681.
108 Q. She, D. Hou, J. Liu, K. H. Tan and C. Y. Tang, *J. Membr. Sci.*, 2013, **445**, 170–182.

109 E. Sivertsen, T. Holt, W. Thelin and G. Brekke, *Desalination*, 2013, **312**, 107–123.
110 S. Chou, R. Wang, L. Shi, Q. She, C. Tang and A. G. Fane, *J. Membr. Sci.*, 2012, **389**, 25–33.
111 S. Chou, R. Wang and A. G. Fane, *J. Membr. Sci.*, 2013, **448**, 44–54.
112 P. G. Ingole, W. Choi, K.-H. Kim, H.-D. Jo, W.-K. Choi, J.-S. Park and H.-K. Lee, *Desalination*, 2014, **345**, 136–145.
113 P. G. Ingole, W. Choi, K. H. Kim, C. H. Park, W. K. Choi and H. K. Lee, *Chem. Eng. J.*, 2014, **243**, 137–146.
114 F.-J. Fu, S.-P. Sun, S. Zhang and T.-S. Chung, *J. Membr. Sci.*, 2014, **469**, 488–498.
115 X. Li, T. Cai and T.-S. Chung, *Environ. Sci. Technol.*, 2014, **48**, 9898–9907.
116 P. G. Ingole, K. H. Kim, C. H. Park, W. K. Choi and H. K. Lee, *RSC Adv.*, 2014, **4**, 51430–51439.
117 Y. Zhang, J. L. Li, T. Cai, Z. L. Cheng, X. Li and T.-S. Chung, *J. Membr. Sci.*, 2018, **563**, 521–530.
118 D. L. Zhao, S. Das and T.-S. Chung, *Environ. Sci. Technol.*, 2017, **51**, 14016–14023.
119 W. Gai, D. L. Zhao and T.-S. Chung, *J. Membr. Sci.*, 2018, **551**, 94–102.
120 M. J. Park, S. Lim, R. R. Gonzales, S. Phuntsho, D. S. Han, A. Abdel-Wahab, S. Adham and H. K. Shon, *Desalination*, 2019, **464**, 63–75.
121 D. Zhao, G. Qiu, X. Li, C. Wan, K. Lu and T.-S. Chung, *Water Res.*, 2016, **104**, 389–396.
122 N. L. Le, N. M. S. Bettahalli, S. P. Nunes and T.-S. Chung, *J. Membr. Sci.*, 2016, **505**, 157–166.
123 G. Han, P. Wang and T.-S. Chung, *Environ. Sci. Technol.*, 2013, **47**, 8070–8077.
124 S. Zhang, F. Fu and T.-S. Chung, *Chem. Eng. Sci.*, 2013, **87**, 40–50.
125 X. Li, T.-S. Chung and T.-S. Chung, *AIChE J.*, 2013, **59**, 4749–4761.
126 X. Song, Z. Liu and D. D. Sun, *Energy Environ. Sci.*, 2013, **6**, 1199.
127 Y. Cui, X.-Y. Liu and T.-S. Chung, *Chem. Eng. J.*, 2014, **242**, 195–203.
128 A. P. Straub, N. Y. Yip and M. Elimelech, *Environ. Sci. Technol. Lett.*, 2014, **1**, 55–59.
129 Y. Li, R. Wang, S. Qi and C. Tang, *J. Membr. Sci.*, 2015, **488**, 143–153.
130 Q. She, J. Wei, N. Ma, V. Sim, A. G. Fane, R. Wang and C. Y. Tang, *J. Membr. Sci.*, 2016, **504**, 75–88.
131 J. A. Idarraga-Mora, D. A. Ladner and S. M. Husson, *J. Membr. Sci.*, 2018, **549**, 251–259.
132 Y. Sun, L. Cheng, T. Shintani, Y. Tanaka, T. Takahashi, T. Itai, S. Wang, L. Fang and H. Matsuyama, *Ind. Eng. Chem. Res.*, 2018, **57**, 13528–13538.
133 X. Tong, X. Wang, S. Liu, H. Gao, C. Xu, J. Crittenden and Y. Chen, *Carbon*, 2018, **138**, 410–418.
134 S. J. Moon, S. M. Lee, J. H. Kim, S. H. Park, H. H. Wang, J. H. Kim and Y. M. Lee, *Desalination*, 2020, **483**, 114409.
135 F.-J. Fu, S. Zhang, S.-P. Sun, K.-Y. Wang and T.-S. Chung, *J. Membr. Sci.*, 2013, **443**, 144–155.
136 S.-P. Sun and T.-S. Chung, *Environ. Sci. Technol.*, 2013, **47**, 13167–13174.
137 S. Zhang, P. Sukitpaneenit and T.-S. Chung, *Chem. Eng. J.*, 2014, **241**, 457–465.
138 G. Han and T.-S. Chung, *AIChE J.*, 2014, **60**, 1107–1119.
139 G. Han, Q. Ge and T.-S. Chung, *Appl. Energy*, 2014, **132**, 383–393.
140 S. C. Chen, C. F. Wan and T.-S. Chung, *J. Membr. Sci.*, 2015, **479**, 190–203.
141 F.-J. Fu, S. Zhang and T.-S. Chung, *Desalination*, 2015, **376**, 73–81.
142 Z. L. Cheng, X. Li, Y. D. Liu and T.-S. Chung, *J. Membr. Sci.*, 2016, **506**, 119–129.
143 W. Gai, X. Li, J. Y. Xiong, C. F. Wan and T.-S. Chung, *J. Membr. Sci.*, 2016, **516**, 104–112.
144 L. Zhang, Q. She, R. Wang, S. Wongchitphimon, Y. Chen and A. G. Fane, *Desalination*, 2016, **389**, 119–128.
145 Y. Chen, L. Setiawan, S. Chou, X. Hu and R. Wang, *J. Membr. Sci.*, 2016, **503**, 90–100.
146 N. Lieu Le, M. Quilitzsch, H. Cheng, P.-Y. Hong, M. Ulbricht, S. P. Nunes and T.-S. Chung, *J. Membr. Sci.*, 2017, **522**, 1–11.
147 Z. L. Cheng, X. Li, Y. Feng, C. F. Wan and T.-S. Chung, *J. Membr. Sci.*, 2017, **524**, 97–107.
148 C. F. Wan, B. Li, T. Yang and T.-S. Chung, *Sep. Purif. Technol.*, 2017, **172**, 32–42.
149 G. Han, Z. L. Cheng and T.-S. Chung, *J. Membr. Sci.*, 2017, **523**, 497–504.
150 C. F. Wan, T. Yang, W. Gai, Y. D. Lee and T.-S. Chung, *J. Membr. Sci.*, 2018, **555**, 388–397.
151 Y. Chen, C. H. Loh, L. Zhang, L. Setiawan, Q. She, W. Fang, X. Hu and R. Wang, *J. Membr. Sci.*, 2018, **548**, 398–407.
152 Y. Li, S. Zhao, L. Setiawan, L. Zhang and R. Wang, *J. Membr. Sci.*, 2018, **550**, 163–172.
153 Y. H. Cho, S. D. Kim, J. F. Kim, H.-G. Choi, Y. Kim, S.-E. Nam, Y.-I. Park and H. Park, *J. Membr. Sci.*, 2019, **579**, 329–341.
154 R. R. Gonzales, Y. Yang, M. J. Park, T.-H. Bae, A. Abdel-Wahab, S. Phuntsho and H. K. Shon, *Desalination*, 2020, **496**, 114756.
155 K. Gerstandt, K. V. Peinemann, S. E. Skilhagen, T. Thorsen and T. Holt, *Desalination*, 2008, **224**, 64–70.
156 S. AL Mashrafi, N. Diaz-Elsayed, J. Benjamin, M. E. Arias and Q. Zhang, *Desalination*, 2022, **537**, 115869.
157 Q. A. Khasawneh, B. Tashtoush, A. Nawafleh and B. Kan'an, *Energies*, 2018, **11**, 3118.
158 T. N. American, *Crown Princess of Norway to Open the World's First Osmotic Power Plant*, **https://www.norwegianamerican.com/crown-princess-ofnorway-to-open-the-worlds-first-osmotic-power-plant/**, 2009.
159 C. Lee, S. H. Chae, E. Yang, S. Kim, J. H. Kim and I. S. Kim, *Desalination*, 2020, **491**, 114501.
160 *Osmotic Power Plant Opened*, REUK.Co.Uk.
161 M. Kurihara and H. Takeuchi, *Water*, 2018, **10**, 48.
162 R. E. Pattle, *Nature*, 1954, **174**, 660–660.
163 R. E. Lacey, *Ocean Eng.*, 1980, **7**, 1–47.

164 A. Galama, J. Post, H. Hamelers, V. Nikonenko and P. Biesheuvel, *J. Membr. Sci. Res.*, 2016, **2**, 128–140.

165 T. Teorell, *Proc. Soc. Exp. Biol. Med.*, 1935, **33**, 282–285.

166 F. Morrison Jr and J. Osterle, *J. Chem. Phys.*, 1965, **43**, 2111–2115.

167 A. Siria, P. Poncharal, A.-L. Biance, R. Fulcrand, X. Blase, S. T. Purcell and L. Bocquet, *Nature*, 2013, **494**, 455–458.

168 Z. Tang, Q.-A. Huang, Y.-J. Wang, F. Zhang, W. Li, A. Li, L. Zhang and J. Zhang, *J. Power Sources*, 2020, **468**, 228361.

169 Y. Brahmi and A. Colin, *Energy Convers. Manage.*, 2022, **254**, 115297.

170 J. Veerman, M. Saakes, S. J. Metz and G. J. Harmsen, *J. Appl. Electrochem.*, 2010, **40**, 1461–1474.

171 J. Jagur-Grodzinski and R. Kramer, *Ind. Eng. Chem. Process Des. Dev.*, 1986, **25**, 443–449.

172 J. Veerman, M. Saakes, S. J. Metz and G. J. Harmsen, *Environ. Sci. Technol.*, 2010, **44**, 9207–9212.

173 A. Daniilidis, D. A. Vermaas, R. Herber and K. Nijmeijer, *Renewable Energy*, 2014, **64**, 123–131.

174 J. Veerman, R. M. de Jong, M. Saakes, S. J. Metz and G. J. Harmsen, *J. Membr. Sci.*, 2009, **343**, 7–15.

175 J. Veerman and D. Vermaas, *Sustainable Energy from Salinity Gradients*, Elsevier, 2016, pp. 77–133.

176 D. A. Vermaas, M. Saakes and K. Nijmeijer, *Environ. Sci. Technol.*, 2011, **45**, 7089–7095.

177 M. Turek, B. Bandura and P. Dydo, *Desalination*, 2008, **221**, 462–466.

178 R. Audinos, *J. Power Sources*, 1983, **10**, 203–217.

179 P. Dlugolecki, K. Nymeijer, S. Metz and M. Wessling, *J. Membr. Sci.*, 2008, **319**, 214–222.

180 J. Moreno, V. Díez, M. Saakes and K. Nijmeijer, *J. Membr. Sci.*, 2018, **550**, 155–162.

181 S. Mehdizadeh, Y. Kakihana, T. Abo, Q. Yuan and M. Higa, *Membranes*, 2021, **11**, 27.

182 M. Tedesco, E. Brauns, A. Cipollina, G. Micale, P. Modica, G. Russo and J. Helsen, *J. Membr. Sci.*, 2015, **492**, 9–20.

183 J. G. Hong and Y. Chen, *J. Membr. Sci.*, 2014, **460**, 139–147.

184 D. A. Vermaas, J. Veerman, M. Saakes and K. Nijmeijer, *Energy Environ. Sci.*, 2014, **7**, 1434–1445.

185 A. H. Avci, D. A. Messana, S. Santoro, R. A. Tufa, E. Curcio, G. Di Profio and E. Fontananova, *Membranes*, 2020, **10**, 168.

186 E. Güler, R. Elizen, D. A. Vermaas, M. Saakes and K. Nijmeijer, *J. Membr. Sci.*, 2013, **446**, 266–276.

187 T. Rijnaarts, J. Moreno, M. Saakes, W. M. de Vos and K. Nijmeijer, *Colloids Surf., A*, 2019, **560**, 198–204.

188 M. Y. Kariduraganavar, R. K. Nagarale, A. A. Kittur and S. S. Kulkarni, *Desalination*, 2006, **197**, 225–246.

189 N. D. Pismenskaya, E. V. Pokhidnia, G. Pourcelly and V. V. Nikonenko, *J. Membr. Sci.*, 2018, **566**, 54–68.

190 J. Veerman, M. Saakes, S. Metz and G. Harmsen, *J. Membr. Sci.*, 2009, **327**, 136–144.

191 D. A. Vermaas, M. Saakes and K. Nijmeijer, *J. Membr. Sci.*, 2011, **385–386**, 234–242.

192 E. Guler, Y. Zhang, M. Saakes and K. Nijmeijer, *ChemSusChem*, 2012, **5**, 2262–2270.

193 D. A. Vermaas, M. Saakes and K. Nijmeijer, *J. Membr. Sci.*, 2014, **453**, 312–319.

194 M. Tedesco, C. Scalici, D. Vaccari, A. Cipollina, A. Tamburini and G. Micale, *J. Membr. Sci.*, 2016, **500**, 33–45.

195 A. H. Avci, R. A. Tufa, E. Fontananova, G. Di Profio and E. Curcio, *Energy*, 2018, **165**, 512–521.

196 H. Kim, S. Yang, J. Choi, J.-O. Kim and N. Jeong, *Desalination*, 2021, **497**, 114676.

197 J. Gao, X. Liu, Y. Jiang, L. Ding, L. Jiang and W. Guo, *Small*, 2019, **15**, 1804279.

198 X. Liu, M. He, D. Calvani, H. Qi, K. B. Gupta, H. J. de Groot, G. Sevink, F. Buda, U. Kaiser and G. F. Schneider, *Nat. Nanotechnol.*, 2020, **15**, 307–312.

199 C. Li, L. Wen, X. Sui, Y. Cheng, L. Gao and L. Jiang, *Sci. Adv.*, 2021, **7**, eabg2183.

200 A. A. Moya, *J. Membr. Sci.*, 2020, **598**, 117784.

201 R. A. Tufa, E. Curcio, W. van Baak, J. Veerman, S. Grasman, E. Fontananova and G. D. Profio, *RSC Adv.*, 2014, **4**, 42617–42623.

202 R. S. Kingsbury, F. Liu, S. Zhu, C. Boggs, M. D. Armstrong, D. F. Call and O. Coronell, *J. Membr. Sci.*, 2017, **541**, 621–632.

203 A. Cosenza, G. Campisi, F. Giacalone, S. Randazzo, A. Cipollina, A. Tamburini and G. Micale, *Energies*, 2022, **15**, 4177.

204 D. A. Vermaas, D. Kunteng, M. Saakes and K. Nijmeijer, *Water Res.*, 2013, **47**, 1289–1298.

205 B. Vital, E. V. Torres, T. Sleutels, M. C. Gagliano, M. Saakes and H. V. M. Hamelers, *Desalination*, 2021, **518**, 115277.

206 Z. He, X. Gao, Y. Zhang, Y. Wang and J. Wang, *Desalin. Water Treat.*, 2016, **57**, 28176–28186.

207 M. Vaselbehagh, H. Karkhanechi, R. Takagi and H. Matsuyama, *J. Membr. Sci.*, 2017, **530**, 232–239.

208 H. Gao, B. Zhang, X. Tong and Y. Chen, *J. Membr. Sci.*, 2018, **567**, 68–75.

209 M. Tedesco, A. Cipollina, A. Tamburini and G. Micale, *J. Membr. Sci.*, 2017, **522**, 226–236.

210 J.-Y. Nam, K.-S. Hwang, H.-C. Kim, H. Jeong, H. Kim, E. Jwa, S. Yang, J. Choi, C.-S. Kim, J.-H. Han and N. Jeong, *Water Res.*, 2019, **148**, 261–271.

211 M. Yasukawa, S. Mehdizadeh, T. Sakurada, T. Abo, M. Kuno and M. Higa, *Desalination*, 2020, **491**, 114449.

212 C. Simões, B. Vital, T. Sleutels, M. Saakes and W. Brilman, *Chem. Eng. J.*, 2022, **450**, 138412.

213 J.-Y. Nam, K.-S. Hwang, H.-C. Kim, H. Jeong, H. Kim, E. Jwa, S. Yang, J. Choi, C.-S. Kim, J.-H. Han and N. Jeong, *Water Res.*, 2019, **148**, 261–271.

214 A. Daniilidis, R. Herber and D. A. Vermaas, *Appl. Energy*, 2014, **119**, 257–265.

215 R. A. Tufa, S. Pawlowski, J. Veerman, K. Bouzek, E. Fontananova, G. di Profio, S. Velizarov, J. Goulão Crespo, K. Nijmeijer and E. Curcio, *Appl. Energy*, 2018, **225**, 290–331.

216 M. Turek and B. Bandura, *Desalination*, 2007, **205**, 67–74.

217 J. W. Post, C. H. Goeting, J. Valk, S. Goinga, J. Veerman, H. V. M. Hamelers and P. J. F. M. Hack, *Desalin. Water Treat.*, 2010, **16**, 182–193.

218 M. Toupin, K. Malek and A. Mokrini, *World Electr. Veh. J.*, 2016, **8**, 431–442.

219 F. Giacalone, M. Papapetrou, G. Kosmadakis, A. Tamburini, G. Micale and A. Cipollina, *Energy*, 2019, **181**, 532–547.

220 W.-S. Hsu, A. Preet, T.-Y. Lin and T.-E. Lin, *Molecules*, 2021, **26**, 5469.

221 R. B. Sadeglian, O. Pantchenko, D. Tate and A. Shakouri, *Appl. Phys. Lett.*, 2011, **99**, 173702.

222 Z.-H. Lin, W.-S. Hsu, A. Preet, L.-H. Yeh, Y.-H. Chen, Y.-P. Pao, S.-F. Lin, S. Lee, J.-C. Fan and L. Wang, *et al.*, *Nano Energy*, 2021, **79**, 105440.

223 S. Roundy, P. K. Wright and J. Rabaey, *Comput. Commun.*, 2003, **26**, 1131–1144.

224 M. Pruvost, W. J. Smit, C. Monteux, P. Poulin and A. Colin, *Multifunct. Mater.*, 2018, **1**, 015004.

225 K. E. Mueller, J. T. Thomas, J. X. Johnson, J. F. DeCarolis and D. F. Call, *J. Ind. Ecol.*, 2021, **25**, 1194–1206.

226 C. Tristán, M. Rumayor, A. Dominguez-Ramos, M. Fallanza, R. Ibáñez and I. Ortiz, *Sustainable Energy Fuels*, 2020, **4**, 4273–4284.

227 F. Giacalone, P. Catrini, A. Tamburini, A. Cipollina, A. Piacentino and G. Micale, *Energy Convers. Manage.*, 2018, **164**, 588–602.

228 D. Brogioli, *Phys. Rev. Lett.*, 2009, **103**, 058501.

229 P. Sharma and T. S. Bhatti, *Energy Convers. Manage.*, 2010, **51**, 2901–2912.

230 D. Brogioli, R. Ziano, R. A. Rica, D. Salerno, O. Kozynchenko, H. V. M. Hamelers and F. Mantegazza, *Energy Environ. Sci.*, 2012, **5**, 9870–9880.

231 S. Porada, R. Zhao, A. van der Wal, V. Presser and P. Biesheuvel, *Prog. Mater. Sci.*, 2013, **58**, 1388–1442.

232 D. Brogioli, R. Ziano, R. Rica, D. Salerno and F. Mantegazza, *J. Colloid Interface Sci.*, 2013, **407**, 457–466.

233 F. La Mantia, M. Pasta, H. D. Deshazer, B. E. Logan and Y. Cui, *Nano Lett.*, 2011, **11**, 1810–1813.

234 M. Ye, M. Pasta, X. Xie, K. L. Dubrawski, J. Xu, C. Liu, Y. Cui and C. S. Criddle, *ACS Omega*, 2019, **4**, 11785–11790.

235 M. C. Hatzell, K. B. Hatzell and B. E. Logan, *Environ. Sci. Technol. Lett.*, 2014, **1**, 474–478.

236 I. Hwang, D. Lee, Y. Jung, K. Park, Y.-G. Jung, D. Kim, G.-H. Cho, S.-I. Jeon, Y.-K. Byeun, U. Paik, S. Yang and T. Song, *ACS Sustainable Chem. Eng.*, 2021, **9**, 13514–13525.

237 D. Lee, J. S. Roh, I. Hwang, Y. Jung, H. Lee, I. W. Ock, S. Kim, S. Sun, S. Yang, H. B. Park, U. Paik and T. Song, *ACS Sustainable Chem. Eng.*, 2022, **10**, 7625–7634.

238 S. Ahualli, M. L. Jiménez, M. M. Fernández, G. Iglesias, D. Brogioli and Á. V. Delgado, *Phys. Chem. Chem. Phys.*, 2014, **16**, 25241–25246.

239 A. Siekierka, K. Smolínska-Kempisty and M. Bryjak, *Desalination*, 2020, **495**, 114670.

240 R. A. Rica, R. Ziano, D. Salerno, F. Mantegazza and D. Brogioli, *Phys. Rev. Lett.*, 2012, **109**, 156103.

241 X. Kong, A. Gallegos, D. Lu, Z. Liu and J. Wu, *Phys. Chem. Chem. Phys.*, 2015, **17**, 23970–23976.

242 M. Nasir, Y. Nakanishi, A. Patmonoaji and T. Suekane, *Renewable Energy*, 2020, **155**, 278–285.

243 D. Moreno and M. C. Hatzell, *ACS Sustainable Chem. Eng.*, 2019, **7**, 11334–11340.

244 S. Ahualli, M. L. Jiménez, Z. Amador, M. M. Fernández, G. R. Iglesias and A. V. Delgado, *Sustainable Energy Fuels*, 2021, **5**, 3321–3329.

245 Z. Zou, L. Liu, S. Meng and X. Bian, *Energy Rep.*, 2022, **8**, 7325–7335.

246 G. R. Iglesias, S. Ahualli, M. M. Fernández, M. L. Jiménez and Á. V. Delgado, *J. Power Sources*, 2016, **318**, 283–290.

247 F. Liu, T. F. W. Donkers, R. M. Wagterveld, O. Schaetzle, M. Saakes, C. J. N. Buisman and H. V. M. Hamelers, *Electrochim. Acta*, 2016, **187**, 104–112.

248 D. A. Vermaas, S. Bajracharya, B. B. Sales, M. Saakes, B. Hamelers and K. Nijmeijer, *Energy Environ. Sci.*, 2013, **6**, 643–651.

249 F. Zhan, Z. Wang, T. Wu, Q. Dong, C. Zhao, G. Wang and J. Qiu, *J. Mater. Chem. A*, 2018, **6**, 4981–4987.

250 H. Zhu, W. Xu, G. Tan, E. Whiddon, Y. Wang, C. G. Arges and X. Zhu, *Electrochim. Acta*, 2019, **294**, 240–248.

251 M. Röttger, T. Domenech, R. van der Weegen, A. Breuillac, R. Nicolaÿ and L. Leibler, *Science*, 2017, **356**, 62–65.

252 B. Nath, *Resonance*, 2019, **24**, 575–582.

A.2 Comparison of miniaturized mechanical and osmotic energy harvesting systems

Wu, N., Derkenne, T., Tregouet, C., and Colin, A. Comparison of miniaturized mechanical and osmotic energy harvesting systems. 118:109004.

In this appendix, we present the review article published on the miniaturized mechanical and osmotic energy harvesting systems. It refers to the Chapter 1 of this thesis manuscript.

Nano Energy 118 (2023) 109004

Contents lists available at ScienceDirect

Nano Energy

journal homepage: www.elsevier.com/locate/nanoen

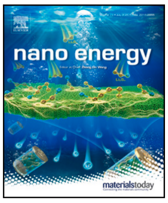

Full paper

Comparison of miniaturized mechanical and osmotic energy harvesting systems

Nan Wu, Timothée Derkenne, Corentin Tregouet, Annie Colin *

ESPCI Paris, PSL Research University, MIE-CBI, CNRS UMR 8231, 10, Rue Vauquelin, F-75231 Paris Cedex 05, France

ARTICLE INFO

Keywords:
Energy harvesting for IoT
Osmotic energy
Electrets
Triboelectricity
Piezoelectricity
Electrostriction

ABSTRACT

IoT stands for Internet of Things. It refers to the network of physical objects or "things" embedded with sensors, softwares, and other technologies that enable them to connect and exchange data with other devices and systems over the internet. The IoT has the potential to transform many areas of our lives, including home automation, healthcare, transportation, manufacturing, etc. By collecting and analyzing data from connected devices, businesses and organizations can gain insights that can help them make better decisions, improve efficiency, and reduce costs. Naturally, IoT requires energy to work and many techniques have been developed to limit the power consumption of the devices. These objects now need very little power to work, of the order of the mW or the µW. However, the IoT devices need to run for long periods of time without being replaced or recharged. This is especially important for devices deployed in remote or hard-to-reach locations. In this framework, it is of great importance to develop energy harvesting systems for IoT. It is of prime importance to use energy from their environment rather than relying on conventional power sources like batteries or mains electricity. By reducing the need for disposable batteries, energy harvesting can help to reduce waste and minimize the environmental impact of IoT devices. Energy can be found in ambient light, temperature differences, vibrations, or electromagnetic radiation. In this review article we will focus on the recovery of energy from mechanical vibrations and on the recovery of mixing energy: these methods have in common to be based on material surface charges. We will detail different modes of operation: the realization of sensors that do not need power, the realization of energy recovery generators which store energy for sensor consumption, and finally the realization of energy recovery generators feeding directly sensors. We will describe the different physical mechanisms of these processes. We will then illustrate them with examples of outstanding achievements.

1. Introduction

The Internet of Things (IoT) refers to a network of intelligent objects which are able to collect information, communicate, exchange data and possibly react towards environmental changes [1–3]. In addition to the conventional electronic objects, such as computers, tablets, and smart phones, IoT could also connect ordinary physical objects of all scales which are embedded with sensors, and living objects as humans and animals. The conception of IoT could facilitate automation process and thus derive new services and applications. The IoT market has maintained rapid growth in recent years, with its market size reaching 650 billion USD by the year of 2026, corresponding to a compound annual growth rate (CAGR) of 16.7% [4]. In terms of application areas, the IoT market is segmented into industries including healthcare, agriculture, automotive, manufacturing, predictive maintenance [5] and smart cities. According to a report by MarketsandMarkets, the healthcare IoT market is expected to reach USD 158.07 billion by 2025, growing at a CAGR of 30.8% from 2020 to 2025 [4]. The IoT industry is a fast-growing and promising market with a wide range of applications and opportunities.

In terms of electrical consumption, the IoT-related energy is estimated to be around 200 TWh per year in 2025, which corresponds to 0.7% share of the global electrical consumption [6]. Considering an estimation of 40 billion connected objects in 2025, the energy consumption in IoT is estimated to be 0.6 mW per device, which is considered as a rather low consumption. However, most of these devices need to operate disconnected from the electrical grid for an extended working time, in conditions where battery replacement is impractical. Such is the case for vibration and stress sensors inserted in bridge structures or for medical use. Thus, development of miniaturized power supply systems for intelligent IoT objects remains a key issue [7].

---

* Corresponding author.
E-mail address: annie.colin@espci.psl.eu (A. Colin).

https://doi.org/10.1016/j.nanoen.2023.109004
Received 1 May 2023; Received in revised form 22 August 2023; Accepted 19 October 2023

To tackle the above-mentioned power-supply problem, the first step is to reduce power consumption. Various factors can affect IoT power consumption. By choosing suitable hardware devices, i.e., microcontrollers, sensors, and wireless modules, it is possible to manage power consumption and extend the device battery life. The communication protocols used in IoT devices can also affect power consumption. For example, compared with Wi-Fi and cellular connectivity, Bluetooth or Zigbee consume much less power, which are certainly more suitable for low-power applications. Additionally, sending data at high frequencies would quickly drain the device's battery: it is thus important to optimize data transmission and minimize the frequency of data transfers. In the last decades, significant progress was achieved in electronics technologies for the development of ultra-low consumption devices. To name of few, the Phoenix processor has a sleep power consumption of only 3 pW in sleep mode and 200 nW in active mode [8], and Lin et al. developed a temperature sensor which consumes only 220 nW [9].

The second step is to design self-powered IoT objects by integrating energy harvesting systems to exploit energy sources in surrounding environments. Such design could decrease or even eliminate the use of batteries in IoT objects. In fact, large quantities of untapped energy sources could be considered for IoT objects powering. These sources either come from human activities or derive from ambient energies, such as chemical energy (chemistry, biochemistry), thermal energy (fatal heat, temperature gradients, variations), radiant energy (sun, infrared, radio frequencies) and mechanical sources (vibrations, deformations) [10]. The energy-harvesting process extracts energy from the surrounding environment and converts it into electrical energy.

A natural idea is to miniaturize the existing mature technologies for energy harvesting, such as wind technology. However, due to its bulky and complex structure, the miniaturization remains difficult. Considering the energy densities of untapped sources, outdoor solar energy is the highest energy source with a power density of 15,000 μW cm^{-3} [10]. It drops to 100 μW cm^{-3} for indoor environments. The theoretical limit of solar cell on a single junction is 29.1%. The world record for solar-cell efficiency of 46% was achieved by using multi-junction concentration cells [11]. Based on exotic materials such as gallium arsenide, this technology remains until now economically non-viable.

The second untapped environmental energy source is mechanical vibrations which can be found almost everywhere, from human bodies to industrial installations. The source of mechanical energy can be a vibrating structure (a bridge, a building, a window in a noisy street) or a moving object (a washing machine). Each vibration is characterized by a frequency f and an amplitude of oscillations Y_0. The mechanical power generated by vibrations can be harvested using an inertial device composed of a seismic mass m and a spring with an elastic constant k. In such a device, the amount of power generated is proportional to the cube of the vibration frequency. The generated power writes $\frac{mY_0^2 8\pi^3 f^3}{4\xi}$ where ξ is the damping factor [12]. Using this framework, we can estimate the power of classical vibrations in daily life. For example, common activities as walking corresponds to a source of mechanical energy with a power of 67 W, breathing of 0.83 W, finger typing of 0.01 W. These values correspond to the energy consumption of the IoT objects. A typical harvesting power density is of the order of 100 μW/cm^3 [13].

Close to mechanical energy, osmotic energy is considered as the third ambient environmental sources. When 1 cm^3 of river water is mixed with 1 cm^3 of sea water, an energy of 2.73 J is released. Considering all the rivers and effluents running to the sea, a global power of around 2 Terawatts is estimated, which corresponds to 75% of the world's electrical power consumption in 2021 [14,15]. The current devices for the recovery of osmotic energy based on selective membranes enable the recovery of 100 μW cm^{-2}, which makes this form of energy, nicknamed blue energy, the second most important source of recoverable energy on a par with the energy recoverable from mechanical vibrations. Thermal gradient, thermal variation, Infrared sources, radio frequency are energy sources present in our environment but at lower available energy levels [16]. For this reason, and because the corresponding harvesting technologies are less mature, we have decided not to deal with them here. Mechanical vibrations and osmotic energy seem to be suitable energy sources to power sensors. The potentially recoverable values are in agreement with power demand of IoT objects. In this review, we will focus on energy-harvesting systems both for mechanical-vibration energy sources and osmotic energy sources.

They have indeed a lot in common since they are both based on surface-charge effect. Several technologies have been developed for converting mechanical waste energy. They present different advantages or disadvantages, in particular according to the intended application. A classic principle for converting mechanical vibrations into electricity is to use electromagnetic generators. The operating principle of an electromagnetic mechanical vibration energy sensor involves the use of a magnet, a coil and a mass–spring system [17]. When the sensor is subjected to mechanical vibrations, the mass–spring system undergoes oscillations, causing the magnet and coil to move relatively to each other. This relative movement induces a changing magnetic flux through the coil in accordance with Faraday's law of electromagnetic induction. The changing magnetic flux induces an electromotive force (EMF) in the coil, generating a voltage across it. This voltage can be used to pass an electric current through a load, for example to charge a battery or power electronic devices. Electromagnetic energy generation is a well-established technology, and the use of this transduction mechanism in small-scale energy harvesting applications is the subject of much research. Fundamental principles and analysis of generators tested to date clearly show that electromagnetic devices do not lend themselves to downscaling [18]. The normalized power measured for an acceleration of 1 m s^{-2} is less than 0.5 μW cm^{-3} and decreases for smaller size [17]. For this reason, we have decided not to mention these generators in the review and to focus on piezolectric device, electrostrictive materials, electrets device and triboelectricity.

In all these situations, vibrations induce an alternative capacitive current that requires rectification before use.

In the osmotic energy situation, selective membranes or highly charged membranes are used to produce an ionic flux which is converted at the electrode level into an electronic current. The electrodes can be capacitive (generation of an alternative current) or faradaic (generation of a continuous current). In this review, we will focus on the development of energy-harvesting systems to power miniaturized sensors based on material surface charge. In each case, we will describe the main working principles, discuss the limitations and advantages, and then illustrate the process by describing practical applications. There are numerous reviews in the literature on each of these technologies (see [19–22] for triboelectric nanogenerators, [23–26] for piezolectric device, [27–29] for electrostrictive materials, [15,30,31] for osmotic energy). The originality of our work consists in presenting 4 different energy-recovery modes and comparing them.

2. Mechanical vibration energy harvesting using piezoelectric materials for sensor powering

2.1. Piezoelectricity

Piezoelectricity was discovered by Pierre and Jacques Curie in 1880 while studying quartz and tourmaline crystals [32]. Piezoelectric materials have the ability to produce voltage when deformed due to vibrations (direct effect). Conversely, they deform when subjected to an externally applied voltage (inverse effect).

Piezoelectricity originates from the distribution of ions of certain crystals. A piezoelectrical crystal has no center of symmetry [33,34]. In the absence of deformation, the electric dipoles created by the charge distribution cancel each other out exactly, which leads to the absence of net charge on the crystal faces. When the crystal is compressed, the absence of a center of symmetry of the lattice induces that the barycenters of the positive and negative charges no longer coincide. In this case, the electric dipoles no longer cancel each other out, which leads to the appearance of net positive and negative charges on the opposite sides of the crystal.

There are 32 crystallographic classes, out of which 21 are non-centrosymmetric (lacking center of symmetry). 20 of them exhibit direct piezoelectricity, with the 21st one being the cubic class [35]. However, in most cases, these materials are not a perfect crystal. This is always the case with polymers which are never in a monocrystalline form. To obtain a piezoelectric response of these materials, it is necessary to orientate the dipoles in the material at rest. This requires an important process called "poling" during which the molecular dipoles of the material are reoriented by exerting a high electric field in the range of 5–100 MV m^{-1} at high temperature (300 °C), followed by a subsequent cooling.

The electro-mechanical behavior of piezoelectric materials can be described by two constitutive equations.

$$S = [s^E]T + [d]E \tag{1}$$

$$D = [d^t]T + [\epsilon^T]E \tag{2}$$

where S is the strain tensor, vector D is the dielectric displacement vector in N m V^{-1} or C m^{-2}, $[\epsilon^T]$ is the permittivity tensor, $[s^E]$ the elastic compliance tensor, E is the applied electric field vector in V m^{-1}, and T is the shear stress. The superscripts T and E indicate that the quantity is measured at constant stress and constant electric field, respectively. $[d]$ is the direct piezoelectric-effect matrix, $[d^t]$ is the matrix which describes the converse piezoelectric effect. In this situation, the superscript t determines the transposition matrix.

Axis 3 is generally chosen according to the direction of the remanent polarization field. The axes 1, 2 and 3 form a direct trihedron. The piezoelectric-effect matrix d has coefficients d_{ij}. The first index i corresponds to the direction of the electric field, i.e. the direction perpendicular to the electrodes, the second index to the direction of the mechanical action. The material can be used according to the mode 33 or 31 depending on the mechanical stress is perpendicular or parallel to the electrodes. Usually, the mode 33 show better performances in term of electromechanical properties than the mode 31. The electromechanical coefficient k_{ij} is typically used to attest the quality of the electromechanical conversion. For a mechanical stress perpendicular to the electrodes, k_{ij} can be expressed as $k_{ij}^2 = \frac{d_{ij}^2}{\epsilon_{ij}^T s_{ij}^E}$. The coefficient k_{ij}^2 corresponds to the energy conversion ratio, i.e. the value of the stored electrical energy divided by the input mechanical energy. A high coupling factor k_{ij} does not necessarily quantify the energy harvesting capability of a material. Instead, it is associated with the efficiency of converting input mechanical or electrical energy into stored electrical or mechanical energy and not energy harvested by the circuit. Piezoelectric energy harvesters, on the other hand, need to convert mechanical energy into useable, or output, electrical energy. Based upon this analysis, Roscow et al. [36] defined under applied strain the factor of merit as the ratio of the output harvested energy divided by the input mechanical energy is given by : $FoM = \frac{d_{ij}^2 Y^2}{\epsilon_{ij}^T}$.

There are 4 main classes of piezoelectric materials: ceramics (lead zirconatate titanate (PZT) [37,38], $BaTiO_3$ [39], $LiNbO_3$ [40]), metal-oxide single crystals (PMN-PT [41,42] a solid solution of lead-magnesium-niobate (PMN) and lead titanate (PT)) polymers (Polyvinylidene fluoride (PVDF) [43,44]) and composites (PZT polymer composite [45,46], $BaTiO_3$ PDMS composite [47], flexible cellulose nanofibril/MoS_2 nanosheet composite [48]). Lead (Pb) based ceramics such as PZT, exhibit high piezoelectric coefficients. However, their rigidity, brittleness, and toxicity limit their applications [49]. Polymers are neither rigid nor brittle. However, they present much weaker piezoelectric properties than other materials which exhibit huge polarization in their crystalline structure. As an example, the k_{33} coefficients of the PZT-5H ceramic is equal to 0.75 [50], that of the PVDF to 0.22 [51] and that of the single crystal PMN-32PT with (001) orientation to 0.93 [50].

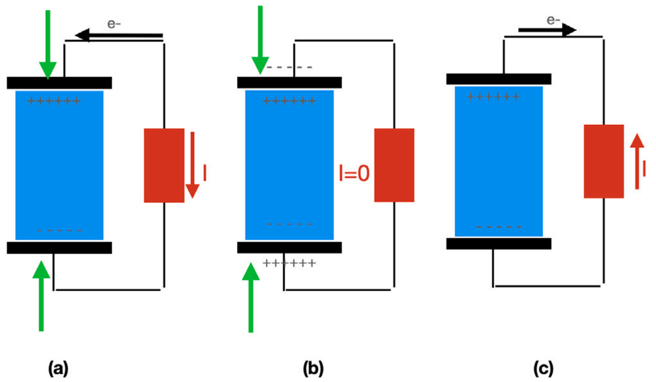

Fig. 1. Piezoelectric material based energy harvesting system. (a) The piezoelectric material is loaded between two electrodes. A force is applied on the material and create charges at the top and the bottom of the material. An electronic current appears to balance these charges. (b) The dipole created by the force is balanced by the charges. The current intensity is zero. (c) the Force is released. The charges go back to their initial position. An inverse electronic current is produced.

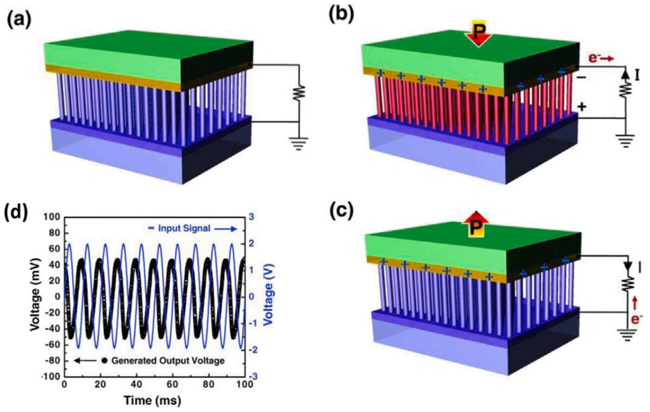

Fig. 2. Production of electric current by a piezoelectric. (a) Piezoelectric ZnO nanowire arrays placed between two electrodes coated with Platinum. (b) The pressure wave creates a dipole and the appearance of charge on the electrodes. This leads to a potential difference between the top and the bottom of the polarized sample and thus to an electron flow which balances the charges and equalizes the electric potentials on both sides. (c) the decompression causes the cancellation of the internal dipole and thus the transfer of charges in the opposite direction. A current of opposite direction appears. (d) The input signal for the generation of a sound wave and the output voltage from the piezoelectric ZnO nanowire arrays due to the sound wave. The phase difference between the signals is due to the impedance of the intrinsic capacitance and reactance within the piezoelectric circuit.

Source: Figures and captions reproduced from [52] with permission from John Wiley and Sons, copyright 2010.

2.2. Piezoelectric materials and piezotronics

In the applications linked to energy harvesting from mechanical vibrations, the direct piezoelectric effect is used [23,53]. In order to recover energy from vibrations, piezoelectric materials are integrated into host oscillating structures such as cantilevers. The polarized material is placed between two electrodes which are connected by an electrical circuit.

The mechanical compression induces the appearance of charge on the crystal and a flow of electrons from the electrode in the electric circuit. This flow stops when the electric field created by the distribution of electrons in the electric circuit cancels the electric field created by the compression of the material. At this stage the current is zero. When the compression is released, the electric dipoles of the material are no longer deformed. Thus the barycenter of positive and negative charges coincide again and the charges disappear on the faces of the crystal.

The electrons initially displaced in the electric circuit will then return to their initial position. This will lead to an electric current of opposite direction in the circuit. In the situation of piezoelectric materials, there is no transfer of electrons from the piezoelectric material to the external circuit and the system behaves like a simple capacitor. The generated electric signal by the piezoelectric material under mechanical vibrations is thus a alternating capacitive signal. The voltage may have positive and negative minima, as well as areas of zero values (Fig. 1). To exploit the harvested energy, a rectifier bridge is required to convert the alternative signals into direct ones.

Wang et al. [54] introduced a new field coined piezotronics [55,56]. This field is based on piezoelectric materials that display semiconductor properties. In those situations, electrical charges can be transferred from the material to the electrode. We will start with the situation where such a material is placed between two platinum electrodes. This situation is illustrated in Fig. 2 where a ZnO-based device is used under a sound wave. At the level of the electrodes, the ZnO–Pt contacts are Schottky diodes. In the compressive mode, whatever the phase of the displacement, one of the two diodes is polarized in the wrong direction, which prevents the departure of the charges from ZnO. The generated current is capacitive and alternating. There is no transfer of electrons between the electrodes and the material in this situation. The system behavior is close to the one involved in classical piezoelectric materials as a simple capacitor.

The main breakthrough of piezotronics appears when the contacts between the material and the electrodes involve an ohmic contact on one side and a Schottky diode contact on the other. In this situation it is possible to produce a direct current [57,58]. Wang et al. developed a nanogenerator fabricated with vertically aligned arrays of zinc oxide nanowires (ZnO NWs) placed under a zigzag metal electrode with a small gap. Mechanical vibrations move the electrode up and down to bend and/or vibrate the nanowires. Unlike the previous device, the zinc nanowires are connected with a silver plate at bottom and with a platinum plate on top. It is to mention that the ZnO–silver contact is ohmic, while the ZnO–platinum contact is a Schottky diode.

When the platinum-covered tooth of the electrode deforms the nanowire, the curvature of the piezoelectric material causes a dipole to appear perpendicular to the main direction of the nanowire [54] (Fig. 3). In the stretched area, the potential of the nanowire is higher than the potential of the platinum metal. The Schottky diode is reverse biased and no electrons are allowed to pass in the electrical circuit. This phase corresponds to an electron displacement in the nanowire from the stretched area to the compressed area perpendicular to the main direction of the nanowire. When the tooth is placed deeper, the nanowire twists more and the contact is made with the compressed zone. The potential of this zone is lower than the potential of the platinum, the diode allows the current to flow and electrons can circulate in the closed circuit. Their passage tends to make the lateral potential difference disappear which closes the Schottky diode again. The current from the nanowire decreases and is cancelled. The global measured current is the sum of these milli-currents all oriented in the same direction. The output electricity generated is continuous and stable. The output averaged power density is comprised between 1 and 4 W m^{-3} [59].

The output power of piezoelectric and piezotronic devices depends both on intrinsic parameters, including the piezoelectric and mechanical properties of the material and the resonance frequency of the piezoelectric element, and extrinsic factors such as the features of the mechanical vibrations (frequency, amplitude) and the mechanical features of the host structure. This explains why in the literature, the level of power output of piezoelectric energy harvesters varies greatly from 100 μW cm^{-3} [60] to 10 000 mW cm^{-3} (KNN/MNC material [61]). In order to fix ideas, we propose in the following a series of outstanding examples which enable the performance comparison between piezoelectric systems and the other energy recovery systems.

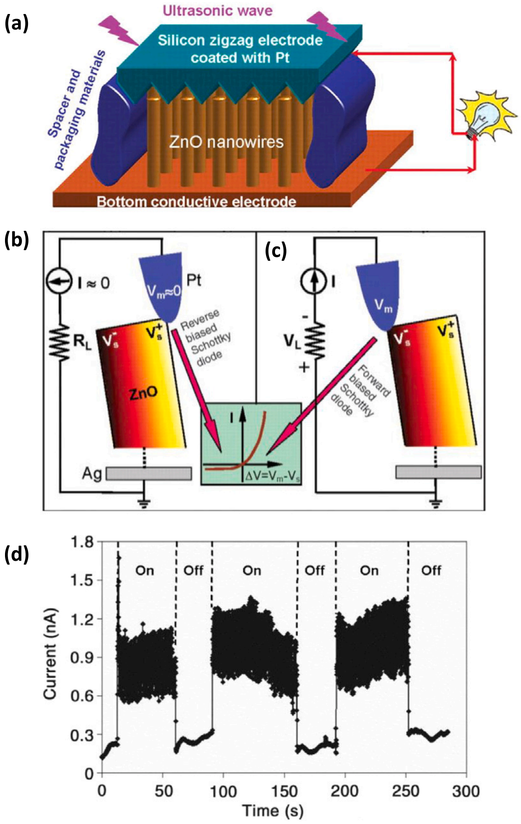

Fig. 3. (a) Schematic diagram showing the design and structure of the nanogenerator. Aligned ZnO NWs grown on a solid/polymer substrate are covered by a zigzag electrode. The substrate and the electrode are directly connected to an external load. (b) Contact between the tooth covered with Platinum and the semiconductor ZnO NW showing reverse biased Schottky rectifying behavior. The process in (b) is to separate and maintain the charges as well as build up the potential. (c) Contact between the tooth covered with Platinum and the semiconductor ZnO NW showing reverse forward Schottky rectifying behavior. The process in (c) is to discharge the potential and generates electric current. Figures and captions reproduced from [54] with permission from The American Association for the Advancement of Science, copyright 2006. (d) Measurement of the output current intensity in presence and absence of ultrasound. Figures and captions reproduced from [59] with permission from The American Association for the Advancement of Science, copyright 2007.

Using PZT-5H piezoceramics, Roundy et al. [62] reported an average outpower of 60 μW for a volume of 1 cm^3 and an acceleration of 2.25 m s^{-2}. Platt et al. [63] showed that by stacking 145 layers of PZT in a 2 cm^3 volume, they measured an average outpower of 1.6 mW (800 W m^{-3}) under a 900 N load and at a vibration frequency of 1 Hz. PMN-25-PT single crystal [41] displays an outpower density of 60 mW cm^{-3} (60 000 W m^{-3}) for a vibration of an amplitude of 150 μm and a frequency of 900 Hz. Under the same conditions, a device containing PZT ceramics displays a 20-time-lower power density [64].

PVDF is the most frequently used piezolelectric polymer. Compared with piezoelectric ceramics, PVDF has much lower piezolectric performances. For comparison, Kendall [65] showed that under 2 Hz excitation and 68 kg weight, a PVDF-based sole flexing system provides an output power of 0.6 mW, while the same device with a PZT-based sole could reach a power output of 5 mW. Wind energy harvesters using PVDF films were studied as well. their performances does not exceed 2 mW cm^{-3} in 7 m s^{-1} wind [66]. A way to improve polymer properties is to make thin film stacks. Godard et al. [67] showed that a stack of 10 thin layers of poly(vinylidene fluoride trifluoro-ethylene) screen printed on a polymer substrate harvests up to 0.97 mW at 33 Hz with an area of only 2.4 cm^2. The structure in N thin films allows to increase the recovered energy by a factor N^2 compared to the same overall polymer thickness.

Liao et al. [68] developed a fiber-based hybrid nanogenerator consisting of ZnO NWs/carbon fibers and Au-coated ZnO-papers, which can be used in converting mechanical energy into electricity. An output current with a peak value of 35 nA was generated. The desired electrical output is obtained by adjusting the external strain rate and the number of devices connected in parallel or in series. The electrical energy generated by the multi-fiber based NG was stored and used to light up a LED. Qin et al. [69] obtained an instantaneous (not averaged) power density of 5.1 mW cm^{-2} from one ZnO nanogenerator under a pressure of 0.44 kg cm^{-2} and a fixed frequency of 1000 Hz.

Piezoelectric vibration energy harvesting has also gained significant attention due to its compatibility with Microelectromechanical Systems (MEMS) technology [70].

Park et al. [71] introduce a piezoelectric microelectromechanical systems (MEMS) energy harvester that utilizes the d_{33} piezoelectric mode. To enhance the piezoelectric properties of the sol–gel spin-coated PZT (Lead Zirconate Titanate) thin film, a PbTiO3 seed layer was implemented as an interlayer between the ZrO2 layer and PZT thin films. The fabricated cantilever PZT film, featuring an interdigital-shaped electrode, exhibited a remnant polarization of 18.5 C cm^{-2}, a coercive field below 60 kV cm^{-1}, a relative dielectric constant of 1125.1, and a d_{33} piezoelectric constant of 50 pC N^{-1}.

The fabricated energy-harvesting device achieved an electrical power output of 1.1 W when subjected to a vibration with an acceleration of 0.39 g at its resonant frequency of 528 Hz, under a load of 2.2 MΩ with a 4.4 V peak-to-peak voltage. The corresponding power density was calculated as 7.3 mW cm^{-3} g^{-2} (rescaled by the acceleration 0.39 g), or a 1.1 mW cm^{-3}. The experimental results were compared with numerical calculations derived from dynamic and analytical modeling equations. Additionally, a comparison was made between the fabricated device and other piezoelectric MEMS energy-harvesting devices.

In summary, this study presents the modeling, fabrication, and characterization of a piezoelectric MEMS energy harvester utilizing the d_{33} piezoelectric mode. The implementation of a $PbTiO_3$ seed layer in the device's structure improved its piezoelectric properties. The fabricated device demonstrated significant power generation capabilities, as validated by experimental and numerical comparisons with other similar energy-harvesting devices.

It involves using cantilever beams with one or two piezoelectric layers and an elastic layer to convert mechanical vibrations into electrical energy. The configuration with two piezoelectric layers, known as a bimorph, has the potential to generate larger electric power. However, as the size of the cantilever-type vibration-energy harvester (VEH) decreases, it becomes more challenging to lower the resonance frequency and achieve sufficient electric power for sensor node batteries.

To address this issue, Tsukamoto et al. [72] display a bimorph VEH with a flexible 3D mesh structure. The purpose of this structure is to control the bending stiffness, thereby simultaneously lowering the resonance frequency and increasing the electric power output. The device consists of two PVDF (Polyvinylidene fluoride) piezoelectric layers bonded on both sides of a 3D mesh elastic layer, with a proof mass attached at the tip. The sum of the line spacing and line length in the mesh is 100 μm.

The study confirms the effectiveness of the bimorph VEH with a 3D mesh structure as an elastic layer through various experiments. Firstly, they demonstrate that the bending stiffness of the mesh harvester can be controlled by adjusting the line spacing in the mesh. Secondly, in vibration tests, it is observed that the resonance frequency of the mesh harvester is lowered by 26% compared to a flat-plate VEH, and the tip deflection is 1.3 times larger. Finally, the total output power of the device is measured to be 20.4 μW, which is sufficient to power low-consumption sensor nodes for Wireless Sensor Networks (WSNs).

All these figures are difficult to compare. Some powers are instantaneous and others are averaged, which is radically different because of the particular shape of the electrical signal. Moreover, they are obtained under different conditions of solicitation. These works do not present a energy conversion ratio which compares the recovered energy with the energy injected into the system. Only a few authors indicate the energy conversion rates in their work. For example, self poled PVDF-WS_2 composite displays a record energy conversion of 25.6% for piezolectric nanocomposites [73]. This value is closed to the one obtained by Chang et al. [64] (25%) for thin films of PVDF fibers. It is higher than the one reported for PVDF-DNA films (2.7%) [74], for PVDF/AlO-rGO (aluminum oxides decorated reduced graphene oxide incorporated PVDF based nanocomposite) Flexible Nanocomposite (12%) [75] and PZT nanocrystals (5%) [42].

All these features show that piezoelectric and piezotronic nanogenerators are among the most efficient nanogenerators [76]. These devices are unaffected by temperature and humidity [77] and can produce alternating current in a range from μW (microwatts) to mW (milliwatts) [78]. These nanogenerators require limited moving parts, zero external voltage sources and are of low cost [79]. They can generate power output with voltage levels that can be easily conditioned (i.e., converted to DC) [80] and sufficient for sensor powering demand. In the last decades, many achievements have been made [81]. We resume some significant examples in the section below.

2.3. *Sensors powered by piezoelectricity*

In the last decade, many self-powered sensors based on piezoelectric nanogenerators have been developed [82]. It is possible to separate the achievements made in three categories: devices that use the electrical signal created by vibrations to probe their environment (Simple Autonomous Sensor) [83], devices that store electrical energy and then restore it to connected objects (Sensor powered by a Nanogenerator With Storage System), and devices that directly power connected objects (Sensor powered by a nanogenerator without storage system). In the following we will discuss these three categories.

2.3.1. *Simple autonomous sensor*

Deng et al. [84] designed a self-powered flexible piezoelectric sensor (PES) based on cowpea structured PVDF/ZnO nanofibers (CPZN) for remote gesture control in a human-machine interactive system. The sensor exhibits excellent bending sensitivity of 4.4 mV deg^{-1} in a range of 44° to 122° and a fast response time of 76 ms. It does not need to be powered. They incorporated this sensor in a chain of devices allowing the remote control of a robotic hand. While the human hand performs movements, these movements are detected and captured by the piezoelectric sensor. The electrical signal is then transferred, analyzed, and transformed into commands that guide the movement of the robotic palm.

In the field of smart sports and high performance sports training, Tian et al. [85] designed a self-powered, lamellar crystal-rich, baklava-structured PZT/PVDF piezoelectric sensor. This sensor has a high sensitivity (6.38 mV/N) along with a short response time of 21 ms. They used this composite to fabricate a ping pong racket which integrates 36 different sensors distributed on the racket. During training, it is possible to see the force of the impact and the centering of the ball on the racket.

Piezoelectric biosensors/bioactuators [86] are developed with new materials and advanced encapsulation methods to avoid the toxicity of conventional lead-based piezoelectric materials. These materials such as poly(lactic acid) polymer (PLLA) can be used in the human body for biomedical pressure sensing applications. Curry et al. have implanted a PLLA piezosensor inside the abdominal cavity of a mouse to monitor the pressure of diaphragmatic contraction [87]. Liu et al. [88] developed a PVDF piezoelectric sensor for respiration sensing and healthcare monitoring.

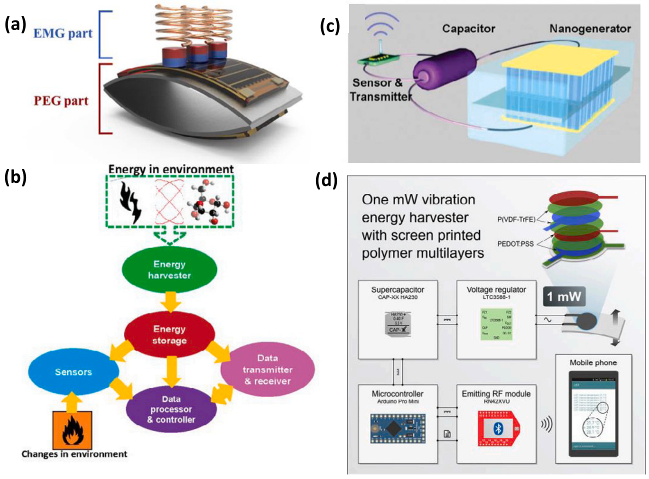

Fig. 4. (a) Schematic image and pictures of the hybrid energy harvester based on PEG and EMG [90]. Figures and captions adapted from [90] with permission from Elsevier, copyright 2020. (b) Schematic diagram of the integrated self-powered system. An integrated system can be divided into five modules: energy harvester, energy storage, sensors, data processor and controller, and data transmitter and receiver. (c) The prototype of an integrated self-powered system by using a nanogenerator as the energy harvester [89]. Figures and captions adapted from [89] with permission from American Chemical Society, copyright 2011. (d) Godard et al. show that 2.4 cm^2 of screen-printed multilayers of a piezoelectric polymer, P(VDF-TrFE), can harvest up to 1 mW at 33 Hz. They demonstrate that this is sufficient for an autonomous sensor to communicate with a mobile phone independently of any other energy source [67]. Figures and captions adapted from [67] with permission from Elsevier, copyright 2020.

2.3.2. *Sensors powered by a nanogenerator with storage system*

In 2011, Hu et al. [89] presented one of the first self-powered connected objects. For this they covered a cantilever equipped with electrodes of polymer substrate and textured ZnO films. Subjected to vibrations which induce a deformation of 0.12% at a deformation rate of 3.56% s^{-1}, the 1 cm^2 device produces a power of 6 μW (see Fig. 4). This power is not enough to power a connected object and requires a storage system consisting of a rectification circuit and a capacitor (Type 1210, 22 μF ± 10%, AVX). This system powers a sensor and a radio frequency data transmitter. Thanks to this storage system, they were able to autonomously transmit wireless signals at distances of 5–10 m.

Godard [67] et al. used a stack of 10 thin layers of poly(vinylidene fluoride trifluoro-ethylene) connected to a rectifier circuit and a voltage regulator (LTC3588-1, Linear Technology) to power a micro-controller (Arduino Pro Mini) connected to a radiofrequency (RF) emitter (RN-42 Blue-tooth module from Microchip). Temperature values recorded by the microcontroller internal temperature sensor were successfully transmitted via RF signal to a mobile phone for 10 s (see Fig. 4).

2.3.3. *Sensors powered by a nanogenerator without storage system*

This approach is more difficult. Despite the realization of many piezoelectric nanogenerators that can produce powers of a few mW, it is difficult to find complete devices integrating a nanogenerator and a commercial Internet of Things (IoT) sensor in the literature. The main reason is that direct plugging requires power of at least 5 mW, which remains a complex aim to reach [90].

Jung et al. [90] succeeded in producing an average output power of 25.45 mW at 60 Hz and 0.5 G input vibration by coupling a piezoelectric nanogenerator made of macro-fiber composite (MFC) piezoelectric plates on the substrates and an electromagnetic nanogenerator. The optimization of the coupling requires an electrical impedance matching and the minimization of the mechanical damping (see Fig. 4). They managed to use this device for direct power supply of a commercial IoT sensor (CC2650 Bluetooth SensorTag, Texas Instruments Corp) without the use of storage system.

Hwang et al. [91] used a new generation of single crystal $(1-x)\mathrm{Pb}(\mathrm{Mg}_{1/3}\mathrm{Nb}_{2/3})\mathrm{O}_3 - x\mathrm{PbTiO}_3$ (PMN-PT) to prepare a piezoelectric nanogenerator. This material exhibits an exceptional piezoelectric charge constant of d_{33} up to 2500 pC N^{-1}, which is almost 4 times higher than PZT, 20 times higher than $BaTiO_3$ and 90 times higher than ZnO. Using this material, they achieved a self-powered artificial pacemaker with significantly increased electrical output current. No battery is needed to store the recovered energy.

2.4. *Summary and outlooks for piezoelectric materials*

The previous results show that the piezoelectric nanogenerators reported in the literature are capable of powering sensors. This allows us to be very optimistic for their deployment for IoT objects, especially in the field of building monitoring [76]. Wireless sensor networks have become an essential part of building environment monitoring, covering multiple functionalities including temperature, light usage, object movement, humidity, air velocity in a ventilation duct and etc. The real-time monitoring of these parameters enables an intelligent regulation and control of the building environment with reduced energy demand. All these sensors require an electrical power between 0.5 and 100 μW.

It is possible to recover energy from environmental sources, such as air flows in ventilation systems or the movement of people on the floor. To provide a quantitative point of view, the reported powers range from 37.4 to 800 μW in ventilation systems and from 66 μW to 55 mW for floors [76]. Even if it remains complex to remove the energy storage system from the module, these piezoelectricity based systems could significantly extend the classical battery systems and decrease the energy cost of the IoT. Piezoelectricity based technologies have already been applied by several companies around the world, as in the case of Kinergizer and EnOcean [92].

Despite the great progress in piezoelectricity-based systems, there are still technological challenges which require extensive research works before the manufacture of matured autonomous IoT devices. The key issue consists in the output power and the need for intermediate energy storage. Future research works should dedicate more attention to the management and modelization of energy generation and storage exchange, the integration of bio-source materials and the technology cost reduction [7].

3. Mechanical vibration energy harvesting using electrostrictive materials for sensor powering

3.1. *Electrostriction*

Electrostriction is a mechanism that all materials possess. When subjected to an electric field E, materials deform. Their deformation S is proportional to the square of the electric field E and therefore does not depend on the direction of the field.

The microscopic origin of this phenomenon comes from two phenomena (see Fig. 5). First, when a material is placed in an electric field, the charges of this material move with respect to their initial position. This results in the appearance of a net charge on the surfaces of the material, the charge on the upper surface balancing the charge on the lower surface. The action of the field compresses the material. This mechanism is at the origin of the breakdown voltage of capacitors containing soft polymer dielectrics. The deformation is given by $S = -E^2\frac{\epsilon_0\epsilon_r}{2Y}$ where Y is the young modulus of the material, ϵ_0 the vacuum permittivity and ϵ_r the dielectric constant of the material.

Second, some polymers exhibit intrinsic electrostriction properties resulting from the change in their dielectric constant under the effect of the electric field. The electrical field modifies the relative position of the electric dipoles of the material. In this situation and for an uniaxial compression, the deformation S is given by $S = \frac{a_1+a_2(1-\nu)}{\epsilon_r}E^2$ where ν is

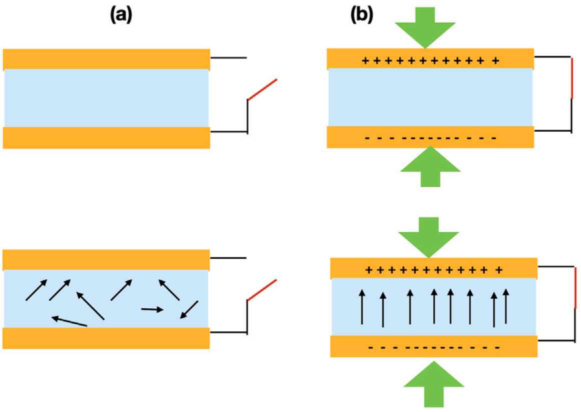

Fig. 5. Electrostriction origin. (a) Maxwell stress that originates from the Coulomb interaction between oppositely charged compliant electrodes. (b) Intrinsic electrostatic effect that originates from direct coupling between the polarization and the mechanical response.

the Poisson coefficient, a_1 and a_2 parameters describing the evolution of the dielectric constant as a function of the deformation.

These two deformations add up to describe the global response of the material [93]. $S = M_{33}E^2 = (\frac{a_1+a_2(1-\nu)}{\epsilon_r} - \frac{\epsilon_0\epsilon_r}{2Y})E^2$. The coefficient M_{33} is the electrostriction coefficient under an uniaxial compression along the electrical field direction. We report here measured M_{33} values. We will see in the following paragraph that it is necessary to define a figure of merit to compare the different materials between them and that only this coefficient is not suitable to qualify the performances. Muensit et al. [94] studied electrostrictive properties of polyaniline(PANI)/polyurethane(PU) composites at low fillers concentration. The intrinsic electrostriction modulus ($M_{33} = -6.10^{-16}$ m^2 V^{-2}) increases by a factor of 1.6 compared to pure PU. Yin et al. [95] investigated carbon black/P(VDF-TrFE-CFE) composites fabricated via a simple blending method. The composite displays an increase of the electrostriction modulus $M_{33} = -2.4.10^{-16}$ m^2 V^{-2} by a factor 2 compared to the polymer. A huge electrostriction modulus ($M_{33} = -2.4.10^{-14}$ m^2 V^{-2}) was reported by Yuan et al. [96] studying reduced graphene oxide/composite.

3.2. Electrostrictive material

In order to recover energy from vibrations, electrostrictive materials based variable capacitors are integrated into a host oscillating structure. Unlike piezoelectric or triboelectric materials, electrostrictive materials requires excitation from external voltage sources to be activated. A capacitor consists of two electrodes separated by a dielectric material. The capacitance of the capacitor is given for a flat capacitor by $C = \frac{Q}{U} = \frac{A}{\epsilon_0\epsilon_r d}$ where Q is the charge stored by the capacitor and U the potential difference across the capacitor, d the distance between the two electrodes, ϵ_0 the vacuum permittivity, and ϵ_r the dielectric constant of the material. A variable capacitor is defined as a capacitor whose capacity varies according to the mechanical vibrations. An example would be the capacitance variation caused by the distance variation between two electrodes in a capacitor.

By applying a variable capacitor, it is possible to design an energy conversion process from mechanical energy towards electrical energy. When the capacitor is polarized by a voltage U, it acquires a charge $Q_1 = C_1U$ and an energy $E = \frac{U^2}{2C_1}$. Considering the situation where the vibration initially moves the electrodes away from each other, the capacitance of the capacitor decreases and reaches a value of C_2. This induces at fixed U a displacement of electron in the electric circuit which connects the two electrodes so as to decrease the charge Q_1 carried by the electrodes to $Q_2 = C_2U$. When the two plates come together again, an electron displacement in the opposite direction occurs to increase the charge again and make it correspond to the value Q_1. The energy converted in a cycle in absence of losses with fixed U is equal to $E = \frac{1}{2}U^2(C_1 - C_2)$. By analyzing the electrical response of an electrostrictive material subjected to vibration, Lallart et al. [28,97] show that the maximum recoverable power is given by:

$$P_{max} = \frac{2\pi}{\epsilon}(M_{33}Y)^2 A l E_{dc}^2 f S_M^2 \tag{3}$$

where A is the surface of the material, l its thickness, f the vibration frequency, S_M the strain magnitude, E_{dc} the applied electrical field, ϵ_r the value of the dielectric constant, M_{33} the electrostriction coefficient under an uniaxial compression along the electrical field direction, Y the young modulus of the material under compression. They define a Figure of merit (FOM) F dependent only upon the properties of the electrostrictive material equal to: $P_{max} = FAlE_{dc}^2 f S_M^2$ with $F = \frac{2\pi}{\epsilon}(M_{33}Y)^2$.

Fig. 6(c) displays the FOM F of materials from the literature. Polyurethane displays lower performances than Nylon. PVDF is most suited polymer for these applications. The FOM values are enhanced when polymers are loaded with conductive particles. PVDF loaded with carbon nanotubes has a higher figure of merit than pure PVDF. PDMS-carbon black particles composite [100] exhibit the highest figure of merit (F = 7 10^{-8}, M_{33} = 8.46 10^{-15} m^2 V^{-2}). The excellent properties of composites are due to two reasons [28,100]. First, composite materials exhibit a large increase of dielectric permittivity in the vicinity of the percolation threshold. Second, the structure of a network of particles close to percolation can also be used to create intrinsic electrostrictive properties. Indeed, when a material close to percolation is strained, a local variation of filler concentration can be induced. Consequently, a variation of dielectric permittivity is observed. To be effective, this concentration variation must not be too important and lead to the creation of a percolation path in the sample which would make the latter an electrical conductor.

As explained previously, electrostrictive materials are materials that must be subjected to a voltage to be active. If these materials are conductive, ohmic losses occur. The loss magnitude is characterized by a loss factor $\frac{\sigma\omega}{\epsilon_0\epsilon_r}$ where σ is the net conductivity, and ω the electric pulsation. It is to mention that the losses are not taken into consideration in the calculation of FOM. In order to limit these losses, it is possible to add a thin insulation layer to the surface of the composites. Pruvost et al. [100,102] show that this allows to decrease the loss factor by a factor of 10 while maintaining the electrostrictive properties of the material.

3.3. Energy harvested by electrostrictive systems

Electrostrictive materials used in variable capacitors can target applications ranging from small to very large scales, which is not the case for piezoelectric materials. We recall that the frequency at resonance varies as $1/(\sqrt{m})$ where m is the mass of the system. Small frequencies are therefore accessible to large devices.

In this context, applications to wave energy recovery have been proposed. Bosch Company [103] makes a demonstrator model to convert wave energy into electricity with a disruptive design. A float is positioned on the surface of the ocean and is firmly anchored at the bottom of the ocean. The two halves are connected with a thousand sheets of dielectric polymers. Every 3 to 10 s, these sheets are deformed by the movement of the waves and allow current to be generated. Moretti [104] et al. demonstrated the ability of a dielectric elastomer to convert the oscillating energy carried by water waves into electricity. They build a harvester prototype using a commercial polyacrylate film as electrostrictive polymer. In resonant conditions, their system demonstrates a delivery power per unit mass of 197 W kg^{-1}.

At microscale, electrostrictive polymers can be used as an electroactive composite based on reduced graphite oxide sheets in a PDMS

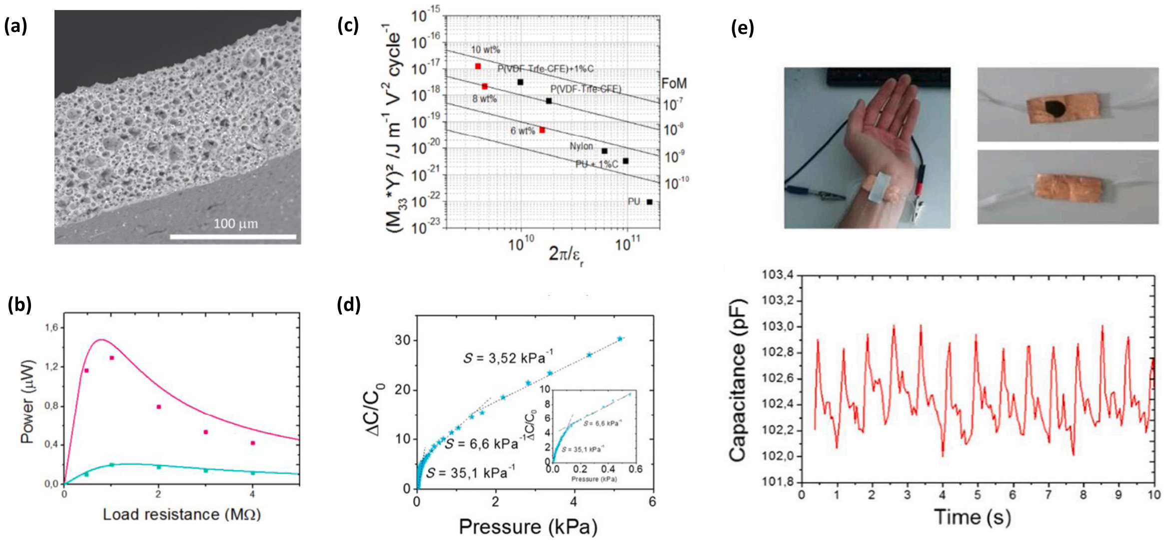

Fig. 6. Illustration of two possible applications of an electrostrictive porous carbon black composite : energy harvestor or capacitive sensor (a) Electron microscope picture of a cross-cut of a porous carbon black composite. (b) Energy harvestor: Harvested power of the composites with 8 CB wt% (green) and 10 CB wt% (pink) with insulating layer as a function of the load resistance. Squares are experimental data and lines are theoretical predictions using equation. The strain frequency is 100 Hz and the applied voltage over the composite Vdc = 32 V. (c) Energy harvestor: Comparison of the electromechanical performances at 100 Hz using the figure of merit (FoM) proposed by Guyomar et al. [97–99] Thick lines have the same FoM. Black spots refer to materials from the literature [97–99]. Figures and captions reproduced from [100] with permission from Institute of Physics Publishing Ltd., copyright 2018. (d) Capacitive sensor: Sensitivity measurements S after 100 cycles for three different pressure ranges (10 wt % CB). (e) Arterial signals measured with the sensor. Figures and captions reproduced from [100,101] with permission from Springer Nature, copyright 2019.

matrix. Applying a sinusoidal acceleration (0.5 g, 15 Hz), Nesser et al. [105] succeed in harvesting a power density of 6 μW cm^{-3} under a static electrical field of 0.4 V μm^{-1}. Cottinet et al. [99] measured a 280 μW cm^{-3} power density using a P(VDF-TrFE-CFE) polymer for a transverse strain of 0.2% with a static electric field of 10 V μm^{-1} at 100 Hz.

In the two previous studies, the ohmic losses are not evaluated. These are probably very low in the case of polymers but can be very important in the case of composites including conductive particles. In order to limit the electrical conduction of systems that have structures close to percolation, Pruvost et al. [100,102] used PDMS foams. During the synthesis the conductive particles are localized in the drops of an inverse emulsion of PDMS. After drying and cross-linking of the continuous medium and for moderate water fractions, the particles are trapped in the unconnected bubbles. This structure prevents the creation of connected paths. By introducing these foams in a cantilever structure and by using an thin insulating layer, they measure a 1 μW cm^{-2} (75 μW cm^{-3}) under a voltage of 200 V (thickness of the layer 125 μm i.e $E = 1.6$ V μm^{-1}) and an acceleration of 7 g. For this material the losses correspond to 1% of the harvested power.

From the data reported by Pruvost et al. [102], the conversion rate of the injected mechanical power can be calculated. In this device, the variation of the capacitance comes not only from the electrostrictive properties of the material but also from the creation of a very low capacitance when the electrodes of the capacitor are detached and separated by the vacuum. The energy supplied to the system is the kinetic energy of the upper part, and can be calculated from the mass of the upper electrode (m = 3 g) the relative displacement speed of the two electrodes ($v = e \times f = 1 \times 10^{-3} \times 40 = 0.04$ m s^{-1}) where f is the oscillation frequency and e the size of the air gap. The kinetic power is equal to 96 μW and the recovered power 7.5 μW leading to a conversion factor of 8%. This is lower than the performances reported by Lallart et al. who measured a conversion factor of 34% for P(VDF-TrFE-CTFE) composite with bis (2-ethylhexyl) phtalate [95]. In this situation, an electrical power density of 4.31 mW cm^{-3} was achieved for the modified terpolymer working at a DC bias electric field of 30 MV m^{-1}.

3.4. Sensors powered by electrostrictive materials

As presented above, there are three ways to power sensors using the energy around us: autonomous sensors, sensors powered by a nanogenerator with storage system, sensors powered by a nanogenerator without a storage system. In the following paragraph we discuss these applications.

3.4.1. Electrostrictive autonomous sensors

Electrostrictive materials have been widely used to fabricate capacitive sensors, whose working principle is mainly based on the variation of capacitance. They are usually composed of two stretchable electrodes between which is placed an elastomer dielectric film to form a well-known parallel plate capacitor. Such sensors allow in particular the local measurement of pressure or temperature and are excessively low energy consumers compared with resistive sensors.

The sensitivity to pressure SP is given by $P = \frac{\Delta C}{\sigma C_0} = \frac{\Delta C}{\epsilon Y C_0}$ where C_0 is the initial capacitance, ΔC the variation of the capacitance, σ the shear stress, ϵ the strain, and Y the young modulus. So to get a high sensitivity, low young modulus are required. Dielectric polymers with a low young modulus as PDMS are traditionally used. In this context, the capacitive sensitivity of a pyramid-structured PDMS film was investigated by Bao [106]. A sensitivity of 0.55 kPa^{-1} was reported compared to 0.02 kPa^{-1} for an unstructurated film (see Fig. 7). Structured PDMS has a high permittivity variation. Indeed, the air pockets are gradually and reversibly replaced by polymer during the deformation process. This leads to a variation of the dielectric constant by a factor of 2 or 3.

To increase the sensitivity of such devices without using additional energy, Pruvost et al. [100,101] have proposed to use PDMS foams whose bubbles are lined with conductive particles. Due to the elastic behavior of the foam pores, a sensitivity ten times higher than previously reported is measured. The sensitivity exceeds 35 kPa^{-1} for a pressure lower than 0.2 kPa (see Fig. 6(d) and (e)). These materials are inexpensive, easy to prepare, and have high capacitance values that are easy to measure using inexpensive electronic devices. These materials are part of the development of electronic skin systems [107]. Liu et al. [108] used an electrostrictive polymer to detect compressive force. This sensor consists of a series of elements made of DE membrane with out-of-plane deformation. Each element experiences

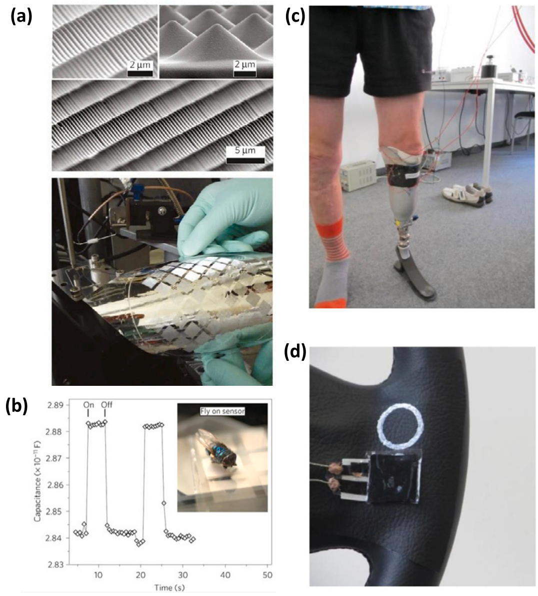

Fig. 7. (a) SEM images of the microstructured PDMS films. The pressure-sensitive structured PDMS films can be molded at full-wafer scale (100 mm) with high uniformity and fidelity on a variety of flexible, plastic substrates. (b) The microstructured PDMS films are able to sense the application of very small pressures. Shown is the capacitance change on placing and removing a bluebottle fly (20 mg) on an area of 64 mm2, corresponding to a pressure of only 3 Pa [106]. Figures and caption from [106] with permission from Springer Nature, copyright 2010. (c) Electrostrictive pressure sensor attached on the liner of a knee prosthesis for an experimental evaluation [111]. (d) Control interface with electrostrictive pressure sensors integrated into an automotive steering wheel [112]. Figures and caption from [111,112] with permission from Society of Photo-Optical Instrumentation Engineers (SPIE), copyright 2016 and copyright 2017.

highly inhomogeneous large deformation to obtain high sensitivity. The sensitivities of the sensor element are about 105 pF N^{-1}. Capacitive sensors [109] are designed to monitor the pressure exerted on a chair by a person, the pressure distribution on a shoe, and the pressure exerted by a knee prosthesis on an amputee who could be seriously affected by an arising decubitus [110,111].

These sensors can also be used for human machine interfaces. It is possible to synchronize the current intensity with the pressure intensity received in the sensor, so as to modulate the LED lighting [112]. This kind of device can be integrated into a car steering wheel for the purpose of illumination or temperature control [112] (see Fig. 7). Unlike conventional robots [113], soft robots can operate freely in our environment because they cause less damage in case of impact. Dielectric soft sensors are the sensors of choice that can be integrated into soft robots. They can measure pressure but also deformation and shear. The challenge is to use many sensors in parallel.

3.5. *Sensors powered by a nanogenerator without storage system*

Hyper Drive Corp has created a small electric power generator utilizing an electrostrictive polymer, which has a mass of around 1 g and a diameter of 8 cm . When the device central part is pushed by 4–5 mm once every second, it generates roughly 0.12 W of power [114]. This amount of energy can power various LEDs, and through coupling with a wireless system, it can turn remote devices on and off. The generator only supplies electricity to the devices when it receives mechanical energy, making it an effective switching system. Its uncomplicated design makes it simple to integrate into a wireless network. Electrostrictive generators [115] attached to the soles of shoes can produce electric power through deformation caused by walking. Adult men, in experimental settings, were able to generate 0.8–1 W of power by walking at a pace of one step per second.

3.6. *Summary and outlooks for electrostrictive materials*

As shown in the previous paragraph, electrostrictive materials, particularly polymeric materials, have very important applications as autonomous sensors. Unlike piezoelectric ceramics, electrostrictive polymer materials are cheap and soft. They are therefore perfectly suited for developing commercial sensor applications. The company StrechSense established in 2015 developed a custom-made electrostrictive-material-based pressure sensors and shear sensors [27]. In the case of medium size devices the results obtained are better than the results of piezoelectric materials. It seems to us that there are prospects in this axis, especially in the recovery of energy from human movements. The powers generated by these electrostatic devices are of one or two orders of magnitude higher than the one obtained with piezoelectric materials. 0.8 W are reported for a shoe equipped with an electrostrictive polymer generator [115] where as 5 mW are reported for a shoe equipped with an piezoelectric ceramic generator [65].

4. Mechanical vibration energy harvesting using electrets for sensor powering

4.1. *Electrets*

Electrets are dielectrics able to keep an electric field for years thanks to charge trapping [116,117]. They are equivalent in electrostatics to magnets in magnetostatics. Trapped “electric charge” can take many forms. It may be excess charge on the surface or in the bulk of the material, but it may also be polarizations in the bulk (fixed aligned dipoles for polar dielectrics, or space charges for polar and non-polar dielectrics), or a composition of both [118]. Electrets are obtained by implanting electric charges into dielectrics. Theoretically, dielectrics do not conduct electricity; therefore, the implanted charges stay trapped inside. Electret research began in earnest when Mototaro Eguchi [119] prepared one of the first electrets by cooling down a molten mixture of Carnauba wax and resin with a little beeswax, while applying an electric field of around 10 kV/cm to the mixture. Currently, many techniques exist to manufacture electrets [120]: thermal charging by heating up and cooling down in a constant electric field [119], tribo-charging by contact or friction on metallic or dielectric objects, corona-charging, electron or ion injections, liquid contact charging, photo-charging and radiation charging. Tribolelectric contact is not covered in this section. In view of the literature generated in recent years on this subject and the advances made in this field, a special section is devoted to triboelectric nanogenerators (TENG) and follows this section [119].

Corana-charging is the most used technique. It consists of a point-grid-plane structure whose point is subjected to a strong electric field: this leads to the creation of a plasma, made of ions. These ions are projected onto the surface of the sample to charge, and transfer their charges to its surface. The key to all these steps is to find materials that will keep the load they carry over time. Dielectrics are not perfect insulators and implanted charges can move inside the material or can be compensated by other charges or environmental conditions, and finally disappear. A focal area of research on electrets concerns their stability [121–123]. Nowadays, many materials are known as good electrets, able to keep their charges for years: for example, PTFE (which is one of the best insulating polymers with low conductivity of 10^{-22} Ω^{-1} cm^{-1}) and silicon dioxide (SiO_2) whose stability is estimated at more than 100 years [124,125]. As an electret, Teflon can contain charge densities of 5.10^{-4} C/m^2 [126].

The key issue in studying electret materials is to know how the charge distribution in an electret influence the electric field around it. The drop of electrical potential V_e across the electret is linked to the volume charge distribution $\rho_e(x)$ by $V_e = \frac{1}{\epsilon_O \epsilon_e} \int_0^{e_e} \rho_e(x)dx$ where e_e is the thickness of the electret, ϵ_0 the vacum permittivity, ϵ_e the relative permittivity of the electret. To make a generator from an electret,

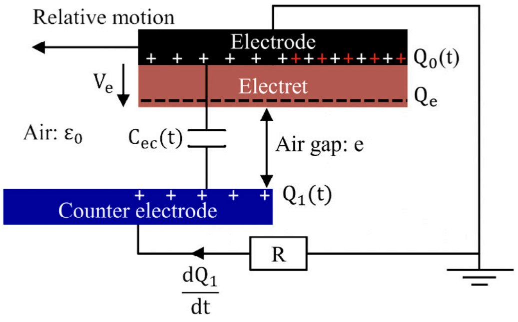

Fig. 8. Electret-based converter with a simple load R. *Source:* Figure reproduced from [127] with permission from IOP Publishing, Ltd, copyright 2016.

it must be placed between two electrodes. By compensation, charges will appear on the electrodes. Gauss's theorem implies that the charge carried by the electret is equal and of opposite sign to the sum of those carried by the electrodes ($Q_o(t) + Q_1(t) + Q_e) = 0$ on Fig. 8). The relative movement between the electret and the electrodes will induce a permanent reorganization of the charges between the two electrodes. An electric current will flow through the charge resistance R connecting them (see Fig. 8). Its intensity is given by the Kirchhoff's law and writes: $I(t) + \frac{Q_1(t)}{RC_{ec}(t)} = -\frac{Ve}{R}$ where $I(t) = \frac{dQ_1(t)}{dt}$ and $C_{ec}(t)$ is the capacitance between the two electrodes. The average power P_r harvested by the resistor R (during a period of time T) is given by $P_r = \frac{1}{T}\int_0^T R(\frac{dQ_1}{dt})^2 dt$. The output power is exactly proportional to the frequency f of the periodic displacement and to the electret's surface voltage squared (V_e^2) [127,128].

4.2. Electrets nanogenerators

There are two typical devices for generating electricity from electrets: rotating devices and conventional variable-capacity devices. From a historical point of view, rotating devices were first introduced.

Jefimenko et al. [129] have developed a rotating electret generator consisting of two electrets of different charge placed between two pairs of conductive half-discs. Two electrodes are created by connecting each half-disc of one pair to a half-disc of the other pair. In this generator, charge transfer is due to the variation in charge displacement induced on the two pairs of electrodes during rotation of the two oppositely charged electret discs. Walker's initial generator is a large one. Its diameter is 152.4 mm. It produces a power of 0.025 W at a rotation speed of 6000 rpm and a load resistance of 10 MΩ. This generator has a high internal impedance, which facilitates energy storage and provides an important potential difference. An electret generator with a radius of 45 mm was developed by Tada [130]. Maximum reported power output from an electret generator was 1.02 mW. Tai et al. miniaturized this set up [131]. Their prototype generates 25 µW with an electret of radius 4 mm, thickness of 9 µm, effective charge density of $-2.8 \cdot 10^4$ C m^{-2} and rotational speed of 4170 rpm.

Currently, the most common and simple structure used is those of a variable capacitor. In some devices, the electrodes are fixed and the electret is moved between them. In other devices, the electret can be attached to one electrode and move vertically or horizontally in relation to another. By laterally moving an electret attached to one electrode relative to another, Arakawa and al [132] obtain a power of 6 µW for an oscillation of 1 mm amplitude at 10 Hz. The surface of the electret is 9 cm^2, the thickness of the electret is 20 µm. The electret was made by using a fluorocarbon polymer CYTOP.

By using a different type of sliding geometry (the two electrodes are placed on the stator and the electret moves laterally in relation to it), Lo and al [133] obtain a power of 17.98 µW at 50 Hz with an external load of 80 MΩ. For low frequencies, the generator can harvest 7.7 µW at 10 Hz and 8.23 µW at 20 Hz. The electret was made with a charged parylene HTR thin-film polymer. The surface charge of the film after corona charge implantation is as high as 3.69 C m^{-2}. The size of the device was 9 cm^2.

An electret energy harvester was developed by J. Nakano, K. Komori, Y. Hattori, and Y. Suzuki [134] to capture the kinetic energy generated by human motion. The electret layer in this device is composed of a fluorinated polymer known as CYTOP EGG. The rotor of the energy harvester features fan-shaped electret and guard electrodes, while the stator has interdigital electrodes to collect the induced charges. The rotor and stator are connected through a miniature ball bearing, allowing free rotation around the center. The assumed parameters for the device include a rotational speed of 1 Hz, an outer radius of the rotor measuring 20 mm, an innermost diameter of the electrodes measuring 9 mm, an air gap of 100 µm between the top and bottom substrates, and a surface charge density of 1 mC m^{-2}. The early prototype achieved a power output of up to 3.6 µW at a rotation rate of 1 revolution per second (rps).

Mahanty et al. developed [135] a flexible sponge-like nanogenerator based on ZnO nanoparticles and etched porous electret poly (vinylidene fluoride–hexafluoropropylene) (P(VDF-HFP)) film. This electret possesses improved dielectric and ferroelectric properties than neat P(VDF-HFP) film. The system has a significant remnant polarization P,P = 1.9 µC cm^{-2} (i.e., aligned dipoles). It does not require pooling or Corana charging. The authors harvest a power density of 1.21 mW cm^{-2} and energy conversion efficiency of 0.3%.

The power densities recovered are of the order of 1 mW cm^{-2} i.e. 10 W m^{-2}. As we shall see later, they are slightly higher than that recovered by triboelectric materials.

Microelectromechanical systems (MEMS) is the most suitable technology to realize IoT-sensing nodes because it enables integrated fabrication of sensors-actuators, electronic circuits for information processing and radio frequency communication, antennas, and energy harvesters on a single chip or in a package [70].

Honma et al. [136] developed an electrostatic induction-type MEMS energy harvesters. For this purpose they use silicon micromachined comb-electrode oscillators. The fixed electrodes are covered by an electret. Their surface is coated with a negatively charged silicon oxide. The charges are bound with the positive charge at the silicon oxide/silicon interface at the rest position. When the movable electrode (which has not been covered by a silicon oxide coating and which does not bear negative charges) is inserted into the fixed ones, the electrical flux between the negative and positive charges are rearranged in part, and the released electrons flow out, thereby converting the mechanical work into the electrical energy (Fig. 9(a) and (b)). A total of 900 pairs of comb electrodes are integrated into a 30 mm X 20 mm chip (Fig. 9(c)). The resonant frequency of the device was specifically designed at 125 Hz to capture environmental vibrations, which were identified as the desired energy source through experimental characterization. When the electret film was polarized to −200 V, the maximal achievable for power for improved geometries was measured to be only 70 µW at an acceleration of 0.05 g.

A new type of in-plane MEMS electret energy harvester has been developed by Qianyan Fu and Yuji Suzuki [138]. This harvester utilizes combined electrodes of overlapping-area-change and gap-closing types to achieve significant power output under both low and high vibration accelerations. The researchers have successfully fabricated an initial prototype using the single layer silicon-on-insulator process. To ensure uniform surface potential, soft-X-ray charging is utilized to establish approximately 60 V on vertical electrets located on the sidewall of the comb fingers. The harvester has demonstrated an output power of up to 1.19 µW at a frequency of 552 Hz and an acceleration of 2.15 g, resulting in an impressive effectiveness of 27.2%.

Lu et all [139] present the first instance of a fully flexible electret-based e-KEH. The proposed electret utilizes PVDF-PTFD nanofibrous

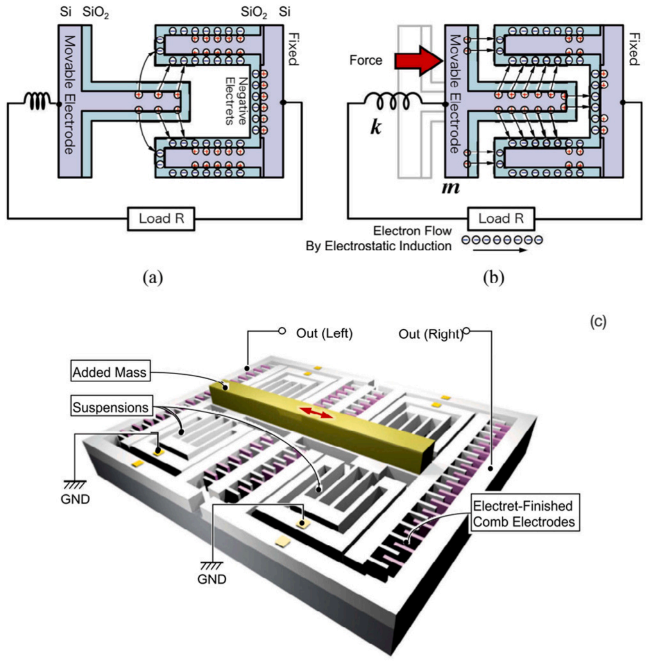

Fig. 9. (a) Detailed view of the electrostatic induction. The surface of the fixed electrode is coated with a negatively charged silicon oxide. The charges are bound with the positive charge at the silicon oxide/silicon interface at the rest position. (b) When the movable electrode is inserted into the fixed ones, the electrical flux between the negative and positive charges are rearranged in part, and the released electrons flow out, thereby converting the mechanical work into the electrical energy. (c) Schematic illustration of electrostatic induction type VDRG. High-density comb electrodes are used to increase the areal mechano-electric coupling. A mass is attached on the movable electrode to increase the mechanical quality factor.
Source: Figure and Captions reproduced from [137] with permission from National Institute for Materials science in partnership with Taylor & Francis Group, copyright 2019.

material, covered with a layer of Parylene C. This arrangement offers several advantages, including faster stabilization of surface potential compared to a flat Parylene C thin film, as well as enhanced charge storage stability. During a pressing operation with a maximum force of 0.5 N and a 3-layers electret configuration, the device's capacitance increases significantly from 25 to 100 pF.

When operated with an optimal resistive load of 16 MΩ and manually pressed, the device demonstrates impressive performance metrics. It achieves a peak instantaneous power output of up to 45.6 μW and an average energy output of 54 nJ per stroke. These values translate to a peak instantaneous power density of 7.3 μW cm^{-2} and an average energy density of 8.6 nJ cm^{-2} per stroke.

Over the span of 450 manual strokes, the prototype effectively charges a 10 nF capacitor to 8.5 V using a full-wave diode bridge. In a separate experiment involving a 1 μF capacitor, a pressing movement frequency of 10 Hz driven by a vibrator with a maximum force of 0.5 N results in an energy delivery rate of 9.9 nJ per stroke.

4.3. Sensors powered by electrets

Stand-alone sensors were produced using electrets [140]. Zhu and colleagues [141] have presented their findings on a flexible comb-electrode triboelectric-electret coupling nanogenerator. This nanogenerator incorporates a separated friction microfiber object, enabling self-powered tracking of position, motion direction, and acceleration, as well as energy harvesting capabilities. The power generation occurs through the coupling of electrostatic and triboelectric effects among the separated triboelectric object, a polytetrafluoroethylene (PTFE) film, and interdigital electrodes. Under an acceleration of 1 m s^{-2}, the PTFE film charged with corona exhibited three times higher short-circuit current (I_{sc}) and six times higher open-circuit voltage (V_{oc}) compared to the uncharged PTFE film. This indicates a significant increase in power generation. The device demonstrates promising potential as a self-powered acceleration tracking sensor, thanks to the stable voltage output during the friction process between the separated components and the numerical relationship between I_{sc} and increased accelerations.

Chen et al. [142] have developed a pressure sensor capable of achieving both high sensitivity and a wide pressure range presented in Fig. 10. To enhance sensing performance, they designed a hierarchical elastomer microstructure (HEM) consisting of two-stage conical polydimethylsiloxane (PDMS) structures with heights of approximately 900 μm and 450 μm. These structures serve as supporting elements to create a highly compressible and adjustable gap. This is crucial because the natural air gap in flexible conformal sensors, without supporting structures, is often small and challenging to control. Such limitations can restrict the sensor's pressure sensing range and sensitivity. The PDMS structures in the HEM are covered with two ultrathin films. The first film is a fluorinated ethylene propylene (FEP)/Ag film with a thickness of around 12.5 μm, and the second film is an Ag/polyethylene terephthalate (PET) film measuring approximately 8 μm. Before assembling the device, the polymer side of the FEP/Ag film is treated with negative corona charging to transform it into an electret. The charge stability of the FEP electret initially decays rapidly within the first ten days but then stabilizes at approximately −1.1 mC m^{-2}. The Highly Sensitive Pressure Sensor operates similarly to traditional self-powered pressure sensors based on electrostatic nanogenerators. When external pressure is applied, the deformation of the PDMS elastomer causes electrons to flow from the bottom electrode to the top electrode in a short-circuit state. Upon pressure release, the PDMS elastomer rebounds, causing reverse charge flow. This cyclic compression and release generate a potential difference between the electrodes, driving charges to flow in an external circuit. The resulting hierarchical self-powered pressure sensor (HSPS) exhibits impressive characteristics. It achieves a high sensitivity of 7.989 V kPa^{-1}, a wide working pressure range of 0.1–60 kPa, a fast response time of 40 ms, and a high signal-to-noise ratio of 38 dB. Additionally, the HSPS demonstrates excellent stability, making it suitable for various applications, including pulse, artery, heart condition, and blood pressure monitoring.

Electrets have gained significant attention in numerous biomedical applications, including bone regeneration, wound healing, nerve regeneration, drug delivery, and wearable electronics, due to their excellent performance, strong resilience, reliability, extended charging lifespan, and capacity to deliver internal electrical stimulation. Yu et al. [143] developed a novel electret-based bio-nanogenerator specifically for electrically stimulated osteogenesis. The fabrication process involved utilizing a two-component-dispersed coaxial electrospinning technique to create porous aligning nanofibers. These nanofibers functioned as a surface charge self-recovery electret mat, enabling energy conversion. Upon implantation, the electret mat interacted with interstitial fluid and the host's stimulated objects, forming a host-coupling bio-nanogenerator (HCBG). During movement of muscle groups, the HCBG effectively harvested biomechanical energy and established an electrical stimulation environment to trigger osteogenesis. The performance of the HCBG was comprehensively evaluated both theoretically and experimentally under various conditions. Remarkable enhancements in osteogenic differentiation in vitro and successful bone repair in vivo were observed. Furthermore, the study delved into the mechanism of calcium ion-induced osteogenesis under electrical stimulation. This research introduces the concept of host coupling for implantable self-powered energy conversion systems and represents an exploratory step towards the field of tissue regeneration therapy.

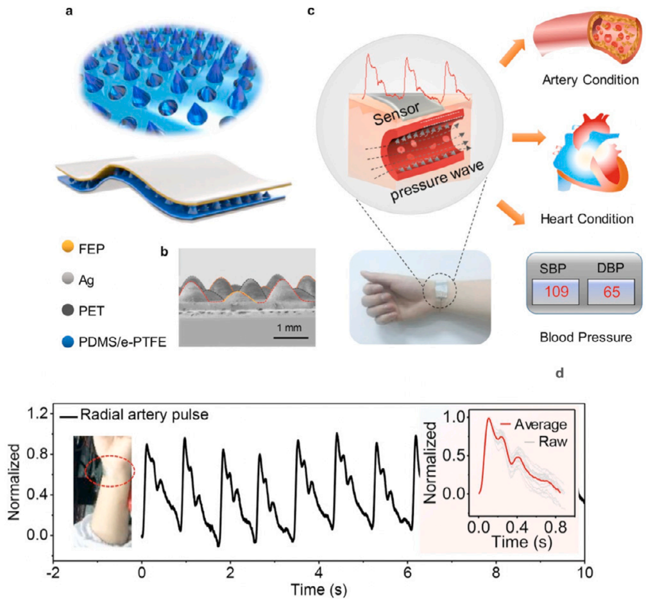

Fig. 10. (a) Schematic structure of pressure sensor and the illustration of the pressure sensor for real-time continuous cardiovascular monitoring. (b) SEM image of the hierarchical structure. (c) The pressure sensor is capable of multifunctional cardiovascular motoring (d) Radial arterial pulse waves of a 30 years old healthy female. Inset is the enlarged view of each cycle. Figure and Captions reproduced from [142] with permission from Elsevier, copyright 2020.

4.4. Conclusions and outlooks for electrets

Electrets have been extensively studied and proven to possess several advantages, including permanent polarization, low cost, stable performance, and good biocompatibility. Moreover, they have the ability to generate endogenous electrical stimulation when exposed to an external electric field. However, there are key issues that need to be addressed to further advance the development of electrets. Charging electrets is an issue. Various charging methods, such as corona charging, soft X-ray irradiation, thermal charging, contact charging, and electron beam injection, have been developed. It is first required to simplify the charging method that hinder industrial-scale production. Charge density is a crucial parameter for assessing the charge storage capacity of electrets. Currently, most electret charges are stored on the surface of dielectric materials and often lack sufficient charge density to meet practical application requirements. To enhance charge density, future development could focus on promoting charge generation inside the dielectric material. This could be achieved through the fabrication of solid porous electrets or hydrogel electrets with a network structure. Last but not the least, long-term stability is a crucial factor for the practical application of electrets. The charge stored in electret materials tends to decay over time, leading to a decrease in performance. Therefore, it is important to develop strategies to improve the long-term stability of electrets, such as exploring new dielectric materials with enhanced charge retention properties or incorporating stabilizing additives.

It is essential to address these challenges in order to drive the further progress of electrets, unlocking their full potential in various applications.

5. Mechanical vibration energy harvesting using triboelectric materials for sensor powering

5.1. Triboelectricity

Due to external mechanical energy, two different materials may become electrically charged after being into contacts. This phenomenon, called tribo-electrification, may be used to produce electricity. During a contact-separation phase, two materials, if connected by electrodes and an electric circuit, will produce electric currents. This process relies on two mechanisms: contact electrification and electrostatic induction.

5.1.1. Contact electrification

Although known since antiquity, the microscopic origin of tribo-electrification is still under debate. The charge transfer might originate from three different processes: electron transfer, ion transfer [144,145], and material abrasion and deposition of charged debris [146] on both sides of the material. As we will see in the following, the main picture that is currently emerging links these phenomena mainly to electron transport [147]. In the case of metal–metal contact, electrons are transferred [148]. Before contact, the levels of the vacuum are aligned, while after the contact, the Fermi levels are aligned. To reach this equilibrium, electrons of the metal which has the highest Fermi level (noted as A) will go to the metal which has the lowest Fermi level (noted as B). Therefore, the interface on the side (A) is positively charged, while the interface on the (B) side is negatively charged. At the equilibrium, since the Fermi level are equal, a contact potential is established as: $V_C = \phi_B - \phi_A$ where $\phi_B = E_{vac} - E_{F,B}$ and $\phi_A = E_{vac} - E_{F,A}$ with E_{vac} the vacuum energy, $E_{F,A}$ and $E_{F,B}$ the Fermi energy of metal A and B, respectively. After contact, a charge remains trapped on the metals. This charge is equal to $Q = CoV_C$ where Co is the capacitance of the contact at separation x_t where tunneling effect disappears. As x_t is small, the potential at x_t is roughly equal to the contact potential V_C. At first sight, Q might depend on the rate at which the metals are separated. This dependence is very low and not significant for practical purposes. The time scale involved in the decay of the charge is equal to $\tau = RC$ where R is the resistance of the contact and C its capacitance at distance x. For distances x below x_t, the characteristic time is very short as R is low and C varies slowly as a function of the separation. The system goes very fast to equilibrium and charges go back to metal A. For distances x higher than x_t, the tunneling resistance is infinite whereas C still varies slowly. The characteristic time involved in the metal separation becomes shorter than τ: charges are trapped and remains fixed beyond this point. This picture has been validated experimentally. The trapped charge varies linearly with the contact potential both measured by the traditional Kelvin technique [148].

Concerning metal–ceramic tribo-electrification, experimental evidences of electron transfers have been reported. The analysis of the decay of the charge trapped in the materials after contact electrification, [149] evidences electron thermionic emission on ceramic materials such as SiO_2 or Al_2O_3 [149] (see Fig. 11).

It is possible to account for the electrification of a ceramic–metal contact by using an energy band diagram. The energy levels of a metal are characterized by a Fermi energy. The energy levels of a dielectric are characterized by its conduction band and its valence band. To understand electronic transfer, it is necessary to consider specific surface states that have an energy in the band gap. At the contact with the metal, the valence and conduction bands of the dielectric are deformed. If the edge of the valence band is below the Fermi level, electrons of the metal will be able to populate surface states of the dielectric, they leave the metal and make appear a positive charge on it. This phenomenon is accompanied as before by the appearance of a contact potential between the dielectric and the metal which is responsible for the capture of charges. The energy band model explains the electrification of metal–metal and metal–dielectric contacts, but fails to describe the contact between two polymers, as there are no quantified energy in polymers. To explain the case of polymer–polymer contact, we suppose that an atom is a potential well in which the outer-shell electrons are loosely bounded [150] (see Fig. 12).

Before the contact, the electron clouds have different energies E_A and E_B. However, electrons cannot be transferred from one material

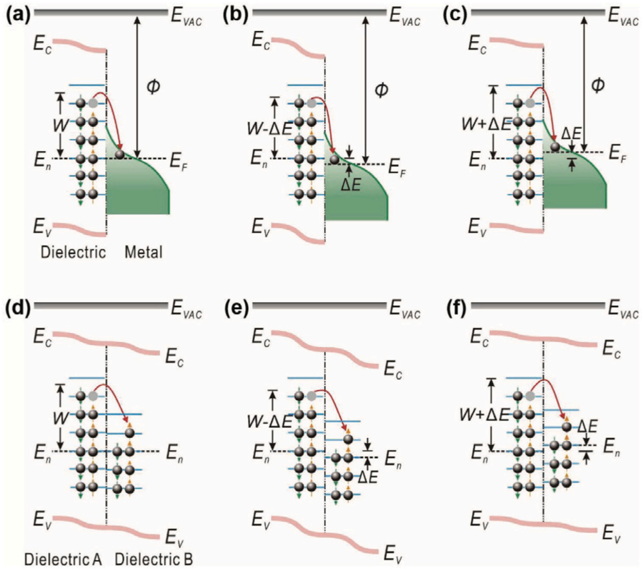

Fig. 11. Surface state models for explaining the regulation of the potential barrier height of materials during CE, depending on the work function or contact potential difference of the contacted materials. Charge transfer between a dielectric (with initial negative charges) and a metal when En of the former is (a) as high as, (b) higher than, and (c) lower than Ef of the latter. Charge transfer between dielectric A (with initial negative charges) and dielectric B when En of the former is (d) as high as, (e) higher than, and (f) lower than that of the latter. EVAC, vacuum level; EC, conduction band; EV, valence band; En, neutral level of surface states; W, potential barrier; *Φ*, work function; and EF, Fermi level.

Source: Figure and Captions reproduced from [149] with permission from John Wiley and Sons, copyright 2019.

to the other because of the potential wells and the value of the extraction energy. However while in contact, the electron clouds overlap. The extraction energies disappear, and the electrons transfer from the material where the energy is the highest to the one where the energy is the lowest. This transfer is strengthened by the mechanical energy that presses the contact. After separation, the charges remains as static charge on the material surface.

Although electrons are or can be clearly involved in the electrification of metal–metal, metal–dielectric and that the previous model can be generalized to polymer–polymer contacts [151], some electrification between two polymer surface clearly seems to rely on the transfer of ions or matter. Using Kelvin force microscopy, Baytekin and al. [146] showed that after electrification between two polymers, each surface bears nanoscale areas of different charges that they dubbed charge mosaics. They argued that contact charging could involve heterolytic bond breaking and that the creation of the charge mosaics comes from the transfer of patches of charged material between contacting surfaces. Everyday life surfaces do not exist in a world without humidity. It is thus necessary to take into account the role of atmospheric humidity and the presence of layers of water adsorbed on surfaces to understand the mechanisms at play. In studies of polymers containing covalently bonded and mobile ions, Diaz and coworkers [144,145] showed that the maximum trapped charge was obtained at 30 percent relative humidity. At high humidity, the presence of a large water layer increases the surface conductivity and thus the departure of accumulated charges to the bulk. In the absence of humidity, the lack of electrification of the contact suggests that the charges transported are ions. The presence of a water bridge and the high dielectric constant of water indicate that during contact, the mobile ions are distributed evenly in the water bridge. The charge separation takes place when the water bridge breaks into two thin films. The counter-ions released by the polymer with the most mobile counter-ions near the second surface are trapped by the separation. Both surfaces achieve a charge. This mechanism allows to understand what happens for neutral polymers without mobile counter ions. Anions in general and the hydroxide ion in particular tend to adsorb at the water/solid or water/air interfaces. This leads to the appearance of a negative surface potential more or less large depending on the absorption. When two different polymers are brought into contact, a rapid equilibrium of the hydroxide ions takes place, the polymer with the stronger affinity for the hydroxide ions covering itself with a greater quantity ion. The rupture of the liquid film leads, as in the previous case, to a surface separation. This mechanism is corroborated by the correlation between surface charge during electrification and zeta potential of the polymer [152].

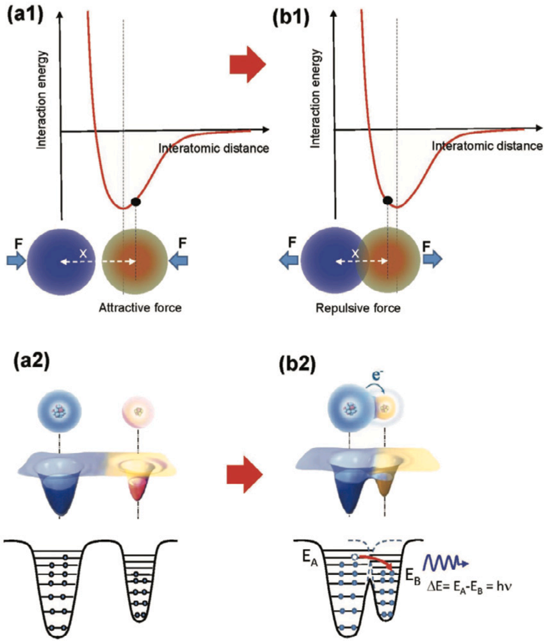

Fig. 12. The overlapped electron-cloud model proposed for explaining CE and charge transfer between two atoms for a general case. (a1,b1) Interatomic interaction potential between two atoms when the force between the two is attractive and repulsive, respectively, by applying an external compressive force. Experiments found that electron transfer occurs only when the two atoms are in the repulsive interaction, for example, in the case when the two atoms have strong electron-cloud overlap. (a2,b2) Schematic of the electron cloud and potential energy well model of two atoms belonging to two materials A and B when they are separated and in close contact, respectively. Electron transition from A atom to B atom is possible due to the lowered potential barrier by the external force, resulting in the occurrence of CE. This is simply referred to as Wang transition for CE.

Source: Figure and Captions reproduced from [150] with permission from John Wiley and Sons, copyright 2020.

To conclude, there is no single picture of contact electrification. At least four mechanisms may be involved:the transfer of electrons between metal–metal and metal–dielectric, the transfer of counter-ions from ionic layers, the transfer of hydroxide ion and the breakage of covalent bonds. However, electron transfer seems to be the predominant mechanism [153].

5.1.2. Electrostatic induction

The production of electricity in triboelectric materials originates in an electrostatic induction phenomenon. In order to take into account the charges created by the contact, Wang introduced in 2017 [147] an additional polarization term P_s in the definition of the displacement vector D.

$$D = \epsilon_o E + P + P_s \tag{4}$$

The first term P is due to the existence of an external field and the second P_s to the existence of the charges that are independent of the external electrical field and come from the contact electrification.

In this framework, the displacement current density J writes $J = \frac{\partial D}{\partial t} = \epsilon_o \epsilon_r \frac{\partial D}{\partial t} + \frac{\partial P_s}{\partial t}$. By integrating J on the surface the displacement current $I_d = \frac{dQ}{dt}$ can be found. It writes [19,154,155]: $I_d = A\sigma_T \frac{dH}{dt} \frac{\frac{d_1\epsilon_0}{\epsilon_1}+\frac{d_2\epsilon_0}{\epsilon_2}}{(\frac{d_1\epsilon_0}{\epsilon_1}+\frac{d_2\epsilon_0}{\epsilon_2}+z)^2}$ where A is the contact surface, $\frac{dH}{dt}$ the variation of the contact/separation between the two material ($\frac{dH}{dt}$ depends upon the nature of the mechanical solicitation i.e. sliding or compressing), d_1 (respectively d_2) the thickness of the material 1 (respectively 2), ϵ_1 (respectively ϵ_2) the dielectric constant of material 1 (respectively 2), ϵ_0 the permittivity the vacuum, z the distance between the two triboelectric materials. The dielectric constants ϵ_1 and ϵ_2 are intrinsic properties of the materials, σ_T depends upon many factors and notably of the surface chemistry and structure.

5.2. Triboelectric materials

The triboelectric properties of materials are represented by their triboelectric surface charge density (TEDC after undergoing a triboelectrification process (contact/separation or sliding) with a reference material (mercury and contact/separation in [156]). A triboelectric table is set up which classifies materials according to their TEDC versus mercury.

Chemical-Resistant Viton Fluoroelastomer, Rubber Acetal, Flame-retardant garolite, Garolite G-10 Clear cellulose display the highest negative TEDC close to −150 μC m^{-2}. Delrin® Acetal Resin, Wood (marine-grade plywood) Wear-resistant slippery garolite, Super-stretchable and abrasion-resistant natural rubber, Oil-resistant buna-N rubber and Food-grade oil-resistant buna-N/vinyl rubber display the lowest negative or even positive value comprised between −10 μC m^{-2} and +10 μC m^{-2}. This table cannot quantitatively predict the charge that will be recovered in a contact between two different materials. However, if the contact mode is the same as the one used to establish the table, two materials displaying highly different charges with mercury will give rise to a high contact charge. On the contrary, two materials with close TEDC values result in a low charge. Moreover, the amplitude of the charge is qualitatively related to the relative positions of the materials in the table [156]. Note that the term $\left(\frac{d_1\epsilon_0}{\epsilon_1}+\frac{d_2\epsilon_0}{\epsilon_2}\right) / \left(\frac{d_1\epsilon_0}{\epsilon_1}+\frac{d_2\epsilon_0}{\epsilon_2}+z\right)^2$ which represents electrostatic induction is roughly the same for all the classical materials. Finally, apart from the material, the performance of a triboelectric device depends on the $\frac{dH}{dt}$ term, which is dominated by the mechanical structure of the device and by the loss from the frictional force [157]. Working in non-contact mode or transforming linear motion into rotational motion (due to lack of space) is one way to improve the process. Many studies focused on modifying and increasing the surface charge. A solution for surface charge increase is to enlarge the effective surface during contact. Kim et al. [158] obtained a contact charge of 788 μC m^{-2} by using a gold electrode covered with gold nanodots for effective surface increase. While increasing effective surface by roughness, the second material must also be soft and flexible (elastic materials or liquid metal) in order to cover the created roughness.

Cheng et al. coupled a triboelectric nanogenerator (TENG) in contact mode with a variable capacitor [160]. They used the TENG and a rectifier circuit to charge the capacitor. The latter subjected to vibrations transmits an electric current. This technique allows to work with important electric charges. Indeed, as there is no contact between the two surfaces of the capacitor, it is more difficult to create an electric field that leads to the ionization of the air. They obtained a maximum effective charge density of 490 μC m^{-2}.

Liu et al. [161] coupled a TENG in contact mode with a generator and a fixed value capacitor. They achieve charge excitation through applying voltage to the main TENG, and an alternating current is produced by using a fixed value ceramic capacitor to store charges. Charges as high as 1.25 mC m^{-2} can be achieved. Other strategy concerns surface chemical modifications and insertion of charge trap layer (mixture of carbon nanotube and polymer for example in the material bulk [162]).

An important strategy concerns the use of an intermediate storage layer. Chun et al. reported [159] a TENG device composed of three layers : a top layer made Aluminum/polydimethylsiloxane, a bottom layer made of Aluminum and an inserted electric double layer made of Aluminum coated by gold nanoparticles. They obtained a power density of 480 W m^{-2} for a load resistance of 10 MΩ. The device of centimeter size (2 cm × 2 cm) was operated in contact/separation mode at a frequency of 3 Hz under a force of 60 N and an amplitude of displacement of 1.5 cm. The conversion rate of the injected energy into recovered energy is equal to 0.224. The principle of the process is given in Figs. 13 and 14. When a force is applied to the nanogenerator, the porous film and the intermediate layer are brought into contact. Positive charges appear on the surface of the intermediate layer and negative charges on the porous film. When the force is continued to be applied, the two layers come into contact with the ground and then with the bottom layer. When the force is withdrawn, the three layers separate simultaneously. The positive charges of the intermediate layer induce the flow of electrons from the ground to the intermediate layer and the negative charges of the porous film induce a movement of electrons from the upper electrode to the lower electrode. After the first cycle, the upper electrode is positively charged and the porous film is negatively charged, while the lower electrode is negatively charged and the intermediate layer is neutral (see Fig. 13). When an external force is again applied to the nanogenerator, the displacement of the negatively charged porous film electrostatically induces positive charges on the middle layer surface, while negative charges are induced on the opposite layer surface. When the force is further applied, the negative charges on the middle layer induce positive charges on the bottom layer, resulting in a flow of electrons through the external circuit. Then, the middle layer contacts the ground point and the electrons flow to ground, resulting in a current in the circuit connected to ground. When the force is removed, the three layers separate simultaneously. The electrons go from the ground to the central layer (see the 4 electrons drawn in blue in Fig. 14 the red line). An important flow of electrons is set up from the top electrode to the bottom one (see the 8 electrons drawn in red on Fig. 14 the red line). Such working principle is different from the charge generation mechanism of a conventional TENG. And it accounts for a considerably higher electrical potential, ideally twice higher, compared to a conventional TENG (see Fig. 14). Using this same approach with a silver particle layer, a polystyrene layer and a fluoropolymer layer, Kim et al. [163] produced a power equal to 818 mW m^{-2}.

Xu et al. [164] used a structure with three layers to get high density energy. A charge pump is devised to pump charges into the floating layer. A charge pump is devised to pump charges into the floating layer simultaneously. This device can achieve ultrahigh effective surface charge density of 1.02 mC m^{-2}.

5.3. Triboelectric nanogenerators (TENG)

The triboelectricity mechanism is successfully used to produce electricity through TriboelEctricity NanoGenerators (TENG).

5.3.1. TENG working principle and modes

There exists 4 basic working modes of TENGs (see Fig. 15): contact–separation (CS) mode, single electrode (SE) mode, sliding (S) mode and freestanding triboelectric-layer (FT) mode.

The CS mode uses a displacement perpendicular to the two materials. When the two materials come into contact they become charged. The CS mode involves a closed circuit. In a closed circuit (i.e. if the two materials are connected by an electrical circuit), the negative charges present in material A induce a displacement of electrons from the electrode connected to A to the electrode connected to material B. This flow of electrons stops when the electrode connected to B acquires a

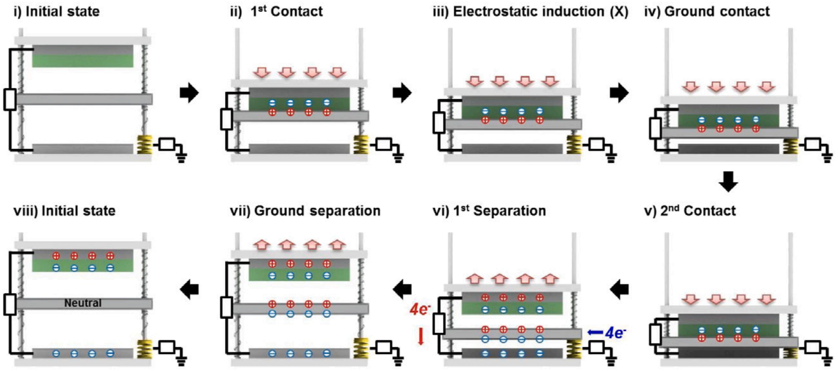

Fig. 13. Working mechanism for the generation of output voltage and current in the TENG under external force. First cycle. *Source:* Figure reproduced from [159] with permission from Springer Nature, copyright 2016.

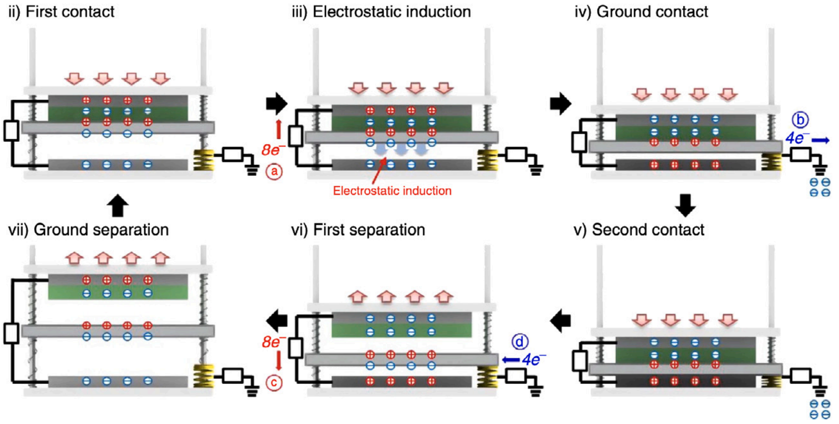

Fig. 14. Working mechanism for the generation of output voltage and current in the TENG under external force after the first cycle. *Source:* Figure reproduced from [159] with permission from Springer Nature, copyright 2016.

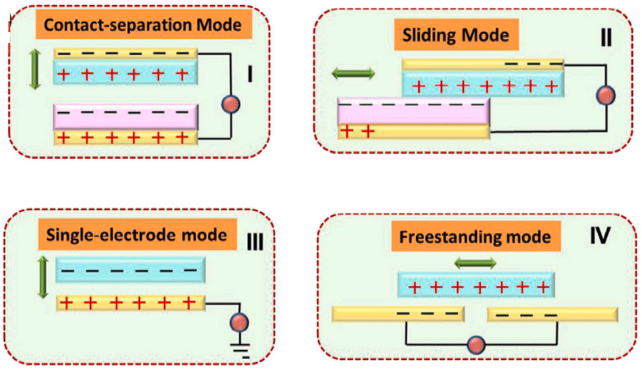

Fig. 15. Four basic working modes of TENGs from [22] with permission from John Wiley and Sons, copyright 2020.

charge equal in absolute value and opposite to the charge carried by the material B.

The single electrode (SE) mode is comparable to the (CS) mode but operates in an open system. The two materials are not electrically connected. When they separate, the material that is not connected to the ground carries charges. The material that is connected to the ground has charges and an electron flow is established between the ground and the material. When the two materials come closer together, a reverse flow is established. The sliding mode (S) involves a movement parallel to the surface of the materials. The materials are in contact and the electrodes covering them are electrically connected. When the contact surface between the two materials decreases, unbalanced electrical charges appear within the two materials. To compensate for these charges, a movement of electrons takes place from one electrode to the other. A reverse movement takes place when the contact surface between the two materials increases. The free standing mode (FT) is a mode comparable to the (S) mode. It involves two materials in contact and a displacement along the plane of the materials. However, as in the SE mode, the two materials are not electrically connected. Instead, the bottom material is cut in two and the electron current flows through the electrodes covering the two identical materials at the bottom. Most applications are not limited to a single mode but use these modes in a coordinated way.

5.3.2. TENG performances

It is difficult to compare the performances reported in the different works in the literature, since the excitation conditions are often very different, especially in terms of applied force and frequency. A figure of merit was calculated and developed by Zi et al. [165]. The figure of merit FOM_p allows to compare the performances of TENGs taking into account their environment. In sliding mode, it is defined by $FOM_p = \frac{2\epsilon_O E_m}{A x_{max}}$, where A is the triboelectrification area, x_{max} the maximum displacement. E_m is given by $E_m = \frac{1}{2}Q_{max}(V_{OCV,max} + V'_{max})$ where Q_{max} is the maximum short circuit transferred charge, $V_{OCV,max}$ is the maximum absolute achievable voltage at $Q = 0$ and V'_{max} is the maximum absolute achievable voltage at Q_{max}. This figure of merit is unfortunately little used. To compare different results presented below, we must therefore keep in mind that the experimental conditions, especially the excitation conditions, are different.

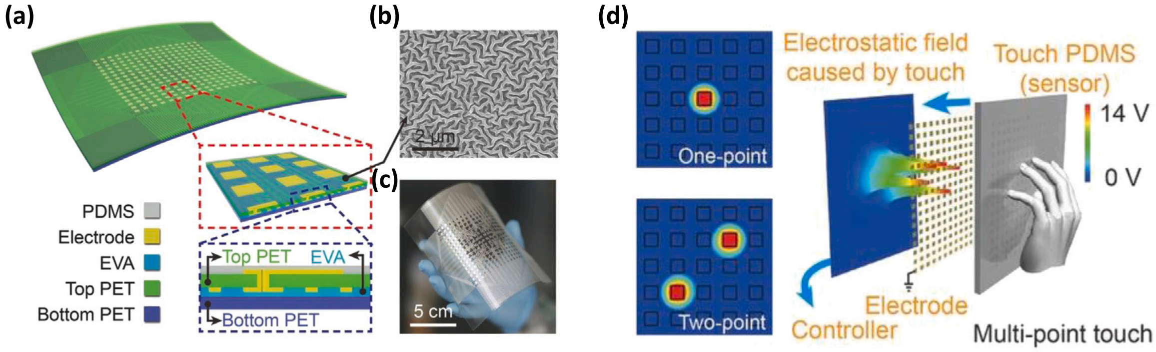

Fig. 16. (a) Schematic of a 16 × 16 TESM. Insets: Partially enlarged tilted view and cross-sectional view of the structural design of the top and bottom, respectively. (b) Scanning electron microscopy (SEM) image of the etched PDMS surface microstructure. (c) Photograph of a fabricated 16 × 16 TESM with good flexibility (d) Schematic of the pressure mapping process.
Source: Figures and Captions adapted from [166] with permission from John Wiley and Sons, copyright 2016.

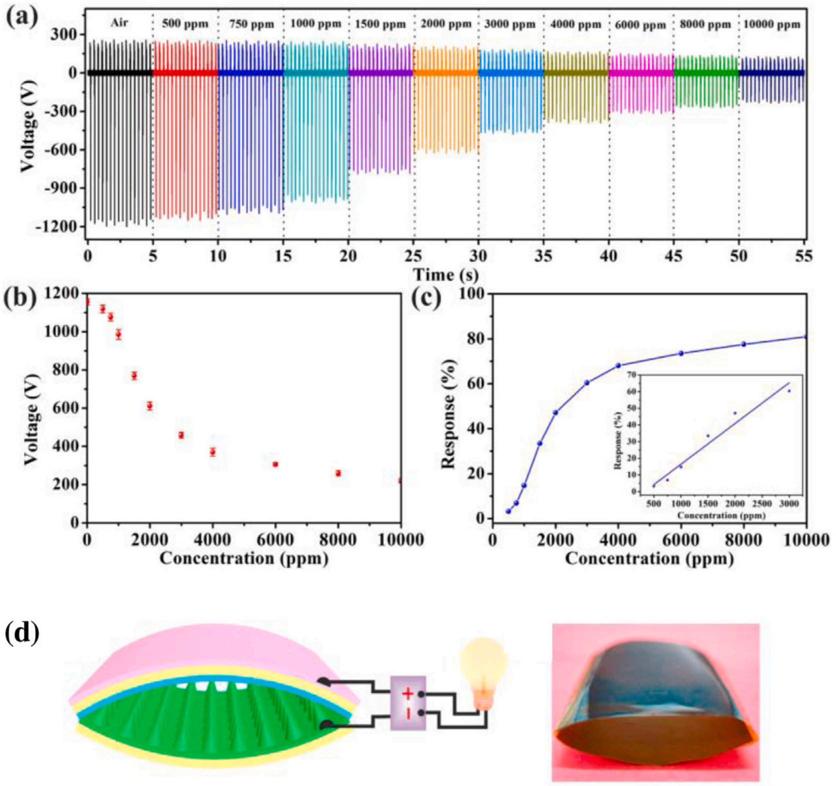

Fig. 17. (a) (b) The output voltage of C PANI TENG based nanosensor at room temperature in air and NH3 with various concentrations (from 500 ppm to 10,000 ppm), (c) The relationship between the response of the C PANI TENG ((Vair-Vgas)/Vair) and the concentration of NH3. Inset is the response curve with NH3 concentration ranging from 500 ppm to 10,000 ppm. (d) Schematic illustrate and photograph of the designed PANI based TENG with an arch-shaped structure. Figures and captions adapted from [168] with permission from Elsevier, copyright 2018.

By integrating a mechanical spring-based system in a TENG made with a copper plate and a PTFE film as triboelectric layers, Wang et al. [167] succeeded in obtaining an average power density of 2 mW m^{-2} under the experimental conditions of a frequency of 3.5 Hz, under a force of 0.6 N, a displacement amplitude of 2 cm, for a load resistance of 10 MΩ. The conversion rate of the injected energy into recovered energy is equal to 0.18.

Pruvost et al. [102] obtained an average power density of 2.25 mW m^{-2} for a frequency of 40 Hz under a force of 0.012 N, an amplitude of displacement of 0.5 mm for a load resistance of 10 MΩ. The conversion rate of the injected energy into recovered energy is equal to 0.10. The experimental results reported in the above-mentioned works do not take into account the electrical conversion. therefore, they do not discuss the problem of impedance matching.

As notice before, Chun at al. [159] obtained a power density of 480 W m^{-2} for a load resistance of 10 MΩ using a TENG device composed of three layers Using this same approach with a silver particle layer, a polystyrene layer and a fluoropolymer layer, Kim et al. [163] produced a power equal to 818 mW m^{-2}.

Zhang et al. [171] obtained a power density of 307 W m^{-2} ie 30 mW cm^{-2} for a load resistance of 5 MΩ using a all-green device made of cellulose-based material and commercial cellophane as tribological layers and graphite sheets as electrodes. To get these performances, the device of centimeter size (5 cm × 5 cm) was operated in contact/separation mode at a frequency of 5 Hz. A 98 W m^{-2} power density was obtained on a 3 cm × 3 cm on a TENG connected to a linear motor at a contact speed of 1 m s^{-1}. The device shows similar

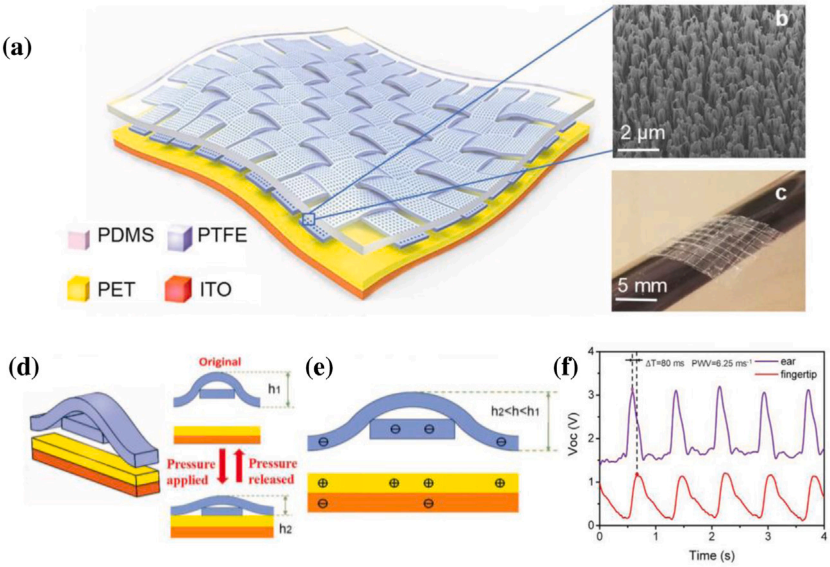

Fig. 18. A weaving constructed self-powered pressure sensor (WCSPS) for self-powered measurement of human Pulse Wave Velocity and Blood Pressure. (a) Schematic illustration of the flexible weaving constructed self-powered pressure sensor. (b) A SEM image of plasma-etched PTFE nanowires. The scale bar is 2 μm. (c) A photograph showing an as-fabricated WCSPS, which is flexible, lightweight, and can be easily wrapped onto a curved surface. The scale bar is 5 mm. (d) Schematic diagram of the cross-sectional view of a single unit of the WCSPS. The right side illustrates the two conditions that when the device is in its original state (h1) and when the external pressure was applied (h2). (e) An illustration showing the electrical signal generation process of the WCSPS [169] (f) The real-time health monitoring of middle-aged and aged people.
Source: Figures and captions adapted from [169] with permission from John Wiley and Sons, copyright 2018.

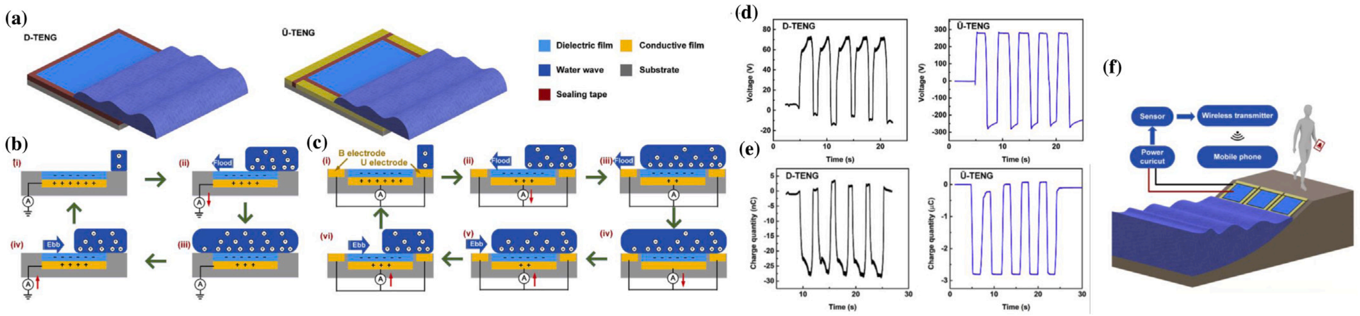

Fig. 19. (a) The structure of the D-TENG and the U-TENG. (b) Work mechanism of the D-TENG. (c) Work mechanism of the U-TENG. (d) Open-circuit voltage comparison of the D-TENG and the U-TENG. (e) Transfer charge quantity comparison of the D-TENG and the U-TENG (f) Flow chart diagram of applications of U-TENG as blue energy harvester. Figure reproduced from [170] with permission from Elsevier, copyright 2019.

performances than fluoropolymer based TENGs [172] (power density 6 W m^{-2} for a load resistance of 1 MΩ with an output current of 1.5 mA under 6 N of pushing force at 5 Hz). This device is not sensitive to humidity.

An important problem is hindered in the reported powers above. It is complex to recover these powers in output circuits. The capacitance of a TENG is of the order of 100 pF. Such characteristics result in a low energy transfer efficiency, both for battery charging and electronic device powering. It is to notice that electronic devices generally have a much lower impedance (100 of μF). To recover energy, a simple rectifier circuit with diodes is not enough. In order to transfer a maximum amount of energy, it is important to insert an electronic stage between the battery or the supercapacitors that allows to adapt the impedance. This can be achieved by using N capacitors in series on charge and in parallel on discharge (basic switched capacitor convertor) or a fractal design based switched-capacitor-convertor (FSCC) [173]. In the last situation, a energy transfer of 94% with an impedance reduction of 750 has been demonstrated. The use of an original system with two stages has also been proposed by Wang et al. [174]. In the first stage the energy is transferred to a low capacitance capacitor with a conversion ratio of 0.75% through a rectifier circuit. Then, the low capacity capacitor is connected, thanks to two automatic electronic switches, to a coupled inductance circuit that allows impedance matching [175].

5.4. Sensors powered by triboelectricity

TENG technology can be used for both power supply and sensing in IoT applications [176]. There are already many insightful reviews with numerous examples [47,177–180]. Our goal here is not to be exhaustive but to show some examples of applications. It is to be noted that the literature on this activity is much more important than on the piezoelectric or electrostrictive themes.

5.4.1. TENG as sensor in IoT applications

Various autonomous physical signal sensors have been designed using the principle of triboelectricity [22]. As explained in the previous paragraphs, pressure measuring presents wide applications in medical monitoring, building monitoring, hand held control of connected objects, and sensory robotics. In this context, many triboelectricity based pressure sensors have been developed.

Wang et al. [166] reported a self-powered touch pad with 36 × 20 pixels using a triboelectric generator (see Fig. 16). A PDMS film serves as an electrofication layer that generates a triboelectric effect upon contact with the silver nanoprinted electrodes. The system is durable and presents excellent performance with a pressure sensitivity exceeding 0.06 kPa^{-1}. The response time is less than a few milli seconds. A stylus writing on the touch pad with a velocity of the order of 50 mm s^{-1} can be easily detected. Cui et al. [168] reported a self-powered NH_3 nanosensor based on TENG (see Fig. 17). PANI nanofibers are a common NH_3 sensing material. The adsorption of NH_3 can transform C-PANI nanofibers into N-Nani nanofibers. The triboelectric properties of the two fibers are very different due to dissimilar electrical conductivity properties. The authors constructed a conventional device by inserting a PANI fiber film and a PVDF film into two electrodes. These signals are obtained at a frequency of 3vHz under the action of a linear motor that simulates the environment. The TENG is solicited in contact mode. The C-PANI-TENG has a much higher output performance than the N-PANI-TENG. The peak short-circuit current value and output voltage of C-PANI-TENG reach 45.70 μA and 1186 V, respectively, which are one hundred times higher than those of N-PANI-TENG (0.26 μA and 6.70 V). Tracking these measurements after calibration provides a measure of gas concentration. The system is durable and shows no variation after 15,000 cycles. In the presence of NH_3, the output voltage of the TENG decreases rapidly to a relatively stable value within 40 s (response time). If pure air is injected again, the voltage rises again within 250 s. The longer recovery time is due to a lower desorption rate of NH_3 molecules on the PANI compared with its absorption rate. The sensor works for NH_3 concentrations between 500 ppm and 10 000 ppm. TENGs present also wide applications as biomedical sensors. Numerous research works have been performed in this direction in the last decades. It is based on the energy harvesting of vital signals (heart sounds, blood pressure, breathing) to analyze patient's health state or to its reactions to an aggressive environment. These devices are designed to be worn directly on the skin or integrated into textiles. In the same spirit CO_2 sensors have been developed [153,181]. Cardiology is one of the most popular applications for TENG biomedical sensor which can measure heart pulse or monitor arterial pressure. In 2015, Yang et al. [182] developed a sensor made by a TENG, encompassing a polytetrafluoroethylene (PTFE) membrane layer and a nylon layer as the triboelectric pairs. The nylon layer was covered by an indium tin oxide (ITO) electrode. Yang et al. utilized this sensor to monitor human arterial pulse waves in real-time at the carotid, wrist, and chest. The device has a low detection limit of 2.5 Pa and a high sensitivity 51 mV Pa^{-1}. Bai et al. [183] placed a fluorinated ethylene propylene membrane and a latex membrane where between two copper electrodes to build a TENG. This very simple device was used to monitor respirations and heart beat for security surveillance.

Others TENGs have been developed to monitor the shape of the heart wave and not simply the rate of the heart wave. It is not a easy task to measure blood pressures, which remains one of the most important vital signals for disease evolution monitoring and patient condition tracking. To achieve this goal, Meng et al. [169] designed a pressure sensor based on a TENG realized in simple contact mode (see Fig. 18). Plasma etched polytetrafluoroethylene(PTFE), polyethylene terephthalate (PTE) and indium tin oxide (ITO) electrode serve as triboelectric materials. At the constant frequency of 2 Hz, the pressure sensitivity of 45.7 mV Pa^{-1} is achieved in the lower-pressure (<0.71 kPa) region. The authors measured the shape of the arterial signal on two points of the body. They deduced from the temporal shift of the signals an important parameter the pulse wave velocity (PWV) which depends linearly on the arterial pressure. This calibration requires the use of studies on patient cohorts. In a simpler way, it allows to track the condition evolution of a given patient.

Yi et al. [184] produced a stretchable rubber based TENG made of a layer of elastic rubber and a layer of Aluminum. The respiration movements cause the stretching of the elastic rubber and provide a change of triboelectric charge distribution and density on the rubber surface relative to the Al surface. This leads to a change of triboelectric charge distribution and a detectable alternating charge flow.

5.4.2. Sensors powered by a TENG with a storage system

Liu et al. [170] developed a triboelectric system based on contact between seawater and a triboelectric material. The authors constructed a triboelectric device (coined D-TENG) from a thin PFE foil and an aluminum electrode placed between two Kapton and PVC insulators. On top of the device an aluminum U-shaped electrode is connected to the aluminum plate. This device is coined U-TENG. In a conventional device without aluminum on top (D-TENG), the sea water arrives on the PET film which has a negative charge acquired during the first contacts with the sea water. This charge is balanced by positive charges on the aluminum. The seawater partly screens the negative charges of the PET. Electrons come from the earth to compensate. At equilibrium, there are more charges on the aluminum that are compensated by less persistent charges not balanced by seawater. When the seawater withdraws, the reverse process starts. If an aluminum electrode is placed above the device, the electrons no longer come from the earth but from this electrode. They maintain a strong negative charge on the high part of the device and thus fill completely the positive charge on the aluminum part. This device thus makes it possible to exacerbate the operation of TENG (see Fig. 19). Open-circuit voltage increases from 73.1 V to 283.1 V, transfer charge quantity increases from 28.4 nC to 2.8 μC and short-circuit current increases from 0.4 μA to 10.8 μA using this strategy. Based on this system, the authors present a WIFI data transmission system that is powered by the energy stored in the capacitors. This wireless signal transmission system is important for further seashore IoT applications, inspectors can obtain information from distributed signal transmitting station when they take an inspection tour of seashore area.

5.4.3. Sensors powered by a TENG without a storage system

Wang [174] first applied TENGs to human signal energy harvesting. He developed a multilayer contact-mode TENG made of aluminum and fluorinated ethylene propylene films. Integrated into the soles of shoes, the walking of a human being can drive this TENG to generate a charge of about 2.2 mC and an output voltage of about 700 V. By using an impedance matching system, they manage to charge a battery. The performances obtained are remarkable. (see Fig. 20). With a light palm tap at 1.6 Hz as the only power source, this device delivers 1.044 mW of direct current (7.34 W m^{-3}). There is neither battery in the system, nor storage system. The device can be used as a standard infinite life power source to continuously power many conventional electronic devices, such as thermometers, electrocardiographs, pedometers, wearable watches, scientific calculators, and wireless radio frequency communication systems. TENGs are particularly suited for IoT applications.

Kim et al. [163] reported a TENG for a self-powered security IoT system. The device includes a silver nanowire layer, a polystyrene layer, and a fluoropolymer contact layer. The presence of the transparent polystyrene layer acts as an intermediate charge storage layer and increases the power density of the ST-TENG to 818 mW m^{-2}. The 11 cm × 11 cm size system is included in a floor. The passage of a passer-by allows to generate an electric signal strong enough to send messages to a data acquisition board. Then, the data acquisition board reads and converts the transmitted analog electric signal to a digital signal by ADC conversion, and the board wirelessly sent the signal of the invader to the smartphone. All this connection is done through a simple AC-DC conversion bridge and capacitors without the use of batteries. The power generated by this device is important enough to avoid the use of complex energy transfer systems.

5.5. Conclusions and outlooks for TENG

The development of triboelectric nanogenerators has reached an exponential increase since the beginning of the century. All currents generated by a TENG type nanogenerator show alternating characteristics, which require a rectification process before use. The power densities obtained by the TENG reach an order of 0.1–1 mW cm^2 under

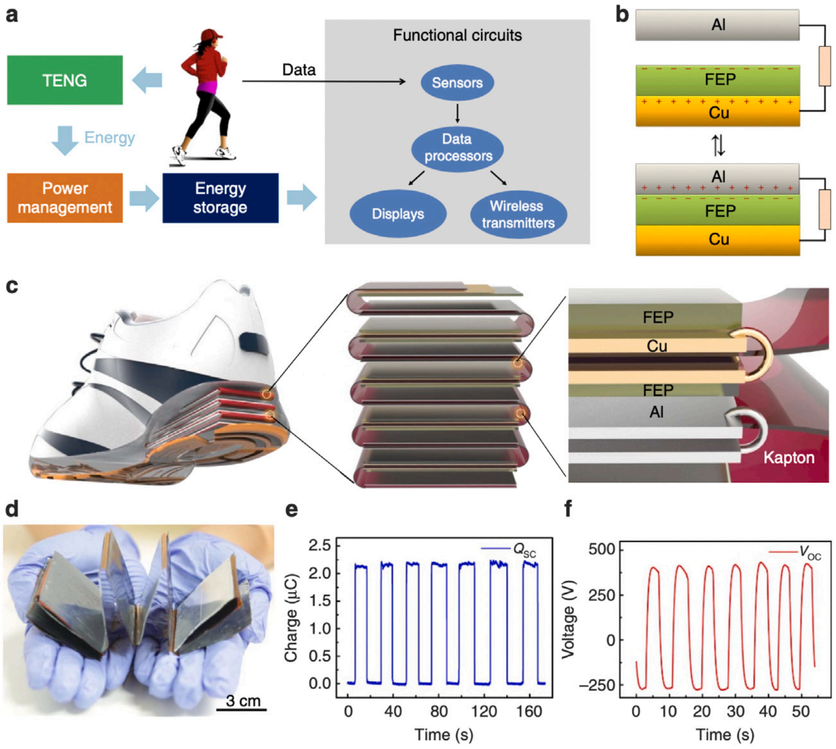

Fig. 20. (a) System diagram of a TENG-based self-powered system. (b) Working mechanism of an attached-electrode contact-mode TENG. (c) Structure of the designed multilayer TENG. (d) Photo of an as-fabricated TENG. (e) Short-circuit current output and (f) open-circuit voltage output of the as-fabricated TENG.
Source: Figure reproduced from [174] with permission from Springer Nature, copyright 2015.

moderate forces. Such performance is lower than that reported for piezoelectric materials, which is around 1–10 mW cm^2 under the same solicitations. However, triboelectric devices have many advantages. There are almost unlimited candidates of materials due to the nature of triboelectric effect [22]. It is possible to integrate materials of low cost and of biosources. TENG devices are mechanically reliable. They endure over thousands to millions of cyclic impacts without significant failures of the structures or decay of the output performance [22]. The challenges concerning TENG devices are the control of humidity and the reduction in size of the devices. Existing devices are of medium size due to limited power density.

6. Osmotic energy harvesting systems

There is an energy in nature whose resources are practically equal to those of mechanical energy.: the energy of mixing or the osmotic energy. The osmotic energy (also named as Blue energy) [185,186] is an underestimated energy source which presents major advantages both in its large energy potential and in its wide availability in all scales. Osmotic energy harvesting harnesses the energy released during the mixing procedure of solutions of different salinity [187] or of different solute concentrations. The potential of blue energy can be estimated by the theoretical calculations of Gibbs free energy ΔG_{mix}. According to research works, a global power of 2.4–2.6 Terawatts is estimated for blue energy potential, considering all the rivers and effluents running to the sea [188]. This feature takes into account only the mixing of solutions of different salinity.

As illustrated in Fig. 21, three major osmotic energy harvesting technologies, including pressure retarded osmosis (PRO), reverse electrodialysis (RED) and Capmixing, can be used to harvest osmotic energy. Briefly speaking, PRO is a semi-permeable membrane based technology where water flux driven by osmotic effect results in the volume increase of the pressurized concentrated solution chamber. The mechanical energy is then used to propel the turbine systems for electricity generation [190,191]. Similarly, RED is also a membrane-based technology. Ion-exchange membranes (IEMs) are used to create an ionic flux under osmotic effect, which is then converted into electric current by redox reactions at electrodes [192,193]. Capmixing systems

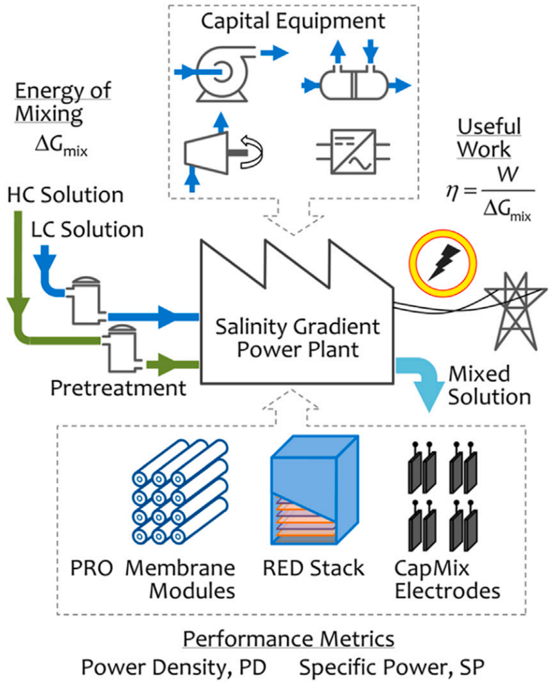

Fig. 21. Schematic representation of a salinity gradient power generation facility.
Source: Figure reproduced from [189] with permission from American Chemical Society, copyright 2016.

designs a precise and engineered cycle to use double layer expansion on capacitive electrodes for osmotic energy harvesting [194]. Apart from large volume mixing of river and sea water at natural estuaries, which is limited by the salt solubility in the water (about 350 g/L), it is also possible to exploit systems with pH gradient. As reported by Kim et al. the mineralizing of CO_2 gas in industrial alkaline wastes ($NaHCO_3$ solutions) could effectively modify the pH in solution [195]. It is thus possible to establish a pH ratio across two compartments of CO_2 and air-parged alkaline solutions separated by a non-selective membrane. The use of MnO_2 electrodes in the system could efficiently develop a pH-gradient dependent potential difference. This is realized due to a reversible redox reaction through intercalation/deintercalation or adsorption/desorption of protons. It is reported that a power density of 0.82 W m^{-2} is achieved in such system [195].

Osmotic energy exists widely in other forms at much smaller scale range. An example could be the biological salinity gradients of physiological fluids established across cell membranes or organs. Accordingly, we can also imagine miniaturized osmotic energy harvesting systems in small-scale applications including analytical sensor devices [196], ionic circuits [197] and biomedical applications [198,199]. In this review, we mainly focus on miniaturized blue energy harvesting systems. Considering the complex accessory equipment (pump and turbine systems for PRO systems and hydraulic circuits for flow sweeping in Capmixing systems), RED systems remain the easiest method for miniaturized system powering. Thus we will restrict our discussions on RED systems. In the following sections, we will firstly begin with a detailed description of RED working principle and its current performances. This will be followed by a summary of miniaturized RED applications, along with the developing trend in the field.

6.1. How to generate electric power from osmosis

Blue energy recovery devices use selective membranes. We will first recall the operating principles of these membranes.

6.1.1. Membrane potential and selectivity

Ion exchange membranes (IEMs) possess fixed charges and are generally classified into 3 categories: cation exchange membranes (CEMs), anion exchange membranes (AEMs) and bipolar membranes [200]. Negatively charged chemical groups of strong or weak acids, including sulphonate (SO_3^-), phosphorate (PO_3^-), carboxyl groups (COO^-), are used in CEMs. AEMs, on the contrary, possess positively charged groups, such as ammonium ($-NR_3^+$), primary amine ($-NH_2$), and etc. In addition to CEMs and AEMs, bipolar membranes possess both positive and negative chemical groups and are widely applied in water splitting procedures [201].

When an IEM is placed in middle of two solutions chambers of different concentrations ($c_{bulk,L}$ and $c_{bulk,R}$) as illustrated in Fig. 22, an electrical potential difference ϕ_m for a chemical species i is established. In order to explain ion transportation, here we define the electrochemical potential $\tilde{\mu}_i$ (J/mol) as the combination of chemical potential term μ_i (J/mol) and electrical potential term ϕ (V).

$$\tilde{\mu}_i = \mu_i + z_i F\phi = \mu_i^0 + RT ln(\gamma_i c_i) + z_i F\phi \tag{5}$$

where z_i is the ion valence, F the Faraday constant, R the gas constant, T temperature, γ_i activity coefficient of species i, and c_i the ion concentration. According to Donnan equilibrium, the electrochemical potential at the solution-membrane interface is identical [202]. Thus it is possible to establish the equation below:

$$\mu_i^0 + RT ln(\gamma_{i,s} c_{i,s}) + z_i F\phi_s = \mu_i^0 + RT ln(\gamma_{i,m} c_{i,m}) + z_i F\phi_m \tag{6}$$

where subfix s and m represents the physical parameters in solution and in membrane, respectively. This leads to,

$$\Delta\phi_D = \phi_s - \phi_m = \frac{RT}{z_i F} ln(\frac{\gamma_{i,m} c_{i,m}}{\gamma_{i,s} c_{i,s}}) \tag{7}$$

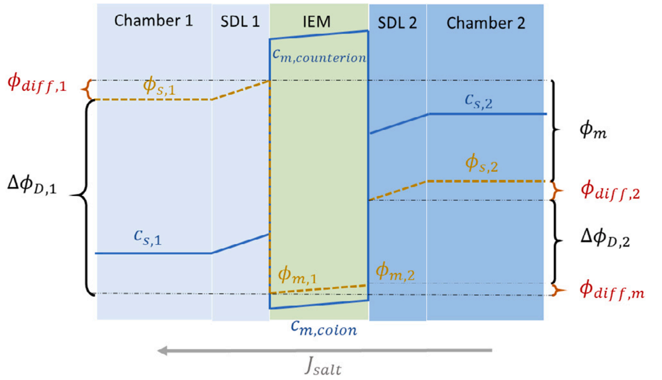

Fig. 22. Schematic representation of concentration c, and potential ϕ, profile in the bulk solutions, the stagnant diffusion layers (SDLs), and in an ion exchange membrane (IEM) in open-circuit conditions.

This potential difference $\Delta\phi_D$ is known as Donnan potential. According to Eq. (7), we have:

$$c_{i,m} \propto c_{i,s} exp(\frac{z_i F}{RT}\Delta\phi_D) \tag{8}$$

According to the definition of Donnan potential established above, we can deduce $\Delta\phi_D > 0$ for CEMs and $\Delta\phi_D < 0$ for AEMs. As co-ions and counter-ions have opposite charge valences, the exponential part is correspondingly greater than 1 for counter-ions and less than 1 for co-ions [203]. This simple calculation explains the important concentration difference of co-ions and counter-ions in IEMs under Donnan exclusion effect. When IEM is placed between two chambers (1 and 2) of different salinities, two Donnan potentials appear separately at the both solution-membrane interfaces. The concentration difference established across the IEM could also result in a diffusion potential ϕ_{diff}. This occurs due to the differences in ionic mobility in the IEM, which leads to a charge separation phenomenon [204,205]. Similarly, stagnant diffusion layers (SDL) could establish on either side of the membrane, which leads to diffusion electrical potentials [206,207]. Such phenomenon (concentration polarization effect) derives from the limitations of ion transportation at solution-membrane interfaces, and leads to an important effective potential drop [208–211]. Combining these above-mentioned terms will lead to the membrane potential difference ϕ_m, as illustrated in Fig. 22.

$$\phi_m = \Delta\phi_{D,1} - \Delta\phi_{D,2} + \phi_{diff,m} + \phi_{diff,1} + \phi_{diff,2} \tag{9}$$

In the case of a rigorously selective membrane, zero co-ion flows present in membrane phase. Due to the electroneutrality condition, the diffusion potentials vanishes. Thus, the membrane potential is simplified as:

$$\phi_m = \frac{RT}{z_i F} ln(\frac{\gamma_{i,2} c_{i,2}}{\gamma_{i,1} c_{i,1}}) \tag{10}$$

However, in real applications, membranes are never perfect. Dlugolecki et al. suggested a simple method for apparent selectivity measurement [212]. The experimental setup consists of a membrane placed in the middle of a saltwater chamber and a freshwater chamber with fixed concentration. The overall electrical potential established across the membrane E_{exp} can thus be measured at steady state. Then the perm-selectivity of the counter-ion is defined as

$$\alpha = \frac{E_{exp}}{\phi_m} \tag{11}$$

It is to notice that an ideal selectivity is obtained when α is of unit value. In the case where selectivity is zero, the membrane is completely non-selective. The selectivity of membranes come from their morphology. The morphology of IEM membranes is quite complex. For example, the structure of Nafion membranes encompasses a connected network of hydrophilic clusters in a hydrophobic and semi-crystalline perfluorocarbon phase [213]. The structural nature of the ionic domains, such as the size, shape, and spatial distributions of the clusters is still under debate. The size of the channels in the connected network is assumed to be less than 0.5 nm. These channels are covered with surface charges coming from the sulphate group SO_3^- in the Nafion situation. Due to the charge neutrality, counterions are attracted by the surface charges, leading to the formation of Electric Double Layer (EDL) composed of Stern layer and Gouy-Chapman layer [214,215]. The thickness of EDL is characterized by the Debye length, which indicates the spatial range of unscreened ionic charges under electrostatic effect [216]. Typically for water at room temperature, the Debye length is estimated at 0.3 nm for a salt concentration of a 1 M [217]. Considering that the pore size in IEMs is comparable to Debye length, the surface charge thus governs the transportation of ions in this case. In fact, the permselectivity could be intuitively explained from an electrostatic point of view : counter-ions are attracted by the fixed charges in membranes while co-ions are electrically repulsed The selectivity decrease is generally related to the existence of co-ion flux and water flux across the membrane [218]. A highly selective membrane is therefore a membrane with very small pore holes. The use of membranes in osmotic energy recovery devices requires the use of membranes that allow a large number of ions to pass through them, thus very permeable membranes. There is therefore a trade off to be found between permeability and selectivity.

This problem seemed to be solved for a while by the introduction of highly charged large hole membranes. Studies on single nanopores of a few tens of microns seemed to imply that gigantic powers could be obtained by using this type of membrane [219]. It is reported that a power density of 4 kW/m^2 is achieved with such nanofluidic system [219]. Gao et al. [220] showed that this way was a dead end. Collective effects prevent the scaling up of this process. When cations (or anions) are brought in excessively from one side of the membrane, there is a diffusion movement of the anions to cancel the electric charge. This creates a heterogeneous concentration distribution in the system called polarization concentration. This has the effect of decreasing the concentration difference on both sides of the membrane and therefore of strongly decreasing the membrane potential. When a single nanotube is considered the ions can diffuse from an infinite 3D space. When several nanotubes are close to each other, the polarization zones interact and the phenomenon is very important. This explains the failure of the scaling.

6.1.2. Working principle of RED

RED devices take advantage of the potential difference that appears on an ion exchange membrane when it separates two saline solutions of different concentrations. A series of pairs of cationic and anionic exchange membranes are placed in salt gradients. Under the effect of the saline gradient and the apparition of the potential difference, the ions migrate from the most concentrated solutions to the most diluted solutions. With the membranes being selective, an ionic flux is established. This is converted into an electronic flux at the electrodes by Faradaic reactions. The maximal gross power density produced under Faradaic conversion (i.e., the power density neglecting the viscous losses due to pumping and the process efficiency) is given by $P_{max} = \frac{E_{ocv}^2}{4SR_{cell}}$, where E_{ocv} is the open-circuit voltage, R_{cell} is the inner resistance of the cell and S is the surface of the membrane. E_{ocv} is the sum of the membranes potentials and of the electrodes drop potentials. The larger the membrane surface there is in a device, the higher power is generated. R_{cell} refers to the resistance of the cell and can be divided into two primary components. The first component, known as the ohmic component, pertains to the conductivity of the cell's components (such as the membrane, solutions, spacers, etc.). The second component, known as the non-ohmic component, is influenced by changes in concentration inside the cell. This non-ohmic component is caused by the polarization effect that occurs near membranes and by variations in salt concentration along the water channel [15].

6.1.3. Power produced using RED

Pattle et al. [221] used over 45 membranes in their RED system, but only achieved a mild power density of 0.2 W m^{-2} due to the low efficiency of their stack. As a result, numerous studies have been conducted to increase the output power density of RED systems. Długołecki et al. [212] investigated the performance of various membranes commonly used in RED and predicted that a power density of 6 W m^{-2} could be achieved using commercial IEMs. Turek et al. [222] achieved a power density of 0.84 W per square meter of membrane with a high salinity gradient (approximately 200), while Veerman et al. obtained a power density of 0.9 W m^{-2} with a salinity difference of 30 g L^{-1} and 1 g L^{-1} of NaCl for the concentrated and diluted solutions, respectively. However, the high cell resistance of RED systems hinders their electrical performance [223]. Vermaas et al. [224] reported that decreasing the spacer thickness from 485 μm to 100 μm can reduce the ohmic resistance of the system by 4, and with this improvement, they achieved a gross power density of 1.8 W m^{-2} using only 5 pairs of IEMs. Nonetheless, thinner spacers were found to lead to a higher pressure loss. In this study, they achieved a net power density of 1.2 W m^{-2}, which remains the highest documented experimental net power density to date.

Increasing the salt concentration and the temperature increases these performances. Using a single membrane and capacitive electrodes, Brahmi et al. [225] reports a net power density output of 2 W m^{-2} was reported, with a concentration ratio of 300 (0.017 M and 5.13 M). For a concentration ratio of 500 (salted water 5 M, fresh water 0.01 M), Daniilidis et al. [226] measure a gross power of 4 W m^{-2} at 25 °C and 7 W m^{-2} at 60 °C. The powers that we have just reported are powers of the order of 1 W m^{-2} ie 100 μW cm^{-2}. They are therefore compatible with IoT type applications. We will see in the next frame applications along this line. Unlike the previous principles, the RED does not draw its energy from a mechanical signal. The current produced does not therefore allow the analysis of a pressure signal or the analysis of a vibration or a shock. It is therefore not possible to build pressure sensors or deformation sensors from reverse electrodialysis devices. The only possible approach is to build energy producing devices that will allow to power sensors. The plan of the review will therefore differ from the previous paragraphs. We will simply focus on small-scale power generating systems and their application to sensors.

6.2. Harvesting devices

6.2.1. Miniaturized RED systems

One of the major advantages of RED technologies is its potential in both scaling up and miniaturization. Emerging researches focus on the development of mini-RED stacks in order to power future wearable devices, implantable sensors, bio-compatible and clinical implant systems, etc. To realize mini-RED devices, researchers can always find an exquisite and highly efficient example from nature: the electric organ of eels [227]. The electric organ is composed of long and thin cells separated by ion gradients [228]. The adjustment of K^+ channels and Na^+ channels could efficiently switch between rest stage (where zero voltage is generated) and firing stage (where a voltage of 150 mV appears across one single cell) [229], as illustrated in Fig. 23(a) and (b).

Inspired by electrolyte in an electric eel which can generate potentials of 600 V, Xu and Lavan proposed in 2008 the artificial cell conception for biological ion concentration gradient harvesting [230]. Based on the model established for natural electrogenic cell, they proposed methods for constructing artificial cells which have higher power density output and energy conversion efficiency according to their theoretical calculation. Also inspired by electric-eel organs, Schroeder et al. realized an excellent design of scalable stacking of miniature polyacrylamide hydrogel compartments coupled with series of alternative cation- and anion-selective hydrogel membranes [229]. Such design consists of a mini-RED repeating module composed of concentrated

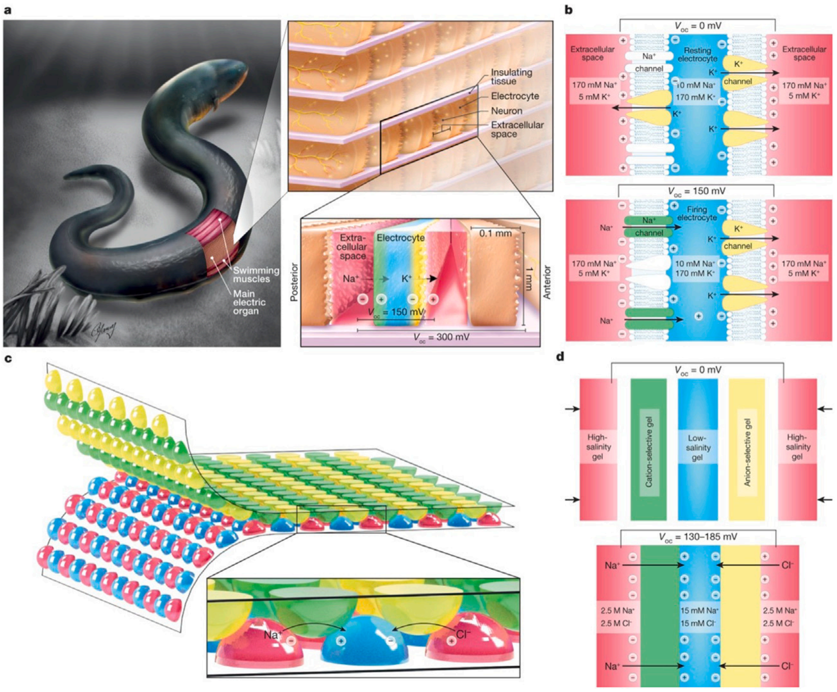

Fig. 23. Morphology and mechanism of action of the eel's electric organ and the artificial electric organ. (a), Electrophorus electricus. The top inset shows the arrangement of electrocytes within the electric organs of Electrophorus electricus. The bottom inset shows ion fluxes in the firing state. (b), Mechanism of voltage generation in electrocytes. (c), Artificial electric organ in its printed implementation. (d), Mechanism of voltage generation in the artificial electric organ.
Source: Figures and captions reproduced from [229] with permission from Springer Nature, copyright 2017.

salinity hydrogel, cation-selective gel membrane, diluted salinity hydrogel and anion-selective gel membrane (Fig. 23(c) and (d)). While stacking these modules in series up to 2449 units, an open-circuit potential of 110 V, along with a power density of 27 mW m^{-2} per tetrameric gel cell is reported. The afore-mentioned work was followed by a similar ionic hydrogel battery in a microfluidic version realized by He et al. [231] They designed typical well arrays and microfluidic channels to enable fast hydrogel assembly within several minutes. This microfluidic design avoids the time-consuming step for hydrogel assembling and provides a further insight for the wide application of power supply for soft and wearable devices.

To fulfill the power supply demand of small scale devices, miniaturized batteries are being extensively studied. In the work of Banan Sadeghian et al. miniaturized RED systems with a diameter of 5 mm are developed for energy generation [232]. Such system is coupled with a microfiltration AEM and copper electrodes. To avoid the use of pumping systems, the solution in the reservoir is not refreshed. This miniaturized system is reported to obtain a maximum energy density of 0.4 mJ cm^{-3} with an operation time of 3 h when connected with a 2 kΩ resistor. Considering the low energy efficiency estimated at 0.44%, system optimization is required to open up its application field. Tsai et al. reported a circular microchamber system containing a homemade Nafion microchannel with a typical surface of 23 × 500 μm^2 and a channel length of 1–3 mm [233]. Ag/AgCl electrodes and KCl solutions of a concentration ratio of 2000:1 are used in the experiment, resulting in a maximum power density of 755 mW m^{-2}. Chang et al. reported a pump-less paper-based RED system for power supply [234]. The unique design avoids the use of traditional pumping systems. In fact, both concentrated solution and diluted solution are driven into the paper-based system under capillary effect. Based on a specific channel design, the injection flow rates are maintained at a constant level. This unique design reduces the system cost and enables an practical integrated power supply device. Despite the low power density (275 nW cm^{-2}) reported in the work, such system presents a rather high operating time (1 h), which presents potentials in powering disposable and cost-less analytical devices.

Lin et al. developed a hydrogel-based RED system, comprising two agarose hydrogel chambers with different potassium chloride concentrations and a cation-selective gellan gum membrane [237]. The RED system is fully designed with bio-compatible materials and presents a open-circuit voltage of 177 mV. In this work, the first TENG-RED combined system is reported. An auxiliary TENG system based on Chitonsan/glycerol and PTFE materials as tribo-layers is developed. The TENG system serves as the charging component while connected with a full-wave rectifier. A maximum charging voltage of RED system is reported at 350 mV.

Informative signals are delivered by electrons in a traditional electronic circuit. However, in biologic systems, information transmission is realized by ions and molecules. The concept of iontronics is positioned between these two systems, where only ions are used for signal transmission in polyelectrolyte gels or electrolytes in aqueous solutions [238]. Currently, various ionic components are extensively studied to complete the iontronic toolbox [197,239,240]. The development of iontronics aims to realize biocompatible information processors to open up the possibility of biological communications directly with living organs [240]. Hopefully, based on this neuron-like and biocommunicable system, an aqueous computer could be developed in the future.

One of the essential obstacles is to design stable and bio compatible power supply systems. The integration of conventional electronic power generators requires the use of electrodes, where faradaic reactions and interfacial resistances could hinder its practical use. In this case, miniaturized electrodeless RED systems become an excellent candidate to power ionic circuits. Han et al. firstly reported a RED-driven complete iontronic circuit as a polyelectrolyte diode [235]. As illustrated in Fig. 24(a), a 25-IEM-packed RED system serves as the power supply of an ionic diode composed of a pair of positively charged poly(diallyldimethylammonium chloride) (pDADMAC) and negatively charged poly(2-acrylamido-2-methyl-1-propanesulfonic acid) (pAMPSA) prepared on a microfluidic chip. A flexible and ion-conducting tube is used for the connection between RED and chip. Experimental results demonstrate the forward bias state and reverse

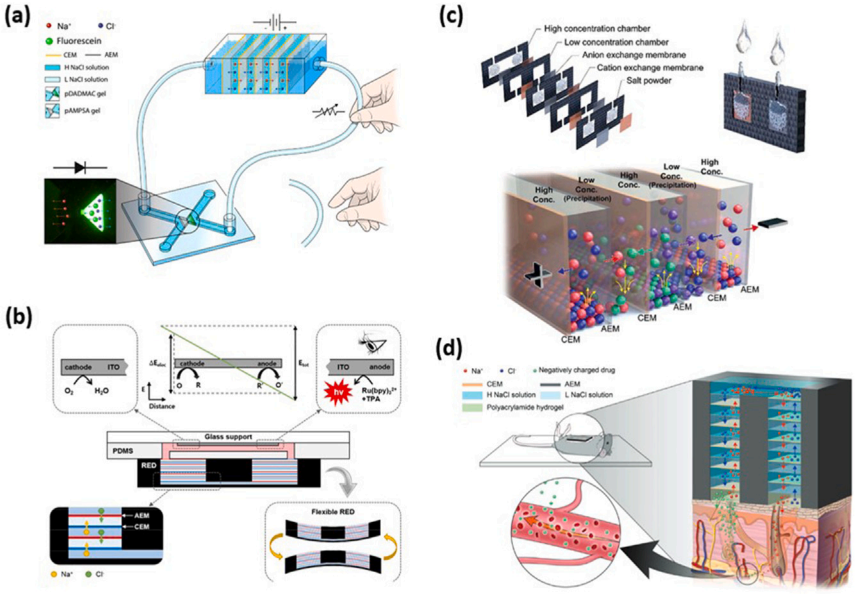

Fig. 24. Miniaturized RED-integrated ionic devices, analytical sensors and biomedical applications. (a), Illustrative schematic of ionic circuit powered by RED. Voltage generated from RED is applied to microfluidic polyelectrolyte diode directly via tubes filled with electrolyte. Figure and captions reproduced from [235] with permission from Springer Nature, copyright 2017. (b), Schematic Design of the RED-Powered Biosensing System. Figure and captions reproduced from [196] with permission from American Chemical Society, copyright 2018. (c), Schematic diagram of ssRED composition, its working principle and the activation process. Entry of water through inlets and dissolution of solid salts in high concentration chambers activate the ssRED. Figure and captions reproduced from [236] with permission from Royal Society of Chemistry, copyright 2018. (d), Schematic representation of the electrodeless RED patch attached on the mouse skin. Figure and captions reproduced from [198] with permission from John Wiley and Sons, copyright 2018.

bias state of the ionic diode powered by miniaturized RED system. The combination of 2 ionic diodes enables the creation of a logic OR gate, which is also experimentally demonstrated in the work.

Miniaturized RED systems could become an excellent candidate for power supply of disposable bio-sensors and microfluidic analytical devices. They possess the advantages of direct ionic flow creation, along with an instant electrical potential difference establishment and IEM stack based scaling up potential, which could be directly integrated into analytical devices to provide electrical energy.

The electrochemiluminescence (ECL)-based bioanalysis platform is a powerful analytical tool while combining with bipolar electrodes (BPE). While faradaic reactions appear on bipolar electrodes under external voltage, the ECL signals could provide information concerning the quantitative analytes on BPE surface. As demonstrated in Fig. 24(b), Baek et al. introduced the use of patch-type mini RED systems to power such platform in an electrode-less and environment-friendly way [196]. The direct ionic flow creation by RED system could avoid the voltage drop and faradaic reaction problems in conventional battery power supply. An integrated analytical system for glucose detection, coupled with RED stack powering system, was demonstrated in their work. The work of Yeon et al. has further promoted the development of disposable solid salt RED (ssRED) power source [236]. They designed a one-shot water-activated RED source where two kinds of salts ($Ag_2SO_4/BaCl_2$) are used alternatively in high concentration chambers (Fig. 24(c)). The activation step requires simply the addition of water into the chambers. As CEMs and AEMs are used alternatively, ions in high concentration chambers penetrated into diluted chambers become insoluble precipitations (AgCl or $BaSO_4$) through metathesis reactions. This ensures a stable concentration ratio, thus a longer operation time of the system. The integration of such system with above-explained BPE system and Ionic diodes are well demonstrated in their work.

Miniaturized RED systems are also widely used in skin-wearable biomedical devices. As presented in the work of Kwon et al. patch-type RED stacks are designed to power active transdermal drug delivery platforms [198]. The electrodeless design of RED patches present excellent advantages in biocompatibility and cost reduction. By adjusting the inserted number of membrane stacks, a controllable voltage is applied on the drug delivery platform to pump ionic drugs to penetrate the skin, as described in Fig. 24(d). Experimental results proved the feasibility of such systems for in vitro drug delivery of 3 representative drugs. Such design could be generalized and integrated for other portable biomedical devices. Pakkaner et al. reported a miniaturized RED driven biopower cell designed for auto-powered implantable medical devices [199]. The power supply is designed to harness the concentration gradient in physiological fluids in renal artery and vein for example. This fluidic device is designed with alternative CEMs and AEMs with a concentration ratio of 7.2 g/L and 9.0 g/L and is kept at 37 °C in order to imitate in vivo conditions. The same group reported an effective way for performance amelioration of the biopower cell: an additional salt-cartridge for concentration ratio boost [241]. Polysulfone (PSf) hollow fiber membranes saturated with NaCl solutions are prepared as salt cartridge. A diluted stream is divided into diluted substream, which is pumped directly into freshwater chambers, and a feed acceptor stream, which passes through the salt cartridge for salinity increase and serves as saltwater chamber reservoirs. A 3-fold increase of OCV of the cell is reported for the salt-cartridge boosted biopower system. It is to mention that although these two works present excellent potentials for miniaturized systems for biomedical applications, the feasibility of practical RED-driven implantable devices is yet to be verified by in vivo experiments.

6.2.2. *Perspectives for RED*

Considering the high energy density and the commercial viability of conventional batteries, it is possible to imagine miniaturized batteries to power small-scaled devices [242]. The tiny batteries widely used at the moment include zinc-air, zinc-silver oxide or lithium-manganese dioxide cells [243]. However, they present major disadvantages due to the necessary battery components of electrodes, electrical connectors and electrolyte. They are difficult to miniaturize due to the limitations of caustic KOH or lithium in batteries and the hazardous chemical products which presents safety problems during integration.

On the contrary, RED systems present major advantages in their small size, their electrode-related cost and redox reaction elimination, and their improved biocompatibility. This enables the integration of

Table 1
Comparison of the different nanotechnologies for energy harvesting.

Technology	Piezoelectricity	Electrostriction	Electrets	Triboelectricity	Osmotic energy
Energy source	Mechanical	Mechanical	Mechanical	Mechanical	Osmotic
Advantages	Mature technology, easy to scale down by using nanomaterials	Low cost, low weight, compatible with microfabrication	Low cost, stable performance, permanent polarization and good biocompatibility	Low cost, implantable device, bio-compatible systems	Direct current, bio-compatible systems
Limitations	Rectification of the current required, pooling, toxic compound (Lead, Perfluorated polymers), ceramics are brittle, need relatively large forces to deform piezoelectric materials	Rectification of the current required, need pre-charge or biasing voltage, large strain required	Rectification of the current required, material have finite lifetime due to slow loss of charges	Rectification of the current required, humidity, low output impedance, energy difficult to store	Technology currently under development, currently high cost

RED systems in sensors, wearable analytical devices and biomedical implants. Different from TENG systems where capacitive currents are generated, RED systems provide a direct ionic flow, along with an open-circuit voltage established across the membrane stack. The RED-driven ionic flow could be used to power iontronic circuits which remain an emerging hot topic today targeting the final goal of bio-communication and processing. In addition, miniaturized pump-free RED systems could also serve as energy storage systems due to the reversible procedures of electrodialysis, where desalination occurs under electricity application, and reverse electrodialysis where salt mixing is harnessed for electricity generation. In this point of view, the combination of RED and TENG system could be imagined as in the work of Lin et al. [237].

In fact, as it is always possible to adapt the number of IEM stacks to reach the power output demand, what hinders the application of mini-RED systems would be the operation lifespan. In the work of Yeon et al. a loss of 10% of current efficiency is reported over several hours [236]. And in the case of a biosensor powered by a RED system, the operation time is estimated to be 15 s [196]. It is thus important to develop functional mini-RED with an elongated working time so that the device could be integrated in implantable systems.

For miniaturized RED stacks, the cost mainly comes from the CEM/AEM membrane stacks in the system. In order to power sensors and ionic circuits, a typical mini-RED of 5–20 membrane stacks is used in the literature, which corresponds to a membrane area of 10–40 cm^2. The commercial membrane price is estimated to be around 1000 € m^{-2} for the widely used commercial brand Nafion. This indicates that the cost of a mini-RED would be around 1–4 €, which corresponds to the typical price of a disposable 1.5 V lithium battery. Considering a price reduction in the membrane research field, the price of a mini-RED could possibly be reduced to less than 1€. In this case, we can imagine economically viable and disposable mini-RED powered systems.

7. Summary and comparison between the different energy harvesting modes

In this work we have reviewed five modes of energy production to power IoT sensors based on mechanical energy sources and osmotic energy sources. These systems have their advantages and disadvantages (see Table 1). The four presented systems for collecting energy from vibrations have similarities. In the three cases (piezoelectric materials, electrostrictive materials, electrets and triboelectric materials), it is possible to use these materials as simple sensors or as materials that produce electric current. It should be noted that unlike piezoelectric materials, electrets and triboelectric materials, electrostrictive materials require a voltage source to polarize them. Although this source does not consume any energy, it is an obstacle to the development of electrostrictive materials.

In all three cases, an alternating electric current is produced. This current must be rectified so that it can be used to charge a battery. Electrostrictive materials need large deformation to perform well, this is not the case for electrets, piezoelectric and triboelectric materials which are adapted to smaller deformations [29]. Note that piezoelectric materials may require high forces. Another important disadvantage of electrostrictive materials is the need to work in the presence of a high voltage. They must be placed in a capacitor with a high potential difference to function, which significantly limits their applications in the IoT field. The techniques based on electrostrictive materials are thus behind the three other types of materials.

The piezoelectric systems are systems that put forward an higher power density compared to electrets and triboelectric systems, they are therefore suitable for miniaturized systems. Totally autonomous systems have been realized [90]. However, piezoelectric materials have their own important disadvantages. Ceramics piezoelectric materials usually contain toxic products (such as lead) and are brittle. Plus, they require high forces. However recent results obtained on polymers [67] are intriguing because of the high power they managed to produce: this could open new routes for energy-harvester design. However, these polymers are mainly perfluorinated products of restricted use in Europe. These products are classified as eternal pollutants due to their non-biodegradable character.

Triboelectric systems have the advantage of being less expensive and mechanically reliable. These points compensate for the lower power carried over compared to piezoelectric systems. The mechanisms of triboelectricity are being better understood, thanks to the work of Professor Wang's team [147,153]. These devices are particularly well adapted for medium size energy recovery systems. It must also be noted that the materials used are not very expensive and can be biosourced. Fully autonomous systems have been developed in many fields. Among them, major research efforts are devoted to harvesting energy from human movements (such as breathing and walking) without disturbing the movement or bothering the user. Triboelectric nanogenerators offer a broad selection of materials and structural designs, thanks to their various operational modes. Implantable and absorbable triboelectric nanogenerators can be designed using natural materials, while wearable and conformal triboelectric nanogenerators can be made using elastic electrode materials [246]. Moreover, TENGs with distinct structures can be custom-designed to match specific regions of the human body that require suitable binding sites [247].

In the last part, we present more preliminary works concerning the recovery of osmotic energy. These works have not yet reached the maturity of the studies on the recovery of mechanical energy but remain promising. Unlike previous systems, reverse electrodialysis devices produce a direct current that does not need to be rectified. After maturation, osmotic energy would become an important energy source because of all its possibilities and particularities. Small-scale applications already begin to spread over biology and chemistry applications. Compared to other types of sensors and nanogenerators that already existed, it offers a new type of solution for energy harvesting. Several research examples are mentioned above for directly using the ionic current or the potential to enhance a designed behavior. Some researchers are even thinking about using ionic current and diode-like effect [248] of semi-permeable membranes to create logic circuit.

Table 2

Comparison of the harvested power for different technologies. The large variety of harvested powers is difficult to interpret since there is no standard conditions or protocol (frequency, amplitude) which would enable a rigorous analysis.

Technology	Reference	Power or energy density by unit surface or volume	Volume (V) or Area (A) of the device	Frequency of the vibrations
Piezoelelectricity	[62]	70 μW cm^{-3}	V = 1 cm^3	100 Hz
Piezoelelectricity	[63]	800 μW cm^{-3}	V = 2 cm^3	1–10 Hz
Piezoelelectricity	[41]	55 000 μW cm^{-3}	V = 1 cm^3	900 Hz
Piezoelelectricity	[65]	77 μW cm^{-2}	A = 65 cm^2	1 Hz (sole, PZT)
Piezoelelectricity	[65]	9 μW cm^{-2}	A = 65 cm^2	1 Hz (sole, PVDF)
Electrostrictive materials	[105]	6 μW cm^{-3}	V = 1 cm^3	10 Hz
Electrostrictive materials	[98]	0.002 μW cm^{-3}	V = 4 cm^3	20 Hz
Electrostrictive materials	[102]	1 μW cm^{-2}	A = 7.5 cm^2	40 Hz
Electrostrictive materials	[115]	16 600 μW cm^{-2}	A = 60 cm^2	1 Hz (sole)
Electrets	[135]	1210 μW cm^{-2}	A = 3.6 cm^2	5 Hz
Electrets	[136]	62.5 μW cm^{-3}	V = 1.1 cm^3	125 Hz
Electrets	[138]	1.2 μW cm^{-2}	A = 1 cm^2	552 Hz
Triboelelectricity	[167]	0.2 μW cm^{-2}	A = 10 cm^2	2–5 Hz
Triboelelectricity	[102]	0.3 μW cm^{-2}	A = 7.5 cm^2	40–60 Hz
Triboelelectricity	[159]	48 000 μW cm^{-2}	A = 4 cm^2	3 Hz
Triboelelectricity	[158]	81.8 μW cm^{-2}	A = 25 cm^2	1 Hz
Triboelelectricity	[171]	30 700 μW cm^{-2}	A = 25 cm^2	1–10 Hz
Triboelelectricity	[174]	3.3 μW cm^{-2}	A = 300 cm^2	1 Hz (sole)
Triboelelectricity	[244]	16.6 μW cm^{-2}	A = 300 cm^2	1 Hz (sole)
Osmotic energy	[225]	220 μW cm^{-2}	A = 3 cm^2	–
Osmotic energy	[232]	0.004 μW cm^{-3}	A = 0.2 cm^2	–
Osmotic energy	[245]	2750 μW cm^{-2}	A = 0.1 cm^2	–

It could lead in the coming years to a new type of information and calculation support and even to the ionic computer.

A simple price evaluation of mini-RED devices estimates a cost around 1 €. This considers the current membrane price and RED performances. The later is very low mostly due to concentration polarization phenomena. As explained, researchers start to study this effect with simulations and electrical measurements. This open problem is maybe a greater challenge to work on. Between single-pore devices and commercial porous membrane, a power density of the order of 10^6 W m^{-2} is reduced by 6 orders of magnitude. If a way of suppressing or at least reducing the concentration polarization is found, the mini-RED device price could be reduced by the same 6 order of magnitude. That would make the osmotic energy an incomparably dense and easy way to generate ionic or electric current.

Most of the nanogenerators presented here collect energy efficiently. It should be noted that all these systems are a long way from commercialization. Comparing these different techniques remains difficult. Different parameters are needed to judge the efficiency of a device. At the application level, power density per volume or per surface is the parameter of choice.

Table 2 compiles recovered power values. An initial analysis can focus on the performances measured, even if they are under very different conditions. The best performance in the literature concerns piezoelectric crystals [41], and generally speaking, the best performances are achieved with the different piezoelectric materials. Electrets have capacities very close to those of triboelectric materials However, this classification is strongly influenced by the framework of the experiments carried out. Even the indicated volume or surface is not the same for the various work : some authors refer to the whole device, while others refer only to the volume or surface of the active material. As an example, while the devices of ref [225,245] work under continuous flow, the device of [232] works with finite volumes of solutions without flow.

To be able to compare systems with each other, you need standardized examples of use. There is an example of an emblematic device that allows the comparison of the recovered powers: the sole of a shoe. In this context, the results obtained with electrostrictive polymers are two orders of magnitude higher than the other systems [29]. 0.8 W are generated with an electrostrictive sole [115] while 5 mW are generated with a piezoelectric sole [65] and between 1 mW [174] and 5 mW [244] with a triboelectric sole. When the devices are at smaller scales and the solicitations are less important, the performances regrouping the piezoelectric and the triboelectric materials can for example exceed the results of performing electrostrictive materials [102]. Here we make an important point. The size of the device that can recover energy is an important parameter for choosing the material. In the case of large devices undergoing strong deformation, electrostrictive materials are preferable. Conversely, for smaller objects (cm^2 size), piezoelectricity, triboelectricity or even osmotic energy are recommended.

8. Perspectives

The analysis we have just carried out enables us to outline the prospects for energy recovery for the IOT. We think that the 3 following axis are key points: Performance characterization, Performance enhancement, Industrial manufacturing processes. In the following we will detail these points.

8.1. Performance characterization

To take this approach further, a common standard is needed to quantify, compare and evaluate the performance of nanogenerators. As presented in the text, three merit factors have been presented in the literature [97,165,249]. The definition of these respective factors of merit highlights the important parameters of both mechanisms (triboelectric charge for TENG, dielectric constant for electrostriction, piezoelectric coefficients). They provide guidelines for comparing and qualifying materials within the same framework, but are not sufficient to compare techniques between them. It is difficult to define standard experiments, as the different modes of loading (sliding contact, frontal contact for triboelectrics, rotation for electrets) can have a significant influence on the value of the harvested power. However, a few standard experiments where the force applied to the system is well controlled seem necessary. This could involve, for example, experiments with a cantilever whose size and frequency of displacement could be controlled and varied. This type of experiment is suitable for electrets, piezoelectric, triboelectric and electrostrictive materials. Beyond these standard tests, we believe that the best way is to define and use an efficiency parameter η defined as the ratio of the output energy E_{out} by the input energy E_{int}, $\eta = \frac{E_{out}}{E_{int}}$. Some data are displayed in the literature or in this article [165], but this approach has to become the rule. This parameter must be calculated in the presence and absence of energy storage.

8.2. Performance enhancement

One of the most important criteria is the increase in power. At the present stage of research, it seems that variations in materials will only allow incremental increases in power. It seems to us that the breakthrough must come from the coupled use of different energy recovery mechanisms. By hybridizing these different technologies [250] significant progress can be made. Lagomarsini et al. have developed an electrostrictive device [251] that does not require an external polarization voltage. Instead, they utilize the charge generated by the piezoelectric material when subjected to external mechanical excitation as the polarization source for the Dielectric Elastomer Generator (DEG). They have created two distinct prototypes: one employing a piezoelectric ceramic as the polarization element of an acrylic-based DEG, and the other using a piezoelectric polymer. To ensure perfect mechanical and electrical synchronization, a smart frame is incorporated. These prototypes demonstrate a noteworthy level of scavenged energy density, reaching up to 1 $\mu J\ g^{-1}$ and 0.39 $\mu J\ g^{-1}$, respectively. Moreover, compared to existing solutions in the literature, these devices are compact and eliminate the need for external polarization voltage. The use of devices drawing on different energy sources can make it possible to take better advantage of the environment. To overcome the weather-dependent limitations of solar cells, it is possible to integrate a solar cell with a TENG (triboelectric nanogenerator). This will permit to continually harness energy from the environment. The TENG in the device developed by Zhang et al. [252], made of a transparent and flexible polymer material, serves both as a component of the triboelectric nanogenerator and as a protective coating for the solar cells.

8.3. Industrial manufacturing processes

Most of the energy recovery systems presented in this review are unique systems developed in laboratories. If we are to make progress in this field, we need to move on to the industrialization of these systems. This requires the implementation of large-scale production protocols (roll-to-roll techniques for manufacturing materials), the search for inexpensive, non-toxic materials available in large quantities, and the implementation of material and quality control protocols. In this context, the MEMS approach is surely the most advanced, since it can benefit from electronics standards. Accelerated system ageing tests need to be introduced. Conditions of resistance to humidity, heat and cold must be clearly identified. This approach must also define marketing standards and norms, and enable buyers to understand how much power they will be able to recover according to the demands made on them. Without this, the market will remain a niche market.

CRediT authorship contribution statement

Nan Wu: Reviewed and edited the manuscript. **Timothée Derkenne:** Reviewed and edited the manuscript. **Corentin Tregouet:** Reviewed and edited the manuscript. **Annie Colin:** Reviewed and edited the manuscript, Supervised the redaction of the manuscript.

Declaration of competing interest

The authors declare the following financial interests/personal relationships which may be considered as potential competing interests: Nan Wu reports financial support was provided by China Scholarship Council. Timothee Derkenne reports financial support was provided by PSL University.

Data availability

No data was used for the research described in the article.

References

[1] K. Rose, S. Eldridge, L. Chapin, The Internet of Things: An Overview, Vol. 80, The internet society (ISOC), 2015, pp. 1–50.

[2] H. Kopetz, W. Steiner, Internet of things, in: Real-Time Systems: Design Principles for Distributed Embedded Applications, Springer, 2022, pp. 325–341.

[3] J. Gubbi, R. Buyya, S. Marusic, M. Palaniswami, Internet of Things (IoT): A vision, architectural elements, and future directions, Future Gener. Comput. Syst. 29 (7) (2013) 1645–1660.

[4] IoT Market by Component (Hardware, Software Solutions and Services), Orgaization Size, Focus Area (Smart Manufacturing), Smart Energy and Utilities and Smart Retail) and Region- Global Forecasts to 2026, Tech. Rep. TC 2895, Marketsandmarkets, 2022.

[5] V.M. Rohokale, N.R. Prasad, R. Prasad, A cooperative Internet of Things (IoT) for rural healthcare monitoring and control, in: 2011 2nd International Conference on Wireless Communication, Vehicular Technology, Information Theory and Aerospace & Electronic Systems Technology (Wireless VITAE), IEEE, 2011, pp. 1–6.

[6] A. Faure, M. Harfi, A. Naboulet, É. Tranier, C. Kirchner, Le Monde De L'internet Des Objets : Des Dynamiques À Maîtriser, Tech. rep., France Stratégie, 2022.

[7] T. Sanislav, G.D. Mois, S. Zeadally, S.C. Folea, Energy harvesting techniques for internet of things (IoT), IEEE Access 9 (2021) 39530–39549.

[8] M. Seok, S. Hanson, Y.-S. Lin, Z. Foo, D. Kim, Y. Lee, N. Liu, D. Sylvester, D. Blaauw, The Phoenix Processor: A 30pW platform for sensor applications, in: 2008 IEEE Symposium on VLSI Circuits, IEEE, 2008, pp. 188–189.

[9] Y.-S. Lin, D. Sylvester, D. Blaauw, An ultra low power 1v, 220nW temperature sensor for passive wireless applications, in: 2008 IEEE Custom Integrated Circuits Conference, IEEE, 2008, pp. 507–510.

[10] S. Boisseau, G. Despesse, B.A. Seddik, Electrostatic conversion for vibration energy harvesting, in: M. Lallart (Ed.), Small-Scale Energy Harvesting, IntechOpen, Rijeka, 2012, http://dx.doi.org/10.5772/51360.

[11] K. Yoshikawa, H. Kawasaki, W. Yoshida, T. Irie, K. Konishi, K. Nakano, T. Uto, D. Adachi, M. Kanematsu, H. Uzu, et al., Silicon heterojunction solar cell with interdigitated back contacts for a photoconversion efficiency over 26%, Nat. Energy 2 (5) (2017) 1–8.

[12] C. Williams, R.B. Yates, Analysis of a micro-electric generator for microsystems, Sensors Actuators A 52 (1–3) (1996) 8–11.

[13] S.D. Moss, O.R. Payne, G.A. Hart, C. Ung, Scaling and power density metrics of electromagnetic vibration energy harvesting devices, Smart Mater. Struct. 24 (2) (2015) http://dx.doi.org/10.1088/0964-1726/24/2/023001.

[14] N.Y. Yip, D. Brogioli, H.V. Hamelers, K. Nijmeijer, Salinity gradients for sustainable energy: primer, progress, and prospects, Environ. Sci. Technol. 50 (22) (2016) 12072–12094.

[15] N. Wu, Y. Brahmi, A. Colin, Fluidics for energy harvesting: from nano to milli scales, Lab Chip 23 (7) (2023) 1034–1065.

[16] M. Lallart, Small-Scale Energy Harvesting, BoD–Books on Demand, 2012.

[17] S.P. Beeby, T. O'Donnell, Electromagnetic energy harvesting, in: Energy Harvesting Technologies, Springer, 2009, pp. 129–161.

[18] M. Geisler, S. Boisseau, M. Perez, I. Ait-Ali, S. Perraud, Scaling effects in a non-linear electromagnetic energy harvester for wearable sensors, in: Journal of Physics: Conference Series, Vol. 773, IOP Publishing, 2016, 012044.

[19] D. Liu, Y. Gao, L. Zhou, J. Wang, Z.L. Wang, Recent advances in high-performance triboelectric nanogenerators, Nano Res. (2023) 1–20.

[20] W. Akram, Q. Chen, G. Xia, J. Fang, A review of single electrode triboelectric nanogenerators, Nano Energy (2022) 108043.

[21] S.A. Lone, K.C. Lim, K. Kaswan, S. Chatterjee, K.-P. Fan, D. Choi, S. Lee, H. Zhang, J. Cheng, Z.-H. Lin, Recent advancements for improving the performance of triboelectric nanogenerator devices, Nano Energy 99 (2022) 107318.

[22] J. Zhu, M. Zhu, Q. Shi, F. Wen, L. Liu, B. Dong, A. Haroun, Y. Yang, P. Vachon, X. Guo, et al., Progress in TENG technology—A journey from energy harvesting to nanoenergy and nanosystem, EcoMat 2 (4) (2020) e12058.

[23] N. Sezer, M. Koç, A comprehensive review on the state-of-the-art of piezoelectric energy harvesting, Nano Energy 80 (2021) 105567.

[24] C. Covaci, A. Gontean, Piezoelectric energy harvesting solutions: A review, Sensors 20 (12) (2020) 3512.

[25] M. Safaei, H.A. Sodano, S.R. Anton, A review of energy harvesting using piezoelectric materials: state-of-the-art a decade later (2008–2018), Smart Mater. Struct. 28 (11) (2019) 113001.

[26] K. Uchino, The development of piezoelectric materials and the new perspective, in: Advanced Piezoelectric Materials, Elsevier, 2017, pp. 1–92.

[27] Y. Zhao, L.-J. Yin, S.-L. Zhong, J.-W. Zha, Z.-M. Dang, Review of dielectric elastomers for actuators, generators and sensors, Iet Nanodielectrics 3 (4) (2020) 99–106.

[28] M. Lallart, P.-J. Cottinet, D. Guyomar, L. Lebrun, Electrostrictive polymers for mechanical energy harvesting, J. Polym. Sci. B 50 (8) (2012) 523–535.

[29] X. Yuan, S. Changgeng, G. Yan, Z. Zhenghong, Application review of dielectric electroactive polymers (DEAPs) and piezoelectric materials for vibration energy harvesting, in: Journal of Physics: Conference Series, Vol. 744, IOP Publishing, 2016, 012077.

[30] Z. Zhang, L. Wen, L. Jiang, Nanofluidics for osmotic energy conversion, Nat. Rev. Mater. 6 (7) (2021) 622–639.

[31] G. Laucirica, M.E. Toimil-Molares, C. Trautmann, W. Marmisollé, O. Azzaroni, Nanofluidic osmotic power generators–advanced nanoporous membranes and nanochannels for blue energy harvesting, Chem. Sci. 12 (39) (2021) 12874–12910.

[32] J. Curie, P. Curie, Développement par compression de l'électricité polaire dans les cristaux hémièdres à faces inclinées, Bull. Minéral. 3 (4) (1880) 90–93.

[33] J. Yang, et al., An introduction to the theory of piezoelectricity, 9 (2005).

[34] R.M. Martin, Piezoelectricity, Phys. Rev. B 5 (4) (1972) 1607.

[35] W.G. Cady, Piezoelectricity: Volume Two: An Introduction To the Theory and Applications of Electromechanical Phenomena in Crystals, Courier Dover Publications, 2018.

[36] J.I. Roscow, H. Pearce, H. Khanbareh, S. Kar-Narayan, C.R. Bowen, Modified energy harvesting figures of merit for stress-and strain-driven piezoelectric systems, Eur. Phys. J. Spec. Top. 228 (2019) 1537–1554.

[37] T.-B. Xu, E.J. Siochi, J.H. Kang, L. Zuo, W. Zhou, X. Tang, X. Jiang, Energy harvesting using a PZT ceramic multilayer stack, Smart Mater. Struct. 22 (6) (2013) 065015.

[38] P. Muralt, M. Marzencki, B. Belgacem, F. Calame, S. Basrour, Vibration energy harvesting with PZT micro device, Procedia Chem. 1 (1) (2009) 1191–1194.

[39] Y. Liu, Y. Chang, E. Sun, F. Li, S. Zhang, B. Yang, Y. Sun, J. Wu, W. Cao, Significantly enhanced energy-harvesting performance and superior fatigue-resistant behavior in [001] c-textured BaTiO3-based lead-free piezoceramics, ACS Appl. Mater. Interfaces 10 (37) (2018) 31488–31497.

[40] Z. Vakulov, A. Geldash, D. Khakhulin, M.V. Il'ina, O.I. Il'in, V.S. Klimin, V.N. Dzhuplin, B.G. Konoplev, Z. He, O.A. Ageev, Piezoelectric energy harvester based on LiNbO3 thin films, Materials 13 (18) (2020) 3984.

[41] A. Badel, A. Benayad, E. Lefeuvre, L. Lebrun, C. Richard, D. Guyomar, Single crystals and nonlinear process for outstanding vibration-powered electrical generators, IEEE Trans. Ultrason. Ferroelectr. Freq. Control 53 (4) (2006) 673–684.

[42] Z. Yang, J. Zu, Comparison of PZN-PT, PMN-PT single crystals and PZT ceramic for vibration energy harvesting, Energy Convers. Manage. 122 (2016) 321–329.

[43] L. Lu, W. Ding, J. Liu, B. Yang, Flexible PVDF based piezoelectric nanogenerators, Nano Energy 78 (2020) 105251.

[44] S. Sukumaran, S. Chatbouri, D. Rouxel, E. Tisserand, F. Thiebaud, T. Ben Zineb, Recent advances in flexible PVDF based piezoelectric polymer devices for energy harvesting applications, J. Intell. Mater. Syst. Struct. 32 (7) (2021) 746–780.

[45] M. Koç, L. Paralı, O. Şan, Fabrication and vibrational energy harvesting characterization of flexible piezoelectric nanogenerator (PEN) based on PVDF/PZT, Polym. Test. 90 (2020) 106695.

[46] K.T. Arul, M. Ramanjaneyulu, M.R. Rao, Energy harvesting of PZT/PMMA composite flexible films, Curr. Appl. Phys. 19 (4) (2019) 375–380.

[47] P. Zhang, W. Zhang, L. Deng, H. Zhang, A triboelectric nanogenerator based on temperature-stable high dielectric BaTiO3-based ceramic powder for energy harvesting, Nano Energy 87 (2021) 106176.

[48] T. Wu, Y. Song, Z. Shi, D. Liu, S. Chen, C. Xiong, Q. Yang, High-performance nanogenerators based on flexible cellulose nanofibril/MoS2 nanosheet composite piezoelectric films for energy harvesting, Nano Energy 80 (2021) 105541.

[49] R. Rai, I. Coondoo, R. Lopes, I. Bdikin, R. Ayouchi, S. Bhattacharaya, R. Schwarz, A. Kholkin, Development of lead-free materials for piezoelectric energy harvesting, in: MRS Online Proceedings Library (OPL), Vol. 1325, Cambridge University Press, 2011, mrss11–1325–e06–03.

[50] H. Li, C. Tian, Z.D. Deng, Energy harvesting from low frequency applications using piezoelectric materials, Appl. Phys. Rev. 1 (4) (2014) 041301.

[51] W.A. Smith, New opportunities in ultrasonic transducers emerging from innovations in piezoelectric materials, in: New Developments in Ultrasonic Transducers and Transducer Systems, Vol. 1733, SPIE, 1992, pp. 3–26.

[52] S.N. Cha, J.-S. Seo, S.M. Kim, H.J. Kim, Y.J. Park, S.-W. Kim, J.M. Kim, Sound-driven piezoelectric nanowire-based nanogenerators, Adv. Mater. 22 (42) (2010) 4726–4730.

[53] A. Erturk, D.J. Inman, Piezoelectric Energy Harvesting, John Wiley & Sons, 2011.

[54] Z.L. Wang, J. Song, Piezoelectric nanogenerators based on zinc oxide nanowire arrays, Science 312 (5771) (2006) 242–246.

[55] Z.L. Wang, Piezotronic and piezophototronic effects, J. Phys. Chem. Lett. 1 (9) (2010) 1388–1393.

[56] H. Yuan, T. Lei, Y. Qin, R. Yang, Flexible electronic skins based on piezoelectric nanogenerators and piezotronics, Nano Energy 59 (2019) 84–90.

[57] H.-K. Park, K.Y. Lee, J.-S. Seo, J.-A. Jeong, H.-K. Kim, D. Choi, S.-W. Kim, Charge-generating mode control in high-performance transparent flexible piezoelectric nanogenerators, Adv. Funct. Mater. 21 (6) (2011) 1187–1193.

[58] B. Kumar, S.-W. Kim, Energy harvesting based on semiconducting piezoelectric ZnO nanostructures, Nano Energy 1 (3) (2012) 342–355.

[59] X. Wang, J. Song, J. Liu, Z.L. Wang, Direct-current nanogenerator driven by ultrasonic waves, Science 316 (5821) (2007) 102–105.

[60] N.E. Dutoit, B.L. Wardle, S.-G. Kim, Design considerations for MEMS-scale piezoelectric mechanical vibration energy harvesters, Integr. Ferroelectr. 71 (1) (2005) 121–160.

[61] D. Lin, M. Guo, K.H. Lam, K.W. Kwok, H. Chan, Lead-free piezoelectric ceramic (K0. 5Na0. 5) NbO3 with MnO2 and K5. 4Cu1. 3Ta10O29 doping for piezoelectric transformer application, Smart Mater. Struct. 17 (3) (2008) 035002.

[62] S. Roundy, P.K. Wright, J. Rabaey, A study of low level vibrations as a power source for wireless sensor nodes, Comput. Commun. 26 (11) (2003) 1131–1144.

[63] S.R. Platt, S. Farritor, K. Garvin, H. Haider, The use of piezoelectric ceramics for electric power generation within orthopedic implants, IEEE/ASME Trans. Mechatronics 10 (4) (2005) 455–461.

[64] A. Chang, C. Uy, X. Xiao, X. Xiao, J. Chen, Self-powered environmental monitoring via a triboelectric nanogenerator, Nano Energy 98 (2022) 107282, http://dx.doi.org/10.1016/j.nanoen.2022.107282, URL https://www.sciencedirect.com/science/article/pii/S2211285522003615.

[65] C.J. Kendall, Parasitic Power Collection in Shoe Mounted Devices (Ph.D. thesis), Citeseer, 1998.

[66] S. Li, J. Yuan, H. Lipson, Ambient wind energy harvesting using cross-flow fluttering, 2011.

[67] N. Godard, L. Allirol, A. Latour, S. Glinsek, M. Gérard, J. Polesel, F.D. Dos Santos, E. Defay, 1-mW vibration energy harvester based on a cantilever with printed polymer multilayers, Cell Rep. Phys. Sci. 1 (6) (2020) 100068.

[68] Q. Liao, Z. Zhang, X. Zhang, M. Mohr, Y. Zhang, H.-J. Fecht, Flexible piezoelectric nanogenerators based on a fiber/ZnO nanowires/paper hybrid structure for energy harvesting, Nano Res. 7 (2014) 917–928.

[69] W. Qin, T. Li, Y. Li, J. Qiu, X. Ma, X. Chen, X. Hu, W. Zhang, A high power ZnO thin film piezoelectric generator, Appl. Surface Sci. 364 (2016) 670–675.

[70] H. Toshiyoshi, S. Ju, H. Honma, C.-H. Ji, H. Fujita, MEMS vibrational energy harvesters, Sci. Technol. Adv. Mater. 20 (1) (2019) 124–143.

[71] J.C. Park, J.Y. Park, Y.-P. Lee, Modeling and characterization of piezoelectric *d*_{33}-mode MEMS energy harvester, J. Microelectromech. Syst. 19 (5) (2010) 1215–1222.

[72] T. Tsukamoto, Y. Umino, S. Shiomi, K. Yamada, T. Suzuki, Bimorph piezoelectric vibration energy harvester with flexible 3D meshed-core structure for low frequency vibration, Sci. Technol. Adv. Mater. 19 (1) (2018) 660–668.

[73] D. Bhattacharya, S. Bayan, R.K. Mitra, S.K. Ray, 2D WS 2 embedded PVDF nanocomposites for photosensitive piezoelectric nanogenerators with a colossal energy conversion efficiency of 25.6%, Nanoscale 13 (37) (2021) 15819–15829.

[74] A. Tamang, S.K. Ghosh, S. Garain, M.M. Alam, J. Haeberle, K. Henkel, D. Schmeisser, D. Mandal, DNA-assisted β-phase nucleation and alignment of molecular dipoles in PVDF film: a realization of self-poled bioinspired flexible polymer nanogenerator for portable electronic devices, ACS Appl. Mater. Interfaces 7 (30) (2015) 16143–16147.

[75] S.K. Karan, R. Bera, S. Paria, A.K. Das, S. Maiti, A. Maitra, B.B. Khatua, An approach to design highly durable piezoelectric nanogenerator based on self-poled PVDF/AlO-rGO flexible nanocomposite with high power density and energy conversion efficiency, Adv. Energy Mater. 6 (20) (2016) 1601016.

[76] R. Hidalgo-Leon, J. Urquizo, C.E. Silva, J. Silva-Leon, J. Wu, P. Singh, G. Soriano, Powering nodes of wireless sensor networks with energy harvesters for intelligent buildings: A review, Energy Rep. 8 (2022) 3809–3826.

[77] N.R. Alluri, B. Saravanakumar, S.-J. Kim, Flexible, hybrid piezoelectric film (BaTi (1–x) Zr x O3)/PVDF nanogenerator as a self-powered fluid velocity sensor, ACS Appl. Mater. Interfaces 7 (18) (2015) 9831–9840.

[78] M. Shim, J. Kim, J. Jeong, S. Park, C. Kim, Self-powered 30 μW to 10 mW piezoelectric energy harvesting system with 9.09 ms/V maximum power point tracking time, IEEE J. Solid-State Circuits 50 (10) (2015) 2367–2379.

[79] J. Tao, N. Viet, A. Carpinteri, Q. Wang, Energy harvesting from wind by a piezoelectric harvester, Eng. Struct. 133 (2017) 74–80.

[80] A. Nechibvute, A. Chawanda, P. Luhanga, Piezoelectric energy harvesting devices: An alternative energy source for wireless sensors, in: M. Lallart (Ed.), Smart Mater. Res. 2012 (2012) 853481, http://dx.doi.org/10.1155/2012/853481.

[81] Y. Hu, Z.L. Wang, Recent progress in piezoelectric nanogenerators as a sustainable power source in self-powered systems and active sensors, Nano Energy 14 (2015) 3–14.

[82] D. Zhang, D. Wang, Z. Xu, X. Zhang, Y. Yang, J. Guo, B. Zhang, W. Zhao, Diversiform sensors and sensing systems driven by triboelectric and piezoelectric nanogenerators, Coord. Chem. Rev. 427 (2021) 213597.

[83] J. Zhong, Y. Ma, Y. Song, Q. Zhong, Y. Chu, I. Karakurt, D.B. Bogy, L. Lin, A flexible piezoelectret actuator/sensor patch for mechanical human–machine interfaces, ACS Nano 13 (6) (2019) 7107–7116.

[84] W. Deng, T. Yang, L. Jin, C. Yan, H. Huang, X. Chu, Z. Wang, D. Xiong, G. Tian, Y. Gao, et al., Cowpea-structured PVDF/ZnO nanofibers based flexible self-powered piezoelectric bending motion sensor towards remote control of gestures, Nano Energy 55 (2019) 516–525.

[85] G. Tian, W. Deng, Y. Gao, D. Xiong, C. Yan, X. He, T. Yang, L. Jin, X. Chu, H. Zhang, et al., Rich lamellar crystal baklava-structured PZT/PVDF piezoelectric sensor toward individual table tennis training, Nano Energy 59 (2019) 574–581.

[86] M.T. Chorsi, E.J. Curry, H.T. Chorsi, R. Das, J. Baroody, P.K. Purohit, H. Ilies, T.D. Nguyen, Piezoelectric biomaterials for sensors and actuators, Adv. Mater. 31 (1) (2019) 1802084.

[87] E.J. Curry, K. Ke, M.T. Chorsi, K.S. Wrobel, A.N. Miller III, A. Patel, I. Kim, J. Feng, L. Yue, Q. Wu, et al., Biodegradable piezoelectric force sensor, Proc. Natl. Acad. Sci. 115 (5) (2018) 909–914.

[88] Z. Liu, S. Zhang, Y. Jin, H. Ouyang, Y. Zou, X. Wang, L. Xie, Z. Li, Flexible piezoelectric nanogenerator in wearable self-powered active sensor for respiration and healthcare monitoring, Semicond. Sci. Technol. 32 (6) (2017) 064004.

[89] Y. Hu, Y. Zhang, C. Xu, L. Lin, R.L. Snyder, Z.L. Wang, Self-powered system with wireless data transmission, Nano Lett. 11 (6) (2011) 2572–2577.

[90] I. Jung, J. Choi, H.-J. Park, T.-G. Lee, S. Nahm, H.-C. Song, S. Kim, C.-Y. Kang, Design principles for coupled piezoelectric and electromagnetic hybrid energy harvesters for autonomous sensor systems, Nano Energy 75 (2020) 104921.

[91] G.-T. Hwang, H. Park, J.-H. Lee, S. Oh, K.-I. Park, M. Byun, H. Park, G. Ahn, C.K. Jeong, K. No, et al., Self-powered cardiac pacemaker enabled by flexible single crystalline PMN-PT piezoelectric energy harvester, Adv. Mater. 26 (28) (2014) 4880–4887.

[92] W.Y. Lionel, O. Chunlian, G. Yuandong, Inexhaustible battery: An energy harvester based battery for IoT applications, in: 2018 IEEE 13th Annual International Conference on Nano/Micro Engineered and Molecular Systems (NEMS), IEEE, 2018, pp. 495–498.

[93] H.Y. Lee, Y. Peng, Y.M. Shkel, Strain-dielectric response of dielectrics as foundation for electrostriction stresses, J. Appl. Phys. 98 (7) (2005) 074104.

[94] D. Jaaoh, C. Putson, N. Muensit, Enhanced strain response and energy harvesting capabilities of electrostrictive polyurethane composites filled with conducting polyaniline, Compos. Sci. Technol. 122 (2016) 97–103.

[95] X. Yin, M. Lallart, P.-J. Cottinet, D. Guyomar, J.-F. Capsal, Mechanical energy harvesting via a plasticizer-modified electrostrictive polymer, Appl. Phys. Lett. 108 (4) (2016) 042901.

[96] J. Yuan, A. Luna, W. Neri, C. Zakri, T. Schilling, A. Colin, P. Poulin, Graphene liquid crystal retarded percolation for new high-k materials, Nat. Commun. 6 (1) (2015) 1–8.

[97] M. Lallart, P.-J. Cottinet, L. Lebrun, B. Guiffard, D. Guyomar, Evaluation of energy harvesting performance of electrostrictive polymer and carbon-filled terpolymer composites, J. Appl. Phys. 108 (3) (2010) 034901.

[98] P.-J. Cottinet, D. Guyomar, B. Guiffard, C. Putson, L. Lebrun, Modeling and experimentation on an electrostrictive polymer composite for energy harvesting, IEEE Trans. Ultrason., Ferroelectr., Freq. Control 57 (4) (2010) 774–784.

[99] P.-J. Cottinet, M. Lallart, D. Guyomar, B. Guiffard, L. Lebrun, G. Sebald, C. Putson, Analysis of AC-DC conversion for energy harvesting using an electrostrictive polymer P (VDF-TrFE-CFE), IEEE Trans. Ultrason. Ferroelectr. Freq. Control 58 (1) (2011) 30–42.

[100] M. Pruvost, W.J. Smit, C. Monteux, P. Poulin, A. Colin, Microporous electrostrictive materials for vibrational energy harvesting, Multifunct. Mater. 1 (1) (2018) 015004.

[101] M. Pruvost, W.J. Smit, C. Monteux, P. Poulin, A. Colin, Polymeric foams for flexible and highly sensitive low-pressure capacitive sensors, Npj Flex. Electron. 3 (1) (2019) 7.

[102] M. Pruvost, W.J. Smit, C. Monteux, P. Del Corro, I. Dufour, C. Ayela, P. Poulin, A. Colin, Integration of a soft dielectric composite into a cantilever beam for mechanical energy harvesting, comparison between capacitive and triboelectric transducers, Sci. Rep. 10 (1) (2020) 1–14.

[103] Internet of things, https://www.bosch-presse.de/pressportal/de/de/tagpage/hashtag-topic-55554.html.

[104] G. Moretti, G.P.R. Papini, M. Righi, D. Forehand, D. Ingram, R. Vertechy, M. Fontana, Resonant wave energy harvester based on dielectric elastomer generator, Smart Mater. Struct. 27 (3) (2018) 035015.

[105] H. Nesser, H. Debeda, J. Yuan, A. Colin, P. Poulin, I. Dufour, C. Ayela, All-organic microelectromechanical systems integrating electrostrictive nanocomposite for mechanical energy harvesting, Nano Energy 44 (2018) 1–6.

[106] S.C. Mannsfeld, B.C. Tee, R.M. Stoltenberg, C.V.H. Chen, S. Barman, B.V. Muir, A.N. Sokolov, C. Reese, Z. Bao, Highly sensitive flexible pressure sensors with microstructured rubber dielectric layers, Nat. Mater. 9 (10) (2010) 859–864.

[107] G. Schwartz, B.C.-K. Tee, J. Mei, A.L. Appleton, D.H. Kim, H. Wang, Z. Bao, Flexible polymer transistors with high pressure sensitivity for application in electronic skin and health monitoring, Nat. Commun. 4 (1) (2013) 1859.

[108] J. Liu, G. Mao, X. Huang, Z. Zou, S. Qu, Enhanced compressive sensing of dielectric elastomer sensor using a novel structure, J. Appl. Mech. 82 (10) (2015) 101004.

[109] H. Böse, J. Ehrlich, Dielectric elastomer sensors with advanced designs and their applications, in: Actuators, Vol. 12, MDPI, 2023, p. 115.

[110] H. Böse, J. Ehrlich, T. Gerlach, T. Shinkar, D. Uhl, Dielectric elastomer strain sensors with enhanced measuring sensitivity, in: Electroactive Polymer Actuators and Devices (EAPAD) XXIV, Vol. 12042, SPIE, 2022, pp. 181–193.

[111] H. Böse, D. Ocak, J. Ehrlich, Applications of pressure-sensitive dielectric elastomer sensors, in: Electroactive Polymer Actuators and Devices (EAPAD) 2016, Vol. 9798, SPIE, 2016, pp. 451–463.

[112] H. Böse, D. Müller, J. Ehrlich, Operation tools with dielectric elastomer pressure sensors, in: Electroactive Polymer Actuators and Devices (EAPAD) 2017, Vol. 10163, SPIE, 2017, pp. 32–42.

[113] B. Shih, D. Shah, J. Li, T.G. Thuruthel, Y.-L. Park, F. Iida, Z. Bao, R. Kramer-Bottiglio, M.T. Tolley, Electronic skins and machine learning for intelligent soft robots, Science Robotics 5 (41) (2020) eaaz9239.

[114] S. Chiba, M. Waki, R. Kornbluh, R. Pelrine, Extending applications of dielectric elastomer artificial muscle, in: Electroactive Polymer Actuators and Devices (EAPAD) 2007, Vol. 6524, SPIE, 2007, pp. 621–625.

[115] R.D. Kornbluh, R. Pelrine, H. Prahlad, A. Wong-Foy, B. McCoy, S. Kim, J. Eckerle, T. Low, From boots to buoys: promises and challenges of dielectric elastomer energy harvesting, in: Electroactivity in Polymeric Materials, Springer, 2012, pp. 67–93.

[116] G. Sessler, Electrets, chapter 2, 1987.

[117] H. Unz, Oliver heaviside (185o-1925), IEEE Trans. Educ. 6 (1) (1963) 30–33.

[118] K.C. Kao, Dielectric Phenomena in Solids, Elsevier, 2004.

[119] E. Mototarô, On dielectric polarisation, Tokyo Sugaku-Buturigakkwai Kizi Dai 2 Ki 1 (10–11) (1919) 326–331.

[120] M. Borisova, S. Koikov, Electret effect in dielectrics, Sov. Phys. J. 22 (1979) 58–69.

[121] P. Kotrappa, Long term stability of electrets used in electret ion chambers, J. Electrost. 66 (7–8) (2008) 407–409.

[122] P. Kotrappa, J. Dempsey, J. Hickey, L. Stieff, An electret passive environmental 222Rn monitor based on ionization measurement, Health Phys. 54 (1) (1988) 47–56.

[123] H. Zhang, N. Liu, Q. Zeng, J. Liu, X. Zhang, M. Ge, W. Zhang, S. Li, Y. Fu, Y. Zhang, Design of polypropylene electret melt blown nonwovens with superior filtration efficiency stability through thermally stimulated charging, Polymers 12 (10) (2020) 2341.

[124] Z. Xia, A. Wedel, R. Danz, Charge storage and its dynamics in porous polytetrafluoroethylene (PTFE) film electrets, IEEE Trans. Dielectr. Electr. Insul. 10 (1) (2003) 102–108.

[125] T. Sugiyama, M. Aoyama, Y. Shibata, M. Suzuki, T. Konno, M. Ataka, H. Fujita, G. Hashiguchi, SiO2 electret generated by potassium ions on a comb-drive actuator, Appl. Phys. Express 4 (11) (2011) 114103.

[126] J. Małecki, Linear decay of charge in electrets, Phys. Rev. B 59 (15) (1999) 9954.

[127] M. Perez, S. Boisseau, P. Gasnier, J. Willemin, M. Geisler, J. Reboud, A cm scale electret-based electrostatic wind turbine for low-speed energy harvesting applications, Smart Mater. Struct. 25 (4) (2016) 045015.

[128] R. Hinchet, A. Ghaffarinejad, Y. Lu, J.Y. Hasani, S.-W. Kim, P. Basset, Understanding and modeling of triboelectric-electret nanogenerator, Nano Energy 47 (2018) 401–409.

[129] O.D. Jefimenko, D.K. Walker, Electrostatic current generator having a disk electret as an active element, IEEE Trans. Ind. Appl. (6) (1978) 537–540.

[130] Y.T.Y. Tada, Experimental characteristics of electret generator, using polymer film electrets, Japan. J. Appl. Phys. 31 (3R) (1992) 846.

[131] J. Boland, Y.-H. Chao, Y. Suzuki, Y. Tai, Micro electret power generator, in: The Sixteenth Annual International Conference on Micro Electro Mechanical Systems, 2003. MEMS-03 Kyoto. IEEE, IEEE, 2003, pp. 538–541.

[132] Y. Arakawa, Y. Suzuki, N. Kasagi, Micro seismic power generator using electret polymer film, Proc. PowerMEMS 187 (190) (2004) 17.

[133] H.-w. Lo, Y.-C. Tai, Parylene-based electret power generators, J. Micromech. Microeng. 18 (10) (2008) 104006.

[134] J. Nakano, K. Komori, Y. Hattori, Y. Suzuki, MEMS rotational electret energy harvester for human motion, in: Journal of Physics: Conference Series, Vol. 660, IOP Publishing, 2015, 012052.

[135] B. Mahanty, S.K. Ghosh, S. Garain, D. Mandal, An effective flexible wireless energy harvester/sensor based on porous electret piezoelectric polymer, Mater. Chem. Phys. 186 (2017) 327–332.

[136] H. Honma, H. Mitsuya, G. Hashiguchi, H. Fujita, H. Toshiyoshi, Improvement of energy conversion effectiveness and maximum output power of electrostatic induction-type MEMS energy harvesters by using symmetric comb-electrode structures, J. Micromech. Microeng. 28 (6) (2018) 064005.

[137] H. Toshiyoshi, S. Ju, H. Honma, C.-H. Ji, H. Fujita, MEMS vibrational energy harvesters, Sci. Technol. Adv. Mater. (2019).

[138] Q. Fu, Y. Suzuki, Large-dynamic-range MEMS electret energy harvester with combined gap-closing/overlapping-area-change electrodes, in: Journal of Physics: Conference Series, Vol. 476, IOP Publishing, 2013, 012112.

[139] Y. Lu, M. Capo-Chichi, Y. Leprince-Wang, P. Basset, A flexible electrostatic kinetic energy harvester based on electret films of electrospun nanofibers, Smart Mater. Struct. 27 (1) (2017) 014001, http://dx.doi.org/10.1088/1361-665X/aa87da.

[140] J. Zhu, Y. Yang, H. Zhang, Z. Zhao, T. Hu, L. Liu, More than energy harvesting in electret electronics-moving toward next-generation functional system, Adv. Funct. Mater. 33 (17) (2023) 2214859.

[141] J. Zhu, C. Chen, X. Guo, Suspended polytetrafluoroethylene nanostructure electret film in dual variable cavities for self-powered micro-shock sensing, Mater. Res. Express 5 (4) (2018) 046305.

[142] S. Chen, N. Wu, S. Lin, J. Duan, Z. Xu, Y. Pan, H. Zhang, Z. Xu, L. Huang, B. Hu, et al., Hierarchical elastomer tuned self-powered pressure sensor for wearable multifunctional cardiovascular electronics, Nano Energy 70 (2020) 104460.

[143] B. Yu, Z. Qiao, J. Cui, M. Lian, Y. Han, X. Zhang, W. Wang, X. Yu, H. Yu, X. Wang, et al., A host-coupling bio-nanogenerator for electrically stimulated osteogenesis, Biomaterials 276 (2021) 120997.

[144] A. Diaz, D. Wollmann, D. Dreblow, Contact electrification: ion transfer to metals and polymers, Chem. Mater. 3 (6) (1991) 997–999.

[145] A. Diaz, Contact electrification of materials: the chemistry of ions on polymer surfaces, J. Adhes. 67 (1–4) (1998) 111–122.

[146] H. Baytekin, A. Patashinski, M. Branicki, B. Baytekin, S. Soh, B.A. Grzybowski, The mosaic of surface charge in contact electrification, Science 333 (6040) (2011) 308–312.

[147] Z.L. Wang, T. Jiang, L. Xu, Toward the blue energy dream by triboelectric nanogenerator networks, Nano Energy 39 (2017) 9–23.

[148] J. Lowell, Contact electrification of metals, J. Phys. D: Appl. Phys. 8 (1) (1975) 53.

[149] C. Xu, B. Zhang, A.C. Wang, W. Cai, Y. Zi, P. Feng, Z.L. Wang, Effects of metal work function and contact potential difference on electron thermionic emission in contact electrification, Adv. Funct. Mater. 29 (29) (2019) 1903142.

[150] Z.L. Wang, Triboelectric nanogenerator (TENG)—sparking an energy and sensor revolution, Adv. Energy Mater. 10 (17) (2020) 2000137.

[151] W.-G. Kim, D.-W. Kim, I.-W. Tcho, J.-K. Kim, M.-S. Kim, Y.-K. Choi, Triboelectric nanogenerator: Structure, mechanism, and applications, Acs Nano 15 (1) (2021) 258–287.

[152] L.S. McCarty, G.M. Whitesides, Electrostatic charging due to separation of ions at interfaces: contact electrification of ionic electrets, Angew. Chem. Int. Ed. 47 (12) (2008) 2188–2207.

[153] Z. Wang, Y. Wang, Q. Gao, G. Bao, T. Cheng, Z.L. Wang, Triboelectric fluid sensors: Principles, development, and perspectives, Adv. Mater. Technol. 8 (5) (2023) 2201029.

[154] R. Zhang, H. Olin, Material choices for triboelectric nanogenerators: a critical review, EcoMat 2 (4) (2020) e12062.

[155] Z.L. Wang, On the first principle theory of nanogenerators from Maxwell's equations, Nano Energy 68 (2020) 104272.

[156] H. Zou, Y. Zhang, L. Guo, P. Wang, X. He, G. Dai, H. Zheng, C. Chen, A.C. Wang, C. Xu, et al., Quantifying the triboelectric series, Nat. Commun. 10 (1) (2019) 1–9.

[157] J. Chen, H. Guo, C. Hu, Z.L. Wang, Robust triboelectric nanogenerator achieved by centrifugal force induced automatic working mode transition, Adv. Energy Mater. 10 (23) (2020) 2000886.

[158] D. Kim, S.-B. Jeon, J.Y. Kim, M.-L. Seol, S.O. Kim, Y.-K. Choi, High-performance nanopattern triboelectric generator by block copolymer lithography, Nano Energy 12 (2015) 331–338.

[159] J. Chun, B.U. Ye, J.W. Lee, D. Choi, C.-Y. Kang, S.-W. Kim, Z.L. Wang, J.M. Baik, Boosted output performance of triboelectric nanogenerator via electric double layer effect, Nat. Commun. 7 (1) (2016) 1–9.

[160] L. Cheng, Q. Xu, Y. Zheng, X. Jia, Y. Qin, A self-improving triboelectric nanogenerator with improved charge density and increased charge accumulation speed, Nat. Commun. 9 (1) (2018) 3773.

[161] W. Liu, Z. Wang, G. Wang, G. Liu, J. Chen, X. Pu, Y. Xi, X. Wang, H. Guo, C. Hu, et al., Integrated charge excitation triboelectric nanogenerator, Nat. Commun. 10 (1) (2019) 1–9.

[162] N. Cui, L. Gu, Y. Lei, J. Liu, Y. Qin, X. Ma, Y. Hao, Z.L. Wang, Dynamic behavior of the triboelectric charges and structural optimization of the friction layer for a triboelectric nanogenerator, ACS Nano 10 (6) (2016) 6131–6138.

[163] B. Kim, J.Y. Song, M.-c. Kim, Z.-H. Lin, D. Choi, S.M. Park, et al., All-aerosol-sprayed high-performance transparent triboelectric nanogenerator with embedded charge-storage layer for self-powered invisible security IoT system and raindrop-solar hybrid energy harvester, Nano Energy 104 (2022) 107878.

[164] L. Xu, T.Z. Bu, X.D. Yang, C. Zhang, Z.L. Wang, Ultrahigh charge density realized by charge pumping at ambient conditions for triboelectric nanogenerators, Nano Energy 49 (2018) 625–633.

[165] Y. Zi, S. Niu, J. Wang, Z. Wen, W. Tang, Z.L. Wang, Standards and figure-of-merits for quantifying the performance of triboelectric nanogenerators, Nat. Commun. 6 (1) (2015) 8376.

[166] X. Wang, H. Zhang, L. Dong, X. Han, W. Du, J. Zhai, C. Pan, Z.L. Wang, Self-powered high-resolution and pressure-sensitive triboelectric sensor matrix for real-time tactile mapping, Adv. Mater. 28 (15) (2016) 2896–2903.

[167] C. Wu, R. Liu, J. Wang, Y. Zi, L. Lin, Z.L. Wang, A spring-based resonance coupling for hugely enhancing the performance of triboelectric nanogenerators for harvesting low-frequency vibration energy, Nano Energy 32 (2017) 287–293.

[168] S. Cui, Y. Zheng, T. Zhang, D. Wang, F. Zhou, W. Liu, Self-powered ammonia nanosensor based on the integration of the gas sensor and triboelectric nanogenerator, Nano Energy 49 (2018) 31–39.

[169] K. Meng, J. Chen, X. Li, Y. Wu, W. Fan, Z. Zhou, Q. He, X. Wang, X. Fan, Y. Zhang, et al., Flexible weaving constructed self-powered pressure sensor enabling continuous diagnosis of cardiovascular disease and measurement of cuffless blood pressure, Adv. Funct. Mater. 29 (5) (2019) 1806388.

[170] L. Liu, Q. Shi, J.S. Ho, C. Lee, Study of thin film blue energy harvester based on triboelectric nanogenerator and seashore IoT applications, Nano Energy 66 (2019) 104167.

[171] R. Zhang, C. Dahlström, H. Zou, J. Jonzon, M. Hummelgård, J. Örtegren, N. Blomquist, Y. Yang, H. Andersson, M. Olsen, et al., Cellulose-based fully green triboelectric nanogenerators with output power density of 300 W m- 2, Adv. Mater. 32 (38) (2020) 2002824.

[172] W. Seung, H.-J. Yoon, T.Y. Kim, H. Ryu, J. Kim, J.-H. Lee, J.H. Lee, S. Kim, Y.K. Park, Y.J. Park, et al., Boosting power-generating performance of triboelectric nanogenerators via artificial control of ferroelectric polarization and dielectric properties, Adv. Energy Mater. 7 (2) (2017) 1600988.

[173] W. Liu, Z. Wang, G. Wang, Q. Zeng, W. He, L. Liu, X. Wang, Y. Xi, H. Guo, C. Hu, et al., Switched-capacitor-convertors based on fractal design for output power management of triboelectric nanogenerator, Nat. Commun. 11 (1) (2020) 1–10.

[174] S. Niu, X. Wang, F. Yi, Y.S. Zhou, Z.L. Wang, A universal self-charging system driven by random biomechanical energy for sustainable operation of mobile electronics, Nat. Commun. 6 (1) (2015) 8975.

[175] S. Boisseau, G. Despesse, S. Monfray, O. Puscasu, T. Skotnicki, Semi-flexible bimetal-based thermal energy harvesters, Smart Mater. Struct. 22 (2) (2013) 025021.

[176] T. Tat, A. Libanori, C. Au, A. Yau, J. Chen, Advances in triboelectric nanogenerators for biomedical sensing, Biosens. Bioelectron. 171 (2021) 112714.

[177] A. Ahmed, I. Hassan, M.F. El-Kady, A. Radhi, C.K. Jeong, P.R. Selvaganapathy, J. Zu, S. Ren, Q. Wang, R.B. Kaner, Integrated triboelectric nanogenerators in the era of the internet of things, Adv. Sci. 6 (24) (2019) 1802230.

[178] J. Li, C. Wu, I. Dharmasena, X. Ni, Z. Wang, H. Shen, S.-L. Huang, W. Ding, Triboelectric nanogenerators enabled internet of things: A survey, Intell. Converged Netw. 1 (2) (2020) 115–141.

[179] Y. Yang, X. Guo, M. Zhu, Z. Sun, Z. Zhang, T. He, C. Lee, Triboelectric nanogenerator enabled wearable sensors and electronics for sustainable internet of things integrated green earth, Adv. Energy Mater. 13 (1) (2023) 2203040.

[180] Y. Zhou, M. Shen, X. Cui, Y. Shao, L. Li, Y. Zhang, Triboelectric nanogenerator based self-powered sensor for artificial intelligence, Nano Energy 84 (2021) 105887.

[181] K. Zhao, G. Gu, Y. Zhang, B. Zhang, F. Yang, L. Zhao, M. Zheng, G. Cheng, Z. Du, The self-powered CO2 gas sensor based on gas discharge induced by triboelectric nanogenerator, Nano Energy 53 (2018) 898–905.

[182] J. Yang, J. Chen, Y. Su, Q. Jing, Z. Li, F. Yi, X. Wen, Z. Wang, Z.L. Wang, Eardrum-inspired active sensors for self-powered cardiovascular system characterization and throat-attached anti-interference voice recognition, Adv. Mater. 27 (8) (2015) 1316–1326.

[183] P. Bai, G. Zhu, Q. Jing, J. Yang, J. Chen, Y. Su, J. Ma, G. Zhang, Z.L. Wang, Membrane-based self-powered triboelectric sensors for pressure change detection and its uses in security surveillance and healthcare monitoring, Adv. Funct. Mater. 24 (37) (2014) 5807–5813.

[184] F. Yi, L. Lin, S. Niu, P.K. Yang, Z. Wang, J. Chen, Y. Zhou, Y. Zi, J. Wang, Q. Liao, et al., Stretchable-rubber-based triboelectric nanogenerator and its application as self-powered body motion sensors, Adv. Funct. Mater. 25 (24) (2015) 3688–3696.

[185] Z. Jia, B. Wang, S. Song, Y. Fan, Blue energy: Current technologies for sustainable power generation from water salinity gradient, Renew. Sustain. Energy Rev. 31 (2014) 91–100, http://dx.doi.org/10.1016/j.rser.2013.11.049.

[186] R.S. Norman, Water salination: A source of energy, Science 186 (4161) (1974) 350–352, http://dx.doi.org/10.1126/science.186.4161.350.

[187] R.A. Tufa, S. Pawlowski, J. Veerman, K. Bouzek, E. Fontananova, G. di Profio, S. Velizarov, J. Goulão Crespo, K. Nijmeijer, E. Curcio, Progress and prospects in reverse electrodialysis for salinity gradient energy conversion and storage, Appl. Energy 225 (2018) 290–331, http://dx.doi.org/10.1016/j.apenergy.2018.04.111.

[188] B.E. Logan, M. Elimelech, Membrane-based processes for sustainable power generation using water, Nature 488 (7411) (2012) 313–319, http://dx.doi.org/10.1038/nature11477.

[189] N.Y. Yip, D. Brogioli, H.V.M. Hamelers, K. Nijmeijer, Salinity gradients for sustainable energy: Primer, progress and prospects, Environ. Sci. Technol. 50 (22) (2016) 12072–12094, http://dx.doi.org/10.1021/acs.est.6b03448.

[190] A. Achilli, A.E. Childress, Pressure retarded osmosis: From the vision of sidney loeb to the first prototype installation —Review, Desalination 261 (3) (2010) 205–211, http://dx.doi.org/10.1016/j.desal.2010.06.017.

[191] S. Sarp, Z. Li, J. Saththasivam, Pressure Retarded Osmosis (PRO): Past experiences, current developments, and future prospects, Desalination 389 (2016) 2–14, http://dx.doi.org/10.1016/j.desal.2015.12.008.

[192] J. Veerman, M. Saakes, S. Metz, G. Harmsen, Reverse electrodialysis: A validated process model for design and optimization, Chem. Eng. J. 166 (1) (2011) 256–268, http://dx.doi.org/10.1016/j.cej.2010.10.071.

[193] A.H. Avci, R.A. Tufa, E. Fontananova, G.D. Profio, E. Curcio, Reverse electrodialysis for energy production from natural river water and seawater, Energy 165 (2018) 512–521, http://dx.doi.org/10.1016/j.energy.2018.09.111, URL https://www.sciencedirect.com/science/article/pii/S0360544218318759.

[194] D. Brogioli, Extracting renewable energy from a salinity difference using a capacitor, Phys. Rev. Lett. 103 (5) (2009) 058501, http://dx.doi.org/10.1103/PhysRevLett.103.058501.

[195] T. Kim, B.E. Logan, C.A. Gorski, A pH-gradient flow cell for converting waste co_2 into electricity, Environ. Sci. Technol. Lett. 4 (2) (2017) 49–53, http://dx.doi.org/10.1021/acs.estlett.6b00467.

[196] S. Baek, S.-R. Kwon, S.Y. Yeon, S.-H. Yoon, C.M. Kang, S.H. Han, D. Lee, T.D. Chung, Miniaturized reverse electrodialysis-powered biosensor using electrochemiluminescence on bipolar electrode, Anal. Chem. 90 (7) (2018) 4749–4755, http://dx.doi.org/10.1021/acs.analchem.7b05425.

[197] J.-H. Han, K.B. Kim, H.C. Kim, T.D. Chung, Ionic circuits based on polyelectrolyte diodes on a microchip, Angew. Chem. Int. Ed. 48 (21) (2009) 3830–3833, http://dx.doi.org/10.1002/anie.200900045.

[198] S.-R. Kwon, S.H. Nam, C.Y. Park, S. Baek, J. Jang, X. Che, S.H. Kwak, Y.-R. Choi, N.-R. Park, J.-Y. Choi, Y. Lee, T.D. Chung, Electrodeless reverse electrodialysis patches as an ionic power source for active transdermal drug delivery, Adv. Funct. Mater. 28 (15) (2018) 1705952, http://dx.doi.org/10.1002/adfm.201705952.

[199] E. Pakkaner, C. Smith, C. Trexler, J. Hestekin, C. Hestekin, Blood driven biopower cells: Acquiring energy from reverse electrodialysis using sodium concentrations from the flow of human blood, J. Power Sources 488 (2021) 229440, http://dx.doi.org/10.1016/j.jpowsour.2020.229440.

[200] T. Luo, S. Abdu, M. Wessling, Selectivity of ion exchange membranes: A review, J. Membr. Sci. 555 (2018) 429–454, http://dx.doi.org/10.1016/j.memsci.2018.03.051.

[201] N. Wu, Y. Brahmi, A. Colin, Fluidics for energy harvesting: From nano to milli scales, Lab Chip 23 (5) (2023) 1034–1065, http://dx.doi.org/10.1039/D2LC00946C.

[202] F.G. Donnan, The theory of membrane equilibria, Chem. Rev. 1 (1) (1924) 73–90, http://dx.doi.org/10.1021/cr60001a003.

[203] H. Fan, Y. Huang, N.Y. Yip, Advancing ion-exchange membranes to ion-selective membranes: Principles, status, and opportunities, Front. Environ. Sci. Eng. 17 (2) (2022) 25, http://dx.doi.org/10.1007/s11783-023-1625-0.

[204] K.N. Mikhelson, A. Lewenstam, S.E. Didina, Contribution of the diffusion potential to the membrane potential and to the ion-selective electrode response, Electroanalysis 11 (10–11) (1999) 793–798, http://dx.doi.org/10.1002/(SICI)1521-4109(199907)11:10/11<793::AID-ELAN793>3.0.CO;2-K.

[205] Y. Oren, A. Litan, State of the solution-membrane interface during ion transport across an ion-exchange membrane, J. Phys. Chem. 78 (18) (1974) 1805–1811, http://dx.doi.org/10.1021/j100611a007.

[206] F.G. Helfferich, Ion Exchange, Courier Corporation, 1995.

[207] H. Strathmann, Ion-Exchange Membrane Separation Processes, Elsevier, 2004.

[208] I. Rubinstein, Theory of concentration polarization effects in electrodialysis on counter-ion selectivity of ion-exchange membranes with differing counter-ion distribution coefficients, J. Chem. Soc., Faraday Trans. 86 (10) (1990) 1857–1861, http://dx.doi.org/10.1039/FT9908601857.

[209] V.I. Zabolotsky, J.A. Manzanares, V.V. Nikonenko, K.A. Lebedev, E.G. Lovtsov, Space charge effect on competitive ion transport through ion-exchange membranes, Desalination 147 (1) (2002) 387–392, http://dx.doi.org/10.1016/S0011-9164(02)00614-8.

[210] C. Tang, M.L. Bruening, Ion separations with membranes, J. Polym. Sci. 58 (20) (2020) 2831–2856, http://dx.doi.org/10.1002/pol.20200500.

[211] R. abu Rjal, V. Chinaryan, M.Z. Bazant, I. Rubinstein, B. Zaltzman, Effect of concentration polarization on permselectivity, Phys. Rev. E 89 (1) (2014) 012302, http://dx.doi.org/10.1103/PhysRevE.89.012302.

[212] P. Dlugolecki, K. Nymeijer, S. Metz, M. Wessling, Current status of ion exchange membranes for power generation from salinity gradients, J. Membr. Sci. 319 (1) (2008) 214–222, http://dx.doi.org/10.1016/j.memsci.2008.03.037.

[213] A.-L. Rollet, O. Diat, G. Gebel, A new insight into nafion structure, J. Phys. Chem. B 106 (12) (2002) 3033–3036.

[214] O. Stern, The theory of the electrolytic double-layer, Z. Elektrochem 30 (508) (1924) 1014–1020.

[215] M. Gouy, Sur la constitution de la charge électrique à la surface d'un électrolyte, J. Phys. Théor. Appl. 9 (1) (1910) 457–468, http://dx.doi.org/10.1051/jphystap:019100090045700.

[216] Z. Zhang, L. Wen, L. Jiang, Nanofluidics for osmotic energy conversion, Nat. Rev. Mater. 6 (7) (2021) 622–639, http://dx.doi.org/10.1038/s41578-021-00300-4.

[217] S. Marbach, L. Bocquet, Osmosis, from molecular insights to large-scale applications, Chem. Soc. Rev. 48 (11) (2019) 3102–3144, http://dx.doi.org/10.1039/C8CS00420J.

[218] N.Y. Yip, D.A. Vermaas, K. Nijmeijer, M. Elimelech, Thermodynamic, energy efficiency and power density analysis of reverse electrodialysis power generation with natural salinity gradients, Environ. Sci. Technol. 48 (9) (2014) 4925–4936, http://dx.doi.org/10.1021/es5005413.

[219] A. Siria, P. Poncharal, A.-L. Biance, R. Fulcrand, X. Blase, S.T. Purcell, L. Bocquet, Giant osmotic energy conversion measured in a single transmembrane boron nitride nanotube, Nature 494 (7438) (2013) 455–458, http://dx.doi.org/10.1038/nature11876.

[220] J. Gao, X. Liu, Y. Jiang, L. Ding, L. Jiang, W. Guo, Understanding the giant gap between single-pore- and membrane-based nanofluidic osmotic power generators, Small 15 (11) (2019) 1804279, http://dx.doi.org/10.1002/smll.201804279.

[221] R. Pattle, Production of electric power by mixing fresh and salt water in the hydroelectric pile, Nature 174 (1954) 660.

[222] M. Turek, B. Bandura, P. Dydo, Power production from coal-mine brine utilizing reversed electrodialysis, Desalination 221 (1–3) (2008) 462–466.

[223] J. Veerman, M. Saakes, S. Metz, G. Harmsen, Reverse electrodialysis: Performance of a stack with 50 cells on the mixing of sea and river water, J. Membr. Sci. 327 (1–2) (2009) 136–144.

[224] D.A. Vermaas, M. Saakes, K. Nijmeijer, Doubled power density from salinity gradients at reduced intermembrane distance, Environ. Sci. Technol. 45 (16) (2011) 7089–7095.

[225] Y. Brahmi, A. Colin, New membrane and electrode assembly concept to improve salinity energy harvesting, Energy Convers. Manage. 254 (2022) 115297, http://dx.doi.org/10.1016/j.enconman.2022.115297.

[226] A. Daniilidis, D.A. Vermaas, R. Herber, K. Nijmeijer, Experimentally obtainable energy from mixing river water, seawater or brines with reverse electrodialysis, Renew. Energy 64 (2014) 123–131.

[227] A.L. Gotter, M.A. Kaetzel, J.R. Dedman, Electrophorus electricus as a model system for the study of membrane excitability, Comp. Biochem. Physiol. A 119 (1) (1998) 225–241, http://dx.doi.org/10.1016/S1095-6433(97)00414-5.

[228] M.V. Brown, The electric discharge of the electric EEL, Electr. Eng. 69 (2) (1950) 145–147, http://dx.doi.org/10.1109/EE.1950.6434151.

[229] T.B.H. Schroeder, A. Guha, A. Lamoureux, G. VanRenterghem, D. Sept, M. Shtein, J. Yang, M. Mayer, An electric-eel-inspired soft power source from stacked hydrogels, Nature 552 (7684) (2017) 214–218, http://dx.doi.org/10.1038/nature24670.

[230] J. Xu, D.A. Lavan, Designing artificial cells to harness the biological ion concentration gradient, Nature Nanotechnol. 3 (11) (2008) 666–670, http://dx.doi.org/10.1038/nnano.2008.274.

[231] P. He, J. He, Z. Huo, D. Li, Microfluidics-based fabrication of flexible ionic hydrogel batteries inspired by electric eels, Energy Storage Mater. 49 (2022) 348–359, http://dx.doi.org/10.1016/j.ensm.2022.04.019.

[232] R. Banan Sadeghian, O. Pantchenko, D. Tate, A. Shakouri, Miniaturized concentration cells for small-scale energy harvesting based on reverse electrodialysis, Appl. Phys. Lett. 99 (17) (2011) 173702, http://dx.doi.org/10.1063/1.3656279.

[233] T.-C. Tsai, C.-W. Liu, R.-J. Yang, Power generation by reverse electrodialysis in a microfluidic device with a nafion ion-selective membrane, Micromachines 7 (11) (2016) 205, http://dx.doi.org/10.3390/mi7110205.

[234] H.-K. Chang, E. Choi, J. Park, Paper-based energy harvesting from salinity gradients, Lab Chip 16 (4) (2016) 700–708, http://dx.doi.org/10.1039/C5LC01232E.

[235] S.H. Han, S.-R. Kwon, S. Baek, T.-D. Chung, Ionic circuits powered by reverse electrodialysis for an ultimate iontronic system, Sci. Rep. 7 (1) (2017) 14068.

[236] S.Y. Yeon, J. Yun, S.-h. Yoon, D. Lee, W. Jang, S.H. Han, C.M. Kang, T.D. Chung, A miniaturized solid salt reverse electrodialysis battery: A durable and fully ionic power source, Chem. Sci. 9 (42) (2018) 8071–8076, http://dx.doi.org/10.1039/C8SC02954G.

[237] Z.-H. Lin, W.-S. Hsu, A. Preet, L.-H. Yeh, Y.-H. Chen, Y.-P. Pao, S.-F. Lin, S. Lee, J.-C. Fan, L. Wang, Y.-P. Chiu, B.-S. Yip, T.-E. Lin, Ingestible polysaccharide battery coupled with a self-charging nanogenerator for controllable disinfection system, Nano Energy 79 (2021) 105440, http://dx.doi.org/10.1016/j.nanoen.2020.105440.

[238] M. Tepermeister, N. Bosnjak, J. Dai, X. Zhang, S.M. Kielar, Z. Wang, Z. Tian, J. Suntivich, M.N. Silberstein, Soft ionics: Governing physics and state of technologies, Front. Phys. (2022) 453.

[239] K. Tybrandt, K.C. Larsson, A. Richter-Dahlfors, M. Berggren, Ion bipolar junction transistors, Proc. Natl. Acad. Sci. 107 (22) (2010) 9929–9932, http://dx.doi.org/10.1073/pnas.0913911107.

[240] P. Janson, E.O. Gabrielsson, K.J. Lee, M. Berggren, D.T. Simon, An ionic capacitor for integrated iontronic circuits, Adv. Mater. Technol. 4 (4) (2019) 1800494, http://dx.doi.org/10.1002/admt.201800494.

[241] E. Pakkaner, J.L. Orton, C.G. Campbell, J.A. Hestekin, C.N. Hestekin, Development of an integrated salt cartridge-reverse electrodialysis (red) device to increase electrolyte concentrations to biomedical devices, Membranes 12 (10) (2022) 990, http://dx.doi.org/10.3390/membranes12100990.

[242] M. Zhu, O.G. Schmidt, Tiny robots and sensors need tiny batteries — Here's How to Do It, Nature 589 (7841) (2021) 195–197, http://dx.doi.org/10.1038/d41586-021-00021-2.

[243] A. Heller, Potentially implantable miniature batteries, Anal. Bioanal. Chem. 385 (3) (2006) 469–473, http://dx.doi.org/10.1007/s00216-006-0326-4.

[244] Z. Lin, Y. Wu, Q. He, C. Sun, E. Fan, Z. Zhou, M. Liu, W. Wei, J. Yang, An airtight-cavity-structural triboelectric nanogenerator-based insole for high performance biomechanical energy harvesting, Nanoscale 11 (14) (2019) 6802–6809.

[245] H.-K. Chang, E. Choi, J. Park, Based energy harvesting from salinity gradients, Lab Chip 16 (4) (2016) 700–708.

[246] Y. Liu, C. Hu, Triboelectric nanogenerators based on elastic electrodes, Nanoscale 12 (39) (2020) 20118–20130.
[247] Z. Li, Q. Zheng, Z.L. Wang, Z. Li, Nanogenerator-based self-powered sensors for wearable and implantable electronics, Research 2020 (2020).
[248] J. Gao, W. Guo, D. Feng, H. Wang, D. Zhao, L. Jiang, High-performance ionic diode membrane for salinity gradient power generation, J. Am. Chem. Soc. 136 (35) (2014) 12265–12272, http://dx.doi.org/10.1021/ja503692z, arXiv:https://doi.org/10.1021/ja503692z, PMID: 25137214.
[249] D.B. Deutz, J.-A. Pascoe, B. Schelen, S. Van Der Zwaag, D.M. De Leeuw, P. Groen, Analysis and experimental validation of the figure of merit for piezoelectric energy harvesters, Mater. Horiz. 5 (3) (2018) 444–453.
[250] T. Zhang, T. Yang, M. Zhang, C.R. Bowen, Y. Yang, Recent progress in hybridized nanogenerators for energy scavenging, Iscience 23 (11) (2020) 101689.
[251] C. Lagomarsini, C. Jean-Mistral, G. Lombardi, A. Sylvestre, Hybrid piezoelectric–electrostatic generators for wearable energy harvesting applications, Smart Mater. Struct. 28 (3) (2019) 035003.
[252] X.-S. Zhang, M. Han, B. Kim, J.-F. Bao, J. Brugger, H. Zhang, All-in-one self-powered flexible microsystems based on triboelectric nanogenerators, Nano Energy 47 (2018) 410–426.

Nan Wu received her bachelor's degree and master's degree from Beihang University. She received her general engineering degree from Ecole Centrale de Lyon. She currently holds a position as a Ph. D candidate at the laboratory of Matériaux Innovants pour l'Energie (MIE) in ESPCI-Paris at Paris Sciences & Lettres University (PSL). Her research focuses on developing innovative and efficient blue energy harvesting systems, especially enhancing energy harvesting efficiency of capacitive reverse electrodialysis systems. Her research interests include energy harvesting systems, capacitive reverse electrodialysis and capacitive electrodes.

Timothée Derkenne received bachelor's degree and master's degree from École Normale Supérieure de Rennes. He also received a master degree in microfluidics in the Institut Pierre Gilles de Gennes for microfluidics. He currently holds a position as a Ph. D candidate at the laboratory of Matériaux Innovants pour l'Energie (MIE) in ESPCI-Paris at Paris Sciences & Lettres University (PSL). His research focuses on transport phenomena in nanoporous materials coupled to fluid dynamics and interfaces, applied to osmotic flow for Blue Energy.

Corentin Tregouet is lecturer in the lab of Matériaux Innovants pour l'Energie (MIE) in ESPCI Paris PSL. He graduated from École Polytechnique in 2013 and defended his Ph.D. on chemical physics in ESPCI Paris - PSL in 2016 about the interfacial rheology of microcapsules. His research focuses on transport phenomena coupled to fluid dynamics and interfaces, applied to foam and emulsion dynamics, interfacial rheology, and ionic transport in membranes.

Annie Colin is a professor at ESPCI Paris PSL and director of the Institut Pierre Gilles de Gennes. She is internationally recognized for her original contributions in the field of soft matter, rheology, materials for energy and microfluidics through her 160 papers and 15 patents.

A.3 A Strategy for power density amelioration of capacitive reverse electrodialysis systems with a single membrane

Nan Wu, Youcef Brahmi, and Annie Colin. A Strategy for Power Density Amelioration of Capacitive Reverse Electrodialysis Systems with a Single Membrane. Environmental Science & Technology, 57(40):14973–14982, 2023.

In this appendix, we present the research article published on the boosting strategy for power density performance amelioration of CRED system. It refers to the Chapter 2 of this thesis manuscript.

Environmental Science & Technology
pubs.acs.org/est
Article

A Strategy for Power Density Amelioration of Capacitive Reverse Electrodialysis Systems with a Single Membrane

Nan Wu,[†] Youcef Brahmi,[†] and Annie Colin*

Cite This: *Environ. Sci. Technol.* 2023, 57, 14973−14982

ABSTRACT: Blue energy refers to the osmotic energy released while combining solutions of different salinity. Recently, single-membrane-based capacitive reverse electrodialysis cells were developed for blue energy harvesting. The performance of these cells is limited by the low ion-electron flux transfer efficiency of the capacitive electrodes in the current operating regimes. To optimize it, we point out an original boosting strategy of using a secondary voltage source E_0 placed in series with the capacitive concentration cell. The net recovered power is defined as the difference between the power dissipated in the load resistor and the power supplied by the secondary voltage. Experimental results indicate a maximum power density of 5.26 $\text{W}\cdot\text{m}^{-2}$ (where the salinity difference is 0.17 and 5.13 M), which corresponds to a 59.8% increase compared with its power density of 3.29 $\text{W}\cdot\text{m}^{-2}$ without boosting strategy. A good agreement on power density is reached for theoretical simulations and experimental results. Influential factors are systematically studied to further reveal the boosting strategy.

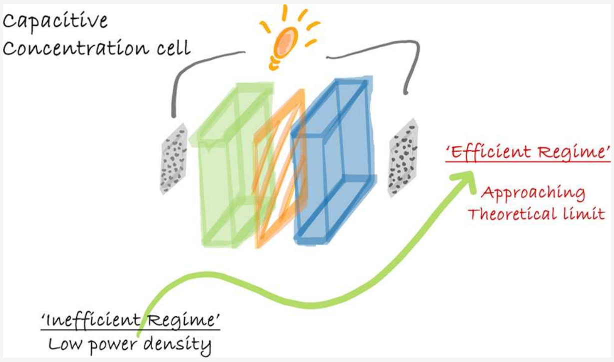

KEYWORDS: *Renewable energy from oceans, Osmotic energy, Capacitive device with a single membrane*

■ INTRODUCTION

Facing the worldwide environmental problems and the threat of long-term climate change, people call for an effective energy transition toward alternative and renewable energy resources.[1−3] According to a report by the think tank Ember[4] released in March 2022, solar and wind have crossed 10% of the global electricity share. Despite their strong growth, diversifying renewable energy sources remains a challenge. In this context, the blue energy released during the mixing of solutions of different salinity is a promising avenue to explore.[5−9] Considering the suitability, sustainability, and reliability of the exploitation, the blue energy power is estimated as 700 kWh/year, which corresponds to 2.5% share of global electricity consumption in 2021.[10]

Proposed by Pattle in the early 1950s,[11] Reverse Electro-Dialysis (RED) is one of the most promising techniques for blue energy harvesting.[12,13] RED devices recover the Donnan potential appeared across ion exchange membranes placed between solutions of different salinities.[14,15] Under an osmotic effect, ions migrate from concentrated solutions to diluted solutions.[7,16] With the membranes being selective, an ionic flux is established.[17] In a standard RED configuration, the conversion of ionic flux toward electronic flux is realized by Faradaic electrodes with redox reactions.[18] The maximal gross power density produced under Faradaic conversion (i.e., the power density neglecting the viscous losses due to pumping, the overvoltages at the electrodes, and the process efficiency) is given by $P_{\max}=\frac{E_{\text{OCV}}^2}{4SR_{\text{cell}}}$, where E_{OCV} is the open-circuit voltage, R_{cell} is the inner resistance of the cell, and S is the membrane surface.

To reduce the cost of the device, Vermaas et al. proposed to use capacitive electrodes in reverse electrodialysis systems (CRED).[19] Carbon-based capacitive electrodes eliminate the loss due to overpotential at the faradaic electrodes and are less expensive than conventional faradaic systems.[20,21] Their use eliminates oxidation−reduction reactions at the electrodes and provides a more sustainable, environmental-friendly, and economical approach.[22,23] In this spirit, Zhu et al.[24] developed capacitive concentration cells with a single selective membrane. They obtained an average power density of 0.95 $\text{W}\cdot\text{m}^{-2}$ for a salt concentration of 0.017 and 0.513 M for fresh water and salt water, respectively. These results are impressive compared with Capmixing devices (less than 400 $\text{mW}\cdot\text{m}^{-2}$)[23,25] and are

Received: July 24, 2023
Revised: September 17, 2023
Accepted: September 19, 2023
Published: September 28, 2023

https://doi.org/10.1021/acs.est.3c05835

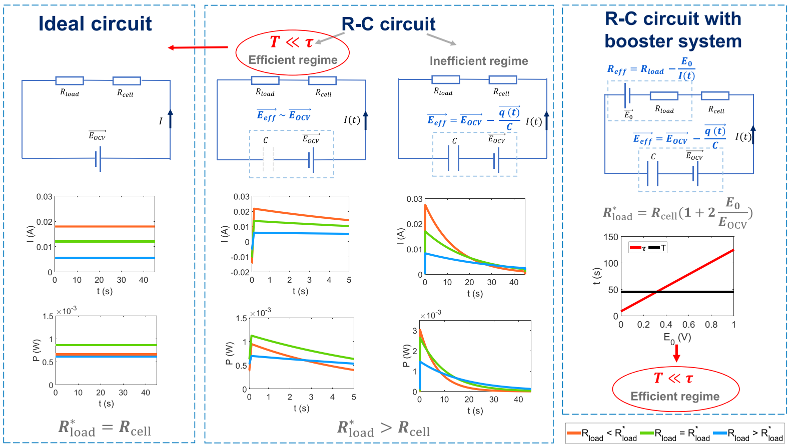

Figure 1. Theoretical analysis of power density performance for the ideal circuit, R-C circuit, and R-C circuit with a booster system, respectively. We illustrate the electrical current curve and power curve within the fixed period T for each case. The power performance loss is due to the current decay in R-C circuits, which fails to satisfy the condition $T \ll \tau$ in the "inefficient regime". The use of an additional booster system enlarges the time window and shifts the working regime toward "efficient regime".

comparable to the results obtained in the RED experiments under the same salinities.[26]

Using the same approach, we developed earlier a novel cell design composed of a single selective membrane and two inexpensive capacitive electrodes.[27] A net power density output of 2 W·m^{-2} was reported, with a salinity ratio of 300 (0.017 and 5.13 M). However, it is worth noting that the power density performance of such capacitive systems remains 60 to 70% below the maximum theoretical value P_{max}. This phenomenon is due to the capacitive response of the electrodes. It seems thus essential to optimize the collection of the ionic current and its transformation into an electric current for capacitive electrodes. In this work, we provide a novel boosting strategy of using a secondary voltage source to promote the power density performance of capacitive concentration cells. A maximum power density of 5.26 W·m^{-2} is achieved in this work, which corresponds to an increase of 59.8% of its performance without booster. The power density obtained under the boosting strategy approaches the theoretical value of an ideal cell $P_{max} = \frac{E^2_{OCV}}{4SR_{cell}}$. This novel path would accelerate the maturity process of capacitive concentration cell systems. The article is as follows. We recall first the working principle of the capacitive concentration cell and its power density performance measurements. Based on this capacitive cell, we present our boosting strategy and explain why the use of a secondary voltage will increase the efficiency of capacitive electrodes. Experiments and modeling are then displayed to confirm our proposal.

CAPACITIVE CONCENTRATION CELL: WORKING PRINCIPLE AND OUTPUT POWER

The general principle of the capacitive concentration cell with a single membrane is illustrated in Supporting Information (see section S1) and has been described at length by Brahmi et al.[27] A cationic ion-exchange membrane (CEM) is placed in the middle of the cell between two compartments of different salinity. This membrane allows the passage of cations and blocks the anions and water molecules.[28,29] Thanks to this selectivity, an electrical potential difference appears between these two solutions of different salinity. In open-circuit cases, the cell voltage E_{OCV} is the sum of Donnan potential E_{mem} and electrode potential E_{elec}. E_{elec} results from the ion adsorption on the electrodes and depends upon the value of the local salt concentration.When the circuit is closed, due to the potential drop, an electric current circulates. The presence of capacitance causes the electric current to decay over time. The produced electric current stops when the capacitor is fully charged. At this stage, the potential difference across its terminals balances the membrane potential E_{mem} and the potential created by the adsorbed layers E_{elec}. It is then necessary to switch the fresh water and salt water supplies in order to reverse the membrane and electrode potential to unblock the electricity production. This generates an electric current in the opposite direction.

Based on electrochemical characterizations (Open-circuit voltage OCV measurement and chronopotentiometry CP studies, Supporting Information), it is possible to measure the open-circuit voltage E_{OCV}, cell inner resistance R_{cell}, and its capacitance C and establish an equivalent R-C circuit for this capacitive concentration cell (Figure S2 (B), Supporting Information). To measure the power density output of the cell system, a resistor is directly connected to electrodes in order to close the circuit. The power density output P_{nb} of the cell in a complete switching period is defined as follows:$P_{nb} = \frac{1}{S0.2T} \times \int_0^{2T} \frac{E_{load}(t)^2}{R_{load}} dt$. S refers to the effective surface of the ion-selective membrane; T is the half period of the salt concentration signal.

As illustrated in Figure 1, an ideal battery is featured by an electromotive force equal to E_{OCV}, an internal resistance R_{cell}, and ideal electrodes with no overpotential and no resistance. While enclosed by a load resistance R_{load}, such a system delivers a maximum power of $\frac{E^2_{OCV}}{4R_{cell}}$ in the situation of $R_{cell} = R_{load}$. Indeed, we're looking to supply power to the load resistance and not to the internal resistance, which means that we must have $R_{cell} < R_{load}$. In the situation where the electrodes are ideal (faradaic without overvoltage and no resistance), the current intensity is constant, as described by the following equation: $I = \frac{E_{ocv}}{R_{load} + R_{cell}}$. It is therefore the maximum for the smallest R_{load}. Combining both conditions leads to $R^*_{load} = R_{cell}$, where $R_{\rm load}^*$ is the resistance that allows to recover the maximum power $P_{\max}=\frac{E_{\rm ocv}^2}{4R_{\rm cell}}$. While equipped with capacitive electrodes, the concentration cells behave differently. As demonstrated in Figure 1, an additional capacitor is added into the equivalent circuit, forming a typical R-C circuit. In this case, the current intensity $I(t)$ varies upon time. The effective electromotive force $E_{\rm eff}$ equals the difference between the electromotive force of the battery and the potential difference across the capacitor of the capacitive electrode $E_{\rm eff}=E_{\rm ocv}-\frac{q(t)}{C}$. For R-C circuits, the electrical characteristic time $\tau = (R_{\rm cell} + R_{\rm load})C$ represents the time required for the capacitor charging or discharging. It plays an important role in electrical performances of the capacitive concentration cells. For operation time T that is much less than the characteristic time τ, the capacitor does not have sufficient time for charging. Thus, the effective electromotive force $E_{\rm eff}$ remains close to $E_{\rm ocv}$. We name this case an "efficient regime". While the electric capacitor charge remains low in this regime, the current intensity maintains a rather high value close to $I=\frac{E_{\rm OCV}}{R_{\rm load}+R_{\rm cell}}$. The efficient regime reaches the situation of an ideal cell. Thus, the maximum power is obtained when $R_{\rm load}^* = R_{\rm cell}$. The recorded density power at $R_{\rm load}^*$ remains constant with time and equal to $P_{\max}=\frac{E_{\rm OCV}^2}{4R_{\rm cell}}$. For T comparable to or even higher than τ, we can no longer neglect the capacitor charging process. The system behaves in a so-called "inefficient regime". As described by the definition of effective electromotive force, $E_{\rm eff}$, the presence of a capacitor reduces the electromotive force and therefore reduces the power dissipated in the load resistor. In addition, the optimal resistance $R_{\rm load}^*$ is higher than that in the previous case. This is due to the decay of current intensity over time. The previous balance between the voltage divider and electrical current results in an optimal condition of $R_{\rm load}^* = R_{\rm cell}$ for ideal cell performance optimization. For capacitive concentration cells, the load resistor $R_{\rm load}$ has an impact on the electrical characteristic time τ. A higher load resistance could prevent current decay in RC circuits and thus is beneficial for power density amelioration. This additional factor tilts the balance toward a higher optimal load resistance. In summary, $R_{\rm load}^*$ is therefore greater than $R_{\rm cell}$ in the situation of capacitive electrodes. The recorded density power varies with time and is less than $P_{\max}=\frac{E_{\rm OCV}^2}{4R_{\rm cell}}$.

■ BOOSTING STRATEGY

Based on the analysis, it is clear that capacitive systems present systematic lower power density performances compared with ideal cells. The performance gap is due to the capacitive current decay response of a typical R-C circuit. However, it is possible for capacitive systems to behave as ideal cells and reach the maximum theoretical value of $P_{\max}$. The key issue is to ensure the condition $T \ll \tau$, so that the capacitive system operates at an "efficient regime".

For capacitive concentration cells, a trivial way to satisfy the condition is to shorten the switching period T. However, such a method is constrained in practical use. While making a water compartment switch, the saltwater reservoir (freshwater reservoir) will be replaced by freshwater flows (saltwater flows). The uncontrolled mixing procedure will lead to a decreasing energy harvesting efficiency and remains an inevitable dynamic transition. The filling time is given by $\tau_{\rm fill} = \frac{ewL}{Q}$ where Q is the flow rate, w is the cell width, and L is the cell length. To ensure energy harvesting efficiency, it is essential to ensure $\tau_{\rm fill} \ll T$. A fast filling time does not lead to a long constant for discharge but ensures the efficiency of the process by suppressing the period where the electrical potential is not well-defined. This can be achieved by decreasing e and increasing Q. This approach has its limits, as it leads to an increase in viscous losses.[27] On an industrial cell, this constraint can be suppressed by keeping e to 1.4 mm, w to 1 m, and L to 12.5 cm. This results in a filling time of 9 s, which is shorter than the concentration inversion time of 90−100 s. We anticipate that boosting will make it possible to use very long inversion times while maintaining efficient power production.

Another way of increasing the efficiency of capacitive electrodes is to use supercapacitors, i.e., capacitors with very high capacitances.[21,30,31] In this case, the electrical characteristic time τ is prolonged to satisfy the condition $T \ll \tau$. From a practical point of view, to recover maximum power, $T < 2\tau$ is required. Assuming $T = 90$ s and taking $T = 0.1 \times 2\tau$ as a criterion, this leads to a characteristic time of 450 s. For a capacitive cell of 1 m^2, the resistance is estimated at 9.6×10^{-4} Ω. The cell capacitance must be 468 750 F·m^{-2}, i.e., 46.8 F·cm^{-2}. It is difficult to achieve such a high capacitance density in conventional systems.

In this work we present a novel strategy to ensure an efficient regime for capacitive concentration cells. Our boosting strategy consists of connecting the capacitive cell to a secondary source of voltage E_0. In this case, the net power output is defined as the difference between gross power dissipated in the load resistor and the additional power supplied by the secondary source $P_{\rm b\text{-}net} = R_{\rm load}I(t)^2 - E_0 I(t)$, which is equal to the power supplied by the battery minus the power stored in the capacitor and the power dissipated in the internal resistance $E_{\rm OCV}I(t)-\frac{I(t)q(t)}{C}-R_{\rm cell}I(t)^2$. We underline that $P_{\rm b\text{-}net}$ is the net power delivered by the battery, which is effectively produced by the circuit and can be stored. The power consumed by secondary source $E_0 I(t)$ was taken into account and subtracted.

A closer look at the expression of net power $P_{\rm b\text{-}net}$ shows that the secondary electromotive force acts as if it were lowering the effective value of the load resistor (Figure 1). It is thus possible to define an effective load resistance as $R_{\rm eff}= R_{\rm load} - \frac{E_0}{I(t)}$. If the effective load resistance is negative, i.e., $R_{\rm load} < \frac{E_0}{I(t)}$, the power harvested in the load resistance is less than the power given by the secondary source of voltage. The balance of the circuit is negative. If the effective load resistance is positive, i.e., $R_{\rm load} > \frac{E_0}{I(t)}$, the power harvested in the load resistance is higher than the power given by the secondary source of voltage. The balance of the circuit is positive, and a net energy is produced. We produce in the load resistance an energy that is higher than the energy given by the secondary voltage. This situation can be analyzed in more detail by continuing the analogy with classical capacitive electrodes without a secondary voltage. The net power recovered is that which would be recovered by an effective resistance equal to $R_{\rm eff}= R_{\rm load} - \frac{E_0}{I(t)}$ in a circuit made up of a battery with an electromotive force $E_{\rm ocv}$, an internal resistance $R_{\rm cell}$, and an electrical characteristic

(a) Phase 1: $0 < t < T$

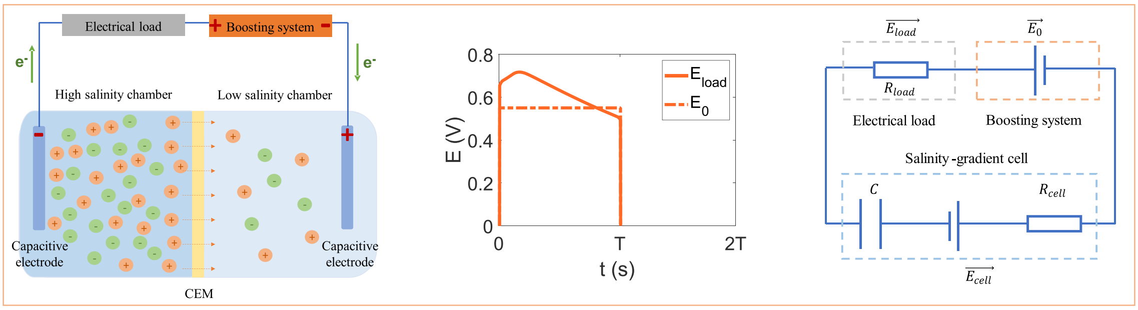

(b) Phase 2: $T < t < 2T$

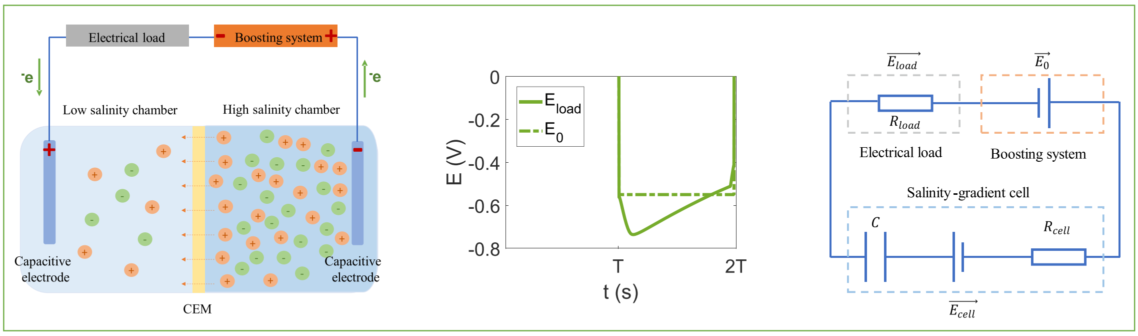

Figure 2. Illustration of the capacitive concentration cell coupled with a booster system in two working phases. (a) Phase 1: $0 < t < T$ and (b) phase 2: $T < t < 2T$. For each phase, we illustrate the temporal measurement of E_{load} and E_0 within a fixed period T. An equivalent circuit is established for each phase based on electrochemical characterizations, respectively.

time equal to $\tau = (R_{\text{load}} + R_{\text{cell}})C$. We're looking to supply power to the effective resistance and not to the internal resistance, which means that we must have $R_{\text{cell}} < R_{\text{eff}}$, i.e., $R_{\text{cell}} + \frac{E_0}{I(t)} < R_{\text{load}}$. This criterion differs from the one in the absence of boosting. It will lead to an increase in the value of the optimal load resistance R^*_{load} and, therefore, to an increase in the characteristic time τ for resistances close to this optimal resistance. The time window governing the efficient regime (i.e., $t < \tau$) is enlarged. In this regime, the intensity is almost constant $I(t) \approx I(0) = \frac{E_0 + E_{\text{OCV}}}{R_{\text{cell}} + R_{\text{eff}}}$. The maximum recovered net power is reached for $R^*_{\text{eff}} = R_{\text{cell}}$, i.e., for $R^*_{\text{load}} = R_{\text{cell}}\left(1 + 2\frac{E_0}{E_{\text{OCV}}}\right)$ and is given by $R_{\text{eff}}I(0)^2 = R_{\text{load}}I(0)^2 - E_0I(0) = \frac{E^2_{\text{OCV}}}{4R_{\text{cell}}}$. For resistances which values are close to the optimal resistance R^*_{load}, the characteristic electrical time τ is close to $2R_{\text{cell}}C\times\left(1 + \frac{E_0}{E_{\text{OCV}}}\right)$. Note that the gross power recovered in the load resistor is $R_{\text{load}}I^2$ and not $R_{\text{eff}}I^2$. $\frac{E^2_{\text{OCV}}}{4R_{\text{cell}}}$ corresponds to the extra power recorded. Although additional energy consumption is required in boosting, due to the efficiency increase, our system not only recovers the additional energy provided by the booster system but also presents higher net power density output. A rigorous calculation is presented in the Supporting Information.

In short, to increase the efficiency of capacitive electrodes, the key issue is to ensure condition $T \ll \tau$. The trivial solution of decreasing the switching period T is restricted by the dynamic filling regime during the water switch. The use of supercapcitors seems quite difficult due to the high capacitance required. To enhance the power density performance, we suggest the use of a secondary source to enlarge the time window and force the capacitive electrodes into the so-called efficient operating regime.

In the following part, we will present the feasibility of using a secondary source for power density enhancement on capacitive concentration cells by experimental results.

RESULTS

Booster System. An alternating voltage power supply (called a booster system) synchronized to the switching period of the cell is placed in series with the cell to promote the power output. The materials and methods are described in the work of Brahmi et al.[27] and in section S2 of the Supporting Information. The electrical potential signal delivered by the power supply corresponds to a rectangular wave with its maximum voltage equal to E_0 and its minimum voltage $-E_0$. As illustrated in Figure 2, the electric potential signal is synchronized in such a way that the signs of E_{load} and E_0 remain the same.

Here, for power density measurement of the cell-booster system, an electrical resistor is directly connected to the cell-booster system to enclose the circuit. A potentiostat is placed in parallel with the resistor for the temporal voltage measurement E_{load}. Therefore, as presented in Figure 2, in a cell-booster system circuit, the voltage applied on the resistor E_{load} remains always the sum of E_0 and E_{cell}.

Thus, the power density directly measured for the resistor is considered as the gross power density $P_{\text{b-gross}}$.

$$P_{\text{b-gross}} = \frac{1}{S.2T}\int_0^{2T}\frac{E_{\text{load}}(t)^2}{R_{\text{load}}}\text{d}t \qquad (1)$$

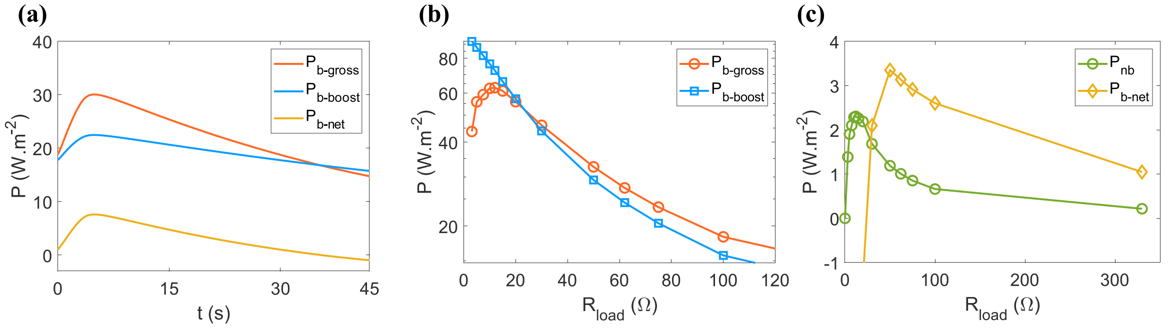

Figure 3. Power density characterization curves for a capacitive cell coupled with a booster system. (a) Power density measurements of $P_{\text{b-gross}}$, $P_{\text{b-boost}}$, and $P_{\text{b-net}}$ as a function of time within a fixed switching period T. Here the load resistance R_{load} is fixed at 75 Ω. (b) Gross power density curve $P_{\text{b-gross}}$ and boosting power density curve $P_{\text{b-boost}}$ as a function of load resistance R_{load}. (c) Net power density curves as a function of R_{load} for a capacitive cell with $P_{\text{b-net}}$ and without P_{nb} as a booster system, respectively. The maximum net power density with booster system surpasses that without a booster system. The experimental conditions in (a−c) are as follows: salinity ratio of 30 (fresh water 0.17 M and salted water 5.13 M), flow rate of 10 mL·min^{-1}, switching period of 45 s, CEM of Nafion 117, and the boosting voltage E_0 is set as 550 mV.

We recall that S refers to the effective surface of the ion-selective membrane.

To obtain the net power density, it is necessary to remove the additional input energy provided by the booster system, which is calculated as follows

$$P_{\text{b-boost}} = \frac{1}{S0.2T}\int_0^{2T} E_0(t)I(t)\ \mathrm{d}t \tag{2}$$

where E_0 refers to the boosting voltage applied in the chronoamperometry (CA) mode by the potentiostat. I refers to the measured boosting current of an electrical circuit. Thus, the net power density of the boost-cell system is calculated as follows.

$$\begin{aligned} P_{\text{b-net}}(E_0) &= P_{\text{b-gross}} - P_{\text{b-boost}} \\ &= \frac{1}{S0.2T}\int_0^{2T}\frac{E_{\text{load}}(t)^2}{R_{\text{load}}}\mathrm{d}t - \frac{1}{S0.2T} \\ &\quad \int_0^{2T} E_0(t)I(t)\ \mathrm{d}t \end{aligned} \tag{3}$$

In Figure 3 (a), power density measurement curves of $P_{\text{b-gross}}$, $P_{\text{b-boost}}$, and $P_{\text{b-net}}$ as a function of time are illustrated. To obtain the maximal power density of the cell-booster system, it is important to describe the variations of $P_{\text{b-gross}}$ and $P_{\text{b-boost}}$ as a function of a series of load resistors R_{load}. Figure 3 (b) presents the power density curves as a function of electrical resistances for $P_{\text{b-gross}}$ and $P_{\text{b-boost}}$. It is clear that $P_{\text{b-gross}}$ first presents a sharp increase at lower electrical resistances, then reaches its maximum at an optimal resistance, and starts the declination for higher electrical resistances. However, $P_{\text{b-boost}}$ remains monotonic, decreasing as a function of resistance. According to the definition equation mentioned above, it is possible to calculate the net power density $P_{\text{b-net}}$ received in a cell-booster system circuit.

Figure 3 (c) illustrates the net power density curve as a function of resistance for a cell coupled with a booster system $P_{\text{b-net}}$ and without a booster system P_{nb} in the case where the concentration is fixed at c_{H} = 5.13 M for the salt water compartment and c_{L} = 0.17 M for the fresh water compartment. The water flows are injected at a fixed flow rate of 10 mL·min^{-1} into the cell with a fixed switching period of 45 s. A cell-booster circuit is enclosed with a boosting voltage of 550 mV.

For a cell-booster system, $P_{\text{b-net}}$ remains negative for low resistances. However, it reaches its maximum at a higher optimal resistance and decreases for higher resistances. It is interesting to notice that the maximal power density recorded in the load resistance surprisingly surpasses that of a pure cell system in the situation of a booster cell system. In this example, the capacitive cell coupled with a booster system could reach a maximum power density of 3.35 W·m^{-2}, which corresponds to a 45.4% increase compared with its maximal power density of 2.30 W·m^{-2} without a booster system. These results are in perfect agreement with the explanation given in the previous section.

Modelings. *Theoretical Models.* A theoretical and mathematical model is proposed based on the equivalent circuit of the system to model the curve. Details of the model and its resolution are given in Supporting Information (see section S3). Here we only give the exact modeling framework and assumptions. As presented in the first section, according to an analysis of the electrochemical impedance spectroscopy, an R-C model is proposed as a simplified fitting model for the cell-booster system.[27] The system inner resistance R_{cell} and capacitance C can be quantitatively characterized by chronopotentiometry (CP) measurements using a potentiostat.

As the cell coupled with a booster system serves as an alternating voltage supply, it is modeled as a constant voltage source of an alternating polarity with a fixed switching period $2T$. The equivalent circuits in positive periods and in negative periods are illustrated in Figure 2.

$E_{\text{mem}}(t)$ is the potential drop over the membrane, $E_{\text{elec}}(t)$ is the electrical potential due to the salt adsorption on the electrodes, $E_0(t)$ is the boosting secondary voltage, and $R_{\text{cell}}(t)$ is the resistance of the cell (including the ohmic and non ohmic resistance of the solvent, the membrane, the carbon felt and the current collector). C is the capacitance of the cell. It comes from the capacitances of the two electrodes. As the electrodes are slightly different, they carry different capacitances, C_1 and C_2, respectively. C is given by $\frac{1}{C} = \frac{1}{C_1} + \frac{1}{C_2}$. The temporal variation of $R_{\text{cell}}(t)$, C, $E_{\text{mem}}(t)$, and $E_{\text{elec}}(t)$ are due to the temporal variation of the ion concentration profile including osmotic potential, diffuse layer establishment, cell filling process after water compartment switching, etc. (see Supporting Information). Note that as capacitances are different, the charges they carry are different, and the kinetics of charging are different. As a result, the cell's characteristic

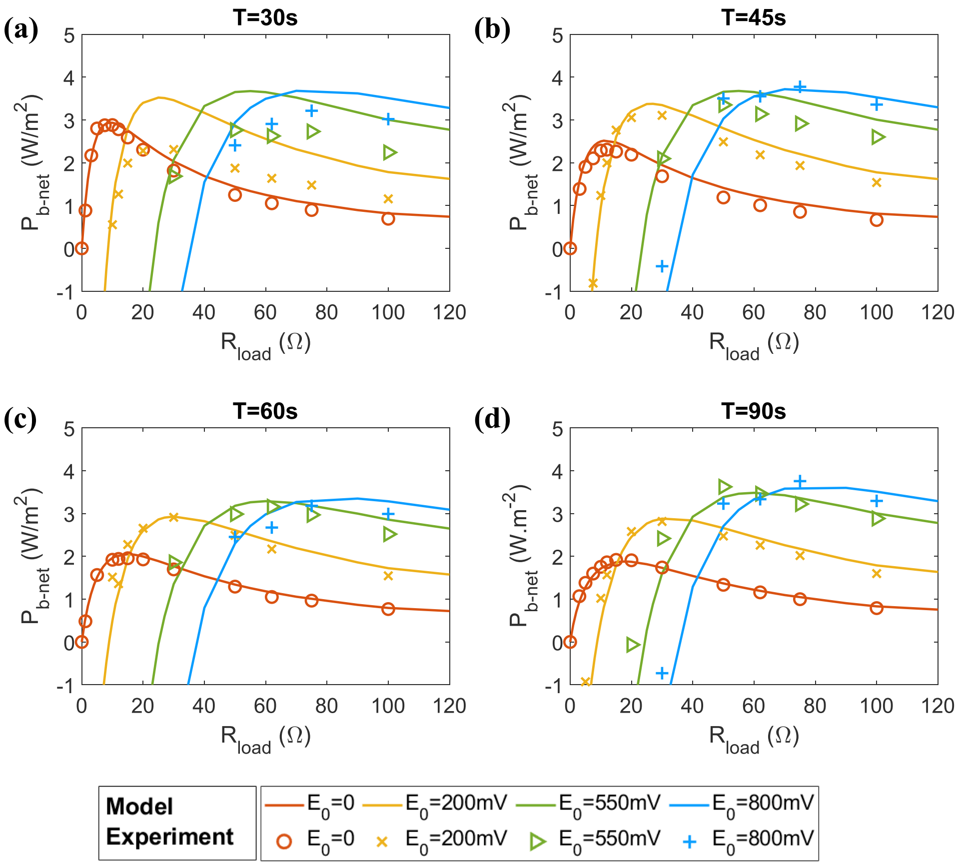

Figure 4. Evolution of the net harvested power density $P_{\text{b-net}}$ as a function of the load resistance R_{load} under a series of boosting voltage E_0. The solid lines correspond to modeling results with fitting parameters fixed at E_{ocv} = 144 mV, R_{cell} = 6 Ω, and C = 1.2 F in the case of (a−c), and E_{ocv} = 148 mV, R_{cell} = 6 Ω, and C = 1.4 F in the case of (d). Experimental dots are presented for various boosting voltages E_0 in the following conditions: salinity gradient of 30 (fresh water concentration 0.17 M, salted water concentration 5.13 M), flow rate of 10 mL·min^{-1}, and CEM of Nafion 117. A quantitative agreement between theoretical and experimental data is found in (b−d) with a switching period T of 45, 60, and 90 s, respectively. An experimental-theory gap is found in (a) with a switching period T of 30 s.

charging time may differ between the two filling phases, as each electrode reacts differently to the change in salinity.

In the following, we will assume that these characteristic times and the filling time of the cell are negligible compared with the switch half period T. Thus, these functions will be modeled simply by window functions: for $0 < t < T$, $E_{\text{mem}}(t) + E_{\text{elec}}(t) = E_{\text{OCV}}$ and for $T < t < 2T$, $E_{\text{mem}}(t) + E_{\text{elec}}(t) = -E_{\text{OCV}}$. In this framework, $R_{\text{cell}}(t)$ does not depend upon t.

For a pure cell-resistor circuit in the absence of boosting, the theoretical equations are written as follows.

For $0 < t < T$:

$$(R_{\text{load}} + R_{\text{cell}})I(t) + \frac{q(t)}{C} = E_{\text{OCV}} \tag{4}$$

For $T < t < 2T$:

$$(R_{\text{load}} + R_{\text{cell}})I(t) + \frac{q(t)}{C} = -E_{\text{OCV}} \tag{5}$$

We apply a secondary voltage in phase with the change of concentrations. Thus, for $0 < t < T$, $E_0(t) = E_0$ and for $T < t < 2T$, $E_0(t) = -E_0$. Thus, while adding a booster system into the circuit, the theoretical equations are written as follows.

For $0 < t < T$:

$$(R_{\text{load}} + R_{\text{cell}})I(t) + \frac{q(t)}{C} = E_{\text{OCV}} + E_0 \tag{6}$$

For $T < t < 2T$:

$$(R_{\text{load}} + R_{\text{cell}})I(t) + \frac{q(t)}{C} = -E_{\text{OCV}} - E_0 \tag{7}$$

Comparison of the Model with the Experimental Data. A comparison of this model with the experimental data in the absence of boosting is displayed in Figure S1 (e) in Supporting Information for various concentration reversal periods (T = 30 s, T = 45 s, T = 60 s, and T = 90 s). A perfect agreement is found for all of the periods, while no fitting parameters are used. The validity of this simple model is based on the assumption that E_{OCV} is a window function and that the cell resistance is constant over time. In our experiments, this is correct because the filling time of the cell, the equilibrium times of the membranes, and the potentials of the adsorbed layers are small compared to the period of concentration inversion T.

In the case of boosting, a model-experiment data comparison of the net power density of the capacitive concentration cell is illustrated in Figure 4. No fitting parameters are used. The calculation is based on characterization of the cell features, including open-circuit voltage E_{OCV},

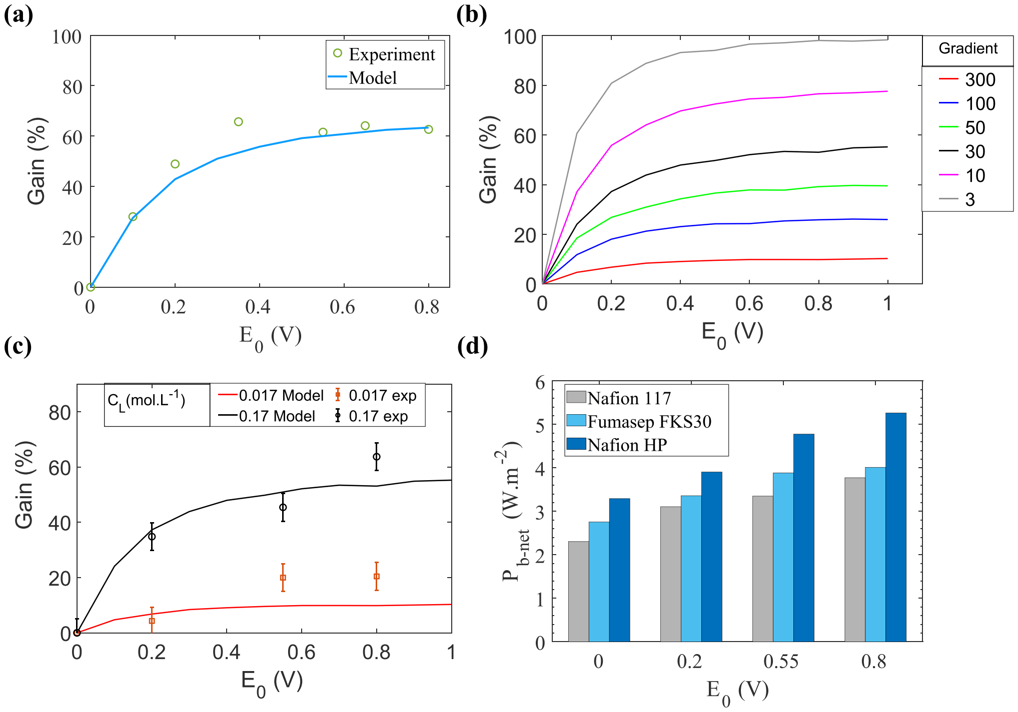

Figure 5. (a) The gain of the harvested power density as a function of the boosting voltage E_0. The experimental conditions are as follows: salinity ratio of 30 (fresh water concentration of 0.17 M and salted water concentration of 5.13 M), flow rate of 10 mL·min^{-1}, switching period of 60 s, and CEM of Nafion 117. (b) Simulation results of gain as a function of the boosting voltage E_0 and the salinity gradient for a fixed concentration of salt solution (5.13 M) and T = 45 s. (c) Impact of the salinity gradient on power density gain for a capacitive salinity-gradient cell coupled with a booster system. The concentration of salt solution and the period are fixed at 5.13 M and 45 s, respectively. (d) Net power density measured for other types of CEMs, including Nafion HP, Nafion 117, and Fumasep FKS-30. The experimental conditions are as follows: salinity ratio of 30 (fresh water concentration of 0.17 M and salted water concentration of 5.13 M), flow rate of 10 mL·min^{-1}, and a switching period T of 45 s.

cell resistance R_{cell}, and cell capacitance C. The solid lines describe the theoretical prediction of the power density profile realized by the model mentioned above, and solid dots represent the experimental data realized in laboratory experiments.

For T higher than or equal to 45 s, experimental results fit well with the theoretical model prediction for various boosting voltages, indicating an excellent theoretical description of the cell-booster system. Note that we did not modify the characteristics of the cell to achieve this agreement. This means that the boosting voltage does not influence the polarization phenomena that occur in the cell in a significant way. We did not have to change the value of the ohmic or nonohmic part of the cell resistance. The maximal power density correlates positively with the boosting voltage. As explained before, each maximal power density is related to an optimal electrical resistance. The optimal resistance value increases as a function of the boosting voltage. Note that the data displayed for T = 90 s in Figure 4 (d) are obtained with a cell displaying different electrical features, i.e., different cell resistance, and a different capacity from the one used in Figure 4 (a−c). It is thus not possible to compare the numerical values between them. However, a quantitative model-experiment agreement is also validated in this case.

For T equal to 30 s, the model does not capture the boosting process, whereas it does in absence of boosting. We believe that these disagreements come from the incomplete modeling. A detailed explanation of this point is available in the discussion part.

Discussions. We now focus on the details of the evolution of the harvested power as a function of several cell parameters. To optimize the power density output of the cell-booster system, a systematic study is carried out in the following to evaluate the impacts of several parameters on the power density output.

Switching Period T. An important influential factor is the switching period T of the cell-booster system. In the presence or absence of boosting, the model predicts that the shortest periods lead to the highest powers. In the absence of boosting, the recovered power decreases as a function of the concentration reversal period in the studied period range, in perfect agreement with the model (see Figure 4). In the case of boosting, the power measured for periods greater than 45 s decreases with the value of the period, as in the case without boosting. The model is in perfect agreement with the data for T = 45, 60, and 90 s. However, the harvested power density is measured to be systematically lower in the case of T = 30 s than for T = 45 s, for all different boosting voltages E_0. In the case of T = 30 s, a power density decrease is even noted for a boosting value of 200 mV compared to a system without booster system (see Figure 4).

The fact that we do not measure a higher power density for a period T = 30 s originates from the neglected processes during model establishment. The filling time of the cell is not taken into account for the modeling. We recall that the filling time is around 2 s. To understand this point, we report in the Supporting Information a numerical model that takes into account the equilibration of cell potentials during mixing by introducing a characteristic time scale for mixing. This numerical analysis shows that the mixing phase affects the process in the presence and absence of boosting and reduces the power recovered. It also shows that the process without boosting is less affected by the mixing phase. In other words, it shows that good agreement can be expected with the simple model without taking mixing into account for $T = 35$ s in the absence of boosting. Periods longer than 50 s are required in the presence of boosting. A detailed explanation is available in Supporting Information section S3.

Boosting Voltage E_0. The boosting voltage E_0 is the additional voltage injected by the booster system. To study its impact on the power density, we measure the power density as a function of electrical resistances for various boosting voltage E_0 at a fixed switching period T. We limit our study to a low boosting voltage (below 1 V) to avoid water hydrolysis.

The gain increases at a low boosting voltage and then saturates. This phenomenon is fully described by the model (see Figure 5 (a)) and comes directly from the electrical equations of the system.

Salinity Gradient. It is interesting to note that the salinity ratio can have two paradoxical effects on the power density output (see Figure 5 (b)). An increase in salinity ratio raises the ionic flux across the membrane induced by the osmotic effect, thus resulting in a higher open-circuit voltage of the cell. As the power density is positively associated with open-circuit voltage in squares, a higher salinity ratio can effectively lead to a higher power output of the system. Meanwhile, the decrease in the salt concentration of the fresh water compartment indicates an electrical resistance increase of the entire cell system, which limits the power output. In the case of a cell-booster system, the simulation prediction indicates that boosting principle is much more efficient for cells with lower electrical resistances (Figure 5 (b)). The gain is higher when the salt concentration is set to 5.13 vs 1.7 M. This simulation is based on the theoretical model explained above and the cell parameters measured by the OCV and CP experiments (Table S1, Supporting Information).

Such a phenomenon is verified by experimental results (see Figure 5 (c)). When the salt concentrations are set to 5.13 M vs 0.17 M, the period at $T = 45$ s and the boosting voltage at 800 mV, the gain can reach 64%, corresponding to a maximum power density of 3.77 $W{\cdot}m^{-2}$. By changing the concentration of the diluted solution to 0.017 M and for the same conditions, this system generated a maximum power density of 4.29 $W{\cdot}m^{-2}$, which corresponds to only 20% increase compared with its maximal power density of 3.53 $W{\cdot}m^{-2}$ without the booster system (Table 1). This can be explained by the fact that, in the second case, the resistance of the cell and the salt ratio are higher than in the first one.

Other Cation-Selective Membranes. The boosting strategy is proven to be applicable to other commercial cationic membranes according to our research results. Here three examples of commercial ion-exchange membranes are presented, including Nafion 117 (Chemours), Nafion HP (Chemours), and Fumasep FKS-30 (Fumatech). The experimental results displayed on Figure 5 (d) are all achieved in the following conditions: salinity ratio of 30 (fresh water concentration of 0.17 M and salted water concentration of 5.13 M), flow rate 10 $mL{\cdot}min^{-1}$, and switching period fixed at 45 s, boosting voltage $E_0 = 0.8$ V.

Table 1. Net Power Density Performances of Capacitive Concentration Cell with Different Commercial CEMs under Boosting Strategy of $E_0 = 0.8$ V

Materials	E_{ocv} (V)	R_{cell} (Ω)	P_{nb} ($W{\cdot}m^{-2}$)	$P_{b\text{-}net}$ ($W{\cdot}m^{-2}$)
Fumasep FKS-30	0.157	6.08	2.75	4.01
Nafion HP	0.158	4.92	3.29	5.26
Nafion 117	0.145	5.4	2.3	3.8

Economical Analysis. In this paper, we propose a novel boosting strategy by using a secondary voltage source in order to enhance the power density output of capacitive RED processes.

This boosting principle is general and applicable to all types of cationic membranes. It remains efficient even at important salt concentrations. It should be noted that the use of this process is relevant for systems with a small number of membranes that must be electronically connected in series. The potential difference to be applied to a system with a high number of membranes could exceed the electrolysis potential of the water, which would be detrimental to the process. It is inevitable to use long switching periods T when scaling up the cell system as a higher filling time is required. Without a booster system, the long switching periods T could easily surpass the characterization time τ. This could become troublesome since the current decays remarkably over time and the average power density decreases significantly with a prolonged switching period. The boosting principle helps to increase the characteristic time τ, which maintains a constant value of current during the switching period for the capacitive systems and leads to a high power density output. To end our analysis, we discuss the economical aspect of this process (see section S4 of the Supporting Information for more details).

The economical analysis of RED unit of 200 kW power realized by Post et al. in 2010 indicates an electricity MWh cost of 104 euros.[32] This figure is in line with current electricity production costs (solar energy 40 €/MWh, wind off shore 120 €/MWh[33]). The calculation includes the cost of membrane, piping, and pumps and a filtration process with a membrane price estimation at 2 €/m^2, which is 500 times over optimistic compared with the price of Nafion membranes at 1000 €/m^2 at the moment. An analysis more in line with reality leads to the introduction of a membrane cost of 10 euros per m^2. This modification induces a production cost of 173 €/ MWh.

In this context, our study allows us to take a small step forward. We were able to produce 5 $W{\cdot}m^{-2}$ with salinity fluids of 300 and 10 $g{\cdot}L^{-1}$. These are not the conditions found at river mouths but, rather, in desalination plants, where solutions are already filtered. In this case, filtration process related costs are eliminated, while boosting related costs, including valves and electronics, are added into economical analysis. Based on the current price and power density performance of two membranes Selemion CMVN (AGC) and Celgard 3401 (Celgard) under boosting strategy, our economical analysis suggests a cost of 5 to 9 times higher than the limits of profitability of 100 €/MWh (Table S2, Supporting Information). They are set to fall as a result of scaleup and market expansion. The development of blue energy techniques requires the discovery of efficient membranes that are selective and avoid mixing. At this stage, the discoveries of recent years give grounds for optimism.[34,35] Sulfonated poly(ether ether ketone) (SPEEK) membranes are of interest.[36−39] These articles claim that they will cost less than 10 € per m^2 and that they are selective. Note that they have not yet been commercialized. Following our analysis, their use will reduce the cost to 81 € per MWh, if their supposed price is maintained.

In the future, we believe that the economic viability of CRED processes depends on innovations that combine different techniques.[40−42] In practical use, we can also imagine the use of a faradaic concentration cell (RED) system as a booster system. To deliver an alternating boosting voltage E_0, a periodic water chamber switch is required. It is then necessary to synchronize the water chamber switching period of capacitive and faradaic systems to apply boosting strategy. Beyond the scope of energy production, CRED with a single membrane could have an important role to play in the storage of renewable energies[43] or in the valorization of CO_2.[44]

■ ASSOCIATED CONTENT

Supporting Information

The Supporting Information is available free of charge at https://pubs.acs.org/doi/10.1021/acs.est.3c05835.

S1 Capacitive concentration cell
S2 Materials and methods
S3 Theoretical models
S4 Economical analysis of boosted capacitive concentration cells (PDF)

■ AUTHOR INFORMATION

Corresponding Author

Annie Colin − *MIE - Chemistry, Biology and Innovation (CBI) UMR8231, ESPCI Paris, CNRS, PSL Research University, Paris 75006, France;* orcid.org/0000-0001-6133-3050; Email: annie.colin@espci.psl.eu

Authors

Nan Wu − *MIE - Chemistry, Biology and Innovation (CBI) UMR8231, ESPCI Paris, CNRS, PSL Research University, Paris 75006, France*

Youcef Brahmi − *MIE - Chemistry, Biology and Innovation (CBI) UMR8231, ESPCI Paris, CNRS, PSL Research University, Paris 75006, France*

Complete contact information is available at: https://pubs.acs.org/10.1021/acs.est.3c05835

Author Contributions

[†]These authors contributed equally to the paper. N.W., Y.B., and A.C. conceived the experiments, N.W. and Y.B conducted the experiment(s), N.W., Y.B., and A.C. analyzed the results. All authors reviewed the manuscript.

Notes

The authors declare no competing financial interest.

■ ACKNOWLEDGMENTS

N.W. acknowledges funding from China Scholarship Council (CSC). Y.B. acknowledges funding from the Institut Pierre-Gilles de Gennes (laboratoire d'excellence PSL). This work has benefited from the technical contribution of the joint service unit CNRS UAR 3750. The authors would like to thank the engineers of this unit (and, in particular, B. Cinquin, A. Jan, K. Phan) for their advice during the development of the experiments.

■ REFERENCES

(1) Chu, S.; Majumdar, A. Opportunities and Challenges for a Sustainable Energy Future. *Nature* **2012**, *488*, 294−303.

(2) Hoffert, M. I.; Caldeira, K.; Benford, G.; Criswell, D. R.; Green, C.; Herzog, H.; Jain, A. K.; Kheshgi, H. S.; Lackner, K. S.; Lewis, J. S.; Lightfoot, H. D.; Manheimer, W.; Mankins, J. C.; Mauel, M. E.; Perkins, L. J.; Schlesinger, M. E.; Volk, T.; Wigley, T. M. L. Advanced Technology Paths to Global Climate Stability: Energy for a Greenhouse Planet. *Science* **2002**, *298*, 981−987.

(3) Norman, R. S. Water Salination: A Source of Energy. *Science* **1974**, *186*, 350−352.

(4) Jones, D. *Global electricity review 2022;* Ember, 2022.

(5) Yip, N. Y.; Brogioli, D.; Hamelers, H. V. M.; Nijmeijer, K. Salinity Gradients for Sustainable Energy: Primer, Progress, and Prospects. *Environ. Sci. Technol.* **2016**, *50*, 12072−12094.

(6) Logan, B. E.; Elimelech, M. Membrane-Based Processes for Sustainable Power Generation Using Water. *Nature* **2012**, *488*, 313−319.

(7) Wu, N.; Brahmi, Y.; Colin, A. Fluidics for Energy Harvesting: From Nano to Milli Scales. *Lab Chip* **2023**, *23*, 1034−1065.

(8) Elimelech, M.; Phillip, W. A. The Future of Seawater Desalination: Energy, Technology, and the Environment. *Science* **2011**, *333*, 712−717.

(9) Marbach, S.; Bocquet, L. Osmosis, from Molecular Insights to Large-Scale Applications. *Chem. Soc. Rev.* **2019**, *48*, 3102−3144.

(10) Alvarez-Silva, O.; Osorio, A. F.; Winter, C. Practical global salinity gradient energy potential. *Renewable and Sustainable Energy Reviews* **2016**, *60*, 1387−1395.

(11) Pattle, R. E. Production of Electric Power by mixing Fresh and Salt Water in the Hydroelectric Pile. *Nature* **1954**, *174*, 660−660.

(12) Yip, N. Y.; Vermaas, D. A.; Nijmeijer, K.; Elimelech, M. Thermodynamic, Energy Efficiency, and Power Density Analysis of Reverse Electrodialysis Power Generation with Natural Salinity Gradients. *Environ. Sci. Technol.* **2014**, *48*, 4925−4936.

(13) Mei, Y.; Tang, C. Y. Recent Developments and Future Perspectives of Reverse Electrodialysis Technology: A Review. *Desalination* **2018**, *425*, 156−174.

(14) Donnan, F. G.; Harris, A. B. CLXXVII.—The Osmotic Pressure and Conductivity of Aqueous Solutions of Congo-Red, and Reversible Membrane Equilibria. *Journal of The Chemical Society, Transactions* **1911**, *99*, 1554−1577.

(15) Donnan, F. G. The Theory of Membrane Equilibria. *Chem. Rev.* **1924**, *1*, 73−90.

(16) Luo, T.; Abdu, S.; Wessling, M. Selectivity of Ion Exchange Membranes: A Review. *J. Membr. Sci.* **2018**, *555*, 429−454.

(17) Aydogan Gokturk, P.; Sujanani, R.; Qian, J.; Wang, Y.; Katz, L. E.; Freeman, B. D.; Crumlin, E. J. The Donnan Potential Revealed. *Nat. Commun.* **2022**, *13*, 5880.

(18) Veerman, J.; Saakes, M.; Metz, S. J.; Harmsen, G. J. Reverse Electrodialysis: Evaluation of Suitable Electrode Systems. *J. Appl. Electrochem.* **2010**, *40*, 1461−1474.

(19) Vermaas, D. A.; Bajracharya, S.; Sales, B. B.; Saakes, M.; Hamelers, B.; Nijmeijer, K. Clean Energy Generation Using Capacitive Electrodes in Reverse Electrodialysis. *Energy Environ. Sci.* **2013**, *6*, 643−651.

(20) Welgemoed, T. J.; Schutte, C. F. Capacitive Deionization Technology^{TM}: An Alternative Desalination Solution. *Desalination* **2005**, *183*, 327−340.

(21) Ratajczak, P.; Suss, M. E.; Kaasik, F.; Béguin, F. Carbon Electrodes for Capacitive Technologies. *Energy Storage Materials* **2019**, *16*, 126−145.

(22) Campione, A.; Cipollina, A.; Toet, E.; Gurreri, L.; Bogle, I. D. L.; Micale, G. Water Desalination by Capacitive Electrodialysis: Experiments and Modelling. *Desalination* **2020**, *473*, 114150.

(23) Kim, T.; Rahimi, M.; Logan, B. E.; Gorski, C. A. Harvesting energy from salinity differences using battery electrodes in a concentration flow cell. *Environ. Sci. Technol.* **2016**, *50*, 9791−9797.

(24) Zhu, H.; Xu, W.; Tan, G.; Whiddon, E.; Wang, Y.; Arges, C. G.; Zhu, X. Carbonized Peat Moss Electrodes for Efficient Salinity Gradient Energy Recovery in a Capacitive Concentration Flow Cell. *Electrochim. Acta* **2019**, *294*, 240−248.

(25) Marino, M.; Misuri, L.; Jiménez, M.; Ahualli, S.; Kozynchenko, O.; Tennison, S.; Bryjak, M.; Brogioli, D. Modification of the surface of activated carbon electrodes for capacitive mixing energy extraction from salinity differences. *J. Colloid Interface Sci.* **2014**, *436*, 146−153.

(26) Vermaas, D. A.; Saakes, M.; Nijmeijer, K. Doubled Power Density from Salinity Gradients at Reduced Intermembrane Distance. *Environ. Sci. Technol.* **2011**, *45*, 7089−7095.

(27) Brahmi, Y.; Colin, A. New Membrane and Electrode Assembly Concept to Improve Salinity Energy Harvesting. *Energy Conversion and Management* **2022**, *254*, 115297.

(28) Fan, H.; Huang, Y.; Yip, N. Y. Advancing Ion-Exchange Membranes to Ion-Selective Membranes: Principles, Status, and Opportunities. *Front. Environ. Sci. Eng.* **2023**, *17*, 25.

(29) Zuo, K.; Wang, K.; DuChanois, R. M.; Fang, Q.; Deemer, E. M.; Huang, X.; Xin, R.; Said, I. A.; He, Z.; Feng, Y.; Shane Walker, W.; Lou, J.; Elimelech, M.; Huang, X.; Li, Q. Selective Membranes in Water and Wastewater Treatment: Role of Advanced Materials. *Mater. Today* **2021**, *50*, 516−532.

(30) Simon, P.; Gogotsi, Y. Materials for Electrochemical Capacitors. *Nat. Mater.* **2008**, *7*, 845−854.

(31) Raza, W.; Ali, F.; Raza, N.; Luo, Y.; Kim, K.-H.; Yang, J.; Kumar, S.; Mehmood, A.; Kwon, E. E. Recent Advancements in Supercapacitor Technology. *Nano Energy* **2018**, *52*, 441−473.

(32) Post, J.; Goeting, C.; Valk, J.; Goinga, S.; Veerman, J.; Hamelers, H.; Hack, P. Towards implementation of reverse electrodialysis for power generation from salinity gradients. *Desalination and water treatment* **2010**, *16*, 182−193.

(33) *Types of Energy Ranked by Cost Per Megawatt Hour - Solar Power Guide - Infographic.* https://solarpower.guide/solar-energy-insights/energy-ranked-by-cost, (accessed: 2023-09-17).

(34) Wu, Q.-Y.; Wang, C.; Wang, R.; Chen, C.; Gao, J.; Dai, J.; Liu, D.; Lin, Z.; Hu, L. Salinity-gradient power generation with ionized wood membranes. *Adv. Energy Mater.* **2020**, *10*, 1902590.

(35) Chen, W.; Xiang, Y.; Kong, X.-Y.; Wen, L. Polymer-based membranes for promoting osmotic energy conversion. *Giant* **2022**, *10*, 100094.

(36) Güler, E.; Elizen, R.; Vermaas, D. A.; Saakes, M.; Nijmeijer, K. Performance-determining membrane properties in reverse electrodialysis. *Journal of membrane science* **2013**, *446*, 266−276.

(37) Sun, C.-Y.; Zhang, H.; Luo, X.-D.; Chen, N. A comparative study of Nafion and sulfonated poly (ether ether ketone) membrane performance for iron-chromium redox flow battery. *Ionics* **2019**, *25*, 4219−4229.

(38) Yuan, Z.; Liang, L.; Dai, Q.; Li, T.; Song, Q.; Zhang, H.; Hou, G.; Li, X. Low-cost hydrocarbon membrane enables commercial-scale flow batteries for long-duration energy storage. *Joule* **2022**, *6*, 884−905.

(39) Chae, S.; Kim, H.; Gi Hong, J.; Jang, J.; Higa, M.; Pishnamazi, M.; Choi, J.-Y.; Chandula Walgama, R.; Bae, C.; Kim, I. S.; Park, J.-S. Clean power generation from salinity gradient using reverse electrodialysis technologies: Recent advances, bottlenecks, and future direction. *Chemical Engineering Journal* **2023**, *452*, 139482.

(40) Simões, C.; Saakes, M.; Brilman, D. Toward Redox-Free Reverse Electrodialysis with Carbon-Based Slurry Electrodes. *Ind. Eng. Chem. Res.* **2023**, *62*, 1665−1675.

(41) Nazemi, M.; Padgett, J.; Hatzell, M. C. Acid/Base Multi-Ion Exchange Membrane-Based Electrolysis System for Water Splitting. *Energy Technology* **2017**, *5*, 1191−1194.

(42) Kim, T.; Logan, B. E.; Gorski, C. A. A pH-Gradient Flow Cell for Converting Waste CO $_2$ into Electricity. *Environmental Science & Technology Letters* **2017**, *4*, 49−53.

(43) van Egmond, W. J.; Saakes, M.; Noor, I.; Porada, S.; Buisman, C. J. N.; Hamelers, H. Performance of an Environmentally Benign Acid Base Flow Battery at High Energy Density. *International Journal of Energy Research* **2018**, *42*, 1524−1535.

(44) Cheng, C.; Wang, S.; Wu, Y.; Bello, I. T.; Dai, Y.; Cheng, R.; Zhai, S.; Wang, Y.; Feng, S.-P.; Ni, M. Thermally Regenerative CO2-Induced pH-Gradient Cell for Waste-to-Energy Conversion. *ACS Energy Letters* **2021**, *6*, 3221−3227.

A.4 Mitigating the Influence of Multivalent Ions on Power Density Performance in a Single-Membrane Capacitive Reverse Electrodialysis Cell

Nan Wu, Michael Levant, Youcef Brahmi, Corentin Tregouet, and Annie Colin. Mitigating the influence of multivalent ions on power density performance in a single-membrane capacitive reverse electrodialysis cell. Scientific Reports, 14(1):16984, 2024.

In this appendix, we present the research article published on the impact of divalent ion mixing on CRED system. It refers to the Chapter 3 of this thesis manuscript.

www.nature.com/scientificreports

scientific reports

OPEN

Mitigating the influence of multivalent ions on power density performance in a single-membrane capacitive reverse electrodialysis cell

Nan Wu[1], Michael Levant[2], Youcef Brahmi[1], Corentin Tregouet[1] & Annie Colin[1]✉

In recent years, the energy generated by the salinity gradient has become a subject of growing interest as a source of renewable energy. One of the most widely used processes is reverse electrodialysis (RED), based on the use of ion exchange membranes and Faradaic electrodes. However, the use of real salt solutions containing mixtures of divalent and monovalent ions in the RED process results in a significant loss of recovered power, compared with salt solutions containing only monovalent ions. From an original point of view, in this work we study and explain the influence of divalent ions and complex solutions in reverse electrodialysis devices equipped with capacitive electrodes with a single membrane (CREDSM). We show that CREDSM mitigates the impact of divalent ions. From a quantitative point of view, the power recovered in a Faradaic cell drops by more than 75% when the solutions contain 50 % molar fraction of divalent ions and by 33 % when the solutions contain 10 % molar fraction of divalent ions. For similar low-cost membranes with fairly low selectivity, recovered power drops by only 34 % when solutions contain 60% moles of divalent ions in CREDSM. We show that only the membrane potential, which makes up half of the cell's open circuit potential, is affected. The potential of capacitive electrodes which counts for half of the potential cell does not decrease in the presence of divalents. For the same membrane under the same conditions, we estimate a loss of 62% in a RED device Furthermore, the membrane is not poisoned by divalent ions because we periodically change the electrical current direction, by means of switching the feed waters. CREDSM devices do not show any variation in membrane resistance or membrane selectivity. The techno-economic analysis suggests further valorization of salinity gradients in industrial operations.

In the face of global environmental challenges and the looming threat of persistent climate change[1,2], there is a growing demand for a decisive shift towards alternative and sustainable energy sources to mitigate these issues[3–5]. Despite the impressive progress of solar and wind energy, the diversification of renewable energy resources remains a complex objective. In this context, the exploitation of blue energy generated by the mixing of solutions with varying salinities presents a promising avenue for exploration[6–8]. Considering factors such as viability, sustainability, and reliability, the potential of blue energy is estimated to generate more than 600 TWh per year[9], which is equivalent to approximately 2.5% of the global electricity consumption in 2021. These promises have led European Commission to recognize blue energy as a renewable energy source for the past 2 years. However, it's worth pointing out that this technology is still confined to research, even if a few industrial pilots have existed, exist or are under construction[10].

Introduced by Pattle in the early 1950s[11] and developed as an energy production method by Loeb[12], Reverse Electrodialysis (RED) stands out as one of the most promising methods for harnessing blue energy[13,14]. RED devices capitalize on the Donnan potential difference across ion exchange membranes positioned between solutions of differing salinities[15,16]. This osmotic phenomenon propels ions to migrate from concentrated to diluted

[1]ESPCI Paris, PSL Research University, MIE-CBI, CNRS UMR 8231, 10, Rue Vauquelin, 75231 Paris Cedex 05, France. [2]Total Energies, PERL - Pôle d'Etudes et de Recherches de Lacq, 64170 Lacq, France. ✉email: annie.colin@espci.psl.eu

solutions[8,17]. By leveraging selective membranes, an ionic flux is established[18]. In a standard RED setup, the conversion of this ionic flux into electronic flux is achieved through Faradaic electrodes that undergo redox reactions[19].

Post et al. reported in 2009 the impact of multivalent ion mixing on energy performance of RED system[20]. They observed a significant stack voltage drop, due to the presence of multivalent ions. The cell potential drops by 20% (from 0.85 V to 0.6 V) when the dilute solution changes from 3 mmol/L sodium chloride to 3 mmol/L sodium chloride and 4 mmol/L magnesium sulphate while the concentrate consisted of 0.45 mol/L sodium chloride and 0.05 mol/L magnesium sulphate is kept constant.

Similarly, Vermaas et al.[1] reported that the introduction of $MgSO_4$ in feed solutions in RED systems led to a reduction in stack voltage, leading to a detrimental power density decrease of more than 50 % in the situation when a molar percentage of 25% or more was accounted for by $MgSO_4$ for both feed water streams. The total salt concentration of the concentrated solution was 0.508 M in all cases,whereas the total salt concentration of the dilute solution was always 0.017 M. The remaining amount of dissolved salt was NaCl. The negative effect due to the presence of multivalent ions is confirmed in various research works[21,22].

To go beyond lab-scale experiments, pilot scale experiments were carried out with real-world solutions. All the works report a significant power performance drop of over 50% due to the presence of multivalent ions[23–25]. Veerman et al.[2] studied a RED module for salinity gradient energy extraction made of 20 membranes pairs of FKS-75 and FAS-75. When only sodium chloride was included in the feed stream of typical composition of 0.5 M for the artificial sea water and 0.02 M for the artificial river water , the harvested power density was equal to 0.743 W m^{-2} of membranes. It decreases to 0.5 W m^{-2} when 0.06 M is added to the more concentrated brine and 0.0024 M to the more dilute one. This corresponds to a power decrease of 33 % when a 10% molar fraction of $MgCl_2$ is added. Using such an approach, Tedesco et al. built a pilot plant with 400 m^2 of low cost membranes (selectivity 0.6) which reaches almost 350 W of gross power capacity using real brine and brackish water[26]. This corresponds to a power density of 0.875 W per m^2 of membranes. Tedesco et al. pointed out a significant power diminution due to the divalent ions presence in seawater. In fact, the produced power is doubled when divalent-free artificial solutions are used[26]. Following the techno-economic analysis of Giacalone et al.[27] with a power density of 0.875 W/m^2 of membranes, we estimate a cost of 1200 € per MWh if the brackish water is filtered. This cost remains high compared to the solar energy (40€ per MWh) and wind energy (120€ per MWh). In fact, one of the major cause of the RED system's high cost relies in the low power density production, which is significantly reduced in real-life feed solution due to the presence of divalent ions, particularly Mg^{2+} and Ca^{2+}. Divalent ions have a negative effect on RED. The second reason why the open circuit potential is lower is that the ratio of the activity coefficients of divalent ions is lower than that of divalent ions. The activity of monovalent ions is generally higher than that of multivalent ions, and this effect is more pronounced in seawater due to the higher ionic strength of the solution.

Four major process are at the origin of this decrease[28]: decrease of the open circuit potential, uphill transportation, increase of the resistance of the membrane, and loss of the selectivity of the membrane. From a thermodynamic point of view, the membrane potential decreases when divalent ions are introduced. Firstly, the membrane potential scales as the valence of the ion at the power minus one. Secondly, the ratio of the activity coefficients of divalent ions is lower than that of divalent ions. Because of the valence of the ion, the electromotive force of the monovalent ions is larger than that of the divalent ions. This causes a reversed transportation of multivalent ions against the concentration gradient called uphill transport. The salinity difference is decreased and the harvested power is lower. Uphill transport of divalent ions Mg^{2+} was evidenced experimentally by Avci et al. using Ion Chromatography analysis conducted on inlet and outlet streams of the RED system[29,30].

Additionally, multivalent ions have larger radii, charges and dehydration energies. Their transport across membranes is slowed down, leading to the trapping of multivalent ions in the membrane due to electrostatic bridging of ionic charges with fixed membrane charges. As a result, the electrical resistance of the membrane increases and selectivity decreases. The decrease in selectivity is aided by another phenomenon. Multivalent ions drag along co ions with the same charge as the membrane, reducing the membrane's selectivity[31]. Fontananova et al. conducted systematic studies to evaluate the common ions as Mg^{2+}, Ca^{2+} and SO_4^{2-}[32]. They identified a strong negative effect of divalent ions on both ionic resistance and permselectivity of ion exchange membranes. Oh et al. confirmed that as divalent ions of small hydrated radius presents higher electrical resistance in CEMs[33]. Gomez-Coma et al. studied experimentally the effect of multivalent ion species on membrane resistance[34]. Other possibilities for reducing membrane fouling and avoiding loss of selectivity are to frequently change the direction of the electric current, for example by applying short electric pulses as reported by Cifuentes-Araya et al.[35] or by changing the feed water as reported by Allison[36].

To diminish the power density drop, the use of monovalent ion selective membranes is proposed and suggested in numerous works[37–39]. However, considering the complexity and the high cost of these membranes, an efficient and cost-effective method is required to mitigate the multi-valent ion impact on RED system performance. The second method is to apply a coating with an opposite fixed charge to that of the membrane but once again the cost is not commensurate with the results obtained[40].

In this article, we study the role of divalent ions in a single-membrane capacitive reverse electrodialysis cell (CREDSM). To the best of our knowledge, this study has never been carried out in such conditions. The originality of our work is to show and explain that the presence of divalent ions in brines affects the performance of CRED-type devices less than RED-type devices. From a quantitative point of view, the power recovered in a Faradaic cell drops by more than 75% when the solutions contain 50% molar fraction of divalent ions (see Figure 7 in Vermaas' work[1]) and by 33% when the solutions contain 10% molar fraction of divalent ions (see the results of Veerman[2]).

For similar low-cost membranes with fairly low selectivity, recovered power drops by only 34% when solutions contain 60% moles of divalent ions in CREDSM-type devices. We propose an explanation for this better performance. According to theoretical and experimental results, we identify uphill effect as the only impact factor for the power loss of CREDSM system in presence of divalent ions. Furthermore, CREDSM cells used with a single membrane have little effect on their cell potential because the cell potential is the sum of the cell potential and the electrode potential. The latter, purely capacitive, is not affected by ions. This point has less impact for a RED cell, which contains several membranes for only two faradic electrodes. The membrane poisoning related issues, including additional membrane voltage drop and cell resistance increase, are suppressed by the reversal of water chambers in CREDSM system. Before concluding, we present a life cycle assessment and techno-economic analysis to gauge the extent of progress needed to transition blue energy into viable renewable energy. Additionally, we examine specific scenarios where RED devices demonstrate effectiveness and commercial viability.

Results

Working principle of a capacitive cell with a single membrane

To enhance cost-effectiveness of RED devices, Vermaas et al. suggested the integration of capacitive electrodes within reverse electrodialysis systems (CRED)[41]. They showed that the power density of CRED is roughly the same when compared to stacks with conventional Ti/Pt electrodes and the $Fe(CN)_6^{3-/4-}$ electrode rinse system.[41]. Equipping a RED cell which contains several membranes with capacitive electrodes does not produce more energy. This substitution obviates oxidation-reduction reactions at the electrodes, yielding a more ecologically friendly and economical approach[42–45].

Following this approach, Zhu et al.[46] pioneered the development of capacitive concentration cells employing a single selective membrane CREDSM. Remarkably, they achieved an average power density of 0.95 W m^{-2} for salinity levels of 0.017 M and 0.513 M in fresh water and salt water, respectively. These results stand in stark contrast to the performance of Capmixing devices (producing less than 400 mW m^{-2})[43,47], and they are comparable to outcomes from RED experiments with faradaic electrodes involving the same salinity gradients[48].

In a similar vein, we have pursued an analogous approach, devising a novel cell configuration comprised of a single selective membrane and two cost-effective capacitive electrodes[49]. This design yielded a net power density output of 2 W m^{-2}, achieved with a salinity ratio of 300 (0.017 M and 5.13 M) and of 5.26 W m^{-2} without boosting strategy[50]. All these results have been obtained in absence of divalent ions.

Let us go deeper in the working principle of these devices. The general principle of the CREDSM is illustrated in Figure 7 (Cell preparation, see Methods). A cationic ion-exchange membrane (CEM) is placed in middle of the cell between two compartments of different salinity. This membrane allows the passage of cations and blocks the anions and water molecules[51,52]. Thanks to this selectivity, an electrical potential difference appears between these two solutions of different salinity. In open-circuit cases, the cell voltage E_{OCV} is the sum of the Donnan potential E_{mem} and of electrode potentials E_{elec}. The Donnan potential is given by the Nernst equation, corrected for the activity of the feed waters and the apparent permselectivity of the non-perfect membrane. It is given by :

$$E_m = \frac{\alpha RT}{z_i F} log \frac{a_{i,1}}{a_{i,2}} \tag{1}$$

where E_m represents the electromotive force across the membrane (in volts, V),R stands for the universal gas constant (8.314 J mol^{-1} K^{-1}), T is the temeperature, z_i represents the valence of the ionic species i (dimensionless), F is the Faraday constant (96,485 C mol^{-1}), and a_i signifies the activity of ionic species i in the feed water (in molarity, M).α is the selectivity of the membrane, $\alpha = 1$ corresponds to a perfect selective membrane. In the situation of a cation exchange membrane, $\alpha = 1$ corresponds to a membrane that allows the free passage of cations but blocks all the anions. The subscripts 1 and 2 indicate the side of the membrane. Equation 1 illustrates that a salinity ratio of monovalent ions (such as Na^+, Cl^-) results in twice the voltage generated by an equivalent salinity ratio of divalent ions (such as Mg^{2+}, $SO_4{}^{2-}$), assuming constant activities and apparent membrane permselectivity.

E_{elec} results from the ion adsorption on the electrodes and depends upon the debye lenght and thus upon the value of the local salt concentration. When the circuit is closed, the potential drop between the two electrodes includes the ohmic ionic dissipation both in the membrane and in the electrolyte, as well as the non-ohmic dissipation in the polarization layers built up around the membrane and the electrode. The closing of the circuit also involves the ohmic potential difference in the load resistance and the capacitive potential jump at the electrodes. The presence of capacitance causes the electric current to decay over time. When the capacitor is fully charged, the potential difference across its terminals balances the membrane potential E_{mem} and the potential created by the adsorbed layers E_{elec}. As a result, the produced electric current stops. It is then necessary to switch the fresh water and salt water supplies in order to reverse the membrane and electrode potential to unblock the electricity production. This generates an electric current in the opposite direction.

Divalent ion mixture influence on cell voltages

We will study a highly selective membrane, Nafion ($Nafion^{TM}$ HP, Chemours). We will then display some data on two others less expensive and less selective commercial membranes, Fumasep ($FUMASEP^{TM}$ FS720, Fumatech) and sPEEK ($FUMASEP^{TM}$ E-620 (K), Fumatech).

In order to perform insight studies of the impact of divalent ion mixing on electrical voltages, we conducted measurements to study separately the membrane voltage E_m and capacitive electrode related voltage E_{OCV-c}. This is realized by open-circuit voltage (OCV) measurements both in capacitive and faradaic cells. In the capacitive situation, E_{OCV-c} is twice the sum of the membrane potential E_m and of the electrode potentials E_{elec-c}. In the faradaic situation, E_{OCV-f} is the sum of the membrane potential E_m and of the Ag/AgCl electrode potentials E_{elec-f}. E_{elec-f} is measured separately in a simple set-up containing two electrodes immersed in two beakers containing solutions of different concentration and linked by a salt bridge. As E_m does not depend upon the nature of the electrode, it is then possible to deduce $E_{elec-c} = E_{OCV-c} - E_m$ from the measurement of the open circuit potential performed on a cell equipped with the membrane and capacitive electrodes. A detailed explanation for the voltage measurement and calculation method is available at Methods section.

We carried out a series of 16 experiments with NaCl solutions mixed with $MgCl_2$ and $CaCl_2$ solutions. The compositions of the different solutions used are given in the Table 7. Compared to solutions with only NaCl, part of the NaCl was replaced by $MgCl_2$ or $CaCl_2$, in order to maintain the molarity of the inflowing feed (and hence the conductivity, to a certain degree) constant. The results obtained concerning different electrical voltages under the influence of divalent ion mixing are displayed in the Table 1, 2 and Figure 1.

Data obtained in the absence of divalent ions are comparable to measurements obtained previously in the literature[49]. In these situations, E_m corrected by measured Ag/AgCl electrode potential are 0.107, 0.074 and 0.05 V for Ra value of 100, 30 and 10 respectively. The membrane potential is given by $E_{mem} = \alpha \frac{RT}{F} ln(\frac{\gamma_H c_H \gamma_H}{\gamma_L c_L \gamma_L})$.$\alpha$ is the selectivity of the membrane, $\alpha = 1$ corresponds to a perfect selective membrane, that allows the free passage of cations but blocks anions. Activity coefficients γ_H, γ_L are obtained with the extended Debye-Hückel equation .

$$log(\gamma) = \frac{-0.51z^2\sqrt(I)}{1 + \frac{A}{305}\sqrt(I)} \tag{2}$$

where I is the ionic strength $I = 0.5\Sigma z_i^2 C_i$ and A stands for the diameter of the hydrated ion (in pm). Some values for A are: Na^+: 450 pm, Mg^{2+}: 800 pm, Ca^{2+}: 600 pm. Based on previous values, the selectivities α are calculated to be 0.99, 0.99 and 0.99 for Ra value of 100, 30 and 10 respectively.

In presence of divalent ions, the membrane voltage decreases compared with solutions composed of pure mono-valent ions, as illustrated in Figure 1. As the molar fraction of divalent ions increases, the membrane voltage shows significant further decrease. For a fixed salinity ratio of 100 (30 or 10, respectively) , the membrane potential decreases from 107 mV to 86 mV (75 mV to 63 mV in the case of ratio 30, and 50 mV to 23 mV in the case of ratio 10, respectively) for a molar fraction of 0.4 of $CaCl_2$ and a total salt concentration of 1.71 mol L^{-1} (0.51 mol L^{-1}, 0.17 mol L^{-1}, respectively). The nature of divalent ions does not change E_m and E_{elec}. There are no major difference between the case of $MgCl_2$ and $CaCl_2$. In presence of $MgCl_2$, the drop of potential is comparable to that in presence of $CaCl_2$. For a NaCl salt fraction of 0.4, Ra=30, the membrane potential is equal to 54 mV in presence of $MgCl_2$ and to 57 mV in presence of $CaCl_2$. We have supplemented this series of measurements with membrane potential measurements when divalents are only present in the dilute solution (see Table 2).

The potential of the electrodes behaves differently (see last column of Table 1). It seems less affected than membrane potential by the presence of divalent ions. It depends little of the amount of divalent added and on the nature of the ions. These results have important implications for cell potential. The cell potential consists the sum of the electrode and membrane contribution. While the molar fraction of NaCl drops from 1 to 0.4, the voltage contribution of membranes E_m shows a significant drop of 19.6%, 27.0% and 54.0% for salinity ratio

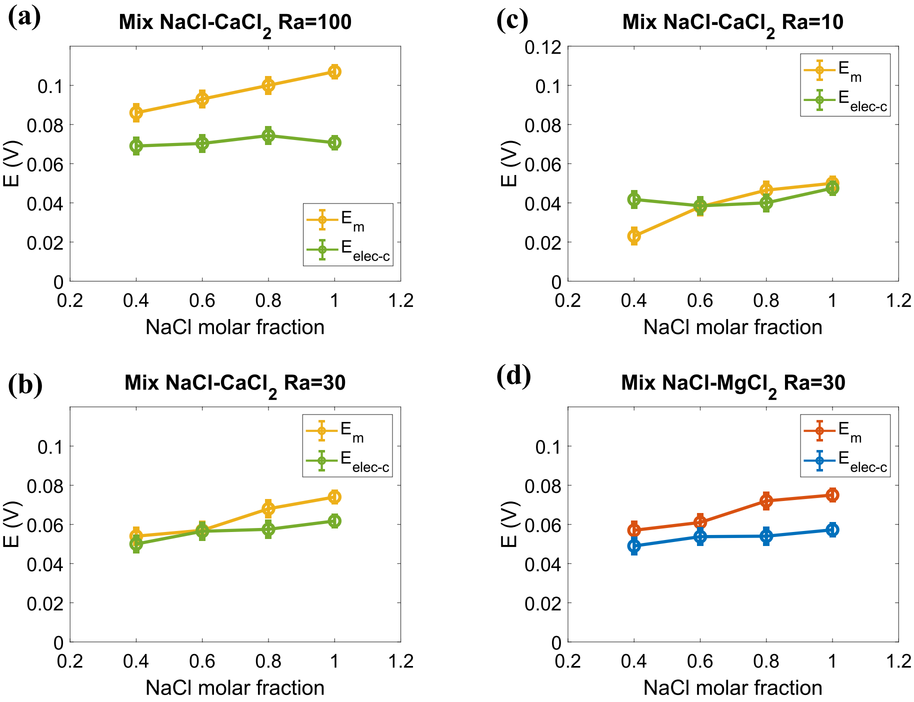

Figure 1. Electrical voltage over membrane E_m and over capacitive electrodes E_{elec-c} as a function of NaCl molar fraction. (**a**), (**b**) and (**c**) represents the variation of voltage of mixing between NaCl and $CaCl_2$ for salinity ratio of 100, 30 and 10, respectively. (**d**) represents the mixing case of NaCl and $MgCl_2$ for a salinity ratio of 30. As molar fraction of divalent ions gets higher, E_m drops significantly while E_{elec-c} remains constant.

NaCl fraction	**$CaCl_2$ fraction**	**Salinity ratio** ***Ra***	**E_{OCV-c} (V)** **$2(E_m + E_{elec-c})$ (V)**	**E_{OCV-f} (V)**	**E_{elec-f} (V)**	**E_m (V)**	**α**	**E_{elec-c} (V)**
1	0	100	0.355	0.203	0.096	0.107	0.99	0.071
0.8	0.2	100	0.349	0.194	0.094	0.100		0.074
0.6	0.4	100	0.327	0.184	0.091	0.093		0.070
0.4	0.6	100	0.310	0.176	0.090	0.086		0.069
1	0	30	0.272	0.151	0.074	0.077	0.99	0.059
0.8	0.2	30	0.251	0.141	0.073	0.068		0.058
0.6	0.4	30	0.227	0.128	0.071	0.057		0.057
0.4	0.6	30	0.209	0.117	0.063	0.054		0.051
1	0	10	0.195	0.101	0.051	0.050	0.98	0.048
0.8	0.2	10	0.173	0.095	0.049	0.047		0.040
0.6	0.4	10	0.153	0.086	0.048	0.038		0.039
0.4	0.6	10	0.130	0.070	0.047	0.023		0.042

Table 1. Electrical voltage measurement split-up table for mixing between NaCl and $CaCl_2$. The electrical voltages measured by experiments consist of open-circuit voltage of a capacitive cell E_{OCV-c} (which corresponds to $2(E_m + E_{elec})$), open-circuit voltage of a faradaic cell E_{OCV-f}, and electrical voltage on faradaic electrodes E_{elec-f}. Based on these measurements, it is possible to deduce the electrical voltage across the membrane E_m and the electrical voltage on capacitive electrodes E_{elec-c}. The measurements are conducted by using solution mixing between NaCl and $CaCl_2$ of different molar fractions (1, 0.8, 0.6 and 0.4 for NaCl molar fraction) for salinity ratios of 10, 30 and 100, respectively. The measurement uncertainties mainly come from the electrode potential contribution in faradaic system E_{elec-f} with a error bar estimated as 1 - 3 mV for different experiment series.

NaCl fraction	**$MgCl_2$ fraction**	**Salinity ratio** ***Ra***	**E_{OCV-c} (V)** **$2(E_m + E_{elec-c})$ (V)**	**E_{OCV-f} (V)**	**E_{elec-f} (V)**	**E_m (V)**	**E_{elec-c} (V)**
Mixing of NaCl–$MgCl_2$ in both solutions							
1	0	30	0.265	0.145	0.070	0.075	0.057
0.8	0.2	30	0.252	0.139	0.067	0.072	0.054
0.6	0.4	30	0.230	0.131	0.070	0.061	0.054
0.4	0.6	30	0.212	0.120	0.065	0.055	0.051
Mixing of NaCl–$MgCl_2$ only in the diluted solution							
1	0	30	–	0.144	0.070	0.074	/
0.8	0.2	30	–	0.142	0.069	0.073	/
0.6	0.4	30	–	0.139	0.069	0.070	/
0.4	0.6	30	–	0.131	0.069	0.062	/
0.2	0.8	30	–	0.120	0.069	0.061	/

Table 2. Electrical voltage measurement split-up table for mixing between NaCl and $MgCl_2$ for a fixed salinity ratio *Ra* of 30. Two scenarios are investigated here: The mixing in both concentrated and diluted solutions, and mixing only in the diluted solution. The measurement uncertainties mainly come from the electrode potential contribution in faradaic system E_{elec-f} with a error bar estimated as 1 - 3 mV for different experiment series.

Ra of 100, 30 and 10, respectively. In the same situations, the voltage contribution of electrodes E_{elec-c} shows a drop of 3%, 16% and 12.4% for salinity ratio *Ra* of 100, 30 and 10, respectively. While the molar fraction of NaCl drops from 1 to 0.4, this induces for a capacitive cell a decrease of the total cell voltage E_{OCV-c} of 12.8%, 23.4%, and 33.6% for salinity ratio *Ra* of 100, 30 and 10, respectively. This decrease is thus much less important than the one occurring for the membrane potential.

We complete this study with some measurements established on less selective membranes. The measured features are displayed on Table 4. The FUMASEP^{TM} FS720 and FUMASEP^{TM} E-620 (K) membrane have a lower initial selectivity than the Nafion membrane respectively 0.87 and 0.74 . When divalents are added, the OCV potential measured in a CREDSM falls by a similar amount to that of the Nafion membrane respectively 26.5 % and 26.4 % compared to 30 %.

To conclude this paragraph, it should be noted that these figures are achieved in a cell where fluxes are permanently exchanged, which is not the case in faradaic cells. We'll come back to this point later.

NaCl-CaCl$_2$				NaCl–MgCl$_2$			
NaCl fraction	CaCl$_2$ fraction	R (Ω cm^2)	C (F cm^{-2})	NaCl fraction	MgCl$_2$ fraction	R (Ω cm^2)	C (F cm^{-2})
1	0	41.2	0.38	1	0	41.2	0.38
0.8	0.2	37.6	0.43	0.8	0.2	34.7	0.44
0.6	0.4	34.06	0.46	0.6	0.4	31.6	0.46
0.4	0.6	31.14	0.47	0.4	0.6	30.8	0.48

Table 3. R-C characterization result table for the capacitive cell system with a fixed salinity ratio of 30 of different divalent ion fraction.

Membrane	Salinity ratio	NaCl fraction	MgCl$_2$ fraction	R(Ω cm^2)	C(F cm^{-2})	E$_m$ (mV)	α
FUMASEP^{TM} FS720	30	1	0	38	0.4	68	0.87
FUMASEP^{TM} FS720	30	0.4	0.6	34	0.42	50	
FUMASEP^{TM} E-620(K)	30	1	0	44	0.375	57.9	0.74
FUMASEP^{TM} E-620(K)	30	0.4	0.6	45	0.38	42.6	

Table 4. Characterization of FUMASEP^{TM} FS720 and FUMASEP^{TM} E-620(K) membrane in presence of divalent ions.

Divalent ion mixture influence on electrochemical properties

In order to characterize changes in cell resistance R_{cell} and cell capacitance C as a function of the nature of the salt solutions, we carried out impedance spectroscopy measurements (see Methods section). As an equivalent R-C circuit can be established for the capacitive cell, for each solution mixture, it is possible to measure the corresponding inner cell resistance and its capacitance by using the Nyquist plot plotted by the PEIS method. Here, by using the impedance result measured at 10 mHz, we characterized R and C for different divalent mixing scenarios. The electrochemical measurement results are illustrated in the Table 3 for two different mixing scenarios: NaCl-CaCl$_2$ and NaCl–MgCl$_2$ with a fixed salinity ratio of 30. It is clear that while the quantity of divalent salts in the mixing is increased, the cell resistance decreases slightly. We believe that this is related to the increase of molar concentration of chloride ions inside the solution. This behavior is also verified by Fumasep-type membranes. We note no increase of the cell resistance in all the cases which suggests that the membrane resistance does not increase much.

Divalent ion mixture influence on energy performance

It is important to characterize the energy performance of the capacitive cell. We will firstly explain the power density characterization method for a simple capacitive cell using pure mono-valent ion based solutions. In general, we connect a load resistor directly to the CREDSM system. We measure the voltage drop on the load resistor $E_{load}(t)$ as a function of time by using the OCV mode in a pontetiostat, as illustrated in Figure 2a. Based on these measurements, it is possible to determine the instantaneous power density output on the load resistor $P(t) = \frac{E_{load}(t)^2}{R_{load}}$, as illustrated in Figure 2b.

The mean gross power density $P_{gross}(t)$, which is the power density without compensating for pumping losses, is a function of time. It is assessed by averaging the signal recorded across the resistance over a time interval of T_s. S denotes the area of the membrane. The expression is as follows:

$$P_{gross}(t) = \frac{1}{T_s \cdot S} \int_t^{T_s+t} \frac{E_{load}^2(u)}{R_{load}} du \tag{3}$$

A priori, $P_{gross}(t)$ depends on time t. In fact, in all our experiments, this power does not depend on time, as shown in the Figure 3b for a few experiments. Figures 2c ,d show the value of stationary power, which is measured from the first cycle.

It's noteworthy that these measurements constitute direct assessments that mirror real-world scenarios. To assess the influence of divalent ion mixing in the capacitive cell, we measure the harvesting power in various salinity gradients with different divalent ion mixing fraction. For each mixing case, the experimental results are presented by dots in Figure 2. The measured power densities show classic variations according to the load resistance. Maximum power recovery decreases from 1.15 W m^{-2} to 0.8 W m^{-2} (respectively 0.75 W m^{-2}) when the CaCl$_2$ (respectively MgCl$_2$) proportion in the brine increases from 0 to 60%. The modeling of the data will be discussed in the following sections.

The same experiments were carried out on the Fumasep (FUMASEP^{TM} FS720, Fumatech) and sPEEK (FUMASEP^{TM} E-620 (K), Fumatech) membranes. The results are shown in Figure 3a, some features are given in Table 4. The addition of divalent causes the maximum power to drop. Note that the power values were measured

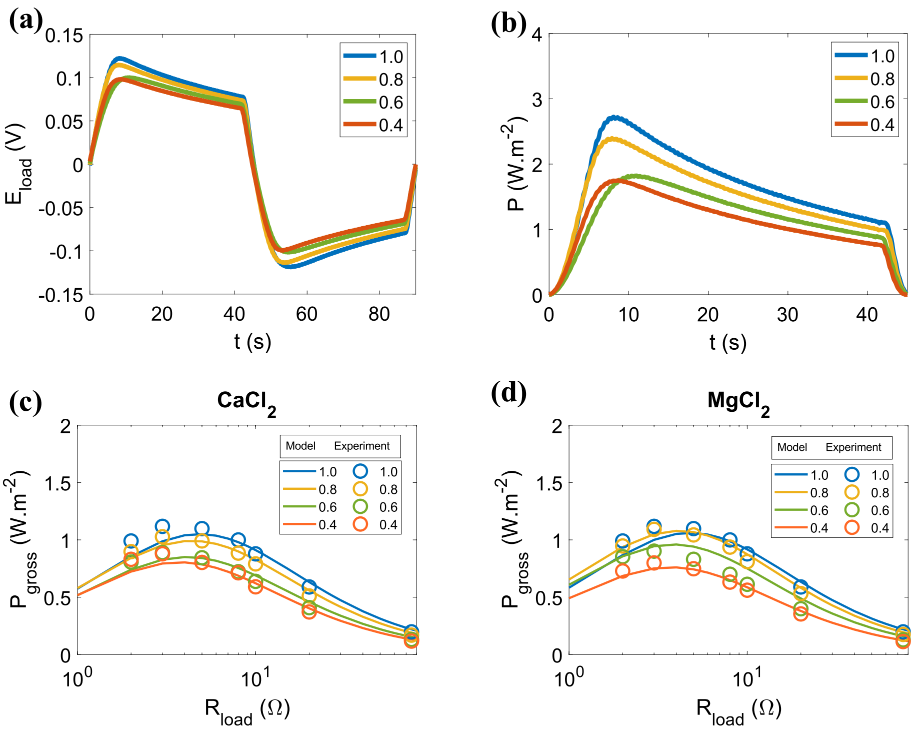

Figure 2. Power density measurement curves. (**a**) Instantaneous voltage measurement as a function of time for a mixing solution of NaCl and $CaCl_2$ of different fractions. A load resistor of 10 Ω is connected to the capacitive cell. The voltage drop on the load resistor E_{load} is measured by a potentiostat. As the solution reversal is realized for a fixed period $T_s = 45$ s, an alternating electrical signal is measured. (**b**) The instantaneous power density P dissipated on the load resistor corresponding to the measurement in (**a**) for a series of mixing fractions. (**c**) The temporal averaged power density P_{gross} as a function of load resistance for divalent ion mixing of NaCl and $CaCl_2$ for a salinity ratio of 30. The solid lines represent the theoretical prediction based on the R-C equivalent circuit. The dots represent the experimental data obtained for a capacitive salinity gradient cell. (**d**) The temporal averaged power density P_{gross} as a function of load resistance for divalent ion mixing of NaCl and $MgCl_2$ for a salinity ratio of 30. The number presented in the legend corresponds to the molar fraction of NaCl.

over 8 hours and no variation was measured over time. The power remains constant, as shown in the figure (see Figure 3b). The modeling of the data will be discussed in the following sections.

Membrane poisoning in Faradaic RED cell

In order to be able to compare the CREDSM and RED devices, it is necessary to carry out new experiments on the membranes we use. The effects of divalents are highly membrane-dependent, and it is not possible to be satisfied with the information available in the literature. To do this, it would be possible to compare the power generated. We have not chosen this approach, however, as it would be complex to construct capacitive cells and Faradaic cells with the same efficiency coefficients, i.e. to recover the same share of the maximum accessible potential. To understand the mechanisms involved, we preferred to focus on how divalent ions modify the intrinsic properties of the membrane.

To probe this more precisely, we close the circuit with the Ag/AgCl electrodes on a resistor which value is closed to R_{cell}. An ionic current passes through the membrane during the experiment. This phase lasts 20 minutes. The current remains constant in the case of the Nafion membrane, drops in the case of the FUMASEP^{TM} FS720 and FUMASEP^{TM} E-620 (K) membranes . We then measure the membrane potential in the Ag/AgCl cell using the OCV measurement. This measurement slightly disturbs the state of the membrane because it requires a reversal of flow. Two flow reversals are used to limit the impact of the measurement on the results. This allows us to calculate membrane selectivity before and after measurement. E_m in presence of divalent varies from 57.9 mV to 56.4 mV in the case of Nafion over 20 minutes, from 50 mV to 42 mV in the situation of FUMASEP^{TM} FS720 and from 42.6 mV to 35 mV in the situation of FUMASEP^{TM} E-620 (K) . We find that the selectivity of the Nafion membrane is unaffected. The selectivity of the FUMASEP^{TM} FS720 membrane decreases by 16% and the one of FUMASEP^{TM} E-620 (K) by 17.8%.

Experiments dealing with real solutions

To complete our study, we designed a series of experiments to test the feasibility of CRED in applications, where complex solution mixtures are used. These imaginary scenarios serve as proxies for some real-life applications, as detailed below, or allow to test some bottlenecks expected in these applications.

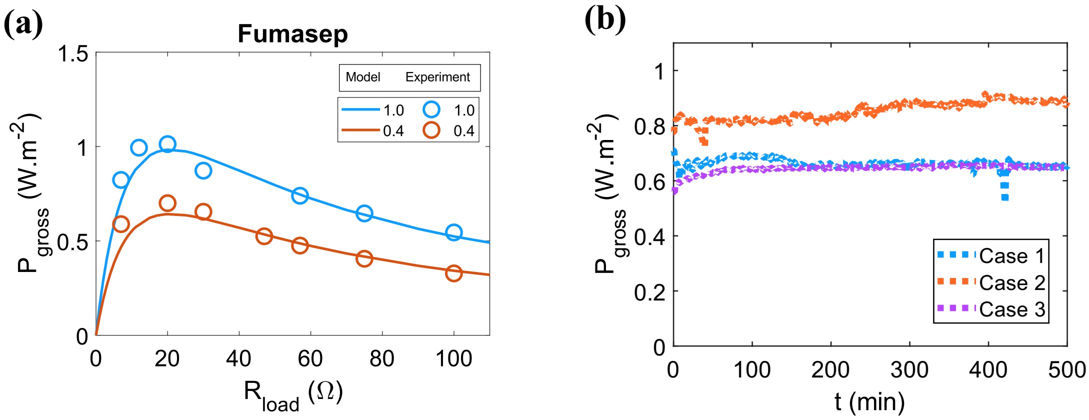

Figure 3. Power density performance characterization. (**a**) The temporal averaged power density P_{gross} as a function of load resistance for artificial NaCl (blue dots) or NaCl (40%) - $CaCl_2$ (60%) mixed solution (red dots) of 30 g L^{-1} vs 1 g L^{-1}. The solid lines represent the theoretical model, the dots represent the experimental results. The result is measured for a CRED system with a FUMASEP^{TM} FS720 membrane with a effective surface of 2.24 cm^2. The figure in the legend refers to the NaCl molar fraction in the mixing. The power density presents a drop of around 30 % in artificial NaCl (40%) - $CaCl_2$ (60%) mixed solution of 30 g L^{-1} vs 1 g L^{-1}. (**b**) Mean gross Power density measurement $P_{gross}(t)$ (see definition Equation 3) of a capacitive salinity gradient cell during an operation duration of 500 min for three different cases. Note that while instantaneous power is a periodic signal due to the capacitive process, power averaged over a period is not. Case 1: the use of artificial NaCl (80%) - $CaCl_2$ (20%) mixed solution with a salinity ratio of 30 g L^{-1} vs 1 g L^{-1}). The membrane used here is Nafion 117 with a load resistor of 10 Ω. Case 2: the use of production water (equivalent NaCl concentration 107 g L^{-1}) with a salinity ratio of 30. The membrane used here is Nafion 117 with a load resistor of 10 Ω. Case 3: the use of artificial NaCl (40%) - $CaCl_2$ (60%) mixed solution with a salinity ratio of 30 g L^{-1} vs 1 g L^{-1}). The membrane used here is FUMASEP^{TM} FS720 with a load resistor of 30 Ω. In all cases, we fix the switching period as T_s = 45s. The power density variation after 10h of operation is within 6%.

In the first scenario (Figure 4a) we consider produced water from an oil well mixing with seawater. Here we used synthetic production water and synthetic seawater prepared in a laboratory from data provided from a field (see composition in[53]). The obtained power density 0.35 W m^{-2} was similar to what what was obtained with NaCl solutions at similarly low salinity ratio of around 4. The amount of osmotic energy is low due to the small difference in salinity. We could conclude that although our results show the feasibility of energy harvesting from production water, unaffected by the presence of divalent ions, advantage of further development of this application is site dependent.

In the second scenario we used real water from the evaporation ponds at the Dead Sea, mixed with the same solution diluted by 30 times (Figure 4b). The extreme salinity conditions of this test could be relevant to projects like the Red sea-Dead sea conveyance, or similar. Remarkably, the high power density of over 2 W m^{-2} indicate the unprecedented feasibility of such application. According to our experimental analysis, the total dissolved salts content in the dead sea solution is on the average 324.9 g L^{-1}. The dominant cation is Mg (62.3 g L^{-1}), followed by Na (32.2 g L^{-1}), Ca (27.5 g L^{-1}) and K (9.3 g L^{-1}). We demonstrated that even in the case where divalent ions (Mg and Ca presenting around 55%) dominate, the measured power density obtained in a capacitive cell is

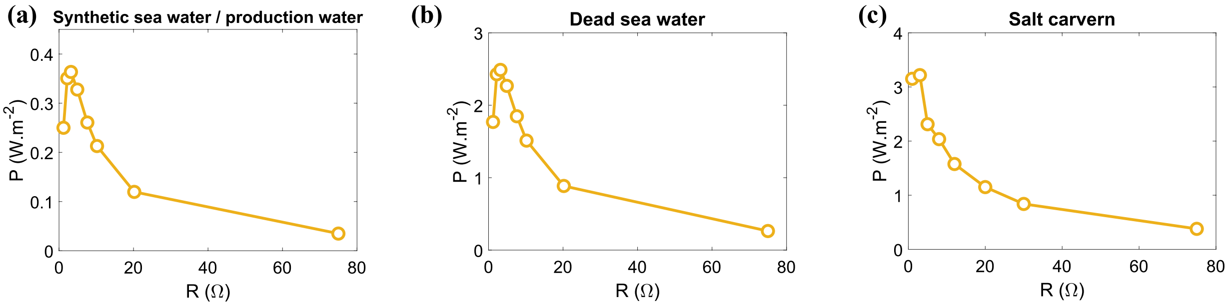

Figure 4. Power density curves for real solutions. (**a**) Power density measurement for the case of synthetic seawater and production water with a salinity ratio of 4. (ESPCI Paris) Power density measurement for the case of Dead sea water with a salinity ratio of 30. (**c**) The case of salt cavern with highly concentrated sea water corresponding to a pure NaCl salt solution of 300 g L^{-1} coupled with an artificial river water. The salinity ratio is 300. All the detailed solution composition is available in the method section. In all cases, the switching period is fixed as T_s = 45 s.

comparable to the value 2.2 W m^{-2} obtained in a pure solution composed of NaCl salts with similar concentration gradients (300 g L^{-1} vs. 10 g L^{-1}) as reported by Wu et al.[50].

In the third scenario (Figure 4c) we imagine creation of salt caverns, either for salt mining or for subsequent hydrogen storage. The caverns are created by dissolution in water, of salinity available on site, injected into the salt deposit. The concentrated solution is therefore saturated brine, mostly composed of NaCl 300 g L^{-1}, and the diluted solution is fresh (used) water or river water, replaced here for simplicity by a 1 g L^{-1} artificial mixture solution of composed of NaCl (40%) and $CaCl_2$ (60%). In this case, a maximum power density of 3.2 W m^{-2} is obtained. The power density shows limited decrease compared with NaCl pure solutions of 300 g L^{-1} and 1 g L^{-1}, which shows a maximum power density of 4 W m^{-2} in the capacitive cell. This scenario also resembles that of a facility constructed between the Great Salt Lake, utilizing water from the lake along with treated wastewater, or a facility situated within the Ettore e Infersa saltworks in Marsala (Trapani, Italy). The Italian location provides freshwater from a coastal well and nearly saturated brine[26,5427].

In our study, the experiments performed with water production and sea water are close to the result obtained with equivalent monovalent ion based solutions as the divalent ions are of low molar fraction (6.7 % in the case of production water and 0.4 % in the case of sea water[53]). For most real sea water solutions, divalent ions are of low molar fraction, as in the example of Mediterranean sea water which contains 3.7% of Mg^{2+} and 1.2% of Ca^{2+} and 33% of Na^{+}[27]). When it comes to Dead Sea water, it is actually dominated by the presence of divalent ions. However, according to our experimental studies, capacitive system presents minor performance decay in this case. We believe that the same results will be obtained when river water containing high levels of divalent ions is taken into account (see Figure 1d). For example, the Amazon river water contains 2.4% of Mg^{2+} and 15% of Ca^{2+} and 3.1% of Na^{+}[27].

We conclude that, within a capacitive cell system, the composition of the brine has a limited impact on performance. We highlight that these performances might be enhanced using an external voltage source[50].

Discussion

To fully understand the mechanisms involved, it is necessary to present a model of the results. The first subsection deals with open-circuit potential measurements. The second subsection of this paragraph deals with power measurements. The last subsection takes advantage of these modelings to explain the measured performances.

Cell open voltage modeling

The preceding measurements show us that divalent ions affect mainly the value of the cell performance of our device and more precisely the open circuit voltage. At this stage, it's important to understand which phenomena induce the drop in potential: is it simply due to the uphill effect where divalent ions migrate into the concentrated compartment as a result of their charge, or is it a phenomenon linked to the variation in membrane selectivity and membrane poisoning? Vermaas et al.[1]has developed a model to quantify the first point, and comparing our data with this model will enable us to answer the question. In their analysis, they propose that the open-circuit equilibrium membrane potential is equal to a potential that cancels out the displacement of divalent ions. This is only possible if a local transfer of matter takes place, inducing a different concentration in the layer of matter near the membrane. More precisely, ion transport across a membrane is a complex phenomenon when monovalent and multivalent ions exist on both sides of an ion exchange membrane. In such situations, ions are exchanged across the membrane to achieve chemical potential equilibrium on both sides. When solutions of NaCl and MgCl are present on either side of a cation exchange membrane (CEM) at varying concentrations but with the same ratio, the electromotive force E_{OCV} resulting from the difference in concentration of Na^{+} is greater than that of Mg^{2+} due to the valence of the ions. We recall that $E_{OCV} = \frac{\alpha RT}{zF} log \frac{a_{i,1}}{a_{i,2}}$. As a result, Mg^{2+} ions are transported from the dilute to the concentrated solution, while twice as many Na^{+} ions move in the opposite direction. This exchange ensures electroneutrality on both sides of the membrane and is described in the literature as uphill transport, corresponding to the movement of Mg^{2+} against the concentration gradient. Using Equation 1 and assuming that the apparent permselectivity is equal for both ionic species, this stationary situation is reached when the ion activities at either side of the membrane obey:

$$\frac{\alpha RT}{z_{Na^{+}}F} log \frac{a_{Na^{+},1}}{a_{Na^{+},2}} = \frac{\alpha RT}{z_{Mg^{2+}}F} log \frac{a_{Mg^{2+},1}}{a_{Mg^{2+},2}} \tag{4}$$

This leads us to :

$$E_m = \frac{\alpha RT}{z_{Na^{+}}F} log \frac{a_{Na^{+},1}}{a_{Na^{+},2}} \tag{5}$$

$$a_{Na^{+},2} = \gamma_{Na^{+},2}(c_{Na^{+},2} + 2J/V_2) \tag{6}$$

$$a_{Na^{+},1} = \gamma_{Na^{+},1}(c_{Na^{+},1} - 2J/V_1) \tag{7}$$

$$\frac{\gamma_{Na^{+},1}(c_{Na^{+},1} - 2J/V_1)}{\gamma_{Na^{+},2}(c_{Na^{+},2} + 2J/V_2)} = (\frac{\gamma_{Mg^{2+},1}(c_{Mg^{2+},1} + J/V_1)}{\gamma_{Mg^{2+},2}(c_{Mg^{2+},2} - J/V_2)})^{(1/2)} \tag{8}$$

J is the molar transport (mol) of Mg^{2+} towards the seawater compartment, and V_1 and V_2 are the volume of the compartments. Activity coefficients in the lower concentration range are obtained with the extended Debye-Hückel equation.

Figure 5 shows a comparison between the model and membrane potential measurements. An excellent agreement is found between measurements and simulation. This agreement shows that the selectivity of the Nafion membrane is not affected when it is used in a capacitive device where the ionic current changes of direction on each half period. In the case of Nafion, no loss of selectivity was neither measured when the ionic current flowed in the same direction for 20 minutes i.e . In all likelihood, Nafion's loss of power is limited to the uphill effect.

In the case of membrane with a poisoning effect as FUMASEP^{TM} FS720, the selectivity is equal to 0.87 in presence of NaCl. The membrane potential drops from 68 to 50 mV in presence of 0.6 Mol $MgCl_2$. This corresponds to a ratio equal to 0.73. The potential of the Nafion membrane drops from 75 mV to 55 mV. This corresponds also to a ratio equal to 0.73. The fact that the two figures are the same shows that the selectivity of the FUMASEP^{TM} FS720 membrane is not affected by the divalent ions in the CREDSM. We recall that no variation of the open potential is measured for more than 8 hours in the CREDSM. It's not the same thing when a direct ionic current flows through the membrane for 20 minutes as in the Faradaic cell. The membrane potential falls to 42 mV, which corresponds to a loss of selectivity of 16%. Same results are obtained with the FUMASEP^{TM} E-620 (K). In the CREDSM the membrane potential is equal to 43 mV in presence of divalent ions and to 58 mV in absence of divalent. This corresponds to a ratio 0.74, same figure than previously , suggesting that the permselectivity is not affected by the divalent ions in the CREDSM. In the Faradaic situation the membrane potential falls to 35 mV, which corresponds to a loss of selectivity of 17.8 %.

To conclude this section, the voltage drop in CREDSM is fully explained by the uphill effect model. However, in faradaic RED system, we observe additional contribution of voltage drop related to the selectivity loss in membrane.

Harvested Power Modeling

Another important point is to verify if the measured cell characteristics, including E_m and R_{cell}, are sufficient to explain the recovered power losses. To check this, we will compare the results with a R-C model that we have validated in previous studies when the cell filling time is small compared to the period. Details can be find in the work of Brahmi et al.[49] and in the method section. This modeling predicts that the power is given by:

$$P_{th} = \frac{2}{ST_s}\frac{CE_{OCV}^2 R_{load}}{R_{load}+R_{cell}} tanh(\frac{T_S}{2(R_{load}+R_{cell})C}) \tag{9}$$

The theoretical prediction is presented by solid lines in Figure 2c and d, it does not involve any fitting parameters. It is demonstrated that experimental power density performances are perfectly described by the classical modeling. For each brine solutions, we have used the measured resistance and capacitance values.

Based on the R-C model derived from the equivalent circuit, it is possible to describe the power density performance of CRED based on the electrochemical characteristics obtained, in the situation of both Nafion and FUMASEP^{TM} FS720.

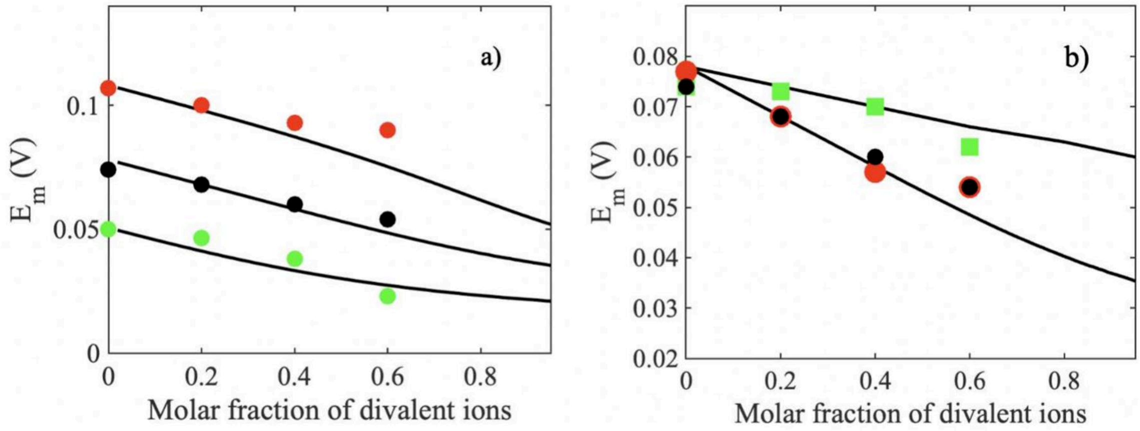

Figure 5. Theoretical interpretation of the membrane voltage E_m decreases as a function of divalent ion molar fraction. (**a**) Theoretical prediction (solid lines) and experimental data (dots) of E_m of different salinity ratio *Ra* of 100, 30 and 10, respectively, for a mixing between NaCl and $CaCl_2$. (**b**) Membrane voltage E_m decrease in two different cases: mixture in both concentrated and diluted solutions, and mixture only in the diluted solution. The feed solution used here is a mixture of NaCl and $MgCl_2$ or NaCl and $CaCl_2$ with a fixed salinity ratio *Ra* of 30. Green squares refer to the case where the $MgCl_2$ is present only in the river water. Black dots refer to the case where NaCl and $MgCl_2$ are present in both feeding solutions. Red dots refer to the case where NaCl and $CaCl_2$ are present in both feeding solutions.

Analysis of our results

The reduction of the harvested power density due to divalent ions is being mitigated when a CRED cell is used. Divalent ions affect the properties of RED devices for two main reasons. The first is the uphill phenomenon, which modifies the membrane potential. This phenomenon is of course common to RED cells with capacitive electrodes and CRED cells. This phenomenon only applies to the membrane potential, not to the electrodes. The CREDSM cells consist only a single membrane and two electrodes. They can be placed in series by repeating this electrode-membrane-electrode unit. In this way, the basic capacitive cell potential is the membrane potential plus the electrode potential. As the latter is not affected by the presence of divalent ions, the potential of a series of single-membrane capacitive cells is less affected than that of a RED cell. The reduction in open-circuit potential is half that of a RED cell. The fact that the impact of divalents is limited in capacitive devices therefore stems primarily not from the capacitances themselves, but from the fact that it is possible to sum the electrode potentials by creating single-membrane cells. It should be remembered that, because of the overpotential on faradaic electrodes, it is not possible to use a single-membrane faradaic cell efficiently. Furthermore, putting faradaic cells in series would raise the problem of high electrode costs and the use of large quantities of toxic electrolytes.

Under these conditions it is possible to calculate the power loss in the presence of divalent ions in the CREDSM and compare it to the RED if there is no loss of membrane selectivity. It should be remembered that the loss of selectivity only occurs on membranes with low selectivity and during a direct ionic current. Assuming that the anionic membrane follows the same trends as the cationic membrane, the open-circuit voltage in a RED device of n membranes equals to $n.E_m$. To simply the calculation, we take the case of a single membrane. The open circuit voltage in a RED device will drop from 107 mV to 86 mV for a salinity ratio of 100, from 77 mV to 54 mV for salinity ratios of 30 and from 50 mV to 23 mV for salinity ratios of 10 when the molar fraction of Na decreases to 0.4. In a CREDSM for salinity ratio Ra of 100, the open circuit voltage will drop from 178 mV to 155 mV for a salinity ratio of 100, from 132 mV to 105 mV for salinity ratios of 30, from 98 mV to 66 mV or salinity ratios of 10 when the molar fraction of Na decreases to 0.4. These figures lead to a decrease of power of 35.4 % for a salinity ratio of 100, of 50.8 % for a salinity ratio of 30, of 78.8 % for salinity ratio of 10 when the molar fraction of Na decreases to 0.4 in a RED device. In comparison, the drop in power in a CREDSM is equal to 24.2 % for a salinity ratio of 100, of 36.7 % for a salinity ratio of 30, of 54.6 % for salinity ratio of 10 when the molar fraction of Na decreases to 0.4. These figures are obtained with the measurement realized by Nafion HP membrane. The results are summarized in Table 5.

The second reason relates to membrane poisoning. Membrane poisoning is influenced by the chemical composition of the membranes. It is relatively rare in Nafion-type membranes but quite common in FUMASEP membranes. This is probably due to the very high surface charge of Nafion membranes, which enables them to avoid poisoning by divalent ions[55]. It leads to a reduction in membrane selectivity, a reduction in electrical potential membrane . The fact that the capacitive process is an alternative process prevents divalent ions from adsorbing permanently to the membrane, which is not the case with continuous processes. The improved properties of CREDSM compared with RED are once again an indirect effect of the alternating flow of the two solutions. It should be noted that this strategy could be applied to RED, as proposed by Vermaas. From a numerical point of view, assuming that the anionic membrane follows the same trends as the cationic membrane, the open circuit voltage in a RED device will drop from 68 mV to 42 mV for a salinity ratio of 30 when the molar fraction of Na decreases to 0.4 along with the selectivity decrease. In a CREDSM for salinity ratio of 30, the open circuit voltage will drop from 125 mV to 101 mV for salinity ratios of 30 when the molar fraction of Na decreases to 0.4. Under these conditions, the power generated by a RED device will fall by 34 % and the power generated by a CREDSM device by 62 %.

The overall underlying mechanism is illustrated in Figure 6.

Life cycle analysis and Techno-economic analysis

Our study shows that capacitive cells can achieve significant power levels compared with the literature when real solutions are used. At this point, it becomes important to ask where blue energy technology stands from an economic and ecological point of view. The current literature can be confusing. Some articles mention the enormous power measured on a single nanotube and extrapolate the enormous power that can be recovered[56], while others write that these techniques will never be marketable and is even not suited for the ecological transition[57,58]. We believe that the situation is halfway between these statements.

Let us first comment on the ecological footprint of the blue energy. A study of the life cycle analysis of our process is outside the scope of this article. However, before making an economic analysis of our process, we would like to remind a few points. Mueller et al.[59] display in 2021 the the first comprehensive life cycle assessment (LCA) of reverse electrodialysis (RED). They conduct a LCA of 1MWh RED plant using natural waters or concentrated brines and compare the results to existing renewable energy technologies, including wind and solar photovoltaics. They studied 9 impact categories: acidification, ecotoxicity eutrophication, global warming, ozone depletion, photochemical oxidation, carcinogenics, non carcinogenics, and respiratory effects. In all the cases, the environmental impacts from RED are found to be comparable to, and sometimes lower than, established renewable energy technologies. The single drawback deals with eutrophication, ecotoxicity, and carcinogenic impacts which are slightly larger for RED than other technologies under the natural water scenario and not the brine one. Processes associated with membrane manufacture are primary contributors to these impact categories. We anticipate that these impacts may be thus decreased by using biosourced membranes such as cellulose membranes in the natural water situation. The authors conclude by saying that RED performs as well as or better than other renewable energy technologies in terms of ecological impact. The footprint is not analyzed in this article, but it is comparable to or better than that of photovoltaic plants. Indeed, despite a power density 30-50 times lower than that of photovoltaic energy, it is possible to produce the same power as a photovoltaic plant on

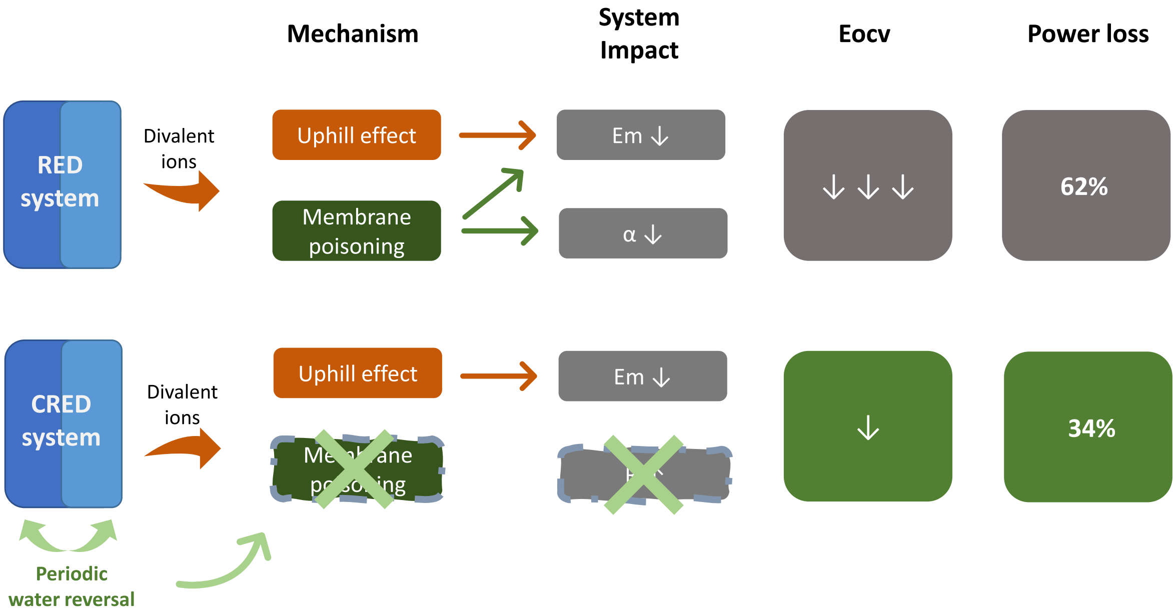

Figure 6. Schematic illustration of the divalent impact mitigation mechanism of CRED system. The diagram summarizes the mechanisms that induce power loss in the presence of divalent ions. In the CREDSM context, only the uphill mechanism affects membrane potential. Electrode potential remains unaffected. This reduces the impact of divalents on the cell potential, which is the sum of the membrane potential and the electrode potential. Flow reversal prevents membrane poisoning. For a molar fraction of 0.6 of $MgCl_2$, this results in a 34% reduction in power. Under the same conditions and for a poorly selective Fumasep-type membrane, membrane poisoning and the cell potential, which is affected twice by the uphill phenomenon, lead to a 62% power density reduction.

		Ratio 10	Ratio 30	Ratio 100
CREDSM	NaCl solution	98 mV	132 mV	178 mV
	NaCl-$CaCl_2$ mixing, fraction 0.4	66 mV	105 mV	155 mV
	Power density drop	54.6%	36.7%	24.2%
RED	NaCl solution	50 mV	77 mV	107 mV
	NaCl-$CaCl_2$ mixing, fraction 0.4	23 mV	54 mV	86 mV
	Power density drop	78.8%	50.8%	35.4%

Table 5. Comparison of power density drop prediction under divalent ion mixing cases of NaCl and $CaCl_2$ for a fraction of 0.4 of NaCl. The voltage values for CRED system corresponds to the open-circuit voltage E_{ocv}. The voltage figures for RED system corresponds to a single membrane voltage E_m, as a simplified case for RED stacks. The calculations are realized for Nafion HP membrane.

smaller surfaces, because RED cells can be stacked on top of each other. Taking into account a thickness of 0.4 mm for two membranes and two liquid compartments (i.e. for the cell repeat pattern) and a density power of 1 W m^{-2}, it is possible to estimate the power of a 1 m × 1 m^2 cell at 5 kW. The basic RED modules will therefore take up 20 times less space than the basic photovoltaic modules, whose density power is estimated at 100 W m^{-2}. Discharges of saltwater solutions are not analyzed in this article, and at this stage there are no studies to show how the fragile ecosystem that makes up an estuary can be affected by withdrawals and discharges of saltwater mixtures. Without getting too far ahead of ourselves in this not-so-simple debate, it is nevertheless important to note that osmotic energy devices mix seawater and river water. It may therefore be possible for the estuary, which does the same, to discharge this water at a point where the salinity is close to that of the mixture. Finally, this impact is less significant when the brine systems studied are industrial brines. In this case, the problem of discharge is already part of the process. All these points are very positive and lead us to ask why RED technology is failing to emerge. One crucial point is the cost. High-performance membranes are expensive membranes. It is important to analyze this point in greater detail and to compare our work with existing results. To do this, we will draw on a techno-economic analyses carried out on RED systems[27,60,61].

Post estimated the cost of a RED device in 2010 for a system producing 200 kW. The calculation includes the costs of construction and membrane (200 000 €), filtration (320 000 €), liquid pumping and maintenance (370 000 €). The fluids pass through the system only once, at a speed 1 $cm.s^{-1}$ comparable to our experiments.

	Post scenario	A scenario	B scenario
Membrane cost (€)	254 000	6 000 000	1 500 000
Piping, fittings and pumps (€)	406 400	406 400	406 400
Valves (€)	0	150000	150000
Filtration (€)	469 900	0	0
Total (€)	1 130 300	6 556 400	2 056 400
Annual Costs (9%) (€)	101 727	590 076	185 076
Total (€)	1 232 027	7 146 476	2 241 476
Net Power (kW)	200	320	320
MWh cost (€)	111	399	125

Table 6. Cost break-down for a membrane reverse electrodialysis unit (membrane surface 100 000 m^2).

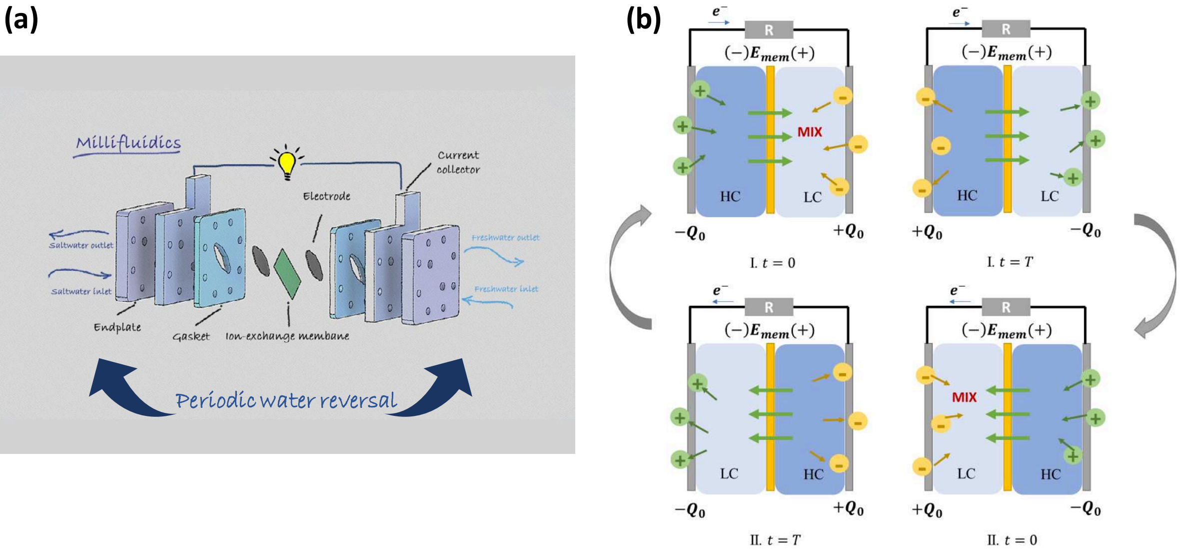

Figure 7. Schematic illustration of the capacitive cell. (**a**) The capacitive system assembly illustration. (**b**) The working principle of the CRED system. The periodic water solution reversal is necessary to ensure the continuous electricity production. The eventual electrical signal delivered by the CRED system will be periodic and alternating.

The calculation takes into account a membrane price of 2 euros per m^2 and a power of 2 W per m^2. Membrane lifetime is 7 years, with production running 8000 hours a year. 9% of the construction and functioning cost are considered to be the exploitation cost over 7 years. Taking inflation into account, this corresponds to a current cost of 1 232 027 euros . This results in a production cost equal to 0.111 € per kWh, i.e. 111 euros per MWh. This figure is in line with current electricity production costs (solar energy 40 € per MWh, wind off shore 120 € per MWh[62]). In this calculation, the price of the membrane is certainly underestimated while the production power is overestimated. More realistically, on the basis of our experimental results, we can envisage several different cases and display two other scenarios in the table. We have measured a power of 3.2 W m^{-2} for a ratio of 300 between a high salinity solution and a fresh water solution in presence of magnesium and calcium. This case mimics that of a plant built between the Great Salt Lake and using water from the lake plus treated wastewater or a plant located in the Ettore e Infersa saltworks in Marsala (Trapani, Italy). The Italian site supplies fresh water from a well on the coast) and almost saturated brine[26,27,54]. These cases are very interesting because all these brines do not require filtration. Algae and microorganisms do not grow in such high salinities and the desalination effluents, treated water effluents or water from a shoreline well are rather clean[54]. We propose an analysis based upon a power density of 3.2 W m^{-2} (equal to our previous measurement) and two cost of membranes.The cost of membrane is difficult to estimate. Post's calculation takes into account a membrane price of 2 euros per m^2 . It's important to note that no membrane currently achieves this cost price. It 's also important to note that the price we pay for a lab scale membrane differs from the commercial price in case of industrialization of the RED process. Because we are interested in real-world greenhouse applications, we will use the commercial price in our cost analysis. Taking into account a lab-scale to commercial cost ratio of Fujifilm membrane equal to 2.8 (based on the lab-scale to commercial cost ratio of the Neosepta membranes), Ahdab et al.[63] propose to use a cost equal to 58 € per m^2 for a Fujifilm membrane. We assume the commercial cost will be same for FUMASEP®FS720

NaCl - CaCl$_2$ solution composition									
	Concentrated solution				Diluted solution				Ratio ;
NaCl	NaCl	NaCl	CaCl$_2$	CaCl$_2$	NaCl	NaCl	CaCl$_2$	CaCl$_2$	Experiment
Molar fraction	g L^{-1}	mol L^{-1}	g L^{-1}	mol L^{-1}	g L^{-1}	mol L^{-1}	g L^{-1}	mol L^{-1}	Number
1	100	1.711	0	0	1	0.017	0	0	100;1
0.8	80	1.369	50.311	0.342	0.8	0.014	0.503	0.003	100;2
0.6	60	1.027	100.623	0.684	0.6	0.010	1.006	0.007	100;3
0.4	40	0.684	150.934	1.027	0.4	0.007	1.509	0.010	100;4
1	30	0.513	0	0	1	0.017	0	0	30;5
0.8	24	0.411	15.093	0.103	0.8	0.014	0.503	0.003	30;6
0.6	18	0.308	30.187	0.205	0.6	0.010	1.006	0.007	30;7
0.4	12	0.205	45.280	0.308	0.4	0.007	1.509	0.010	30;8
1	10	0.171	0	0	1	0.017	0	0	10;9
0.8	8	0.137	5.031	0.034	0.8	0.014	0.503	0.003	10;10
0.6	6	0.103	10.062	0.068	0.6	0.010	1.006	0.007	10;11
0.4	4	0.068	15.093	0.103	0.4	0.007	1.509	0.010	10;12
NaCl - MgCl$_2$ solution composition									
	Concentrated solution				Diluted solution				Ratio ;
NaCl	NaCl	NaCl	MgCl$_2$	MgCl$_2$	NaCl	NaCl	MgCl$_2$	MgCl$_2$	Experiment
Molar fraction	g L^{-1}	mol L^{-1}	g L^{-1}	mol L^{-1}	g L^{-1}	mol L^{-1}	g L^{-1}	mol L^{-1}	Number
1	30	0.513	0	0	1	0.0171	0	0	30;13
0.8	24	0.411	20.872	0.102	0.8	0.014	0.695	0.003	30;14
0.6	18	0.308	41.745	0.205	0.6	0.010	1.389	0.007	30;15
0.4	12	0.205	62.618	0.308	0.4	0.007	2.084	0.010	30;16

Table 7. Brine composition.

membrane. Note that the lab scale price for a FUMASEP®E-620 (K) membranes is 57 € per m^2[64]. We therefore propose a scenario A based on a construction cost of 60 € per m^2 for the membranes in the cell. This cost takes into account the cost of the membrane and the carbon felt.

In another realistic techno-economic analysis, Giacalone et al.[27] consider that the price of highly selected membrane is 15 € per m^2. This price is in line with the recent development of sulfonated poly-ether-ether-ketone, sPEEK membrane. Owing to the low cost of raw material (61.5 € /kg for PEEK polymer), Zhu[65] and Yuan[66] estimate the cost of sPEEK membrane to be as low as 12€ per m^2, which is at least 20 or 30 times lower than that of commercially available Nafion membranes. We will thus propose a B Scenario based over a cost of 15 €per m^{2}for the membrane and the carbon felt. The results are summarized in Table 6.

The viscous loss is estimated at 0.2 W per m^2 of membranes. We have previously measured similar viscous losses in our devices (0.1 W m^{-2}). We thus take into account the same cost of viscous loss and filtration when required. To this figure we need to add the power required to reverse the flows. To estimate the cost of valves additionally used in the capacitive system, we estimate the cost at around 35% of the cost related to piping, fittings and pumps.

This analysis shows that the very salty solutions is economically viable and comparable to other renewable energies 111 € per MWh, if we consider a membrane plus felt price of 15 € per m^2. It remains however high, 399 € per MWh, in the situation where the price of the membrane plus felt equals 60 € per m^2. Note that the obtained values are better than the one predicted following the results of Tedesco[54] and the analysis of Giacalone[27] because the power density is higher (3.2 W m^{-2}), we have considered no filtration and the plant is different as it encompasses 100 000 m^2 of membranes. The main contribution of our work is the fact that we are able to limit the role of the divalent ions. Considering the Dead sea water scenario (a plant built between the Dead sea and a desalination plant[27]) and following the same analysis, the cost will be reaching 200 € per MWh. This was the scenario 2 of our study. Lastly, considering sea water mixed with river water, the harvested power remains slightly higher than 1 W per m^2 and leads to a cost of 400 € per MWh which is too high even in the situation of sPEEK membranes. It will correspond to a cost of 1276 € per MWh for a membrane cost of 60 € per m^2.

Conclusion

In this work, we evaluate the electrochemical characteristics and energy performance of CRED system under the impact of divalent ions. Different from RED systems where significant power density drop is reported, CRED system present limited power density drop . It is demonstrated in different mixing ratios and even real-world solutions that CRED systems are efficient in mitigating the impact of divalent ions. We reveal the underlying mechanism of the minor power density loss of CRED system related to divalent ions. The model-experiment comparison suggests the fact that the open-circuit voltage drop in CRED system can be thoroughly explained by the uphill effect and by the variation of the membrane potential due to thermodynamic considerations (activity of the divalent ions, factor 2 on the Nernst equation). The membrane poisoning issues extensively reported in RED systems, which have a huge impact on membrane selectivity and cell resistance, are not in presence in CRED system. While membrane poisoning occurs within less than in a hour in RED systems, CRED system mitigates the membrane poisoning issues simply by the intrinsic water chamber reversal process in its working regime. This enables a stable power density output over 500 cycles (8 hours), as demonstrated in our research results. Comparing with the expensive and complex design of monovalent selective membranes, the water chamber switch process is cost effective and easy to implement in RED systems. It is surely an efficient method to be generalized in faradaic RED systems.

In addition, as demonstrated in the experimental results, divalent ions have significant impact on membrane related potentials but limited impact on capacitive electrode related potentials. In the scale up process of RED systems, only cationic and anionic membranes are stacked to increase the overall cell voltage. As the majority of the cell voltage contribution is related to the membrane stack, the overall voltage is severely influenced by the divalent ion mixing. However for the scale up of CRED system, the repeating unit comprises a selective membrane and a pair of capacitive electrodes. The electrode related voltage contribution is comparable to that of membrane stack. This indicates a limited open-circuit voltage drop in CRED stacks compared with RED systems.

From an economical point of view, we come to the same conclusion as Giacalone et al.[27]. We demonstrate the potential for brine and freshwater RED plants to become financially sustainable when using highly concentrated brine from a natural lake or sea and treated freshwater. The novelty of our work lies in having obtained these results from experiments where divalent ions are present and not from simulation. We recall that the presence of divalent ions is a key question in the conclusion of Giacalone et al. and that of Tedesco et al.[26]. We have also shown that the process is not cost-effective for freshwater and river estuaries. However, costs using sPEEK membranes are 4 times higher than the cost of renewable energy sources. The difference is substantial enough to hinder the direct application of the results, yet minor enough to encourage continued investigation into the process.

Methods

Capacitive cell: description

The experiments are performed in a capacitive cell. A configuration akin to that detailed in the prior study by Brahmi et al.[49] is employed here (Figure 7a). The cell exhibits symmetrical geometry, featuring an ion-exchange membrane (Nafion^{TM}117, Chemours) sandwiched between two water compartments containing varying salt concentrations. The membrane, with a dry thickness of 183 μm, ensures an average conductivity exceeding 0.1 S.cm^{-1} and a total acid capacity ranging between 0.95 and 1.01 meq.g^{-1}. The effective surface area of the ion-exchange membrane used in our experimentation measures 5.5 cm^2 unless precised. Carbon felt capacitive porous electrodes (Kynol Activated Carbon Felt) are separately positioned within gaskets on either side of the membrane. The graphite current collectors are situated at a distance of 1.4 mm from the membrane and are directly linked to the carbon felt capacitive porous electrodes. The entire assembly is securely sealed by stainless steel endplates and held together using eight bolts torqued to 2 N.m. Note that after the cell has been clamped, there is no space between the electrodes and the capacitive tissue. Saline solutions flow into the pores of the capacitive tissue. Two ports facilitate water inlet and outlet, driven by a peristaltic pump (Longer Multichannel Peristaltic pump) operating at a consistent flow rate of 10 mL.min^{-1}.

While concentrated solution and diluted solution are injected continuously into the capacitive system, a cationic flow is generated from the concentrated part towards the diluted part under the osmotic effect. The cation exchange membrane blocks the anions and water molecules from free passing. In order to generated electricity, it is necessary to convert this cationic flux into a flux of electrons. In a capacitive system, ions are adsorbed onto the capacitive electrode, inducing the movement of electrons in the outer circuit. Due to charge accumulation inside the capacitive electrodes, the system reaches eventually a saturation regime where the fully charged capacitor blocks the creation of cationic flux (Figure 7b). To deblock the saturated regime of capacitive charging, an automated 4-port valve switches water compartments at fixed intervals of T_s. By doing the solution reversal in the chamber, one can reverse the direction of both ionic and electronic flux, thus discharging the accumulated charges in capacitive electrodes and restart the charging process in a reversed direction. This repeated transition within a fixed period T_s unblocks the saturation state, enabling the cell to deliver periodic alternating current. A detailed model can be found in the work of Wu et al.[50].

Preparation and composition of the salted solutions

NaCl, $MgCl_2$, $CaCl_2$ and KCl were purchased from Sigma Aldrich. In this study, we prepared solution mixtures of different concentrations. The compositions of these solutions are described in Tables 7 and 8.

Measurement of the open circuit voltage

To evaluate the inherent potential of the circuit, we initially link the two cell electrodes. One compartment is filled with a high salt concentration while the other contains a low salt concentration. We then wait for equilibrium to be established.

Modeling the temporal progression of the potential necessitates understanding the behavior of both the electrodes and the membrane. Across the entirety of the circuit, there is no voltage drop. This can be expressed as follows:

$$R_{load}I + R_{cell}I + \frac{q}{C} = E_m(t) + E_{elec-c}(t) \tag{10}$$

Scenario 1: Production water / seawater						
	Salinity	**NaCl equivalent**	**NaCl**	**KCl**	**$CaCl_2$,$2H_2O$**	**$MgCl_2$,$6H_2O$**
	Ratio	**$g\,L^{-1}$**	**$g\,L^{-1}$**	**$g\,L^{-1}$**	**$g\,L^{-1}$**	**$g\,L^{-1}$**
Production water	4.28	107	93.9	0.628	11.25	9.32
Sea water	4.28	25	23.63	0.77	0.11	0.20
Scenario 2: Dead Sea water / ×30 diluted						
	Salinity	**NaCl equivalent**	**Na**	**K**	**Ca**	**Mg**
	ratio	**$g\,L^{-1}$**	**$g\,L^{-1}$**	**$g\,L^{-1}$**	**$g\,L^{-1}$**	**$g\,L^{-1}$**
Dead Sea water	30	324.87	32.177	9.27	27.503	62.23
Diluted Dead Sea water	30	10.83	1.073	0.309	0.917	2.074
Scenario 3: Salt caverns						
	Salinity	**NaCl equivalent**	**NaCl**	**KCl**	**$CaCl_2$,$2H_2O$**	**$MgCl_2$,$6H_2O$**
	Ratio	**$g\,L^{-1}$**	**$g\,L^{-1}$**	**$g\,L^{-1}$**	**$g\,L^{-1}$**	**$g\,L^{-1}$**
Salt cavern extraction water	300	300	300	0	0	0
River water	300	1	0.4	0	1.509	0

Table 8. Experiments reproducing possible applications: compositions of solutions.

Here, $E_m(t)$ represents the voltage drop across the membrane, $E_{elec-c}(t)$ signifies the voltage drop across the capacitive layer, I denotes the current intensity, and R_{cell} is the ohmic resistance of the cell, which encompasses the resistance of the solvent, carbon felt, and current collector.

Changes in the concentrations of ions over time cause the temporal evolution of $E_{elec-c}(t)$ and $E_m(t)$. These variations stem from cell filling and the creation of a diffuse ion layer near the electrodes when altering the salt concentration.

At $t = 0$, the system is in a stable state with $I(0) = 0$ and $q(0) = q_0 = C(E_m(\infty) + E_{elec-c}(\infty)$. For t less than 0, the sum of membrane and capacitive layer potentials is given by $E_m(\infty) + E_{elec-c}(\infty)$; at $t = 0$, the flow in both compartments reverses and the signs of membrane and capacitive layer potentials change. Upon reaching steady state after reversal, membrane and capacitive layer potentials are determined by $-E_m(\infty) - E_{elec-c}(\infty)$.

The solution to Equation 10 is straightforward. We arrive at:

$$q = \exp^{-\int_0^t \frac{du}{RC}} \int_0^t -\frac{E_m(s) + E_{elec-c}(s)}{R} \exp^{-\int_0^s \frac{du}{RC}} ds + q_0 \exp^{-\int_0^t \frac{du}{RC}} \tag{11}$$

$$A(t) = \frac{1}{RC} \exp^{-\int_0^t \frac{du}{RC}} \int_0^t -\frac{E_m(s) + E_{elec-c}(s)}{R} \exp^{-\int_0^s \frac{du}{RC}} ds \tag{12}$$

$$I(t) = A(t) - \frac{q_0}{RC(t)} \exp^{-\int_0^t \frac{du}{RC}} - \frac{E_m(t) + E_{elec-c}(t)}{R} \tag{13}$$

$q_0 = C(E_m(\infty) + E_{elec-c}(\infty))$.

This leads to $RI(\infty) = E_{OCV-c} = -2(E_m(\infty) + E_{elec-c}(\infty))$. To conclude, as noted in the main text, the open-circuit measurement for a capacitive cell corresponds to twice the steady-state membrane potential and capacitive layer values.

Experimentally, to measure OCV, we continuously feed the compartments with solutions of different salinities for 300 s, then reverse the flows for 300 s. This process is repeated 5 times. We record the evolution of the open-circuit voltage signal. The cell delivers no electrical current, and only ionic flows are responsible for the measured signal. The signal stabilizes in less than 100 seconds after the flow reversals. The signal is averaged over the 50 seconds preceding the change in concentration. OCV is measured by taking the quater of the difference in signals when saltier water flows into the right-hand compartment and when saltier water flows into the left-hand compartment. The absolute values of the two measurements may differ slightly (by plus or minus 5%) if the two electrodes are not the same. In this situation, we measure the electrode potential plus the electrode membrane. It should be noted that these values are flow-dependent, due to the non-perfect selectivity of membranes.

Measurement of the membrane potential voltage

To gain insight into the individual impact of the membrane and the electrodes on the potential, we conducted separate measurements of the open-circuit potential of the membrane, denoted as E_m. These measurements were performed while subjecting the membrane to salt gradients, utilizing custom-made Faradaic Ag/AgCl electrodes. The experimental procedure is the same for Faradaic and capacitive electrodes. In an open circuit, Faradaic electrodes are not subject to polarization phenomena (no current-induced polarization, no resistive or capacitive effects of Debye layers[67–69], as no current flows through them.

For a Faradaic cell, the OCV voltage corresponds to the sum of the membrane voltage and the Faradaic electrode voltage.

$$E_{OCV-f} = E_m + E_{elec-f} \tag{14}$$

Thus in order to obtain the membrane voltage E_m, it is necessary to measure the Faradaic electrode related voltage E_{elec-f}. In our experiment, we immersed the two home-made Ag/AgCl electrodes into concentrated solution and diluted solution in two beakers separately. The solutions used in experiments follows the same experimental conditions as mentioned above for E_{OCV-c} and E_{OCV-f} measurements (solutions of different saliniy ratios with different divalent molar mixing fractions). The whole circuit is closed by the use of a home-made salt bridge (KCl saturated). Then the electrode potential difference E_{elec-f} is measured by using a potentiostat.

The capacitive cell assembly is described above and we measure the open-circuit voltage E_{OCV-c} for solutions of different salinity ratio with different mixing molar fraction. As explained above, the OCV voltage of a capacitive cell corresponds to twice the sum of the membrane voltage and capacitive electrode voltage.

$$E_{OCV-c} = 2(E_m + E_{elec-c}) \tag{15}$$

Following the above two equations (Equation 14 and Equation 15), we can easily calculate the membrane voltage E_m and capacitive electrode voltage E_{elec-c}.

Measurements of the impedance of the cell

Each compartment of the cell is supplied with a different saline solution under a constant flow rate. The circuit is open, and we wait for steady-state. We then apply 10 mV oscillatory perturbations over the open-circuit voltage. We use a logarithmically spaced frequency range from 200 kHz to 10 mHz for a fixed salinity ratio of 30 g L^{-1} vs. 1 g L^{-1} situation with different divalent ion mixing fraction. A Nyquist plot can be plotted corresponding all to a sweep over a frequency range from 200 kHz to 10 mHz. Note that the exact value of the impedance depends on the tightening. Here, we used the impedance data measured at 10 mHz to characterize the cell inner resistance and capacitance. Variations of 0.5 (Ω cm^2) in real part are measured on consecutive experiments despite the care taken to make the clamping procedure repeatable.

Measurement and modeling of the harvested power

The system under consideration embodies a capacitive configuration. To restore current, a cyclic process reminiscent of cap mixing procedures is employed, where distinct brine flows with varying concentrations are directed into the two compartments. The experimental apparatus incorporates a rotary valve that permits the passage of highly concentrated saltwater into the first compartment for a duration of T_s, succeeded by the circulation of fresh water for an equivalent T_s duration. This procedure is reversed in the second compartment. Here, T_s represents the half period of the salt gradient. The direction of the current shifts with each cycle, which is a distinctive trait of capacitive currents. The use of capacitive electrodes prompts a reevaluation of the methodology employed for measuring the recovered power. The mean gross power density P_{gross} (that is, power density without compensating for pumping losses) is assessed by averaging the signal recorded across the resistance over a time interval of $2T_s$. The parameter A denotes the area of the membrane. The expression is as follows:

$$P_{gross} = \frac{1}{2T_s \cdot A} \int_0^{2T_s} \frac{E_{load}^2(t)}{R_{load}} dt \tag{16}$$

It's noteworthy that these measurements constitute direct assessments that mirror real-world scenarios. These experiments are conducted across various salinity gradients, oscillation periods, and flow rates.

In a previous work[49], we developed a theoretical model that can account for the measured power and that describes the experimental values well when the cell filling time is small compared to the period. Details about the modeling can be find in the work of Brahmi et al.[49]. We recall here only the main point of the theoretical approach. According to an analysis of the electrochemical impedance spectroscopy, a R-C model is proposed as a simplified fitting model for the cell-booster system[49]. The system inner resistance R_{cell} and capacitance C can be quantitatively characterized by Potentiostatic electrochemical impedance spectroscopy (PEIS) measurement using a potentiostat. $E_{mem}(t)$ is the potential drop over the membrane, $E_{elec}(t)$ the electrical potential due to the salt adsorption on the electrodes, $R_{cell}(t)$ the resistance of the cell (including the ohmic and non ohmic resistance of the solvent, the membrane, the carbon felt and the current collector). The temporal variation of $R_{cell}(t)$, $C_{cell}(t)$ $E_{mem}(t)$ and $E_{elec}(t)$ are due to the temporal variation of the ion concentration profile including osmotic potential, diffuse layer establishment, cell filling process after water compartment switching and etc. In the following we will assume that these characteristic times and the filling time of the cell are negligible compared with the switch half period T_s. Thus, these functions will be modeled simply by window functions:for $0 < t < T_s$, $E_{mem}(t) + E_{elec}(t) = E_{OCV}$ and for $T_s < t < 2T_s$, $E_{mem}(t) + E_{elec}(t) = -E_{OCV}$. In this framework, $R_{cell}(t)$ and C do not depend upon t.We recall that T_s is the switch half period.

Following these conditions, we establish the theoretical model for a pure cell-resistor circuit in absence of boosting by the equations below:For $0 < t < T_s$:

$$(R_{load} + R_{cell})I(t) + \frac{q_1(t)}{C} = E_{OCV} \tag{17}$$

For $T_s < t < 2T_s$:

$$(R_{load} + R_{cell})I(t) + \frac{q_1(t)}{C} = -E_{OCV} \tag{18}$$

We solve analytically these equations and calculate the electrical power recovered by the load resistor.We find:

$$P_{th} = \frac{2}{ST_s}\frac{CE_{OCV}^2 R_{load}}{R_{load}+R_{cell}} tanh(\frac{T_S}{2(R_{load}+R_{cell})C}) \tag{19}$$

Conductivity measurement of effluents

To verify the extent of salt mixing inside the CREDSM system, we conducted conductivity measurements during the experiment. Solutions samples are taken in 3 different scenarios to conduct further tests of conductivity. We take solution samples of concentrated part and diluted part before their injection into the CREDSM system. These results are considered as a comparison baselines. Then solution samples of concentrated part and diluted part are taken after their mixing inside the CREDSM system under Open-circuit mode and closed-circuit mode, respectively. The conductivity measurements are realized by a conductivity meter (SevenDirect SD30, Mettler Toledo). On our device CREDSM, the variation of the conductivity depends upon the nature of the membrane.

In the Nafion HP situation, for feed solutions composed of 80%NaCl - 20% $CaCl_2$ of 30g/L and 1g/L, we observe a major conductivity increase of 0.54% in diluted solution and no significant conductivity variation in concentrated solution in Open circuit mode. While the CREDSM is connected to a load resistor to form a closed electrical circuit, a larger conductivity increase of 5.14% is observed in diluted solution. Still we do not observe any conductivity variation in the concentrated solution.

In the Fumasep FS720 situation, for feed solutions composed of 80% NaCl - 20% $CaCl_2$ of 30g/L and 1g/L, we observe a larger conductivity increase of 4.86% in diluted solution and no significant conductivity variation in concentrated solution in Open circuit mode. While the CREDSM is connected to a load resistor to form a closed electrical circuit, a larger conductivity increase of 11.66% is observed in diluted solution. Still we do not observe any conductivity variation in the concentrated solution.

In OCV mode, the conductivity variation is purely due to the imperfection of the membrane selectivity. The mixing observed is thus uncontrolled loss. However, in closed circuit mode, the mixing originates both from the uncontrolled loss and the useful mixing which results in the electricity production. From the above results, it can be deduced that Nafion HP membrane presents higher selectivity than Fumasep FS720. The extent of mixing in the CREDSM system is rather small, with a conductivity variation of 5% for Nafion HP and 10% for Fumasep FS720.

Data availability

The datasets used and/or analyzed during the current study are available from the corresponding author on request.

Received: 3 January 2024; Accepted: 15 July 2024

References

1. Vermaas, D. A., Veerman, J., Saakes, M. & Nijmeijer, K. Influence of multivalent ions on renewable energy generation in reverse electrodialysis. *Energy & Environmental Science* **7**, 1434–1445. https://doi.org/10.1039/C3EE43501F (2014).
2. Veerman, J., Gómez-Coma, L., Ortiz, A. & Ortiz, I. Resistance of ion exchange membranes in aqueous mixtures of monovalent and divalent ions and the effect on reverse electrodialysis. *Membranes* **13**, 322. https://doi.org/10.3390/membranes13030322 (2023).
3. Chu, S. & Majumdar, A. Opportunities and challenges for a sustainable energy future. *Nature* **488**, 294–303. https://doi.org/10.1038/nature11475 (2012).
4. Hoffert, M. I. *et al.* Advanced technology paths to global climate stability: Energy for a greenhouse planet. *Science* **298**, 981–987. https://doi.org/10.1126/science.1072357 (2002).
5. Norman, R. S. Water Salination: A Source of Energy. *Science* **186**, 350–352. https://doi.org/10.1126/science.186.4161.350 (1974).
6. Yip, N. Y., Brogioli, D., Hamelers, H. V. M. & Nijmeijer, K. Salinity gradients for sustainable energy: Primer, progress, and prospects. *Environ. Sci. Technol.* **50**, 12072–12094. https://doi.org/10.1021/acs.est.6b03448 (2016).
7. Logan, B. E. & Elimelech, M. Membrane-based processes for sustainable power generation using water. *Nature* **488**, 313–319. https://doi.org/10.1038/nature11477 (2012).
8. Wu, N., Brahmi, Y. & Colin, A. Fluidics for energy harvesting: From nano to milli scales. *Lab Chip* **23**, 1034–1065. https://doi.org/10.1039/D2LC00946C (2023).
9. Alvarez-Silva, O. A., Osorio, A. F. & Winter, C. Practical global salinity gradient energy potential. *Renew. Sustain. Energy Rev.* **60**, 1387–1395. https://doi.org/10.1016/j.rser.2016.03.021 (2016).
10. https://redstack.nl; https://www.sweetch.energy. *REDSTACK* (2024).
11. Pattle, R. E. Production of electric power by mixing fresh and salt water in the hydroelectric pile. *Nature* **174**, 660–660. https://doi.org/10.1038/174660a0 (1954).
12. Loeb, S. Method and apparatus for generating power utilizing reverse electrodialysis (1979).
13. Yip, N. Y., Vermaas, D. A., Nijmeijer, K. & Elimelech, M. Thermodynamic, energy efficiency, and power density analysis of reverse electrodialysis power generation with natural salinity gradients. *Environ. Sci. Technol.* **48**, 4925–4936. https://doi.org/10.1021/es5005413 (2014).
14. Mei, Y. & Tang, C. Y. Recent developments and future perspectives of reverse electrodialysis technology: A review. *Desalination* **425**, 156–174. https://doi.org/10.1016/j.desal.2017.10.021 (2018).
15. Donnan, F. G. & Harris, A. B. CLXXVII.–The osmotic pressure and conductivity of aqueous solutions of congo-red, and reversible membrane equilibria. *J. Chem. Soc. Trans.* **99**, 1554–1577. https://doi.org/10.1039/CT9119901554 (1911).
16. Donnan, F. G. The theory of membrane equilibria. *Chem. Rev.* **1**, 73–90. https://doi.org/10.1021/cr60001a003 (1924).
17. Luo, T., Abdu, S. & Wessling, M. Selectivity of ion exchange membranes: A review. *J. Membr. Sci.* **555**, 429–454. https://doi.org/10.1016/j.memsci.2018.03.051 (2018).
18. Aydogan Gokturk, P. *et al.* The Donnan potential revealed. *Nat. Commun.* **13**, 5880. https://doi.org/10.1038/s41467-022-33592-3 (2022).
19. Veerman, J., Saakes, M., Metz, S. J. & Harmsen, G. J. Reverse electrodialysis: Evaluation of suitable electrode systems. *J. Appl. Electrochem.* **40**, 1461–1474. https://doi.org/10.1007/s10800-010-0124-8 (2010).

20. Post, J. W., Hamelers, H. V. M. & Buisman, C. J. N. Influence of multivalent ions on power production from mixing salt and fresh water with a reverse electrodialysis system. *J. Membr. Sci.* **330**, 65–72. https://doi.org/10.1016/j.memsci.2008.12.042 (2009).
21. Kaya, T. Z., Altıok, E., Güler, E. & Kabay, N. Effect of co-existing ions on salinity gradient power generation by reverse electrodialysis using different ion exchange membrane pairs. *Membranes* **12**, 1240. https://doi.org/10.3390/membranes12121240 (2022).
22. Wang, Z. *et al.* The effect of trace ions on the performance of reverse electrodialysis using brine/seawater as working pairs. *Front. Energy Res.*https://doi.org/10.3389/fenrg.2022.919878 *(2022).*
23. Tufa, R. A. *et al.* Potential of brackish water and brine for energy generation by salinity gradient power-reverse electrodialysis (SGP-RE). *RSC Adv.* **4**, 42617–42623. https://doi.org/10.1039/C4RA05968A (2014).
24. Tedesco, M. *et al.* Performance of the first reverse electrodialysis pilot plant for power production from saline waters and concentrated brines. *J. Membr. Sci.* **500**, 33–45. https://doi.org/10.1016/j.memsci.2015.10.057 (2016).
25. Tedesco, M., Cipollina, A., Tamburini, A. & Micale, G. Towards 1kW power production in a reverse electrodialysis pilot plant with saline waters and concentrated brines. *J. Membr. Sci.* **522**, 226–236. https://doi.org/10.1016/j.memsci.2016.09.015 (2017).
26. Tedesco, M., Cipollina, A., Tamburini, A. & Micale, G. Towards 1 kW power production in a reverse electrodialysis pilot plant with saline waters and concentrated brines. *J. Membr. Sci.* **522**, 226–236. https://doi.org/10.1016/j.memsci.2016.09.015 (2017).
27. Giacalone, F. *et al.* Application of reverse electrodialysis to site-specific types of saline solutions: A techno-economic assessment. *Energy* **181**, 532–547. https://doi.org/10.1016/j.energy.2019.05.161 (2019).
28. Pintossi, D., Simões, C., Saakes, M., Borneman, Z. & Nijmeijer, K. Predicting reverse electrodialysis performance in the presence of divalent ions for renewable energy generation. *Energy Convers. Manage.* **243**, 114369 (2021).
29. Avci, A. H., Tufa, R. A., Fontananova, E., Di Profio, G. & Curcio, E. Reverse Electrodialysis for energy production from natural river water and seawater. *Energy* **165**, 512–521. https://doi.org/10.1016/j.energy.2018.09.111 (2018).
30. Avci, A. H. *et al.* Energy harvesting from brines by reverse electrodialysis using nafion membranes. *Membranes* **10**, 168. https://doi.org/10.3390/membranes10080168 (2020).
31. Rijnaarts, T., Huerta, E., van Baak, W. & Nijmeijer, K. Effect of divalent cations on red performance and cation exchange membrane selection to enhance power densities. *Environ. Sci. Technol.* **51**, 13028–13035 (2017).
32. Fontananova, E. *et al.* Effect of solution concentration and composition on the electrochemical properties of ion exchange membranes for energy conversion. *J. Power Sour.* **340**, 282–293. https://doi.org/10.1016/j.jpowsour.2016.11.075 (2017).
33. Oh, Y. *et al.* Effects of divalent cations on electrical membrane resistance in reverse electrodialysis for salinity power generation. *Indus. Eng. Chem. Res.* **57**, 15803–15810. https://doi.org/10.1021/acs.iecr.8b03513 (2018).
34. Gómez-Coma, L. *et al.* Modeling the influence of divalent ions on membrane resistance and electric power in reverse electrodialysis. *J. Membr. Sci.* **592**, 117385. https://doi.org/10.1016/j.memsci.2019.117385 (2019).
35. Cifuentes-Araya, N., Pourcelly, G. & Bazinet, L. Impact of pulsed electric field on electrodialysis process performance and membrane fouling during consecutive demineralization of a model salt solution containing a high magnesium/calcium ratio. *J. Colloid Interface Sci.* **361**, 79–89 (2011).
36. Allison, R. P. Electrodialysis reversal in water reuse applications. *Desalination* **103**, 11–18 (1995).
37. Güler, E., van Baak, W., Saakes, M. & Nijmeijer, K. Monovalent-ion-selective membranes for reverse electrodialysis. *J. Membr. Sci.* **455**, 254–270. https://doi.org/10.1016/j.memsci.2013.12.054 (2014).
38. Besha, A. T., Tsehaye, M. T., Aili, D., Zhang, W. & Tufa, R. A. Design of monovalent ion selective membranes for reducing the impacts of multivalent ions in reverse electrodialysis. *Membranes* **10**, 7. https://doi.org/10.3390/membranes10010007 (2020).
39. Rijnaarts, T., Huerta, E., van Baak, W. & Nijmeijer, K. Effect of divalent cations on RED performance and cation exchange membrane selection to enhance power densities. *Environ. Sci. Technol.* **51**, 13028–13035. https://doi.org/10.1021/acs.est.7b03858 (2017).
40. Veerman, J. Concepts and misconceptions concerning the influence of divalent ions on the performance of reverse electrodialysis using natural waters. *Membranes* **13**, 69. https://doi.org/10.3390/membranes13010069 (2023).
41. Vermaas, D. A. *et al.* Clean energy generation using capacitive electrodes in reverse electrodialysis. *Energy Environ. Sci.* **6**, 643–651. https://doi.org/10.1039/c2ee23562e (2013).
42. Campione, A. *et al.* Water desalination by capacitive electrodialysis: Experiments and modelling. *Desalination* **473**, 114150. https://doi.org/10.1016/j.desal.2019.114150 (2020).
43. Kim, T., Rahimi, M., Logan, B. E. & Gorski, C. A. Harvesting energy from salinity differences using battery electrodes in a concentration flow cell. *Environ. Sci. Technol.* **50**, 9791–9797. https://doi.org/10.1021/acs.est.6b02554 (2016).
44. Welgemoed, T. J. & Schutte, C. F. Capacitive deionization technology™: An alternative desalination solution. *Desalination* **183**, 327–340. https://doi.org/10.1016/j.desal.2005.02.054 (2005).
45. Ratajczak, P., Suss, M. E., Kaasik, F. & Béguin, F. Carbon electrodes for capacitive technologies. *Energy Storage Mater.* **16**, 126–145. https://doi.org/10.1016/j.ensm.2018.04.031 (2019).
46. Zhu, H. *et al.* Carbonized peat moss electrodes for efficient salinity gradient energy recovery in a capacitive concentration flow cell. *Electrochim. Acta* **294**, 240–248. https://doi.org/10.1016/j.electacta.2018.10.053 (2019).
47. Marino, M. *et al.* Modification of the surface of activated carbon electrodes for capacitive mixing energy extraction from salinity differences. *J. Colloid Interface Sci.* **436**, 146–153. https://doi.org/10.1016/j.jcis.2014.08.070 (2014).
48. Vermaas, D. A., Saakes, M. & Nijmeijer, K. Doubled power density from salinity gradients at reduced intermembrane distance. *Environ. Sci. Technol.* **45**, 7089–7095. https://doi.org/10.1021/es2012758 (2011).
49. Brahmi, Y. & Colin, A. New membrane and electrode assembly concept to improve salinity energy harvesting. *Energy Convers. Manage.* **254**, 115297. https://doi.org/10.1016/j.enconman.2022.115297 (2022).
50. Wu, N., Brahmi, Y. & Colin, A. A strategy for power density amelioration of capacitive reverse electrodialysis systems with a single membrane. *Environ. Sci. Technol.* **57**, 14973–14982. https://doi.org/10.1021/acs.est.3c05835 (2023).
51. Fan, H., Huang, Y. & Yip, N. Y. Advancing ion-exchange membranes to ion-selective membranes: Principles, status, and opportunities. *Front. Environ. Sci. Eng.* **17**, 25. https://doi.org/10.1007/s11783-023-1625-0 (2022).
52. Zuo, K. *et al.* Selective membranes in water and wastewater treatment: Role of advanced materials. *Mater. Today* **50**, 516–532. https://doi.org/10.1016/j.mattod.2021.06.013 (2021).
53. Le Beulze, A. *et al.* Jams and cakes: A closer look on well clogging mechanisms in microscale produced water reinjection experiments. *Transp. Porous Media* **147**, 143–156. https://doi.org/10.1007/s11242-023-01900-0 (2023).
54. Tedesco, M. *et al.* Performance of the first reverse electrodialysis pilot plant for power production from saline waters and concentrated brines. *J. Membr. Sci.* **500**, 33–45. https://doi.org/10.1016/j.memsci.2015.10.057 (2016).
55. Werges, Y. I. Modelling of reverse electrodialysis in the presence of multivalent ions (2021).
56. Siria, A. *et al.* Giant osmotic energy conversion measured in a single transmembrane boron nitride nanotube. *Nature* **494**, 455–458. https://doi.org/10.1038/nature11876 (2013).
57. Gao, J. *et al.* Understanding the giant gap between single-pore- and membrane-based nanofluidic osmotic power generators. *Small* **15**, 1804279. https://doi.org/10.1002/smll.201804279 (2019).
58. Wang, Z., Wang, L. & Elimelech, M. Viability of harvesting salinity gradient (Blue) energy by nanopore-based osmotic power generation. *Engineering* **9**, 51–60. https://doi.org/10.1016/j.eng.2021.02.016 (2022).
59. Mueller, K. E., Thomas, J. T., Johnson, J. X., DeCarolis, J. F. & Call, D. F. Life cycle assessment of salinity gradient energy recovery using reverse electrodialysis. *J. Ind. Ecol.* **25**, 1194–1206. https://doi.org/10.1111/jiec.13082 (2021).
60. Post, J. W. *et al.* Towards implementation of reverse electrodialysis for power generation from salinity gradients. *Desalin. Water Treat.* **16**, 182–193. https://doi.org/10.5004/dwt.2010.1093 (2010).

61. Kuleszo, J., Kroeze, C., Post, J. & Fekete, B. M. The potential of blue energy for reducing emissions of CO2 and non-CO2 greenhouse gases. *J. Integr. Environ. Sci.* **7**, 89–96. https://doi.org/10.1080/19438151003680850 (2010).
62. Robertson, J. Types of Energy Ranked by Cost Per Megawatt Hour - Solar Power Guide - Infographic. https://solarpower.guide/solar-energy-insights/energy-ranked-by-cost.
63. Ahdab, Y. D., Schucking, G., Rehman, D. & Lienhard, J. H. Cost effectiveness of conventionally and solar powered monovalent selective electrodialysis for seawater desalination in greenhouses. *Appl. Energy* **301**, 117425. https://doi.org/10.1016/j.apenergy.2021.117425 (2021).
64. Quote received from fumasep. *Quote Fumatech* (2024).
65. Zhu, H. SPEEK scaling UP. *Joule* **6**, 718–720. https://doi.org/10.1016/j.joule.2022.03.006 (2022).
66. Yuan, Z. *et al.* Low-cost hydrocarbon membrane enables commercial-scale flow batteries for long-duration energy storage. *Joule* **6**, 884–905. https://doi.org/10.1016/j.joule.2022.02.016 (2022).
67. Chu, K. T. & Bazant, M. Z. Electrochemical thin films at and above the classical limiting current. *SIAM J. Appl. Math.* **65**, 1485–1505. https://doi.org/10.1137/040609926 (2005).
68. Bazant, M. Z., Chu, K. T. & Bayly, B. J. Current-voltage relations for electrochemical thin films. *SIAM J. Appl. Math.* **65**, 1463–1484 (2005).
69. Chu, K. T. & Bazant, M. Z. Electrochemical thin films at and above the classical limiting current. *SIAM J. Appl. Math.* **65**, 1485–1505 (2005).

Acknowledgements

N.W acknowledges funding from CSC. Y.B acknowledges funding from TotalEnergies. M.L and Y.B thank C.Desplobins and M.Questel for their help conducting the experiments in PERL.

Author contributions

M.L, A.C. conceived the experiments, N.W, Y.B conducted the experiments. N.W, M.L, Y.B, C.T, A.C. analyzed the data. N.W, M.L, A.C. wrote the manuscript. All authors reviewed the manuscript.

Competing interests

The authors declare no competing interests.

Additional information

Correspondence and requests for materials should be addressed to A.C.

RÉSUMÉ

Face aux problèmes de réchauffement climatique, trouver des ressources énergétiques propres et durables pour remplacer les combustibles fossiles conventionnels est d'une importance capitale. L'énergie osmotique demeure une ressource énergétique inexploitée avec un potentiel significatif. Dans ce travail, nous parvenons à une conversion efficace de l'énergie osmotique en électricité grâce à un processus de mélange bien contrôlé utilisant un système d'électrodialyse inverse capacitif (CRED). Il est démontré qu'un écart substantiel de densité de puissance existe entre le système CRED et la valeur maximale théorique, principalement en raison de l'efficacité de conversion faible du flux ionique-électronique dans les électrodes capacitifs. Pour pallier cette limitation, nous proposons la stratégie de boosting pour optimiser le régime de fonctionnement du système CRED. Des expériences et des modélisations confirment une amélioration de la performance énergétique du système CRED. Pour avancer vers des applications réelles, nous évaluons les performances du système CRED sous des solutions composées de mélanges ioniques complexes. Contrairement à la chute significative de la densité de puissance observée dans les systèmes RED classiques, le système CRED ne présente qu'une légère diminution lorsqu'il est soumis à des solutions avec un mélange d'ions divalents. Ce phénomène est attribué au renversement périodique des solutions dans les compartiments, qui atténue l'effet d'empoisonnement de la membrane. Ce résultat est ensuite validé par des tests à long terme avec des solutions réelles. Pour généraliser le système CRED dans un spectre plus large, nous proposons une cellule de gradient de pH avec des électrodes de MnO_2 à pseudo-capacité. Elle utilise l'énergie osmotique établie dans un processus de capture de CO_2 basé sur un électrolyte et vise à réduire le coût global du processus de capture de carbone. La cellule de gradient de pH présente une augmentation inattendue de la densité de puissance sous la stratégie de boosting. Cela est dû à la contribution de tension supplémentaire des électrodes en raison du changement de couverture fractionnelle lié aux réactions d'oxydoréduction. Cependant, elle reste dans le cadre du régime capacitif et est bien décrite par une modélisation CRED adaptée.

MOTS CLÉS

Énergie bleue, Gradient salin, Electrode capacitive, Ion divalent, Densité de puissance

ABSTRACT

Given the global warming issues, finding clean and sustainable energy resources to replace conventional fossil fuels is of paramount importance. Osmotic energy remains an untapped energy resource with significant potential. In this work, we achieve efficient conversion of osmotic energy into electricity through a well-controlled mixing process using a capacitive reverse electrodialysis (CRED) system. It is demonstrated that a substantial power density gap exists between the CRED system and the theoretical maximum value, primarily due to the low ionic-electronic flux conversion efficiency in capacitive electrodes. To address this limitation, we propose the boosting strategy to optimize the working regime of the CRED system. Both experiments and modeling confirm an enhanced energy performance of the CRED system. To advance towards real-world applications, we assess the performance of the CRED system under solutions composed of complex ion mixing. In contrast to the significant power density drop observed in classic RED systems, the CRED system exhibits only a minor decrease when subjected to solutions with divalent ion mixing. This phenomenon is attributed to the periodic water chamber reversal, which mitigates the membrane poisoning effect. This result is further validated through long-term testing with real-world solutions. To generalize the CRED system into a broader spectrum, we propose a pH gradient cell with MnO_2 electrodes of pseudo capacitance. It uses the osmotic energy established within an electrolyte based CO_2 capturing process and aims to reduce the overall cost of carbon capturing process. The pH gradient cell presents unexpected power density increase under boosting strategy. This is due to the additional electrode voltage contribution due to fractional coverage change related to redox reactions. However, it stays in the framework of capacitive regime and remains well described by an adapted CRED modeling.

KEYWORDS

Blue energy, Salinity gradient, Capacitive electrode, Divalent ion, Power density